



High Efficiency Centrifugal Compressor for Rotorcraft Applications

*Gorazd Medic, Om P. Sharma, Joo Jongwook, Larry W. Hardin, Duane C. McCormick,
William T. Cousins, Elizabeth A. Lurie, Aamir Shabbir, Brian M. Holley, and Paul R. Van Slooten
United Technologies Research Center, East Hartford, Connecticut*

This Revised Copy, numbered as NASA/CR—2014-218114/REV1, October 2017, supersedes
the previous version, NASA/CR—2014-218114, November 2014, in its entirety.

NASA STI Program . . . in Profile

Since its founding, NASA has been dedicated to the advancement of aeronautics and space science. The NASA Scientific and Technical Information (STI) Program plays a key part in helping NASA maintain this important role.

The NASA STI Program operates under the auspices of the Agency Chief Information Officer. It collects, organizes, provides for archiving, and disseminates NASA's STI. The NASA STI Program provides access to the NASA Technical Report Server—Registered (NTRS Reg) and NASA Technical Report Server—Public (NTRS) thus providing one of the largest collections of aeronautical and space science STI in the world. Results are published in both non-NASA channels and by NASA in the NASA STI Report Series, which includes the following report types:

- **TECHNICAL PUBLICATION.** Reports of completed research or a major significant phase of research that present the results of NASA programs and include extensive data or theoretical analysis. Includes compilations of significant scientific and technical data and information deemed to be of continuing reference value. NASA counter-part of peer-reviewed formal professional papers, but has less stringent limitations on manuscript length and extent of graphic presentations.
- **TECHNICAL MEMORANDUM.** Scientific and technical findings that are preliminary or of specialized interest, e.g., "quick-release" reports, working papers, and bibliographies that contain minimal annotation. Does not contain extensive analysis.
- **CONTRACTOR REPORT.** Scientific and technical findings by NASA-sponsored contractors and grantees.
- **CONFERENCE PUBLICATION.** Collected papers from scientific and technical conferences, symposia, seminars, or other meetings sponsored or co-sponsored by NASA.
- **SPECIAL PUBLICATION.** Scientific, technical, or historical information from NASA programs, projects, and missions, often concerned with subjects having substantial public interest.
- **TECHNICAL TRANSLATION.** English-language translations of foreign scientific and technical material pertinent to NASA's mission.

For more information about the NASA STI program, see the following:

- Access the NASA STI program home page at <http://www.sti.nasa.gov>
- E-mail your question to help@sti.nasa.gov
- Fax your question to the NASA STI Information Desk at 757-864-6500
- Telephone the NASA STI Information Desk at 757-864-9658
- Write to:
NASA STI Program
Mail Stop 148
NASA Langley Research Center
Hampton, VA 23681-2199



High Efficiency Centrifugal Compressor for Rotorcraft Applications

*Gorazd Medic, Om P. Sharma, Joo Jongwook, Larry W. Hardin, Duane C. McCormick,
William T. Cousins, Elizabeth A. Lurie, Aamir Shabbir, Brian M. Holley, and Paul R. Van Slooten
United Technologies Research Center, East Hartford, Connecticut*

This Revised Copy, numbered as NASA/CR—2014-218114/REV1, October 2017, supersedes
the previous version, NASA/CR—2014-218114, November 2014, in its entirety.

National Aeronautics and
Space Administration

Glenn Research Center
Cleveland, Ohio 44135

Acknowledgments

The authors gratefully acknowledge the National Aeronautics and Space Administration for their support under NASA Research Announcement (NRA) contract NNC08CB03C, as part of management of the Rotary Wing Project within the NASA Fundamental Aeronautics Program. The authors appreciate continued technical discussions and dialogue with Dr. Gerard E. Welch, Mr. Edward P. Braunscheidel of NASA Glenn Research Center and Mr. Gary J. Skoch of Army Research Laboratory, Vehicle Technology Directorate, to ensure focus of the current program. The authors are also grateful to Dr. Michael D. Hathaway and Mr. Mark A. Stevens of NASA Glenn Research Center for their assistance during the evolution of the program. The authors also acknowledge the organizations supporting design reviews: NASA, Air Force Research Laboratory, US Army Applied Aviation Technology Directorate, NAVAIR, and ARL-VTD, as well as AFRL on providing the impeller vibrometry support on this effort. The authors are grateful to Dr. Ron-Ho Ni of the AeroDynamic Solutions for providing CFD (LEO) and grid generation codes (WAND) to the CFD based design execution effort at UTRC. The authors are also thankful to Dr. Ron-Ho Ni, Dr. Anthony Jones of PW Aero Systems and Dr. Sam Baghdadi for providing technical guidance during the design execution process. The authors are thankful to William J. Baker of the Agilis Engineering for conducting the mechanical and structural design of the machine and patiently accommodating our requests. The authors are grateful to Mr. Jarso Mulugeta for conducting the preliminary design work. The authors are also grateful to the UTRC management, particularly Dr. David Parekh, Dr. Vince Nardone and Mr. John Zimmerman for their continued support and encouragement during the course of the program.

Revised Copy

This Revised Copy, numbered as NASA/CR—2014-218114/REV1, October 2017, supersedes the previous version, NASA/CR—2014-218114, November 2014, in its entirety.

Numerous changes have been made to Appendixes A and C.

Trade names and trademarks are used in this report for identification only. Their usage does not constitute an official endorsement, either expressed or implied, by the National Aeronautics and Space Administration.

This work was sponsored by the Fundamental Aeronautics Program at the NASA Glenn Research Center.

Level of Review: This material has been technically reviewed by technical management.

Available from

NASA STI Program
Mail Stop 148
NASA Langley Research Center
Hampton, VA 23681-2199

National Technical Information Service
5285 Port Royal Road
Springfield, VA 22161
703-605-6000

This report is available in electronic form at <http://www.sti.nasa.gov/> and <http://ntrs.nasa.gov/>

Executive Summary

The report "High Efficiency Centrifugal Compressor for Rotorcraft Applications" documents the work conducted at UTRC under the NRA Contract NNC08CB03C, with cost share 2/3 NASA, and 1/3 UTRC, that has been extended to 4.5 years. The purpose of this effort was to identify key technical barriers to advancing the state-of-the-art of small centrifugal compressor stages; to delineate the measurements required to provide insight into the flow physics of the technical barriers; to design, fabricate, install, and test a state-of-the-art research compressor that is representative of the rear stage of an axial-centrifugal aero-engine; and to acquire detailed aerodynamic performance and research quality data to clarify flow physics and to establish detailed data sets for future application.

The design activity centered on meeting the goal set outlined in the NASA solicitation—the design target was to increase efficiency at higher work factor, while also reducing the maximum diameter of the stage. To fit within the existing Small Engine Components Test Facility at NASA Glenn Research Center (GRC) and to facilitate component re-use, certain key design parameters were fixed by UTRC, including impeller tip diameter, impeller rotational speed, and impeller inlet hub and shroud radii. This report describes the design effort of the High Efficiency Centrifugal Compressor stage (HECC) and delineation of measurements, fabrication of the compressor, and the initial tests that were performed.

A new High-Efficiency Centrifugal Compressor stage with a very challenging reduction in radius ratio was successfully designed, fabricated and installed at GRC. The testing was successful, with no mechanical problems and the running clearances were achieved without impeller rubs. Overall, measured pressure ratio of 4.68, work factor of 0.81, and at design exit corrected flow rate of 3 lbm/s met the target requirements. Polytropic efficiency of 85.5 percent and stall margin of 7.5 percent were measured at design flow rate and speed. The measured efficiency and stall margin were lower than pre-test CFD predictions by 2.4 percentage points (pt) and 4.5 pt, respectively. Initial impressions from the experimental data indicated that the loss in the efficiency and stall margin can be attributed to a design shortfall in the impeller. However, detailed investigation of experimental data and post-test CFD simulations of higher fidelity than pre-test CFD, and in particular the unsteady CFD simulations and the assessment with a wider range of turbulence models, have indicated that the loss in efficiency is most likely due to the impact of unfavorable unsteady impeller/diffuser interactions induced by diffuser vanes, an impeller/diffuser corrected flow-rate mismatch (and associated incidence levels), and, potentially, flow separation in the radial-to-axial bend.

An experimental program with a vaneless diffuser is recommended to evaluate this observation. A subsequent redesign of the diffuser (and the radial-to-axial bend) is also recommended. The diffuser needs to be redesigned to eliminate the mismatching of the impeller and the diffuser, targeting a slightly higher flow capacity. Furthermore, diffuser vanes need to be adjusted to align the incidence angles, to optimize the splitter vane location (both radially and circumferentially), and to minimize the unsteady interactions with the impeller. The radial-to-axial bend needs to be redesigned to eliminate, or at least minimize, the flow separation at the inner wall, and its impact on the flow in the diffuser upstream.

Lessons were also learned in terms of CFD methodology and the importance of unsteady CFD simulations for centrifugal compressors was highlighted. Inconsistencies in the implementation of a widely used two-equation turbulence model were identified and corrections are recommended. It was also observed that unsteady simulations for centrifugal compressors require significantly longer integration times than what is current practice in industry.

Contents

Executive Summary	iii
1.0 Introduction	1
1.1 Nomenclature	2
2.0 Design Requirements, Technical Challenges and Design Strategy	3
2.1 Design Requirements	3
2.2 Key Technical Challenges	4
2.3 Design Strategy	4
3.0 Compressor Aerodynamic Design	5
3.1 Design Approach	5
3.2 Design Process Readiness	6
3.2.1 CFD Validation for CC3 Compressor	7
3.2.2 Detailed Analysis of CFD Results for CC3 Compressor	9
3.3 Impeller Design	11
3.3.1 3D Aero Concepts	11
3.3.2 Impeller Trailing Edge Shaping—Assessment of Impact for CC3	12
3.4 Impeller Blading and Flowpath Design	13
3.4.1 30° Backsweep	17
3.5 Diffuser Design	22
3.5.1 3D Aero Concepts	22
3.5.2 Diffuser Topology	24
3.5.3 Splitter Vane Placement	27
3.5.4 Vane Thickening	32
3.6 Performance Assessment for Impeller-Diffuser Stage	33
3.7 Exit Guide Vane Design	35
3.8 Radial-to-Axial Bend Design	39
3.9 Final Design Summary	41
4.0 Design-Intent Performance	42
4.1 Stage Performance at 100 percent N_c	42
4.2 Performance Map	43
4.3 Comparison of Predicted Performance to Target Requirements	45
4.4 Stage Performance at Rig Scale and Scaling to the Engine	45
5.0 Compressor Mechanical Design	49
5.1 General Information	49
5.1.1 Impeller Mechanical Design	49
5.2 Shroud Design	50
5.3 Diffuser Mechanical Design	52
5.4 Exit Guide Vane Mechanical Design	54
5.5 Flow Chart of Structural Analysis	56
5.6 Impeller Burst Margin	58
5.7 Impeller Stress Analysis—Low-Cycle Fatigue Analysis	59
5.8 High-Cycle Fatigue Analysis	60
5.9 Campbell Diagrams for Impeller, Diffuser and EGV	61
6.0 Fabrication and Assembly	63
6.1 Impeller	63
6.1.1 Impeller Fabrication Problems and Their Solutions	64
6.1.2 Final Impeller Runouts	66
6.1.3 Final Impeller Imbalance	68
6.1.4 Final Impeller Blade Tip and Hub Profile Measurements	69
6.2 Shroud	71
6.3 Diffuser and EGV Subassembly	72
6.3.1 Holding Fixture for Assembling the Diffuser and EGV to Shroud	73
6.4 Mock Assembly	73
6.5 Diffuser/Shroud Bolted Interface Analysis	74

7.0	Test Instrumentation	75
7.1	Laying Out the Instrumentation	76
8.0	Data Reduction and Test Results	80
8.1	General Information	80
8.2	Steady-State Data	81
8.2.1	Data Reduction Methodology	82
8.2.2	Measured Data	86
8.2.3	Comparison of Steady State Data to Pre-Test CFD	93
8.3	High-Response Pressure Data at 100 percent N_c	103
8.3.1	Phase-Locked Averaged Results	103
8.3.2	RMS Analysis	107
8.3.3	Frequency Response	109
9.0	Post-Test Root Cause Analysis of Differences Between Test Data and Pre-Test CFD Predictions	110
9.1	General Information	111
9.2	Impact of Suppressed Inlet	113
9.3	Sensitivity to Geometry Variation	113
9.3.1	Impact of a 5 mil Step	113
9.3.2	Impact of Restaggering the Splitter Vane	115
9.4	Turbulence Modeling	120
9.5	Unsteady Effects	122
9.6	Revised Performance Audit	126
9.7	Comparison of Post-Test CFD to Steady State Data	126
10.0	Comparison of Post-Test CFD to High-Response Data	130
10.1	Comparison of CFD to Data (100 percent N_c)	130
10.2	Assessment of Unsteady Impeller-Diffuser Interactions in Post-Test CFD	139
11.0	Discussion	144
11.1	Process Shortfalls	144
11.1.1	Application of Steady CFD Code Outside of its Domain of Validation	144
11.1.2	Limitations of Turbulence Models	146
11.1.3	Underestimation of Unsteady Impeller-Diffuser Interactions	146
11.2	Design Shortfalls	147
11.2.1	Impeller-Diffuser Interactions	147
11.2.2	Diffuser Design	149
11.2.3	Radial-to-Axial Bend and EGV	153
11.2.4	Stability and Range	157
11.3	Revisiting Impeller With Vaneless Diffuser	160
12.0	Conclusions and Recommendations	161
12.1	Test Impeller With a Vaneless Diffuser	162
12.2	Redesign Diffuser to Minimize Interactions With Impeller	162
12.3	Lessons Learned	162
Appendix A.	—Tabulated Data for Key Figures	163
Appendix B.	—High-Response Data and Comparison to CFD	181
B.1	Time-Averaged Results	182
B.2	Phase-Locked Averaging	185
B.3	Unsteady Pressure Transducer Correction	197
Appendix C.	—Hot Coordinates	213
C.1	Flowpath	213
C.2	Impeller Main Blade and Splitter	220
C.3	Diffuser Main Vane and Splitter Vane	286
C.4	Exit Guide Vane	298
Appendix D.	—Instrumentation Coordinates	305
Appendix E.	—Catalog of Electronic Files	311
E.1	Detailed Catalogue of Electronic Files	311
E.2	Detailed Compilation of Test Results	311
E.3	Instrumentation Locations	311

E.4	Hot Coordinates.....	311
E.5	100% N_c LEO Speedline For Final Design (Without Fillets).....	311
E.6	100% N_c LEO Speedline for Final Design (With Impeller Fillets).....	311
E.7	100% N_c LEO Speedline For Final Impeller Design	311
E.8	Selected Speedlines From Post-Test CFD Simulations.....	311
E.9	Animations From Post-Test CFD Simulations For Design Point.....	311
E.10	Meanline Results—Overview	311
References		312

List of Tables

Table 1.—Design Requirements	3
Table 2.—Geometric parameters of the newly designed centrifugal compressor stage	41
Table 3.—Comparison of predicted STD performance at design point to target requirements.....	45
Table 4.—The final imbalance readings of the impeller, and their comparison with the drawing specifications.....	68
Table 5.—Comparison of measured data to target design requirements ($N_c = 100$ percent, and 12 mils constant clearance)	86
Table 6.—Comparison of measured data to pre-test CFD ($m_{c,ex} = 3$ lbm/s, $N_c = 100$ percent, and 12 mils constant clearance)	96
Table 7.—Comparison of performance computed in post-test CFD analyses using different approaches presented in Figure 162 to Figure 164 to measured data ($N_c = 100$ percent, and 12 mils constant clearance)	129
Table 8.—Lowest order spinning modes predicted in compressor.....	139
Table 9.—Comparison of post-test CFD results with different turbulence models—adiabatic efficiency at design flow rate	146
Table 10.—Lowest stable flow rate and stall margin for tests with different tip clearances (at 100 percent N_c).....	158
Table A.1.—Data for Figure 48	163
Table A.2.—Data for Figure 49	164
Table A.3.—Data for Figure 50 and Figure 162	165
Table A.4.—Data for Figure 118, Figure 119 and Figure 120	166
Table A.5.—Data for Figures Figure 121, Figure 122, Figure 123, Figure 124, Figure 125, and Figure 126	167
Table A.6.—Data for Figure 127	168
Table A.7.—Data for Figure 128	169
Table A.8.—Data for Figure 129	170
Table A.9.—Data for Figure 130	170
Table A.10.—Data for Figure 140, Figure 141, and Figure 144	171
Table A.11.—Data for Figure 145	172
Table A.12.—Data for Figure 146	172
Table A.13.—Data for Figure 147, Figure 148, Figure 149, and Figure 150	173
Table A.14.—Data for Figure 151	174
Table A.15.—Data for Figure 154, Figure 155, Figure 156, and Figure 157	175
Table A.16.—Data for Figure 163	176
Table A.17.—Data for Figure 164	177
Table A.18.—Data for Figure 187	178
Table A.19.—Data for Figure 189	179
Table A.20.—Data for Figure 195	180
Table A.21.—Data for Figure 204	180
Table B.1.—Original hot positioning (as in CFD setup) for pressure transducer.....	210
Table B.2.—Final clocked cold positioning for pressure transducer.....	211
Table C.1.—Flow path—Hub	213
Table C.2.—Flow path—Shroud	217
Table C.3.—Impeller main blade—Section 1	220
Table C.4.—Impeller main blade—Section 2	223

Table C.5.—Impeller main blade—Section 3.....	226
Table C.6.—Impeller main blade—Section 4.....	229
Table C.7.—Impeller main blade—Section 5.....	232
Table C.8.—Impeller main blade—Section 6.....	235
Table C.9.—Impeller main blade—Section 7.....	238
Table C.10.—Impeller main blade—Section 8.....	241
Table C.11.—Impeller main blade—Section 9.....	244
Table C.12.—Impeller main blade—Section 10.....	247
Table C.13.—Impeller main blade—Section 11.....	250
Table C.14.—Impeller splitter blade—Section 1	253
Table C.15.—Impeller splitter blade—Section 2	256
Table C.16.—Impeller splitter blade—Section 3	259
Table C.17.—Impeller splitter blade—Section 4	262
Table C.18.—Impeller splitter blade—Section 5	265
Table C.19.—Impeller splitter blade—Section 6	268
Table C.20.—Impeller splitter blade—Section 7	271
Table C.21.—Impeller splitter blade—Section 8	274
Table C.22.—Impeller splitter blade—section 9.....	277
Table C.23.—Impeller splitter blade—Section 10.....	280
Table C.24.—Impeller splitter blade—Section 11	283
Table C.25.—Diffuser main vane—Section 1	286
Table C.26.—Diffuser main vane—Section 2	289
Table C.27.—Diffuser splitter vane—Section 1	292
Table C.28.—Diffuser splitter vane—Section 2	295
Table C.29.—EGV Section 1	298
Table C.30.—EGV Section 2	301
Table D.1.—Impeller Shroud Static Pressure Taps	307
Table D.2.—Shroud Static Taps Immediately Upstream of Diffuser.....	308
Table D.3.—Hub Static Taps Immediately Upstream of Diffuser.....	308
Table D.4.—Diffuser Static Pressure Tap Locations	308
Table D.5.—Static Pressure Taps In Bend Between Diffuser and EGVs.....	310
Table D.6.—Exit Guide Vane Static Pressure Taps	310

List of Figures

Figure 1.—Photograph of NASA CC3 Reference Compressor.....	5
Figure 2.—An example of WAND computational grid for a centrifugal impeller.....	7
Figure 3.—Performance map of CC3 impeller with vaneless diffuser, measurements (open symbols) versus steady-state CFD results (closed symbols).....	8
Figure 4.—100 percent N_c design corrected speed compressor map for CC3 stage, measurements (open symbols) versus CFD steady-state (red) and unsteady (green) results.....	9
Figure 5.—Contours of entropy generation for the CC3 impeller at design condition of inlet corrected flow rate of 10 lbm/s at 100 percent N_c	10
Figure 6.—CC3 impeller, circumferentially averaged velocity profiles at radial location 1.18*impeller tip radius, about 2.5 blade widths downstream of the trailing edge, at design condition of inlet corrected flow rate of 10 lbm/s at 100 percent N_c	10
Figure 7.—Velocity vectors in the CC3 diffuser passage at design condition of inlet corrected flow rate of 10 lbm/s at 100 percent N_c	11
Figure 8.—Left to right: Baseline CC3 impeller, CC3 impeller with lean applied, CC3 impeller with bow applied.....	11
Figure 9.—Rounded versus constant radius trailing edge and CFD predicted performance map of CC3 impeller at 100 percent N_c	12
Figure 10.—CFD predicted radial velocity at CC3 impeller exit ($R/R_2 = 1.18$) for impeller and vaneless diffuser. Operating condition is 10 lbm/s inlet corrected flow at 100 percent N_c	13

Figure 11.—Top: CC3 impeller with constant radius trailing edge; Bottom: CC3 impeller with rounded trailing edge.	13
Figure 12.—Results of calibration of meanline (solid symbols) to CC3 data (open symbols), prior to geometry sensitivity studies. Total pressure ratio is shown in blue, and total-to-total adiabatic efficiency in red; results for 100 percent N_c	14
Figure 13.—Meanline study prediction of peak pressure ratio and efficiency for varying exit blade height (blade height increases from right to left), and impeller backsweep angles (from 20 to 50°), at 100 percent N_c	14
Figure 14.—Meanline study prediction of peak efficiency and diffuser throat area for varying impeller blade exit width, for fixed impeller backsweep angle (of 20°), at 100 percent N_c	15
Figure 15.—Comparison of flowpath for CC3 (blue) and HECC impeller design studies (black).	15
Figure 16.—CFD prediction, 100 percent design speed compressor map for parent 20° backsweep impeller (initial design), followed by sequential additions of geometry modifications, at 100 percent N_c	16
Figure 17.—Top: Parent 20° backsweep impeller with constant radius trailing edge. Bottom: Parent 20° backsweep impeller with rounded trailing edge.	17
Figure 18.—Geometric description for the final 30° backsweep impeller design compared to NASA CC3 impeller (Ref 10). Blade angles are shown in top figures, blade thickness in bottom figures. Five spanwise profiles are included (0, 25, 50, 75, and 100 percent span).	18
Figure 19.—Impeller-only performance comparison of the parent 20° backsweep impeller (B20) compared to final 30° backsweep impeller design (B30) and the original CC3 impeller; total pressure ratio (top), adiabatic efficiency, total-to-total (bottom), at 100 percent N_c	19
Figure 20.—Impeller-only performance comparison of the parent 20° backsweep impeller (B20) compared to final 30° backsweep impeller design (B30) and the original CC3 impeller; total-to-static pressure ratio (top), adiabatic efficiency, total-to-static (bottom), at 100 percent N_c	20
Figure 21.—Impeller blade exit circumferentially averaged profiles. Open symbols: CC3. Solid line: Final 30° backsweep impeller design. Results for design flow rate, at 100 percent N_c	21
Figure 22.—Isentropic Mach number versus normalized chord length at varying spanwise locations for NASA CC3 impeller (symbols) and final 30° backsweep impeller design (solid). Results for design flow rate, at 100 percent N_c	22
Figure 23.—Original (blue) and redesigned (black) flowpaths, showing 23 percent reduction in stage maximum diameter. Reducing the exit diameter limits the amount of diffusion available.	23
Figure 24.—Examples of topologies considered at same maximum diameter as original CC3 to define the configuration with highest recovery. Configuration “Reduced thickness with splitter” (with 18 vanes) achieves C_p of 0.822 compared to C_p of 0.783 for CC3 wedge diffuser. Results for design flow rate, at 100 percent N_c	24
Figure 25.—Comparison of vaned diffuser design at diameter ratio of 1.71 (red) to vaned diffuser at diameter ratio of 1.45 (blue). CC3 wedge diffuser is shown for reference (black). A configuration at a somewhat lower inner radius that was considered in the process is also shown (green).	25
Figure 26.—Positioning of the splitter leading edge with respect to diffuser throat (dashed line).	26
Figure 27.—Comparison of stage performance computed with new vaned diffuser configurations with diameter ratio of 1.71 (in green) and 1.45 (in blue).	27
Figure 28.—Comparison of loading distributions for vane diffuser with splitter, for splitter placed identically in mid-passage (right) or shifted in order to balance pressure recovery on both sides (left), at design flow rate, 100 percent N_c	28
Figure 29.—A study showing the impact of vane count for the final vaned diffuser configuration. Vane count of 20 pairs of main and splitter vanes was maintained for better matching with the impeller (for 100 percent N_c).	29
Figure 30.—Comparison of loading distributions as function of radius for the main vane in the new diffuser (solid line) in comparison to CC3 (symbols), at design flow rate and 100 percent N_c	30
Figure 31.—New diffuser design exit profiles—absolute Mach number is approximately 0.3 (top), and the swirl angle is approximately 60° (bottom), at design flow rate and 100 percent N_c	31
Figure 32.—CC3 (left) and new vaned diffuser with shifted splitters (right), as spotted in the diffuser maps. CFD predicted pressure recovery of 0.78 for CC3, and about 0.70 for the new diffuser....	31

Figure 33.—Final thickening of the leading edges of diffuser vanes—action item from the preliminary design review.	32
Figure 34.—Impact of thickening of the diffuser leading edges on performance of the impeller-diffuser stage—CFD with mixing plane predicted a reduction of 0.2 percentage points in peak adiabatic efficiency (for 100 percent N_c).	33
Figure 35.—Steady CFD-predicted performance map for impeller-diffuser stage design run at fixed impeller tip-clearance (12 mil).	34
Figure 36.—Performance for 100 percent design speed for impeller-diffuser stage design with unthickened diffuser vanes and no EGV, as computed with steady (red) and unsteady CFD (green), indicating the pre-test quantification of the level of impact of impeller/diffuser interaction on performance.	35
Figure 37.—Results of EGV airfoil section trade study, in which camber and solidity were varied for two airfoil sections to find minimum total pressure loss that meets target exit swirl angle (at design flow rate at 100 percent N_c). Configurations circled in green were down selected for further analyses via stage calculations.	36
Figure 38.—Variation in total-to-static efficiency due to positioning of EGV row relative to diffuser row (at design point, 100 percent N_c).	37
Figure 39.—Comparison of entropy contours for least favorable (top) and most favorable (bottom) position of EGV row relative to diffuser row (at design point, 100 percent N_c).	37
Figure 40.—Comparison of static pressures and absolute Mach number at EGV mid-span for three EGVs, as computed with different clocking positions: 0.62 pitch (left), 0.75 pitch (middle), and 0.87 pitch (right).	38
Figure 41.—Circumferentially averaged inlet and exit profiles to the EGV row; absolute Mach number at exit has been reduced below 0.16, and the swirl angle below 18° (Results for design flow rate, at 100 percent N_c).	38
Figure 42.—Design process of the initial radial-to-axial bend configuration.	39
Figure 43.—Results of optimization of radial-to-axial bend area, showing original flat bend (blue) and redesigned curved bend (green) from optimization.	40
Figure 44.—Results of optimization of radial-to-axial bend area, showing stage (impeller, diffuser, clocked-EGV) adiabatic efficiency (total-to-total) with the original flat bend (blue) and redesigned curved bend (green) at 100 percent N_c .	40
Figure 45.—Comparison of passage height and area scheduling for radial-to-axial bend area for CC3 (red) and the new design (blue).	40
Figure 46.—NASA CC3 compressor (left) and the new design (right).	41
Figure 47.—Comparison of HECC and CC3 impellers showing improved trailing edge and improved blade angle distribution.	42
Figure 48.—Predicted total pressure ratio (top) and total-to-total adiabatic efficiency (bottom) versus inlet corrected flow for NASA CC3 and final design (at 100 percent N_c).	42
Figure 49.—Predicted total-to-static stage adiabatic (top) and polytropic efficiency (bottom) versus exit corrected flow for NASA CC3 and final HECC design (at 100 percent N_c).	43
Figure 50.—Full compressor map for speeds 85 to 105 percent obtained during steady post-test CFD analyses using standard day inlet conditions and the same vorticity-based $k-\omega$ model that was used in pre-test CFD analyses.	44
Figure 51.—Meanline prediction of total-to-total adiabatic efficiency for varying inlet radius ratio at fixed inlet area, no inlet swirl (at 100 percent N_c).	46
Figure 52.—Estimated efficiency reduction versus diameter ratio, at varying specific speeds. HECC stage is specific speed $N_s=0.6$. Used with permission from ASME. Rodgers, C., and Brown, D., "High Hub/Tip Centrifugal Compressors," GT2009-59012, Proceedings of ASME Turbo Expo 2009, Orlando, FL, June 8-12, 2009.	46
Figure 53.—Adiabatic efficiency(T-T) reduction computed with CFD for the impeller as its diameter ratio is increased to 0.5 (at 100 percent N_c).	47
Figure 54.—The impact of adding the fillets to the final design as estimated with CFD.	48
Figure 55.—Bookkeeping efficiency deltas from rig to engine scale.	48
Figure 56.—Cross-section of the HECC compressor rig showing the new as well as existing parts.	49
Figure 57.—Compressor rig conditions used in the mechanical design.	50

Figure 58.—HECC impeller geometry has 15 main blades and 15 splitter blades. The picture on the right shows the rounded trailing edges and fillets.....	50
Figure 59.—Compressor shroud showing instrumentation holes, and the ablatable material.....	51
Figure 60.—Impeller static probe hole locations on the shroud.....	51
Figure 61.—Assembly of the diffuser vanes with the hub and shroud. The two instrumented modular vanes are shown in red.....	52
Figure 62.—Diffuser vanes were designed to be brazed with the hub and shroud.....	53
Figure 63.—Diffuser vane passage shroud static holes.....	53
Figure 64.—Diffuser vane passage hub static holes.....	54
Figure 65.—EGV assembly has 60 vanes and three of these are instrumented.....	54
Figure 66.—EGVs are designed to be brazed with the hub and shroud.....	55
Figure 67.—There are 31 EGV hub static holes.....	55
Figure 68.—There are 12 exit rakes located around the circumference at the aft of the EGV trailing edge. Each rake has three probes for measuring total pressure, and two probes for measuring total temperature	56
Figure 69.—Flowchart of aerodynamic and structural analyses used during design process.....	57
Figure 70.—Typical flowchart for high cycle fatigue analysis.....	57
Figure 71.—“Higher fidelity” analysis flowchart for high cycle fatigue.....	58
Figure 72.—Impeller 2D analysis—von Mises stress; comparison to NASA CC3 impeller.....	59
Figure 73.—Overall von Mises stresses plot to observe peak stresses locations with high stress regions compared to 80 percent SY to calculate safety margin.	60
Figure 74.—Impeller high-cycle fatigue analysis and impeller Goodman diagram.....	61
Figure 75.—Impeller Campbell diagram (red dots are fundamental modes).....	62
Figure 76.—Diffuser Campbell diagram.....	62
Figure 77.—EGV Campbell diagram.....	63
Figure 78.—The titanium forging was first rough-turned to an oversize impeller volume shape.....	64
Figure 79.—HECC impeller after the final machining.....	64
Figure 80.—Area of impeller damage incurred during machining.....	65
Figure 81.—Summary of the impeller runouts as measured by Anmark.....	65
Figure 82.—Impeller drawing showing various dimensions that are referenced above in the Plan Requirements section.....	67
Figure 83.—Final impeller runouts being checked out after mounting it on the refinished curvic couplings and the new precision arbor.....	67
Figure 84.—The Hoffmann machine showing the imbalance readings after regrinding of the curvic couplings and the impeller. These readings are 10 times larger than the imbalance specified on the drawings.....	68
Figure 85.—The departure of the impeller profiles from the CAD model for the hub surfaces (top), and the impeller main and splitter blade tips (bottom).....	69
Figure 86.—The graphical and pictorial representation of the runouts on the backface of the impeller. The largest negative deviation from the drawing specification is 0.0005 in. (under-size), and the largest positive deviation is 0.0042 in.	70
Figure 87.—The forging for the shroud.....	70
Figure 88.—The shroud during the machining (left), and in the final form (right).....	71
Figure 89.—A close up view of the ablatable coating on the inside of the shroud.....	71
Figure 90.—Diffuser and EGV subassemblies before instrumentation.....	72
Figure 91.—Uninstrumented modular diffuser vanes.....	72
Figure 92.—Diffuser assembly being inspected at UTRC on the 5-axis machine (left), as well as visually.....	72
Figure 93.—Custom built fixture for holding the shroud, and for assembling the stationary parts	73
Figure 94.—Steps involved in the mock assembly. First (top left) placement of the diffuser subassembly on the shroud. Then placing the heat belts around the EGV surfaces and heating it to about 150~160 °F. At that time EGV subassembly is lifted with a crane and moved over the shroud (top right), and lowered using a locating pin. Finally, the removal of the heating pads and check for the fit (bottom picture).....	74
Figure 95.—Detail of the proposed diffuser/shroud bolted interface with threaded studs.....	75
Figure 96.—Exit rake integration in the rig.....	76

Figure 97.—CFD prediction of static pressure near diffuser main blade shroud surface, at choke (top) and near-stall (bottom) conditions. Symbols indicate tap locations.	77
Figure 98.—Diffuser section showing the modular vane instrumented with total-pressure probes.....	78
Figure 99.—Diffuser showing high-response instrumentation.....	79
Figure 100.—Summary of the instrumentation designed into the rig.	79
Figure 101.—NASA Small Engine Component Test Facility.	80
Figure 102.—Tip clearance variation with speed obtained during the mechanical checkout (performance test data was run with maximum clearance of 0.012 in. at the trailing edge).	81
Figure 103.—Station identification used in data reduction.	82
Figure 104.—Hub and shroud static pressure taps used to compute static pressure at diffuser leading edge.....	83
Figure 105.—Hub and shroud static pressure taps used to compute static pressure at EGV LE and TE.....	84
Figure 106.—Inlet suppression run during the test against inlet corrected flow rate for various corrected speeds.....	87
Figure 107.—Compressor speedlines of total pressure ratio against inlet corrected flow rate for various corrected speeds; speedlines were run to near-stall.....	88
Figure 108.—Compressor speedlines of total temperature ratio against inlet corrected flow rate for various corrected speeds.....	88
Figure 109.—Total-to-total adiabatic (blue) and polytropic (green) efficiency against inlet corrected flow rate for various corrected speeds.....	89
Figure 110.—Total-to-static adiabatic (blue) and polytropic (green) efficiency against inlet corrected flow rate for various corrected speeds.....	89
Figure 111.—Total-to-static adiabatic efficiency against exit corrected flow rate for various corrected speeds.....	90
Figure 112.—Total-to-static polytropic efficiency against exit corrected flow rate for various corrected speeds.....	90
Figure 113.—Total pressure ratio for impeller (inlet to diffuser leading edge) against inlet corrected flow rate for various corrected speeds.....	91
Figure 114.—Total-to-total adiabatic (blue) and polytropic (green) efficiency for impeller (inlet to diffuser leading edge) against inlet corrected flow rate for various corrected speeds.....	91
Figure 115.—Total-to-total adiabatic efficiency for impeller (inlet to diffuser leading edge) against exit corrected flow rate for various corrected speeds.....	92
Figure 116.—Total pressure loss from diffuser leading edge to EGV leading edge against inlet corrected flow rate for various corrected speeds.	92
Figure 117.—Total pressure loss from EGV leading edge to exit against inlet corrected flow rate for various corrected speeds.	93
Figure 118.—Total pressure ratio at 100 percent N_c : data against pre-test CFD predictions.....	94
Figure 119.—Total-to-total adiabatic efficiency for 100 percent N_c : data against pre-test CFD predictions.....	95
Figure 120.—Total-to-total polytropic efficiency for 100 percent N_c : data against pre-test CFD predictions.....	95
Figure 121.—Total-to-total adiabatic efficiency for impeller for 100 percent N_c : data against pre-test CFD predictions.....	96
Figure 122.—Total pressure ratio for impeller for 100 percent N_c : data against pre-test CFD predictions.	97
Figure 123.—Total temperature ratio for compressor for 100 percent N_c : data against pre-test CFD predictions.....	97
Figure 124.—Pressure recovery in the diffuser for 100 percent N_c : data against pre-test CFD predictions.....	98
Figure 125.—Pressure recovery for diffuser and EGV combined for 100 percent N_c : data against pre-test CFD predictions.	98
Figure 126.—Total pressure loss from diffuser leading edge to exit for 100 percent N_c : data against pre-test CFD predictions.	99

Figure 127.—Static pressure around main (top figure) and splitter (bottom figure) vanes on the hub for 100 percent N_c at inlet corrected flow of 11 lbm/s: data against pre-test CFD predictions.....	100
Figure 128.—Static pressure around main (top figure) and splitter (bottom figure) vanes on the shroud for 100 percent N_c at inlet corrected flow of 11 lbm/s: data against pre-test CFD predictions.....	101
Figure 129.—Total pressure profile at diffuser modular vane leading edge for 100 percent N_c at inlet corrected flow of 11 lbm/s: data against pre-test CFD predictions.....	102
Figure 130.—Total pressure profile at EGV leading edge for 100 percent N_c at inlet corrected flow of 11 lbm/s: data against pre-test CFD predictions.....	102
Figure 131.—Unsteady pressure results at deep choke operating point.....	104
Figure 132.—Unsteady pressure results choke onset operating point.....	105
Figure 133.—Unsteady pressure results at design operating point.....	106
Figure 134.—Unsteady pressure results at near stall operating point.....	107
Figure 135.—Waterfall plots of RMS component in diffuser passage A.....	108
Figure 136.—Unsteady pressure transfer function (K12=reference).....	109
Figure 137.—Steady state CFD computations for impeller-diffuser configuration at 100 percent N_c : a comparison of adiabatic efficiency computed UTCFD to results from LEO (using the same WAND grid).....	111
Figure 138.—Detail of the computational grid: WAND 2009 grid (left) and UTGRID 2012 grid (right)....	112
Figure 139.—Steady state CFD computations for final HECC configuration at 100 percent N_c : comparing LEO results from 2009 to UTCFD results computed on a finer, better resolved UTGRID grid.....	112
Figure 140.—Steady state CFD computations for final HECC stage configuration at 100 percent N_c using UTCFD—an assessment of the impact of suppressed inlet.....	113
Figure 141.—Steady state CFD computations for final HECC configuration at 100 percent N_c using UTCFD with suppressed inlet—an assessment of the impact of 0.005 in. step on the shroud.....	114
Figure 142.—Comparison of the measured and computed total pressure profile at the diffuser leading edge for inlet corrected flow of 10.55 lbm/s at 100 percent N_c , showing the effect of the 5 mil forward-facing step at the shroud.....	114
Figure 143.—Splitter vane rotated towards the suction side of the main vane for 3°.....	115
Figure 144.—Steady state CFD computations for final HECC configuration at 100 percent N_c using UTCFD with suppressed inlet—an assessment of the impact of restaggering the splitter vane 3° towards the main vane.....	115
Figure 145.—Plot of static pressure around the main (top) and splitter vane (bottom) on the shroud for 100 percent N_c at inlet corrected flow rate of 11 lbm/s—an assessment of the impact of restaggering the splitter vane 3° towards the main vane (closed).....	116
Figure 146.—Total pressure profile at diffuser modular vane leading edge for 100 percent N_c at inlet corrected flow rate of 11 lbm/s—an assessment of the impact of restaggering the splitter vane 3° towards the main vane (shown in blue) in comparison to measured data (red symbols).....	117
Figure 147.—Total pressure ratio for impeller for 100 percent N_c —an assessment of the impact of restaggering the splitter vane 3° towards the main vane.....	118
Figure 148.—Total temperature ratio for impeller at 100 percent N_c —an assessment of the impact of restaggering the splitter vane 3° towards the main vane.....	118
Figure 149.—Adiabatic efficiency for impeller for 100 percent N_c —an assessment of the impact of restaggering the splitter vane 3° towards the main vane.....	119
Figure 150.—Pressure recovery for combined diffuser and EGV for 100 percent N_c —an assessment of the impact of restaggering the splitter vane 3° towards the main vane.....	119
Figure 151.—Steady state CFD computations for final HECC configuration at 100 percent N_c using UTCFD with suppressed inlet—an assessment of the impact of using different turbulence models.....	120
Figure 152.—Total pressure profile at diffuser leading edge for 100 percent N_c at inlet corrected flow rate of 11 lbm/s—an assessment of the impact of using different turbulence models.....	121

Figure 153.—Surface stress lines on the diffuser main vane, as computed for 100 percent N_c at inlet corrected flow rate of approximately 11 lbm/s—an assessment of the impact of using different turbulence models.	121
Figure 154.—Unsteady CFD computations (dashed) for final HECC configuration at 100 percent N_c using UTCFD with suppressed inlet—comparison to steady state solution (solid) for vorticity based $k-\omega$ model.	122
Figure 155.—Unsteady CFD computations (dashed) for final HECC configuration at 100 percent N_c using UTCFD with suppressed inlet—comparison to steady state solution (solid) for strain-rate based $k-\omega$ model.	123
Figure 156.—Unsteady CFD computations (dashed) for final HECC configuration at 100 percent N_c using UTCFD with suppressed inlet—total temperature ratio comparison to steady state solution (solid) for strain-rate based $k-\omega$ model.	123
Figure 157.—Unsteady CFD computations (dashed) for final HECC configuration at 100 percent N_c using UTCFD with suppressed inlet—total pressure ratio comparison to steady state solution (solid) for strain-rate based $k-\omega$ model.	124
Figure 158.—Unsteady CFD computations (dashed) for final HECC configuration at 100 percent N_c using UTCFD with suppressed inlet—comparison of predicted impeller efficiency to steady state solution (solid) for strain-rate based $k-\omega$ model.	124
Figure 159.—Unsteady CFD computations (dashed) for final HECC configuration at 100 percent N_c using UTCFD with suppressed inlet—comparison of predicted diffuser losses to steady state solution (solid) for strain-rate based $k-\omega$ model.	125
Figure 160.—Unsteady CFD computations (dashed) for final HECC configuration at 100 percent N_c using UTCFD with suppressed inlet—comparison of predicted EGV losses to steady state solution (solid) for strain-rate based $k-\omega$ model.	125
Figure 161.—Book-keeping efficiency deltas from rig to engine scale—revised audit, based on post-test CFD.	126
Figure 162.—Full compressor map for speeds 85 to 105 percent obtained during steady post-test CFD analyses using standard-day inlet conditions, (fixed 12 mil clearance), and the same vorticity-based $k-\omega$ model that was used in pre-test CFD analyses as compared to data at suppressed inlet.	127
Figure 163.—Full compressor map for speeds 85 to 105 percent obtained during steady post-test CFD analyses using the suppressed inlet conditions, (fixed 12 mil clearance), and the same vorticity-based $k-\omega$ model that was used in pre-test CFD analyses as compared to data at suppressed inlet.	128
Figure 164.—Full compressor map for speeds 85 to 105 percent obtained during unsteady post-test CFD analyses using suppressed inlet conditions, (fixed 12 mil clearance), and the strain-rate based $k-\omega$ model as compared to data at suppressed inlet.	129
Figure 165.—K18 signal versus CFD at 11 lbm/s (design flow) and 100 percent N_c	131
Figure 166.—K18 signal versus CFD at 10.4 lbm/s (near-stall flow) and 100 percent N_c	131
Figure 167.—K12 signal versus CFD at 11 lbm/s (design flow) and 100 percent N_c	132
Figure 168.—K12 signal versus CFD at 10.4 lbm/s (near-stall flow) and 100 percent N_c	132
Figure 169.—K13 signal versus CFD at 11 lbm/s (design flow) and 100 percent N_c	133
Figure 170.—K13 signal versus CFD at 10.4 lbm/s (near-stall flow) and 100 percent N_c	133
Figure 171.—K19 signal versus CFD at 11 lbm/s (design flow) and 100 percent N_c	134
Figure 172.—K19 signal versus CFD at 10.4 lbm/s (near-stall flow) and 100 percent N_c	134
Figure 173.—K20 signal versus CFD at 11 lbm/s (design flow) and 100 percent N_c	135
Figure 174.—K20 signal versus CFD at 10.4 lbm/s (near-stall flow) and 100 percent N_c	135
Figure 175.—Corrected K7 signal versus CFD at 11 lbm/s (design flow) and 100 percent N_c	136
Figure 176.—Corrected K7 signal versus CFD at 10.4 lbm/s (near-stall flow) and 100 percent N_c	136
Figure 177.—Corrected K8 signal versus CFD at 11 lbm/s (design flow) and 100 percent N_c	137
Figure 178.—Corrected K8 signal versus CFD at 10.4 lbm/s (near-stall flow) and 100 percent N_c	137
Figure 179.—Corrected K9 signal versus CFD at 11 lbm/s (design flow) and 100 percent N_c	138
Figure 180.—Corrected K9 signal versus CFD at 10.4 lbm/s (near-stall flow) and 100 percent N_c	138
Figure 181.—Circumferential lines studied for rotor-stator interaction—at mid-span (dashed).	140
Figure 182.—Raw CFD data for rotor-stator interaction analysis.	140

Figure 183.—Spatial Fourier decomposition for rotor-stator interaction analysis—lower order modes.....	141
Figure 184.—Spatial Fourier decomposition for rotor-stator interaction analysis—higher order modes.....	142
Figure 185.—Reconstructed $m=-5$ mode over one rotor revolution.	143
Figure 186.—Two speedlines at 100 percent N_c for the final 30° backsweep design computed with different location of the inlet (open symbols, B30-D2X, has inlet boundary further upstream compared to B30-D2, solid symbols). The leftmost point for B30-D2X is not well converged, and it eventually diverges. CC3 is also shown for reference.	145
Figure 187.—Impeller efficiency for 100 percent N_c - unsteady CFD results are more representative of the measured data.	148
Figure 188.—Unsteady loading on the impeller main-blade (top) and splitter (bottom) at mid-span for design flow rate at 100 percent N_c , as predicted with unsteady CFD using strain-rate based production in $k-\omega$ model.	148
Figure 189.—Adiabatic efficiency for impeller for 100 percent N_c —restaggering the splitter vane by 3° towards the main vane has a large impact on the performance of the impeller.	149
Figure 190.—Instantaneous contour plot of turbulent kinetic energy in the diffuser at mid-span (from a post-test UTCFD unsteady simulation at 11 lbm/s for 100 percent N_c using strain-rate based production $k-\omega$).	150
Figure 191.—Average diffuser incidence calculated from measurements of flow rate, exit total temperature, and static and total pressure at modular vane (across all speeds).	151
Figure 192.—Measured static pressure near stall for 100 percent N_c shows negative loading on the splitter.....	152
Figure 193.—Measured static pressure near design for 100 percent N_c shows negative loading on the splitter, not predicted by the steady CFD model.	153
Figure 194.—Pressure recovery: from diffuser LE to diffuser TE (top) and from diffuser LE to EGV LE (bottom).	154
Figure 195.—Pressure throughout the bend—comparison of measurements to post-test CFD (unsteady, strain-rate based $k-\omega$ model) at inlet corrected flow rate of 11 lbm/s for 100 percent N_c	155
Figure 196.—Contour plots of radial velocity at three radial cross-sections near the trailing edge of diffuser vanes at inlet corrected flow rate of 11 lbm/s for 100 percent N_c . Flow separation near trailing edge; gray indicates reversed flow - time-averaged flowfield from unsteady post-test CFD (unsteady, strain-rate based $k-\omega$ model).	155
Figure 197.—Contour plots of streamwise velocity at two cross-sections in the bend at inlet corrected flow rate of 11 lbm/s for 100 percent N_c . Flow separation in the bend; gray indicates reversed flow - time-averaged flowfield from unsteady post-test CFD (unsteady, strain-rate based $k-\omega$ model).	156
Figure 198.—Contours of instantaneous Ma number in the EGV at midspan indicate flow separation at inlet corrected flow rate of 11 lbm/s for 100 percent N_c (from unsteady post-test CFD, with strain-rate based $k-\omega$ model).	156
Figure 199.—Range as predicted for HECC and CC3 with both vaned (solid lines) and vaneless diffusers (dashed lines) for 100 percent N_c	158
Figure 200.—Flow incidence angle to HECC impeller (left) and axial velocity profile 0.5 in. upstream of the impeller leading edge (right) for near-stall condition (~ 10 lbm/s), design condition (~ 11 lbm/s), and choke condition (~ 11.6 lbm/s)—at 100 percent N_c	158
Figure 201.—Toolmarks at the hub of the impeller.	159
Figure 202.—Impeller fillets at trailing edge, actual geometry (top), CFD geometry with fillets as computed in pre-test simulations (middle), CFD geometry with no fillets (bottom).	159
Figure 203.—Total-to-total adiabatic efficiency for the impeller with a vaneless diffuser computed using the exit of the computational domain at $R \sim 10$ in. as downstream station—at 100 percent N_c	160
Figure 204.—Total-to-total adiabatic efficiency for the impeller with a vaneless diffuser at 100 percent N_c computed using the radius of modular vane LE ($R \sim 9.1$ in.) as downstream station—a comparison with computations for the vaned configuration (steady and unsteady), using strain rate based $k-\omega$ model. Data for the vaned configuration is also included for reference.	161

Figure B.1.—Location of unsteady pressure transducers.....	181
Figure B.2.—Circumferential location of static taps and unsteady pressure transducer (FWD looking AFT).	182
Figure B.3.—Comparison of static taps and unsteady pressure transducers in diffuser passages (at operating point no.40, 100 percent N_c).	183
Figure B.4.—Comparison of static taps and unsteady pressure transducers in the impeller tip region (at operating point no.54, 100 percent N_c).	184
Figure B.5.—Comparison of impeller shroud static taps with unsteady pressure transducers (at operating point no.50, 100 percent N_c).....	185
Figure B.6.—Phase-locked averaging approach.	186
Figure B.7.—Example phase-locked unsteady pressure with random component.....	187
Figure B.8.—(a) Pressure transducer no.7 (operating points 43, 50, 54, and 56; 100 percent N_c).	188
Figure B.8.—(b) Pressure transducer no.8 (operating points nos. 43, 50, 54, and 56; 100 percent N_c).	189
Figure B.8.—(c) Pressure transducer no. 9 (operating points nos. 43, 50, 54, and 56; 100 percent N_c).	190
Figure B.8.—(d) Pressure transducer no. 18 (operating points nos. 43, 50, 54, and 56; 100 percent N_c).	191
Figure B.8.—(e) Pressure transducer no. 15 (operating points nos. 43, 50, 54, and 56; 100 percent N_c).	192
Figure B.8.—(f) Pressure transducer no. 12 (operating points nos. 28, 35, 40, and 42; 100 percent N_c).	193
Figure B.8.—(g) Pressure transducer no. 13 (operating points nos. 28, 35, 40, and 42; 100 percent N_c).	194
Figure B.8.—(h) Pressure transducer no. 19 (operating points nos. 28, 35, 40, and 42; 100 percent N_c).	195
Figure B.8.—(i) Pressure transducer no. 20 (operating points nos. 28, 35, 40, and 42; 100 percent N_c).	196
Figure B.9.—Pressure transducer installation details.	197
Figure B.10.—Modeling approaches for pressure transducer correction.	198
Figure B.11.—Pressure transducer-to-flowfield pressure ratio as a function of grazing Mach number... .	199
Figure B.12.—Pressure transducer Grazing Mach number (inlet corrected flow of 11 lbm/s, 100 percent N_c).	200
Figure B.13.—(a) Pressure transducer no. 7 comparison with CFD (operating point no. 54 at 100 percent N_c).	201
Figure B.13.—(b) Pressure transducer no. 8 comparison with CFD (operating point no. 54 at 100 percent N_c).	202
Figure B.13.—(c) Pressure transducer no. 9 comparison with CFD (operating point no. 54 at 100 percent N_c).	203
Figure B.13.—(d) Pressure transducer no. 18 comparison with CFD (operating point no. 54 at 100 percent N_c).	204
Figure B.13.—(e) Pressure transducer no. 15 comparison with CFD (operating point no. 54 at 100 percent N_c).	205
Figure B.13.—(f) Pressure transducer no. 12 comparison with CFD (operating point no. 40 at 100 percent N_c).	206
Figure B.13.—(g) Pressure transducer no. 13 comparison with CFD (operating point no. 40 at 100 percent N_c).	207
Figure B.13.—(h) Pressure transducer no. 19 comparison with CFD (operating point no. 40 at 100 percent N_c).	208
Figure B.13.—(i) Pressure transducer no. 20 comparison with CFD (operating point no. 40 at 100 percent N_c).	209
Figure D.1.—Hub and shroud static pressure taps used to compute static pressure at diffuser leading edge.	305
Figure D.2.—Hub and shroud static pressure taps used to compute static pressure at EGV LE and TE	306

High Efficiency Centrifugal Compressor for Rotorcraft Applications

Gorazd Medic, Om P. Sharma, Joo Jongwook, Larry W. Hardin, Duane C. McCormick,
William T. Cousins, Elizabeth A. Lurie, Aamir Shabbir, Brian M. Holley, and Paul R. Van Slooten
United Technologies Research Center
East Hartford, Connecticut 06108

1.0 Introduction

Centrifugal compressors have been extensively used in a variety of products over the last century and in rotorcraft engines over the last 60 years. These devices provide reliable compression in very compact configurations. Extensive databases, design rules, and criteria are available in most design and manufacturing organizations to allow development of these machines. These design processes are highly empirical, utilizing scaling strategies, and rely on prototype testing to achieve design goals. This design process reflects the fact that the flow in these machines is highly complex, dominated by three-dimensional, viscous, and unsteady mechanisms, and results in conservative designs to limit engine program risks. Managing this complex flowfield is a primary limitation to high efficiency designs. Over the past decade, CFD-based tools have begun to be utilized to assess configurations during the detailed design phase. To date these tools have been validated largely by utilizing component level performance metrics. There is a need to validate these tools by utilizing data that elucidates the physics of loss generation mechanisms in these machines, to ensure these tools can be used to define the details of the loss reduction concepts with confidence.

A second limitation to high efficiency centrifugal compressor designs is that the close spacing of the rotating impeller and stationary diffuser rows can cause performance and durability issues. Matching a vane diffuser to an impeller is a nontrivial task due to the complicated flow mechanics involved and the absence of a quantitative understanding of the interaction. Satisfactory performance of an individual component does not guarantee that the combined stage design will also have satisfactory efficiency and flow range. Considerable resources can be spent during an engine development program to rework components that are found only during the rig test phase, not to be well matched. For durability concerns, the unsteady interaction of the impeller-diffuser pair can cause large unsteady blade loads on each, and can be an excitation source for high cycle fatigue. Although there are a number of publications describing impeller-diffuser interaction (for example, Refs. 1, 2, and 3), no clear guidelines exist on optimizing performance by controlling impeller-diffuser gap, diffuser vane solidity, or vane throat area. Because the interaction losses are inherently unsteady, CFD-based design processes must include unsteady analyses to assess its impact on overall performance.

The purpose of this effort is to identify key technical barriers to advancing the state-of-the-art of small centrifugal compressor stages; to delineate the measurements required to provide insight into the flow physics of the technical barriers; to design, fabricate, install, and test a state-of-the-art research compressor that is representative of the rear stage of an axial-centrifugal aero-engine; and to acquire detailed aerodynamic performance and research quality data to clarify flow physics and to establish detailed data sets for future application. The design activity centered on meeting the goal set outlined in the NASA solicitation (Ref. 4) the design target was to increase efficiency at higher work factor, while also reducing the maximum diameter of the stage. To fit within the existing Small Engine Components Test Facility at NASA Glenn Research Center (GRC) and to facilitate component re-use, certain key design parameters were fixed by UTRC, including impeller tip diameter, impeller rotational speed, and impeller inlet hub and shroud radii. This report describes the design effort of the High Efficiency Centrifugal Compressor stage (HECC) and delineation of measurements, fabrication of the compressor, and the initial tests that were performed.

1.1 Nomenclature

A	area
B	blockage (aerodynamic)
c	speed of sound
C_p	pressure recovery coefficient
D_2	impeller trailing edge diameter
D_{\max}	maximum diameter of compressor stage
g_c	gravitational constant
i	incidence angle
LE	leading edge
M, Ma	Mach number
$m_{c, \text{exit}}$	exit corrected mass flow rate
$m_{c, \text{inlet}}$	inlet corrected mass flow rate
M_{isen}	isentropic Mach number
N_c	corrected speed
N_s	specific speed
P, P_s	static pressure
P_0, P_T	total pressure
P_{atm}	atmospheric, standard day pressure
PPS	pounds mass per second
PR	pressure ratio
PT_{loss}	normalized total pressure loss
R	gas constant
r	radius (in.)
R_1	impeller leading edge radius
R_{1h}	impeller inlet hub radius
R_{1s}	impeller inlet shroud radius
R_2	impeller trailing edge radius
RAKE	measurements at exit rakes
Re	Reynolds number
SM	stability margin
Station 1	impeller inlet
Station 1a	impeller exit
Station 2	diffuser inlet
Station 2a	diffuser exit
Station 3	EGV inlet
Station 4	EGV exit
STD	standard day (conditions)
T, T_s	static temperature
T_0, T_T	total temperature
TE	trailing edge
TR	temperature ratio
T-S	total-to-static
T-T	total-to-total
U	wheel speed at a given radius
V_r, C_r	radial velocity
V_t, C_θ	tangential, circumferential velocity
V_x, C_x	axial velocity
$W_{\text{corr, exit}}$	exit corrected mass flow rate
$W_{\text{corr, inlet}}$	inlet corrected mass flow rate
\dot{w}	weight flow
α	angle w.r.t. axial direction
β	angle w.r.t. circumferential direction
η_{ad}	adiabatic efficiency
$\eta_{\text{poly}}, \eta_p$	polytropic efficiency

ρ	density
γ	specific heat ratio
ω	total pressure loss coefficient

2.0 Design Requirements, Technical Challenges and Design Strategy

2.1 Design Requirements

The intent of the design effort is to develop a centrifugal stage that is representative of the final stage of an axicentrifugal compressor for rotorcraft applications. To that end, the performance requirements at engine scale and at rig scale are shown in Table 1. Also included are values for the existing NASA CC3 rig with higher radius ratio diffuser. The rig is geometrically scaled twice as large, approximately, as the engine scale, making it easier to accommodate dense levels of instrumentation. The geometric scale factor varies as described in (Ref. 5):

$$\frac{L_{\text{engine}}}{L_{\text{rig}}} = \sqrt{\frac{\dot{m}_{\text{engine}}}{\dot{m}_{\text{rig}}}} \quad (1)$$

The engine-scale compressor exit temperature of 950 to 1000 °F corresponds to an overall pressure ratio of 25 to 30, which is consistent with advanced turboshaft engines. Also, for a multistage turboshaft engine, the mechanical layout would typically drive the impeller geometry to have impeller inlet hub to shroud radius ratio R1H/R1S of about 0.6 to 0.7 and impeller inlet shroud to tip diameter ratio R1S/R2 of about 0.6. When scaling to the rig environment, these radius ratios should be maintained. In order to minimize changes to the existing rig hardware, however, this requirement was relaxed out of necessity and the original ratios were held, at nominally 0.4 and 0.5, respectively. The effect of not holding inlet radius ratios on performance will be addressed in the section on scaling from rig to engine and in the associated performance audit.

TABLE 1.—DESIGN REQUIREMENTS

Metric	Engine	Rig	CC3 (Existing rig)
Stage pressure ratio	4.0 to 5.0	4.0 to 5.0	4
Exit corrected flow, lbm/s	0.7 to 0.8	2.6 to 3.1	3.1
Work factor, $\Delta H_0/U_2^2$	0.6 to 0.75	0.6 to 0.7	0.6
Polytropic efficiency, TT, %	≥88	≥88	≥86
Compressor exit temperature, °F	950 to 1000	350 to 410	425
D_{\max}/D_2	≤1.45	1.45	1.87
Stability margin, %	13	13	13
Geometric similitude			
Tip clearance, mil	6.6	12	12
Fillets, mil	27/28	50/150	50/150
Surface finish, mil	0.03	0.06	0.06
Engine relevance			
Exit Mach number	0.15	0.15	0.15
Exit swirl angle, deg.	15	15	60
Inlet radius ratio, R_{1H}/R_{1S}	0.6	0.38	0.39
Shroud radius ratio, R_{1S}/R_2	0.6	0.5	0.49

2.2 Key Technical Challenges

One of the objectives of this research effort is to use this opportunity to design a centrifugal research compressor to also enable the characterization and prioritization of key technical barriers and knowledge gaps to advancing the state-of-the-art of small centrifugal compressor stages. As already discussed to some degree in the introduction, the key challenges in this context are well known—they both stem from reduction in diffuser radius and center around minimizing the impeller-diffuser interactions and designing efficient compact diffusers.

Strong impeller-diffuser interactions are expected at high pressure ratios and high impeller exit Mach numbers, and close spacing between the rotating impeller and stationary diffuser vanes. These interactions can have detrimental impact on the performance and structural integrity of both impeller blades and diffuser vanes. No clear guidelines exist on reducing these interactions and optimizing performance by controlling the impeller-diffuser gap, diffuser vane solidity or vane throat area. Other concepts that could be considered for reducing these interactions include low solidity diffuser vanes, three-dimensional designs with sweep, bow and lean applied to diffuser vanes, as well as end-wall contouring in the vaneless space—with the aim of reducing the peak Mach number. The intent is to address these through unsteady simulations.

Due to an overall trend towards reduction in size, compact diffusers are now expected to deliver the needed pressure recovery—however, efficiently diffusing the flow over a limited length remains a challenge. Overcoming this challenge will require a large amount of analytical and experimental work. Design concepts of interest for compact diffusers include splitter vanes and three-dimensional diffuser flowpath with diverging endwalls. Both of these require careful and tedious design optimization procedures. Finally, further reducing losses in the diffuser will require careful handling of the nonuniformity of time-averaged flow coming out of the impeller—by further optimizing the spacing between the impeller and diffuser.

Both of these challenges are further exacerbated by the limitations of CFD routinely used to support turbomachinery design. Steady (mixing-plane) simulations cannot account for unsteady interactions between impeller and diffuser. RANS turbulence models are of limited fidelity when it comes to predicting turbulent flow dominated by strong curvature of the flowpath and strong rotational effects, as well as to predicting turbulent separation in adverse pressure gradients, or, in other words—predicting the flow in diffusers. The intent in this design effort is an extensive use of RANS-based CFD analyses which will allow us to baseline the current state-of-the-art of RANS modeling in turbomachinery.

In conclusion, it is expected that the outcome of this research effort will also support the development of advanced engines for future rotorcraft applications through a clear identification of key technical challenges—including modeling limitations in current design and analysis tools. Finally, the acquisition of detailed experimental datasets will support future development and improvement of physical insight and the validation of design and analysis tools. The test instrumentation plan will be accommodated to allow the acquisition of data specifically focusing on impeller-diffuser interactions and the flow in the diffuser.

2.3 Design Strategy

The design activity centered on meeting the goal set outlined in the NASA solicitation—the design target was to increase efficiency at higher work factor, while also reducing the maximum diameter of the stage. To fit within the existing Small Engine Components Test Facility at GRC and to facilitate component re-use, certain key design parameters were fixed by UTRC, including impeller tip diameter, impeller rotational speed, and impeller inlet hub and shroud radii. This constraint put a particular emphasis on diffuser design, since it implied that the entire reduction in compressor size, to meet the D_{max}/D_2 requirement (< 1.45), would have to come from the reduction in diffuser size.

A design strategy of increasing the impeller work factor through backsweep reduction /optimization, while maintaining performance through advanced 3D aero design concepts was adopted. Another objective for applying 3D aero design concepts was to achieve uniform spanwise profiles at diffuser inlet, facilitating the improvements in diffuser and overall compressor performance.



Figure 1.—Photograph of NASA CC3 Reference Compressor.

Examples of advanced 3D aero design concepts aimed at increasing the performance that were considered include leading and trailing edge shaping, lean and bow, as well as sweep applied to both impeller blades and diffuser vanes, end-wall contouring, as well as alternative topologies with one or multiple splitter vanes in the diffuser and splitter blades in the impeller. An exit guide vane (EGV) row was also to be included in the new design to manage pressure recovery and aerodynamic loading at low radius ratio requirement. The impact of these 3D aero concepts was first to be studied for the reference NASA CC3 compressor, shown in Figure 1.

The NASA CC3 compressor was originally designed by Allison Engine Company as a high efficiency (peak total-total adiabatic efficiency of 85 percent), 1.66 kg/s compressor with a total pressure ratio of about 4. It was subsequently scaled to 4.54 kg/s (10 lbm/s) to provide a test article suitable for detailed diagnostics. The CC3 stage consists of an impeller with 15 main and 15 splitter blades with blunt, constant radius trailing edges, and a 24-bladed wedge diffuser that exits into an annular radial-to-axial bend. The impeller blades have constant backsweep angle of 50° from radial. The impeller running tip clearance was measured to be 0.1524 mm (0.006 in.) near the leading edge, 0.61 mm (0.024 in.) near mid-chord, and 0.203 mm (0.008 in.) near the exit. The diffuser leading edge is located at radius ratio (diffuser leading edge to impeller trailing edge) $R_3/R_2=1.078$ and exits at diffuser trailing edge to impeller trailing edge radius ratio $R_5/R_2=1.68$. The overall diameter of the stage is $D_{max}/D_2=1.87$.

3.0 Compressor Aerodynamic Design

3.1 Design Approach

As an initial assessment of design readiness of CFD tools, detailed comparisons were made to the existing data of the NASA CC3 compressor (Refs. 6 and 7), which was tested in both vaneless diffuser and stage configurations. These CFD simulations showed good agreement with data and provided high confidence in the ability to predict design point performance relatively well. Based on this successful validation of CFD tools for the reference NASA CC3 compressor, a CFD-based design approach was established that was to rely heavily on CFD for performance assessment of different design concepts.

A first step in the design process was the assessment of advanced 3D aero design concepts aimed at increasing the performance for the reference NASA CC3 compressor, and in particular the CC3 impeller. Concepts that were considered included leading and trailing edge shaping, lean and bow, as well as sweep,

and alternative topologies with multiple splitter blades in the impeller. Leading and trailing edge shaping was found to have a large impact on both performance and impeller exit profiles and was implemented in the new design. Several backsweep angles were then considered for the impeller design with the aim of increasing the impeller work factor and achieving more uniform impeller exit profiles. First, a nominal 20° backsweep design was considered, and then a nominal 30° backsweep design was adopted for the final design. Flowpath, blade incidence angles, and blade camber were also optimized in this process.

In parallel, diffuser design proceeded by using the reference CC3 impeller. In order to reduce the maximum diameter of the compressor while increasing overall total-to-static efficiency, alternative diffuser topologies were considered. In particular, splitter vane design showed best results. After completing the new impeller design, final iterations on the diffuser design were conducted using the newly designed impeller.

An exit guide vane (EGV) row was also included in the new design to manage pressure recovery and aerodynamic loading at low radius ratio requirement. EGVs were first studied as an isolated row and were designed to reduce exit Mach number and swirl angle—for a given diffuser exit profile. Radial-to-axial bend was also optimized to achieve the best performance, and a clocking analysis was performed for the final positioning of the EGVs.

Purpose-specific tools were adopted to improve throughput. These included meanline tools from UTC's business units, blade shaping tools such as ANSYS's Blade Modeler and UTRC's Cblade, and CFD grid generation tool WAND and CFD solver LEO from ADS.

Three-dimensional RANS CFD simulations with LEO were used extensively to evaluate the impact of design modifications: over 400 steady state computations were performed for various design configurations that consisted of impeller with a vaneless diffuser, impeller with a vaned diffuser, impeller with a vaned diffuser and EGV row. In these steady simulations, mixing plane interface was used between rotating and stationary rows. Limited unsteady simulations were performed both for CC3 and an intermediate new design and they showed minimal difference with respect to steady simulations.

3.2 Design Process Readiness

As an initial assessment of CFD-based design process, comparisons were made to the existing data of the NASA CC3 compressor (Refs. 6 and 7), which was tested in both vaneless diffuser and stage configurations. For the vaneless diffuser computations, the computational domain extends to approximately 1.18 * impeller tip radius. For the full stage, the computational domain includes the annular radial-to-axial bend and is terminated downstream of the bend.

The commercial solver Code LEO with rapid grid generation Code WAND (Figure 2), provided by AeroDynamic Solutions, Inc., was selected as a CFD tool. The structured grid is an OHHHH topology with distance to the first grid point from the wall set such that the nondimensional wall distance (y^+) is near 1 to capture near-wall effects.

Code LEO is a density-based finite volume CFD code (Ref. 8) that provides numerical solutions on either a multi-block structured mesh or an unstructured mesh; for the present study, structured meshes were used. Code LEO also uses a multi-grid scheme for convergence acceleration on structured meshes. Wilcox's 1998 $k-\omega$ turbulence model (Ref. 9) is implemented in Code LEO, with the production terms based on vorticity. For the present study, the wall integration option is used near solid surfaces.

Grid sensitivity studies had previously been performed by AeroDynamic Solutions for the CC3 configuration; for cases reported here, a grid count of about half-a-million cells per row was utilized. For CC3 this resulted in a grid with about one million cells, for the new compressor design (that also included EGVs) the final grid was with about 1.5 million cells. Impeller tip clearances used for CC3 were chosen to match the measured values—variable clearance was used (0.006 in. at LE, 0.024 at mid-chord, and 0.008 at TE). For the new compressor, a constant tip clearance of 0.012 in. was used throughout the design process, and in post-test CFD analyses.

All steady-state CFD models of stage configurations used a mixing plane interface between impeller and diffuser rows. Unsteady time-accurate CFD analyses use a sliding interface between impeller and diffuser rows. Assumed inlet conditions for all LEO simulations include standard day conditions, 1 percent turbulence intensity and zero inlet swirl. Solid surfaces are treated as adiabatic. The working fluid is air with constant specific heat ratio of $\gamma = 1.395$.

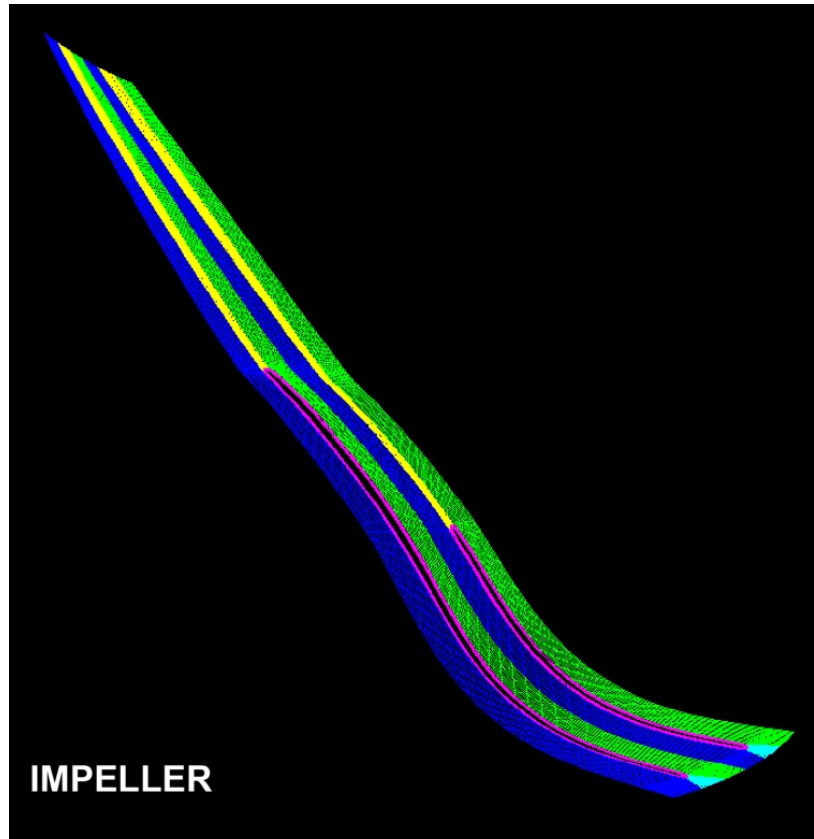


Figure 2.—An example of WAND computational grid for a centrifugal impeller.

3.2.1 CFD Validation for CC3 Compressor

CFD results computed for CC3 compressor are compared to data in Figure 3 and Figure 4. For the impeller with vaneless diffuser, shown in Figure 3, the overall trends of the CFD predictions show good agreement with rig data, considering that the CFD model uses the same running tip clearance for all operating speeds. At 100 percent design speed and inlet corrected flow rate of 10 lbm/sec, steady-state CFD over predicts total-to-total efficiency by 0.9 percentage points and the choke mass flow by less than 1 percent. At low flow, the CFD results include the last stable point as computed using steady simulations.

For the stage, Figure 4, at 100 percent design speed and corrected flow rate of 10 lbm/sec, steady-state CFD tends to over predict total pressure ratio by 3 percent, temperature ratio by 0.3 percent (not shown), total-to-total adiabatic efficiency at design condition by 0.4 pt, and choke mass flow by 4 percent. Unsteady simulations of a 120° sector, consisting of 5 impeller main/splitter blade pairs and 8 diffuser vanes, using a sliding interface and 3000 time steps per revolution (equivalently, 100 time steps per trailing edge pitch). Simulations were run for 2 to 4 revolutions for cyclic convergence. Results of the unsteady simulation compared to data are shown in Figure 4, where it is seen that the predicted efficiency near design point and stall is closer to the measured data, but the choke flow is still over predicted. Overall, these simulations gave us high confidence in our ability to predict the design point performance very well with steady, RANS/mixing-plane codes.

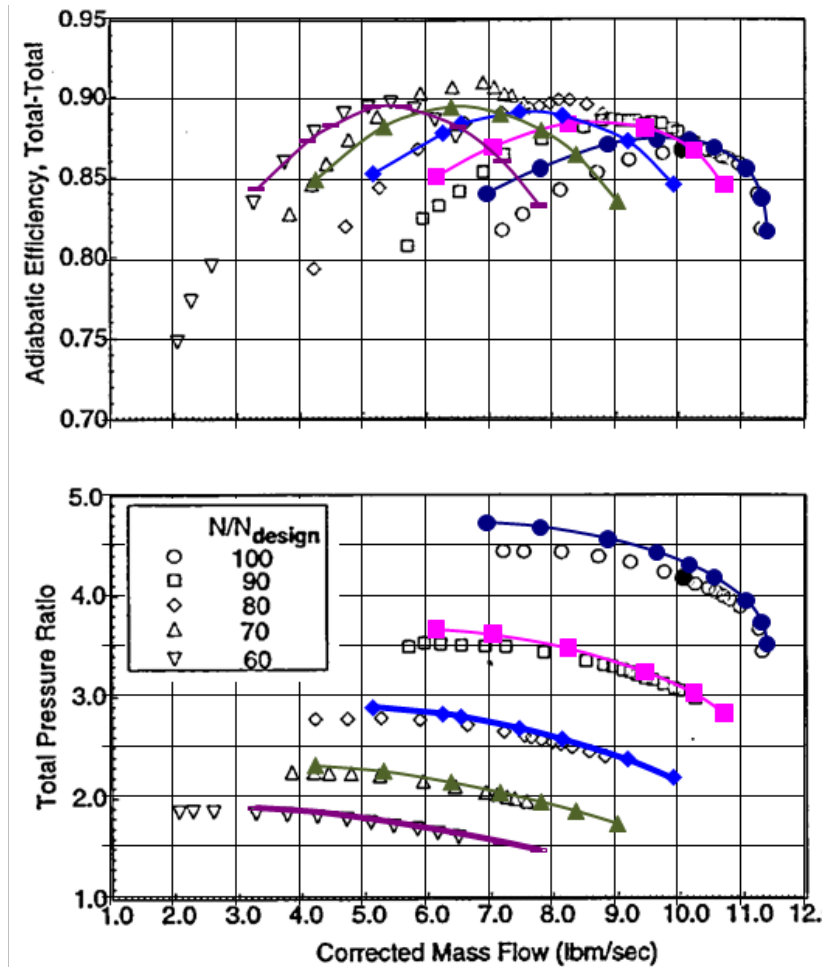


Figure 3.—Performance map of CC3 impeller with vaneless diffuser, measurements (open symbols) versus steady-state CFD results (closed symbols).

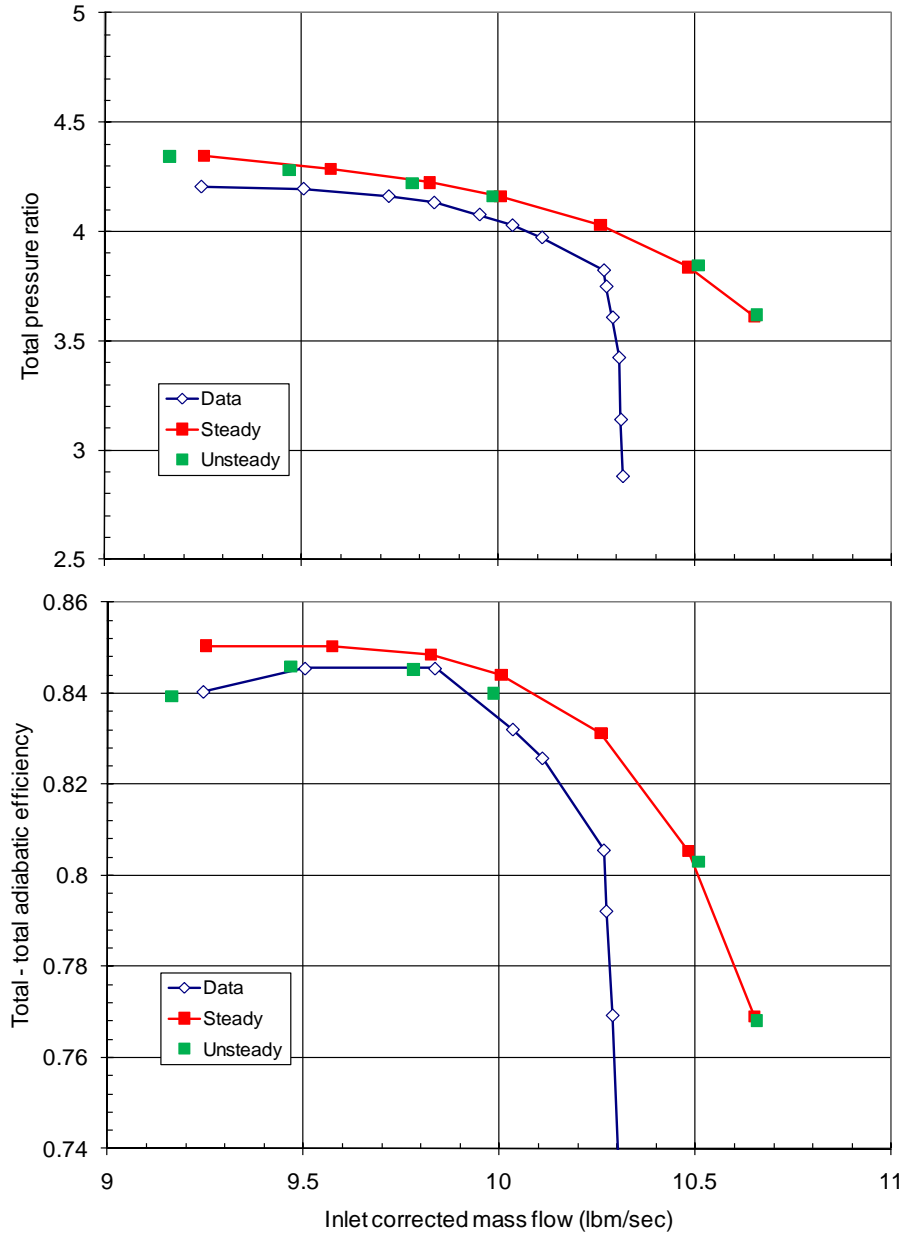


Figure 4.—100 percent N_c design corrected speed compressor map for CC3 stage, measurements (open symbols) versus CFD steady-state (red) and unsteady (green) results.

3.2.2 Detailed Analysis of CFD Results for CC3 Compressor

Following the initial calculations, more detailed inspection of the calculated flow field was conducted in order to illustrate dominant flow physics. Figure 5 shows contours of entropy generation at different locations through the impeller, at the design operating condition. Dominant losses develop in the impeller exducer passage and collect along the shroud. Circumferentially averaged exit profiles for the vaneless diffuser configuration computed at the design operating condition, shown in Figure 6, indicate that the flow is relatively weak at the shroud side, as evidenced by the near-zero radial velocity, in general agreement with measurements (Ref. 7). In the stage computations at design conditions, the velocity vectors in the diffuser passage in the vicinity of the hub, shown in Figure 7, illustrate the presence of separation on the pressure side of the diffuser vane.

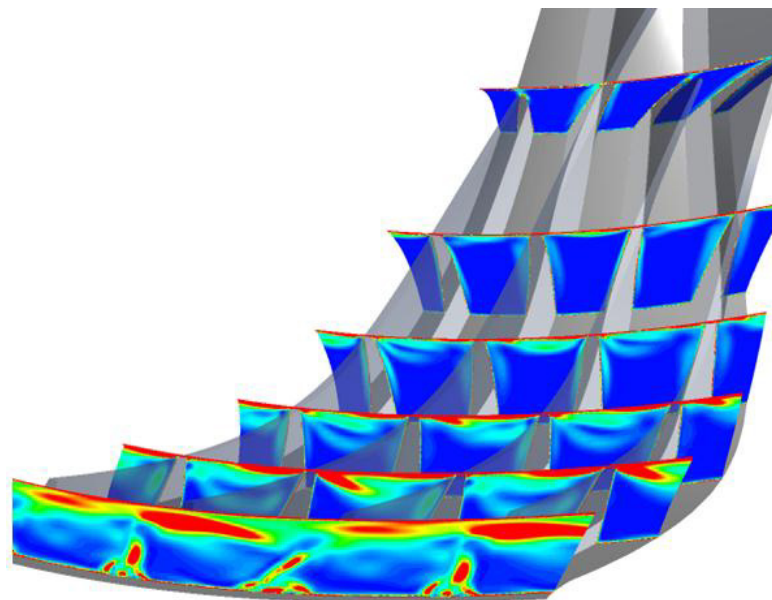


Figure 5.—Contours of entropy generation for the CC3 impeller at design condition of inlet corrected flow rate of 10 lbm/s at 100 percent N_c .

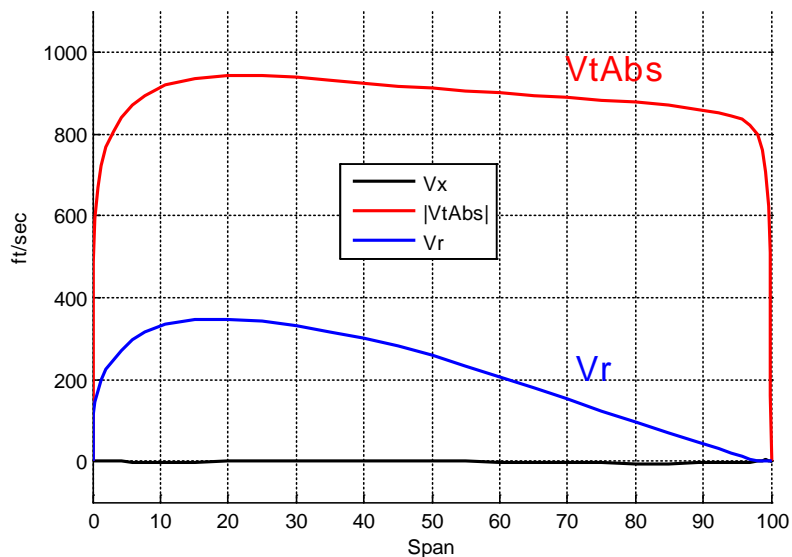


Figure 6.—CC3 impeller, circumferentially averaged velocity profiles at radial location 1.18*impeller tip radius, about 2.5 blade widths downstream of the trailing edge, at design condition of inlet corrected flow rate of 10 lbm/s at 100 percent N_c .

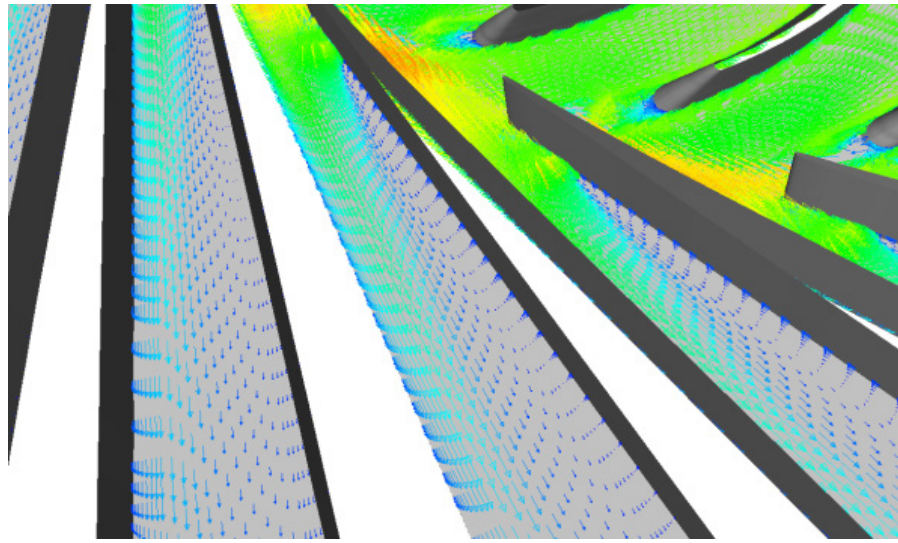


Figure 7.—Velocity vectors in the CC3 diffuser passage at design condition of inlet corrected flow rate of 10 lbm/s at 100 percent N_c .

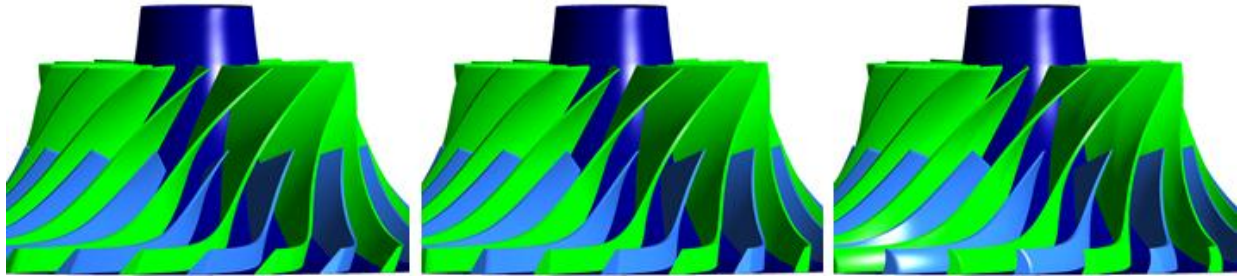


Figure 8.—Left to right: Baseline CC3 impeller, CC3 impeller with lean applied, CC3 impeller with bow applied.

3.3 Impeller Design

3.3.1 3D Aero Concepts

In order to address the weak shroud side flow, a wide range of impeller sensitivity analyses was performed. Three-dimensional aerodynamic concepts that have found success in axial turbomachinery components were applied to the CC3 geometry in order to identify opportunities for improvement. The concepts that were assessed include impeller blade lean, impeller blade bow, impeller leading edge shape and impeller trailing edge shape. Examples of the modified impeller geometries are shown in Figure 8.

For example, blade lean provided 1 percent improvement in pressure ratio, with minimal impact to stage efficiency—an increase of 0.1 percentage points. Similarly, an attempt to bow the blade provided 1.8 percent increase in pressure ratio, with a 0.1 pt decrease in stage efficiency. An impeller with two splitters gave a 0.2 percent increase in pressure ratio, and a 0.1 pt decrease in stage efficiency. Adding an elliptic leading edge to impeller blades showed bigger impact on efficiency—an increase of 0.5 pt was observed—with pressure ratio increasing for about 0.2 percent. Finally, the shaping of trailing edges was found to have the strongest impact on stage efficiency. With elliptic trailing edges an increase of stage efficiency of 0.75 pt was observed, together with a 0.5 percent increase in pressure ratio. Rounded trailing edges showed even more benefit—an increase of 1 pt in stage efficiency and an increase of 1 percent in pressure ratio.

3.3.2 Impeller Trailing Edge Shaping—Assessment of Impact for CC3

Impeller trailing edge shaping was found to have a strong effect on loading, efficiency, and exit profiles, in addition to maximum capacity. This was observed with the CC3 compressor by replacing the existing constant radius trailing edge with a rounded trailing edge, while maintaining the same maximum radius, during the grid generation process. The modified impeller, when combined with a vaneless diffuser, was found to have noticeably higher total pressure ratio and efficiency, as seen in Figure 9. Also, the circumferentially averaged exit profiles for the impeller with rounded trailing edge were found to have less evidence of separation, Figure 10.

The reason for the significant increase in pressure rise is specific to the way in which the trailing edge was rounded and can be explained by referring to Figure 11. In this instance, when moving from constant radius to rounded trailing edge, material is preferentially removed from the suction side of the blade while the pressure side remains largely unchanged. This results in less blade lean and also reduces the backsweep angle; reduced backsweep angle can be shown via the Euler work equation to raise the pressure rise through the impeller (Ref. 5). Also, the presence of more uniform exit velocity profiles is an indication that secondary flows have been reduced through the impeller passage.

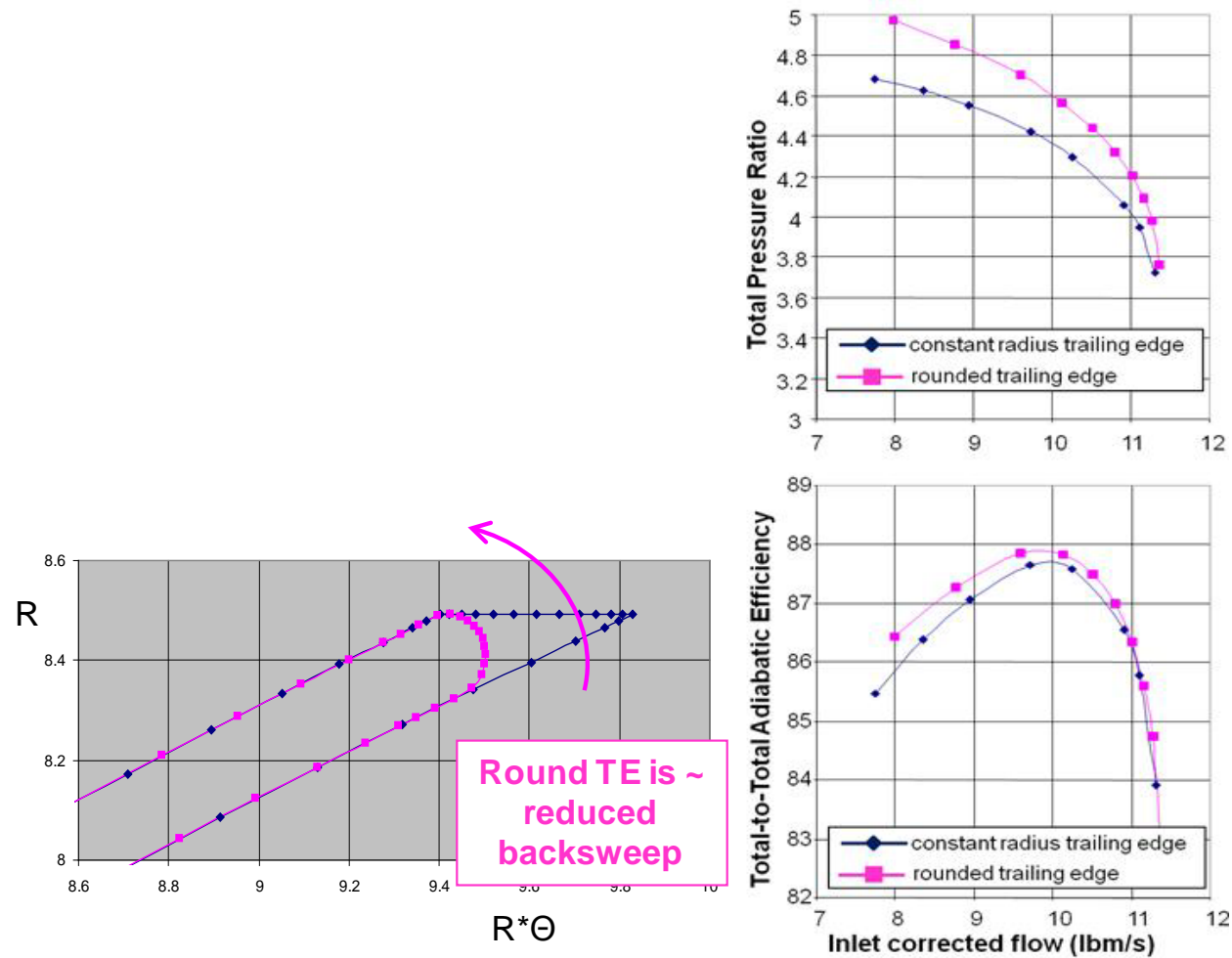


Figure 9.—Rounded versus constant radius trailing edge and CFD predicted performance map of CC3 impeller at 100 percent N_c .

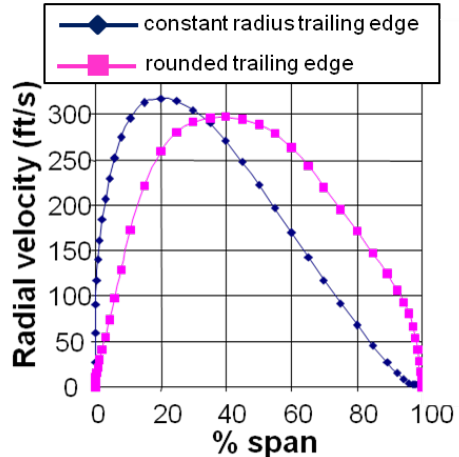


Figure 10.—CFD predicted radial velocity at CC3 impeller exit ($R/R_2 = 1.18$) for impeller and vaneless diffuser. Operating condition is 10 lbm/s inlet corrected flow at 100 percent N_c .

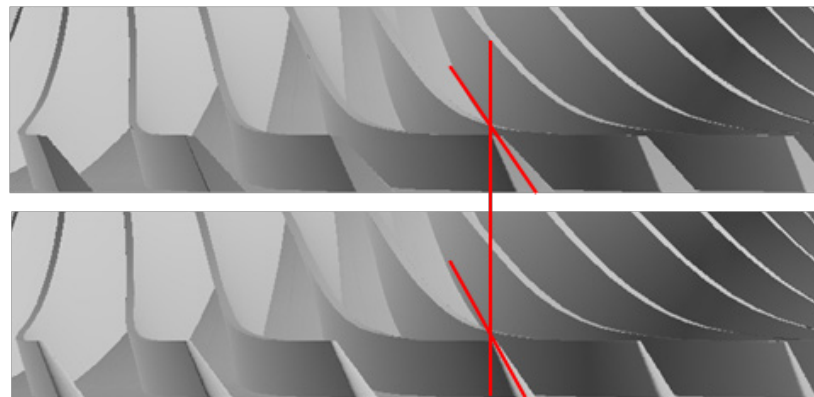


Figure 11.—Top: CC3 impeller with constant radius trailing edge; Bottom: CC3 impeller with rounded trailing edge.

3.4 Impeller Blading and Flowpath Design

Given the results of the scoping studies, then, the design strategy was to target uniform impeller exit profiles, via backsweep distributions, impeller blade shaping, and flowpath shaping, in order to provide uniform entry profiles to the two-dimensional diffuser vanes, and to reduce secondary flows. Concurrently, the overall design goal was to increase the work factor (via backsweep reduction) and efficiency while maintaining stall margin. This strategy, if executed successfully, can decrease specific fuel consumption by increasing stage pressure ratio or by decreasing the required number of axial stages in an axial-centrifugal configuration.

Meanline sensitivity studies were performed to assess the impact of changes in principal blade dimensions on pressure ratio, efficiency, and choke mass flow rate, assuming a fixed impeller diameter and operating speed. The meanline slip factor was calibrated to the CC3 rig data, Figure 12. Examples of the meanline study output are shown in Figure 13 and Figure 14.

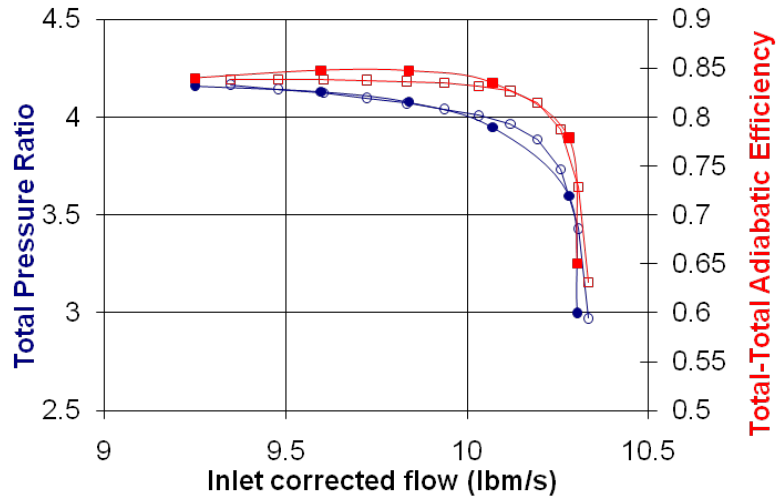


Figure 12.—Results of calibration of meanline (solid symbols) to CC3 data (open symbols), prior to geometry sensitivity studies. Total pressure ratio is shown in blue, and total-to-total adiabatic efficiency in red; results for 100 percent N_c .

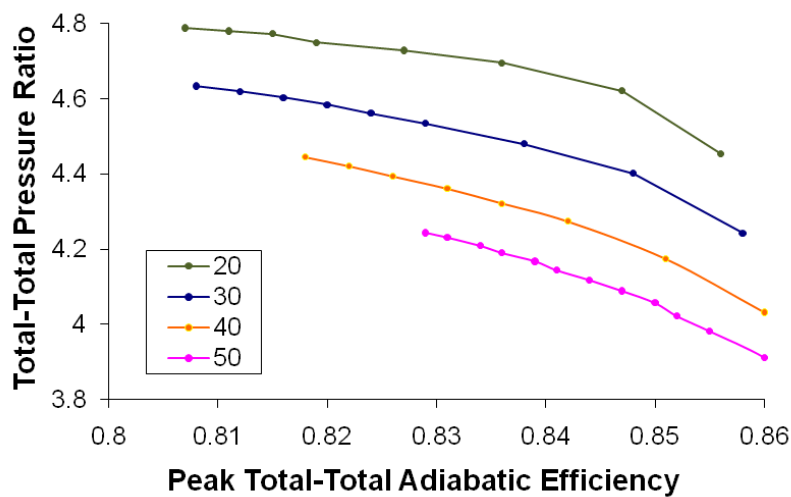


Figure 13.—Meanline study prediction of peak pressure ratio and efficiency for varying exit blade height (blade height increases from right to left), and impeller backsweep angles (from 20 to 50°), at 100 percent N_c .

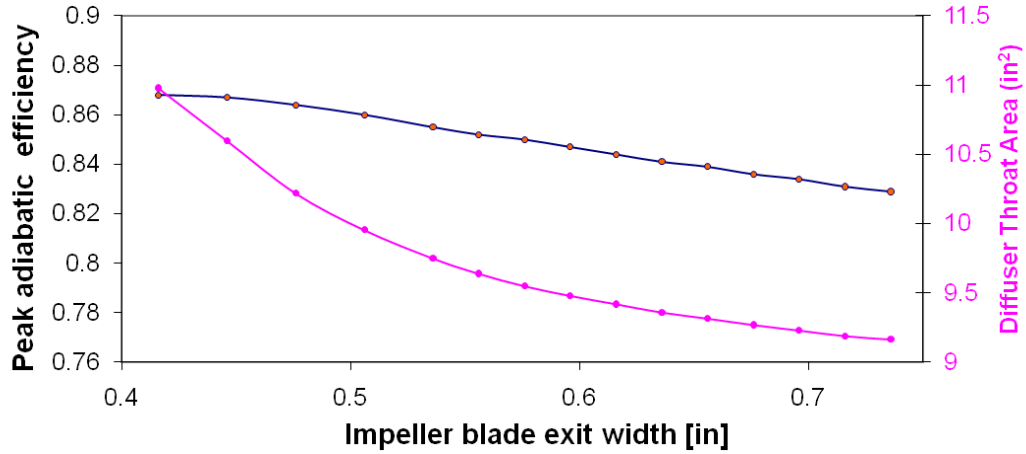


Figure 14.—Meanline study prediction of peak efficiency and diffuser throat area for varying impeller blade exit width, for fixed impeller backsweep angle (of 20°), at 100 percent N_c .

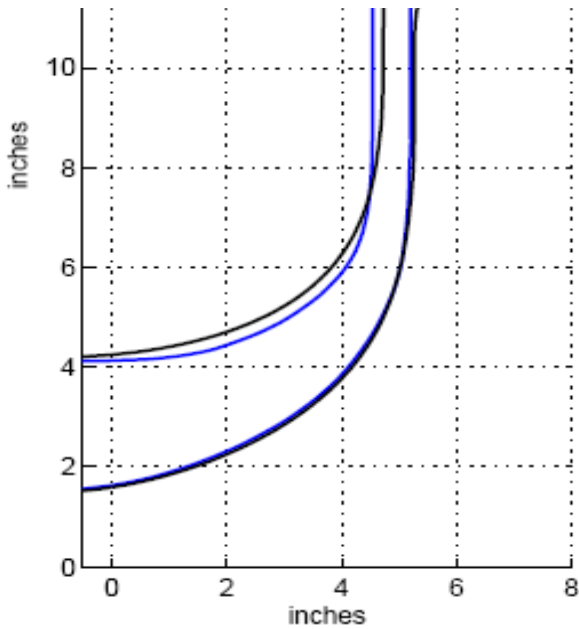


Figure 15.—Comparison of flowpath for CC3 (blue) and HECC impeller design studies (black).

Following the meanline study, detailed impeller blade design began in earnest. A parent impeller with nominal 20° backsweep was selected for study (actual spanwise variation was from 22° to 30° from hub to shroud). Progressively higher backsweep from hub to shroud removes excessively high loads from outer portions of the blade. A series of local blade shape modifications was performed, and the impact of each on overall performance, blade loading, and impeller exit profiles was assessed using CFD. Each impeller was paired with the same vaneless diffuser which extended up to $1.18 \times$ impeller tip diameter (keeping the same computational domain as in the initial CC3 simulations); the meridional flowpath can be seen in Figure 15.

The performance results for the configurations analyzed in this study are shown in Figure 16. It is interesting to note that for this backsweep angle, the modification of the trailing edge has the opposite effect to the effect seen on the CC3 impeller, i.e. rounding the trailing edge reduces the pressure ratio. The blade metal angle is more radial to begin with, and so the effect of rounding is more evenly

distributed to pressure and suction side with no change to lean, Figure 17. Nevertheless, this modification of the trailing edge leads to an increase of peak efficiency of 0.4 pt. Similarly, a change in the impeller incidence further increased the peak efficiency, but also increases the flow capacity by about 4 percent. The best of these nominal 20° backsweep designs (that included all the modifications presented in Figure 16, except the shroud height modification, and is shown in magenta color) was confirmed to have achieved the target two-dimensional exit flowfield. The exit radial velocity is more uniform, especially at the shroud side (span=100 percent), which leads to lower shroud-side endwall losses.

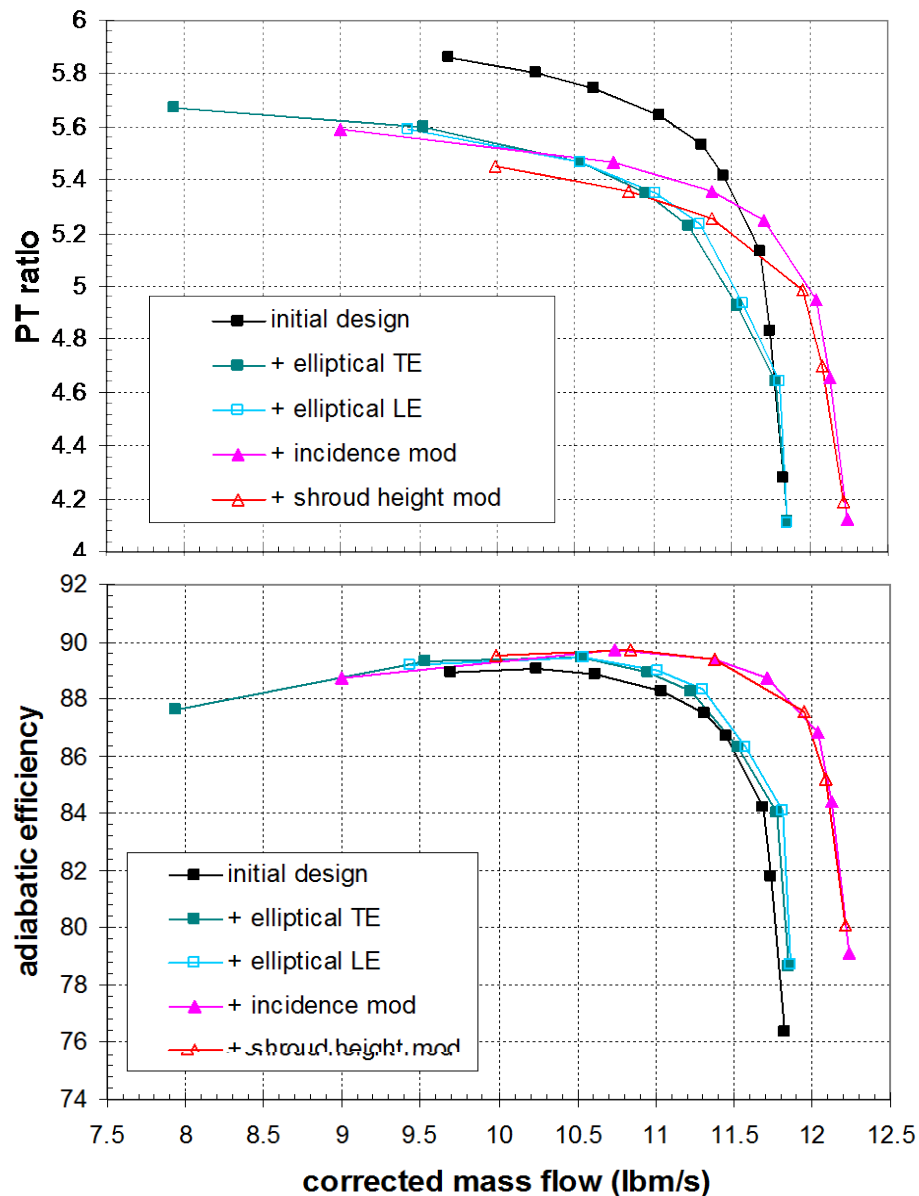


Figure 16.—CFD prediction, 100 percent design speed compressor map for parent 20° backsweep impeller (initial design), followed by sequential additions of geometry modifications, at 100 percent N_c .

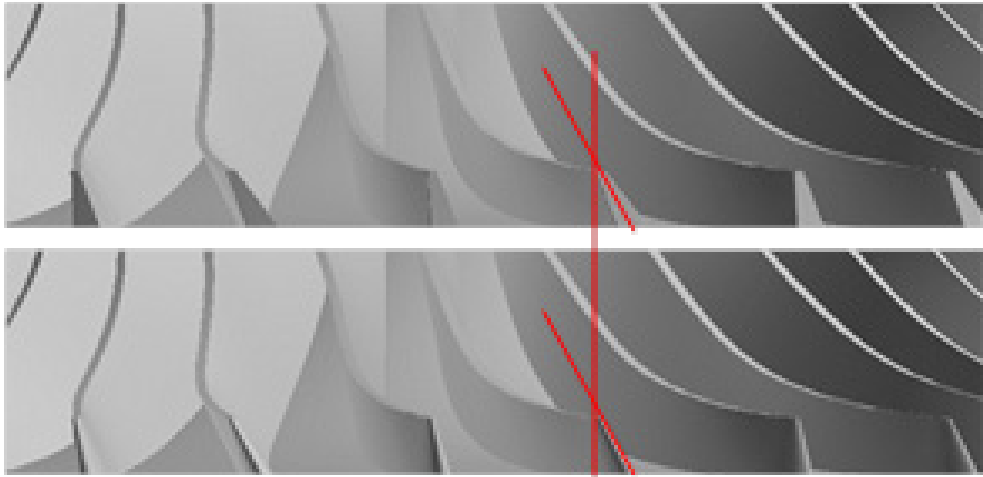


Figure 17.—Top: Parent 20° backsweep impeller with constant radius trailing edge. Bottom: Parent 20° backsweep impeller with rounded trailing edge.

3.4.1 30° Backsweep

The parent 20° backsweep impeller and its derivatives all are predicted to have excess pressure ratio capability, suggesting that the backsweep could be increased to lower pressure ratio and increase stability margin (Ref. 5). This trade of pressure ratio versus stability margin is also more consistent with the NASA goal set and product demand. The best of the 20° backsweep configurations (from Figure 16) was then modified by increasing the nominal backsweep to 30° (spanwise variation was now 32° to 42°). A detailed comparison of the new impeller geometry to CC3 impeller is shown in Figure 18, CC3 has a uniform spanwise distribution of the metal angle at the trailing edge of approximately 47°. Compared to CC3 impeller, the camber has been brought forward in the new design, while the thickness distribution has been maintained.

Performance results comparing the parent 20° backsweep impeller and the new 30° backsweep design to NASA CC3 impeller are shown in Figure 19. The reduction in pressure ratio associated with changing from 20° to 30° backsweep is accompanied by an increase in peak efficiency of about 0.7 pt, and a further increase of flow capacity by about 2.5 percent. Note that for the 30 backsweep design this speedline extends only to about 10 lbm/s. At the same time, compared to parent 20° backsweep design, the peak efficiency shifts further to the right—to flow rates exceeding 11 lbm/s.

Figure 20 presents the same comparison of 20° backsweep design and 30° backsweep design to the original CC3 impeller, but now for total-to-static pressure ratio and total-to-static adiabatic efficiency. The new 30° backsweep design maintains the same pressure ratio as the parent 20° design, but the efficiency is now improved. New 30° backsweep impeller matches CC3 adiabatic total-to-static efficiency, but achieves higher total-to-static pressure ratio. With a good diffuser design, this impeller has a potential to significantly surpass the performance of the CC3 impeller.

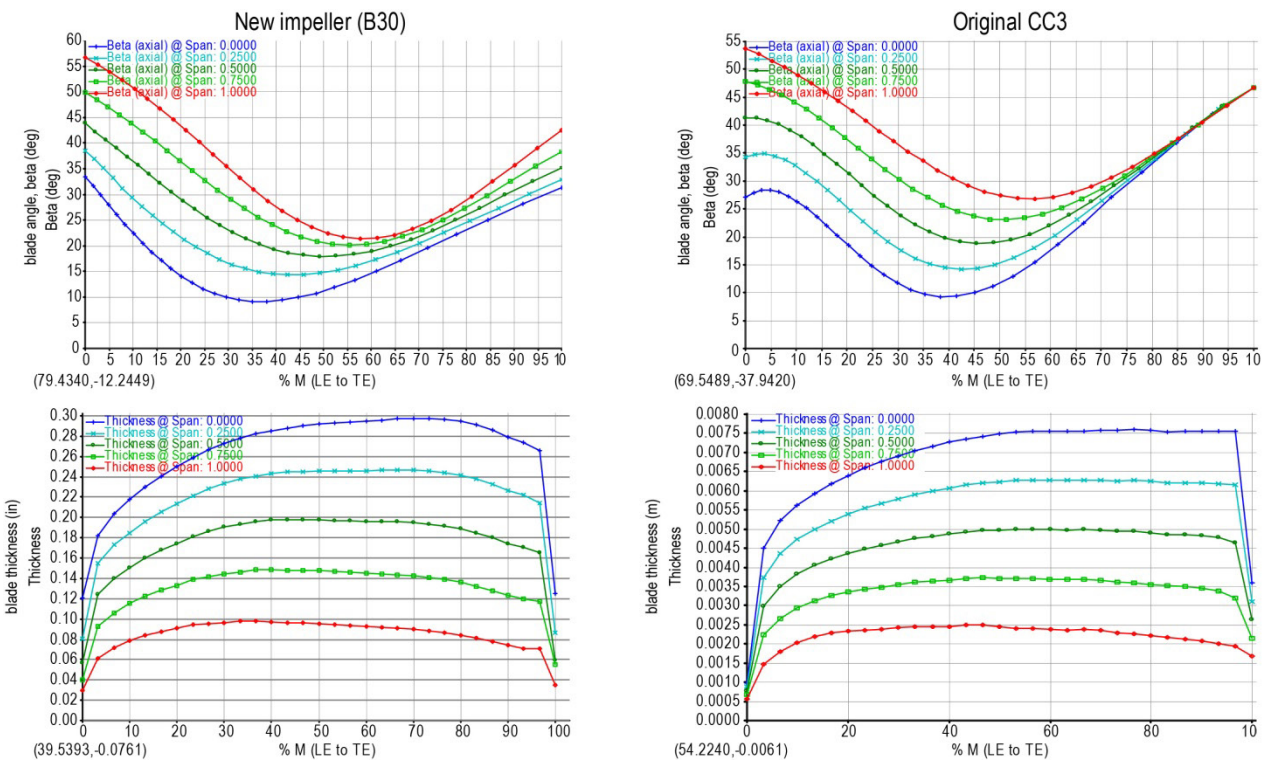


Figure 18.—Geometric description for the final 30° backsweep impeller design compared to NASA CC3 impeller (Ref 10). Blade angles are shown in top figures, blade thickness in bottom figures. Five spanwise profiles are included (0, 25, 50, 75, and 100 percent span).

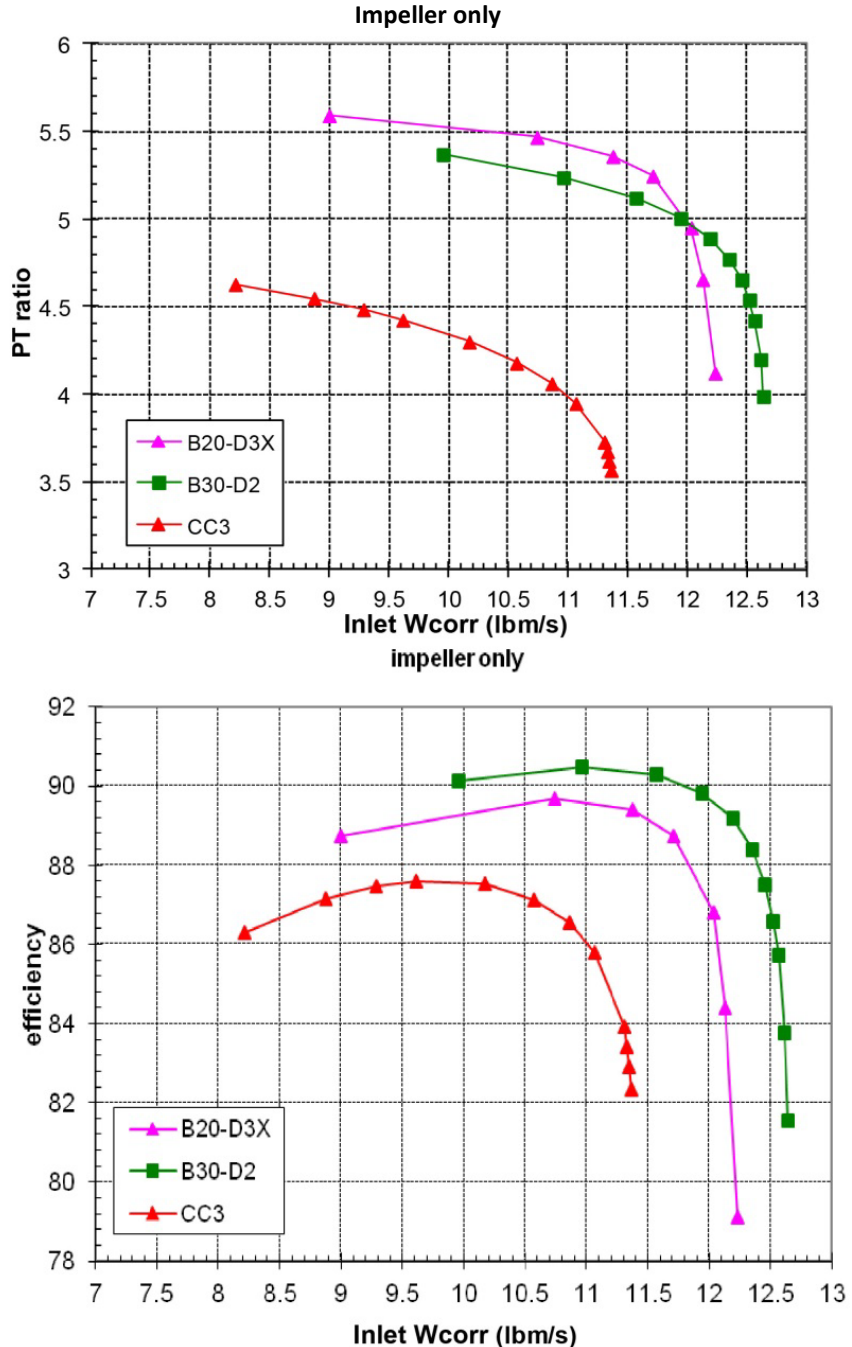


Figure 19.—Impeller-only performance comparison of the parent 20° backswept impeller (B20) compared to final 30° backswept impeller design (B30) and the original CC3 impeller; total pressure ratio (top), adiabatic efficiency, total-to-total (bottom), at 100 percent N_c .

CFD results also show that more uniform 2D exit profiles are maintained with the new 30° backswept design; they are compared to NASA CC3 impeller exit profiles in Figure 21. A comparison of the surface pressure for the final 30° backswept design to the CC3 design at different spanwise stations is shown as isentropic Mach number versus normalized chord length in Figure 22, where it is seen that the new design shifts loading aft, and that the flow is accelerating over the last part of the blade, which reduces the likelihood of separation so often found in the exducer area.

At this point in the design process, an analysis of the impact of blade count on the performance of the final design was conducted showing potential for further efficiency gains (of about 0.4 pt). Similarly, a study with reduced speed (to 93 percent) pointed to opportunities for additional efficiency gains (of about 0.6 pt). Both of these were presented at the preliminary design review, but the final decision was to continue with the original blade count and nominal speed.

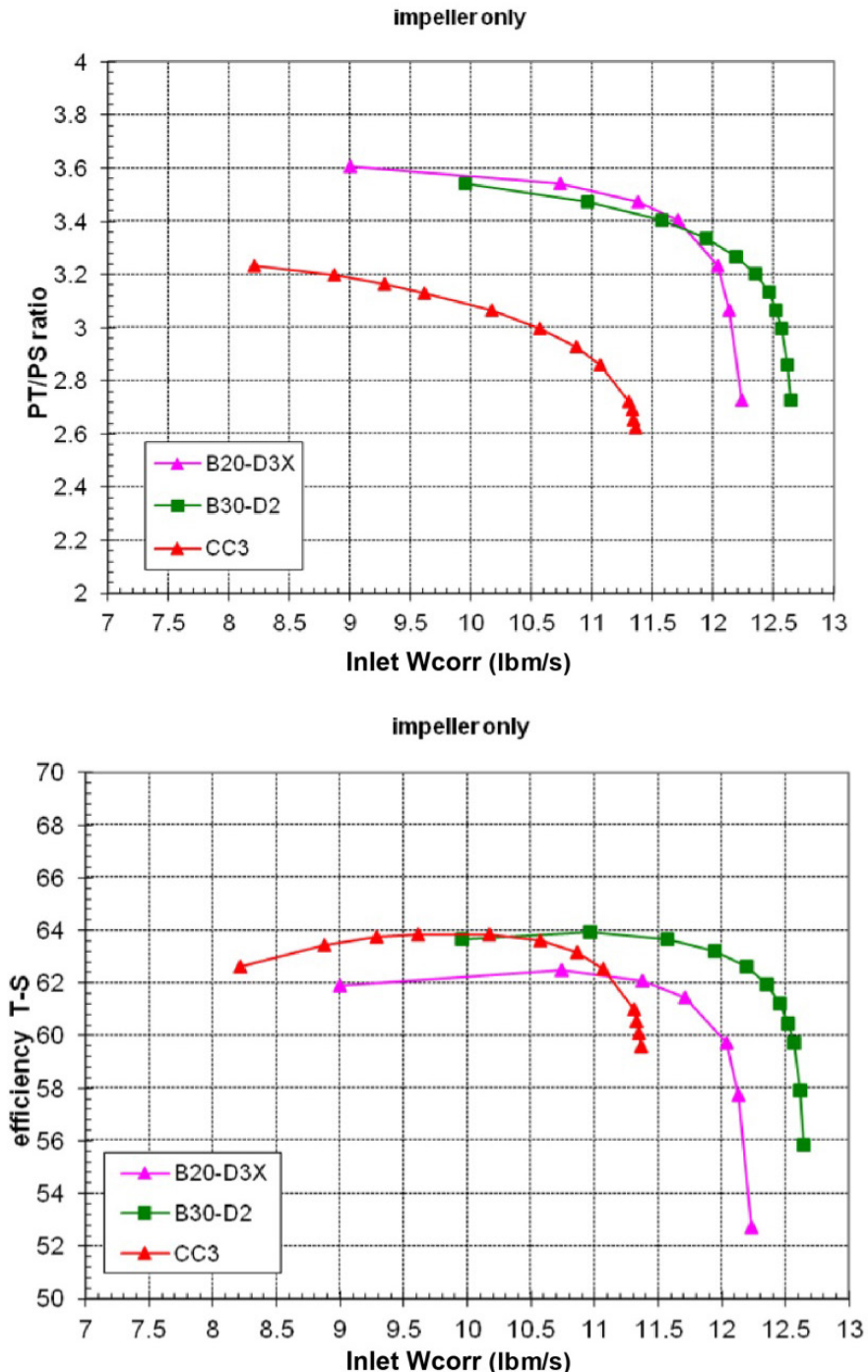


Figure 20.—Impeller-only performance comparison of the parent 20° backsweep impeller (B20) compared to final 30° backsweep impeller design (B30) and the original CC3 impeller; total-to-static pressure ratio (top), adiabatic efficiency, total-to-static (bottom), at 100 percent N_c .

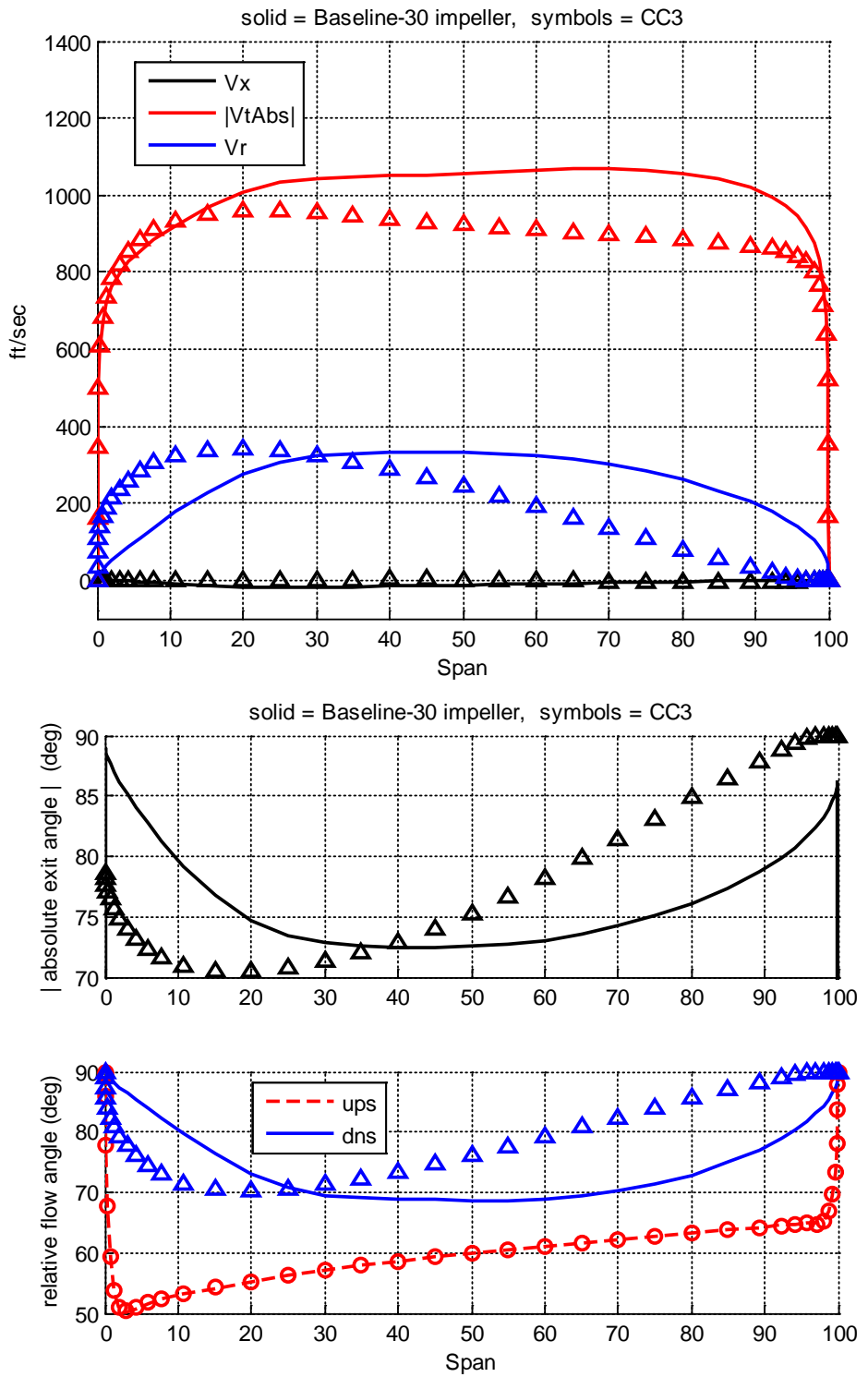


Figure 21.—Impeller blade exit circumferentially averaged profiles. Open symbols: CC3. Solid line: Final 30° backsweep impeller design. Results for design flow rate, at 100 percent N_c .

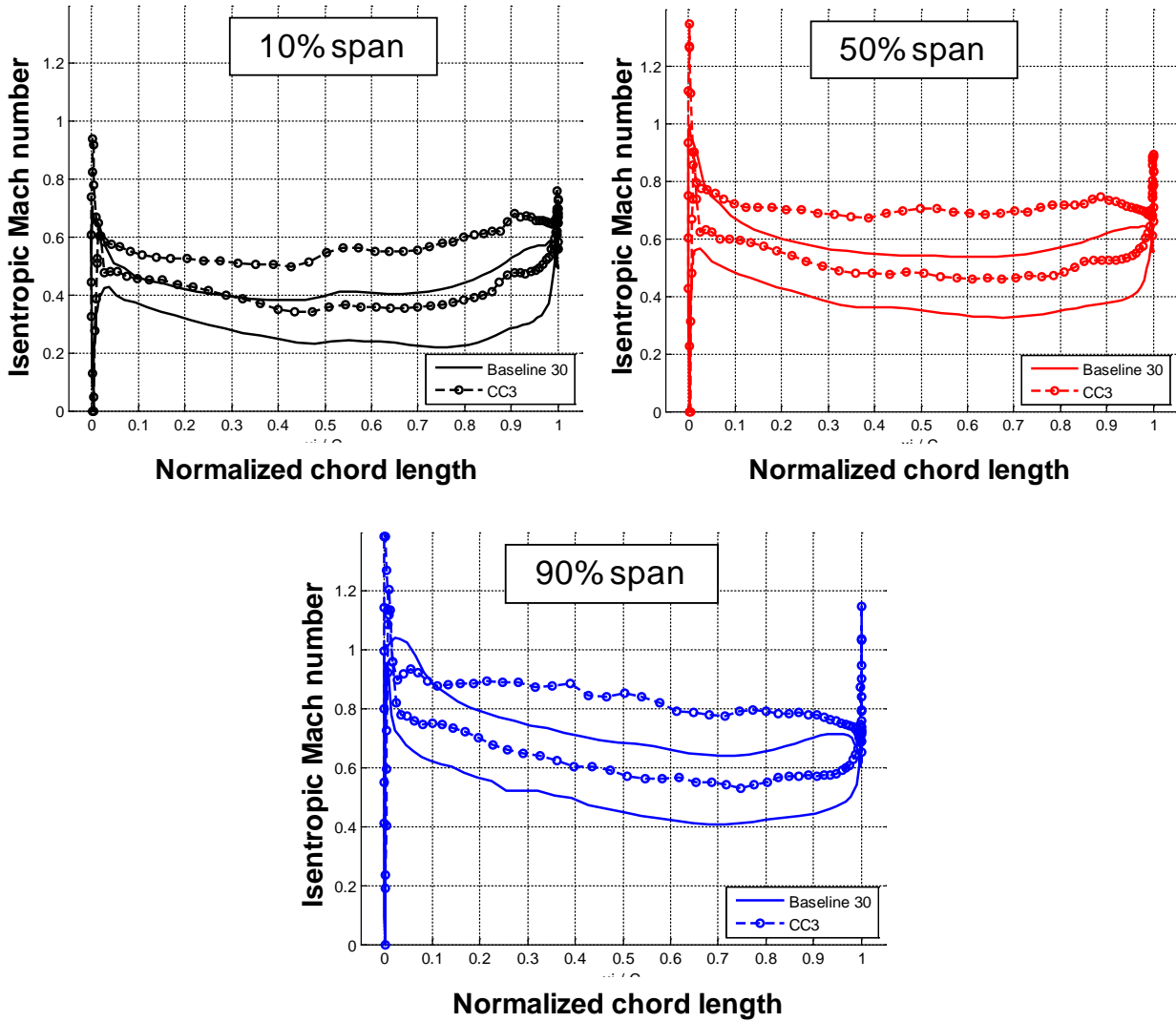


Figure 22.—Isentropic Mach number versus normalized chord length at varying spanwise locations for NASA CC3 impeller (symbols) and final 30° backsweep impeller design (solid). Results for design flow rate, at 100 percent N_c .

3.5 Diffuser Design

In order to reduce the maximum diameter of the compressor while increasing overall total-to-static efficiency, alternative topologies to the wedge diffuser were considered. A view of the target flowpath is shown in Figure 23; the reduction of maximum diameter significantly lowers the attainable pressure recovery in this setup. Careful tailoring of the diffuser geometry is needed to maximize the pressure recovery.

3.5.1 3D Aero Concepts

Similarly to the analysis conducted for the impeller, 3D aero concepts were first applied to the diffuser wedges in the NASA CC3 reference compressor to determine sensitivities. Examples of these include vane sweep, vane lean, vane elliptic leading edges, a reduction in the vane leading edge radius, as well as a vane leading edge fillet on the shroud (100 mils). All were assessed using steady simulations with a mixing plane between impeller and diffuser.

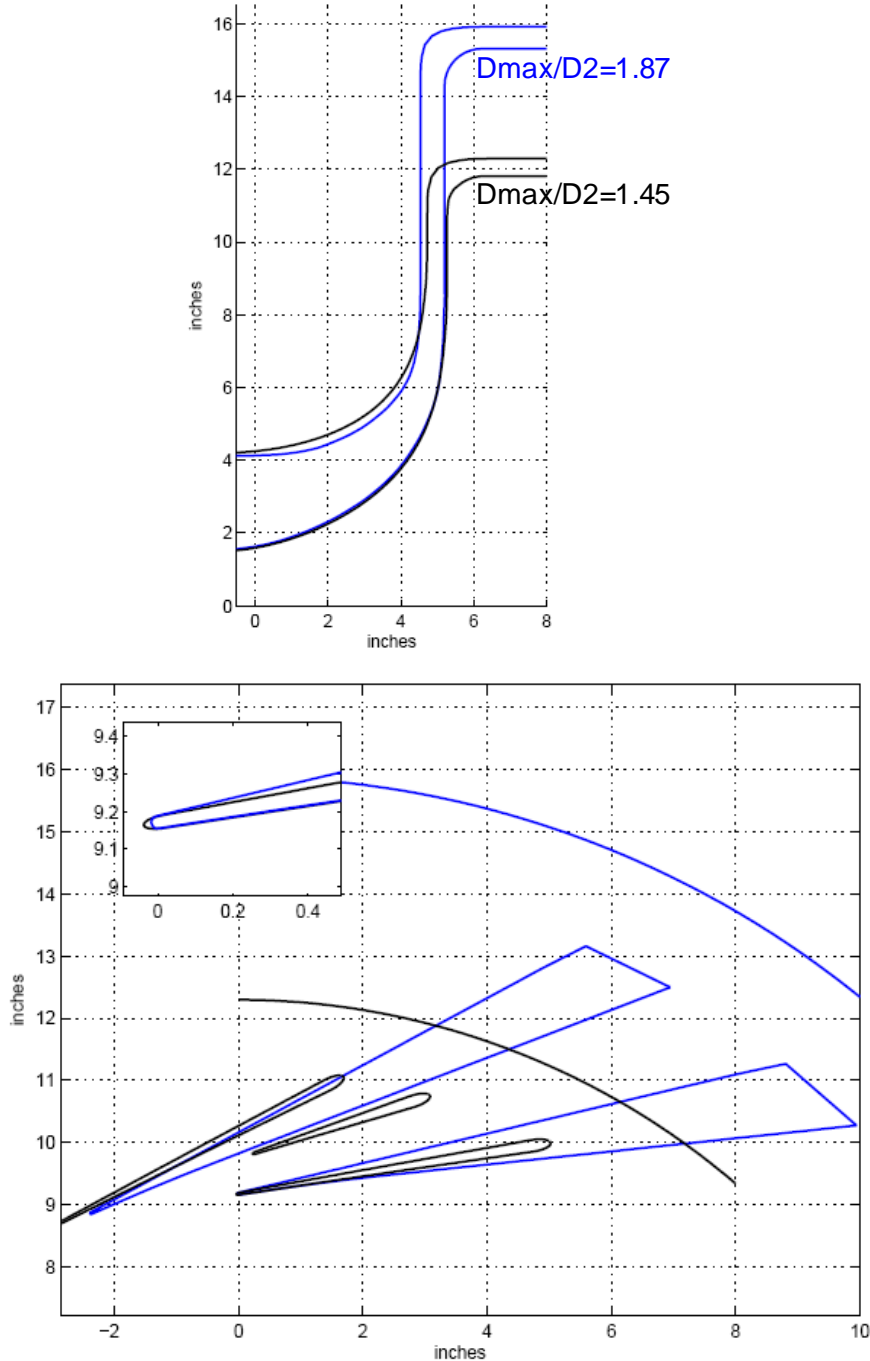


Figure 23.—Original (blue) and redesigned (black) flowpaths, showing 23 percent reduction in stage maximum diameter. Reducing the exit diameter limits the amount of diffusion available.

Vane sweep was found to have an overall neutral impact on the stage performance—with virtually no change in pressure ratio and stage efficiency. Adding vane lean lead to a decrease in pressure ratio of 0.1 percent and a decrease in stage efficiency of 0.2 percentage points. The vane leading edge fillet on the shroud caused a strong detrimental impact with a decrease in pressure ratio of about 0.5 percent and a decrease in stage efficiency of 0.5 pt. Shaping of the vane leading edges was most beneficial; an elliptic leading edge led to a 0.2 percent increase in pressure ratio, as well as to 1.0 point increase in stage

efficiency. Vane leading edge radius reduction had a similar effect: 0.3 percent increase in pressure ratio and 1.2 pt increase in stage efficiency. While shaping of the leading edges was clearly something of interest and would be incorporated in the new design, other concepts did not provide huge performance benefits. The need to maximize pressure recovery in compact diffusers thus lead us to consider alternative diffuser topologies.

3.5.2 Diffuser Topology

As a first step, alternative topologies were considered at the same maximum diameter as the original CC3 together with CC3 impeller, in order to identify the highest recovery layout, as shown in Figure 24. Vane diffusers with splitters were found to maintain total-to-static efficiency with 5 percent increased pressure recovery compared to the original CC3 wedges (0.822 against 0.783), and were selected to be considered for the final reduced diameter design. At this stage in the design process, CC3 impeller was still used to study the diffuser configuration of choice (vanes with splitters) for reduced diameter ratios. First, diameter ratio was reduced to 1.71 for the configuration with splitters (18 pairs of vanes), and similar levels of pressure recovery were still maintained—with $C_p = (p_{out} - p_{in}) / (p_{T,in} - p_{in})$ of 0.818.

At this point, the new impeller design was finalized, and the CFD studies of diffuser geometries were now conducted with this impeller in place of CC3 impeller. These CFD analyses now became the first analyses for the new stage. The same diffuser considered above with the CC3 impeller, with the diameter ratio of 1.71, now produced a pressure recovery C_p of 0.77—for the new impeller with a higher pressure ratio and higher exit Mach number. The next step was to further shrink the diffuser outer diameter which resulted in a new design—still with splitter vanes but now with 20 pairs of vanes—with the target diameter ratio of 1.45. CFD predictions yielded here a recovery of C_p of approximately 0.70.

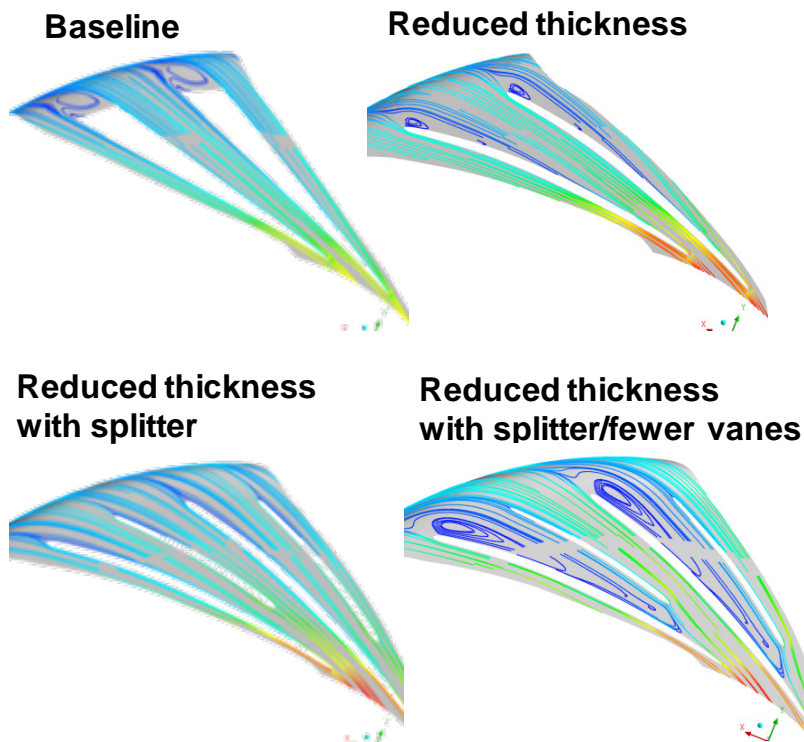


Figure 24.—Examples of topologies considered at same maximum diameter as original CC3 to define the configuration with highest recovery. Configuration “Reduced thickness with splitter” (with 18 vanes) achieves C_p of 0.822 compared to C_p of 0.783 for CC3 wedge diffuser. Results for design flow rate, at 100 percent N_c .

Both of those configurations are shown in Figure 25. Note that the leading edge radius of the final diffuser configuration (shown in blue in Figure 25) is at $1.0715 * \text{impeller TE radius}$, which is slightly lower than CC3 which is at $1.078 * \text{impeller TE radius}$ (shown in black in Figure 25). In the design process, a configuration at a somewhat lower LE radius was also considered (of $1.05 * \text{impeller TE radius}$)—but it was not selected for final design (this configuration is shown in green in Figure 25). Note that not much consideration was given to configurations with increased gap and no designs with gaps larger than in CC3 were analyzed—the challenge here was to balance the need for minimizing the impeller-diffuser interactions with extending the diffuser length needed to achieve desired pressure recovery.

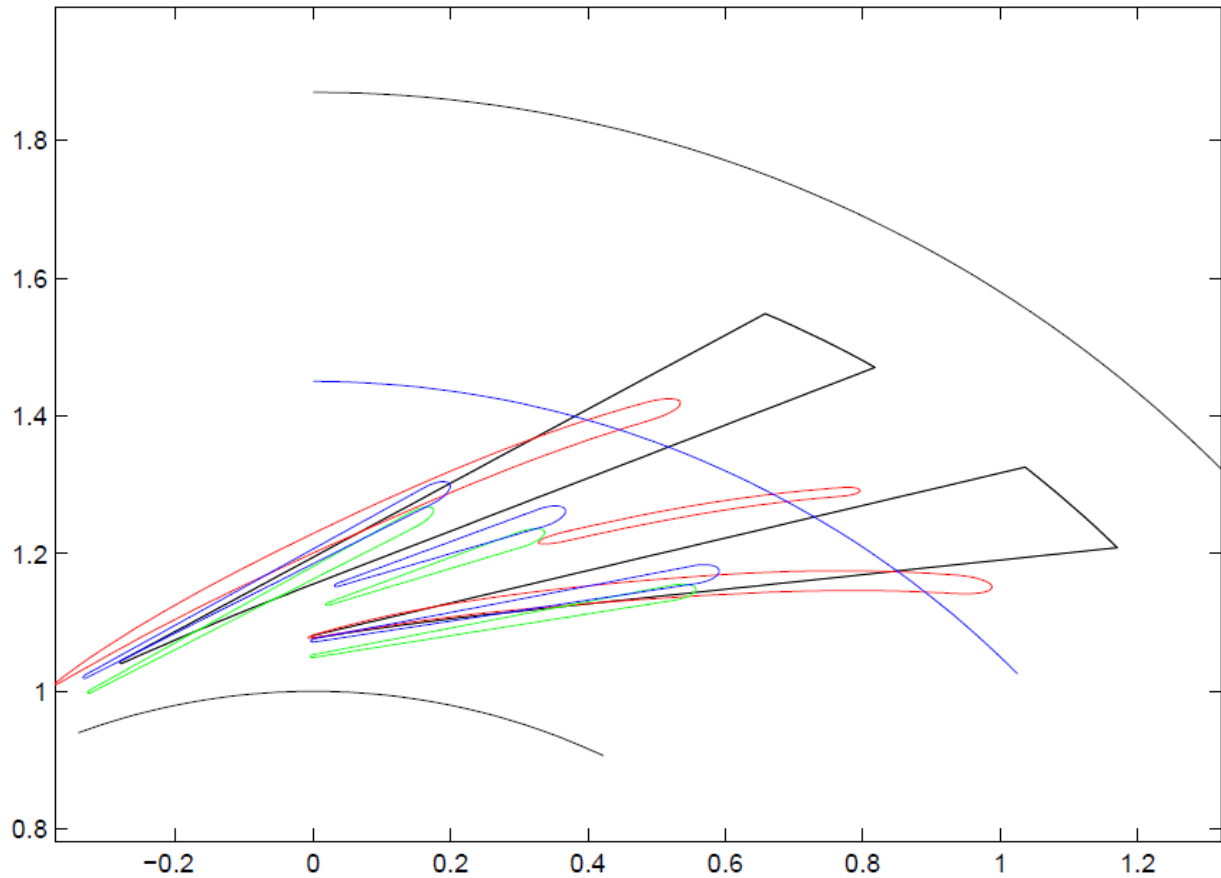


Figure 25.—Comparison of vaned diffuser design at diameter ratio of 1.71 (red) to vaned diffuser at diameter ratio of 1.45 (blue). CC3 wedge diffuser is shown for reference (black). A configuration at a somewhat lower inner radius that was considered in the process is also shown (green).

It is also worth mentioning that several three-dimensional concepts aimed at reducing the impeller-diffuser interactions, such as sweeping or bowing the vanes at leading edge, were considered early in the initial diffuser studies, mostly using steady CFD simulations and were not found to have a large impact on impeller performance. Unsteady simulations would have provided a more accurate assessment of these concepts, particularly at the higher absolute Mach numbers at the diffuser leading edge at the backsweep and flow of the HECC impeller.

The positioning of the leading edge of the splitter was determined by setting it sufficiently downstream of the throat area to avoid very high Mach number flow at its approach. This rationale is illustrated in Figure 26. In retrospect, the exact radial location of the splitter vane should have undergone fine-tuning via unsteady CFD.

Performance plots for the new stage design as computed at this point in the design process are presented in Figure 27. Note that the performance computed for impeller alone is also included in this plot (dashed blue line), and this speed-line is somewhat different from the one presented in Figure 19. While the impeller geometry has not changed, the computational setup has changed and the inlet boundary has been moved further upstream. In addition, a couple of additional operating points were computed. Most notably, one additional operating point was added at a very low flow, seemingly showing a much larger range for the impeller.

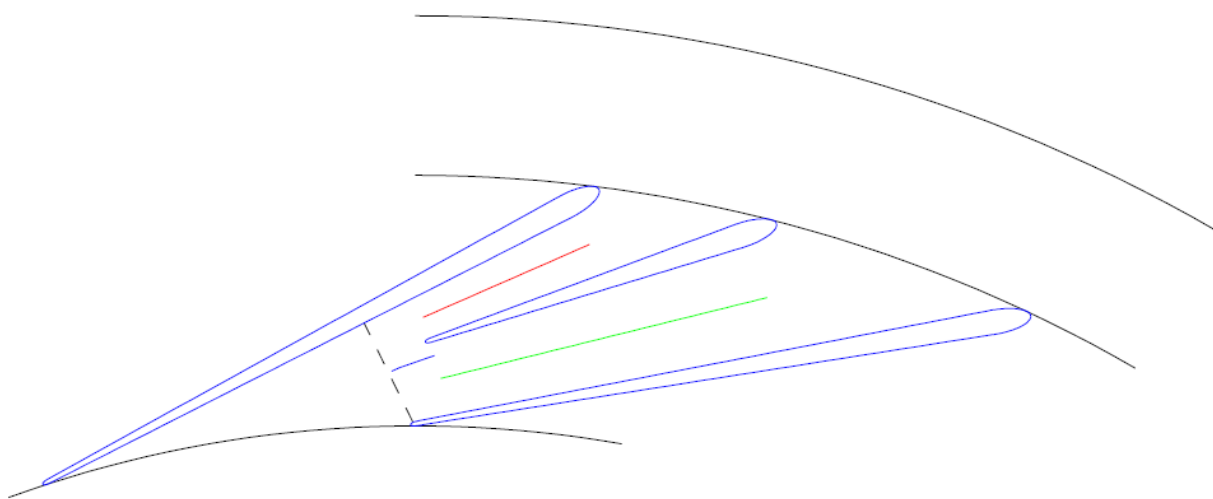


Figure 26.—Positioning of the splitter leading edge with respect to diffuser throat (dashed line).

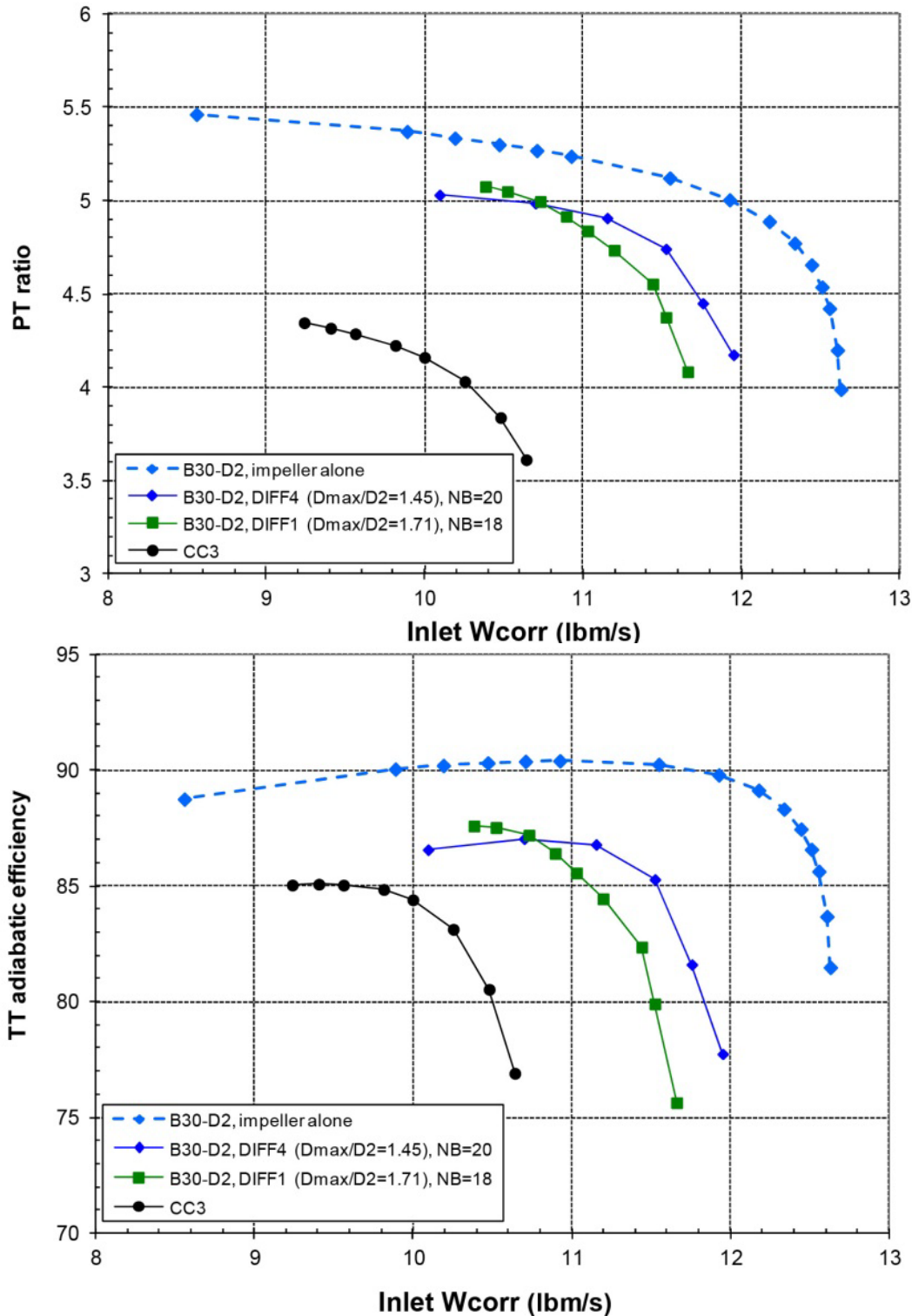


Figure 27.—Comparison of stage performance computed with new vaned diffuser configurations with diameter ratio of 1.71 (in green) and 1.45 (in blue).

3.5.3 Splitter Vane Placement

In order to balance the pressure recovery through both sides of the splitter passage, the splitter was positioned off the mid-passage centerline and at a slightly closed stagger angle, to match each side's

length to width and area ratios, by reference to classic diffuser maps (Ref. 11). By shifting the splitter in this manner, an additional 0.3 pt in total-to-static efficiency are gained over the mid-passage splitter placement. Also, compared to the original surface pressure distributions, the shifted splitter configuration creates more balanced loading between the two elements for radius $R > 10.5$ in., Figure 28.

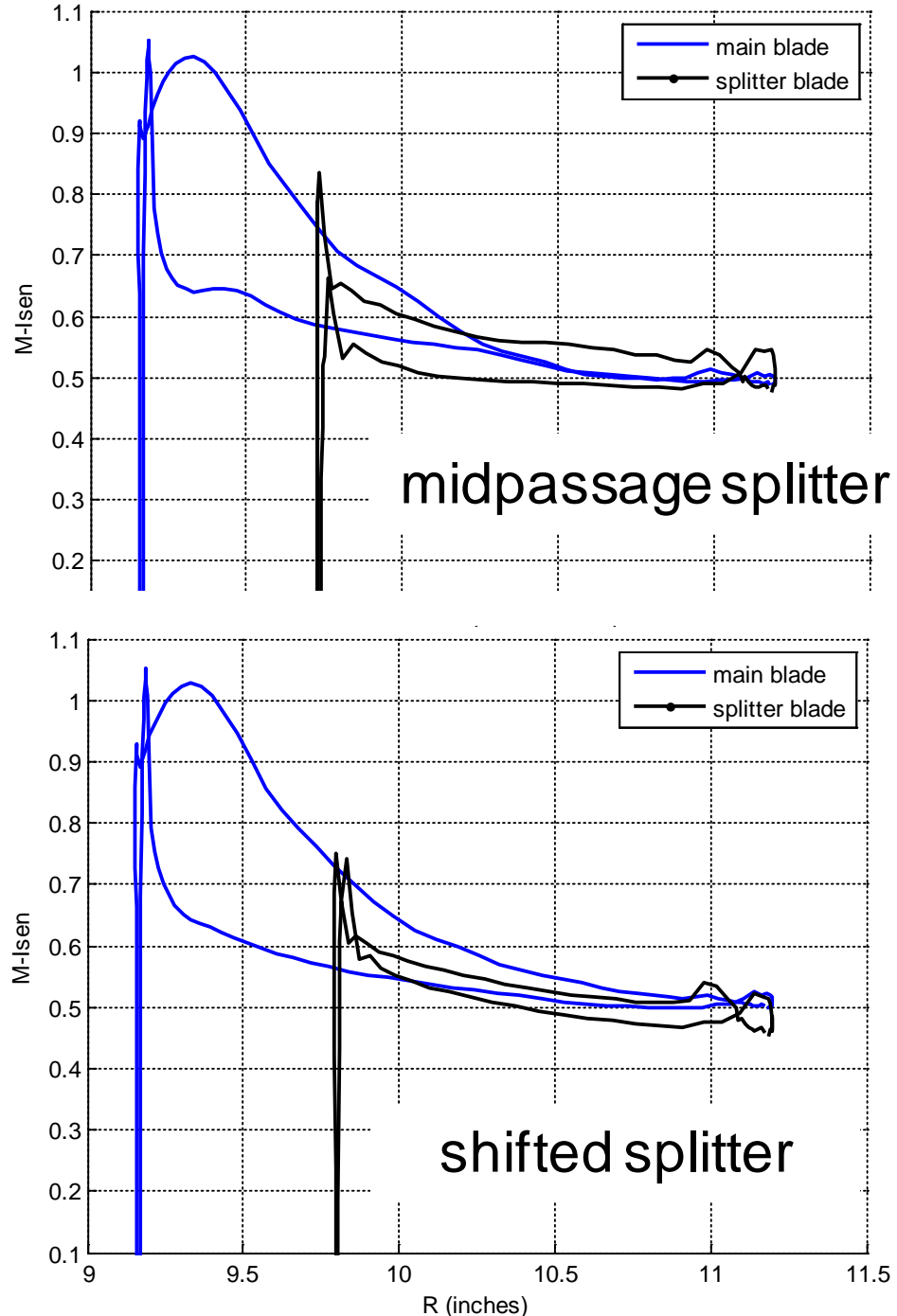


Figure 28.—Comparison of loading distributions for vane diffuser with splitter, for splitter placed identically in mid-passage (right) or shifted in order to balance pressure recovery on both sides (left), at design flow rate, 100 percent N_c

At the same time, a trade-off study was also conducted to assess the optimal number of vanes, as shown in Figure 29. For best matching with the impeller, the vane count of 20 was maintained. Further reducing the vane count (to say, 18) was not considered because it was concluded that would further increase the operating flow rate for the compressor and deviate too far from the original specifications.

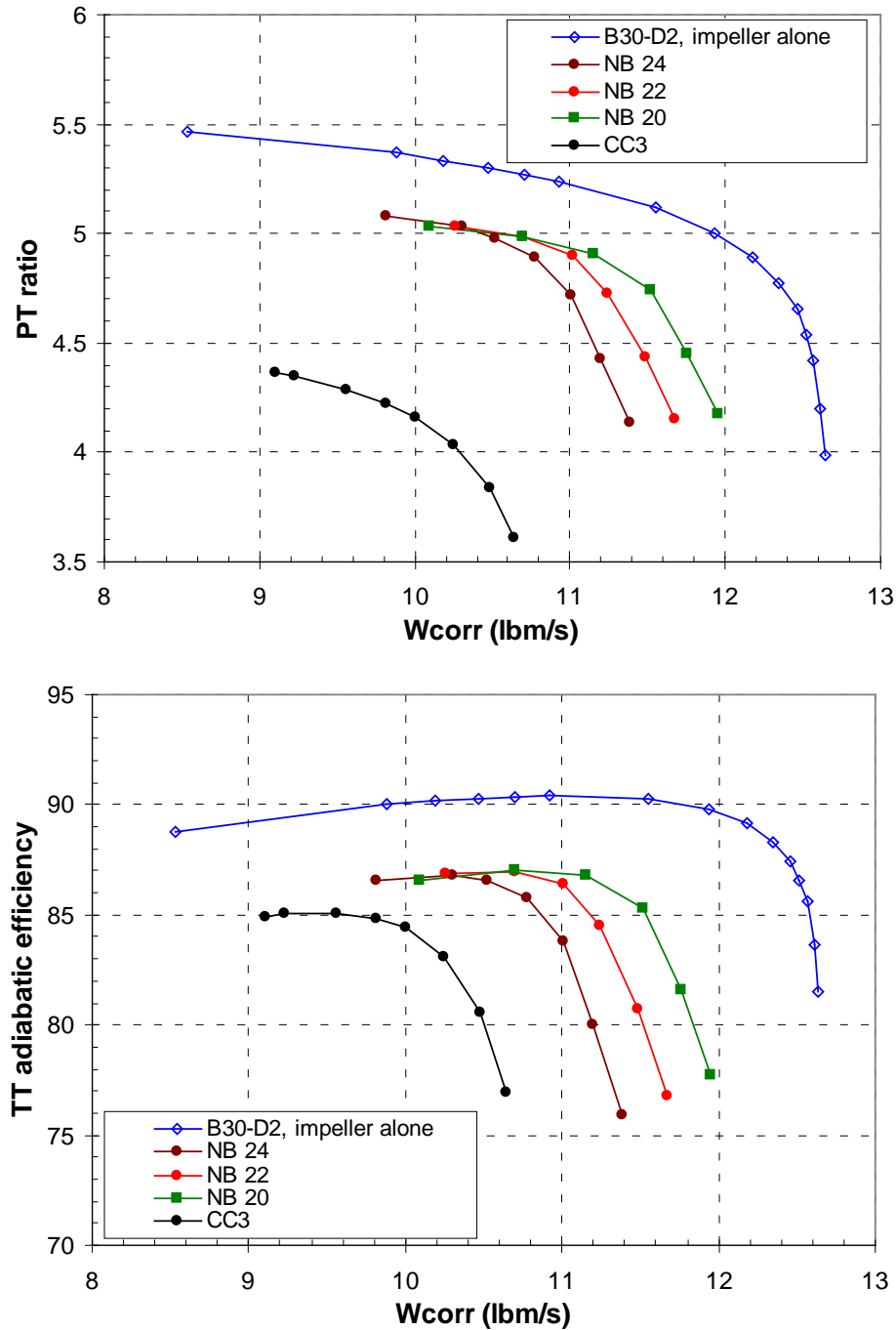


Figure 29.—A study showing the impact of vane count for the final vaned diffuser configuration. Vane count of 20 pairs of main and splitter vanes was maintained for better matching with the impeller (for 100 percent N_c).

In Figure 30, the final configuration is compared to CC3 by plotting the isentropic Mach number at mid-span against radius as computed in CFD simulations. Note that the amount of diffusion in the new diffuser is significantly higher than in the CC3 diffuser. The exit profiles from the full stage for the new impeller/diffuser design are then shown in Figure 31, with absolute Mach number of approximately 0.3 and exit swirl angle of 60°—pointing to the clear need to add the exit guide vanes to further diffuse and deswirl the flow.

Finally, both CC3 diffuser and the new diffuser design are spotted in diffuser maps in Figure 32. Note that the pressure recovery computed with CFD was 0.78 for CC3 and 0.70 for the new diffuser. While for CC3 the CFD seems to be aligned with diffuser maps, for the new diffuser CFD predicted significantly higher recovery.

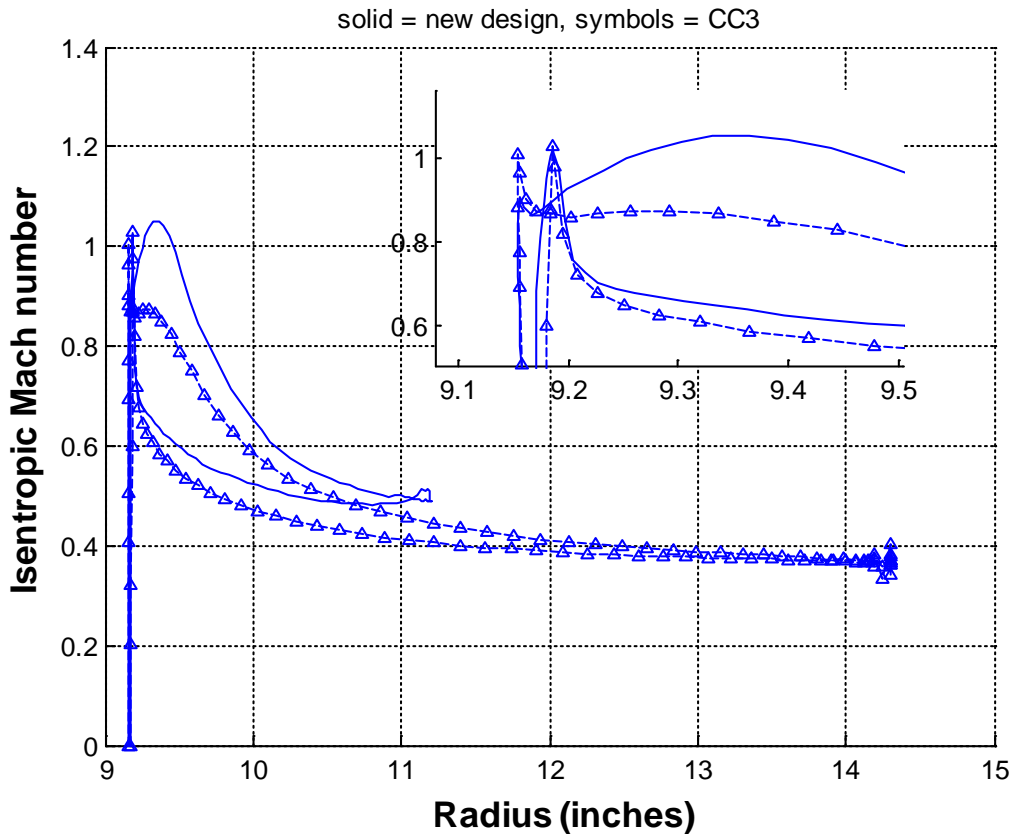


Figure 30.—Comparison of loading distributions as function of radius for the main vane in the new diffuser (solid line) in comparison to CC3 (symbols), at design flow rate and 100 percent N_c .

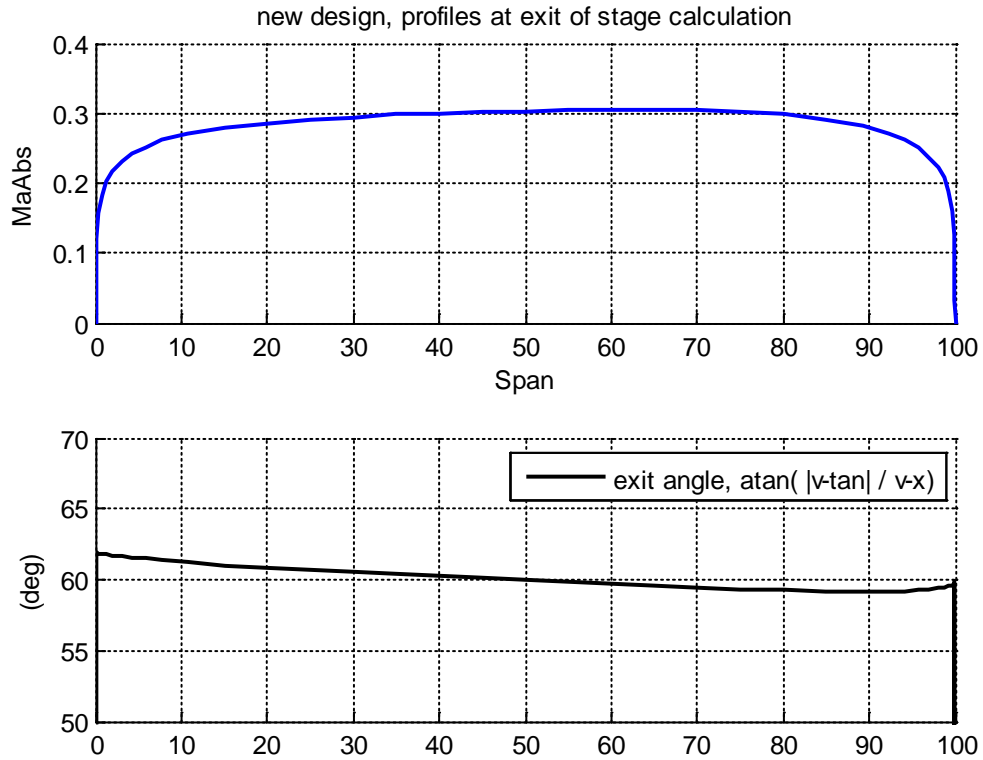


Figure 31.—New diffuser design exit profiles—absolute Mach number is approximately 0.3 (top), and the swirl angle is approximately 60° (bottom), at design flow rate and 100 percent N_c

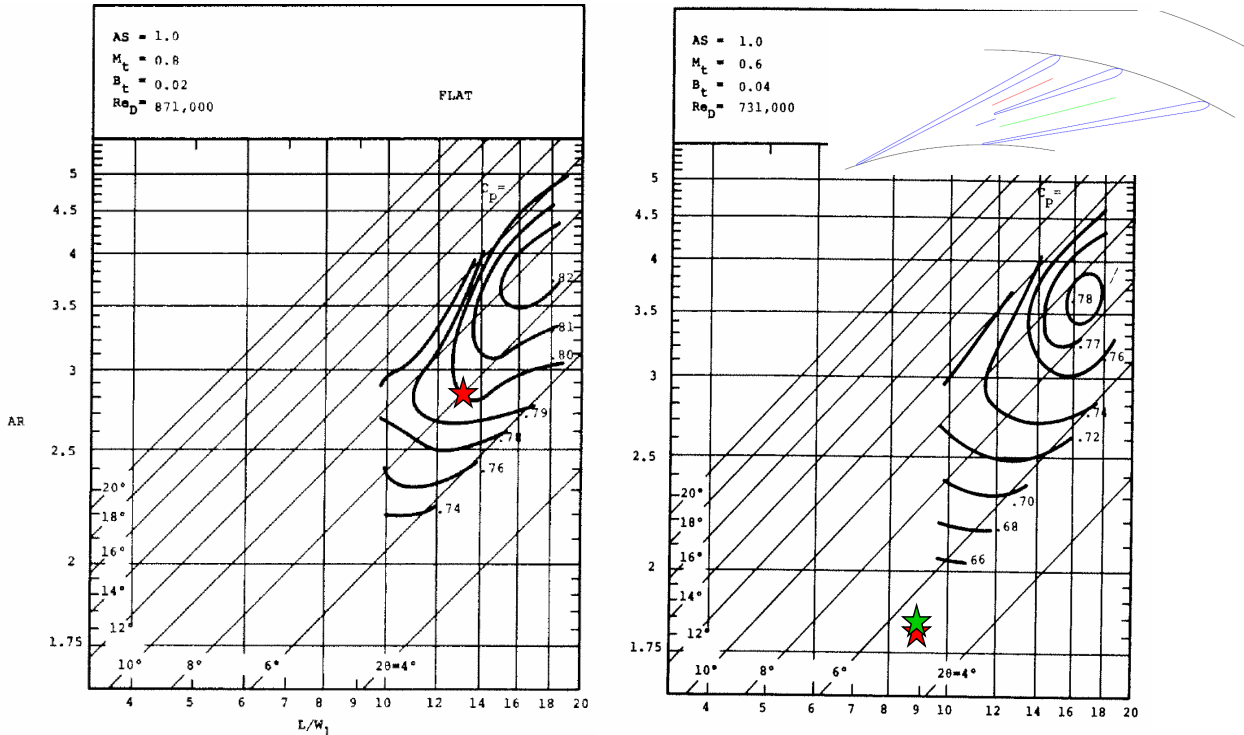


Figure 32.—CC3 (left) and new vanned diffuser with shifted splitters (right), as spotted in the diffuser maps. CFD predicted pressure recovery of 0.78 for CC3, and about 0.70 for the new diffuser.

3.5.4 Vane Thickening

At the preliminary design review the determination was made to increase the thickness of the diffuser vanes—both the main and the splitter vanes—so that engine scale leading edge would meet minimum thickness requirements—the thickness was increased by 18 percent. At the same time, the vanes were restaggered as indicated in the legend of Figure 33. The new geometry is presented in Figure 33, and the impact on performance is illustrated in Figure 34 where the results from steady CFD simulations (with mixing plane in between impeller and diffuser) showed only a 0.2 pt reduction in peak efficiency with the thicker vane leading edges (HECC Iteration 3 represents the modified design). Again, unsteady simulations would have provided a better estimate of the impact of thickening on performance, as the use of mixing plane reduces the potential flow effects upstream of the vanes.

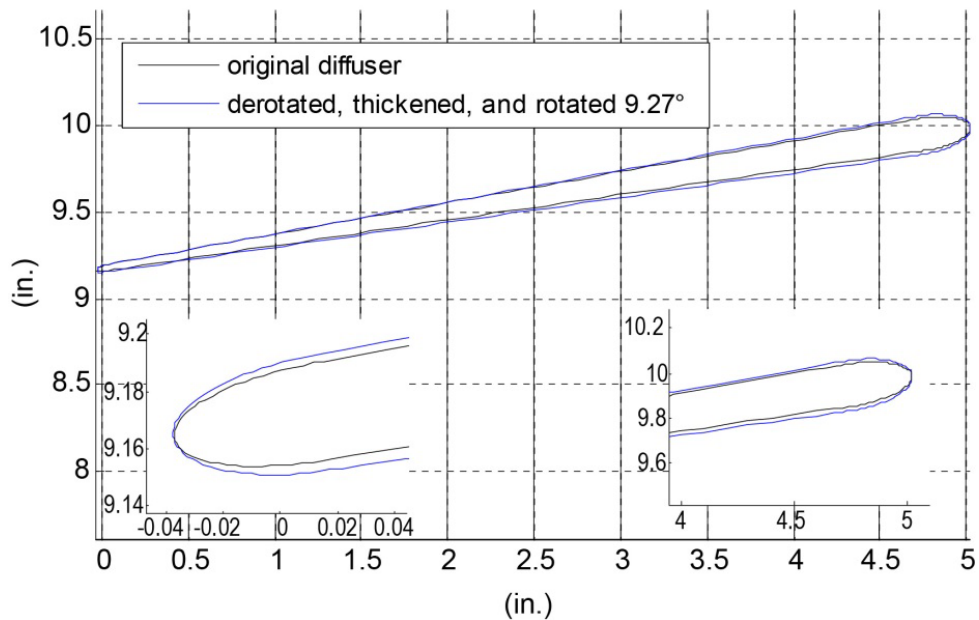


Figure 33.—Final thickening of the leading edges of diffuser vanes—action item from the preliminary design review.

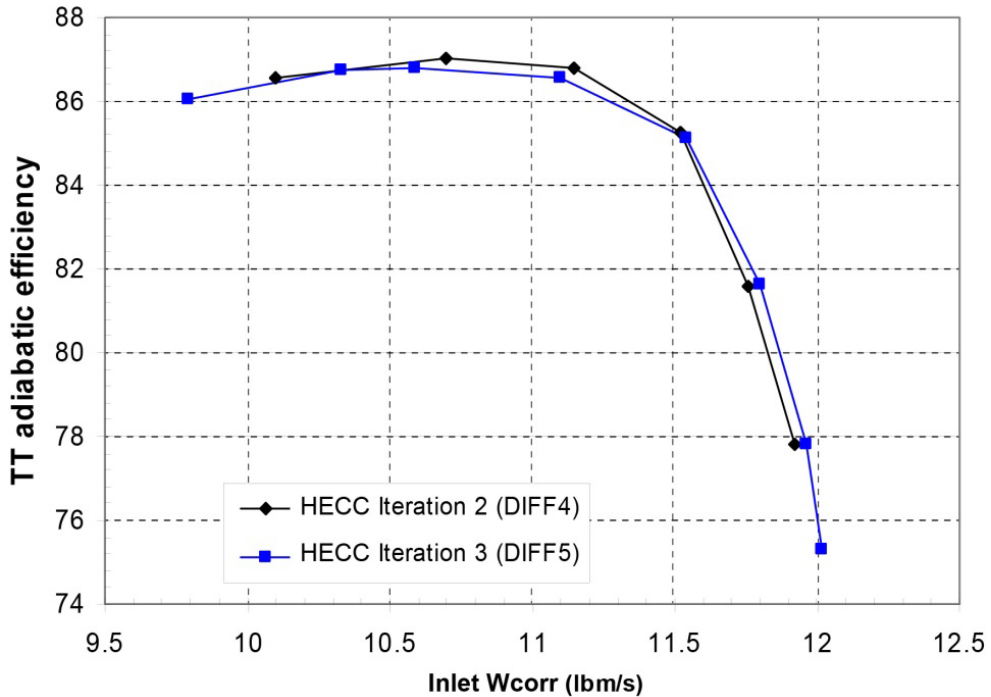


Figure 34.—Impact of thickening of the diffuser leading edges on performance of the impeller-diffuser stage—CFD with mixing plane predicted a reduction of 0.2 percentage points in peak adiabatic efficiency (for 100 percent N_c).

3.6 Performance Assessment for Impeller-Diffuser Stage

After both impeller and diffuser design was completed (but prior to final thickening of diffuser vanes and the completion of the design of exit guide vanes), an entire compressor map was generated, using a steady state CFD model with mixing plane assumption between the rotating and stationary row, Figure 35. This map shows contours of total-to-total polytropic efficiency instead of total-to-static, because it does not include the EGV row. In this map it is also seen that for inlet corrected mass flow rate of 10 lbm/sec best performance is achieved at 95 percent rpm, with total pressure ratio of 4.4 and total-to-total polytropic efficiency of greater than 89 percent.

This same configuration was also considered using an unsteady CFD model of a sector of the stage, which includes a 72° periodic sector of 3 impeller blade passages and 4 diffuser blade passages. The simulations were run for 2 to 4 full revolutions of the impeller, with 100 time-steps per main-to-splitter pitch.

The unsteady calculation was performed to ensure that the predicted performance did not vary substantially from the steady state assumptions when impeller-diffuser interactions were also included. The resulting speedline at 100 percent design speed is given in Figure 36, in which it is seen that the predicted performance is reduced by approximately 0.5 percentage points in the compressor operating area, at no penalty to total pressure ratio. Note that this assessment did not include the thickening of diffuser vanes. Also, this assessment was conducted prior to the addition of the EGVs to the new design, so it also does not account for the impact of the unsteadiness on the EGVs.

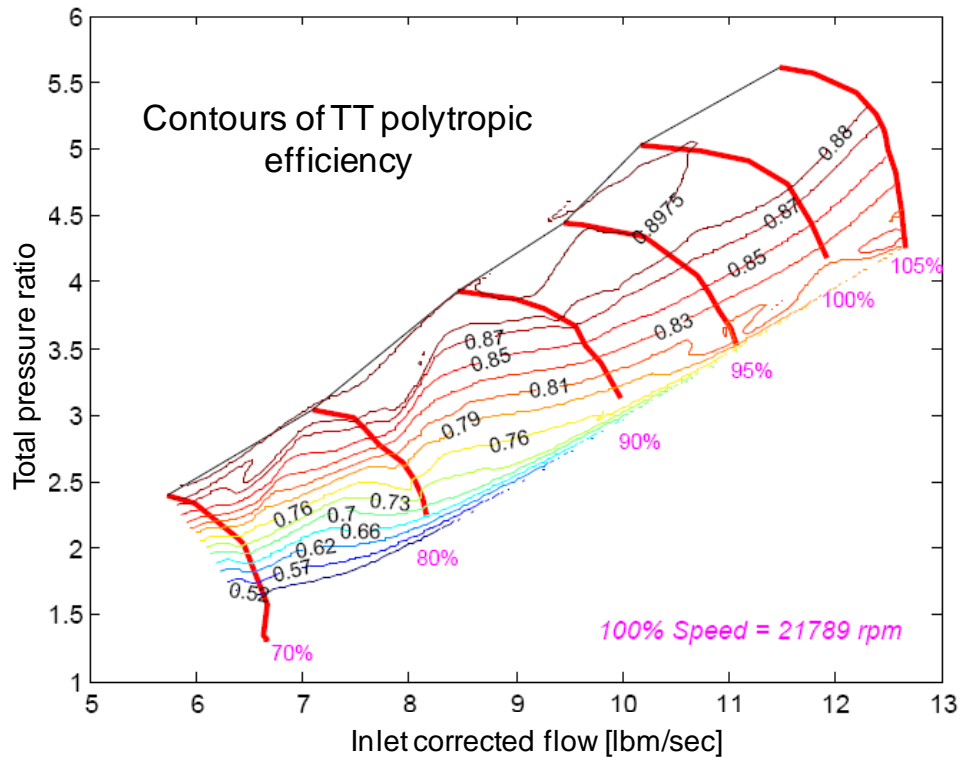


Figure 35.—Steady CFD-predicted performance map for impeller-diffuser stage design run at fixed impeller tip-clearance (12 mil).

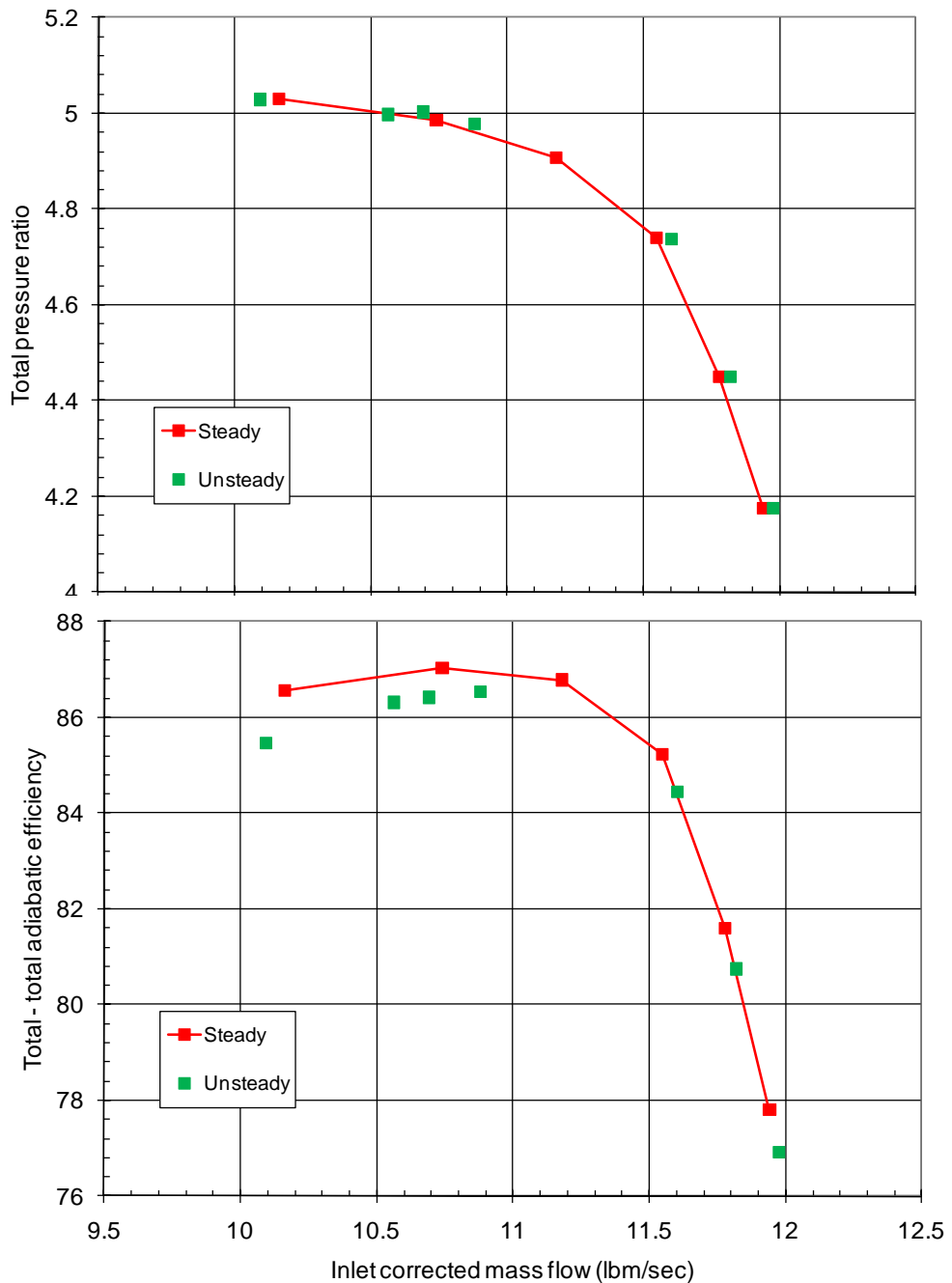


Figure 36.—Performance for 100 percent design speed for impeller-diffuser stage design with unthickened diffuser vanes and no EGV, as computed with steady (red) and unsteady CFD (green), indicating the pre-test quantification of the level of impact of impeller/diffuser interaction on performance

3.7 Exit Guide Vane Design

The exit flow from the diffuser still contains a significant amount of swirl velocity, which must be reduced for satisfactory combustor performance in an engine application. To that end, a row of exit guide vanes was designed to target a stage exit Mach number of 0.15 and swirl angle of 15° from axial. The exit

guide vanes were developed as an isolated row, using the circumferentially averaged exit profiles from the diffuser row as the inlet boundary condition to the three-dimensional CFD model. A trade study was executed that considered variations in solidity (by varying blade count and axial distance) and stagger angle, for two airfoil sections. The goal was to minimize total pressure loss while meeting the target exit swirl angle. After comparing about 50 permutations, shown in Figure 37, two configurations were down-selected for computations of all three components in the stage.

Full stage computations were conducted using a mixing plane between the rotating impeller and stationary diffuser rows, and point-to-point matching of a single passage of the 20-bladed diffuser with three passages of a 60-bladed exit guide vane row. In this way, the effect of clocking the exit guide vanes relative to the diffuser blades could be studied; in the optimal configuration, a “free” increase in total-to-static efficiency of 0.1 pt compared to worst configuration is observed, as illustrated in Figure 38. The difference can be seen by considering the convection of the diffuser wakes through the EGV row at design point, shown in Figure 39; in an engine application, the blade counts of the two stationary rows would be selected such to minimize any periodicity of wake interaction. For the rig, the final clocking angle was selected based on most uniform pressure distribution for each of three blades with EGV at 0.75 pitch, as shown in Figure 40. Exit profiles from the EGVs, shown here for an intermediate configuration considered at PDR, illustrate the absolute Mach number as well as the swirl angle in Figure 41. The maximum value for absolute Mach number at exit has been reduced below 0.16, and the swirl angle below 18°. The mass-averaged values for exit Mach number and swirl angle for the final design were computed as 0.15° and 14°, respectively.

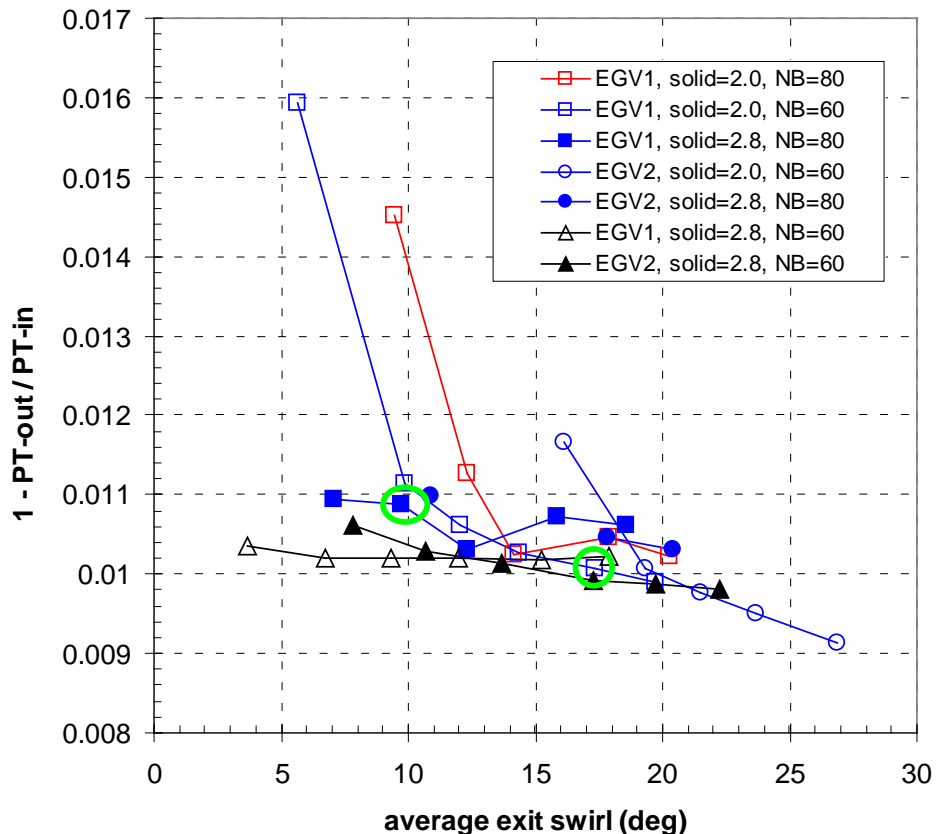


Figure 37.—Results of EGV airfoil section trade study, in which camber and solidity were varied for two airfoil sections to find minimum total pressure loss that meets target exit swirl angle (at design flow rate at 100 percent N_c). Configurations circled in green were down selected for further analyses via stage calculations

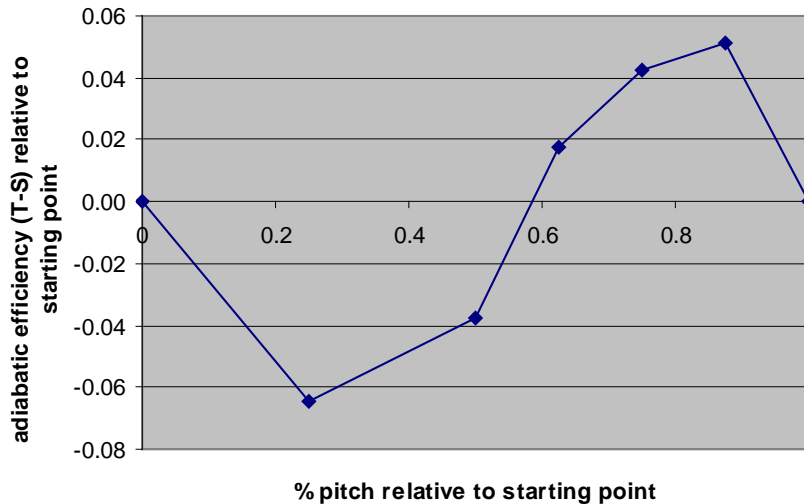


Figure 38.—Variation in total-to-static efficiency due to positioning of EGV row relative to diffuser row (at design point, 100 percent N_c).

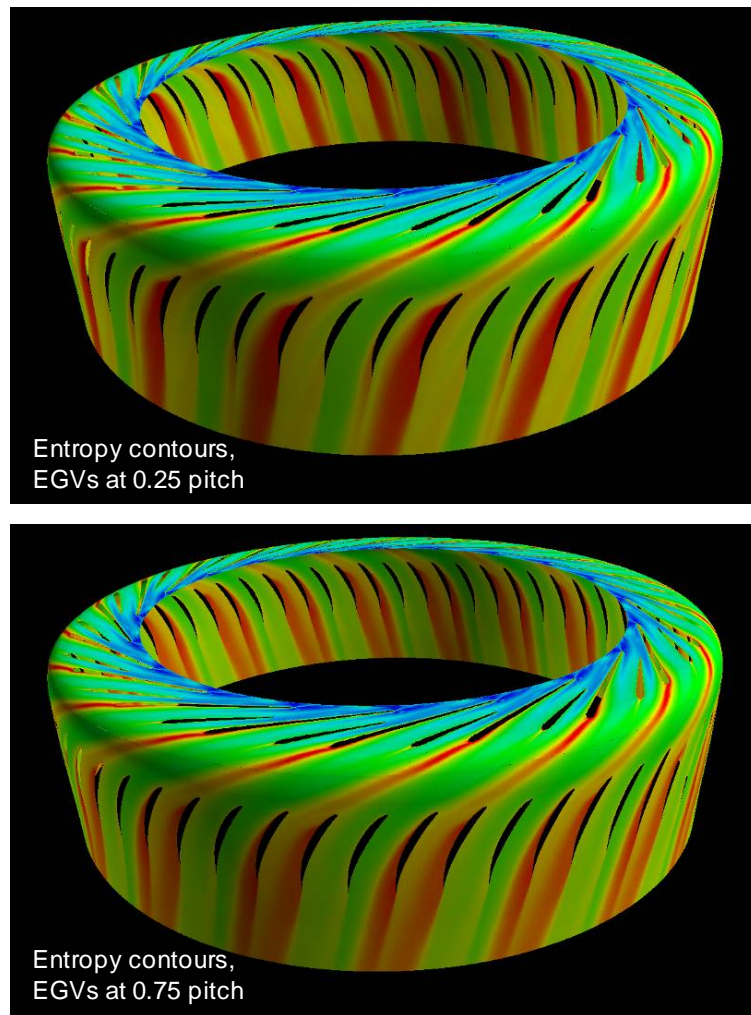


Figure 39.—Comparison of entropy contours for least favorable (top) and most favorable (bottom) position of EGV row relative to diffuser row (at design point, 100 percent N_c).

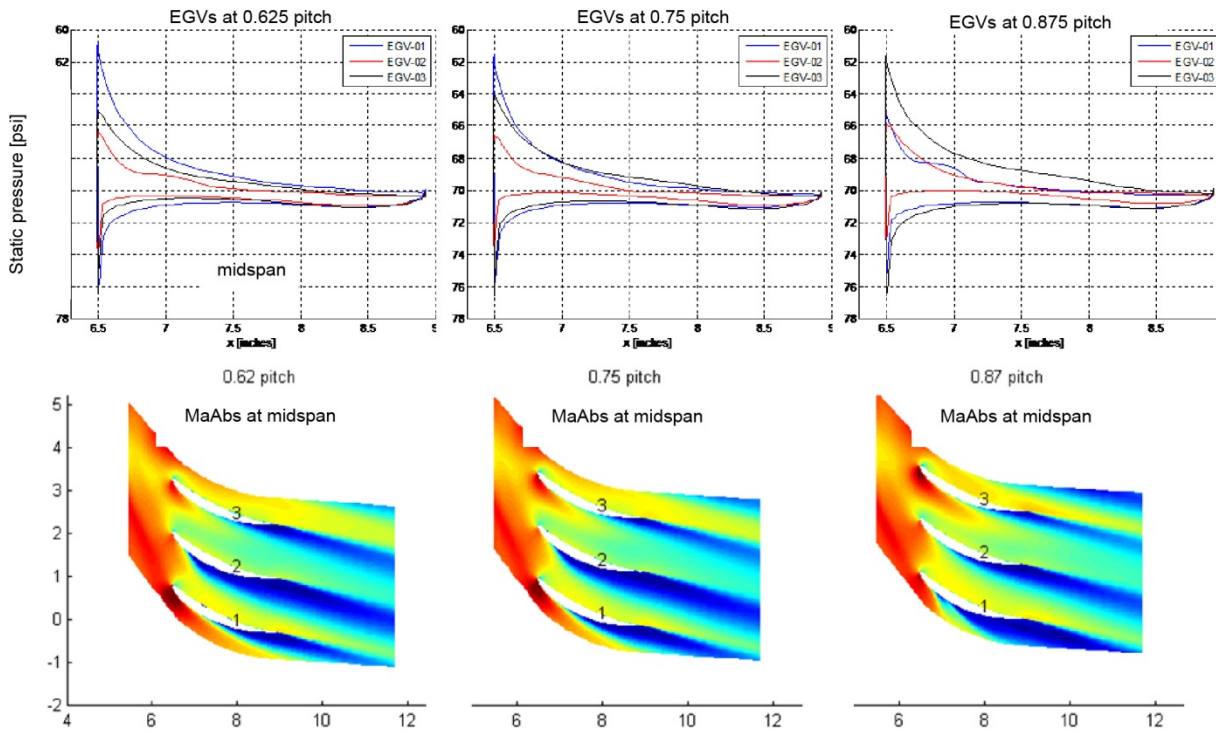


Figure 40.—Comparison of static pressures and absolute Mach number at EGV mid-span for three EGVs, as computed with different clocking positions: 0.62 pitch (left), 0.75 pitch (middle), and 0.87 pitch (right).

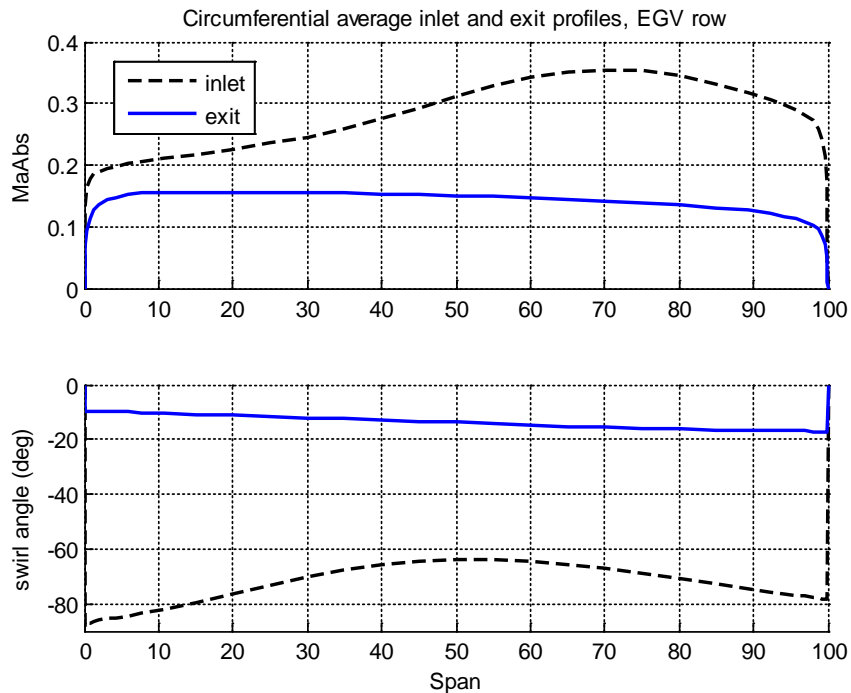


Figure 41.—Circumferentially averaged inlet and exit profiles to the EGV row; absolute Mach number at exit has been reduced below 0.16, and the swirl angle below 18° (Results for design flow rate, at 100 percent N_c).

3.8 Radial-to-Axial Bend Design

The initial design for the radial-to-axial bend was constructed from CC3 geometry with the following adjustments. The outer diameter of the bend was set at the maximum diameter ratio of 1.45. The bend entrance area was set by the design of the new diffuser. The intent was to keep a similar area ratio (from diffuser exit to EGV inlet) as in the CC3. This process is illustrated in Figure 42, where the starting geometry combining the first two constraints above is shown in blue, and the final geometry, that incorporates the notion of similar inlet/outlet area ratio as in CC3 bend, is shown in black.

As a next step, the radial-to-axial bend geometry was optimized in a process that coupled the CFD solver Code LEO to mesh morphing software Sculptor (a product of Optimal Solutions Software, LLC) with optimizer iSight (a product of Simulia of Dassault Systèmes), to minimize total pressure loss. In this instance, the CFD model includes a single passage of the impeller, diffuser, and EGV rows. The bend and EGV flowpath geometry was parameterized using 8 control points on the hub and 8 on the shroud that were allowed to vary radially. The shroud control points are constrained not to exceed the stage maximum diameter. The resulting change in the bend geometry, Figure 43, was found to improve total-to-static adiabatic efficiency by 0.25 pt (as illustrated in Figure 44). Note that the main difference occurred at the hub, well after the bend and inside the EGV passage. Final area scheduling for the new radial-to-axial bend design is compared to CC3 in Figure 45.

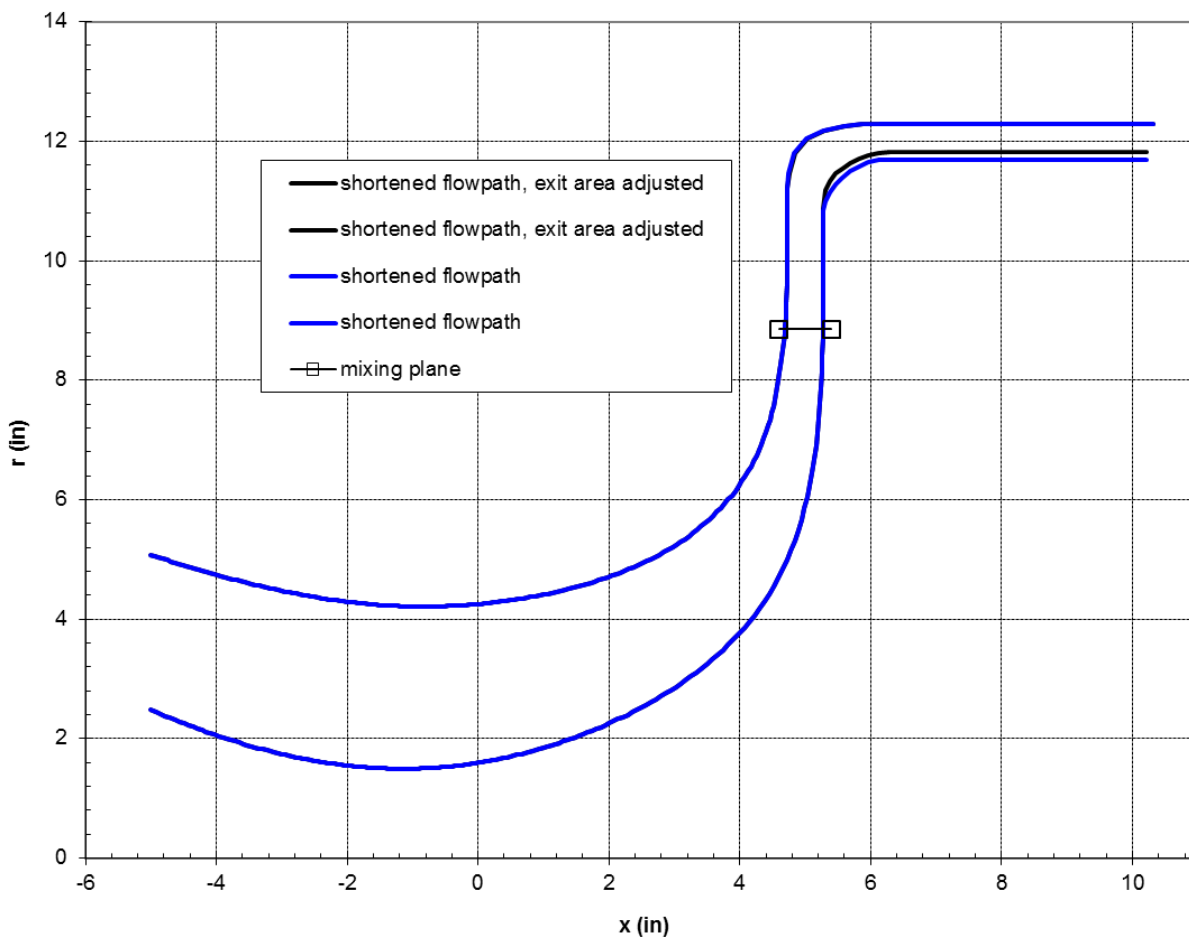


Figure 42.—Design process of the initial radial-to-axial bend configuration

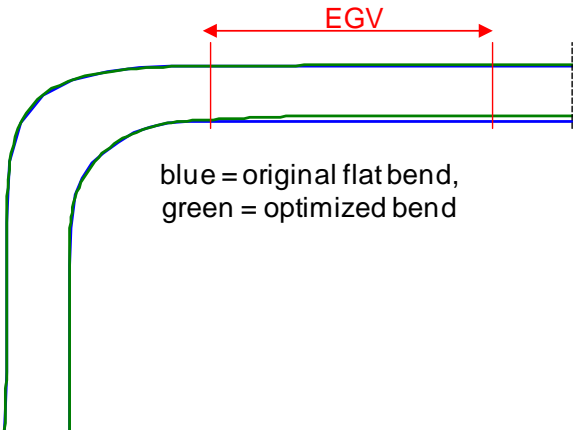


Figure 43.—Results of optimization of radial-to-axial bend area, showing original flat bend (blue) and redesigned curved bend (green) from optimization

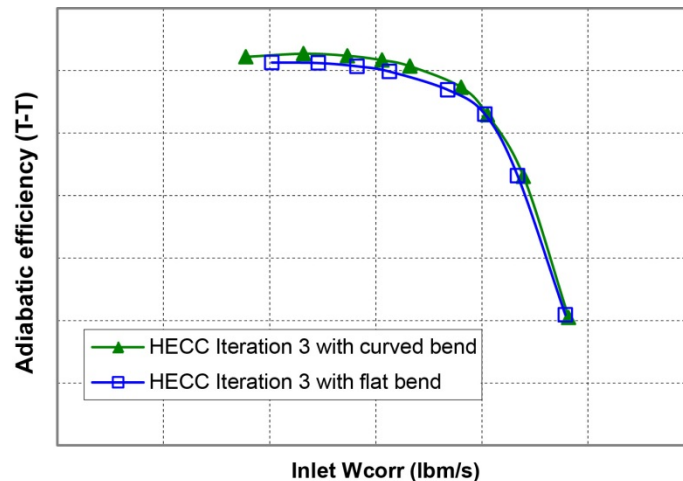


Figure 44.—Results of optimization of radial-to-axial bend area, showing stage (impeller, diffuser, clocked-EGV) adiabatic efficiency (total-to-total) with the original flat bend (blue) and redesigned curved bend (green) at 100 percent N_c

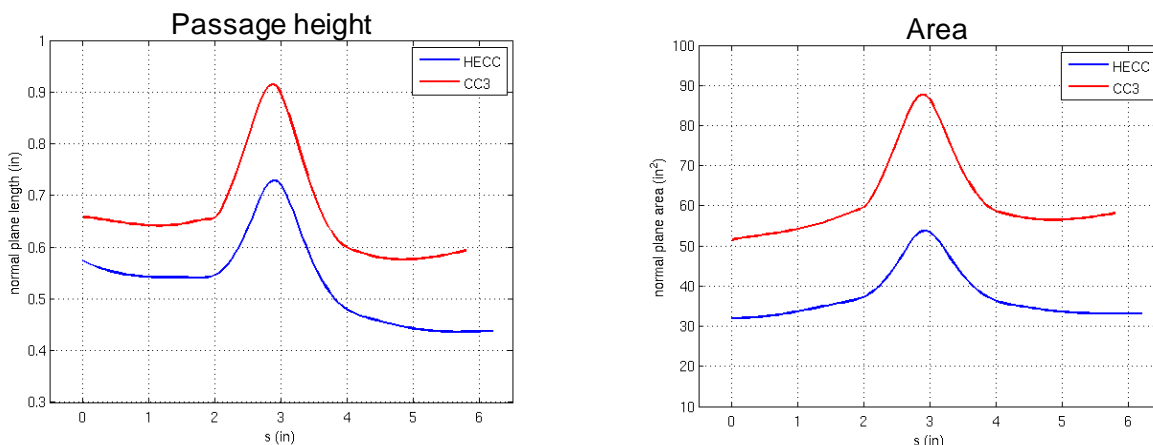


Figure 45.—Comparison of passage height and area scheduling for radial-to-axial bend area for CC3 (red) and the new design (blue)

3.9 Final Design Summary

The final configuration geometry description is given in Table 2. A comparison of the final geometry against the original CC3 compressor is given in Figure 46, and a photograph of the new impeller compared to CC3 impeller is also shown in Figure 47.

TABLE 2.—GEOMETRIC PARAMETERS OF THE NEWLY DESIGNED CENTRIFUGAL COMPRESSOR STAGE

	Value	Hub	Shroud
Impeller blade input diameter, in.		3.190	8.479
Impeller splitter inlet diameter, in.		5.315	9.474
Impeller exit diameter, in.		16.988	16.998
Impeller exit blade height, in.	0.609		
Leading edge lean angle, deg.	-2		
Trailing edge lean angle, deg.	-29		
Number of blade/splitter pairs	15		
Tip clearance, in.	0.012		
Vaned diffuser inlet diameter, in.		18.215	18.215
Vaned diffuser outlet diameter, in.		22.398	22.398
Vaned diffuser channel height, in.	0.559		
Number of vane/splitter pairs	20		
Deswirl blade inlet diameter, in.		23.663	24.594
Deswirl blade exit diameter, in.		23.737	24.610
Deswirl vane axial chord, in.	2.438		
Number of deswirl vanes	60		

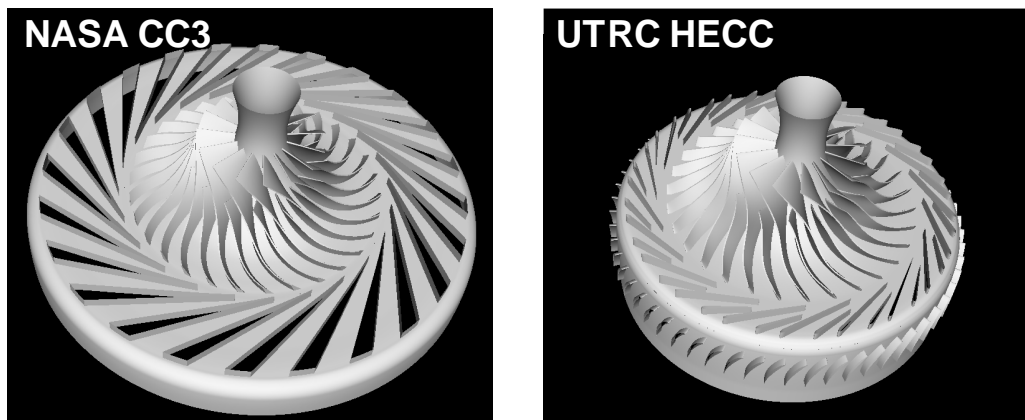


Figure 46.—NASA CC3 compressor (left) and the new design (right).



Figure 47.—Comparison of HECC and CC3 impellers showing improved trailing edge and improved blade angle distribution.

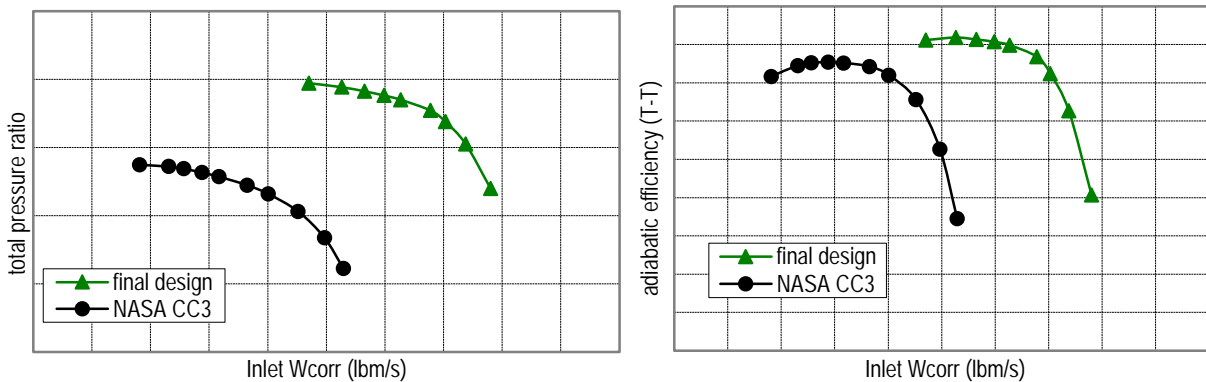


Figure 48.—Predicted total pressure ratio (top) and total-to-total adiabatic efficiency (bottom) versus inlet corrected flow for NASA CC3 and final design (at 100 percent N_c).

4.0 Design-Intent Performance

4.1 Stage Performance at 100 percent N_c

A comparison of the predicted performance for the final geometry (that includes impeller, diffuser, and EGVs), computed with uniform 0.012 in. impeller tip clearance and standard day inlet conditions, to NASA CC3 compressor is shown in Figure 48 and Figure 49. At design-point exit corrected flow rate of 3 lbm/s and 100 percent N_c , the total pressure ratio of 4.85 and the total-to-total adiabatic efficiency of 86.2 percent were predicted. The CFD prediction for the polytropic total-to-total efficiency for the final design at standard day inlet conditions is 88.8 percent. Stall margin of about 12 percent was also predicted. Note that for CC3 compressor, the choke flow was over-predicted by about 4 percent—with a similar over-prediction for HECC, the stall margin quoted above would be significantly reduced. This has not been factored in the pre-test assessment of CFD predictions.

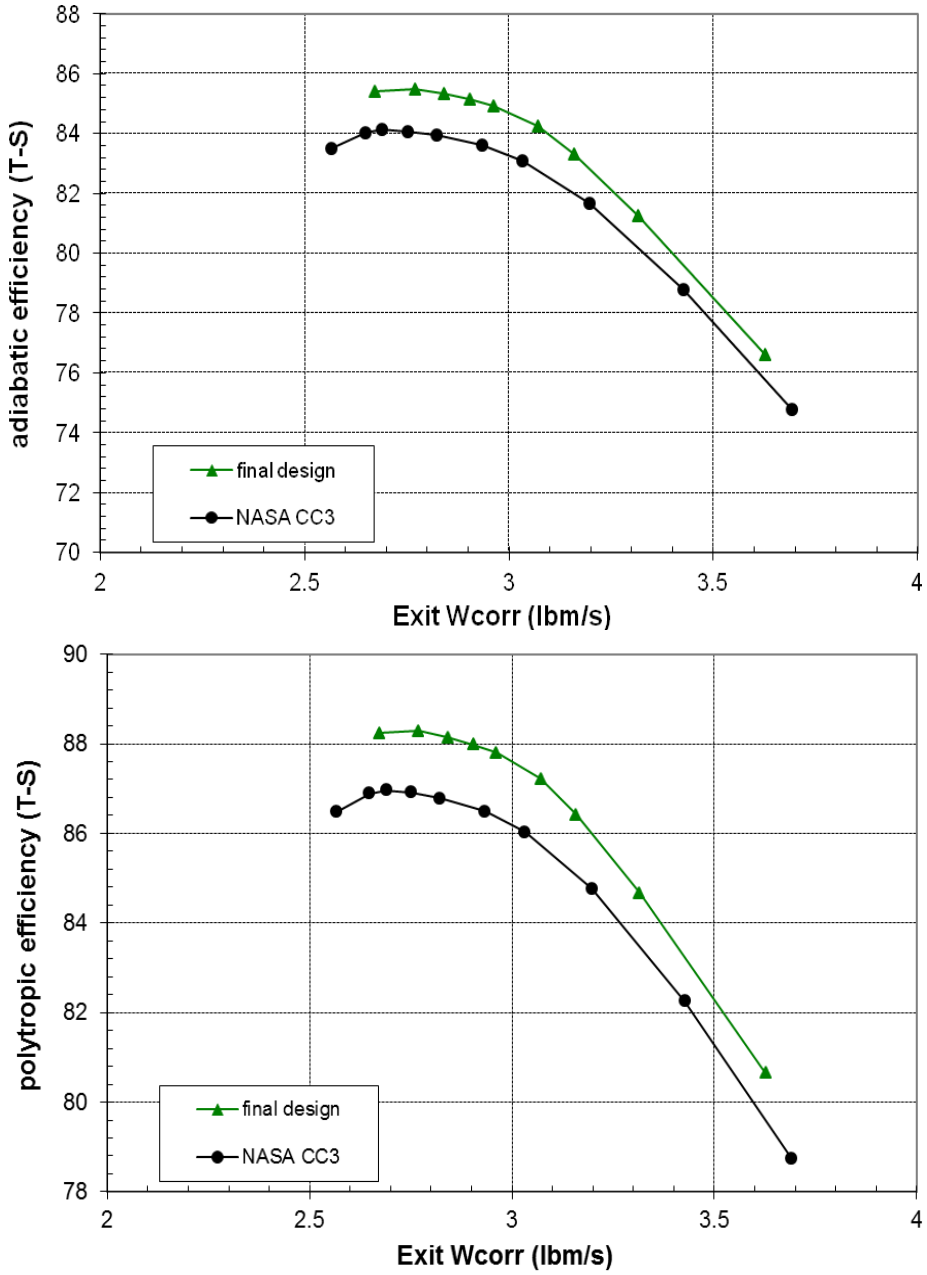


Figure 49.—Predicted total-to-static stage adiabatic (top) and polytropic efficiency (bottom) versus exit corrected flow for NASA CC3 and final HECC design (at 100 percent N_c)

4.2 Performance Map

A full performance map for the final design was not provided to NASA ahead of test, and it was only computed as a part of the post-test CFD analyses. Since UTRC no longer had access to LEO—a new solver, UTCFD (described in Section 9.0), with the baseline vorticity-based $k-\omega$ model, was used for steady simulations with standard day inlet conditions as a surrogate for LEO to generate a “pre-test” performance map. To our best understanding, this represents the design intent performance as assessed with “pre-test” methodology. Note, however, that UTCFD computations conducted on finer grids predict

somewhat higher peak efficiency for 100 percent speed (for about 0.5 percentage points), and somewhat lower choke flow (which reduced from about 11.9 to 11.6 lbm/s)—as shown in Section 9.1, Figure 139.

A performance map that includes total-pressure ratio and total-to-total adiabatic efficiency is shown in Figure 50. Results are presented for 85, 90, 95, 100 and 105 percent corrected speeds. Peak efficiency varies from about 87.3 at 85 percent and 90 percent speed to about 85.8 at 105 percent speed. Total pressure ratio predicted at peak efficiency was about 3.33 at 85 percent speed, 3.8 at 90 percent speed, 4.25 at 95 percent speed, and 5.37 at 105 percent speed.

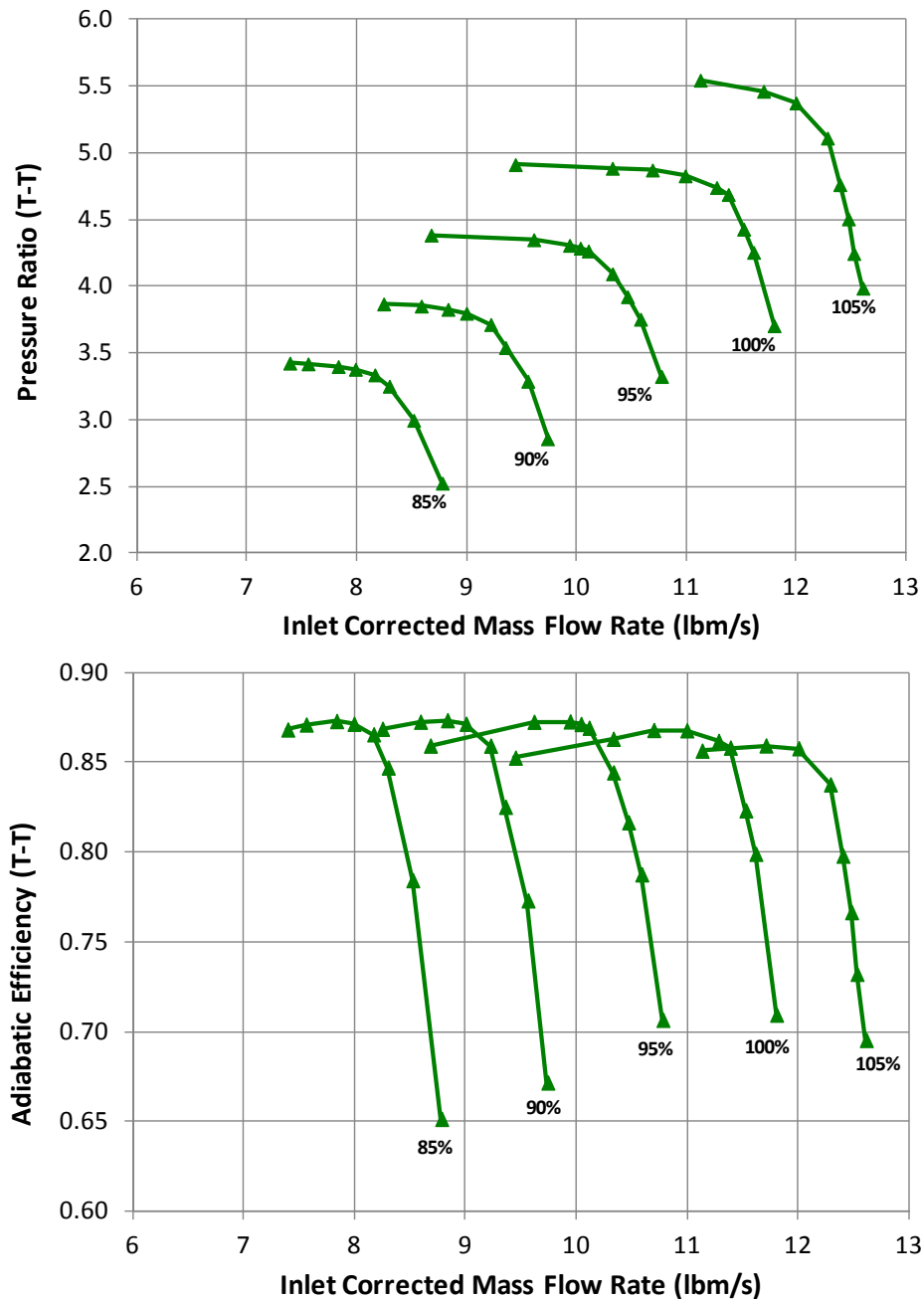


Figure 50.—Full compressor map for speeds 85 to 105 percent obtained during steady post-test CFD analyses using standard day inlet conditions and the same vorticity-based $k-\omega$ model that was used in pre-test CFD analyses.

From these steady computations of the entire performance map, it would also seem that the range was largest for 95 and 100 percent speeds. As discussed at length in Section 11.0, using steady CFD computations for assessment of range is at the least questionable, and could easily lead to misleading conclusions, so this information should be used with caution.

4.3 Comparison of Predicted Performance to Target Requirements

A comparison of CFD predicted performance at design point to target requirements is shown in Table 3. Predicted pressure ratio is 4.85, work factor is 0.79, and polytropic efficiency is 88.8, at exit corrected flow rate of 2.98 lbm/s. Stability margin is approximately 12 percent. Exit Mach number is 0.15 and exit swirl angle is 14°. Apart from the stability margin, the other metrics meet the target requirements.

4.4 Stage Performance at Rig Scale and Scaling to the Engine

In order to project the stage performance to engine scale, three elements are considered: the calibration of CFD to data, the impact of relatively low inlet radius ratio for the rig, and the Reynolds number effect. The geometric scale factor of equation (1) is calculated to be 0.516, assuming the rig operates at 100 percent design speed and exit corrected flow of 3 lbm/sec for the rig and 0.8 lbm/sec for the engine. Other geometric parameters specific for the rig design to be relevant for the smaller engine scale have to be chosen such that by assuring that once scaled down, the minimum thicknesses and leading and trailing edge radii would conform to typical design and manufacturing practices.

The performance delta when moving from rig to engine to capture the effect of inlet radius ratio was considered. Larger inlet radii drives higher inlet tip Mach numbers and associated friction and shock losses. The effect was estimated in two ways. First, meanline predictions for the HECC stage with inlet hub-to-inlet shroud ratio increased from $R_{1H}/R_{1S} = 0.37$ to $R_{1H}/R_{1S} = 0.60$, with fixed inlet area and no inlet swirl, were compared, Figure 51, in which it is seen that the higher radii cause an efficiency penalty of 1 point. Second, a survey of recent literature (Ref. 12) indicates that at similar pressure ratio and work factor to the HECC stage, which has specific speed $N_s=0.6$, and with inlet swirl of 25°, as might be found in a multistage aero-engine, the efficiency penalty for increasing radius ratio is about 0.5 pt, Figure 52. Last, CFD simulations were conducted for the impeller by increasing the radius ratio to 0.5. The peak efficiency drops for about 0.85 pt, as illustrated in Figure 53.

TABLE 3.—COMPARISON OF PREDICTED STD PERFORMANCE
AT DESIGN POINT TO TARGET REQUIREMENTS

Metric	HECC Final Design	
	Target	CFD predicted
Stage Pr	4.0 to 5.0	4.85
Inlet corrected flow, lbm/s	10.0	11.2
Exit corrected flow, lbm/s	2.6 to 3.1	2.98
Work factor, DH_0/U_2^2	0.58 to 0.7	0.79
Poly Eff TT, %	≥ 88	88.8
T3, °F	350 to 410	399
Dmax/Dtip	1.45	1.45
Stability margin, %	13	~12
M_{exit}	0.15	0.15
α_{exit}	15°	14°

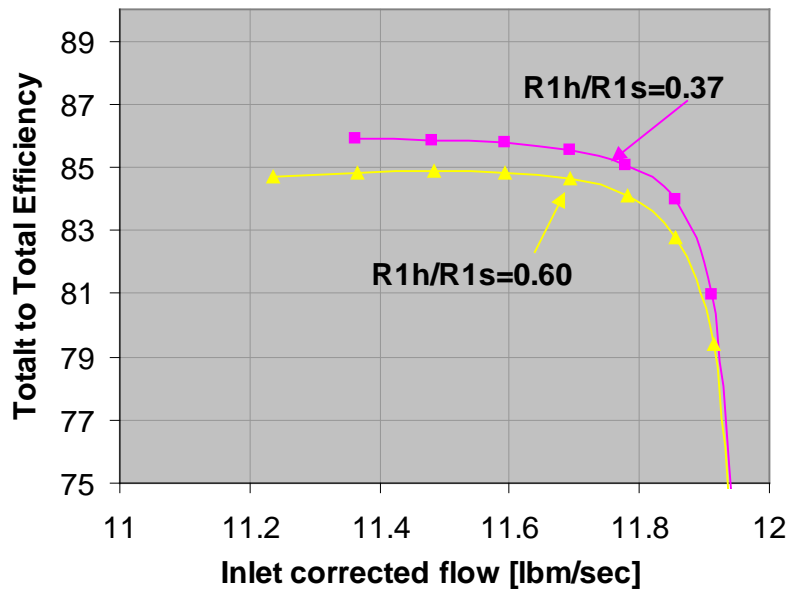


Figure 51.—Meanline prediction of total-to-total adiabatic efficiency for varying inlet radius ratio at fixed inlet area, no inlet swirl (at 100 percent N_c).

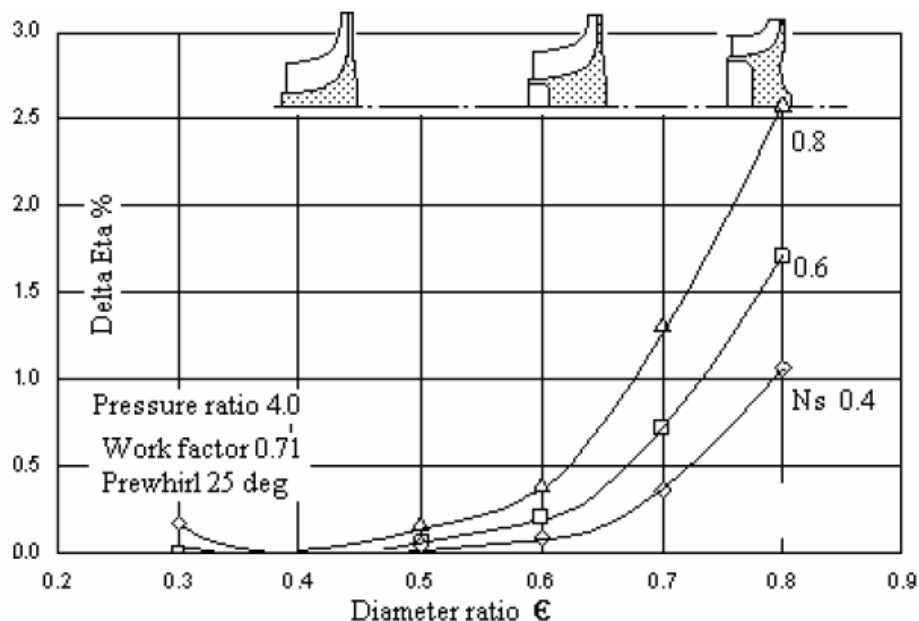


Figure 52.—Estimated efficiency reduction versus diameter ratio, at varying specific speeds. HECC stage is specific speed $N_s = 0.6$. Used with permission from ASME. Rodgers, C., and Brown, D., "High Hub/Tip Centrifugal Compressors," GT2009-59012, Proceedings of ASME Turbo Expo 2009, Orlando, FL, June 8-12, 2009.

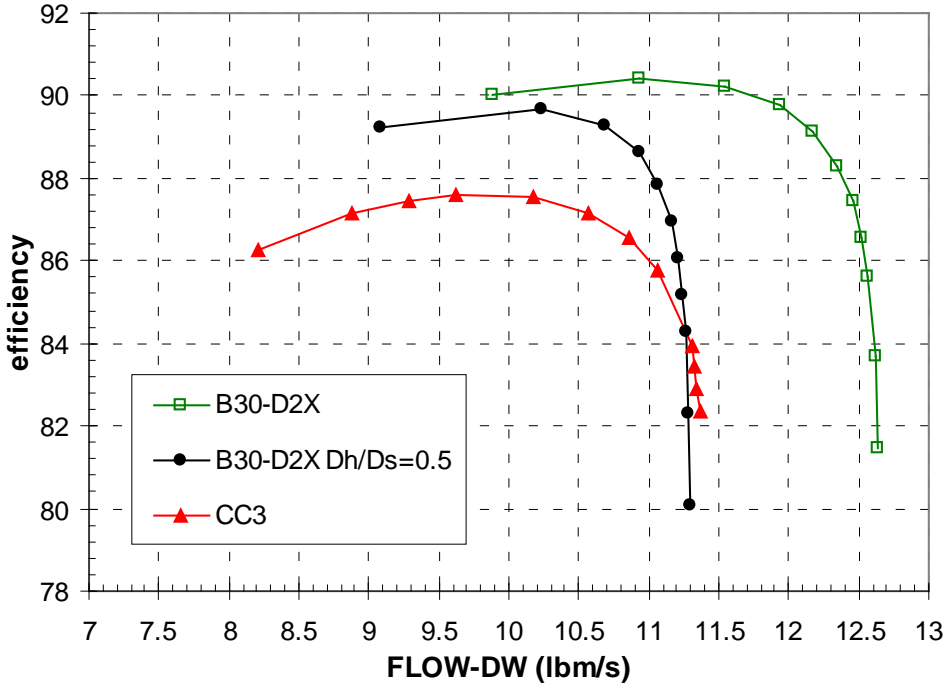


Figure 53.—Adiabatic efficiency(T-T) reduction computed with CFD for the impeller as its diameter ratio is increased to 0.5 (at 100 percent N_c).

The impact of adding fillets has also been estimated by CFD. This is shown in Figure 54 where these rig size fillets seem to have relatively low impact—they add less than 0.1 pt in efficiency improvement, and less than 0.5 percent in increase in capacity. The lowest flow rate achieved in steady CFD computations decreased by about a 1.25 percent.

$$\frac{1 - \eta_{\text{engine}}}{1 - \eta_{\text{rig}}} = \left(\frac{\text{Re}_{\text{rig}}}{\text{Re}_{\text{engine}}} \right)^{0.1} \quad (2)$$

where the Reynolds number is based on inlet flow conditions ρ_1, μ_1 , the mean inlet absolute velocity V_1 , and the tip diameter D_2 . All of the rig quantities are known from the CFD solutions. The engine conditions are found in the following manner. By assuming an overall pressure ratio, and knowing that portion of the pressure rise through the centrifugal stage, then the portion of pressure rise through the engine's axial stages can be assigned and the inlet pressure to the centrifugal can be determined. Based on the design requirements, Table 1, the inlet total temperature is known to be in the range 950 to 1000 °F. The inlet velocity for the engine is found by from the rig inlet Mach number and from the inlet static temperature. Given the range of inlet total temperatures and assumptions of overall pressure ratio in the range 25 to 30, then, the adiabatic efficiency for the engine is expected to be 0.2 to 0.7 pt higher than for the rig. No change in surge margin due to Reynolds number effects is expected in the operating range for the engine, since both rig and engine are in the high Reynolds number regime (Ref. 13).

Finally, the efficiency delta due to Reynolds number effects when scaling from rig to engine is found using the standard formulation (Ref. 13),

Given these estimates, the projected aerodynamic performance of the engine version of the HECC stage is estimated in three steps, as shown in Figure 55. First, the CFD prediction of efficiency is decremented by the amount that the CFD over predicted the data, as based on the CFD results for CC3 stage. This decrement captures the effects of additional losses not captured by the steady-state mixing plane model, any rig inlet flow nonuniformity, backplate bleed, fillets, and any other nonideal geometry not present in the CFD model. In retrospect, this decrementation from CFD results may have been overly optimistic—this will be further elucidated in the discussion in Sections 8.0 and 9.0. For example, the

observed delta of 0.5 pt in adiabatic efficiency between steady and unsteady simulations that have been performed for the impeller-diffuser configuration (and would have likely been higher for the final design) has not been accounted for in this decrementation.

The second step in estimating the performance of the engine version consisted of assessing the range of efficiency penalty due to changes in inlet radius ratio. Last, the range of increase in efficiency due to Reynolds number effects is added. The net result is a predicted polytropic total-to-total efficiency of 87.9 to 88.5 percent (Ref. 14).

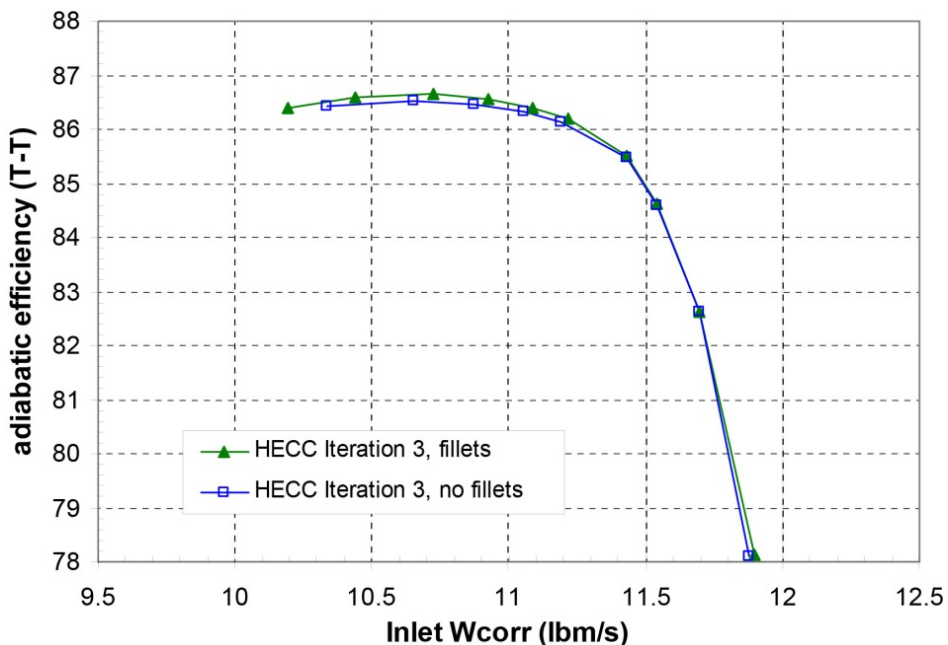


Figure 54.—The impact of adding the fillets to the final design as estimated with CFD.

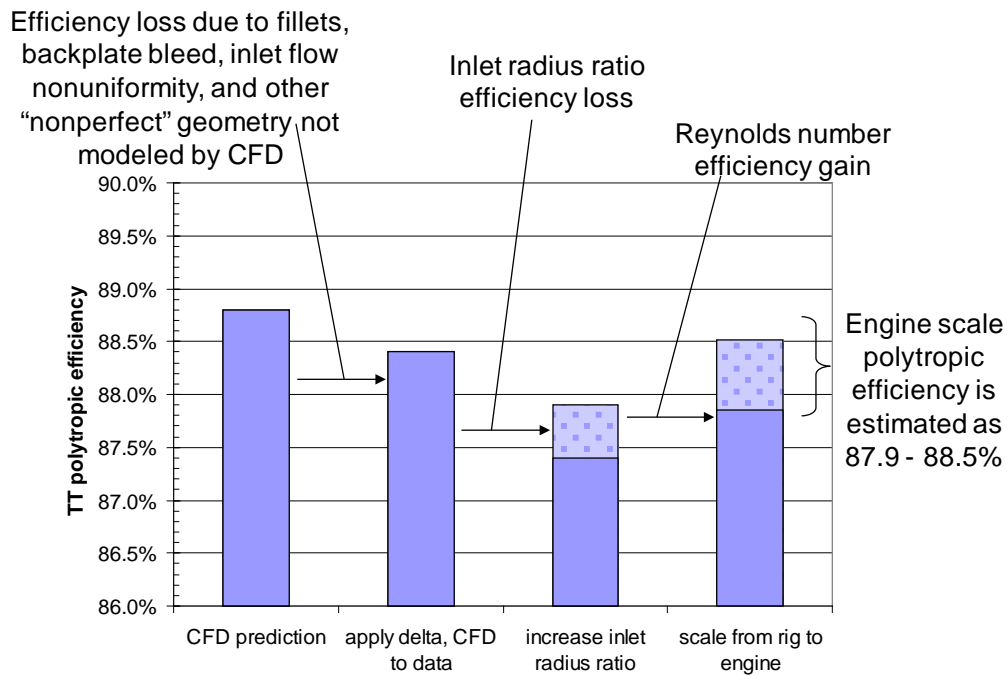


Figure 55.—Bookkeeping efficiency deltas from rig to engine scale.

5.0 Compressor Mechanical Design

5.1 General Information

The High Efficiency Centrifugal Compressor (HECC) was designed to be tested in an existing test rig at GRC where the CC3 compressor was tested (Refs. 6 and 7), and the intent of the aerodynamic design as defined in the NRA solicitation was to maintain/increase efficiency at higher work factor and reduced overall compressor stage radius ratio. For design-point corrected speed was held at that of the NASA CC3 compressor and the HECC was therefore designed to use some of the existing CC3 rig hardware. Figure 56 shows the existing components of the CC3 rig used in conjunction with the new HECC compressor hardware that includes impeller, diffuser, and EGV. The diffuser and EGV assemblies were fabricated as independent subassemblies. All the components are instrumented to acquire detailed experimental data in order to document the aerodynamic performance of the compressor. The HECC compressor design utilizes the existing tip clearance and assembly control system of CC3 rig. Figure 57 shows the total as well as static conditions at key locations along the HECC flowpath. These conditions were used for the mechanical design reported in this document. The following sections briefly describe the mechanical design of each component as well as the associated instrumentation.

5.1.1 Impeller Mechanical Design

The impeller consists of fifteen main and fifteen splitter blades that have rounded trailing edges, and incorporate back sweep and lean as shown in Figure 58. Impeller blades have a compound fillet between the blades and hub. The material for impeller is a titanium alloy (Ti 6Al-4V). The hot hub geometry was transformed to cold geometry using 2D structural analysis, whereas 3D structural analyses were used for transforming the impeller blade geometry from hot to cold. The impeller curvic coupling design is consistent with CC3 compressor. Calculations were carried out to ensure that the curvic coupling design can meet the HECC compressor structural requirements. The impeller design also provided forward and aft balancing zones for material removal during the impeller balancing process.

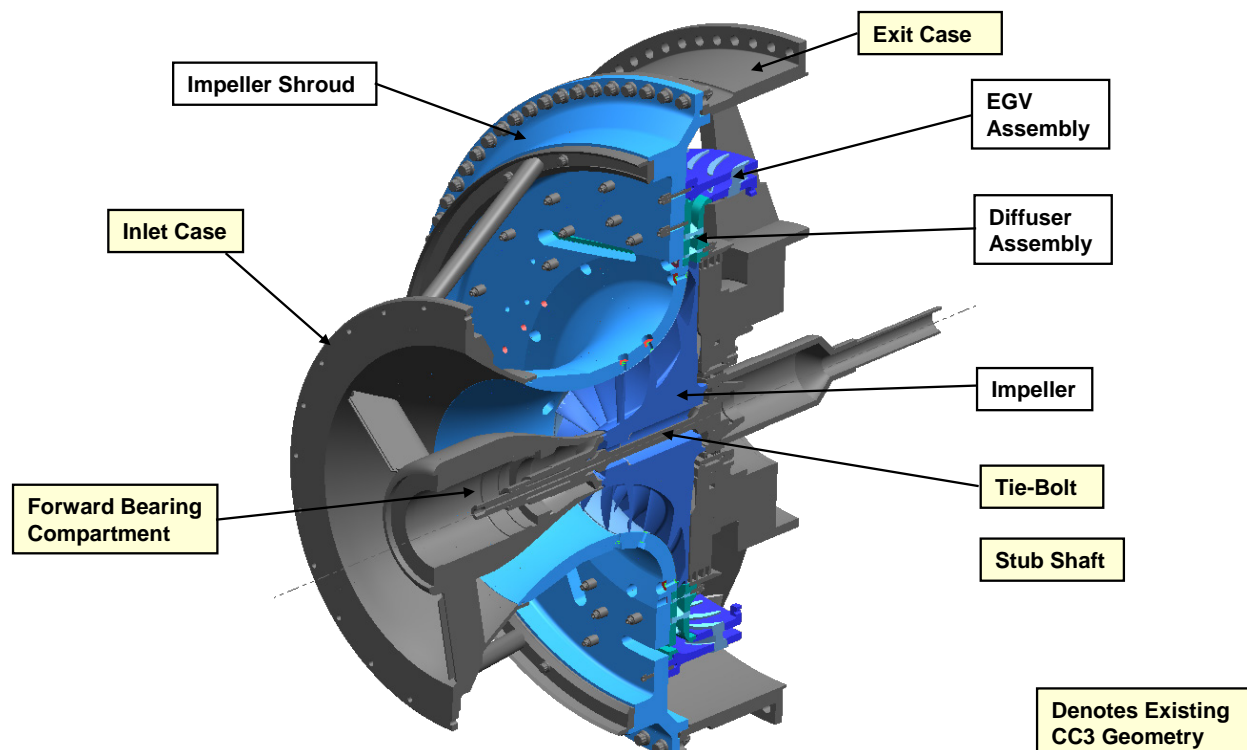


Figure 56.—Cross-section of the HECC compressor rig showing the new as well as existing parts.

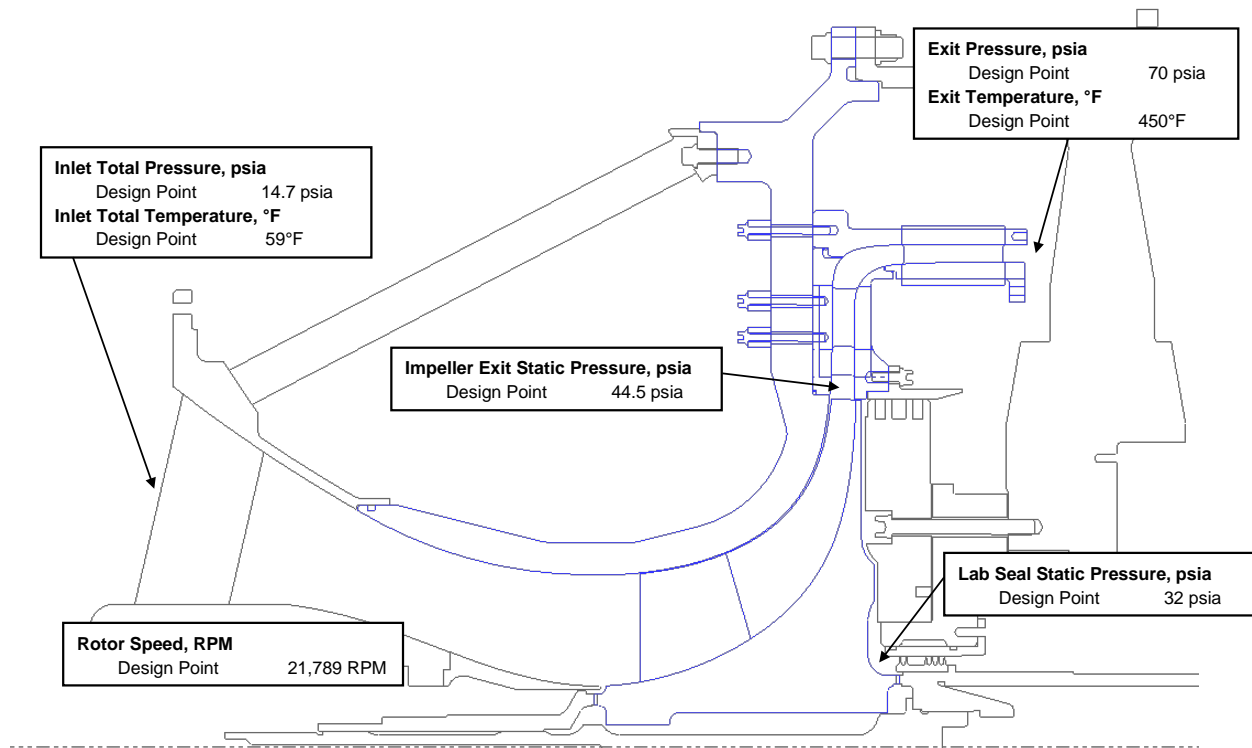


Figure 57.—Compressor rig conditions used in the mechanical design.

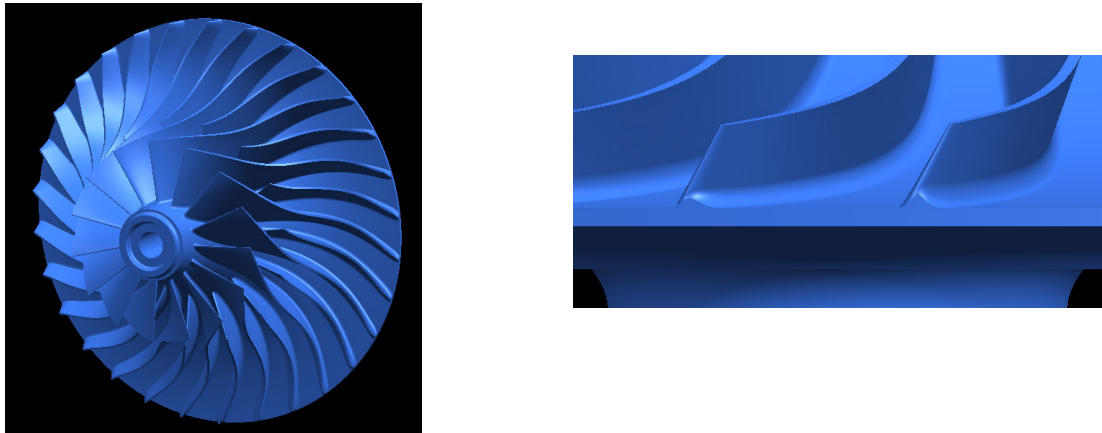


Figure 58.—HECC impeller geometry has 15 main blades and 15 splitter blades. The picture on the right shows the rounded trailing edges and fillets.

5.2 Shroud Design

The shroud is made out of stainless steel (SS 347), and the impeller part of the shroud is coated with an abradable material with a thickness of 0.02 ± 0.005 in. (Figure 59). The shroud cold geometry was calculated from the hot geometry using 2D structural analysis. The shroud design calls for it to be machined from a solid billet. Furthermore, the flowpath was machined with the instrumentation holes plugs in place. Larger slots for instrumentation were milled, whereas the holes for instrumentation were drilled. The finer holes for instrumentation were machined by EDM (electrical discharge machining). In addition, provisions were made for the assembly/disassembly of the shroud with the diffuser and EGV assemblies.

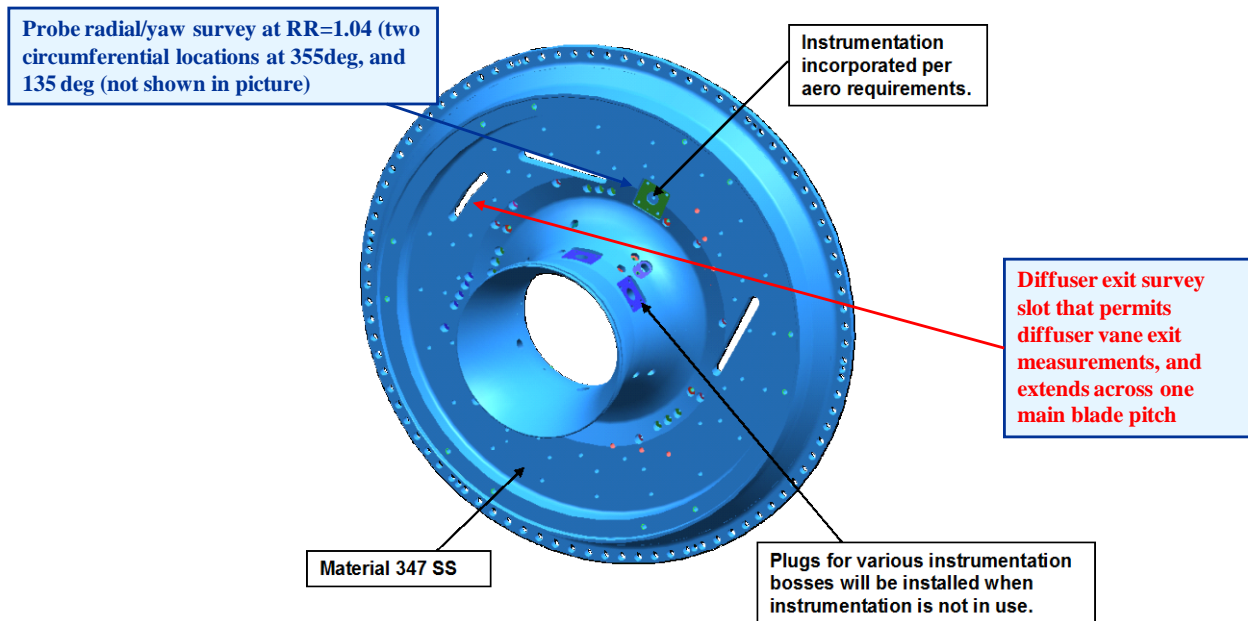


Figure 59.—Compressor shroud showing instrumentation holes, and the abradable material.

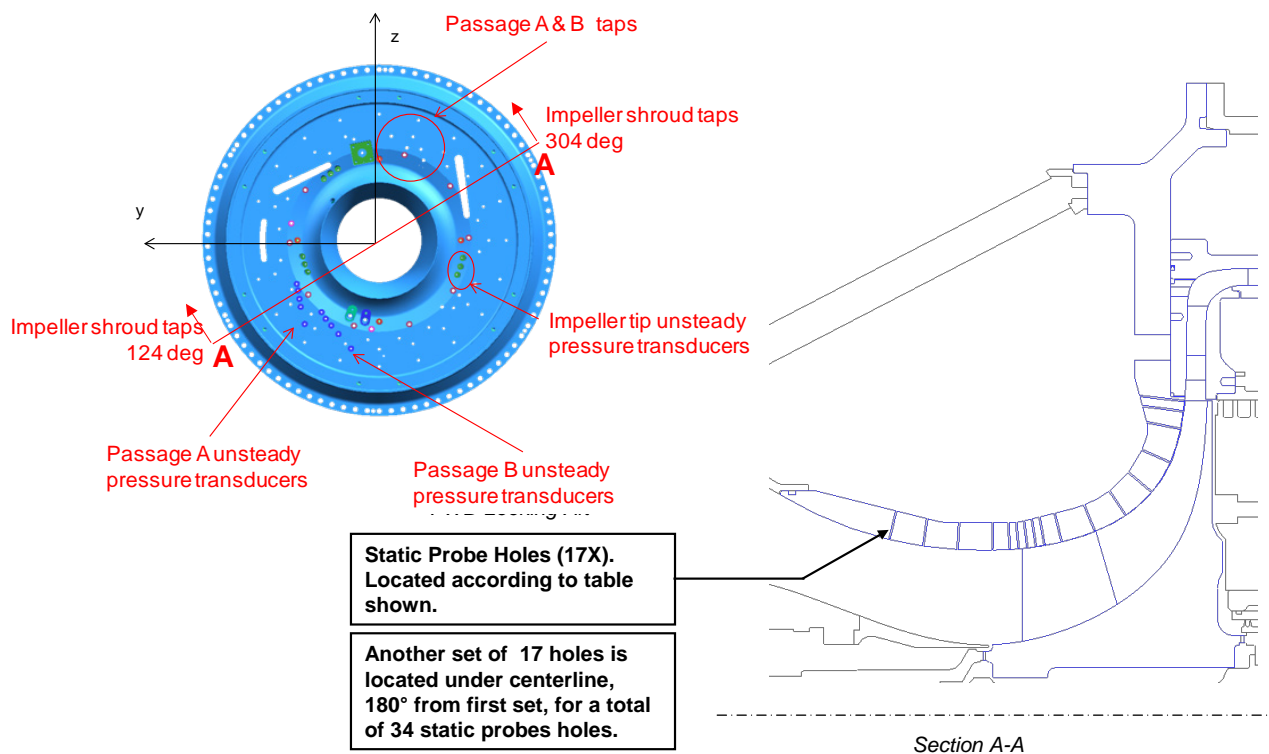


Figure 60.—Impeller static probe hole locations on the shroud.

Two access ports are provided for inlet survey instrumentation. A total of seventeen holes are located on the impeller shroud, starting upstream of the impeller leading edge (Figure 60), with a duplicated set of seventeen holes located 180° from the first set. Two access ports were provided for measurements between the impeller trailing edge and the diffuser leading edge (at radius ratio of 1.04—at two circumferential locations). Provisions for nine Kulite transducers are also located on the impeller shroud. The shroud also has provisions for diffuser and EGV instrumentation, and these are described below where the design of these two parts is discussed. A diffuser exit survey slot is also located at diffuser exit and extends across one main-to-main vane pitch.

5.3 Diffuser Mechanical Design

There are a total of twenty pairs (main/splitter) of diffuser vanes. The diffuser vanes have thin leading edges and are uncambered. These are made of stainless steel (347 SS), and Figure 61 shows the individual components of the entire diffuser assembly. Diffuser hot-to-cold transformation was carried out using 2D structural analysis. The vanes were made by machining a bar stock, and were then brazed with the diffuser hub and shroud using AMS 4777 or AMS 4778 alloy (Figure 62). To facilitate the assembly with the shroud, locating pins are incorporated into the design.

For the diffuser, nine radial Kulite transducers are located over the circumference at 36° increments. A total of 59 shroud vane passage static holes are located around a pair of diffuser vanes that covers one passage of the main and splitter vanes as shown in Figure 63. Another 48 diffuser van passage static holes are located on the diffuser hub (Figure 64). A traversing survey slot is located downstream of the diffuser trailing edge. Three static holes are located on the diffuser shroud bend, and six on the hub bend. A pocket is contoured on the diffuser shroud to route the instrumentation tubing. Four strain gauges are also located on the diffuser vanes. Two of the diffuser vanes are modular, and their design allows for their removal in order to provide instrumentation versatility. More information on the instrumentation location is given in Appendix E.3.

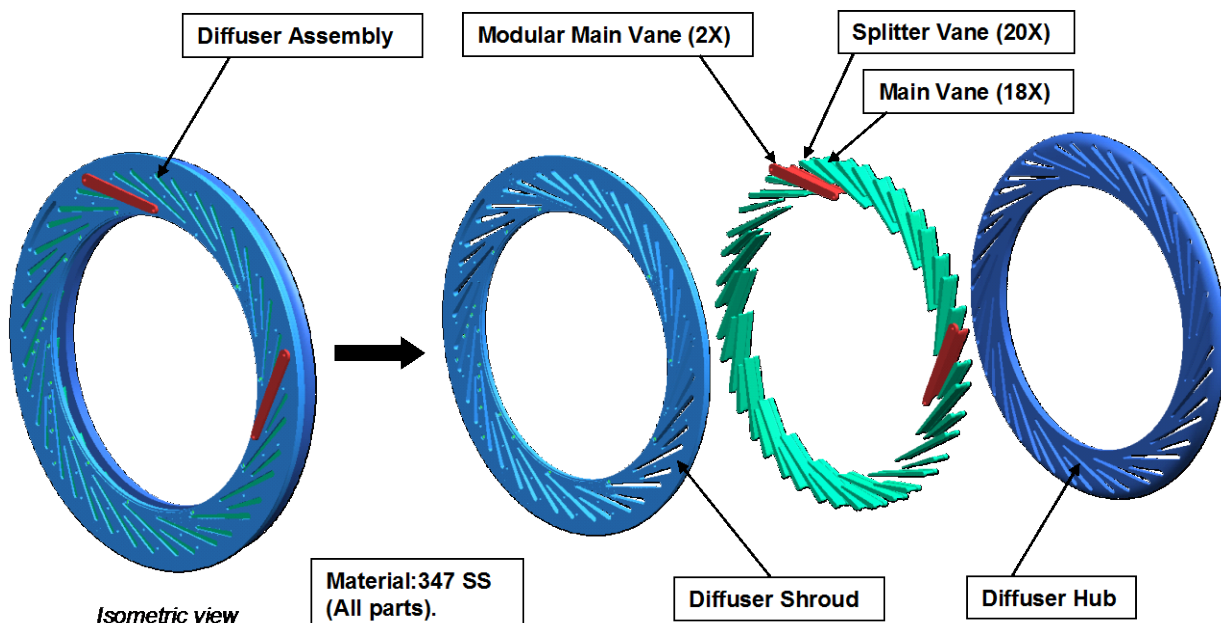


Figure 61.—Assembly of the diffuser vanes with the hub and shroud. The two instrumented modular vanes are shown in red.

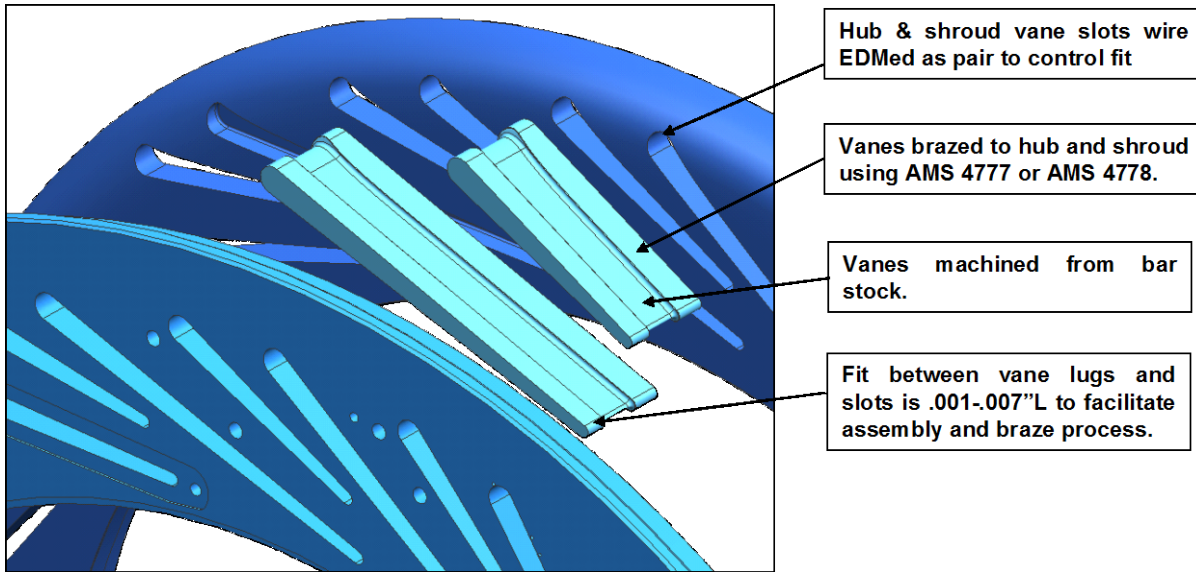


Figure 62.—Diffuser vanes were designed to be brazed with the hub and shroud.

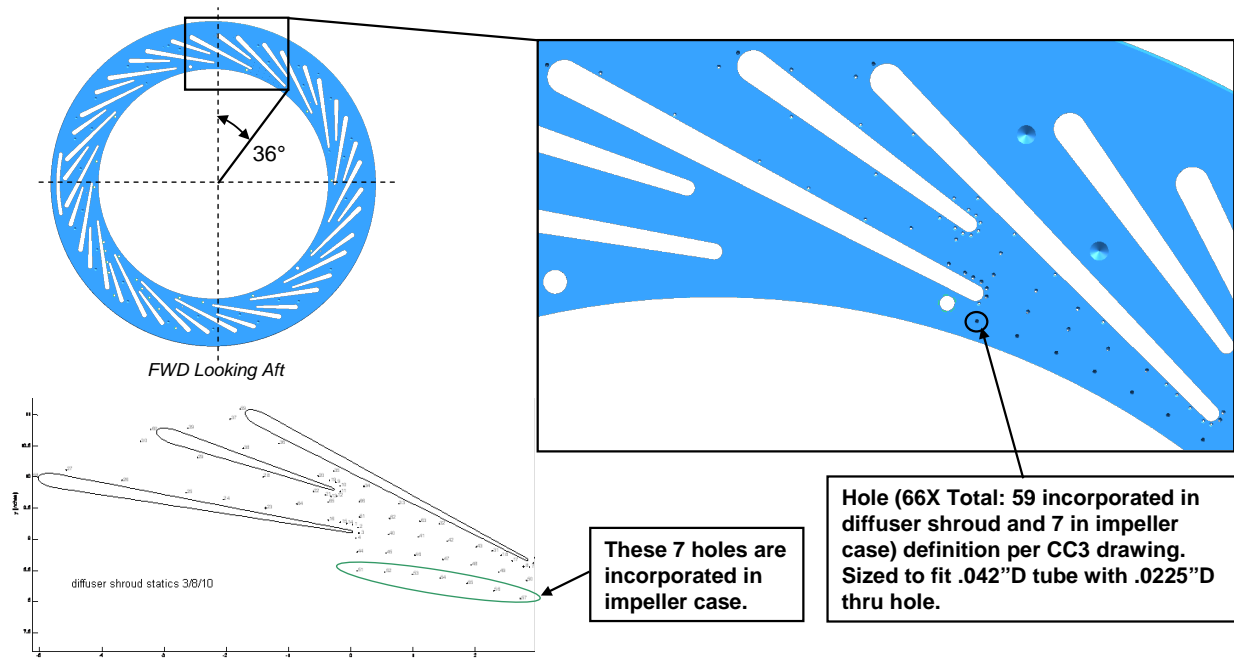


Figure 63.—Diffuser vane passage shroud static holes.

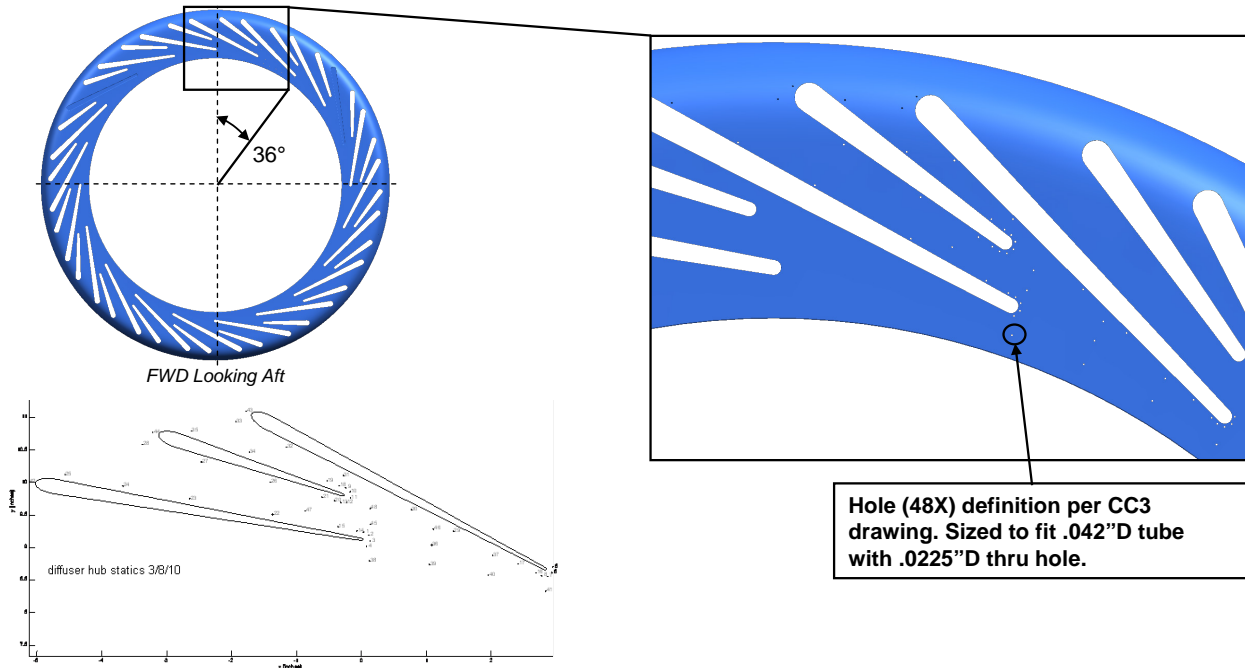


Figure 64.—Diffuser vane passage hub static holes.

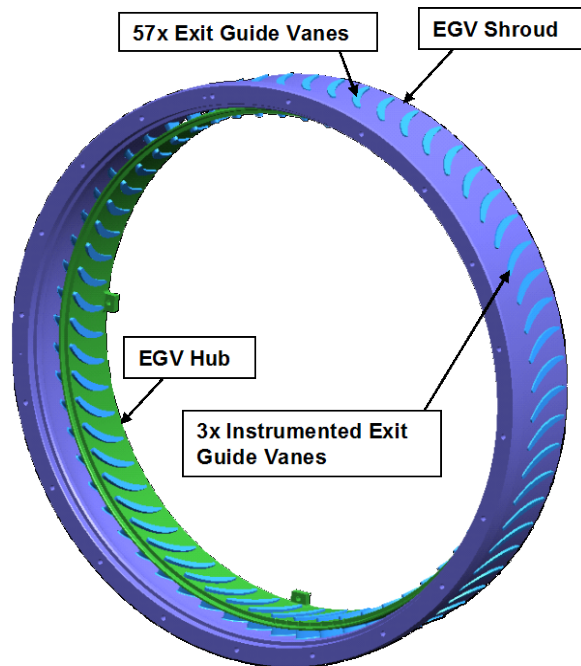


Figure 65.—EGV assembly has 60 vanes and three of these are instrumented.

5.4 Exit Guide Vane Mechanical Design

There are a total of sixty exit guide vanes (EGVs), three of which are instrumented, as shown in Figure 65. The vanes are made out of stainless steel (347 SS) and are machined from a bar stock, and then brazed to hub and shroud using AMS 4777 or AMS 4778 brazing alloy as depicted in Figure 66. Locating pins are provided for properly locating the diffuser and EGV assemblies. The diffuser and EGV

assemblies form a tight fit to seal the flow path, and four jackscrew holes are provided for removing the EGV assembly. A provision allows for future clocking of the EGV relative to diffuser by up to half a vane pitch. The hot-to-cold transformation was done using 2D structural analysis. Axial loads due to thermals are accounted for in order to determine the axial forces on the bolted joints.

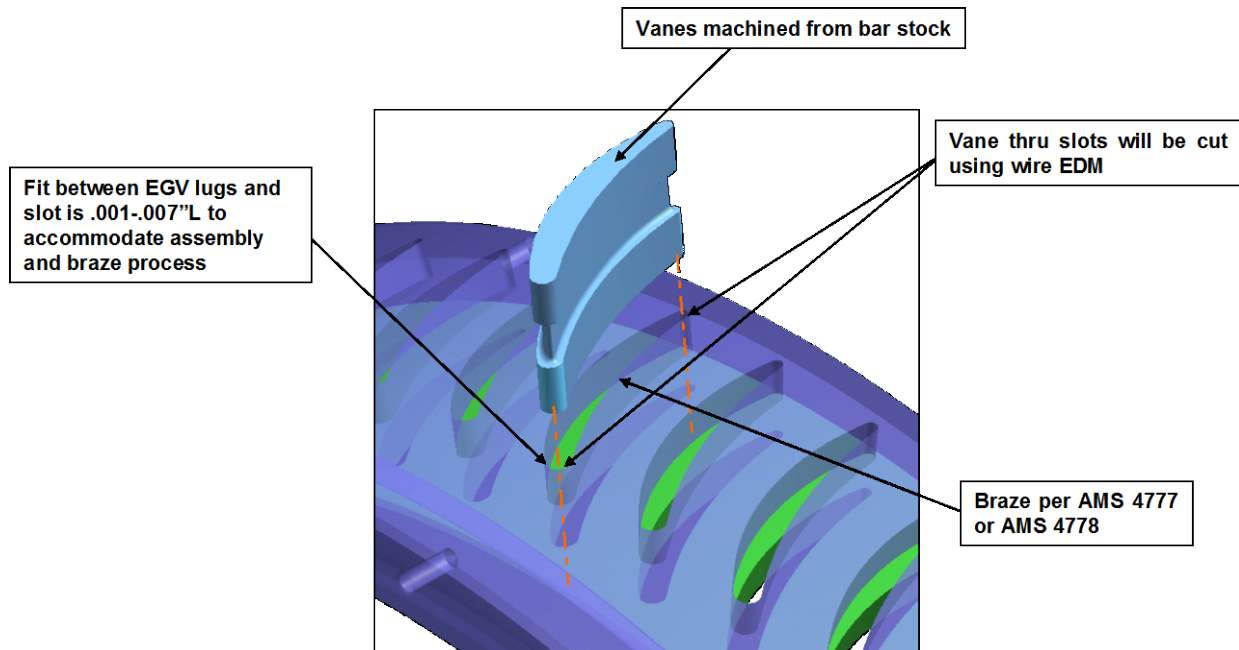


Figure 66.—EGVs are designed to be brazed with the hub and shroud.

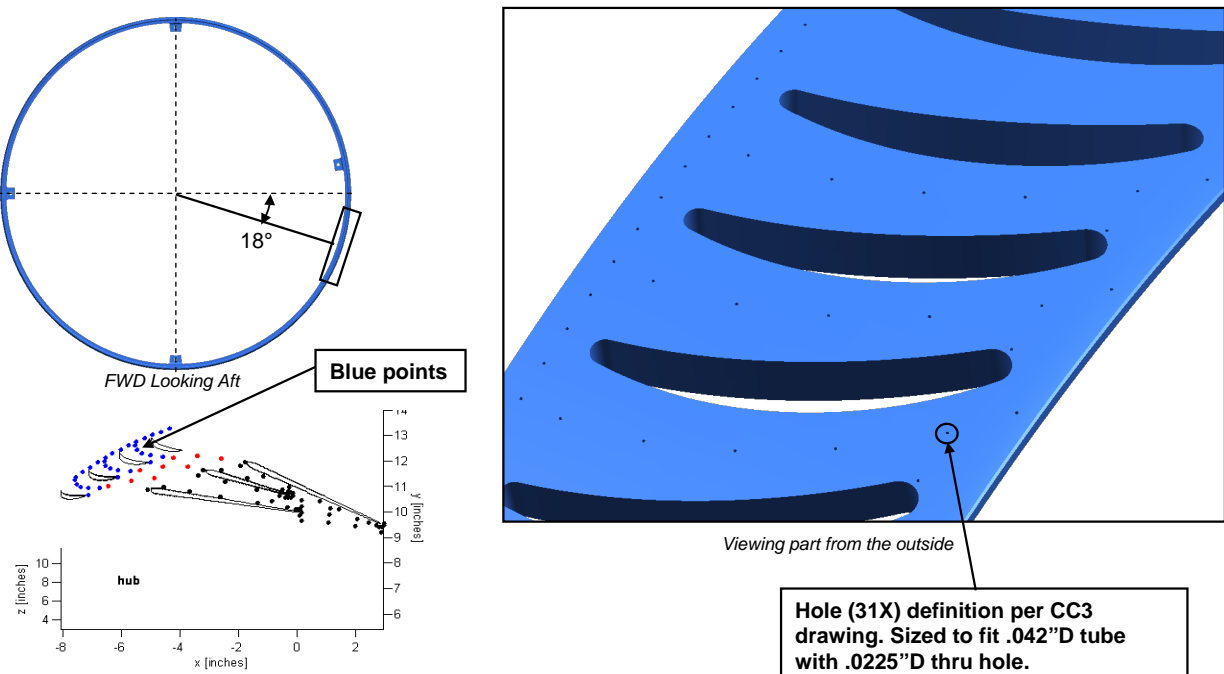


Figure 67.—There are 31 EGV hub static holes.

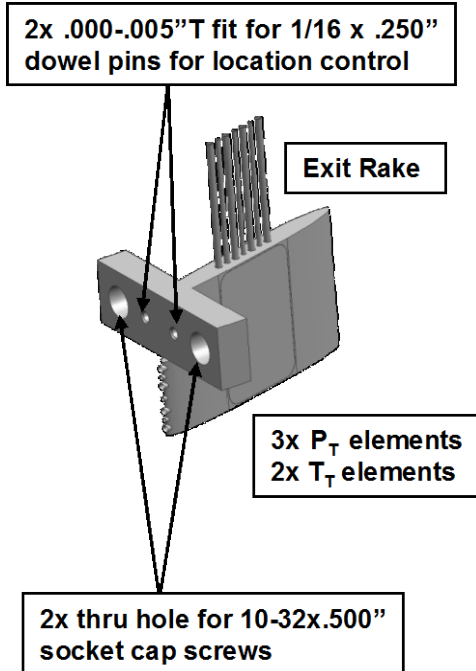


Figure 68.—There are 12 exit rakes located around the circumference at the aft of the EGV trailing edge. Each rake has three probes for measuring total pressure, and two probes for measuring total temperature

Thirty one EGV shroud static holes, and 31 EGV hub static holes are provided as depicted in Figure 67. These statics span over three EGV passages. Twelve exit rakes are placed circumferentially at the aft face of EGV shroud to measure the exit total pressure and temperature. Each rake has three total pressure and two total temperature measuring elements (Figure 68). Six static holes are located on the EGV shroud bend, and three on the hub bend.

5.5 Flow Chart of Structural Analysis

As a follow-up to the PDR, where the concerns were raised about high-cycle fatigue due to relatively thin diffuser blades, various additional structural analyses were performed to assess burst margin, low cycle fatigue limits, and high cycle fatigue capability. A modal analysis was also performed to ensure that no resonant crossings occur in the expected operating range of the rig.

A detailed description of typical engineering practice was prepared. A flow chart of the various analyses performed under this contract, as presented at PDR, is shown in Figure 69. CFD solutions provide boundary conditions for steady-state thermal and stress analyses, from which assessments are made of burst margin, low cycle fatigue (LCF) limits, and high cycle fatigue (HCF) capability. A modal analysis is also performed to assure that no resonant crossings occur in the expected operating range of the rig.

A similar flowchart that corresponds to high cycle fatigue assessment is shown in Figure 70. After performing steady state stress and modal analyses, the margin for the magnitude of vibratory stresses is assessed using a Goodman diagram, which charts the allowable vibratory stress at a given mean stress level for a particular material. A notional criteria is that at a given mean stress levels, there remains 10 ksi of margin in vibratory stress. The frequency at which vibratory stresses occur is assessed using a Campbell diagram, in which the resonant frequencies are compared against the expected vibratory drivers; typical practice is to have some margin between the two frequencies within the operating range. The diffuser design as presented at PDR passes both concerns.

Having passed criteria for both the magnitude and frequencies of vibratory stress allowance, it is common to use strain gages to measure vibratory stresses during a rig or engine test. It is recommended that this additional instrumentation be included in the initial testing of the new design to assure HCF margins.

In some engine development programs, coupled fluid/structure interaction analyses are performed to attempt to predict the magnitude of the vibratory stresses, Figure 71, in situations where the required frequency margins are not met. Experience has shown that such predictions can be unreliable and are used only provide guidance as to which strain gage measurements are most critical.

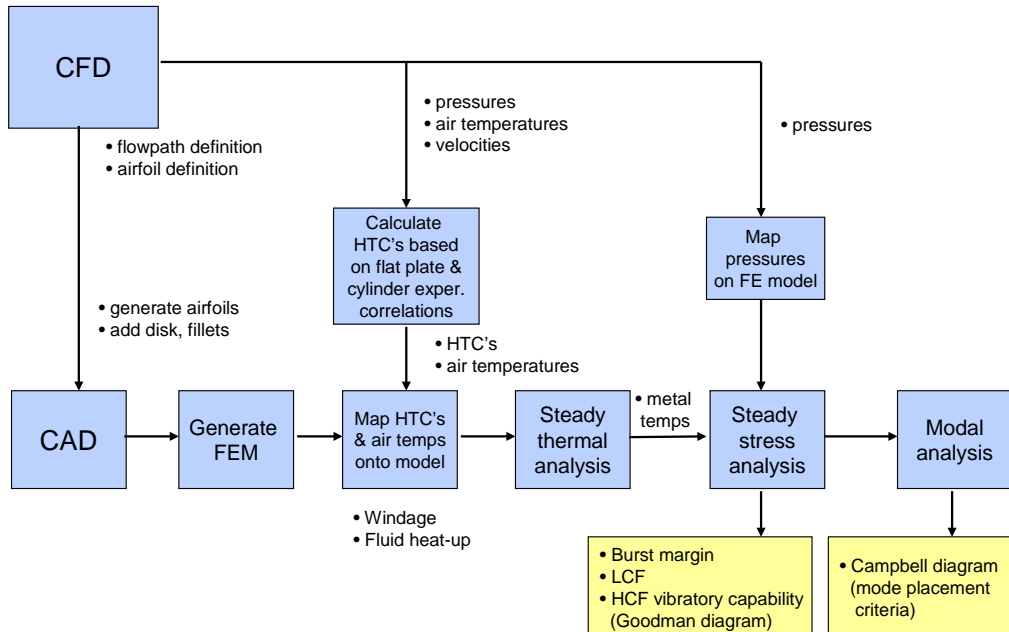


Figure 69.—Flowchart of aerodynamic and structural analyses used during design process.

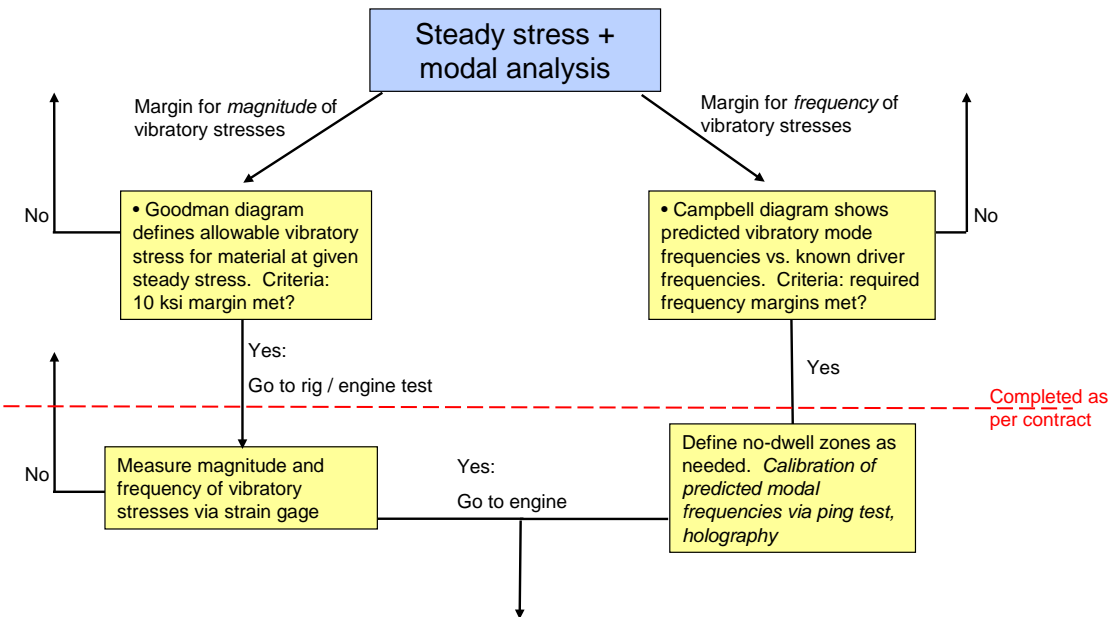


Figure 70.—Typical flowchart for high cycle fatigue analysis.

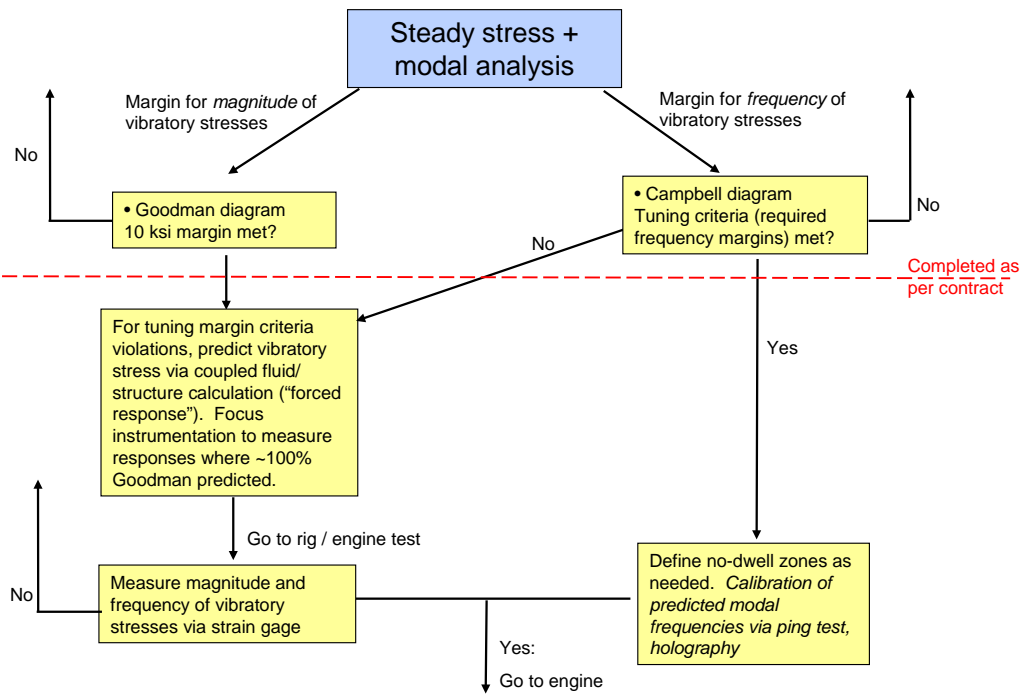


Figure 71.—“Higher fidelity” analysis flowchart for high cycle fatigue.

5.6 Impeller Burst Margin

Results from a 2D analysis of the impeller and the resulting von Mises stress are shown in Figure 72; a comparison to the existing NASA CC3 impeller is also made. Very similar stress levels as CC3 impeller are observed, with plenty of burst margin.

Although the engine stress is 3.05 times higher than the rig, the ultimate tensile strength of nickel is 1.7 times higher than titanium. The equation for burst speed is:

$$\text{Burst speed} = \sqrt{\frac{\sigma_{-3\sigma \text{ UTS}} (.85)}{\sigma_{\text{average hoop}}}}$$

The rig impeller is estimated to have burst speed of about 200 percent design rpm, so scaling this by $\sqrt{1.7/3.05}=149$ percent design speed, which is sufficiently higher than the criteria of 120 percent design speed.

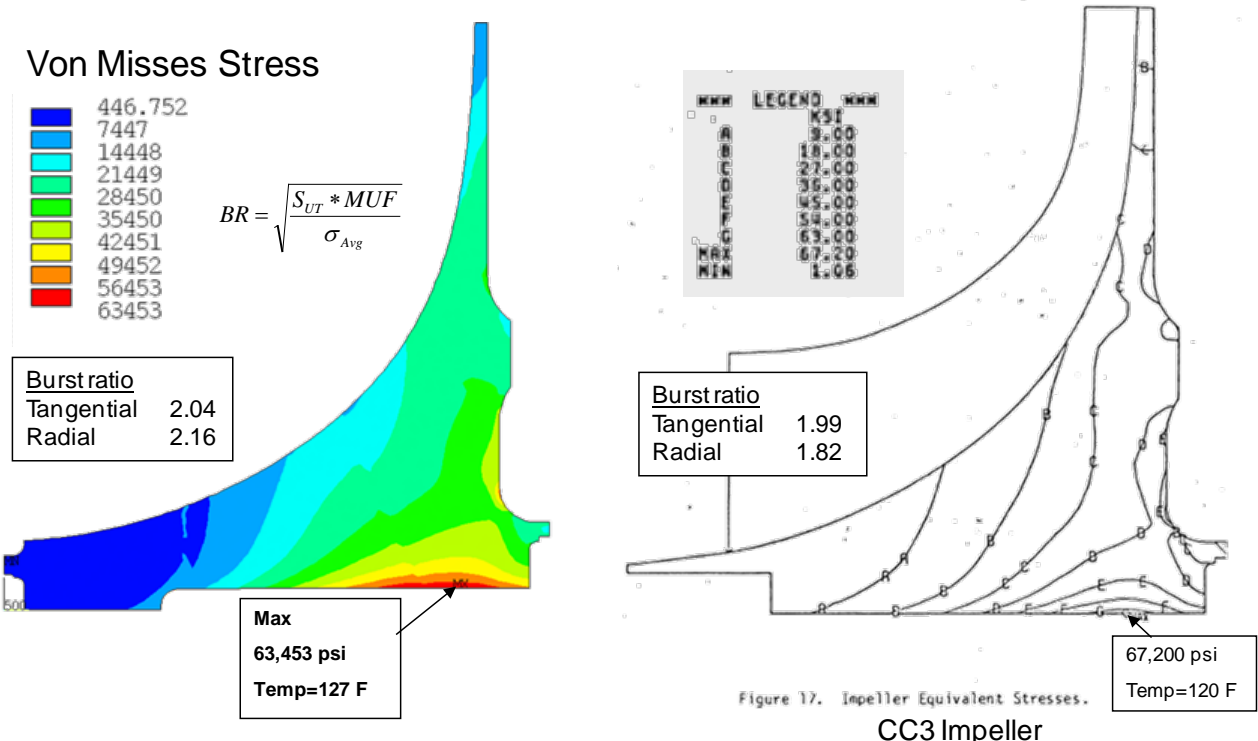
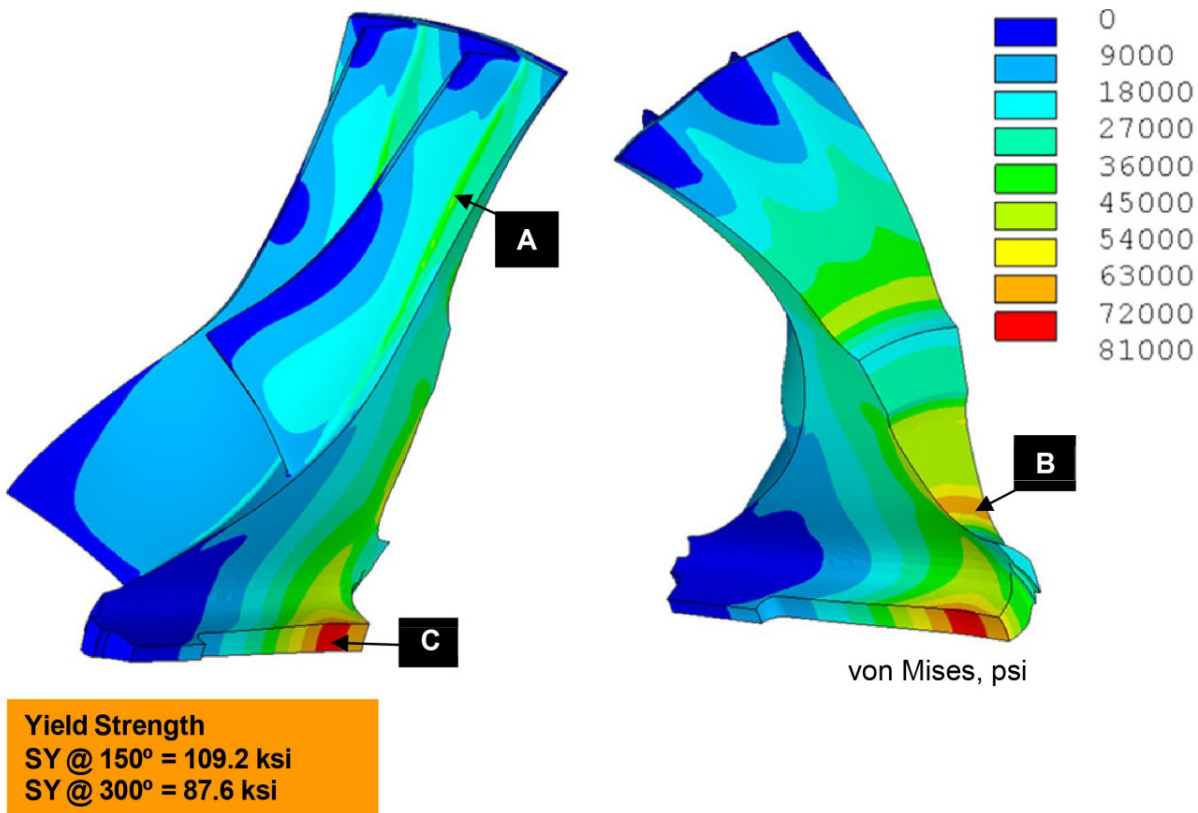


Figure 72.—Impeller 2D analysis—von Mises stress; comparison to NASA CC3 impeller.

5.7 Impeller Stress Analysis—Low-Cycle Fatigue Analysis

Figure 73 presents overall von Mises stresses plot to observe peak stresses locations for the rig. High stress regions are compared to 80 percent yield strength to calculate safety margin.

The engine impeller will have mechanical stresses approximately 3 times higher than the rig, and also higher transient thermal stresses. The magnitude of the estimated transient thermal stresses was made from similar engine impellers to increase the total stress by about 15 percent. The minimum LCF life for Udiment 720 at these combined stress levels and temperatures is estimated to be about 1600 cycles. This is low for a commercial engine, but not a show-stopper: because the burst speed is so much higher than required, it is possible to redesign the impeller disk shape to reduce the mechanical stresses, in order to gain more LCF life. This is a typical design work that would be done in the process of resizing an existing impeller to a new application.



Location	S1 (ksi)	S3 (ksi)	Radial (ksi)	Tangential (ksi)	Axial (ksi)	VM (ksi)	T (°F)	sm (%)
A	57.0	0.66	39.6	44.4	4.33	48.8	300	30.37
B	78.9	0.85	76.2	59.8	3.59	70.5	150	19.30
C	67.7	-14.4	0.07	67.7	-14.4	75.9	150	13.12

Note: safety margin calculated using von Mises stress results and 0.8*SY

Figure 73.—Overall von Mises stresses plot to observe peak stresses locations with high stress regions compared to 80 percent SY to calculate safety margin.

5.8 High-Cycle Fatigue Analysis

Figure 74 shows impeller high-cycle fatigue analysis, and impeller Goodman diagram. Impeller has adequate vibratory capability (>10 ksi). Similarly, the analysis for the diffuser and EGVs shows infinite HCF life for diffuser vanes.

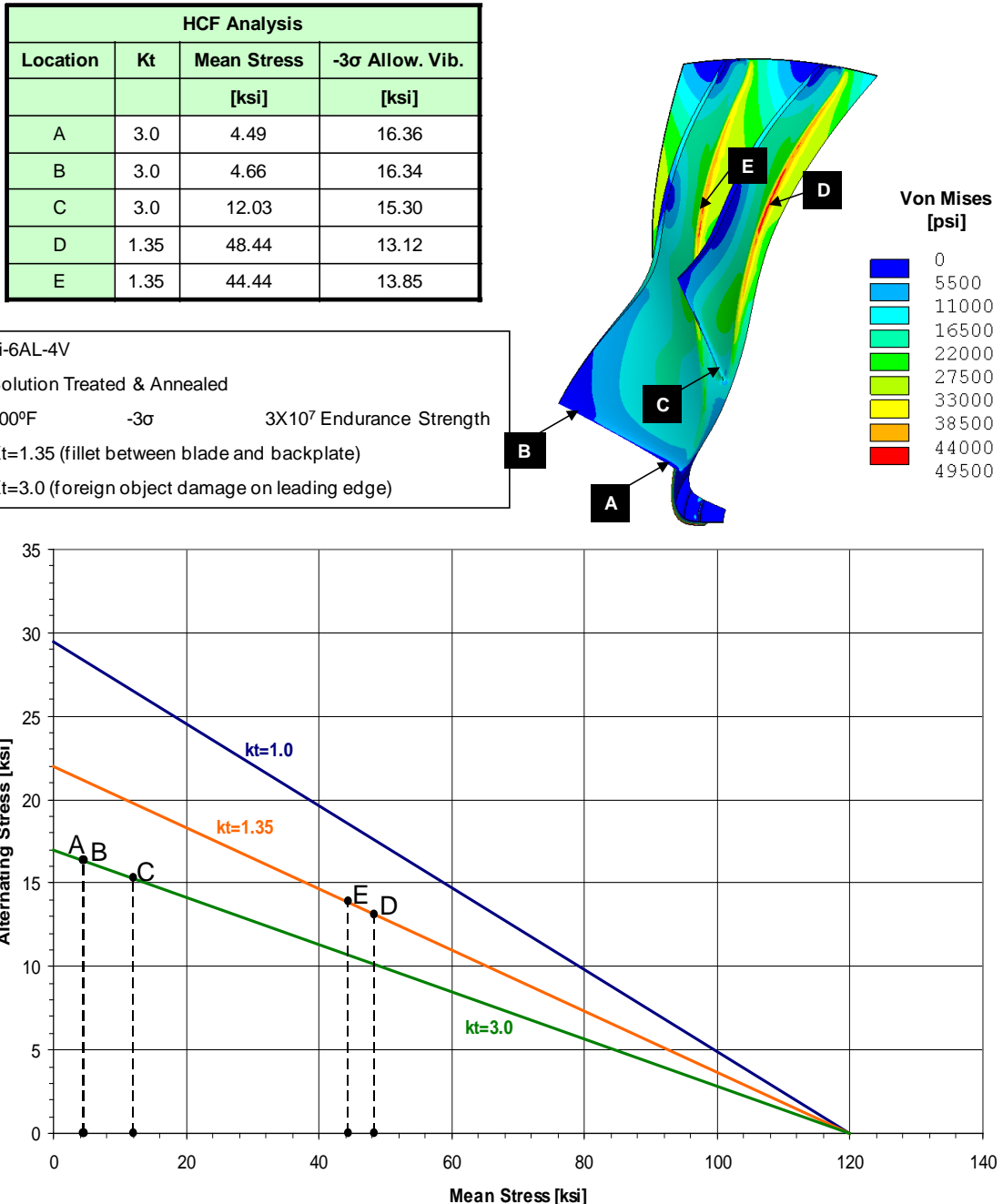


Figure 74.—Impeller high-cycle fatigue analysis and impeller Goodman diagram.

5.9 Campbell Diagrams for Impeller, Diffuser and EGV

Parts of the modal analysis are presented here in the form of Campbell diagrams for the impeller, diffuser and EGV, shown in Figure 75, Figure 76 and Figure 77.

For the impeller the modal analysis in Figure 75 shows acceptable mode placement, with the only recommendation to move the 80 percent steady state operation to 84 percent speed to reduce risk. For the diffuser, shown in Figure 76, there is plenty of margin for all modes and no speed restrictions are necessary (first mode has 51 percent margin above 30EO—impeller blade count). Figure 77 shows that all fundamental EGV modes are above the operating range (with plenty of margin above 30EO and 60EO).

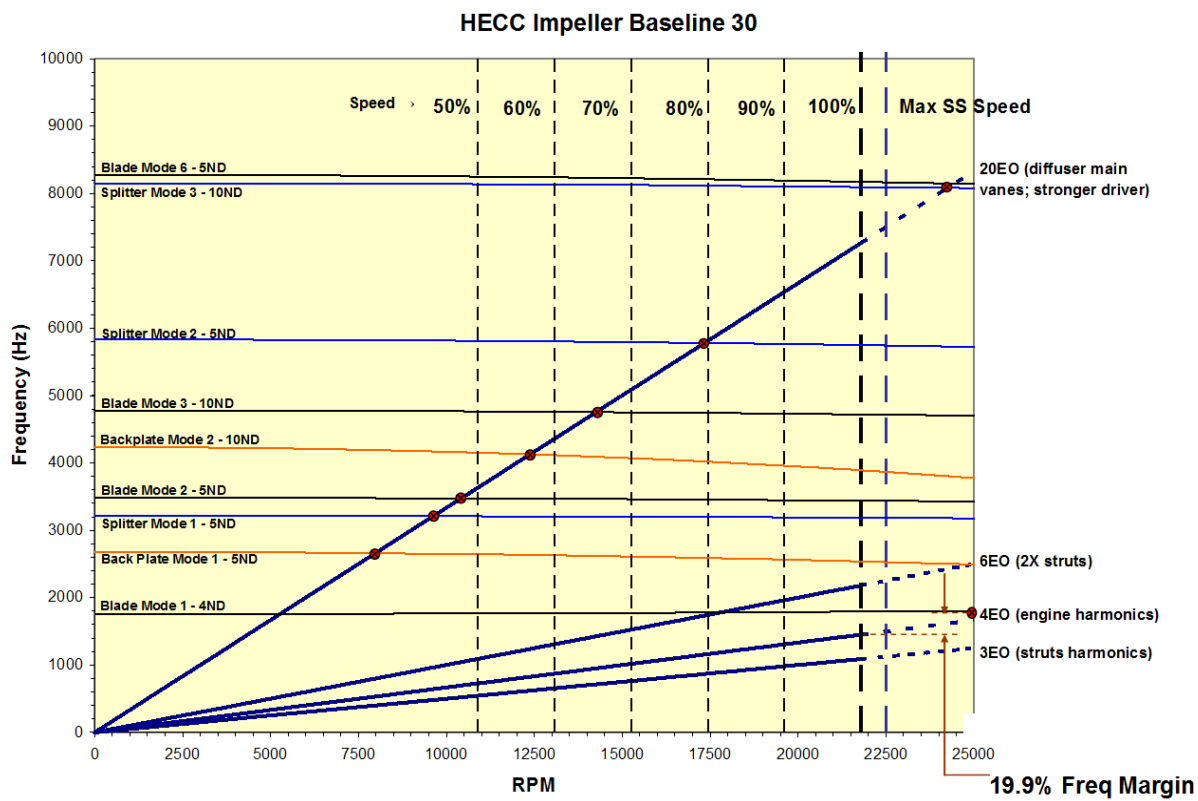


Figure 75.—Impeller Campbell diagram (red dots are fundamental modes).

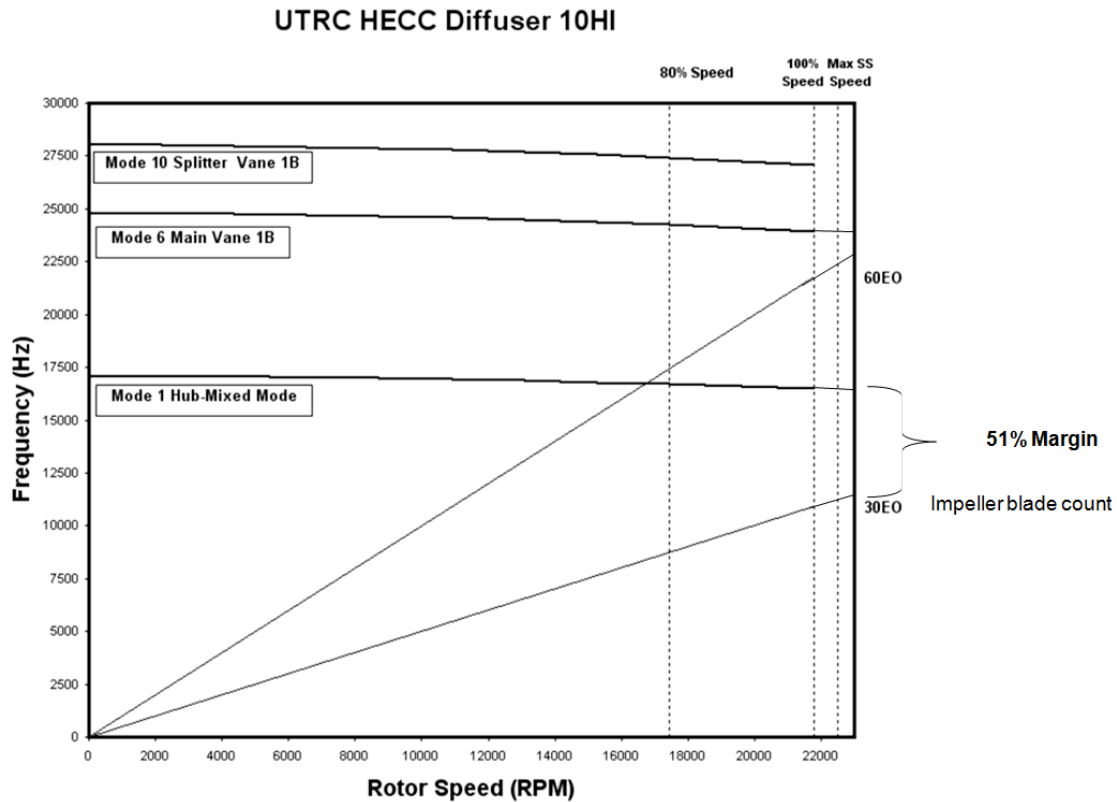


Figure 76.—Diffuser Campbell diagram.

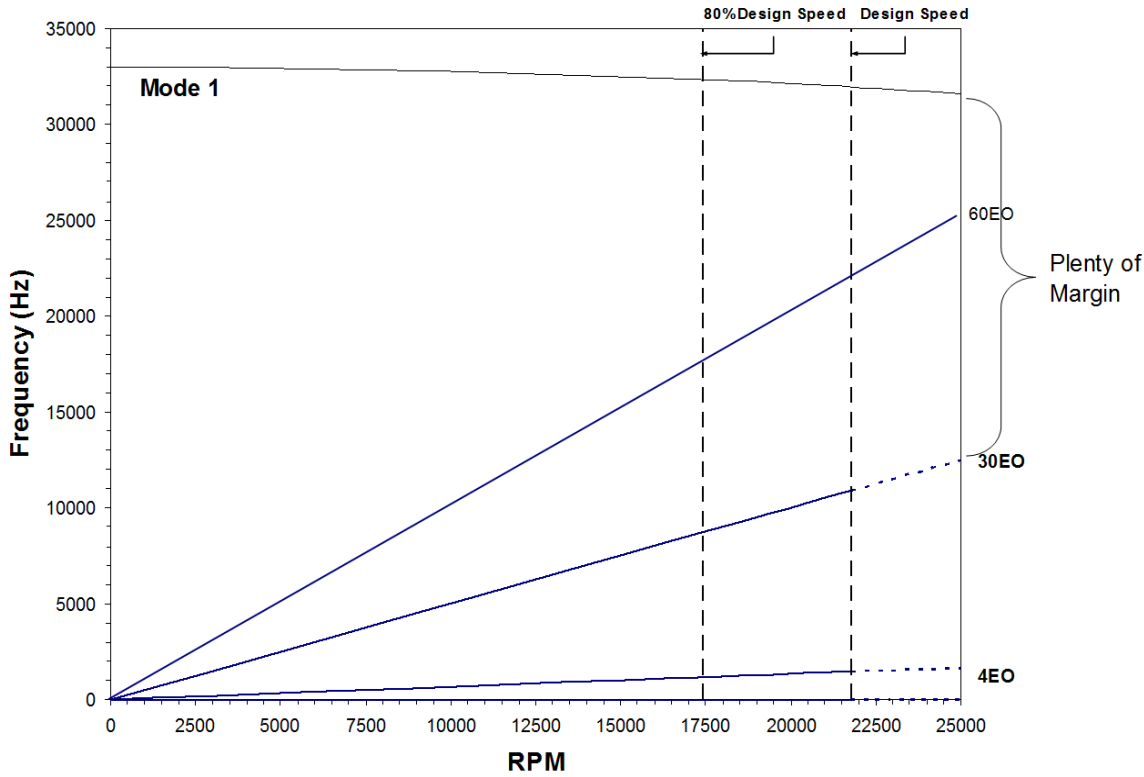


Figure 77.—EGV Campbell diagram.

6.0 Fabrication and Assembly

As noted, GRC has an existing Small Engine Components Compressor Test Facility (Ref. 15) located in the CE-18 test cell. This test cell provides the testing of the advanced axial and centrifugal multistage compressors. Previously the CC3 Centrifugal Compressor Stage was tested in the same test cell (Refs. 6 and 7). Since the HECC compressor will be tested in the CE-18 test cell, it is designed to use some of the existing rig hardware. Figure 56 shows the existing components of the CC3 rig that will be used in conjunction with the new HECC compressor hardware that includes an impeller, a vane diffuser, and an EGV. In order to increase the future versatility of the rig the diffuser and EGV subassemblies are fabricated separately and the design allows for their disassembly. All the components are instrumented to acquire detailed experimental data in order to document the aerodynamic performance of the compressor. The HECC compressor design utilizes existing clearance and assembly control of the CC3 rig.

6.1 Impeller

The titanium forging was first rough-turned to an oversize impeller volume shape as shown in Figure 78. An ultrasonic test of the rough-turned forging was carried out to confirm that there were no cracks or any other internal material defects. This was then sent to Turbocam Inc. for further machining to produce the final impeller (Figure 79). Turbocam used point milling process for both roughing and finishing the impeller blade, hub, and tip surfaces. For this purpose a ball end mill with pass spacing was used to achieve the desired surface finish. All of the milling operations were performed on a simultaneous 5-axis milling machine. The turning of all the two-dimensional features was done on a vertical turn lathe.

After completing the machining the impeller was then sent to Anmark Machine for fabrication of the curvic couplings. In addition the balance adapters were also fabricated for detail balancing of the impeller, which was initially carried out by The Balancing Company, Inc.

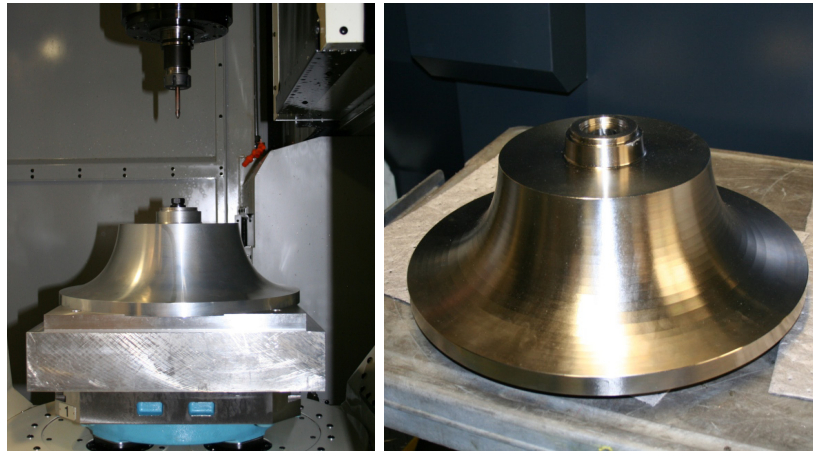


Figure 78.—The titanium forging was first rough-turned to an oversize impeller volume shape.



Figure 79.—HECC impeller after the final machining.

6.1.1 Impeller Fabrication Problems and Their Solutions

Due to a mistake during the machining process, one of the blades near the trailing edge was chipped (Figure 80) and required repair. UTRC consulted with its business units Hamilton Sundstrand-Power Systems (HS-PS), Pratt & Whitney Canada (PWC), and Pratt & Whitney to develop a repair process that was then used by the vendor to repair the blade. The repair process consisted of weld repair, heat treatment, and finish machining to the original specifications. Consideration was given to the tradeoff between the performance debit and the life debit. The repaired blade was inspected after the repair, and it met the required tolerances.

After receiving the balanced impeller and the curvic couplings, GRC carried out measurements using their in-house setup and reported excessive runouts at the impeller OD, as well some imbalance. In an attempt to find the root cause of the problem UTRC talked to all the vendors that worked on the impeller. It included Turbocam, Inc., who machined the impeller, Anmark Machine who fabricated the curvic couplings, and The Balancing Company, Inc. who did the balancing. The inspection reports from these vendors did not indicate any problems, and implied that each vendor was able to meet the tolerances specified on the drawings for their tasks. Anmark and The Balancing Company offered to re-inspect the impeller and associated hardware for their part of the work. After consultation with team members it was decided that the best course of action was to have Anmark recheck the impeller runouts with a more accurate setup than NASA afforded.

The results of the Anmark measurements are summarized in Figure 81 in the form of total-indicator-runout (TIR). The runout on both the ground and the unground area of the hub in front of the impeller leading edge was found to be 0.003 in., instead of 0.002 in. as is called on the drawings. The blade tip runout at approximately mid-chord was 0.003 in., whereas the blade outer diameter (OD) runout was 0.0022 in. Both of these should have been 0.002 in. per drawing specifications.

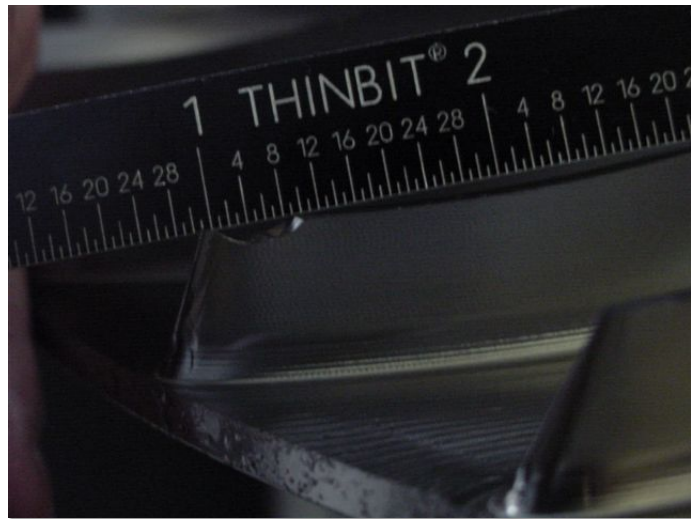


Figure 80.—Area of impeller damage incurred during machining.

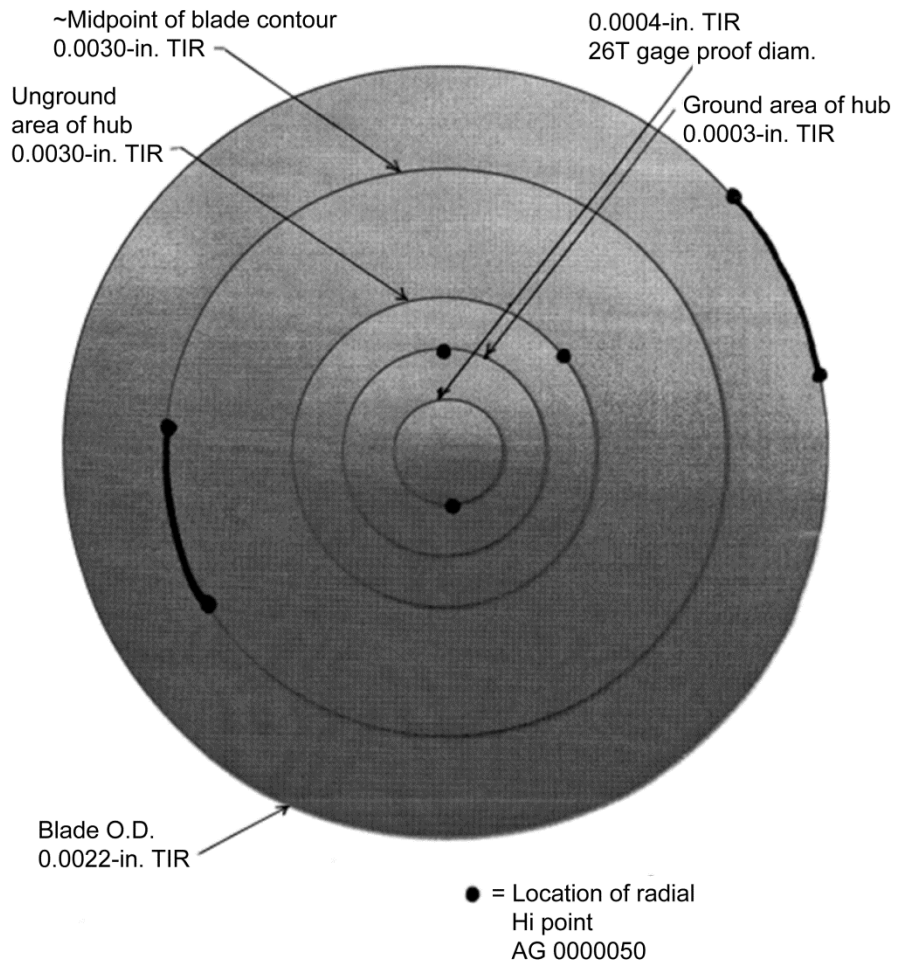


Figure 81.—Summary of the impeller runouts as measured by Anmark.

Since the impeller tip clearance is 0.012 in., a runout of 0.003 in. in the blade tip variation amounted to an undesirable 25 percent variation in the blade tip clearance. So there was a need to bring the impeller runout within the drawing specifications of 0.002 in. However, the entire project team expressed the desire to go a step further and reduce the impeller blade tip runout to 0.001 in. rather than 0.002 in. The reason for this was that a 0.002 in. in the blade tip variation still amounted to about 16 percent variation in the blade tip clearance. In addition the blade tip runout of CC3 impeller at GRC, which had the same diameter as the HECC, was 0.001 in.

Therefore UTRC explored the possibilities that could allow the impeller runout to be brought to 0.001 in. Initial handicap was the fact that the maximum impeller blade tip runout at mid-chord and the maximum blade outer diameter runout were at locations that were circumferentially opposite to each other. These are marked on Figure 81 as "location of radial hi point". A plan was then put together that allowed the regrinding of the curvic couplings to bring the impeller blade tip runout to 0.001 in. while relaxing the blade outer diameter at the back face to be up to 0.002 in. below the lower limit as specified on the drawings. Note that relaxing these two dimensions does not affect the impeller flowpath. The plan requirements and the process that was used to reduce the impeller runouts is summarized below.

Plan Requirements

- The plan required relaxing the axial length of the impeller which was 7.3916 in. The drawing sets this dimension to the range of 7.389 to 7.393 in. as is shown in Figure 6 (this length finally came out to be 7.3838 in.)
- The blade impeller outer diameter (OD) at the back face had to be relaxed. The impeller OD was 16.9595 in. with the lower limit on the drawing to be 16.958 in. This dimension was anticipated to be 0.002 in. below the lower limit (i.e., 16.958 - 0.002 = 16.956 in.).

Process

- Regrind the curvic couplings to bring the impeller profile total indicator runout (TIR) within 0.001 in. The impeller profile also includes the trailing edge where the runout is in axial direction (facial runout). This process of regrinding would essentially bring the impeller rotational axis and the curvic coupling axis closer to each other.
- Re-inspect the TIR of impeller on the curvics by taking impeller profile runout measurements near the impeller leading edge, midpoint, and near the trailing edge.
- Fabricate a new arbor/shaft that would be used for regrinding the blade OD, balancing the impeller, and taking runout measurements. This was needed because the impeller is relatively heavy.
- Regrind the impeller OD at the back face. As noted above under the plan requirement, the final OD would be smaller than the lower limit on the drawing by 0.002 in. The plan was to regrind the curvic couplings first and then the blade OD. Only the continuous part of the blade OD was to be reground, and this did not include the blade trailing edges.
- After bringing the blade profile runout within 0.001 in. and regrinding the impeller blade OD, rebalance the impeller to within the drawing specifications.
- Finally inspect every third blade pair tip and hub profiles on a CMM against the drawing specifications.

6.1.2 Final Impeller Runouts

The effort was successful in meeting its objective. The impeller blade tip runout at the blade leading edges and at midchord is 0.0008 in. compared to the initial value of 0.003 in. The blade tip runout near the blade trailing edge is 0.0012 in. which is only slightly higher than the 0.001 in. target. Note that at this location the runout is in the axial direction. The final blade OD runout is 0.0002 in. compared to the initial value of 0.0043 in.

Measurements by Anmark also showed that the splitter blades and the main blades are not at the same height. There appears to be a 0.0011 in. (maximum) difference between the full blades and the splitter blades at the points where Anmark made the measurements. The difference in height varied from zero to 0.0011 in. between splitter and main blades.

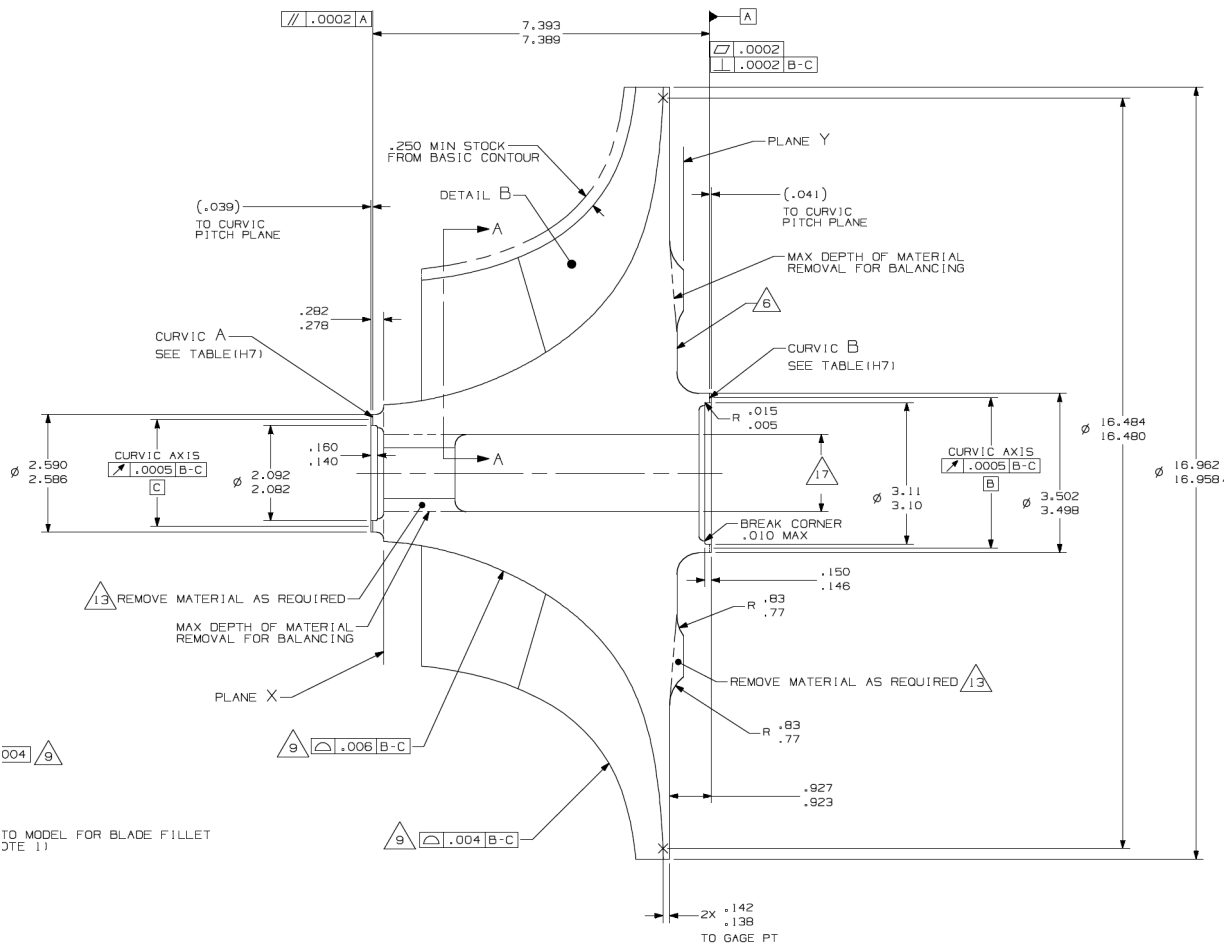


Figure 82.—Impeller drawing showing various dimensions that are referenced above in the Plan Requirements section.

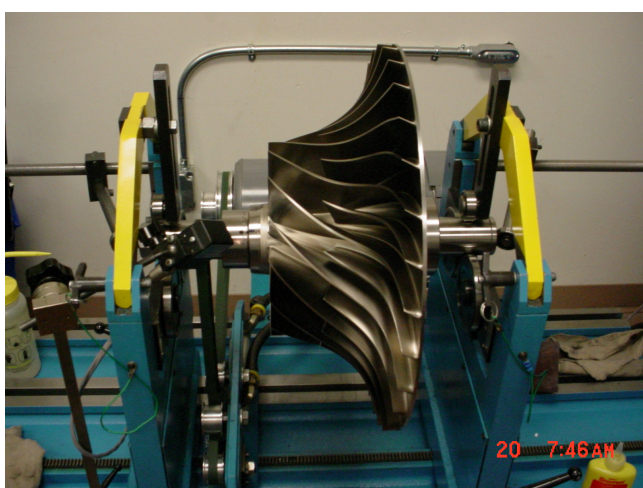


Figure 83.—Final impeller runouts being checked out after mounting it on the refinished curvic couplings and the new precision arbor.

The final impeller axial dimension, also referred to as the stacking dimension is 7.3838 in. which is 0.0012 in. smaller than the minimum of 7.385 in. indicated on the drawings. The plan had allowed it to be as much as 0.002 in. undersize but the final outcome was better than this. The final blade OD is 16.956 in. and this is 0.002 in. smaller than the minimum of 16.958 in. on the drawings. Also note that these dimensions do not affect the flow path and as such are not relevant for the aerodynamic performance of the impeller.

6.1.3 Final Impeller Imbalance

The impeller imbalance after regrinding the curvic couplings and the impeller OD was about 10 times larger than the drawing requirements as is shown in Figure 84. However this imbalance was reduced to comply with the mechanical design requirements and the results, summarized in Table 4, are within drawing specifications.



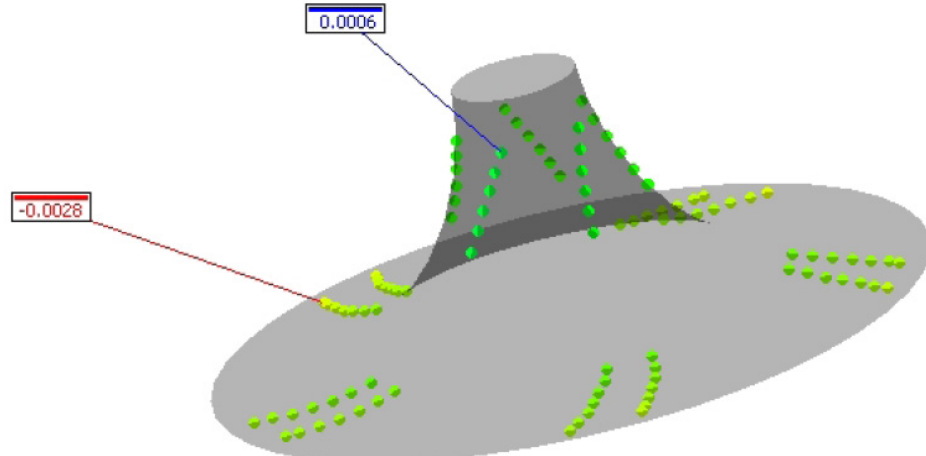
Figure 84.—The Hoffmann machine showing the imbalance readings after regrinding of the curvic couplings and the impeller. These readings are 10 times larger than the imbalance specified on the drawings.

TABLE 4.—THE FINAL IMBALANCE READINGS OF THE IMPELLER, AND THEIR COMPARISON WITH THE DRAWING SPECIFICATIONS

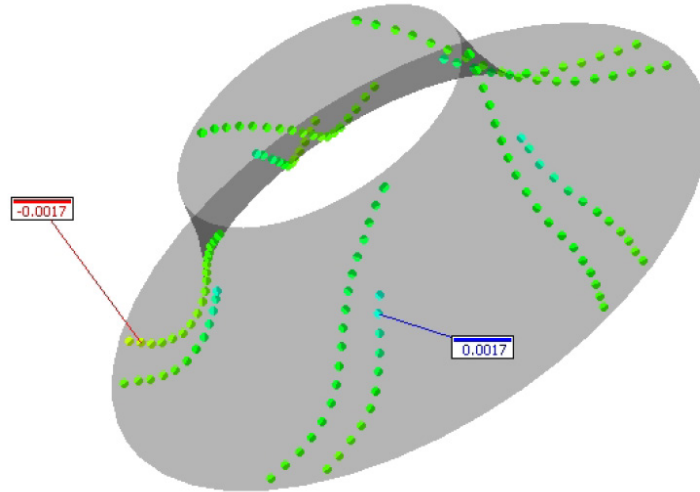
	Initial unbalance, oz-in.	Final unbalance, oz-in.	Final unbalance at 180°, oz-in.	Drawing spec., oz-in.
Plane X	0.299	0.021	0.018	0.03
Plane Y	0.374	0.0077	0.013	0.03

6.1.4 Final Impeller Blade Tip and Hub Profile Measurements

After regrinding of the curvic couplings and the impeller blade OD was completed, Turbocam was asked to take further measurements to check the final impeller geometry relative to the drawings. Turbocam used the CMM to measure the hub and tip profiles of the 6 main and 6 splitter blades (impeller has 15 main and 15 splitter blades). These measurements showed that the impeller hub and tip profiles are within drawing specifications. The results are shown in Figure 85.



Current Unit	Inch, Degree	Measure Sensor	M2_STY_D2R_L20
Measure Time	8/2/2011 1:10:29 PM	Measure Points	105
Upper Tolerance	0.0030	Lower Tolerance	-0.0030
Maximum Error	0.0006	Minimum Error	-0.0028
Maximum Index	85	Minimum Index	84



Current Unit	Inch, Degree	Measure Sensor	M2_STY_D2R_L20
Measure Time	8/2/2011 12:54:08 PM	Measure Points	154
Upper Tolerance	0.0020	Lower Tolerance	-0.0020
Maximum Error	0.0017	Minimum Error	-0.0017
Maximum Index	29	Minimum Index	125

Figure 85.—The departure of the impeller profiles from the CAD model for the hub surfaces (top), and the impeller main and splitter blade tips (bottom).

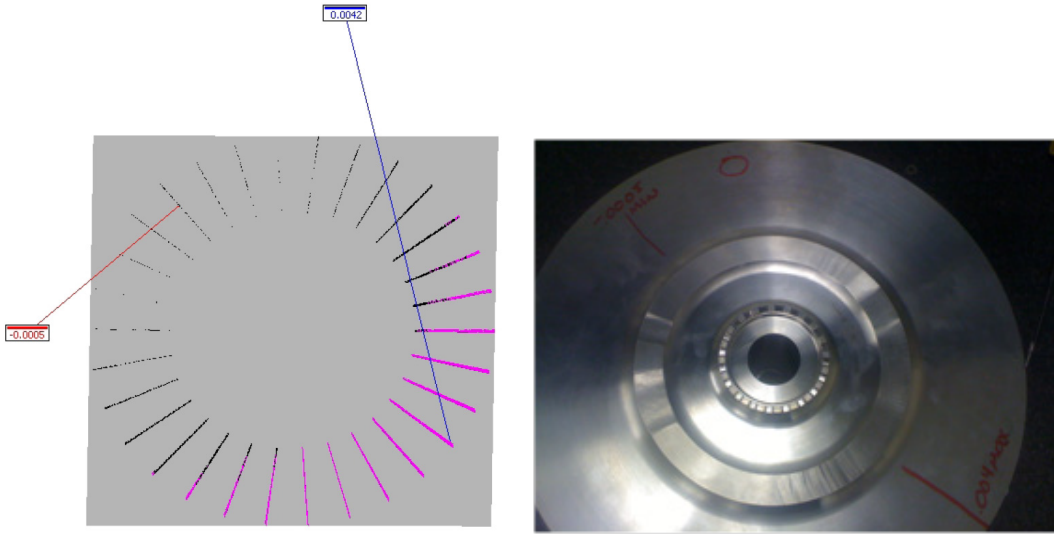


Figure 86.—The graphical and pictorial representation of the runouts on the backface of the impeller. The largest negative deviation from the drawing specification is 0.0005 in. (under-size), and the largest positive deviation is 0.0042 in.



Figure 87.—The forging for the shroud.

Impeller back face flatness was also measured, and the results are graphically and pictorially summarized in Figure 86. These results are consistent with the Anmark's measurements. Note that the Anmark measurements showed that the runout on the back face was 0.004 near the max diameter, and that the axial dimension (also referred to as the stacking length) was 0.0012 in. shorter than the minimum 7.385 in. that is specified on the drawings. Also note that the back face is not part of the flow path, and the drawings specify smaller tolerances on this face primarily to facilitate the final impeller balancing without removing large amounts of material.

6.2 Shroud

The shroud is made of stainless steel and was machined by P&W Canada from a forging that can be seen arriving at the P&W Canada's facility in Figure 87. The shroud during the machining process and in its final form is shown in Figure 88. The part of the shroud that extends over the impeller is coated with a 0.020 ± 0.005 in. thick abradable material (METCO 601) (Figure 89).

The larger holes/provisions in the shroud were made before the application of the abradable material, and finer holes (~0.035 in. and less) were made after the coating was in place. Shroud was checked for cracks etc. with Fluorescent Penetrant Inspection (FPI).

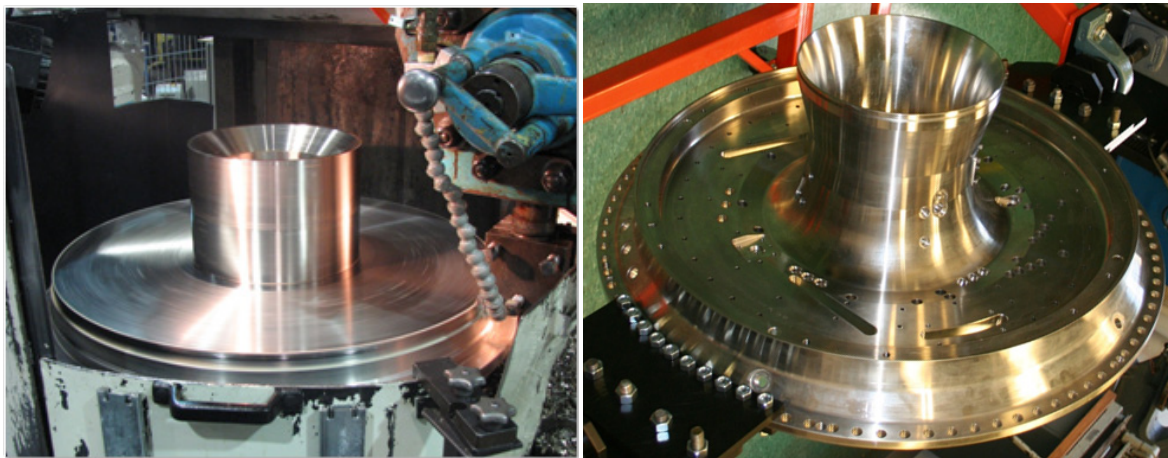


Figure 88.—The shroud during the machining (left), and in the final form (right).

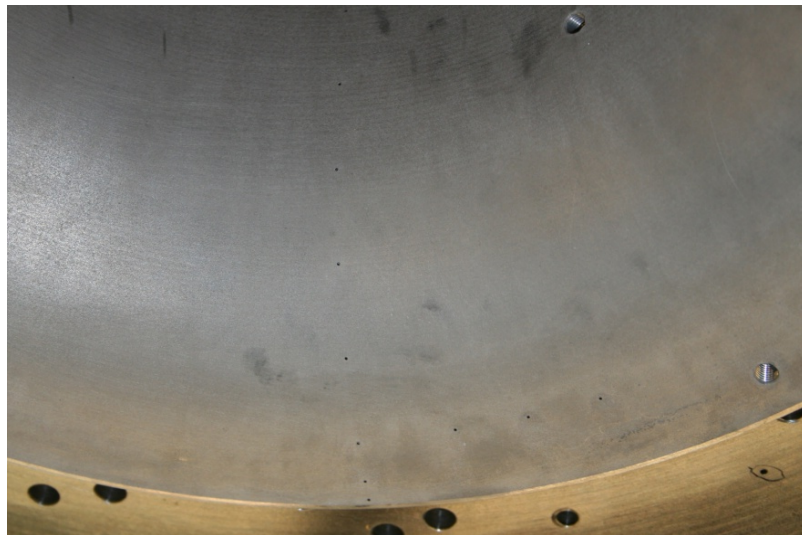


Figure 89.—A close up view of the abradable coating on the inside of the shroud.

6.3 Diffuser and EGV Subassembly

The diffuser and EGV subassemblies are complicated, and therefore the vendor encountered several challenges during the fabrication of these assemblies. These challenges also led to a long delay in the completion of these parts. The completed assemblies were received by UTRC on July 6, 2011. The diffuser and EGV subassemblies are shown in Figure 90. In addition there were two uninstrumented diffuser modular vanes (Figure 91), and two instrumented modular vanes that go with the diffuser assembly. The vendor, Walter's Precision, inspected the assemblies before shipping these out to UTRC. The assemblies were re-inspected by UTRC (Figure 92), and the manufacturer's inspection report was verified. The minor nonconformities were deemed not to have an impact on the assembly, or the performance of these parts. A preliminary check on the fit of the diffuser and EGV assemblies to the shroud had already been carried out during the inspection process.

All the instrumentation holes were checked for clogging by blowing air through them. In addition a sample hypo tube was used to test the size of each of the instrumentation holes on the two assemblies. It was found that some of the instrumentation holes were clogged and had to be cleared.



Figure 90.—Diffuser and EGV subassemblies before instrumentation.



Figure 91.—Uninstrumented modular diffuser vanes.



Figure 92.—Diffuser assembly being inspected at UTRC on the 5-axis machine (left), as well as visually.

Some shortcomings in the diffuser and EGV assemblies were identified and mostly rectified. First of these had to do with the excessive brazing alloy left in some of the diffuser passages. This excessive alloy was located on that area of the flow path where the diffuser vanes meet the hub and the shroud, and the excessive alloy appeared primarily as small beads. Wherever possible, the excessive alloy was hand removed, and the corresponding surfaces hand finished.

It was found that three of the instrumentation holes in the bend area between the diffuser and the EGV were missing (holes number 5000, 5003, 5006 using the labeling convention described in Appendix E.3). These were drilled at UTRC machine shop with the help of the CAD model.

It was also found that the diffuser and EGV assemblies needed some cleaning primarily due to the chemical residue from the fluorescent penetrant inspection. Therefore the two assemblies were ultrasonically cleaned.

6.3.1 Holding Fixture for Assembling the Diffuser and EGV to Shroud

A special holding fixture for assembling the diffuser and EGV subassemblies was built. Figure 93 shows this fixture with the shroud mounted on it. The shroud was instrumented while mounted on this fixture. The fixture allows tilting and rotating of the parts to facilitate instrumentation routing, as well as the assembly of the diffuser and EGV subassemblies to the shroud.

6.4 Mock Assembly

After the in-house inspection of the diffuser and EGV assemblies, UTRC carried out a mock assembly to check out the fitting of these two assemblies to each other and to the shroud. The mock assembly and disassembly were successfully carried out. The steps for the mock assembly are summarized below, and the corresponding pictures are shown in Figure 94.

1. Installed a lifting device onto the diffuser and the EGV subassemblies to facilitate lifting by crane.
2. Secured the shroud to the table fixture.
3. Placed the diffuser sealing rings using vacuum grease.
4. Lowered the diffuser subassembly on to the impeller shroud using TDC mark and locating pins. Then installed the modular vanes to locate the diffuser shroud to the proper position.
5. Installed EGV sealing ring no.2 for the EGV subassembly by using the vacuum grease.
6. A very thin coat of anti-seize (silver goop) was applied to one mating surface before assembly. The use of anti-seize was a precautionary measure for later disassembly. The anti-seize was not used during the final assembly.
7. Installed the heat belts on the inside and outside of the EGV subassembly.
8. Turned on the power to the heat belts, and heated the EGV subassembly for about 2.5 hr to get a temperature of about 150 ~ 160 °F. A temperature probe was used to measure the temperature.
9. Installed the two screws from underneath of the shroud to help locate the subassembly.
10. Lowered the EGV subassembly over the diffuser shroud using the locating pin (only one pin), positioned, and then dropped it in place.
11. Removed the heating belts, and installed the bolts but did not tighten these.
12. Used a feeler gauge and a boroscope to verify the interference fit between the diffuser and the EGV subassemblies.



Figure 93.—Custom built fixture for holding the shroud, and for assembling the stationary parts



Figure 94.—Steps involved in the mock assembly. First (top left) placement of the diffuser subassembly on the shroud. Then placing the heat belts around the EGV surfaces and heating it to about 150~160 °F. At that time EGV subassembly is lifted with a crane and moved over the shroud (top right), and lowered using a locating pin. Finally, the removal of the heating pads and check for the fit (bottom picture).

Disassembly

1. Removed the bolts.
2. Installed the heat belts on the EGV subassembly.
3. Installed four jackscrews onto the pads so that the shroud surface is not marred.
4. Applied power to the heat belts and heated the surfaces for about 1 hr. Afterwards disassembled the EGV from diffuser by using opposite pair of jackscrews. It required only one eighth of a turn of the jackscrews to disassemble the two subassemblies.
5. Used the crane to lift the EGV subassembly.
6. There was no marring of the mating surfaces of the EGV and the diffuser subassemblies, probably because of the initial application of the anti-seize.

6.5 Diffuser/Shroud Bolted Interface Analysis

In 2012, there were some concerns about the diffuser/shroud bolted interface (detail shown in Figure 95). UTRC subsequently carried out a detailed analysis of the interface.

The following observations were noted at the time. Threading a lubricated screw into a blind hole can create a hydraulic lock, resulting in incorrect screw preload. The current design does not allow the screw to be bottomed-out, to engage the full length of the HeliCoil. A gap is required at the bottom of the threaded hole for the joint to be preloaded. The conduction through the screw could cause the screw to

expand at a different rate in the axial direction than one of the two parts being joined. This will impact the screw preload and joint stresses.

These lead to the following concerns. The length of thread engagement and thread shear failure is a concern. The shear failure will have more significant consequences than a bolt bending failure from thermal expansion and is more likely to occur first. Also, the screw preload will be lost over time in the bolted joint.

Detailed analysis at UTRC yielded the following recommendations:

1. Use Belleville spring washer to:
 - a. Build a spring joint to maintain the screw preload
 - b. Reduce the bearing area under the screw head, allowing the screw more freedom to rotate
2. Use threaded studs in the place of screws to:
 - a. Obtain the maximum thread engagement.
 - b. Obtain more accurate fastener thread engagement depth
 - c. Obtain more accurate fastener installation preload
 - d. Eliminate the need for precision in spacer length
 - e. Reduce the bending stress. The tensile area of a socket head 1960 series screw, in the shank, is larger making the screw less flexible in bending than a threaded stud. The higher stiffness translates to higher bending stress in the 1960 series screw.

Initial testing of the rig showed that the temperature gradients across the existing interface never exceeded 50 °F and the temperature limit was determined to be 100 °F. Therefore, the initial installation of socket head bolts was found to be adequate and the high strength studs were not required.

7.0 Test Instrumentation

The steady-state and unsteady CFD results were interrogated for guidance regarding placement of instrumentation, the purpose of which is threefold: to confirm key improvements of the HECC design; to explore technical barriers; and to provide validation for the design community.

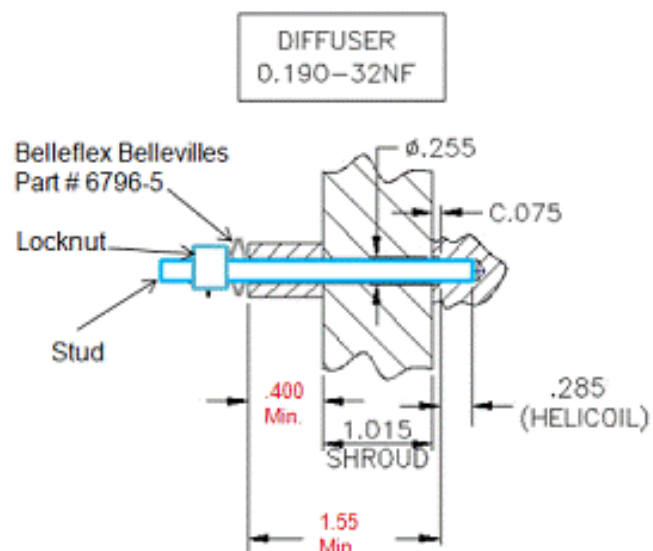


Figure 95.—Detail of the proposed diffuser/shroud bolted interface with threaded studs.

Measurements to confirm key improvements of the HECC design were aimed to determine the overall performance by the use of inlet and exit total pressure and temperature rakes. They were also intended to determine whether the impeller achieves uniform exit profiles to allow for incidence loss reduction in the diffuser, which will be determined via diffuser vane leading edge instrumentation. Another question of great interest is whether the compact diffusion via topology of vane diffusers with splitters is successfully achieved. A dense field of static pressure measurements in the diffuser was designed to provide insights into that. And finally, the details of the overall performance of the stage will be determined by collecting static pressure throughout the flowpath, static pressure on hub and shroud walls mid-passage through 3 EGV passages, total pressure on 3 EGV leading edges and provisions for total pressure probes in axial-to-radial bend.

Measurements to explore technical barriers aimed to answer several questions too. One concerns the loss in performance associated with exit (backplate) bleed, and the variable backplate bleed capability already present in rig could be utilized to investigate it—although no specific research plan has been developed as a part of this effort. A critical question for advancing the state-of-the-art of small centrifugal compressor stages is about the relationship between the unsteady pressure fields created by the impeller at blade passing frequency (BPF) and its interactions with the diffuser vanes and vice versa. Unsteady pressure measurements on the impeller shroud and in the diffuser area with Kulite instrumentation will be conducted to provide insights. They will be also placed in the diffuser splitter region to provide insight into whether the split diffuser achieves the design goal of balanced pressure recovery and mass flow split. Unsteady pressure measurements are also considered upstream of the impeller, in the vaneless space distributed around the circumference, in the diffuser throat, and at the diffuser exit.

Finally, in order to provide good quality validation data for analysis tools, a question of great concern is usually about the inlet flowfield. Inlet rakes to measure turbulence intensity and velocity field (five-hole probe and/or boundary layer probe) could be considered to achieve this goal in future tests.

7.1 Laying Out the Instrumentation

In order to assess the overall performance of the stage, twelve exit rating rakes, containing three total pressure and two total temperature measurements each, are located around the exit, clocked circumferentially by diffuser vane pitch and then in 1.5° increments, in order to provide flowfield measurements across one entire diffuser vane pitch (main-to-main), as shown in Figure 96. Also, there are over 200 static pressure taps throughout the flowpath (coordinates are given in Appendix D): along the impeller shroud, in dense fields surrounding one diffuser passage on both hub and shroud side, through the radial-to-axial bend, along three exit guide vanes, and at the stage exit.

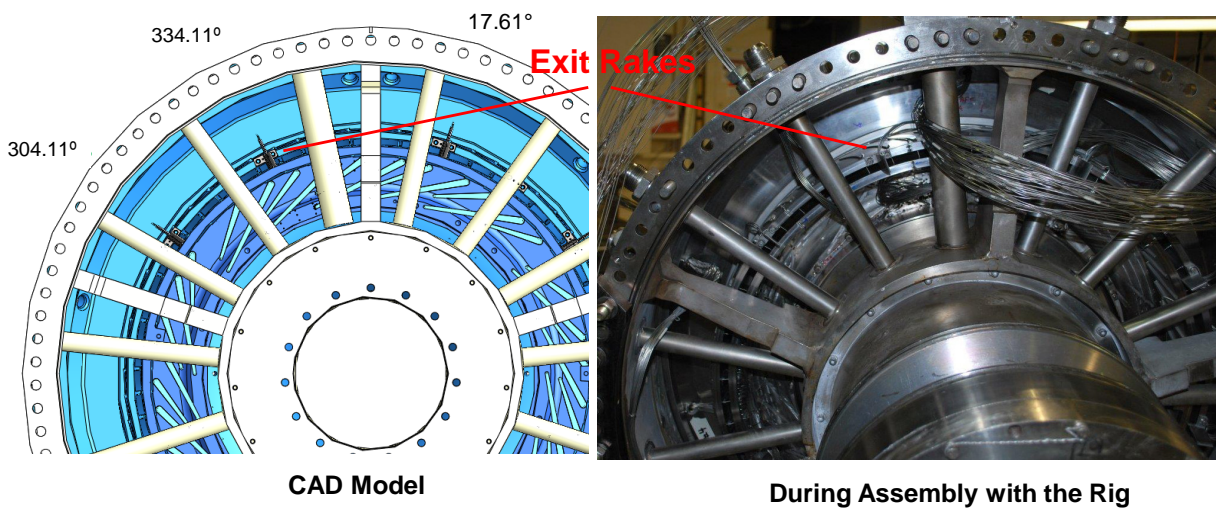


Figure 96.—Exit rake integration in the rig

The selection of tap locations was made based on inspection of the steady-state CFD results for 100 percent design speed, at choke, peak efficiency, and near-stall conditions, with the goal of providing detailed information in relevant locations. An example of that assessment is shown in Figure 97, in which the CFD prediction of static pressure on the shroud surface surrounding the diffuser main blade is shown, along with the static pressure tap locations.

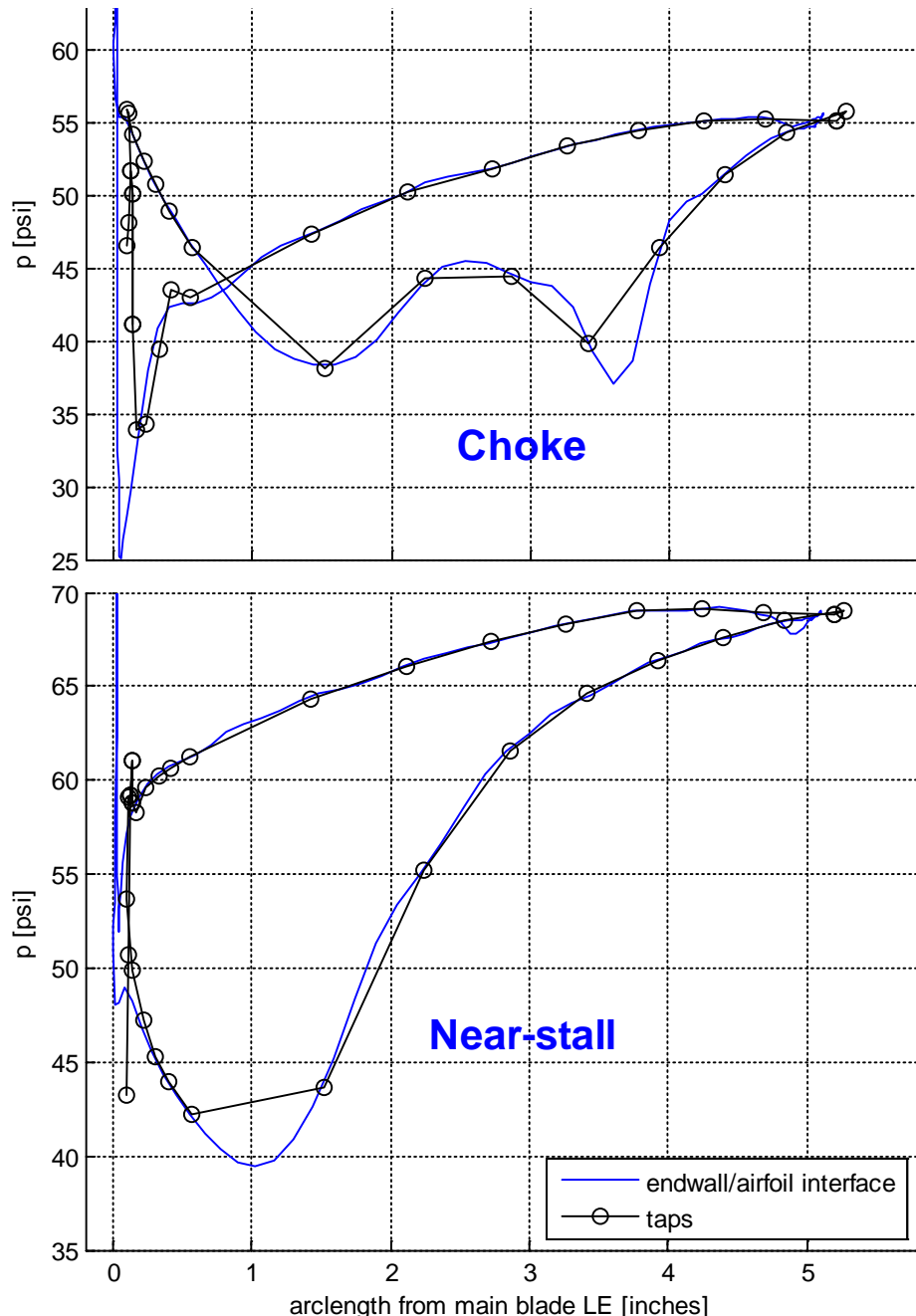


Figure 97.—CFD prediction of static pressure near diffuser main blade shroud surface, at choke (top) and near-stall (bottom) conditions. Symbols indicate tap locations.

To assess the performance of individual components, provisions for probe access were created between the impeller and diffuser, and between the diffuser and exit guide vanes. Two diffuser main vanes have been fabricated in a modular fashion, allowing for future instrumentation development. The initial configuration has seven total pressure measurements along the leading edge, allowing for confirmation of the two-dimensional nature of the impeller exit profiles (Figure 98). Also, one set of three exit guide vanes has total pressure Kiel-head probes installed at three spanwise locations per vane.

To address technical barriers associated with impeller-diffuser interaction and high cycle fatigue, a set of 20 unsteady pressure transducers were laid out in the region between the impeller trailing edge and through the diffuser passage. Locations were selected based on interrogation of unsteady CFD results at near-stall and choke conditions. A 3x3 array of measurements at (90, 96, 100) percent impeller trailing edge radius in (0, 1/3, 2/3) pitch increments will capture the variation of the pressure field in the stationary frame due to the upstream effect of the diffuser blades. Also, a set of ten measurements through the vaneless space and diffuser passage will capture traveling waves and possible pumping of the pressure field along either side of the splitter blade (Figure 99). Finally, in order to assess rotating stall, 12 measurements are located at 1.05 times the impeller tip radius, with ten in a pitchwise location that exhibited very small pressure amplitude in the CFD unsteady simulation and two at (1/3, 2/3) pitchwise increments from the other ten. Because the unsteady CFD model only includes four of twenty diffuser passages, it is not expected to capture unsteady phenomena associated with disturbances on the scale of the entire circumference.

The rig also contains provisions for measuring tip clearance via three tip capacitance probes, located at inlet, knee, and exit of the impeller. Finally, variable backface bleed capability is already present in the rig. A summary of the instrumentation designed into the rig is shown in Figure 100 (see also Appendix D).



Figure 98.—Diffuser section showing the modular vane instrumented with total-pressure probes.

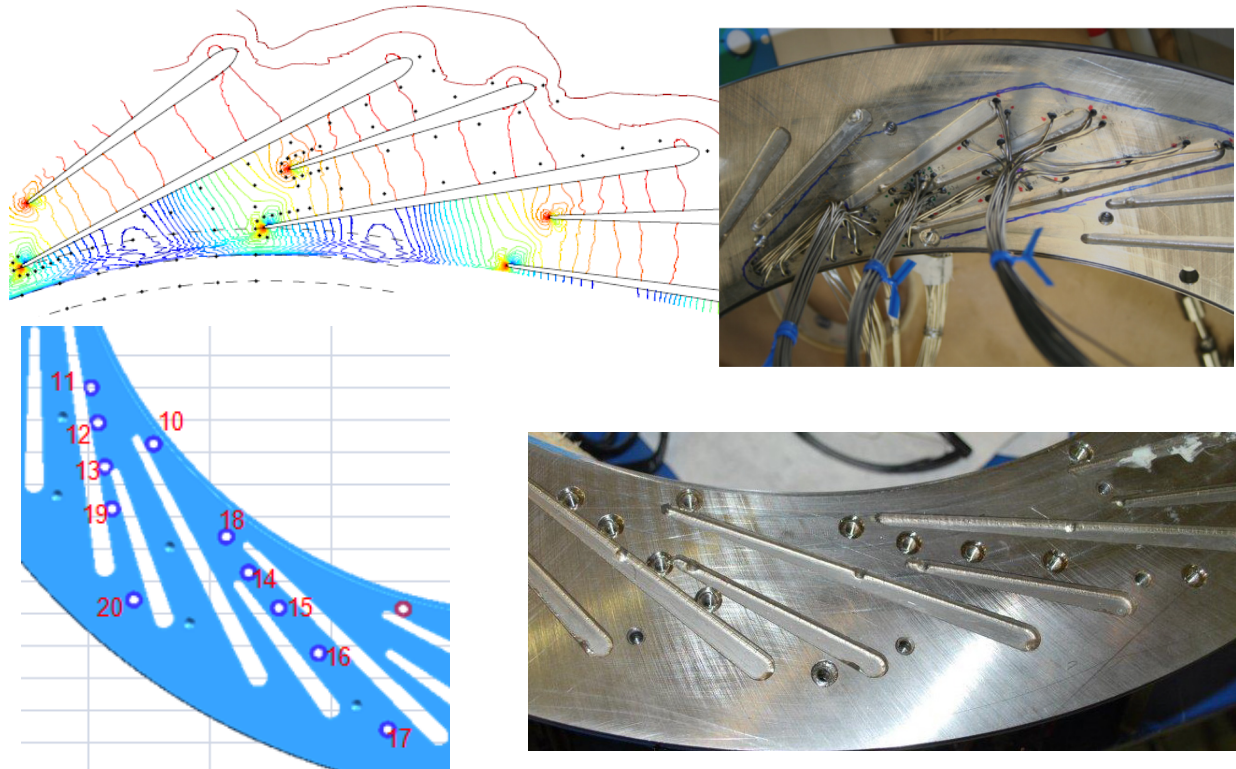


Figure 99.—Diffuser showing high-response instrumentation.

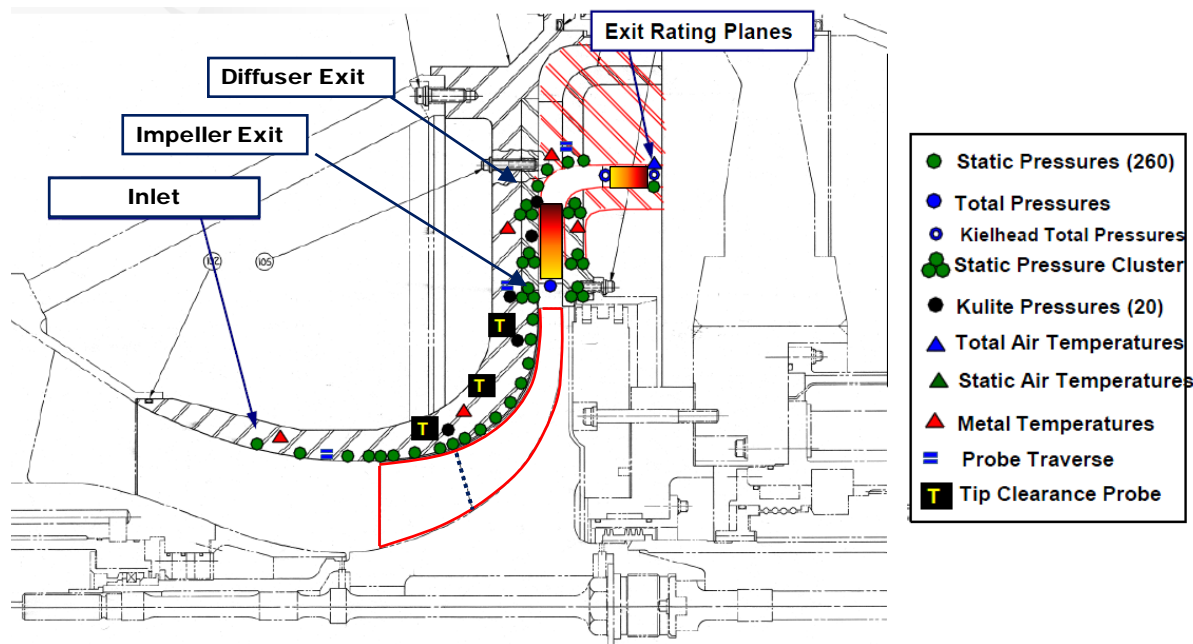


Figure 100.—Summary of the instrumentation designed into the rig.

8.0 Data Reduction and Test Results

8.1 General Information

The HECC was tested in the NASA Small Engine Component Test Facility (CE-18) (Ref. 15) shown in Figure 101. A mechanical checkout was initially performed on the rig to clear the operation to 104 percent corrected speed for detailed testing. Data was acquired for both steady-state instrumentation and the Kulite dynamic measurements. The Kulite measurements, however, were very limited in scope due to only having eight channels of digital data acquisition capability in the test cell. As a result, transducers were switched in and out of the data system to acquire data in the diffuser, which as discussed herein, is necessary to understand the flow field within the diffuser. At NASA's request, provisions for dynamic pressure transducers to be located in the vaneless space were designed into the rig to support examination of stalling behavior. The transducers were not installed during the initial HECC aero-testing of this contract.

During the mechanical checkout of the rig, data were obtained to verify predicted impeller and shroud displacements and to establish running tip clearances. Both of these efforts were successful and no rubs occurred throughout the test. An example of tip-clearance variation with operating speed is shown in Figure 102.

- 6000 hp / 60,000 rpm / 30:1 PR / Max 20" diameter
- Inlet pressures 2-45 psia / Inlet air -20 °F to ambient
- Inlet flow 60 lb_m/s / Exhaust to ambient or 26 in-hg

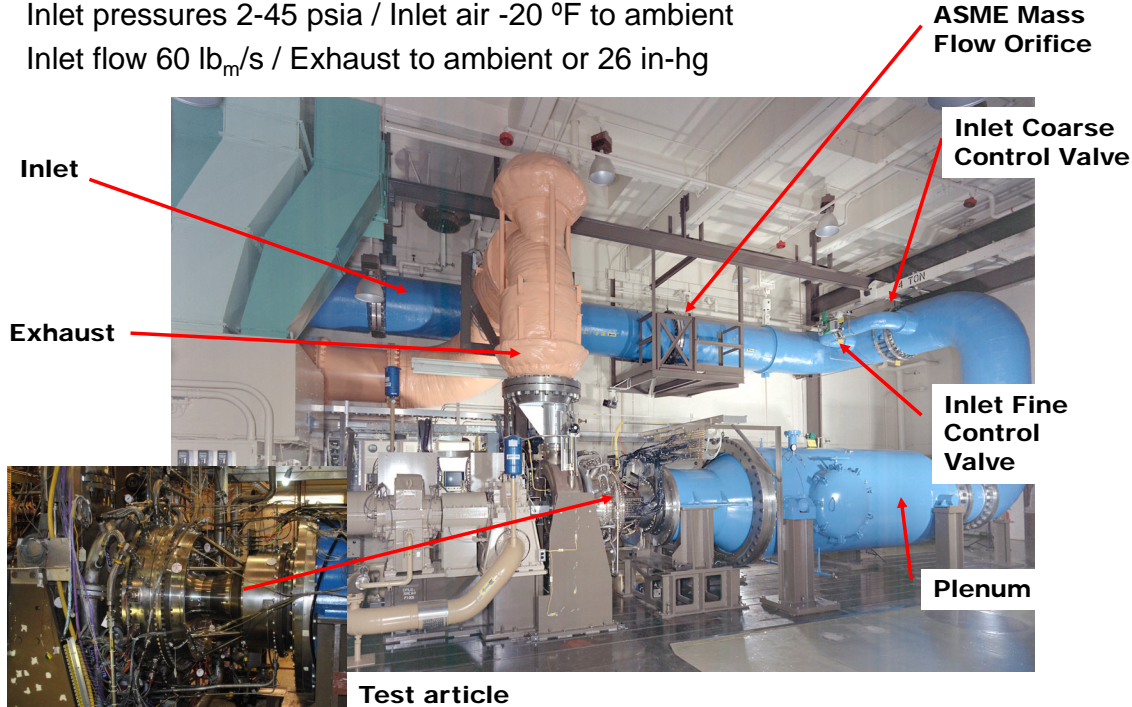


Figure 101.—NASA Small Engine Component Test Facility.

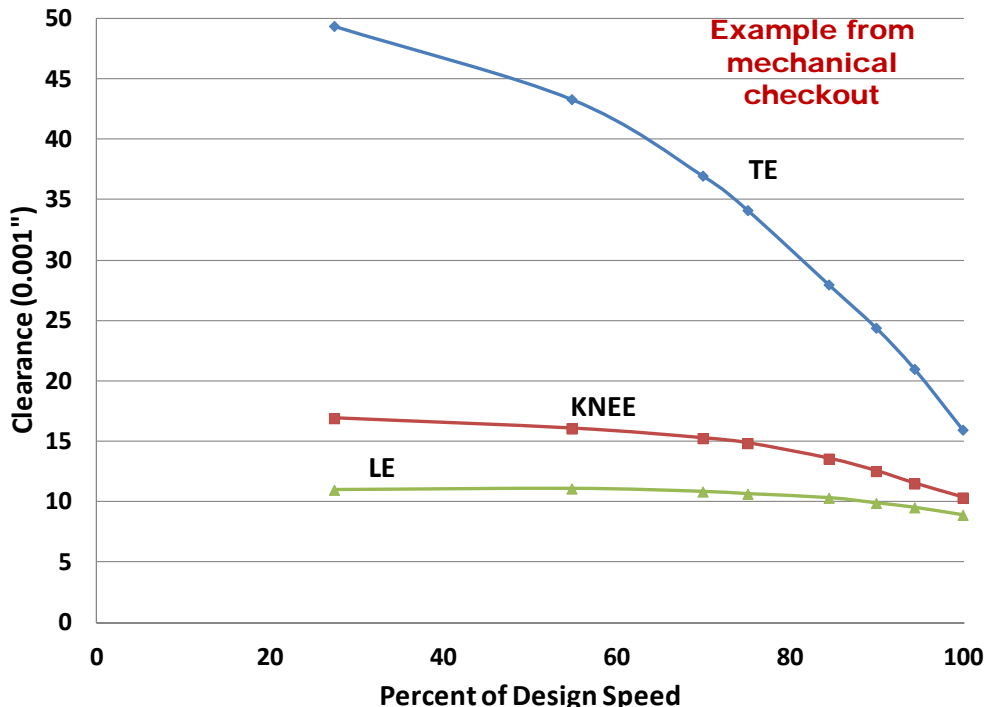


Figure 102.—Tip clearance variation with speed obtained during the mechanical checkout (performance test data was run with maximum clearance of 0.012 in. at the trailing edge).

Due to limits on the rig axial thrust balance capability, testing was performed with a suppressed inlet so that the higher-speeds on the map could be reached. The speedline data evaluated here covers 70 percent (RDG 3840 to 3862), 75 percent (RDG 3484 to 3502), 85 percent (RDG 3568 to 3583), 90 percent (RDG 3809 to 3826), 95 percent (RDG 3398 to 3414), 100 percent (RDG 3616 to 3635) and 105 percent (RDG 3693 to 3713) corrected speed. As discussed, this performance test data was run with maximum clearance of approximately 0.012 in. at the trailing edge (with the maximum values at the inlet being somewhat lower—approximately 0.010 in., and the maximum values at the knee being slightly higher—approximately 0.0125 in.). Note that the circumferential variation was observed, with a min to max variation of 0.003 in. at the trailing edge (this variation is much smaller at the inlet, 0.0005 in., and somewhat similar at the knee, 0.0025 in.).

8.2 Steady-State Data

Some of the key plots derived from steady state data are shown here, whereas the Appendix E.2 includes a much wider range of plots for steady state data. To facilitate evaluation of the data and examine the loss development through the compressor rig, a station definition was developed as shown in Figure 103.

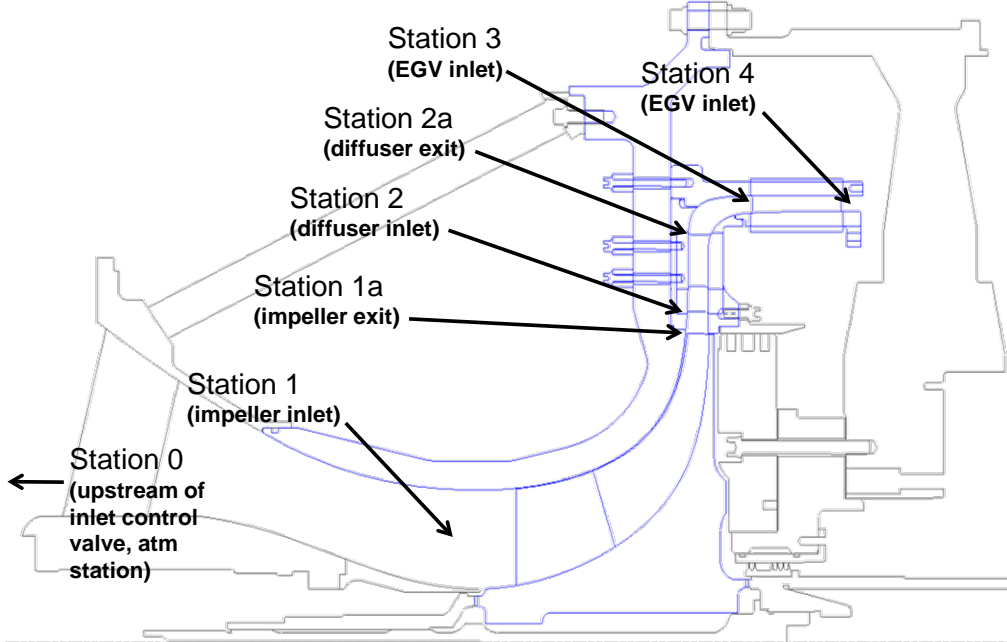


Figure 103.—Station identification used in data reduction.

8.2.1 Data Reduction Methodology

Before presenting the data, a discussion of the averaging process is provided. For the static pressures, an arithmetic average of selected taps is generally used, but where there are known to be significant periodic variations in pressure in the circumferential direction, trapezoidal averaging is used to more accurately handle periodic endpoints. Note that the same process used in analyzing the experimental data is also used to process the results from CFD simulations—whenever the CFD results are compared to data.

The station-averaged total pressure upstream of the diffuser is obtained using a Mach-weighted average of seven equally-spaced total pressure heads mounted to the leading edge of each of two diffuser vanes. The averaging process also allows variable specific heats based on the total temperature which is assumed to be equal to the exit total temperature for lack of any local measurement. The computation process is as follows. First, trapezoidal integration is applied to selected hub and shroud static pressure taps (circled in red in Figure 104) to obtain the station-averaged hub and shroud static pressures. These two pressures are in turn averaged to obtain the static pressure P2.

Mach number is computed using:

$$M_i = \sqrt{\left[\left(\frac{P_{T,i}}{P_2} \right)^{\frac{\gamma-1}{\gamma}} - 1 \right] \left(\frac{2}{\gamma-1} \right)} \quad (3)$$

The Mach-weighted total pressure for each vane is then calculated by using

$$\overline{P_T} = \frac{\sum_{i=1}^N M_i P_{T,i}}{\sum_{i=1}^N M_i} \quad (4)$$

and the two estimates of the total pressure are averaged to yield P02.

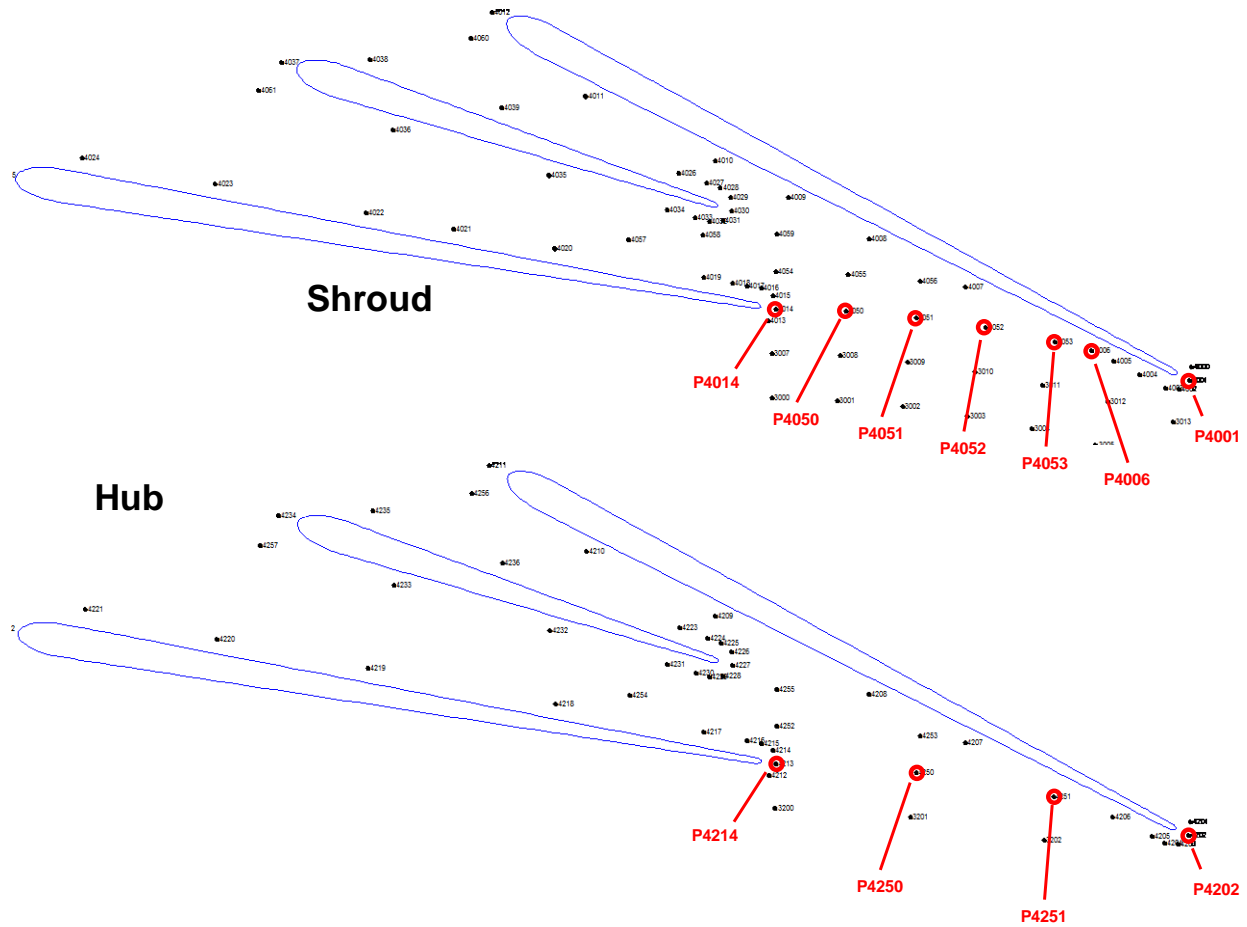


Figure 104.—Hub and shroud static pressure taps used to compute static pressure at diffuser leading edge

For each of the total pressure probes mounted to the leading edge of the diffuser vanes, the local averaging process applied to the hub and shroud static pressure taps for the EGV inlet and exit is quite similar to that used for the diffuser static taps. The taps used to compute leading and trailing edge averages for the hub and shroud are shown in Figure 105 circled in red. One of the leading edge statics on the hub was found to be open to atmospheric pressure and was eliminated from the average. That tap is indicated by the red x.

There are three total pressure probes on each of three EGV leading edges at 25, 50, and 75 percent span. These probes were simply averaged to obtain the total pressure at the leading edge of the EGVs because the pressure profiles are relatively flat.

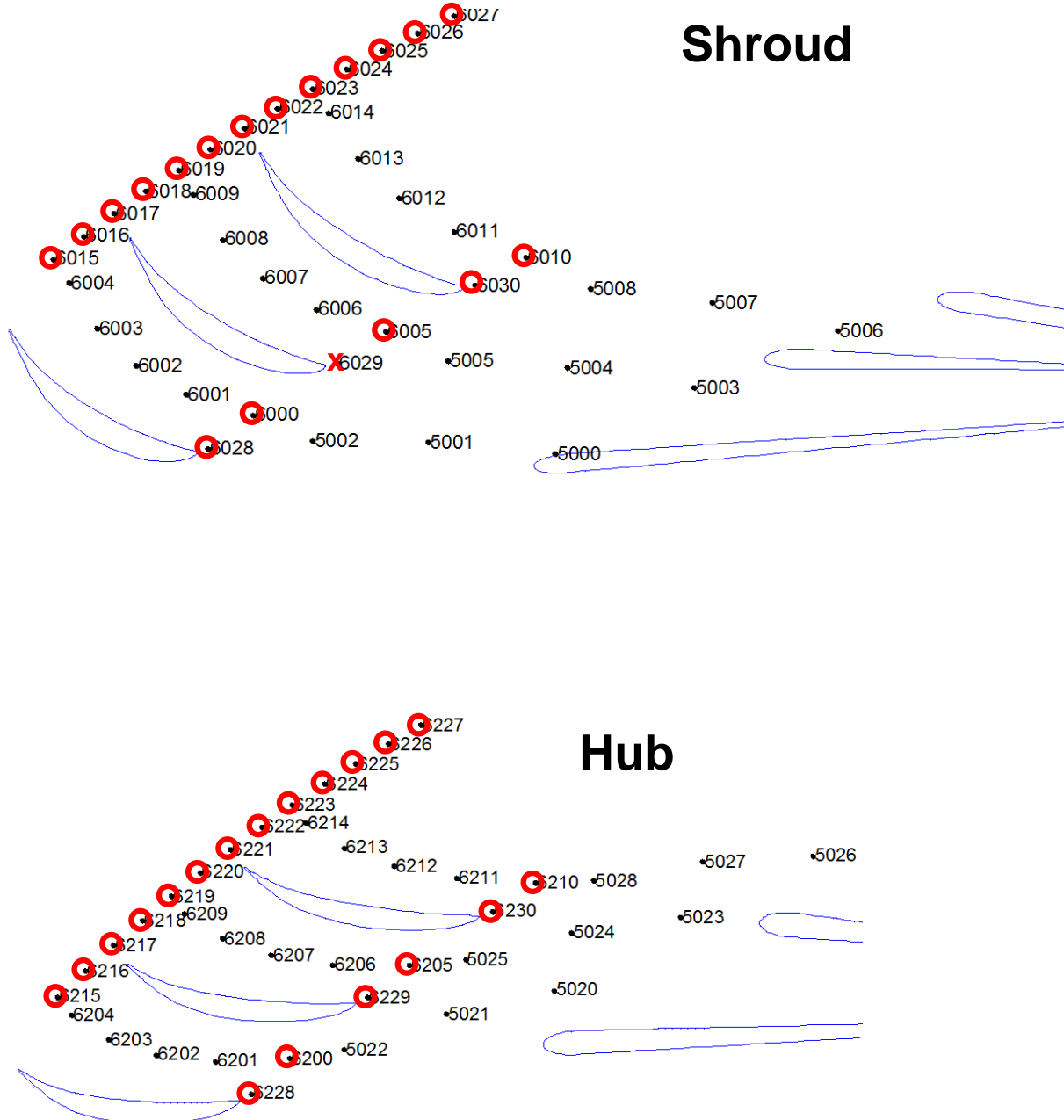


Figure 105.—Hub and shroud static pressure taps used to compute static pressure at EGV LE and TE

8.2.1.1 Inlet Flow Angle to the Rotor

In order to compute the rotor incidence, it is first necessary to compute the axial velocity at the inlet. It is assumed that the velocity over the inlet face is uniform and axial. The area is computed by Equation (5) below.

$$A_I = \pi * (R_{\text{shroud}}^2 - R_{\text{hub}}^2) \quad (5)$$

The axial Mach number is computed by iterating on Equation (6) until the flow equals the measured flow. The axial velocity is then given by applying Equations (7) and (8):

$$\dot{w} = \frac{A_l P_{T0}}{\sqrt{RT_{T0}}} \sqrt{\gamma g_c} M_{AX} \left[1 + \frac{\gamma - 1}{2} M_{AX}^2 \right]^{\left(\frac{\gamma + 1}{2 - 2\gamma} \right)} \quad (6)$$

$$T_s = \frac{T_{T0}}{1 + \frac{\gamma - 1}{2} M_{AX}^2} \quad (7)$$

$$C_X = \sqrt{\gamma g_c RT_s} M_{AX} \quad (8)$$

The tangential velocity (wheel speed) at any radius is given by Equation (9) and the inlet flow angle is then computed by Equation (10). This flow angle is in the NASA notation.

$$U_1 = 2\pi \frac{\text{RPM}}{60} \frac{r_1}{12} \quad (9)$$

$$\beta_1 = \tan^{-1} \left(\frac{-U_1}{C_X} \right) \quad (10)$$

Finally, the incidence is computed as the difference between the inlet flow angle and the metal angle by:
 $i = \beta_1 - \beta_1^*$

8.2.1.2 Inlet Flow Angle to the Diffuser

The exit wheel speed is computed by equation (11) just like the inlet wheel speed was calculated. The rotational speed of the exit flow is computed from the total temperature across the rotor using equation (12). The exit density is calculated from the exit static pressure and temperature by (13) and then the exit radial flow component, which is assumed to be uniform, is calculated from (14) where B is the blockage (the blockage value used here was 0.95).

$$U_2 = 2\pi \frac{\text{RPM}}{60} \frac{r_2}{12} \quad (11)$$

$$C_{\theta 2} = \frac{\gamma R}{\gamma - 1} (T_{T4} - T_{T1}) \frac{g_c}{U_2} \quad (12)$$

$$\rho_2 = \frac{144 P_{S2}}{R T_{S2}} \quad (13)$$

$$C_{R2} = \frac{144 \dot{w}_2}{\rho_2 A_2 B} \quad (14)$$

The exit flow angle is computed by:

$$\beta_2 = \tan^{-1} \left(\frac{C_{\theta 2}}{C_{R2}} \right) \quad (15)$$

and finally the diffuser incidence is computed as the difference between the exit flow angle and the diffuser metal angle by: $i_D = \beta_2 - \beta_D^*$

8.2.1.3 Exit Swirl and Mach Number

The exit swirl angle and Mach number were computed from the exit measurements as follows. The total pressures for the exit rakes were averaged (simple arithmetic average) and saved as $P_{T\text{RAKE}}$. Similarly, the total temperatures for the exit rakes were averaged and saved as $T_{T\text{RAKE}}$. The hub and tip static pressures were averaged to yield $P_{S\text{HUB}}$ and $P_{S\text{SHROUD}}$ and these were averaged to give P_S .

The average gamma was computed by taking the mean of the values calculated from the upstream and downstream total temperatures using a standard polynomial fit. The Mach number was then calculated using equation (16) below:

$$M_{\text{EXIT}} = \sqrt{\left[\left(\frac{P_{T\text{EXIT}}}{P_{S\text{EXIT}}} \right)^{\frac{\gamma-1}{\gamma}} - 1 \right] \frac{2}{\gamma-1}} \quad (16)$$

The weight flow can be computed from the exit total quantities and the axial Mach number at the exit using equation (17):

$$\dot{w} = \frac{A_{\text{EXIT}} P_{T\text{RAKE}}}{\sqrt{RT_{T\text{RAKE}}}} \sqrt{\gamma g_c} M_{AX} \left[1 + \frac{\gamma-1}{2} M^2 \right]^{\frac{\gamma+1}{2-2\gamma}} \quad (17)$$

The axial Mach number is given by equation (18):

$$M_{AX} = M_{\text{EXIT}} * \cos(\alpha) \quad (18)$$

Given the known exit Mach number, the swirl angle is iterated upon until the measured weight flow is matched by equation (17).

8.2.2 Measured Data

A comparison of measured data for the design point at 100 percent speed is shown against the target design requirements in Table 5. As already mentioned, in the test the maximum clearance at the trailing edge was about 0.012 in. for 100 percent speed (with the maximum values at the inlet being somewhat lower—approximately 0.010 in., and the maximum values at the knee being slightly higher—approximately 0.0125 in.). Target pressure ratio, work factor, and exit corrected flow rate are met. Total-to-total polytropic efficiency is at 85.5 percent which is 2.5 pt lower than target. Stall margin is at 7.5 percent, which is 5.5 pt lower than the target of 13 percent. Note that the exit Mach number and exit swirl are also higher than the target.

TABLE 5.—COMPARISON OF MEASURED DATA TO TARGET DESIGN REQUIREMENTS ($N_c = 100$ PERCENT, AND 12 mils CONSTANT CLEARANCE)

	Target	Measured	Delta
PR_{TT}	4.0 to 5.0	4.68	✓
$\eta_{\text{poly},TT}$, %	$\geq 88\%$ pt	85.5	-2.5
$m_{c,ex}$, lbm/s	2.6 to 3.1	3.0	✓
Work factor, $\Delta H_0/U_2^2$	0.58 to 0.7	0.81	✓
M_{exit}	0.15	0.18	0.03
α_{exit}	15°	34.3°	19.3°
SM, %	13 pt	7.5	-5.5

The amount of inlet suppression run is shown in Figure 106. Total pressure ratio and total temperature ratio for the compressor from impeller inlet to EGV exit is shown in Figure 107 and Figure 108, respectively. Figure 109 and Figure 110 show the total-to-total and total-to-static polytropic and adiabatic efficiency maps, plotted against inlet corrected mass flow. Figure 111 and Figure 112 show total-to-static adiabatic and polytropic efficiency plotted against exit corrected flow for all speeds.

Total pressure ratio for the impeller is shown in Figure 113, while total-to-total adiabatic and polytropic efficiencies for the impeller are shown in Figure 114. In Figure 115, total-to-total adiabatic efficiency for the impeller is plotted against exit corrected flow rate. At 100 percent speed and design intent operating condition, the adiabatic efficiency for the impeller is 87.5 percent.

Total pressure loss for the diffuser (this also includes the bend—computed from diffuser LE to EGV LE) is shown in Figure 116, while total pressure loss for the EGV is shown in Figure 117. The former has relatively large values with the minimum of about 0.4 at 100 percent speed. Also, no clear bucket is observed for the diffuser losses. The loss in the EGV shows a clearer loss bucket, with the minimum value for 100 percent of about 0.045.

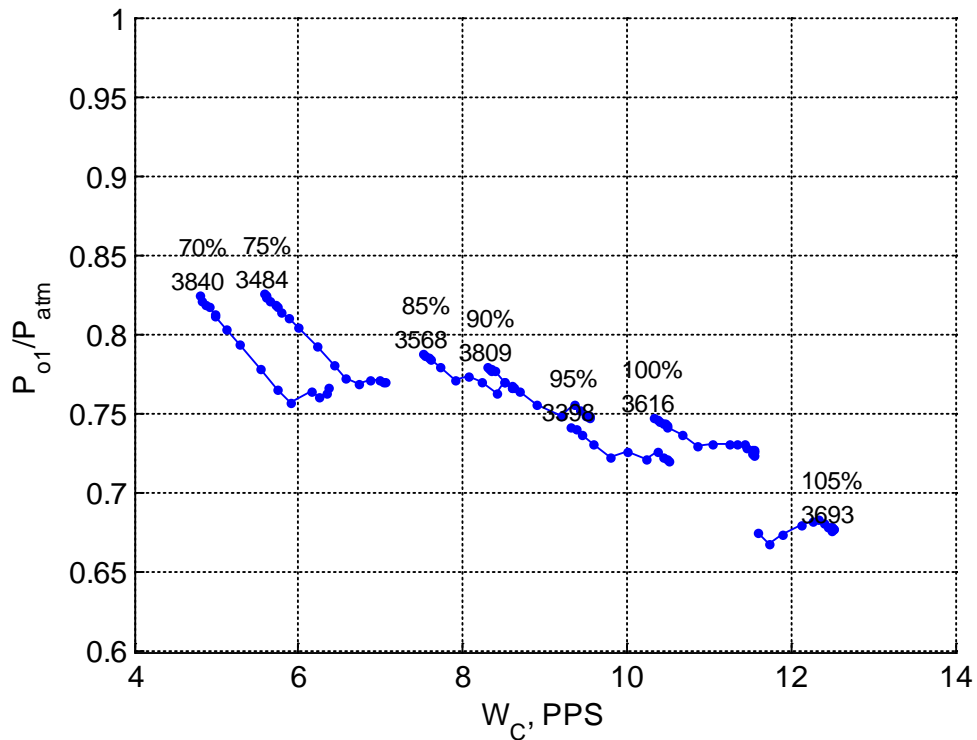


Figure 106.—Inlet suppression run during the test against inlet corrected flow rate for various corrected speeds.

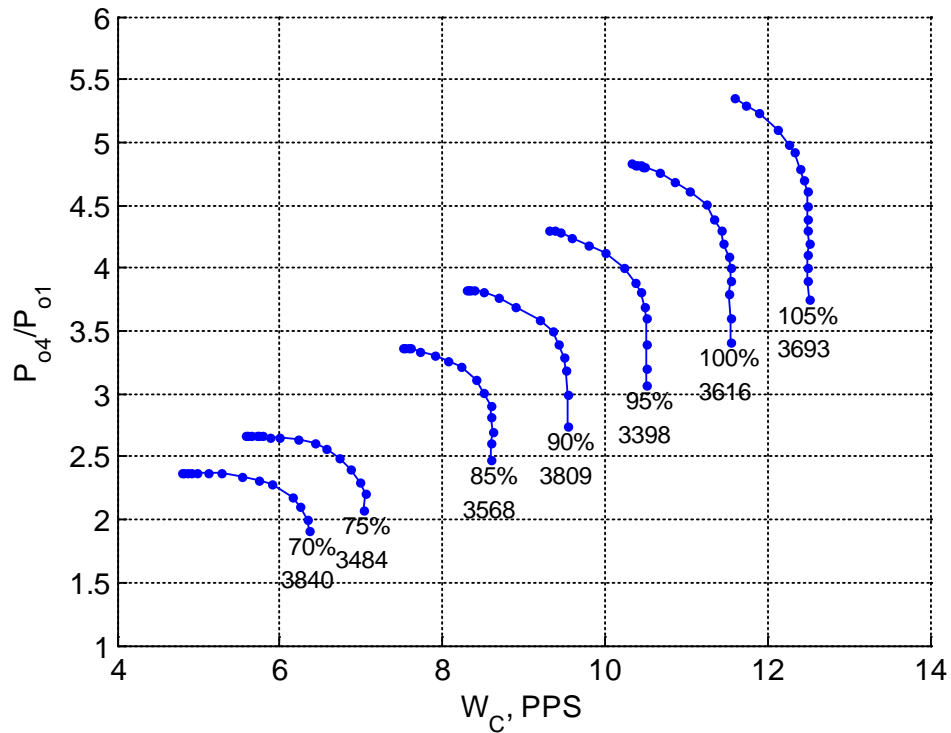


Figure 107.—Compressor speedlines of total pressure ratio against inlet corrected flow rate for various corrected speeds; speedlines were run to near-stall.

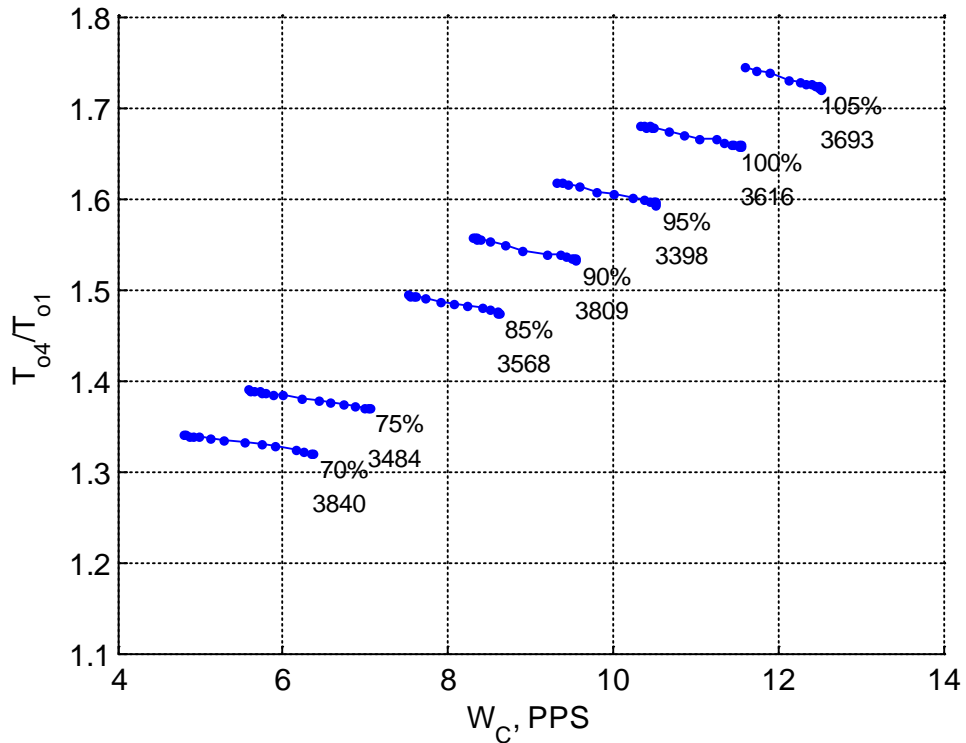


Figure 108.—Compressor speedlines of total temperature ratio against inlet corrected flow rate for various corrected speeds.

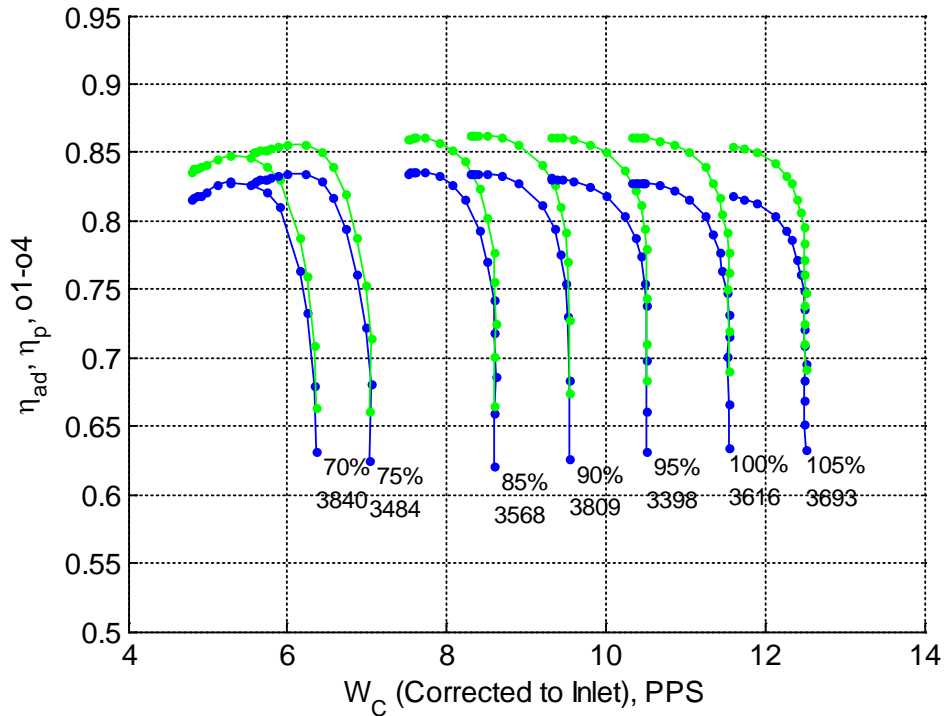


Figure 109.—Total-to-total adiabatic (blue) and polytropic (green) efficiency against inlet corrected flow rate for various corrected speeds.

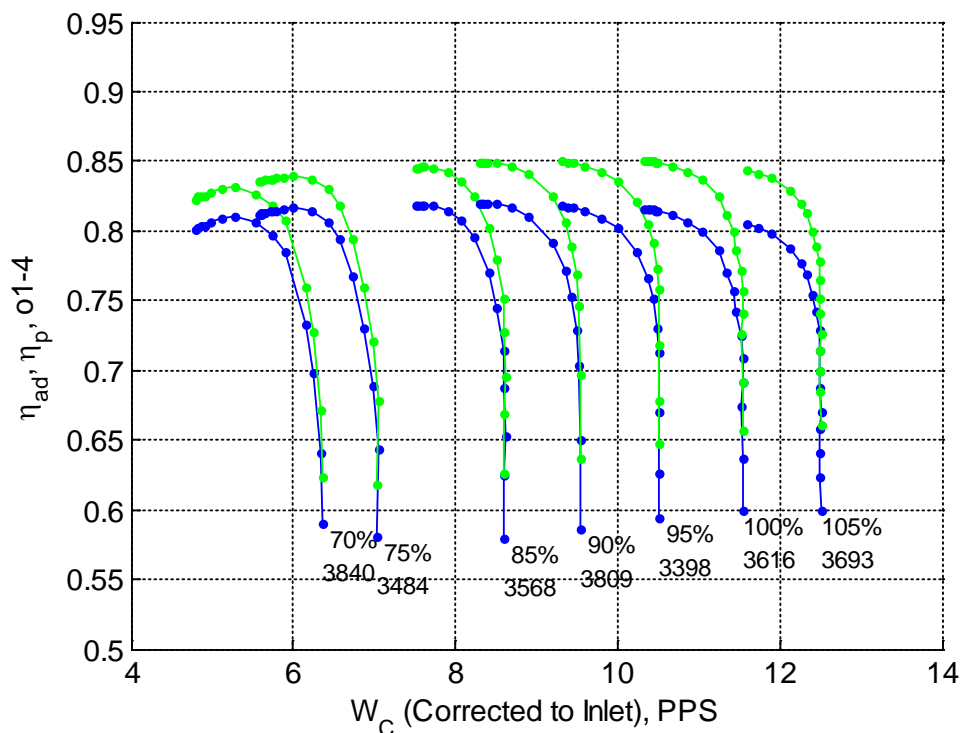


Figure 110.—Total-to-static adiabatic (blue) and polytropic (green) efficiency against inlet corrected flow rate for various corrected speeds.

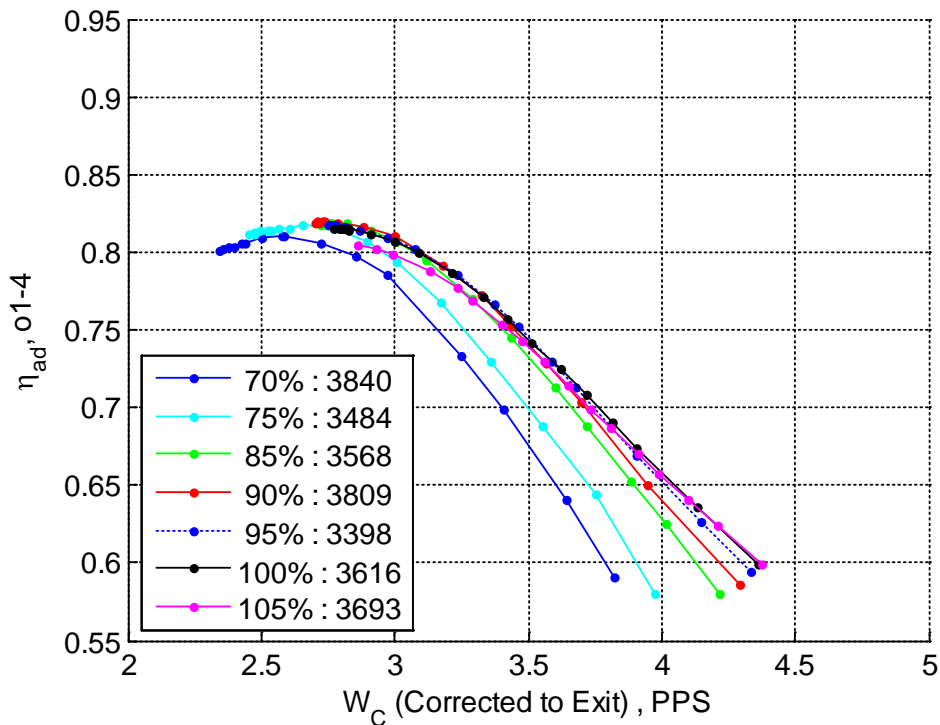


Figure 111.—Total-to-static adiabatic efficiency against exit corrected flow rate for various corrected speeds.

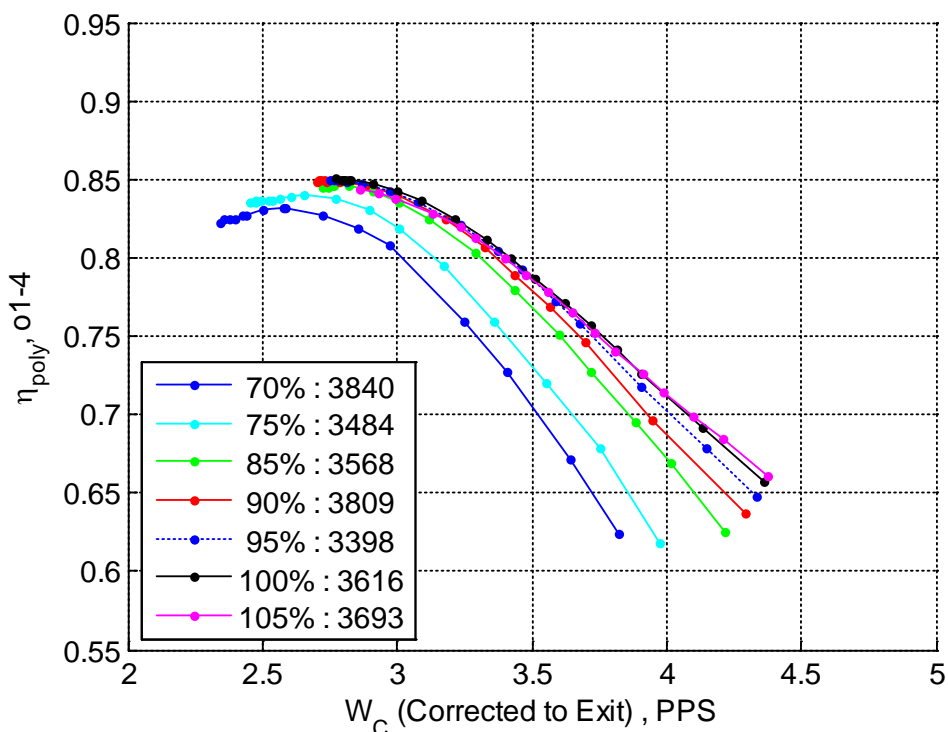


Figure 112.—Total-to-static polytropic efficiency against exit corrected flow rate for various corrected speeds.

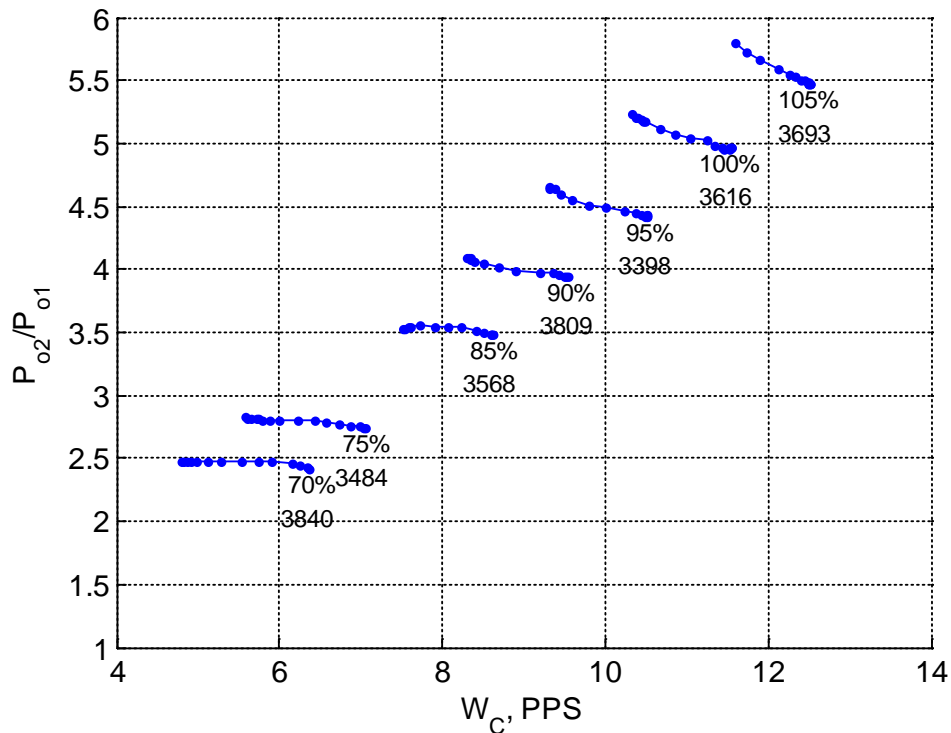


Figure 113.—Total pressure ratio for impeller (inlet to diffuser leading edge) against inlet corrected flow rate for various corrected speeds.

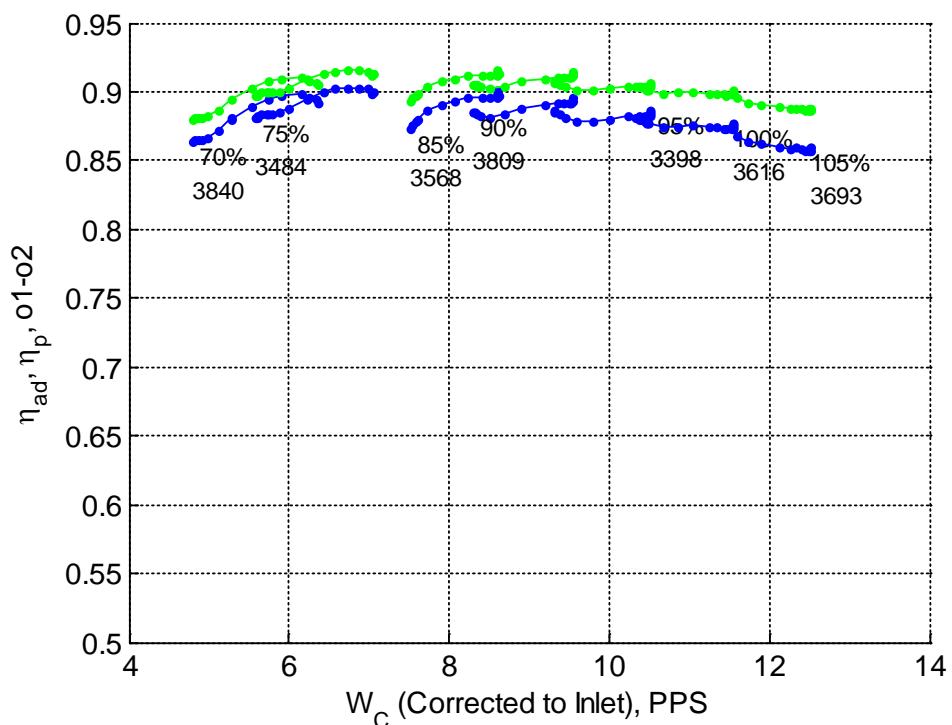


Figure 114.—Total-to-total adiabatic (blue) and polytropic (green) efficiency for impeller (inlet to diffuser leading edge) against inlet corrected flow rate for various corrected speeds.

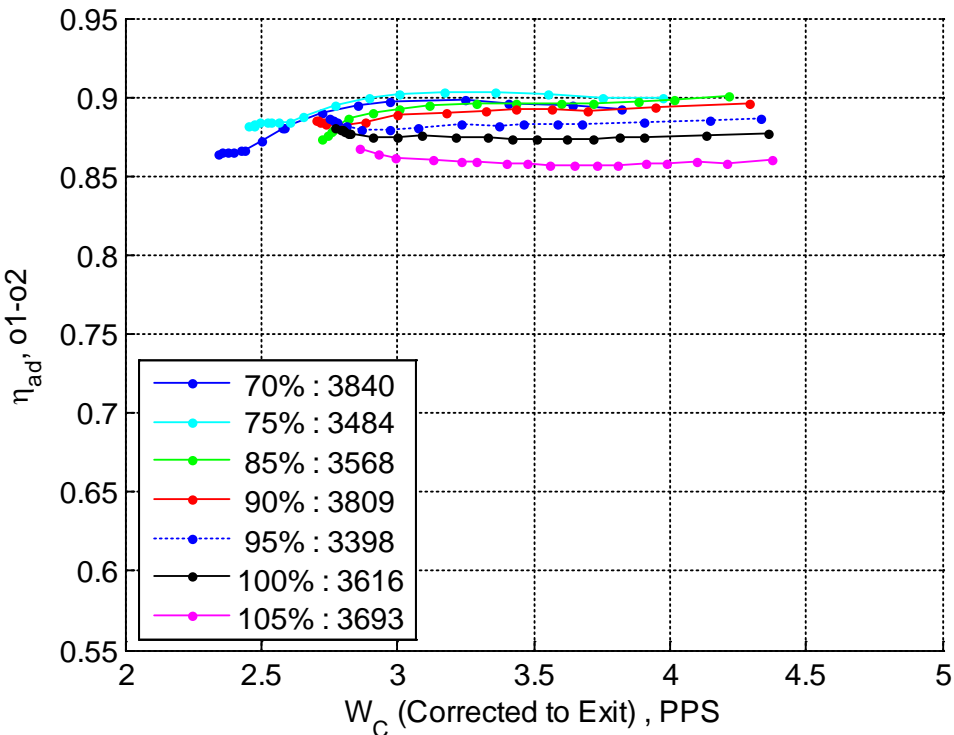


Figure 115.—Total-to-total adiabatic efficiency for impeller (inlet to diffuser leading edge) against exit corrected flow rate for various corrected speeds.

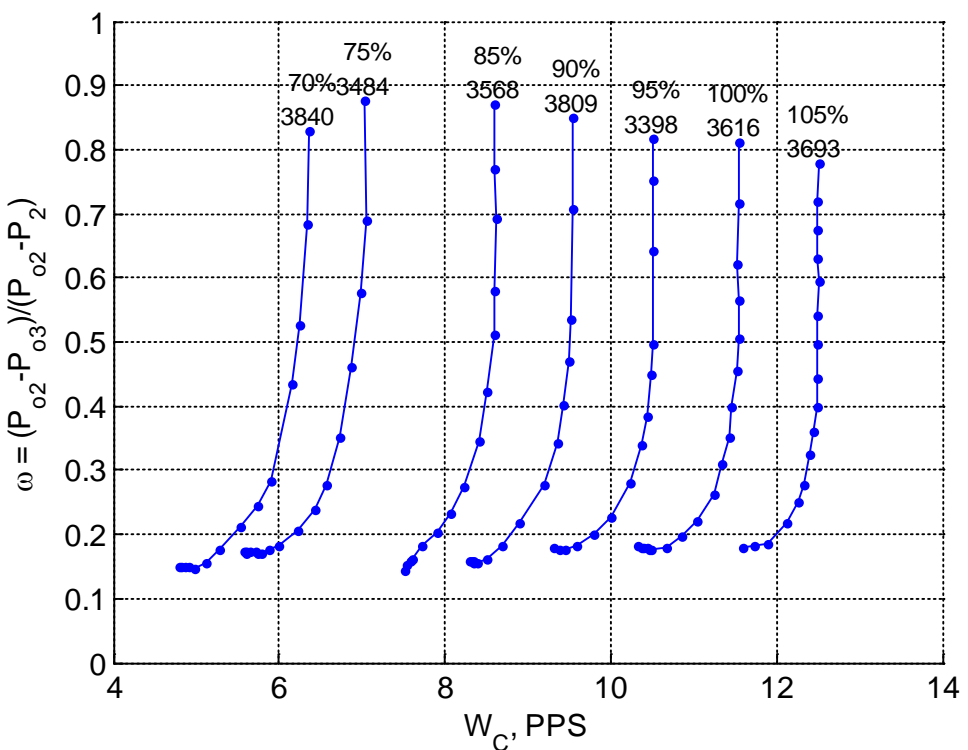


Figure 116.—Total pressure loss from diffuser leading edge to EGV leading edge against inlet corrected flow rate for various corrected speeds.

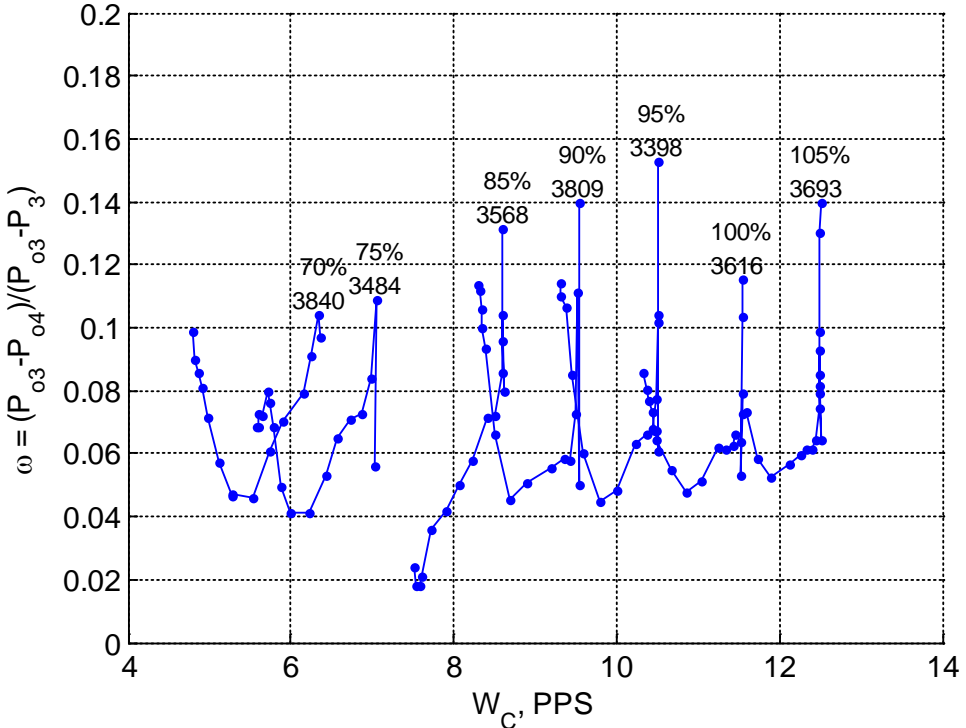


Figure 117.—Total pressure loss from EGV leading edge to exit against inlet corrected flow rate for various corrected speeds.

8.2.3 Comparison of Steady State Data to Pre-Test CFD

A comparison of total pressure ratio for 100 percent speed as computed in the pre-test CFD prediction using LEO is made with the measurements in Figure 118. Total-to-total adiabatic and polytropic efficiency are also compared to data, in Figure 119 and Figure 120, respectively. Overall, the comparison of predicted performance to data is summarized in Table 6. Pre-test CFD significantly over predicts the performance: pressure ratio is over predicted by 3 percent, polytropic efficiency by 2.4 pt and the stall margin by 4.5 pt. Note also that the measured exit Mach number and exit swirl are also higher than what was computed in the pre-test CFD.

Interestingly, the flow rate at which the compressor stalls matches relatively well what was the last stable steady CFD simulation at low flow (see, for example, Figure 118), while there is an over prediction of choke flow rate in CFD by about 4 percent. It's worth noting that this over prediction is similar to what has been observed in the CFD computations for CC3. However, this was not accounted for when discussing the expected range and stall margin for the new HECC compressor.

To investigate the discrepancies between the pre-test predictions the performance of impeller, diffuser and EGV are analyzed separately for 100 percent speed. Total-to-total adiabatic efficiency, total pressure ratio and total temperature ratio for impeller are presented in Figure 121, Figure 122 and Figure 123. Pressure recovery for the diffuser is presented in Figure 124, pressure recovery for combined diffuser and EGV is presented in Figure 125, and total pressure loss from diffuser leading edge to EGV leading edge is presented in Figure 126.

Note that all these quantities are highly dependent on P_{02} , and how accurately it is measured, as well as how the averages from the measurements are computed. Data reduction and the details of processing the total pressure measurements from modular vanes are discussed Section 8.2.1. CFD data is processed in the same way: using the same physical location as in the modular vanes, and is averaged in the same fashion as the experimental data.

Impeller adiabatic efficiency is over predicted by the pre-test CFD—from about 4 pt for the lower flow rates to about 2.5 pt for the higher flow rate conditions. Indeed, CFD over predicted the total pressure at modular vanes, and at the same time under predicted total temperature ratio for the compressor.

Data for the pressure recovery of the diffuser show that it peaks at about 0.67, whereas the CFD predicted peak values of about 0.66. Note that the recovery in the measurements peaks at the lowest flow rate—no bucket is observed. This is consistent with the notion that the diffuser vanes have been designed with large negative incidence—this point will be discussed in more details in Section 9.3.2. For the overall pressure recovery for the diffuser and EGV, CFD is predicting peak values of about 0.74 against measured values of 0.745. As far as recovery is concerned, pre-test CFD agrees with data. Total pressure losses from diffuser leading edge to exit also show that both CFD and measured values are about 7 to 8 percent for design condition.

Plots of static pressure in the diffuser are shown for flow rate of 11 lbm/s in Figure 127 (on the hub) and Figure 128 (on the shroud). Predicted trailing edge pressure is higher than the data, but most interesting is negative loading on the splitter vane shown in the experimental data, which is not present in the CFD results (splitter vane has almost zero loading in CFD). Furthermore, the measured pressure on the suction side of the main vane shows a bump (at radius of about 10 in.) which is also not present in the CFD results. Note also that both of these features on the main and splitter vane are stronger on the shroud, than on the hub. In summary, the diffuser is not behaving as expected based on pre-test analyses. However, note that this does not seem to dramatically impact the diffuser losses, which seem well predicted by pre-test CFD.

Figure 129 and Figure 130 show measured total pressure profiles at diffuser leading edge and EGV leading edge compared to pre-test CFD for 11 lbm/s. The asymmetric shape of both profiles seems to be captured to some degree in the CFD results. As already discussed, pre-test CFD over predicts the pressure ratio in the impeller, while the losses in the diffuser are predicted relatively well. However, for flow rate of 11 lbm/s CFD seems to under predict the total pressure losses in the diffuser a bit more than for the other points on the speedline—resulting in larger delta between CFD and data at the EGV LE than at the diffuser LE.

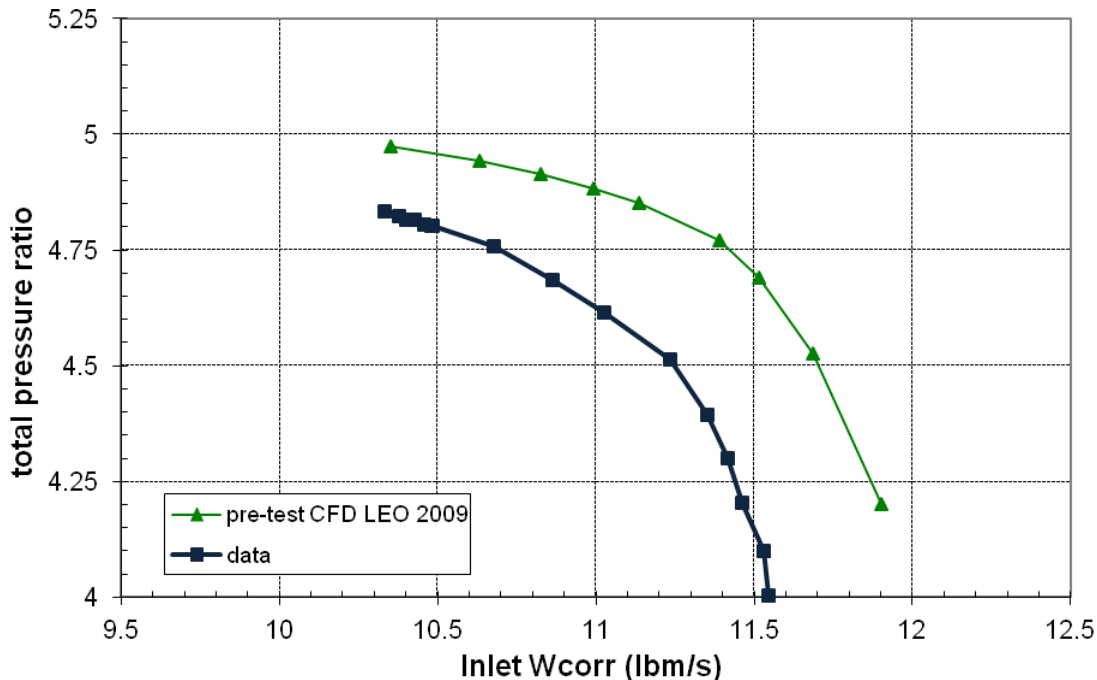


Figure 118.—Total pressure ratio at 100 percent N_c : data against pre-test CFD predictions.

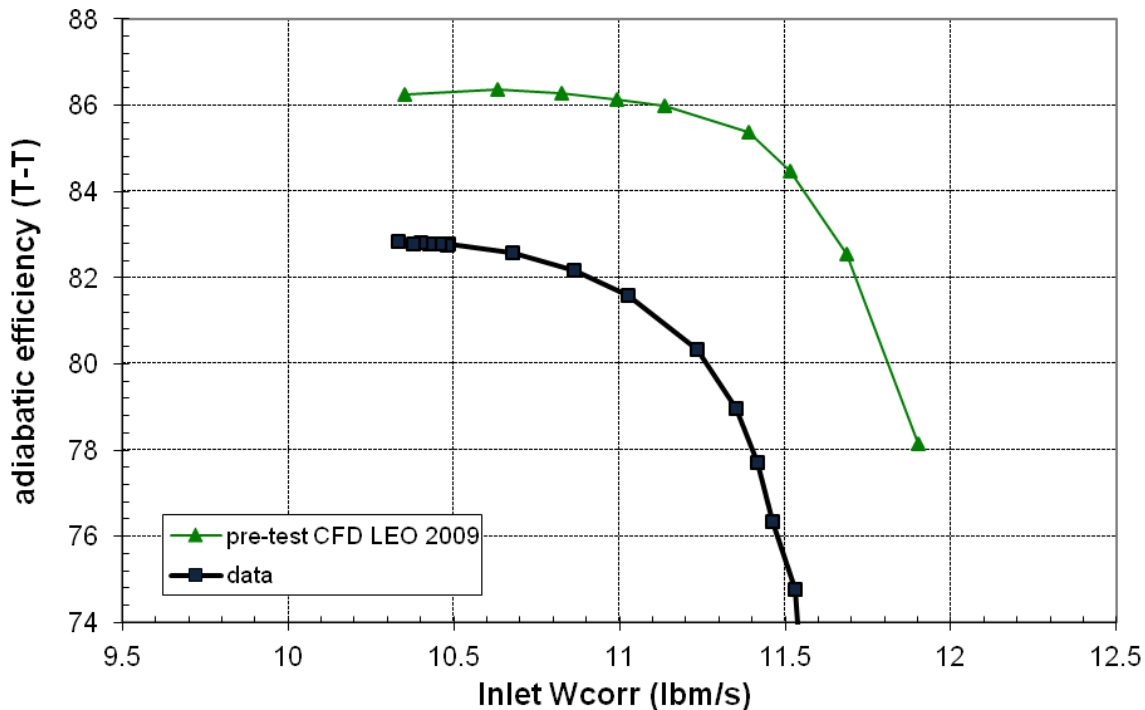


Figure 119.—Total-to-total adiabatic efficiency for 100 percent N_c : data against pre-test CFD predictions.

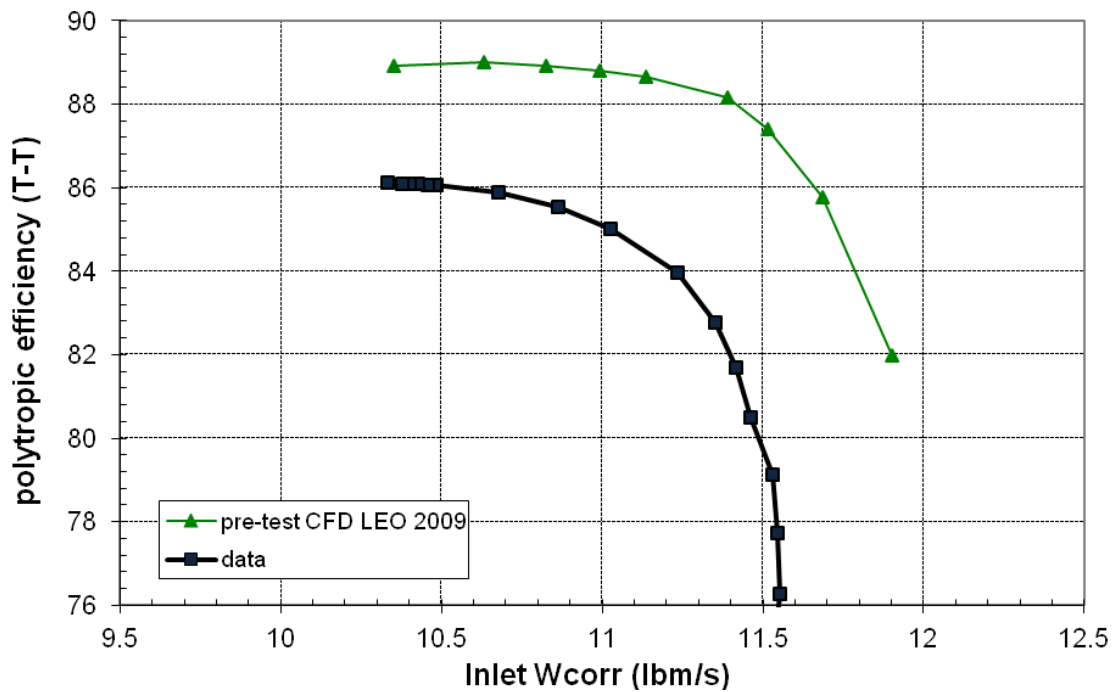


Figure 120.—Total-to-total polytropic efficiency for 100 percent N_c : data against pre-test CFD predictions.

TABLE 6.—COMPARISON OF MEASURED DATA TO PRE-TEST CFD
($m_{c,ex} = 3$ lbm/s, $N_c = 100$ PERCENT, AND 12 mils CONSTANT CLEARANCE)

	Pre-test CFD	Measured	Delta
PR _{TT}	4.85	4.68	-3%
$\eta_{poly,TT}$, %	87.9	85.5	-2.4 pt
$m_{c,in}$, lbm/s	11.1	10.85	-2.5%
Work factor, $\Delta H_0/U_z^2$	0.79	0.81	✓
M_{exit}	0.15	0.18	0.03
α_{exit}	14°	34.3°	20.3°
SM, %	12	7.5	4.5 pt

*Note that the pre-test CFD efficiency and flow rate were corrected for suppressed inlet.

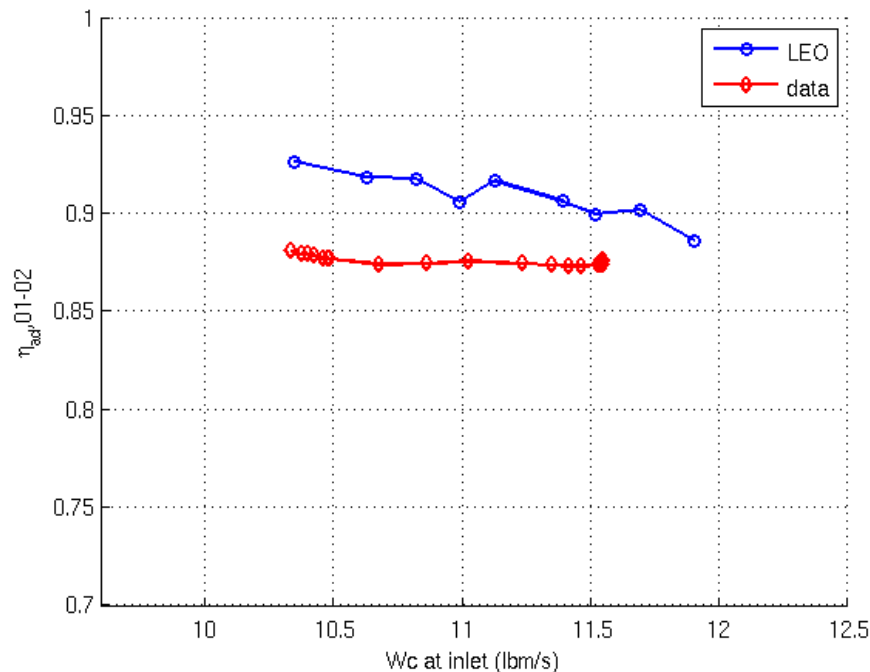


Figure 121.—Total-to-total adiabatic efficiency for impeller for 100 percent N_c : data against pre-test CFD predictions.

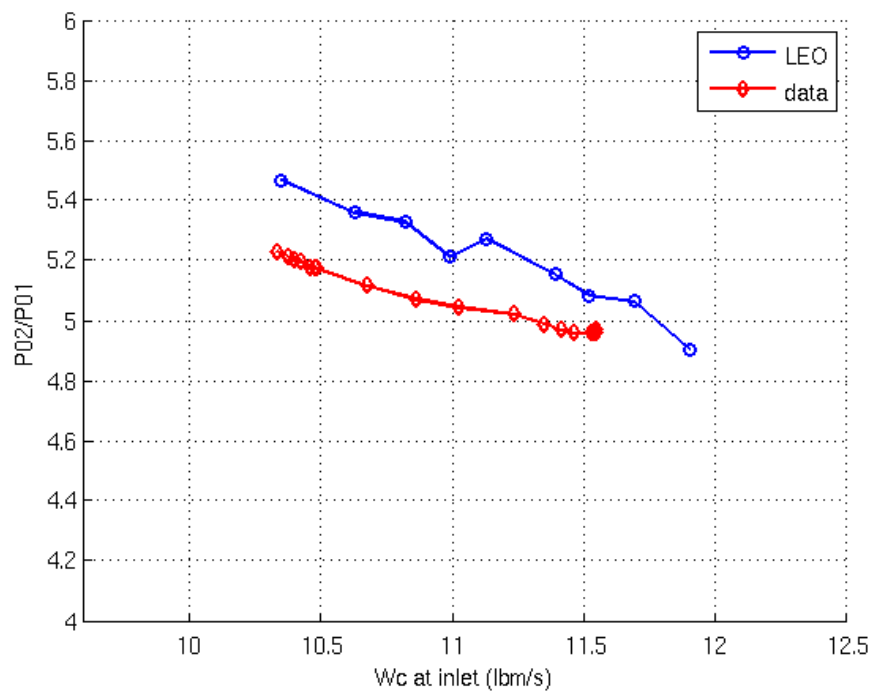


Figure 122.—Total pressure ratio for impeller for 100 percent N_c : data against pre-test CFD predictions.

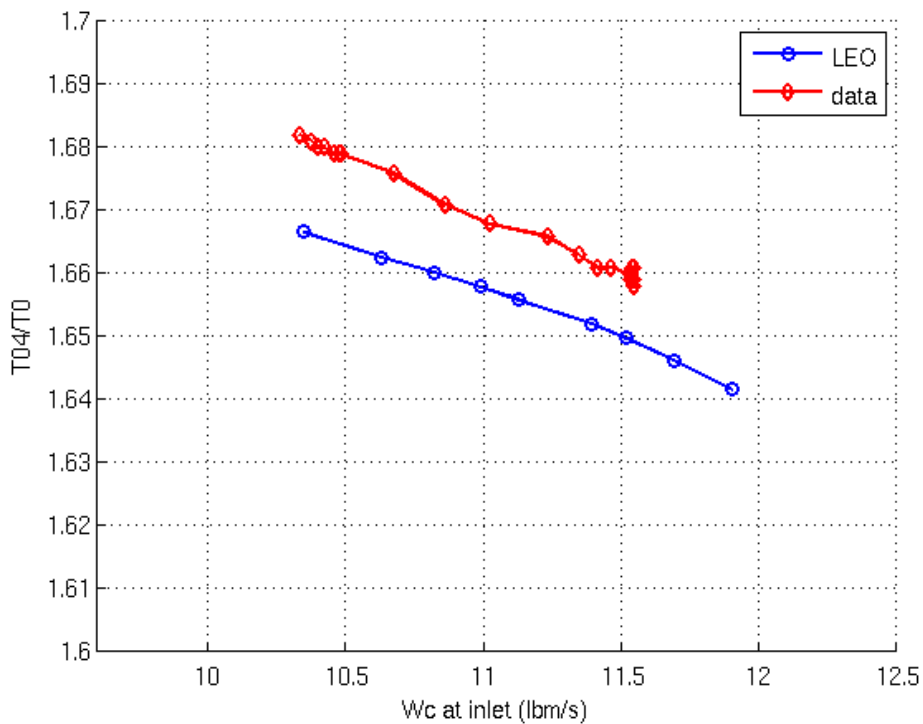


Figure 123.—Total temperature ratio for compressor for 100 percent N_c : data against pre-test CFD predictions.

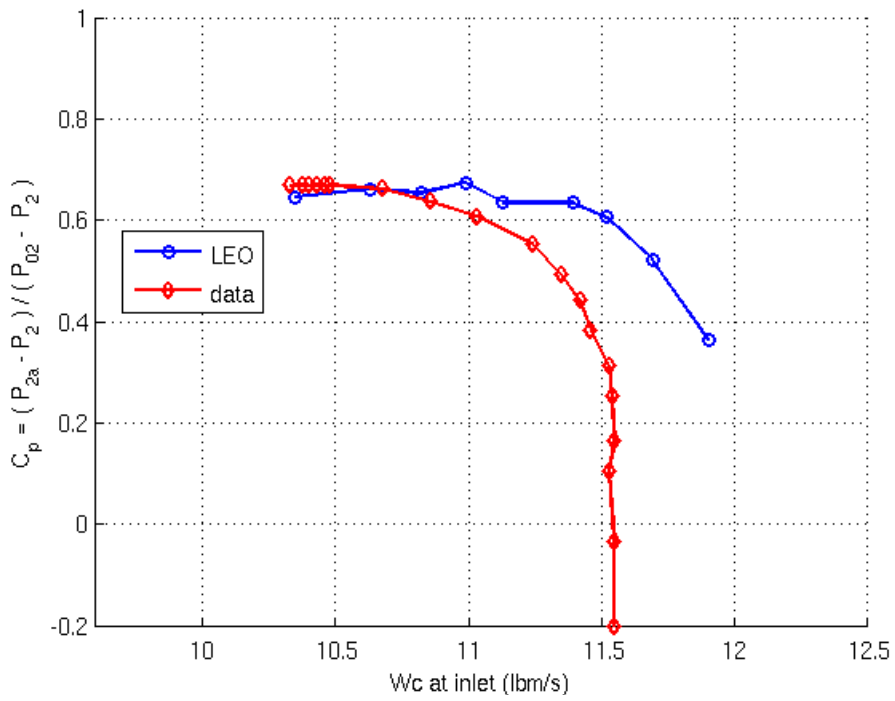


Figure 124.—Pressure recovery in the diffuser for 100 percent N_c : data against pre-test CFD predictions.

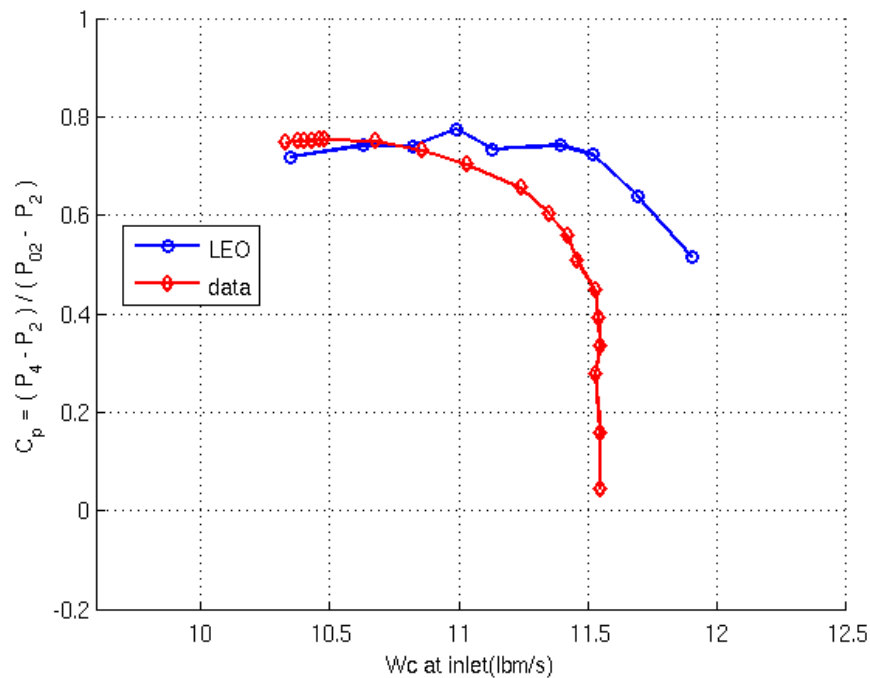


Figure 125.—Pressure recovery for diffuser and EGV combined for 100 percent N_c : data against pre-test CFD predictions.

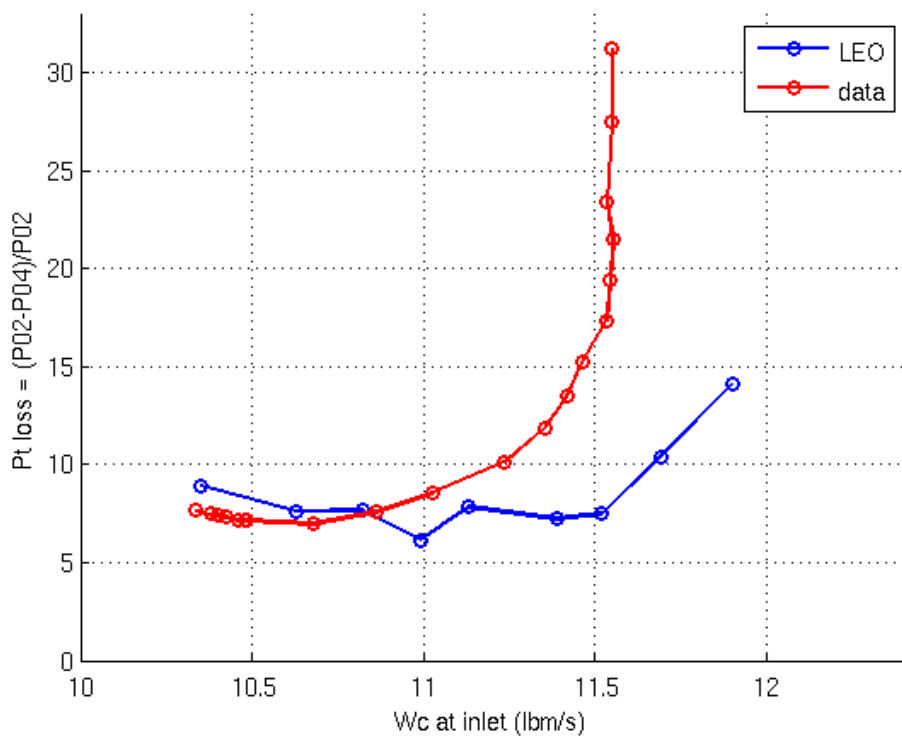


Figure 126.—Total pressure loss from diffuser leading edge to exit for 100 percent N_c : data against pre-test CFD predictions.

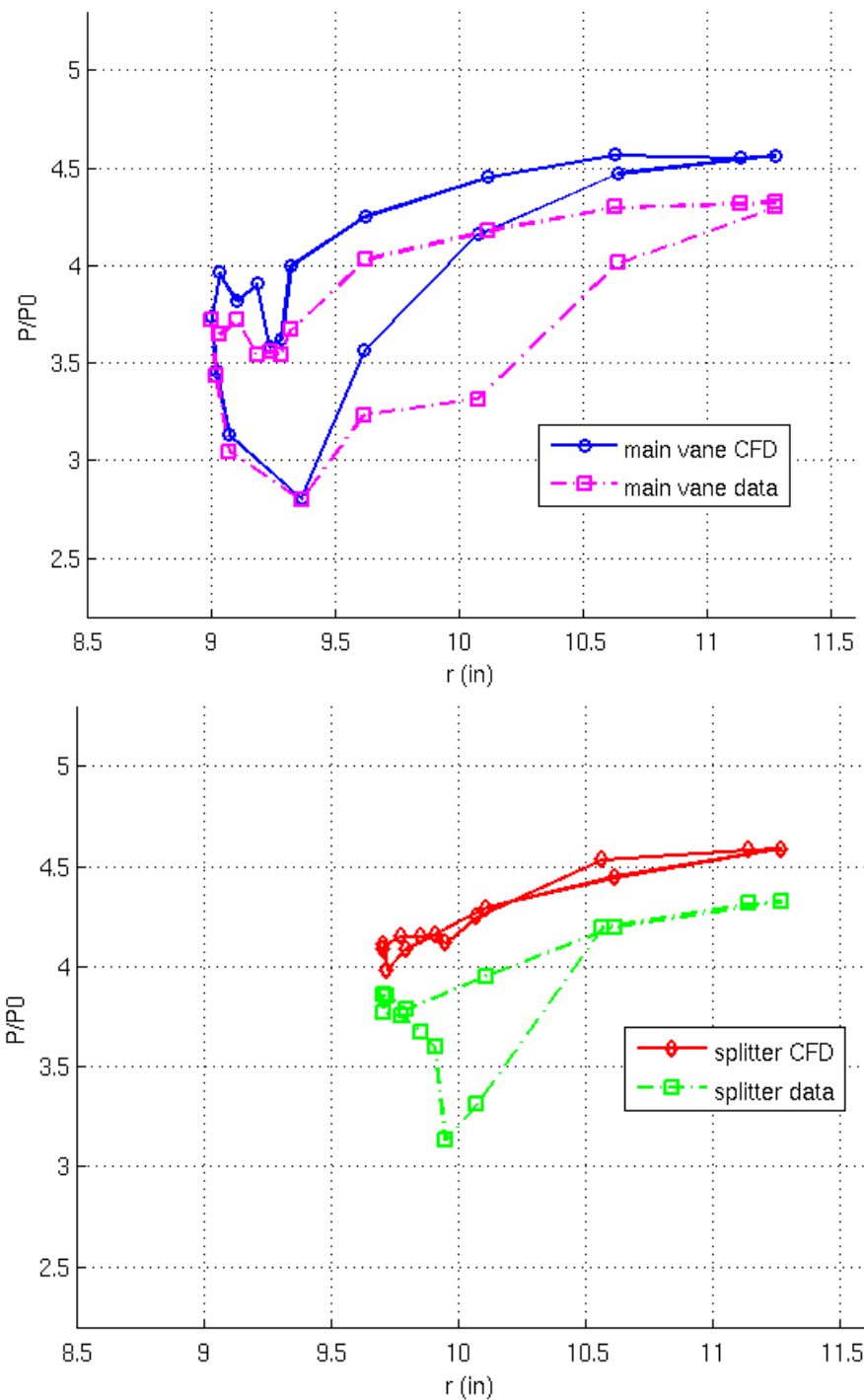


Figure 127.—Static pressure around main (top figure) and splitter (bottom figure) vanes on the hub for 100 percent N_c at inlet corrected flow of 11 lbm/s: data against pre-test CFD predictions.

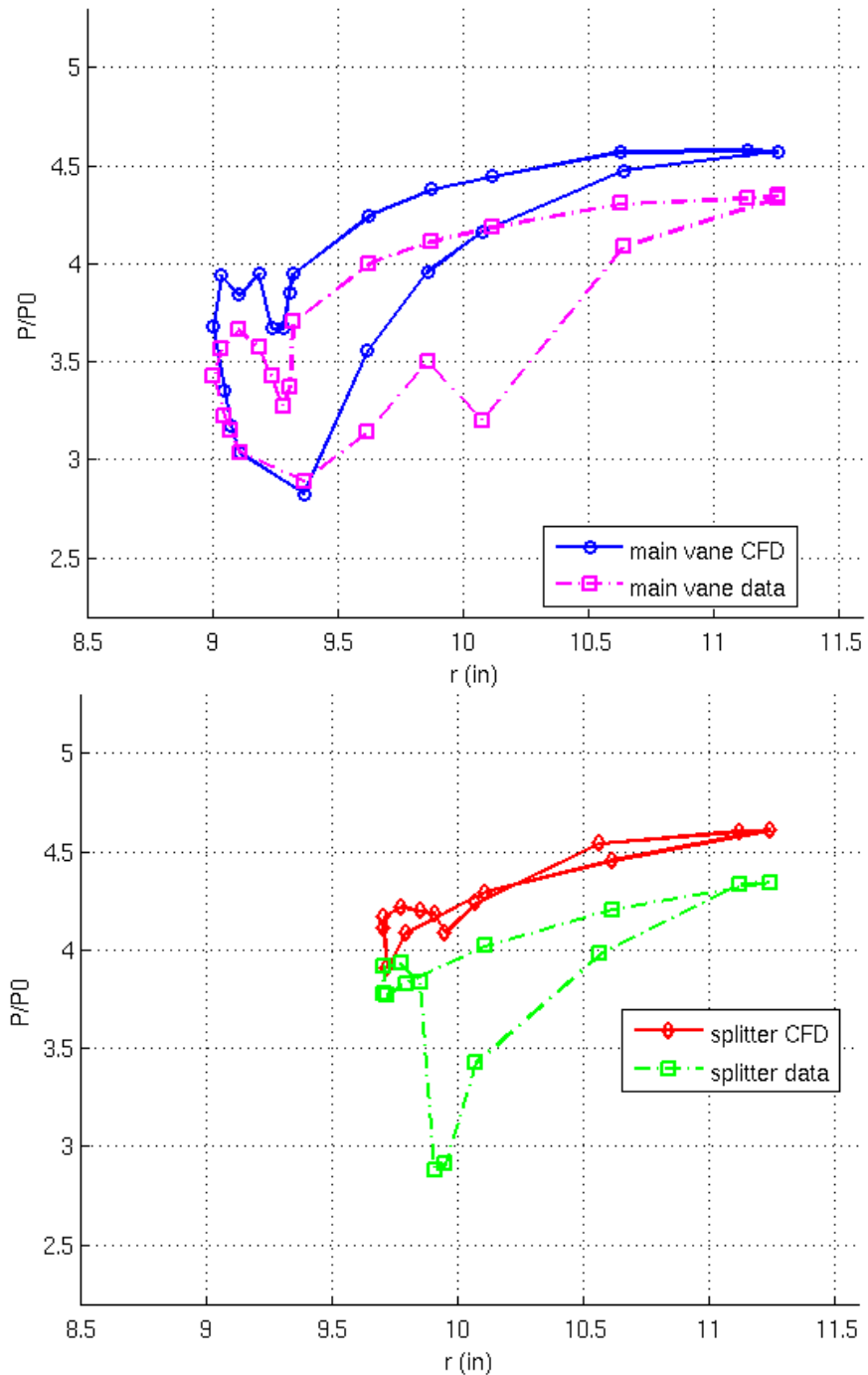


Figure 128.—Static pressure around main (top figure) and splitter (bottom figure) vanes on the shroud for 100 percent N_c at inlet corrected flow of 11 lbm/s: data against pre-test CFD predictions.

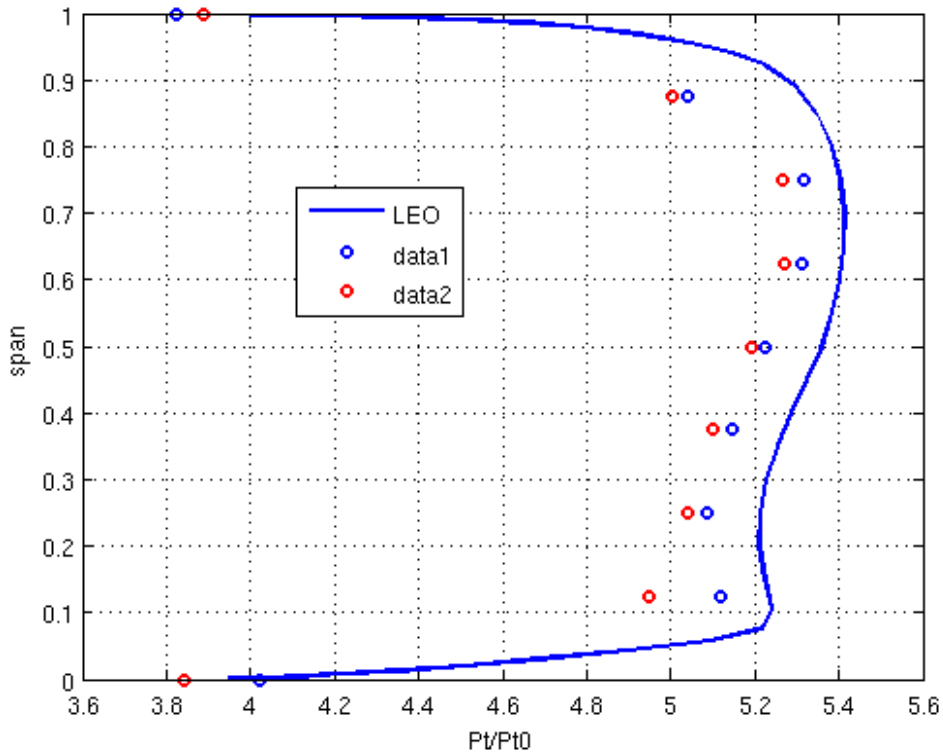


Figure 129.—Total pressure profile at diffuser modular vane leading edge for 100 percent N_c at inlet corrected flow of 11 lbm/s: data against pre-test CFD predictions.

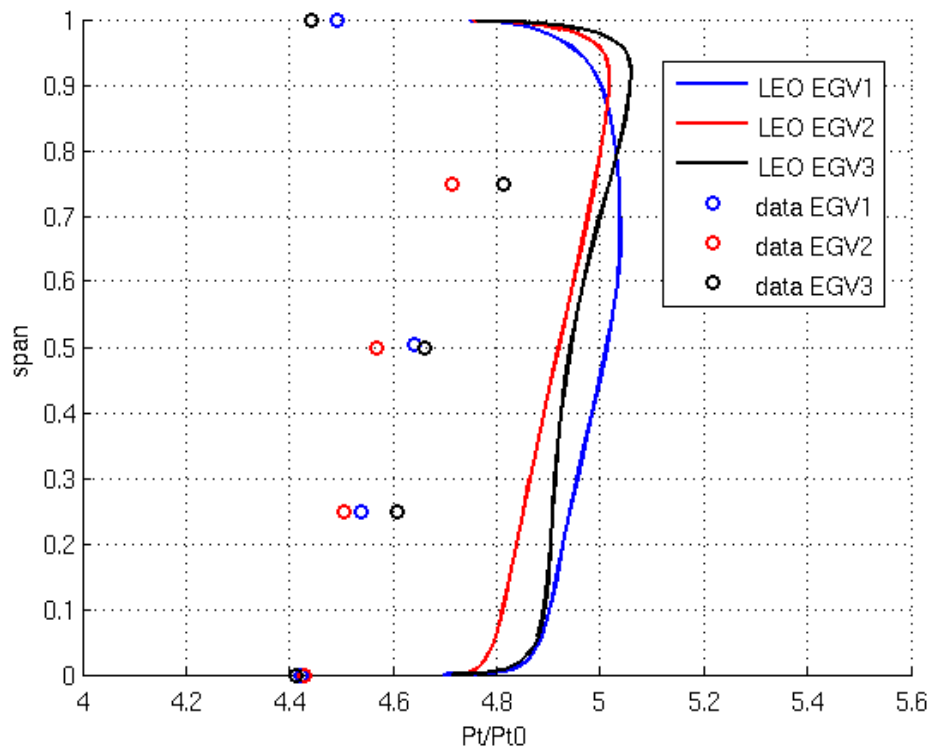


Figure 130.—Total pressure profile at EGV leading edge for 100 percent N_c at inlet corrected flow of 11 lbm/s: data against pre-test CFD predictions.

8.3 High-Response Pressure Data at 100 percent N_c

The following section analyzes the signals from the high-response, unsteady pressure transducers (Kulite XT-190 and XTE-190 sensors) for a range of operating points. As discussed in Section 7.0, these measurements were meant to address technical barriers associated with impeller-diffuser interaction and high cycle fatigue. Figure 131 shows the locations of the diffuser passage transducers which are used to understand acoustic and convective propagation through the diffuser. Data was obtained at locations 12, 13, 15, 18, 19, and 20. In addition, transducers were located at the impeller tip radius (installed on the impeller shroud) at 0, 1/3, and 2/3 vane pitch to capture the variation of the pressure field in the stationary frame due to the upstream effect of the diffuser blades.

Details of the processing (e.g. the phase-locked averaging approach) are described in Appendix A, as well as the Fourier decomposition results, modeling for the installation correction for the impeller tip transducers, and comparison of mean pressure to the static pressure taps.

8.3.1 Phase-Locked Averaged Results

Figure 131 to Figure 134 present the phase-locked averaged pressure data for a range of compressor flows from deep choke to near stall. Each figure gives the results for all the unsteady pressures in terms of the fractional deviation from the mean pressure versus the normalized time (or phase) of one blade passage. The mean pressure is listed in each figure in the lower left corner. The thick, red-colored line in each plot is the phase-locked (to rotor-blade passage) average pressure or deterministic component. The cyan-colored lines are $\pm 2\text{RMS}$ of the uncorrelated/random pressure and the dashed, red-colored lines are the maximum deviation from the averaged pressure that occurred in time record. The Fourier analysis of the phase-locked average pressure is given in Appendix A.

Unsteady pressures at locations 7, 8, and 9 (so-called K7, K8, and K9) are just inboard of the rotor tip diameter and (with the exception of K8) clearly show two cycles of high to low pressure variation over one blade passage interval which gives rise to a strong first harmonic of the blade passage frequency (i.e., $2f_{BP}$). It is inferred that the high pressure regions correspond the passing of the pressure side of the main and splitter blades (and likewise the low pressure regions correspond to the passing of the suction side of the main and splitter blades). In addition, close inspection of K7 and K9 RMS distributions show locally high levels at one of the two high pressure regions. This locally-high RMS level is most likely due to the wake of the main blade (longer boundary layer development than splitter). All the other locations show higher relative frequency content as evident by their nonsinusoidal waveform (see the Fourier analysis in Appendix A) due to the interaction with the diffuser vanes/splitters.

For K7, K8, and K9, the waveform is nearly invariant with operating point and the random part of the signal is low as seen by the tightness of the RMS (cyan) and maximum deviation (red-dashed) lines to the phase-locked curves. With the exception of the near stall point (Figure 134), this observation is also true of K18 which is located just upstream of the lower diffuser passage (so-called “passage B”). K12, the location just upstream of the upper diffuser passage (so-called “passage A”) has likewise invariant waveform and low random component for the choke onset (Figure 132) and deep choke (Figure 131) operating points.

For all the other locations downstream in the diffuser passages (K13, K19, K20—passage A, K15—passage B), the waveform and random component are highly dependent on the compressor operating point mainly due to the location of the transonic region and the existence of a terminating shock wave. For example, for the choke onset operating point (Figure 132), the transonic/choke region can be inferred to be located near the splitter leading edges due to the peaked RMS levels in that region (K13) compared with the RMS levels upstream and downstream of that region.

For the deep choke operating point (Figure 131), a well-established supersonic region can be observed into the diffuser passages by observing the low mean pressure of K15 (passage B) and K19 (passage A). It's interesting to note that these two locations show very high maximum deviations from the phase-locked average on the positive side (upper red-dashed lines). Since the RMS is not correspondingly high, these maximum deviations occur during a low fraction of the time (this observation is better illustrated in Appendix A, Figure B.7, which plots all the instantaneous time histories of K19). The

terminating shock is apparently located between K19 and K20 as seen by the rise in the mean pressure between these two locations.

For the subsonic operating points (design, Figure 133, and near stall, Figure 134), close inspection of the RMS and/or maximum deviation lines for the pressures in passage A, reveals regions in phase space (or normalized time) where the levels are relatively higher and shift with downstream position. This feature is most evident for the near stall operating point for K12, K13, and K19 (Figure 134). Presumably, these regions of higher randomness correspond to wake turbulence from the rotor convecting through the diffuser. This point is better illustrated in the following section which gives waterfall plots of the RMS component for these pressures.

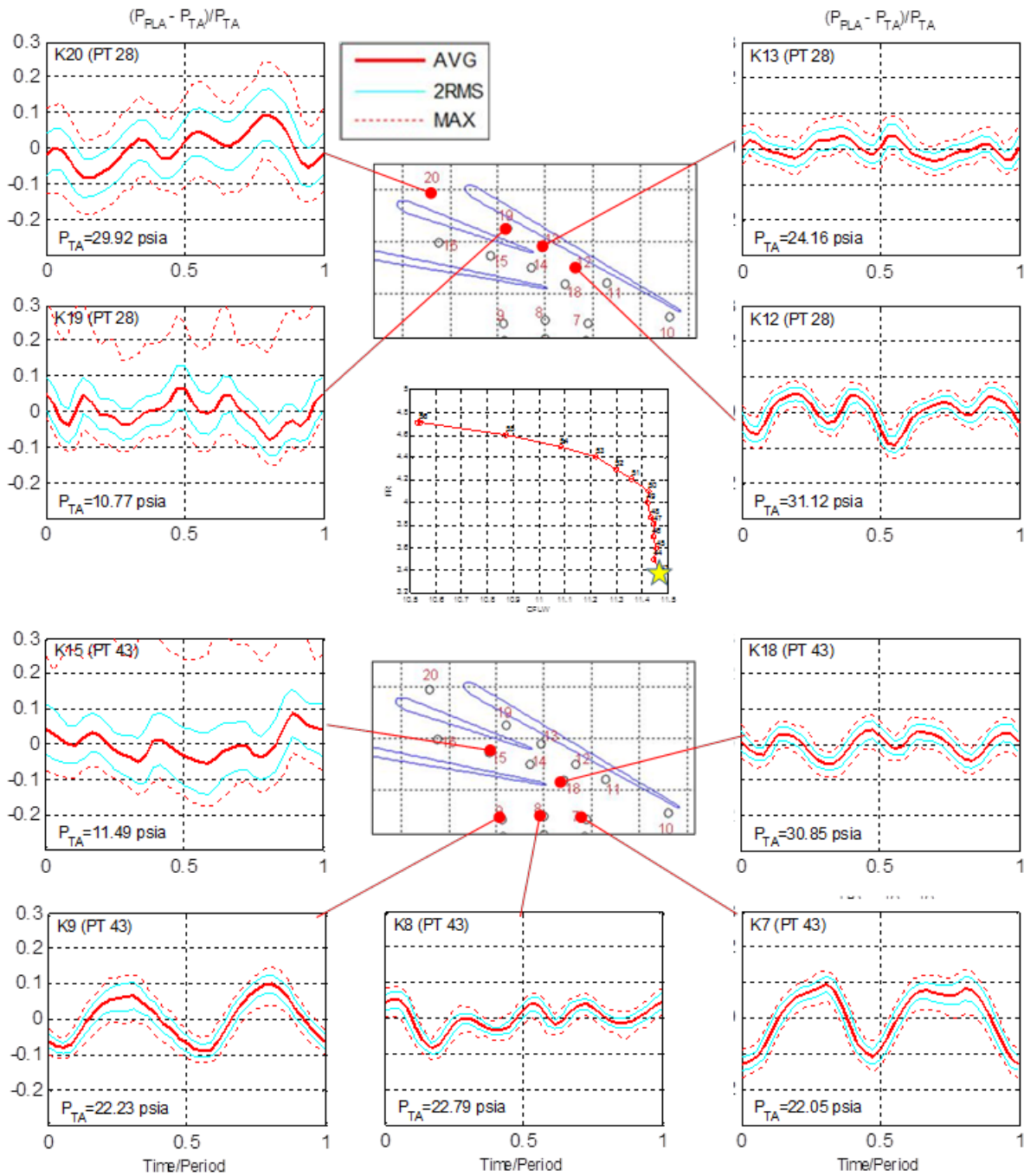


Figure 131.—Unsteady pressure results at deep choke operating point.

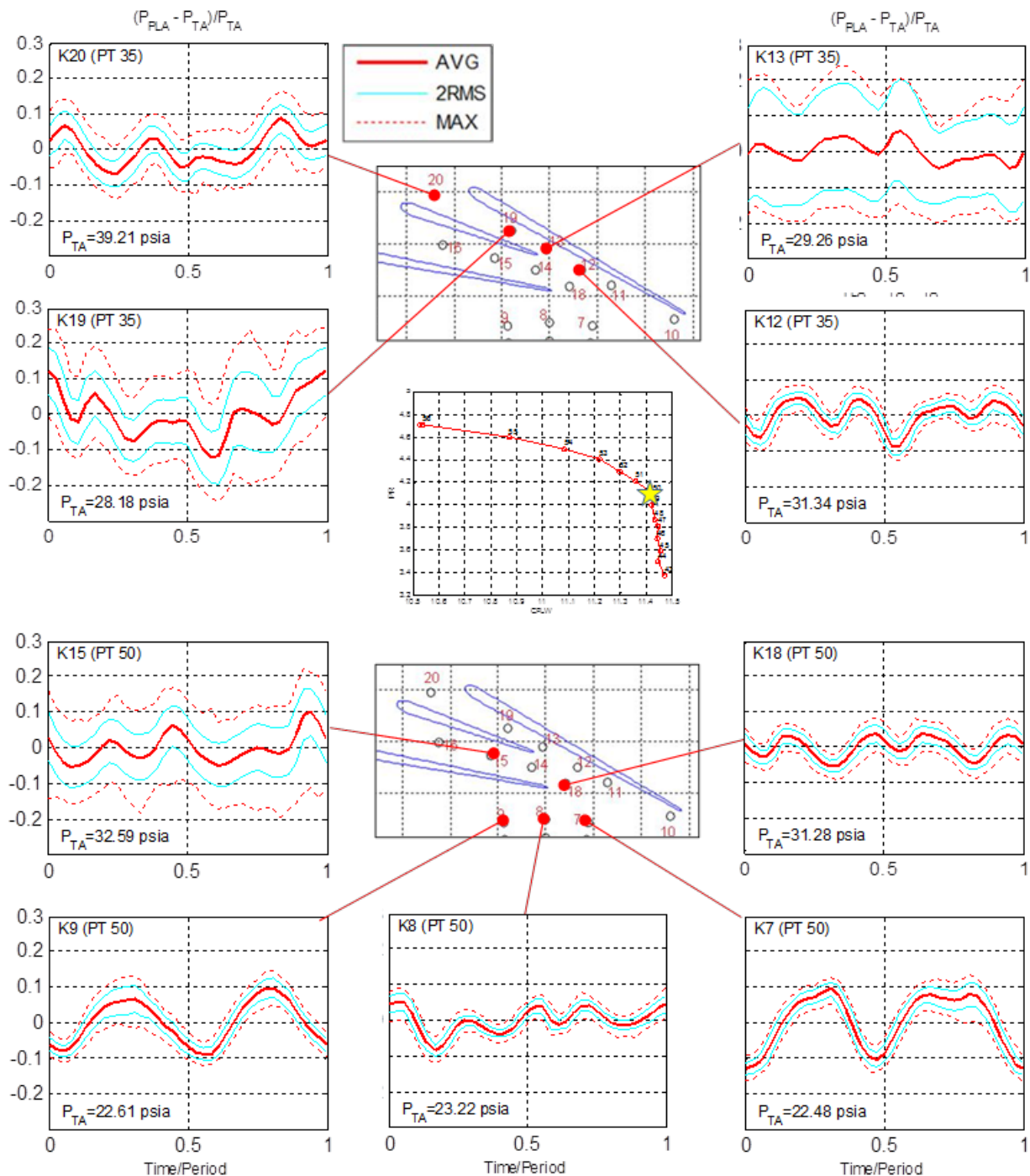


Figure 132.—Unsteady pressure results choke onset operating point.

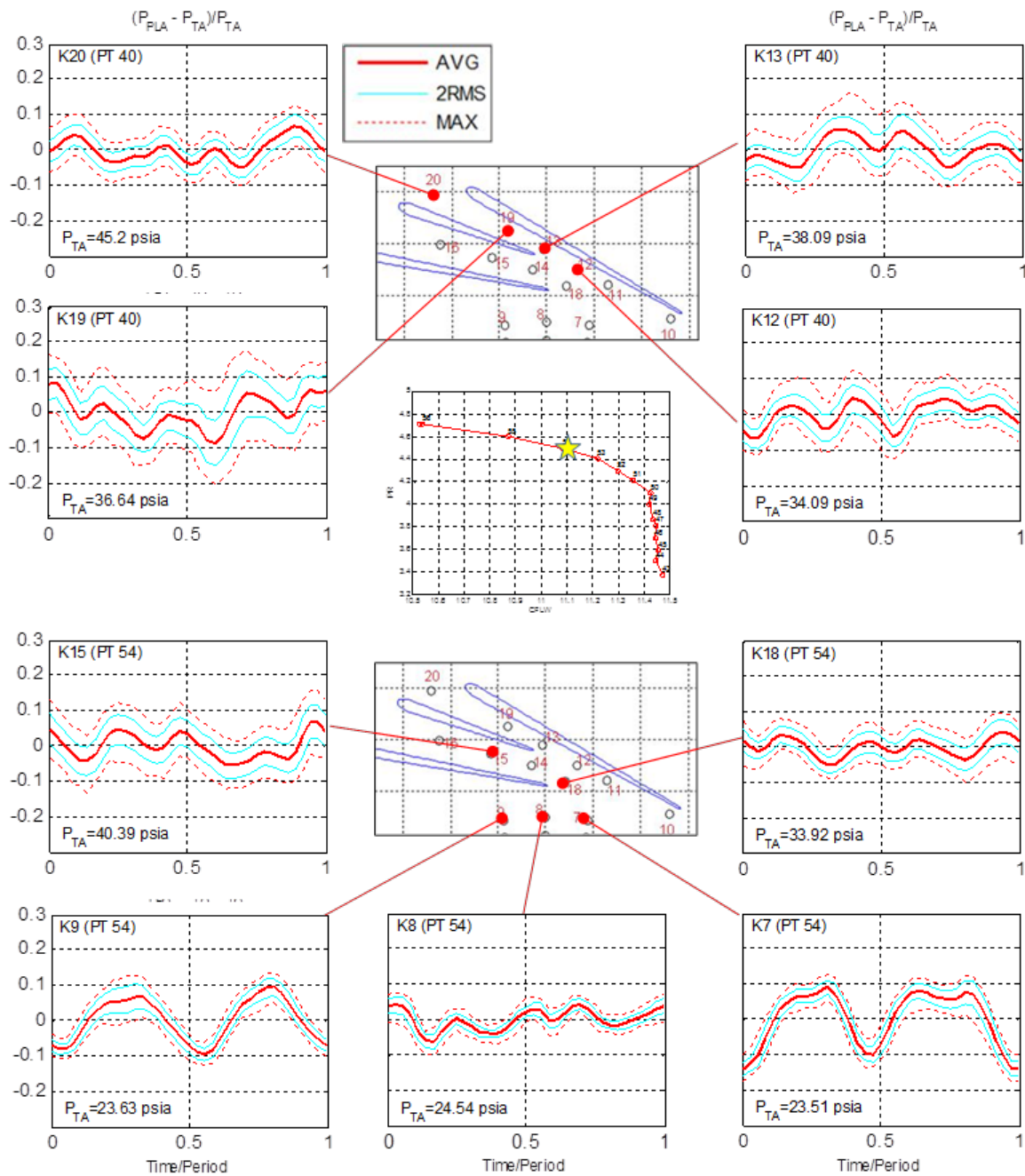


Figure 133.—Unsteady pressure results at design operating point.

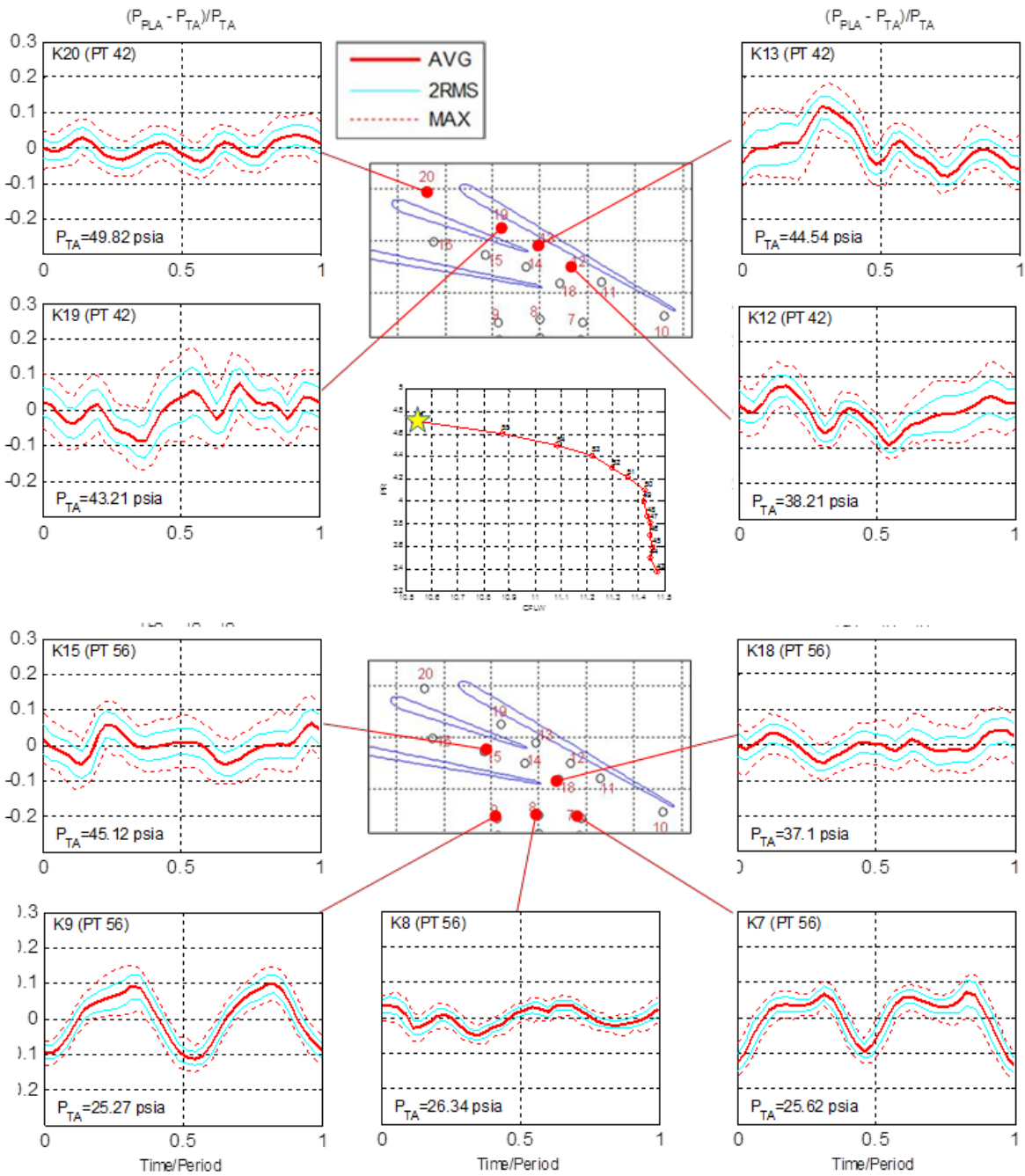


Figure 134.—Unsteady pressure results at near stall operating point.

8.3.2 RMS Analysis

This section discusses the time/space relationship of the random component through the diffuser passage. As mentioned in the previous section, the convection of the rotor wake structure was observed in diffuser passage A where a series of unsteady pressure transducers are located from upstream to downstream (similar resolution was not available for passage B). To quantitatively investigate this observation, waterfall plots of the RMS component for the passage A pressures are given in Figure 135 for the four operating points discussed in the previous section. To better visualize the time/space relationship, three cycles of blade passage are pieced together. The RMS value is normalized by the mean pressure and the distance axis ("s") is the relative spacing from K12.

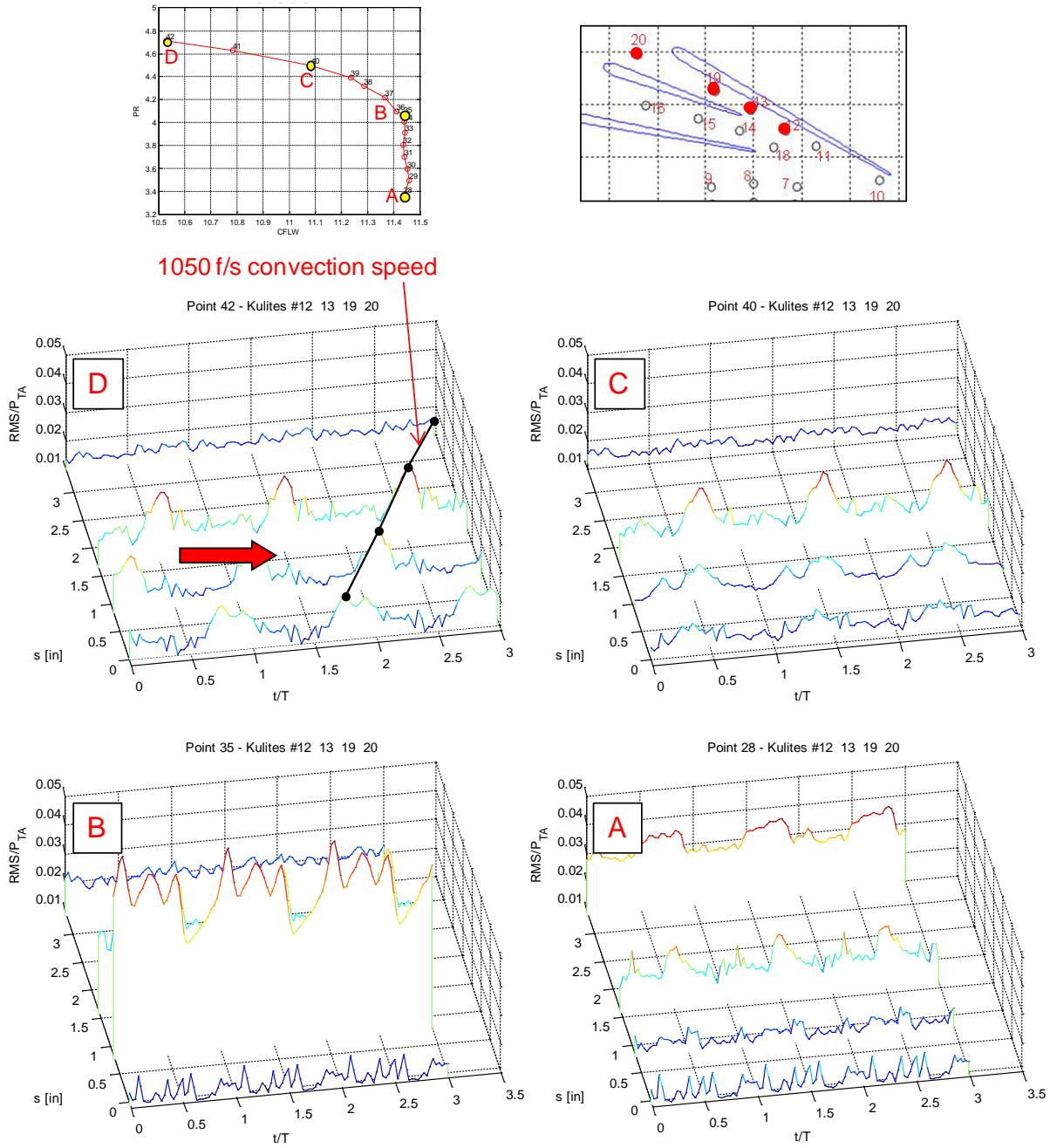


Figure 135.—Waterfall plots of RMS component in diffuser passage A.

The near stall operating point (upper left waterfall plot) clearly shows propagating structures from $s=0$ in. (K12) to $s=1.5$ in. (K19) which are moving at a speed of about 1050 f/s or about $M=0.7$, very close to the velocity predicted by the CFD. Surprisingly, there is no indication of coherent structures at the exit of the diffuser passage ($s=3.5$ in., K20). The design operating point (upper right plot) shows similar features as the near stall operating point.

For the choke onset and deep choke operating points (lower left and right plots, respectively), the RMS distribution is mainly influenced by the terminating shock location (high levels indicating approximate location). The deep choke operating point (lower right plot) does show some indication of a convecting-wake structure.

8.3.3 Frequency Response

This section examines the time/space relationship in the diffuser passage A by computing the frequency response between unsteady pressure transducers (using K12 as a reference). Unlike the previous section which examines the convecting random part of the pressure signal, this analysis considers both the deterministic and random parts of the signal.

Figure 136 shows the phase part of the frequency response between the pressures in diffuser passage A. A coherence analysis between the reference pressure (K12) and the downstream pressures indicated a strong, near unity coherence at blade passage frequency and its harmonics, otherwise, the coherence was very low, $\gamma^2 < 0.1$. Hence, only frequency response is plotted at blade passage and harmonics. Three frequency responses are shown in the figure (K13/K12: red circles, K19/K12: blue squares, and K20/K12: green triangles) for four operating points (A: deep choke, B: choke onset, C: design, D: near stall).

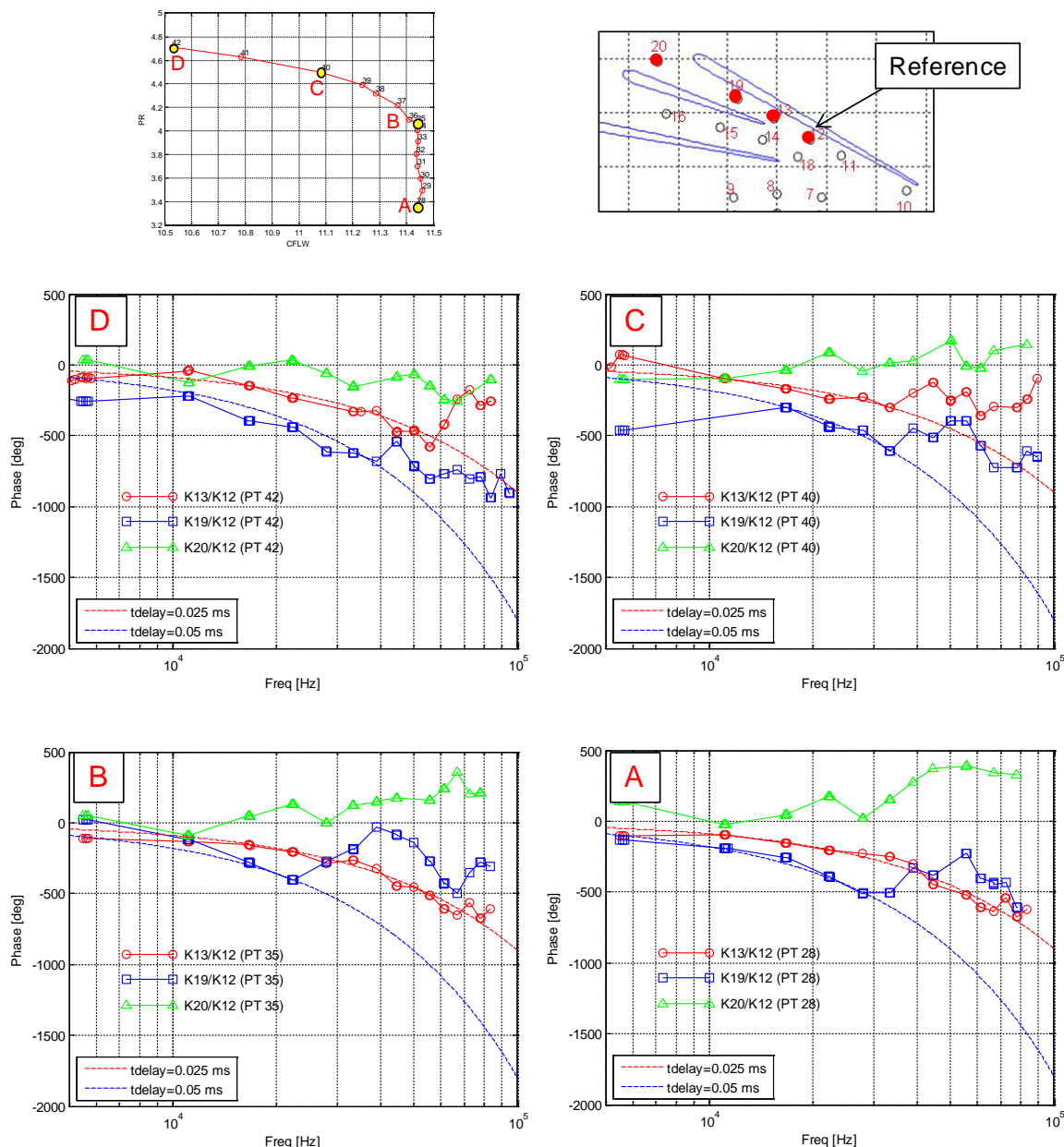


Figure 136.—Unsteady pressure transfer function (K12=reference).

In addition to the pressure frequency responses, the frequency responses for two time delays ($\exp(-i\omega\tau)$) are also plotted in the figure. As seen in the figure, a time delay of $\tau = 0.025$ ms correlates the frequency response between K12 and K13 and $\tau = 0.050$ ms correlates the frequency responses between K12 and K19. The agreement with the time delay response is better for the choke onset and deep choke operating points, but still reasonable for the design and near stall operating points. For the K20/K12 frequency response (vane leading to trailing edge), a time delay relationship does not appear to be present.

Using these time delays, a propagation velocity can be computed to help understand the physical mechanism that is causing the correlation between locations. The distances between K12-K13 and K12-K19 are 0.84 and 1.65 in. Using the time delays $\tau = 0.025$ and 0.05 ms gives propagation velocities of 2800 and 2740 f/s. Since the CFD indicates the Mach number in passage A is M~0.6-0.8 and the speed of sound is c~1500 f/s, these computed propagation speeds are approximately equal to the speed of sound plus the mean velocity and are hence consistent with downstream moving acoustic waves.

In contrast to this propagation speed, the previous section concluded that the random signals correspond to rotor wakes convecting at approximately the mean velocity. Hence, both propagating wake structures and acoustic waves are present in the diffuser passage. It can also be concluded the propagating acoustic waves are the dominate pressure fluctuation since the frequency response analysis with the full signals correlates with acoustic speed.

The lack of a mean flow correlation and an acoustic speed correlation with the most downstream location (K20) is an interesting result. It may indicate that the pressure fluctuations present there are dominated by a physical mechanism that is not present upstream, such as trailing edge separation.

9.0 Post-Test Root Cause Analysis of Differences Between Test Data and Pre-Test CFD Predictions

As the initial test results were made available to UTRC, and it became clear that there is a large discrepancy between test results and pre-test CFD predictions, a new set of CFD analyses was undertaken to conduct a root-cause analysis. Since UTRC had no longer access to ADS software LEO and WAND, UTC's in-house tools were used instead. Specifically, newly developed UTC's next-gen turbomachinery solver UTCFD has been used for CFD analyses, and computational grids were generated using UTRC's new grid generator for centrifugal compressors UTGRID.

UTCFD and UTGRID are both products of the Virtual Aero-Thermal Engineering (VATE) project which is an ongoing UTRC IRAD capability building project initiated in 2008 with the overall goal of developing focused, sustainable, and efficient, high-fidelity computational technology and application processes. These enhanced capabilities are being developed to enable UTRC to conduct large-scale simulations in support of technology and product development programs for all UTC business units. Under this multi-year effort, the common platform project is designed to deliver a long-term, sustainable, computational framework, with a focus on the current bottlenecks of key CFD technology, to achieve maximum benefits in a timely manner. Specifically, the project is expected to deliver CFD technologies and processes on a common computational platform, which will enable the execution of component simulations with increasing levels of complexity in geometry and modeled physics.

At the core of the VATE project is a modern modular CFD library, the next-generation turbomachinery solver UTCFD, that is based on validated in-house CFD methodology for turbomachinery. Pratt & Whitney joined UTRC in developing UTCFD in 2009 and it has pursued it jointly with UTRC ever since, through a sequence of special initiative projects.

From a technical perspective, the modular CFD library UTCFD is based on: (1) a flexible data structure to allow maximum generality in configuring a variable governing equation set, structured or unstructured grid types and time-domain/frequency-domain expressions; (2) separate dependent and independent variables sets to contain the "property table" and equations of state in a centralized module; (3) a general preconditioning system to enable a unified convergence scheme for all speeds including incompressible flows; (4) a modular coding practice to enable extensibility and reusability while limiting or

even removing future maintenance requirements; and (5) a concurrent parallel message passing scheme to maximize the parallel efficiency for large scale computations. In addition, multi-physics and multi-disciplinary simulations are taken into consideration through the design of interfaces between solvers of different physics from the beginning of the code design, rather than as an after-thought.

UTCFD is entirely written in Fortran90 with MPI-based parallelization (it has been tested with several MPI libraries—OPENMPI, HPMPI, etc.). CGNS file format is used for I/O (CGNS 2.5 library is currently used). The code has been successfully compiled and executed on multiple computer clusters within UTC, and in 2011 it was successfully ported to Jaguar/Titan cluster at ORNL, and used as the computational code for our ALCC project “Large-eddy simulations for turbomachinery—advancing state-of-the-art”. In the context of RANS turbulence models, several versions of $k-\omega$ model, as well as Spalart-Allmaras model have been implemented.

9.1 General Information

As a first step to benchmark the new UTCFD solver for HECC, a detailed comparison was conducted to pre-test computations with LEO. First, the impeller-diffuser configuration, studied both with steady and unsteady analyses with LEO prior to PDR, was analyzed with UTCFD. A comparison of CFD results using steady simulations on the same grid and using the same $k-\omega$ model with vorticity-based production in turbulence equations is shown in Figure 137.

Then, the next step was to analyze the final design. A new computational grid was generated with UTGRID. It contained about 4.5 millions of computational cells overall, as compared to approximately 1.5 million in the WAND grid used in pre-test analyses (Figure 138). In particular, improved spanwise resolution was used in the new analyses, 97 computational cells versus 65. Larger O-grids were also used around blades and vanes, better capturing the boundary layers.

A comparison of adiabatic efficiency computed with UTCFD for the final design and compared to LEO pre-test predictions is shown in Figure 139. It shows that UTCFD predicts somewhat higher peak efficiency (for about 0.5 pt), and somewhat lower choke flow (which reduced from about 11.9 to 11.6 lbm/s).

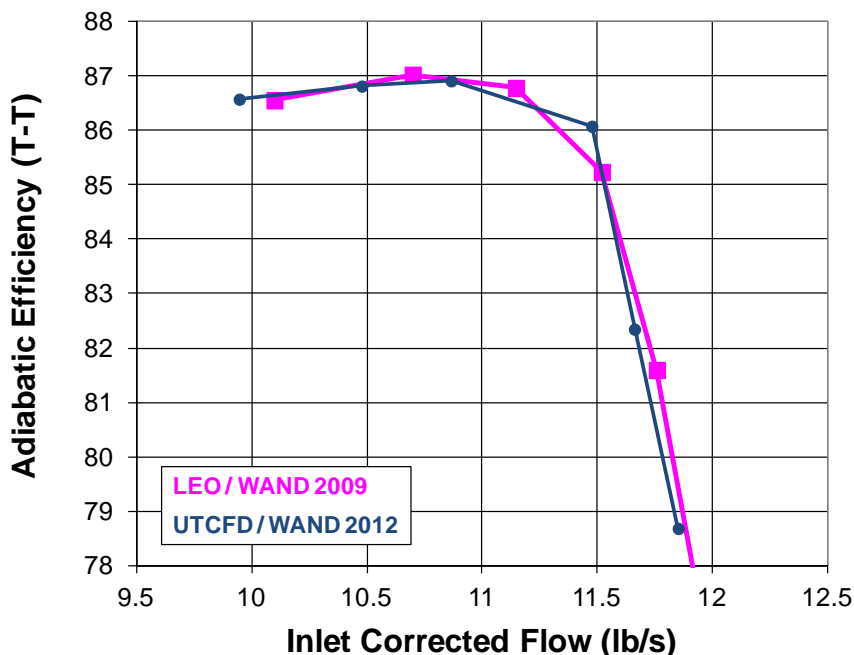


Figure 137.—Steady state CFD computations for impeller-diffuser configuration at 100 percent Nc : a comparison of adiabatic efficiency computed UTCFD to results from LEO (using the same WAND grid).

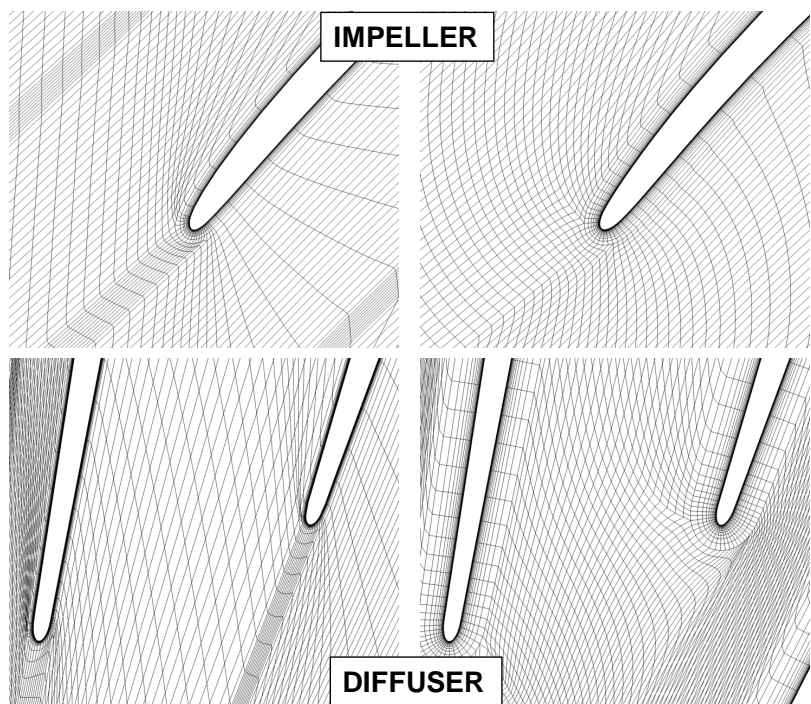


Figure 138.—Detail of the computational grid: WAND 2009 grid (left) and UTGRID 2012 grid (right).

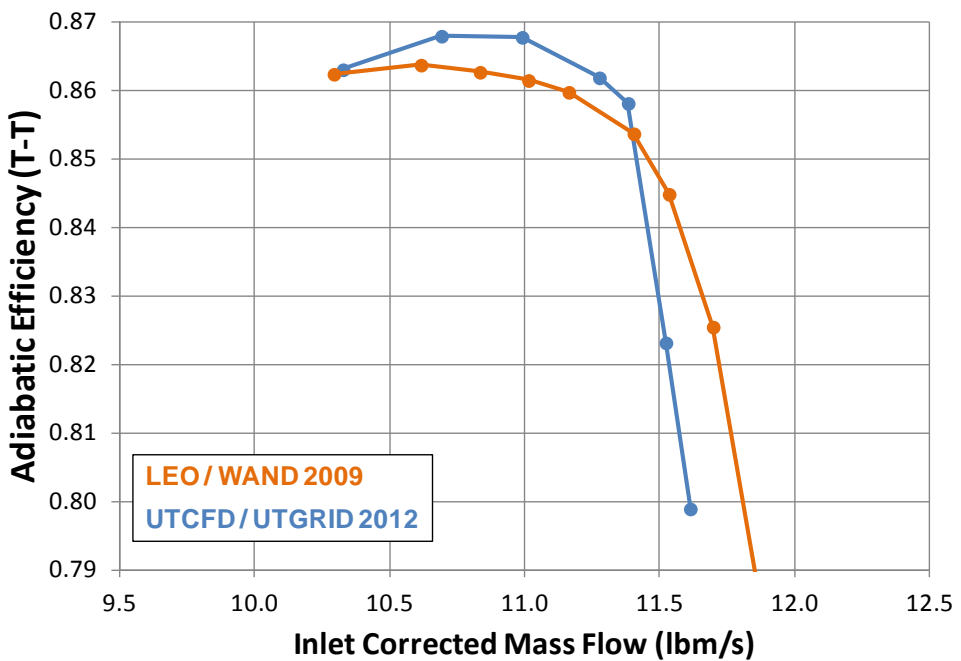


Figure 139.—Steady state CFD computations for final HECC configuration at 100 percent N_c : comparing LEO results from 2009 to UTCFD results computed on a finer, better resolved UTGRID grid.

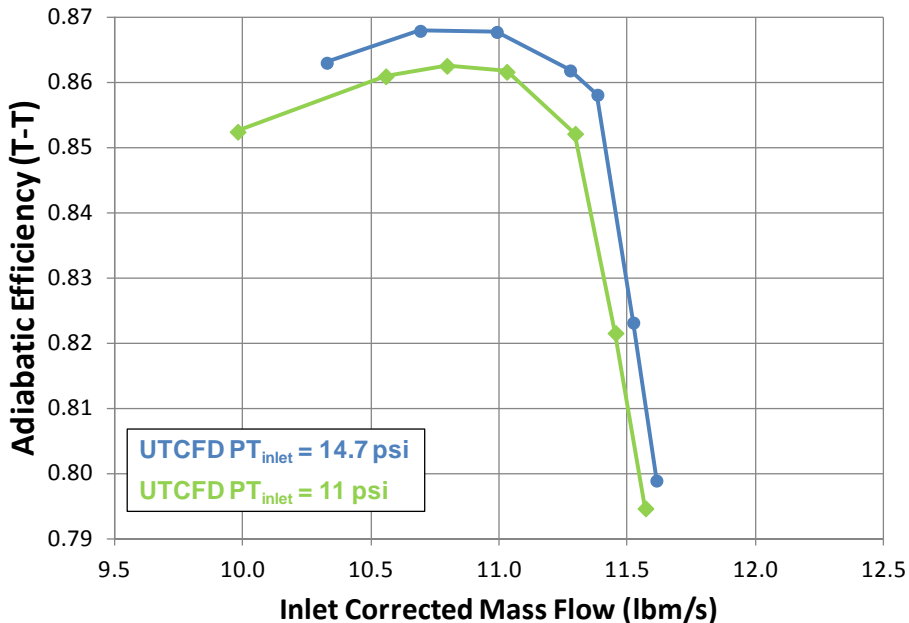


Figure 140.—Steady state CFD computations for final HECC stage configuration at 100 percent N_c using UTCFD—an assessment of the impact of suppressed inlet.

9.2 Impact of Suppressed Inlet

Since the HECC testing was conducted at suppressed inlet (as discussed in Section 7.0), UTCFD was then used to assess the impact of lower inlet total pressure on the performance. Figure 140 presents the adiabatic efficiency computed with inlet total pressure of 14.7 psi, and with 11 psi (using the baseline $k-\omega$ turbulence model). The performance delta that was observed was about 0.6 pt. in total-to-total adiabatic efficiency, which roughly corresponds to the performance reduction due to the Reynolds number effect which the reduction in inlet pressure would produce. Note that the choke flow is also reduced by about 1 percent.

Figure 140 also shows a difference in range between two speedlines. Note that no rigorous effort has been put into determining the last stable point at lowest flow—as predicted by steady CFD. The differences presented in Figure 140 reflect differences in flow rate computed for same exit static pressures, and as such they are somewhat indicative of changes in range. However, as discussed at length in Section 11.1.1, using steady CFD computations for assessment of range is at the least questionable, and could easily lead to misleading conclusions, so this information should be used with caution. This conclusion applies to all speedlines presented in the post-test CFD analysis.

9.3 Sensitivity to Geometry Variation

Initial focus of new CFD analyses was on understanding whether, in case the actual geometry of the compressor components as installed in the rig differs significantly from the one that was originally analyzed with CFD, whether that could account for the observed differences in the performance and specifically the measured static pressure on the diffuser endwalls.

Focus was on two scenarios that were considered as plausible geometrical variations in the rig:

- The impact of a 5 mil step in the shroud flowpath just before the diffuser leading edge,
- The impact of a change in the stagger of the splitter vane for 1° and 3°.

9.3.1 Impact of a 5 mil Step

Upon examination of the rig during teardown, a 5 mil forward-facing step was found on the shroud side of the flowpath, just upstream of the diffuser. The step was not around the full circumferential extent,

but was in the area of one of the instrumented diffuser vanes. A CFD run was made with an axisymmetric step in the flowpath and a significant reduction in adiabatic efficiency was observed, as shown in Figure 141. The results were also compared to the total pressure profile measured with the instrumented diffuser vanes. CFD results with modeled step show better agreement with the measured total pressure profile, as shown in Figure 142. Note that while the impact of step on the measured performance is not clear, this analysis indicates that any feature that causes additional losses in the tip region would have a significant impact on performance.

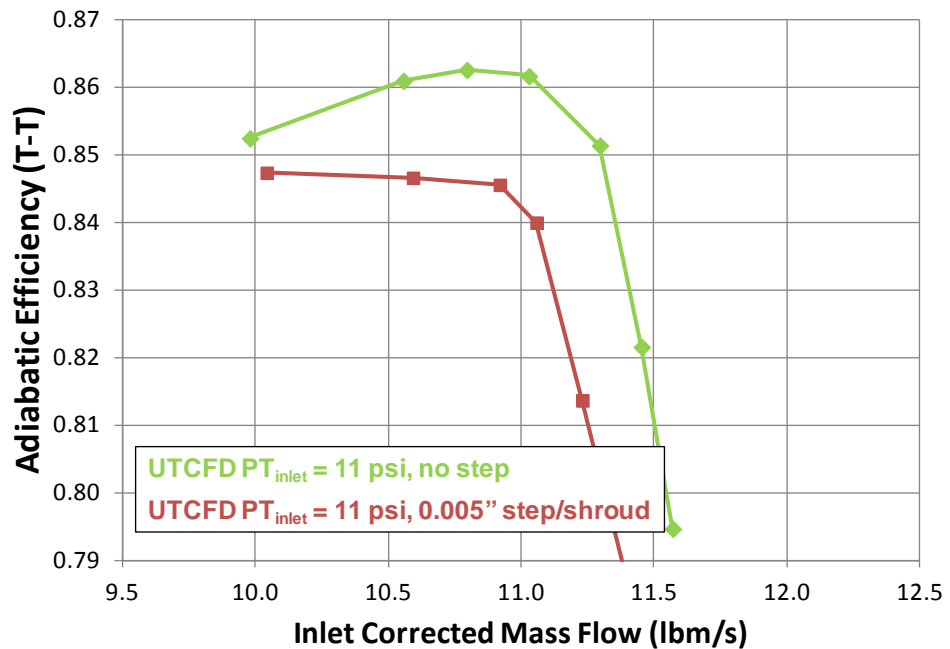


Figure 141.—Steady state CFD computations for final HECC configuration at 100 percent N_c using UTCFD with suppressed inlet—an assessment of the impact of 0.005 in. step on the shroud.

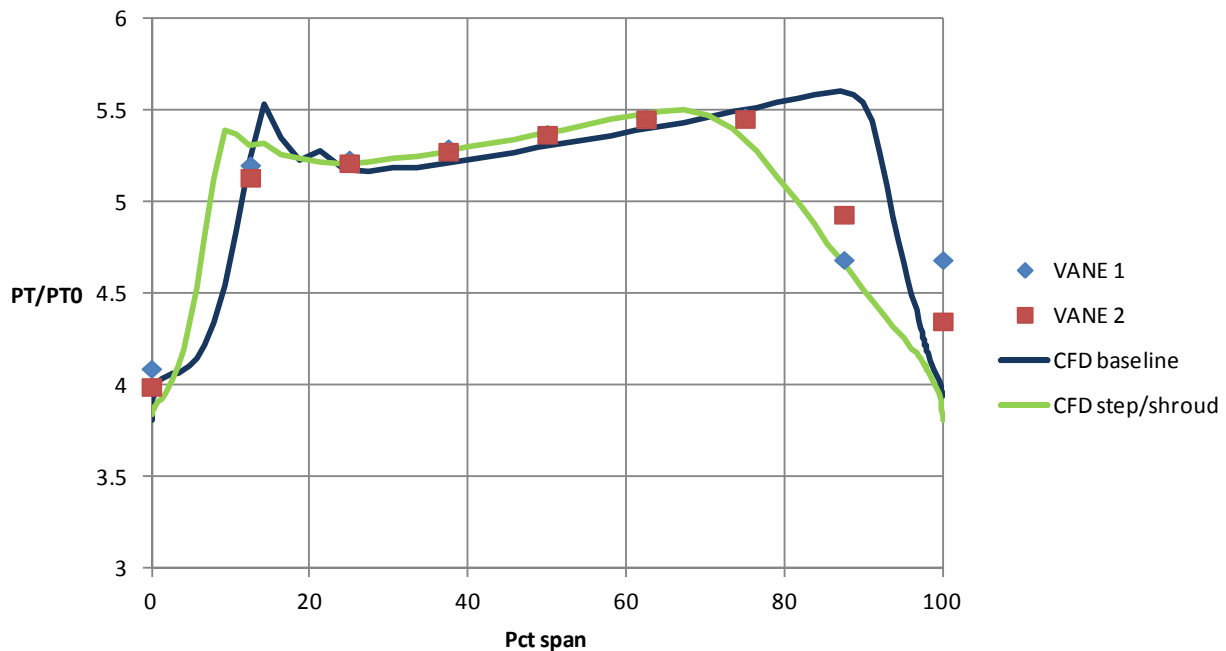


Figure 142.—Comparison of the measured and computed total pressure profile at the diffuser leading edge for inlet corrected flow of 10.55 lbm/s at 100 percent N_c , showing the effect of the 5 mil forward-facing step at the shroud.

9.3.2 Impact of Restaggering the Splitter Vane

Splitter vane was rotated around trailing edge for towards the suction side of the main vane, for 1 and 3° in an attempt to recreate the peculiar pressure distribution on the suction side of the main vane, shown in Figure 127 and Figure 128. This is illustrated for 3° in Figure 143. This modification of the geometry also showed significant performance loss, approximately 1 point in adiabatic efficiency, when run with 3° rotation, at 11 lbm/s, as illustrated in Figure 144.

Furthermore, the plot of static pressure around the main vane (for the run with splitter rotated for 3°) shows an appearance of a feature similar to what has been observed in the experiments—this is shown in Figure 145.

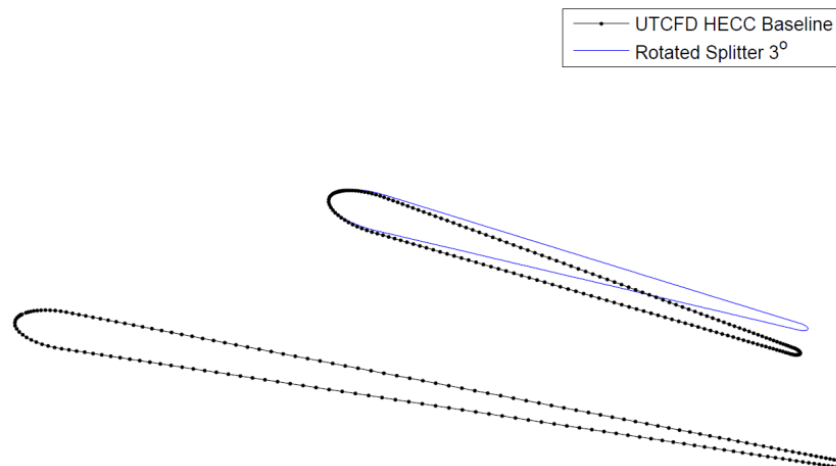


Figure 143.—Splitter vane rotated towards the suction side of the main vane for 3°.

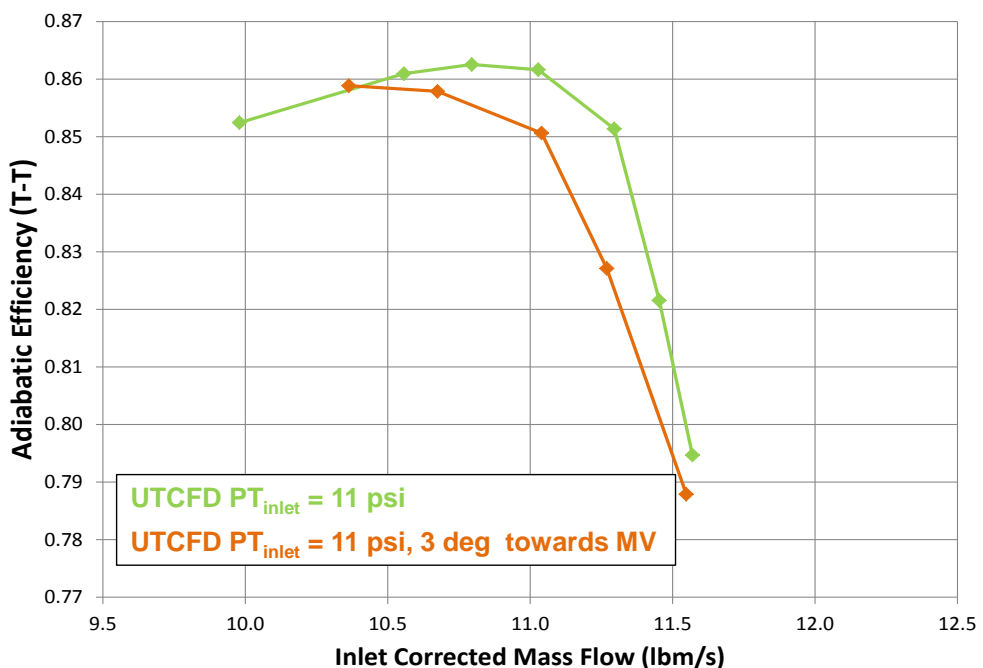


Figure 144.—Steady state CFD computations for final HECC configuration at 100 percent N_c using UTCFD with suppressed inlet—an assessment of the impact of restaggering the splitter vane 3° towards the main vane.

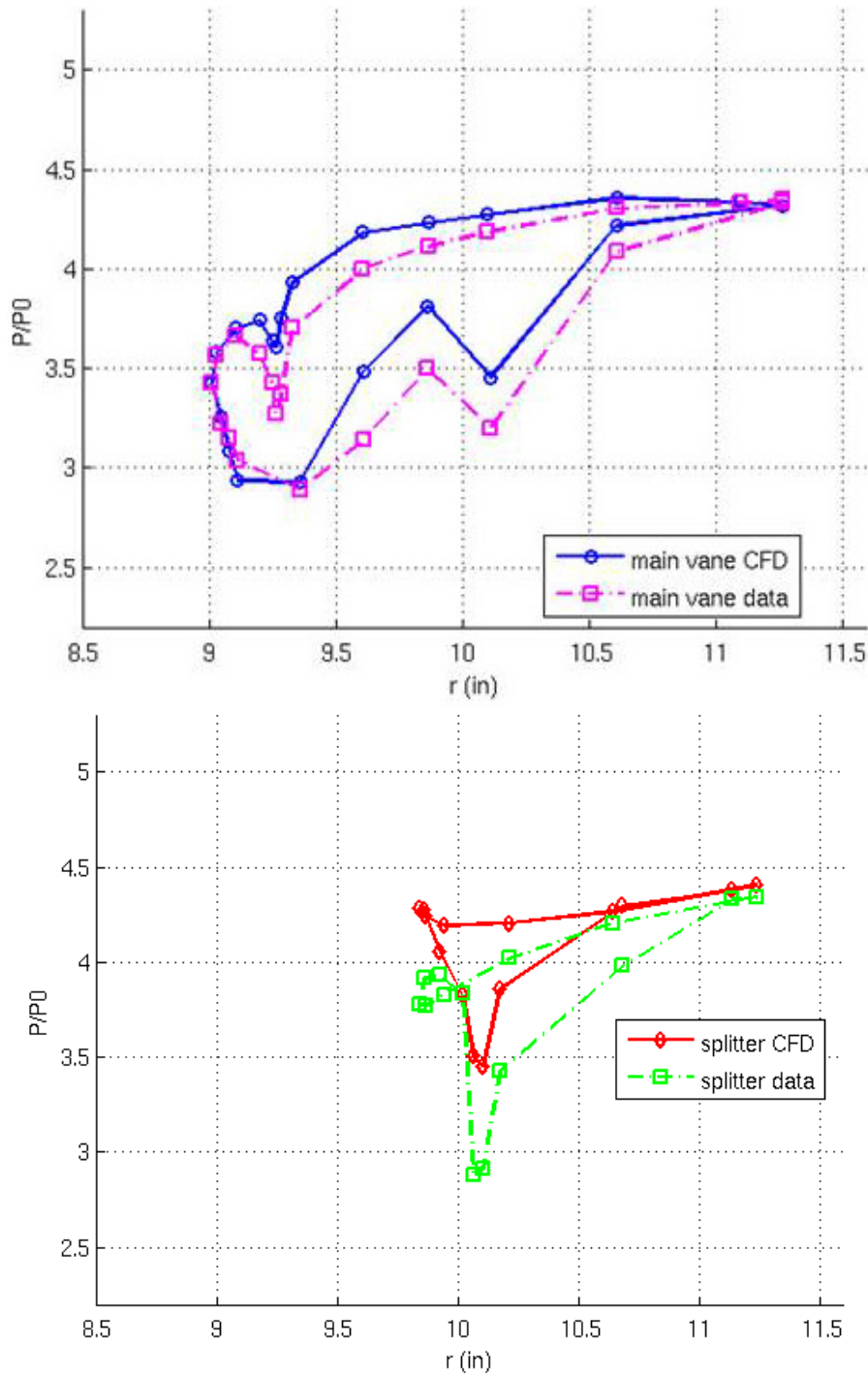


Figure 145.—Plot of static pressure around the main (top) and splitter vane (bottom) on the shroud for 100 percent N_c at inlet corrected flow rate of 11 lbm/s—an assessment of the impact of restaggering the splitter vane 3° towards the main vane (closed).

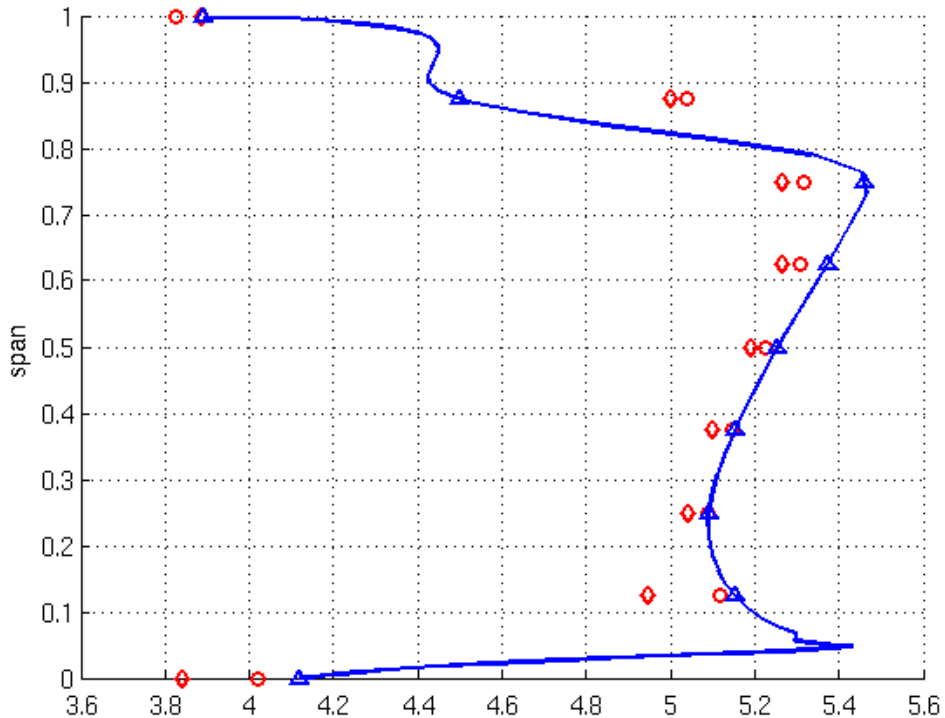


Figure 146.—Total pressure profile at diffuser modular vane leading edge for 100 percent N_c at inlet corrected flow rate of 11 lbm/s—an assessment of the impact of restaggering the splitter vane 3° towards the main vane (shown in blue) in comparison to measured data (red symbols).

Next, the plot of total pressure profile at the diffuser modular vane leading edge is shown in Figure 146. It is very interesting that there seems to be a feedback mechanism when rotating the splitter vane which extends all the way to the leading edge of the main vane. Furthermore, in Figure 147, the total pressure ratio for the impeller matches the data computed using the total pressure from the modular vane very well. Temperature ratio is still off (Figure 148), and so is the adiabatic efficiency presented in Figure 149. However, the delta between CFD and the data has been reduced when compared to pre-test CFD. Finally, pressure recovery coefficient for the combined diffuser and EGV is predicted very well across the speedline—as shown in Figure 150.

These results indicate that when the experimentally observed static pressure distribution around diffuser vanes is mimicked in the computations, there are potentially large interactions with the impeller and a significant impact on impeller performance. To properly account for those interactions—unsteady simulations are needed. They would further reduce the impeller and overall stage efficiency (as will be further discussed in Section 9.5 on the unsteady effects) and improve the agreement with data.

Given that the hardware inspection performed at NASA in late 2012 didn't show large geometrical variations for the diffuser vanes—certainly not variations of a similar magnitude to what was studied here—the unsteady simulations were not pursued further.

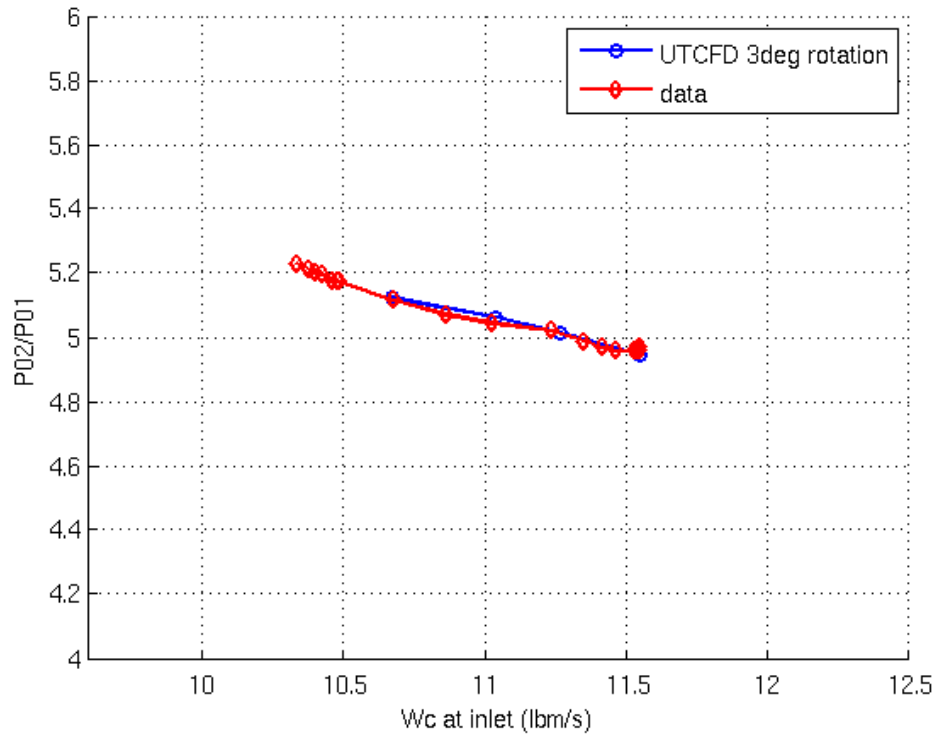


Figure 147.—Total pressure ratio for impeller for 100 percent N_c —an assessment of the impact of restaggering the splitter vane 3° towards the main vane.

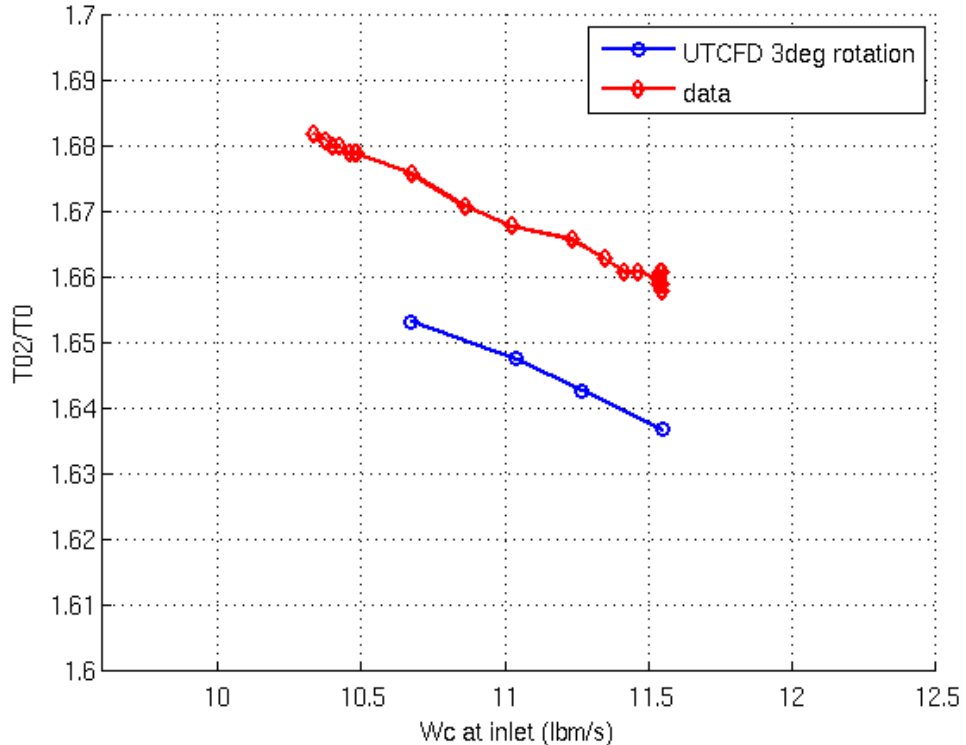


Figure 148.—Total temperature ratio for impeller at 100 percent N_c —an assessment of the impact of restaggering the splitter vane 3° towards the main vane.

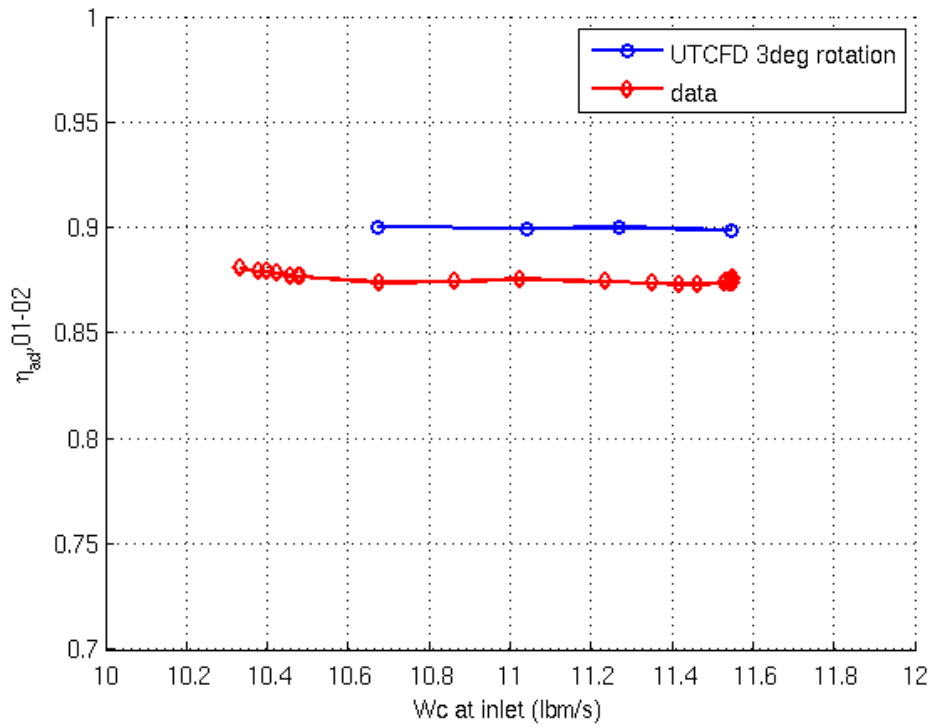


Figure 149.—Adiabatic efficiency for impeller for 100 percent N_c —an assessment of the impact of restaggering the splitter vane 3° towards the main vane.

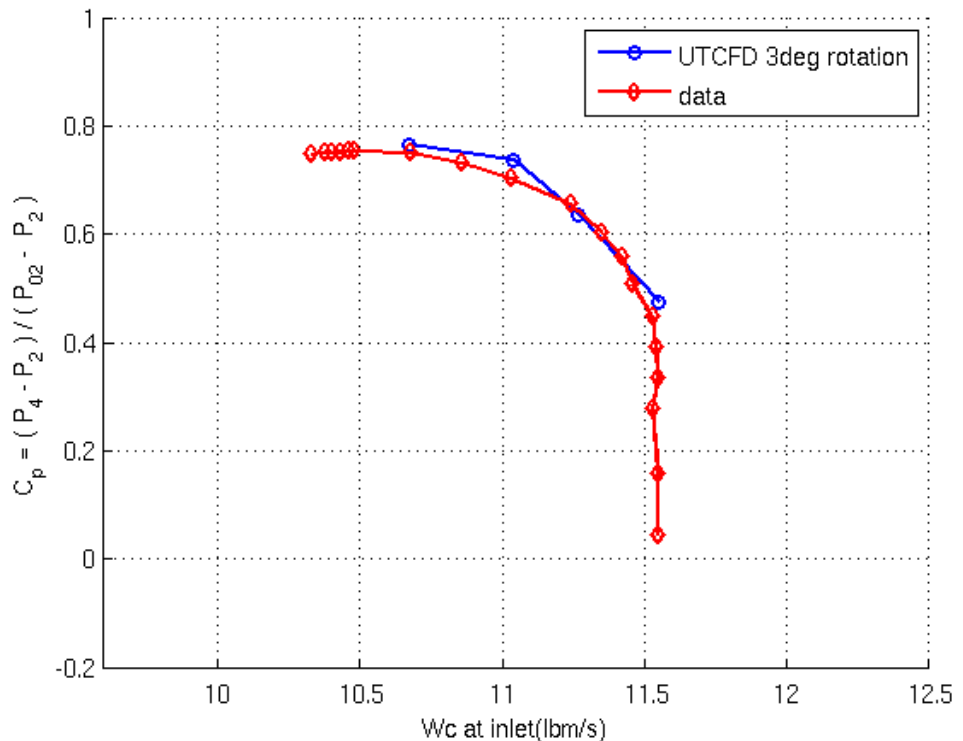


Figure 150.—Pressure recovery for combined diffuser and EGV for 100 percent N_c —an assessment of the impact of restaggering the splitter vane 3° towards the main vane.

9.4 Turbulence Modeling

Another element that was considered in great detail in the post-test CFD analyses was the impact of the choice of turbulence model. The baseline model used in the pre-test CFD with LEO was $k-\omega$ model with vorticity based production. Note that this particular model has well-known issues: the definition of Reynolds stress used in mean flow equations and the turbulent model equations is different, and as such the model does not ensure the conservation of mechanical energy. While the motivation behind this model is a legitimate concern with reducing the anomalous production of turbulent kinetic energy in the leading edge region, in retrospect, the $k-\omega$ model with vorticity based production should have been avoided because the aforementioned concerns.

As a part of the analyses conducted here, three additional models were considered: $k-\omega$ with strain-rate based production, $k-\omega$ with strain-rate based production and SST eddy-viscosity limiter, and Spalart-Allmaras model (which was run with lowest inlet turbulence, effectively making the flow at impeller leading edge most transitional). Adiabatic efficiency (total-to-total) predicted with these models is summarized in Figure 151. While none of these models properly accounts for the high curvature of the flowpath and strong rotational effects in the impeller and it is hard to argue which one should be used, the spread in the results at design condition—about 2 pt in peak efficiency—indicates a very strong sensitivity of CFD in this configuration on how turbulence and the boundary layer development is modeled. Note also the differences in the range predicted by different models—the predictions of the last stable point at lowest flow are quite different. Again, no rigorous effort has been applied to the determination of stable operating range for different models using these steady CFD simulations—the curves merely reflect the behavior of different models with same, or similar, exit boundary conditions. The exception are the runs with Spalart-Allmaras which were only stable for flow rates higher than 11 lbm/s.

The differences between turbulence models are further illustrated by comparing the total pressure profile as measured at diffuser leading edge presented in Figure 152, as well as by comparing surface stress lines for the diffuser main vane, presented in Figure 153. There is a strong variation between different models with respect to both the amount of shroud and hub blockage coming out of the impeller, as well as with respect to flow separation on both suction and pressure side of the main vane. For these steady simulations, the strain-rate based $k-\omega$ model with the SST limiter, as well as Spalart-Allmaras model, show pressure side separation near the hub on the main vane, near leading edge. In addition, Spalart-Allmaras predicts reversed flow near the trailing edge (near the hub, on the pressure side).

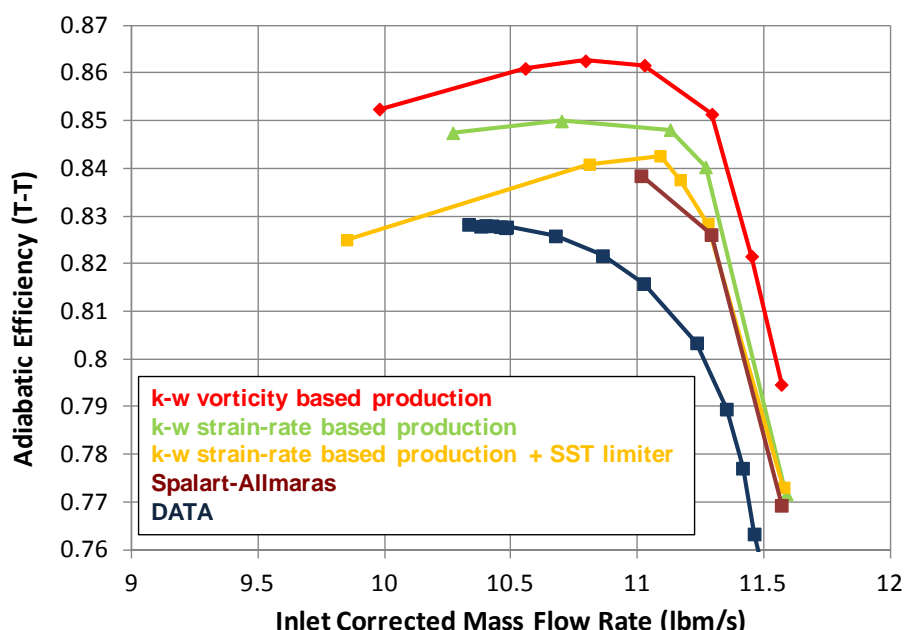


Figure 151.—Steady state CFD computations for final HECC configuration at 100 percent N_c using UTCFD with suppressed inlet—an assessment of the impact of using different turbulence models.

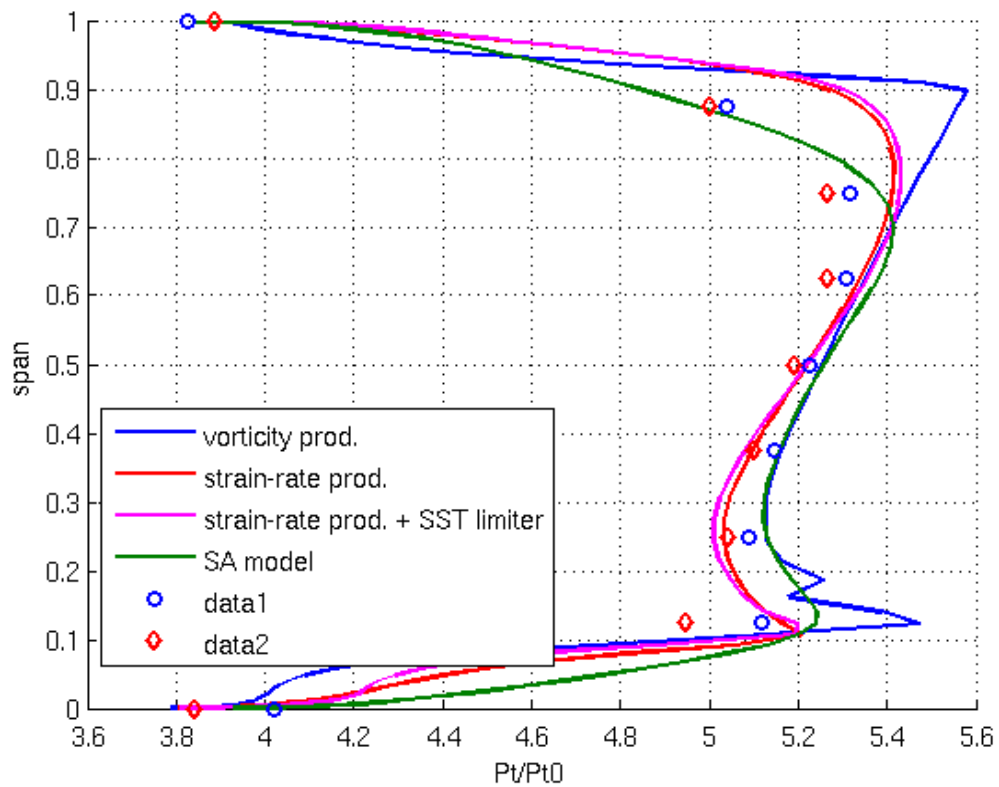


Figure 152.—Total pressure profile at diffuser leading edge for 100 percent N_c at inlet corrected flow rate of 11lbm/s—an assessment of the impact of using different turbulence models.

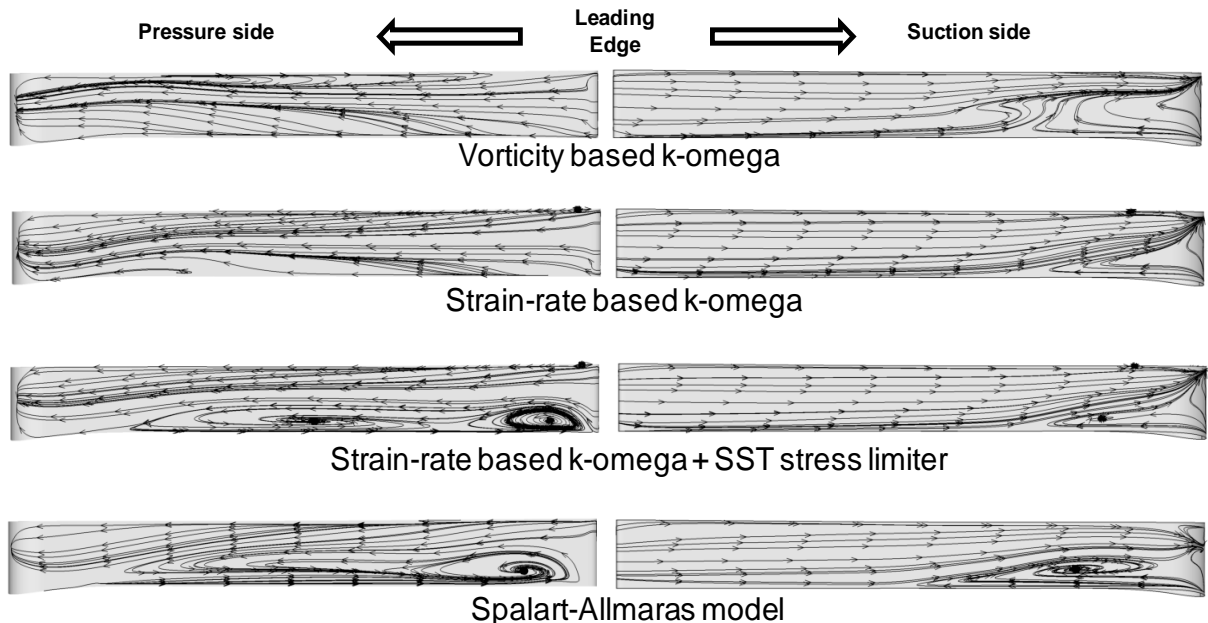


Figure 153.—Surface stress lines on the diffuser main vane, as computed for 100 percent N_c at inlet corrected flow rate of approximately 11 lbm/s—an assessment of the impact of using different turbulence models.

9.5 Unsteady Effects

During the design process, the unsteady simulations were only performed for the design iteration that did not include the EGVs, and with the diffuser vanes prior to the additional thickening of the diffuser vane leading edges requested at the preliminary design review (for structural reasons). A difference to steady results was relatively small at design point—approximately 0.5 pt lower adiabatic efficiency ($T-T$). In addition, the simulations were conducted for only 2 to 4 full revolutions of the impeller.

Post-test unsteady simulations were performed on finer grids and were integrated for a significantly longer time—more than 8 revolutions—and it was observed that 6 revolutions are required for the flow to be converged (in particular, in terms of total temperature at exit). This, coupled with the addition of EGVs and thicker diffuser vane leading-edges into the simulations, resulted in a larger difference between steady and unsteady simulations for the same baseline turbulence model than realized during the design process—approximately 1.2 pt lower adiabatic efficiency at design point (as shown in Figure 154). With strain-based $k-\omega$ model, the delta between steady and unsteady runs is even larger—about 2 pt in the adiabatic efficiency (Figure 155). In addition, the choke flow reduced and approached the data. Interesting to note is that unsteady simulations using strain-rate based model with the SST limiter show very similar results to the ones obtained without the limiter (not shown in Figure 155). Thus, since this approach agreed best with the experimental data, it was chosen to compute the full performance map (discussed in Section 9.7).

Figure 154 and Figure 155 also show differences in the last computed point at lowest flow rate. Note that no rigorous effort has been put into determining those points—these differences merely reflect differences in flow rate computed for same exit static pressures, and as such they are somewhat indicative of changes in range. As already mentioned, and discussed at length in Section 11.0, this information on stability boundaries obtained from steady CFD (or even unsteady CFD with periodic sectors) should be used with caution.

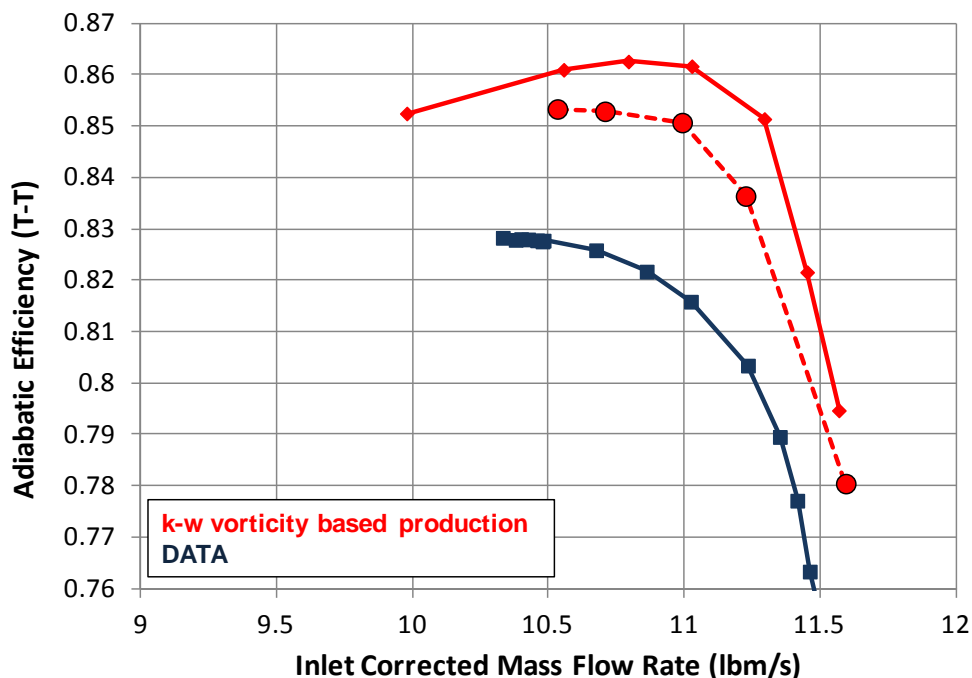


Figure 154.—Unsteady CFD computations (dashed) for final HECC configuration at 100 percent N_c using UTCFD with suppressed inlet—comparison to steady state solution (solid) for vorticity based $k-\omega$ model.

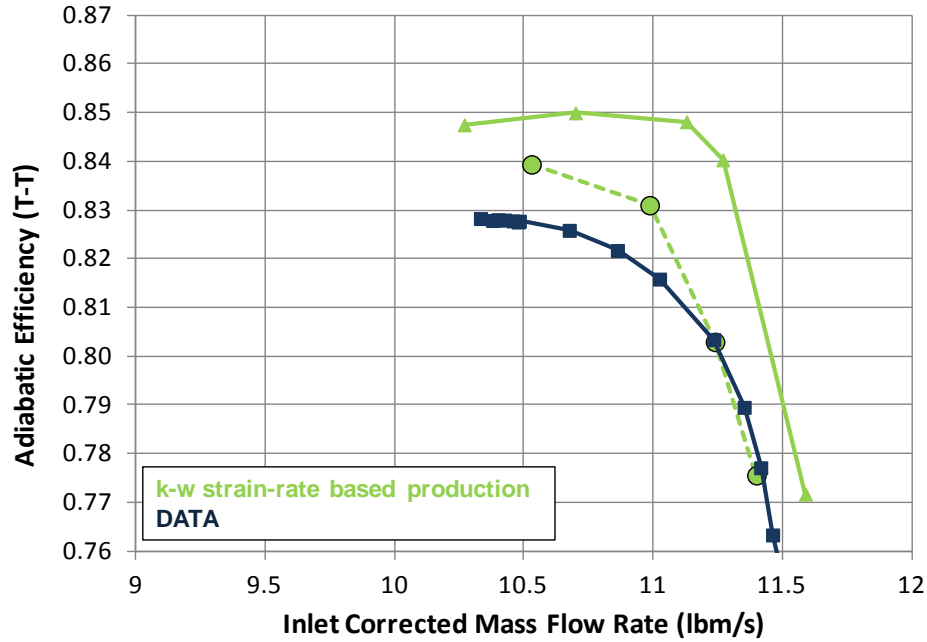


Figure 155.—Unsteady CFD computations (dashed) for final HECC configuration at 100 percent N_c using UTCFD with suppressed inlet—comparison to steady state solution (solid) for strain-rate based $k-\omega$ model.

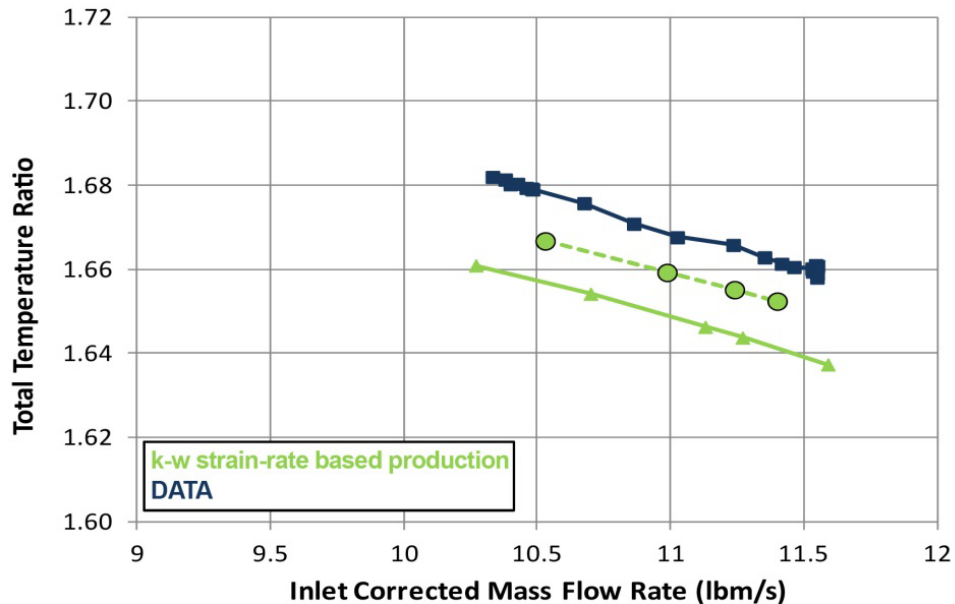


Figure 156.—Unsteady CFD computations (dashed) for final HECC configuration at 100 percent N_c using UTCFD with suppressed inlet—total temperature ratio comparison to steady state solution (solid) for strain-rate based $k-\omega$ model.

Examining the impact of unsteady runs on individual components, one observes that the main difference between steady and unsteady runs comes from the change in temperature ratio (Figure 156), while pressure ratio is relatively similar in steady and unsteady simulations (Figure 157). In other words, the performance of the impeller is more impacted by the unsteadiness than the performance of the diffuser and EGV. This is illustrated by plotting the adiabatic efficiency for the impeller (computed from inlet to the sliding interface), shown in Figure 158, and by plotting the total pressure losses in the diffuser

and EGV, shown in Figure 159 and Figure 160, respectively. Note also a shift in choke flow with unsteady simulations, as well as the change in the shape of total pressure loss curves for diffuser and EGV—clearly indicating the lack of loss bucket (as observed in experiment), which was not that apparent in steady simulations.

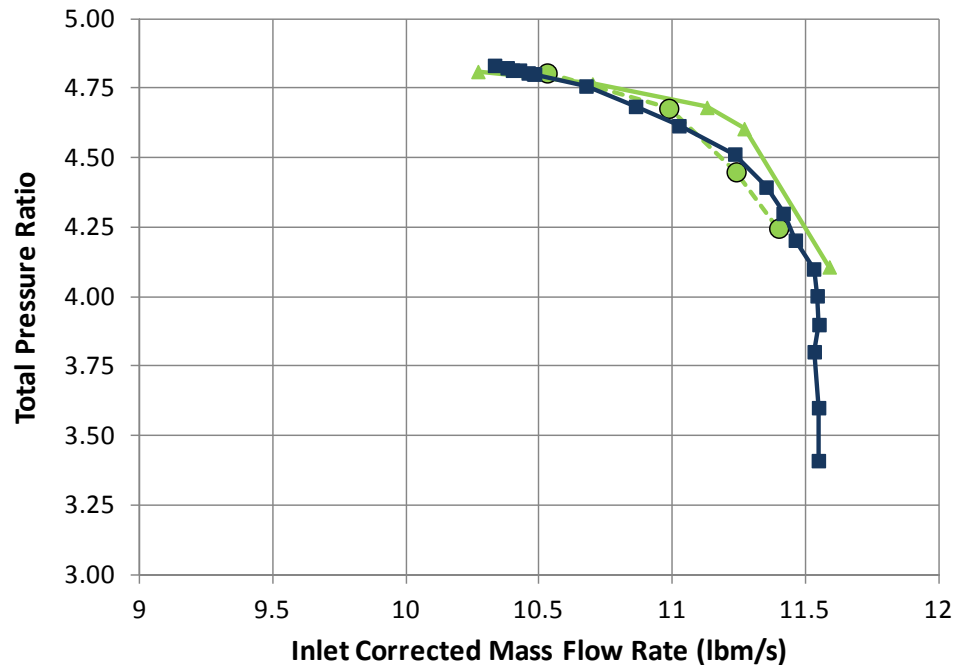


Figure 157.—Unsteady CFD computations (dashed) for final HECC configuration at 100 percent N_c using UTCFD with suppressed inlet—total pressure ratio comparison to steady state solution (solid) for strain-rate based $k-\omega$ model.

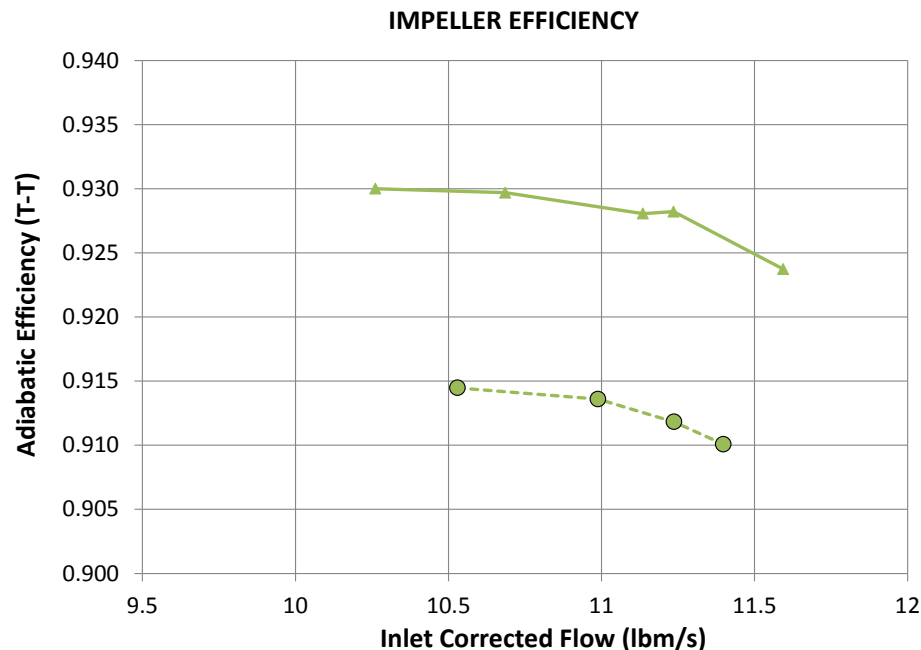


Figure 158.—Unsteady CFD computations (dashed) for final HECC configuration at 100 percent N_c using UTCFD with suppressed inlet—comparison of predicted impeller efficiency to steady state solution (solid) for strain-rate based $k-\omega$ model.

DIFFUSER LOSSES

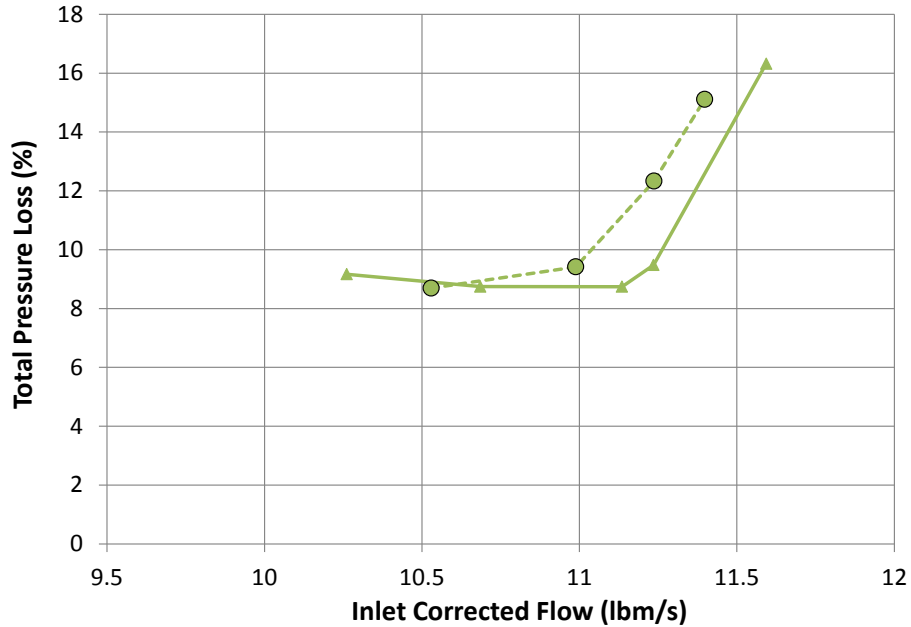


Figure 159.—Unsteady CFD computations (dashed) for final HECC configuration at 100 percent N_c using UTCFD with suppressed inlet—comparison of predicted diffuser losses to steady state solution (solid) for strain-rate based $k-\omega$ model.

EGV LOSSES

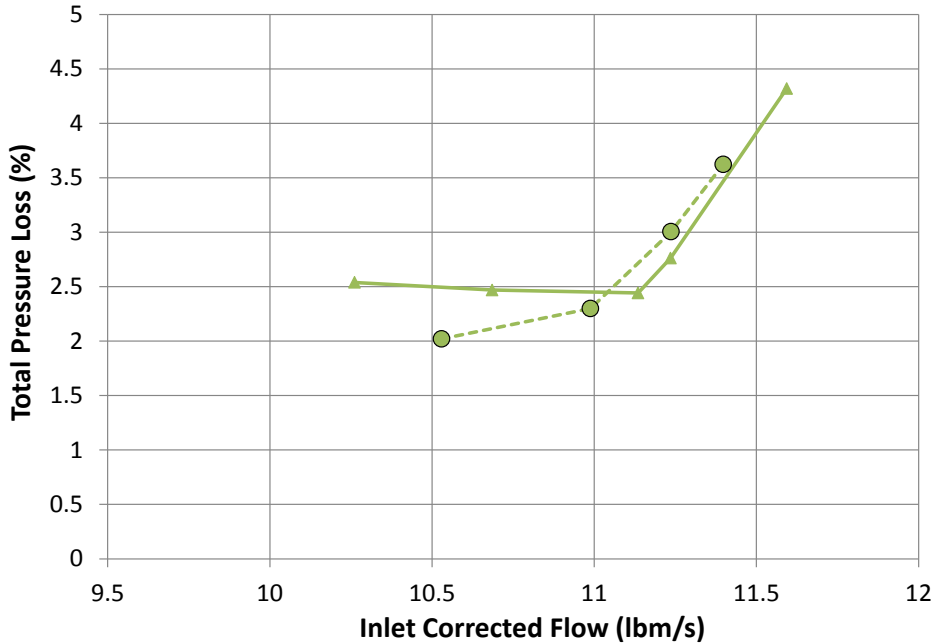


Figure 160.—Unsteady CFD computations (dashed) for final HECC configuration at 100 percent N_c using UTCFD with suppressed inlet—comparison of predicted EGV losses to steady state solution (solid) for strain-rate based $k-\omega$ model.

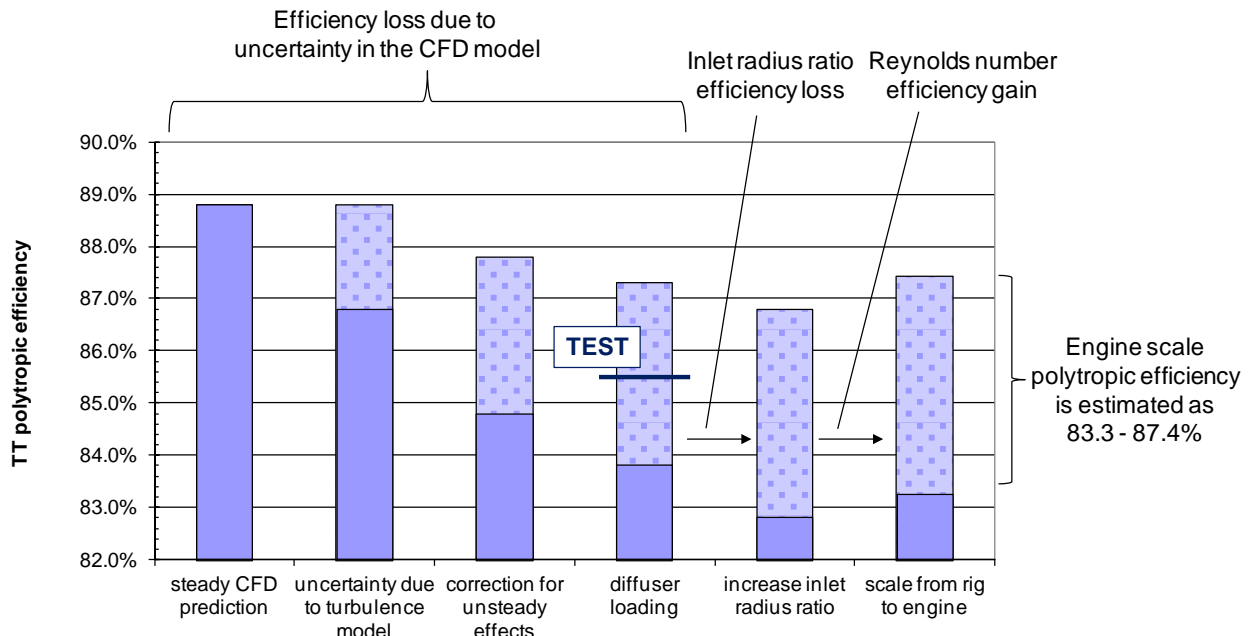


Figure 161.—Book-keeping efficiency deltas from rig to engine scale—revised audit, based on post-test CFD.

9.6 Revised Performance Audit

As the post-test CFD analyses have shown, taking into account the uncertainty in the CFD model both due to turbulence modeling and due to unsteady effects not modeled in the steady simulations used in the design process leads to a more conservative assessment of the expected performance for the compressor.

A revised performance audit consistent with the findings of the post-test CFD analyses is presented in Figure 161. Light purple region indicates the uncertainty range for polytropic efficiency. For example, results with different turbulence models showed that efficiency can be up to 2 pt lower than what was predicted with the model used in pre-test CFD analyses. Similarly, unsteady simulations for different turbulence models showed that the difference to steady runs can be from 1 to 2 pt. Finally, the column labeled “diffuser loading” is meant to reflect the efficiency decrement that is associated with correctly predicting the diffuser loading—which was observed, for example, when rotating the splitter vane by 3°. This delta is from 0.5 to 1 pt.

In summary, the revised result for engine scale polytropic total-to-total efficiency is of 83.3 to 87.4 percent. The polytropic efficiency measured in test of 85.5 percent is also shown—note that the rig operates with a suppressed inlet.

9.7 Comparison of Post-Test CFD to Steady State Data

As a part of the post-test CFD analyses, UTCFD with the baseline vorticity-based $k-\omega$ model was used for steady simulations with standard day inlet conditions as a surrogate for LEO to generate a “pre-test” performance map for 85, 90, 95, 100 and 105 percent speeds. All computations were conducted with a constant impeller tip clearance of 0.012 in. Note that the finer computational grids constructed as a part of post-test analyses were used here—see the discussion in Section 9.1. The performance map that includes total-pressure ratio and total-to-total adiabatic efficiency is shown in Figure 162. Similarly, another performance map was generated using the same approach, but with suppressed inlet, and is shown in Figure 163. With suppressed inlet and the lower Reynolds number, a reduction in pressure ratio

and efficiency is observed for all speeds—similar to what has been already discussed for 100 percent speed in Section 9.2. Predicted choke flow has also been reduced for all speeds, for about 1 percent.

Finally, the performance map was generated using what was deemed the best CFD simulations in post-test analyses: unsteady simulations, with strain-rate based production in $k-\omega$ model, and with suppressed inlet. This result is shown in Figure 164. Pressure ratio is well predicted with unsteady simulations, and the over prediction of adiabatic efficiency is reduced, when compared to steady simulations—as summarized in Table 7. Note that the agreement of predicted adiabatic efficiency with data is better for higher speeds.

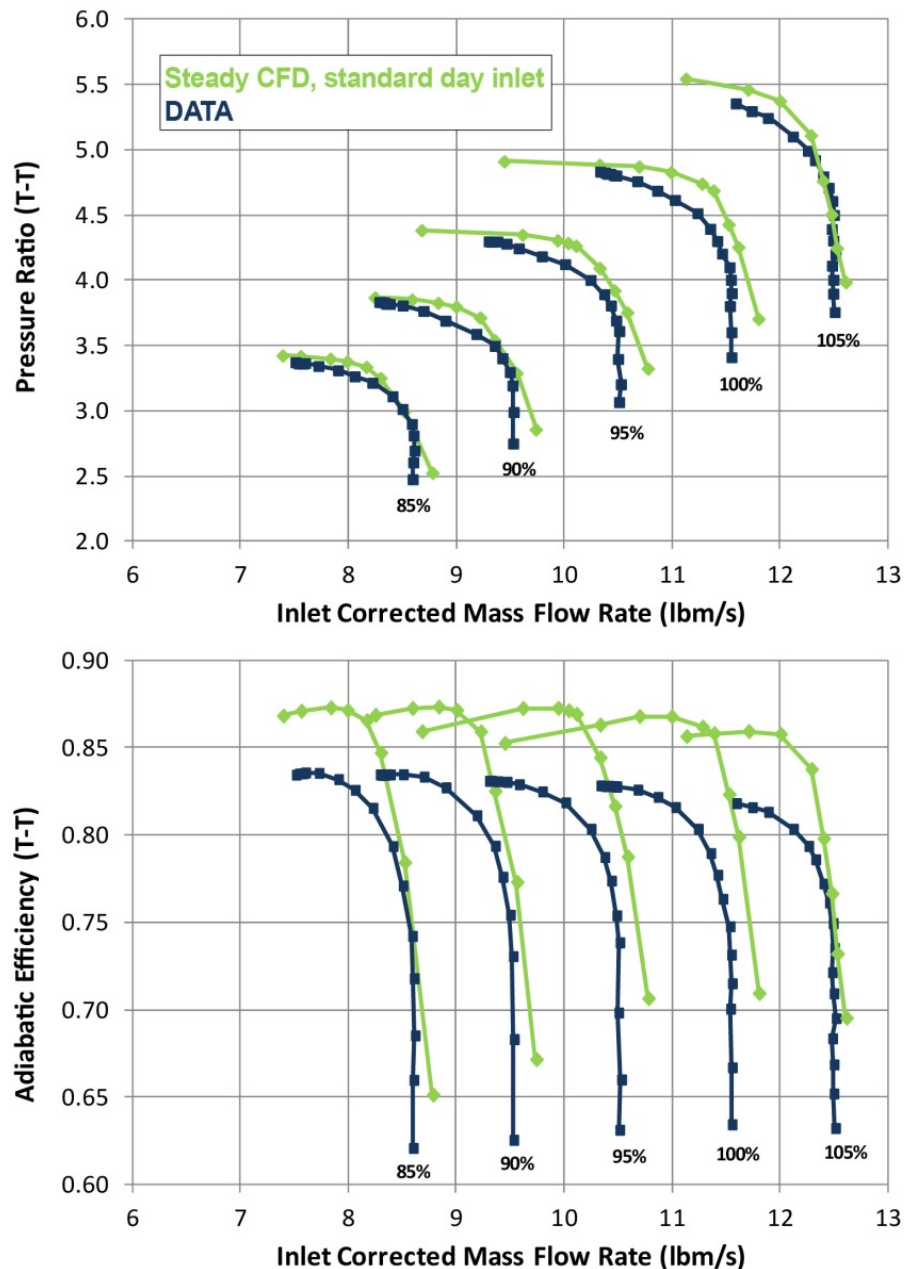


Figure 162.—Full compressor map for speeds 85 to 105 percent obtained during steady post-test CFD analyses using standard-day inlet conditions, (fixed 12 mil clearance), and the same vorticity-based $k-\omega$ model that was used in pre-test CFD analyses as compared to data at suppressed inlet.

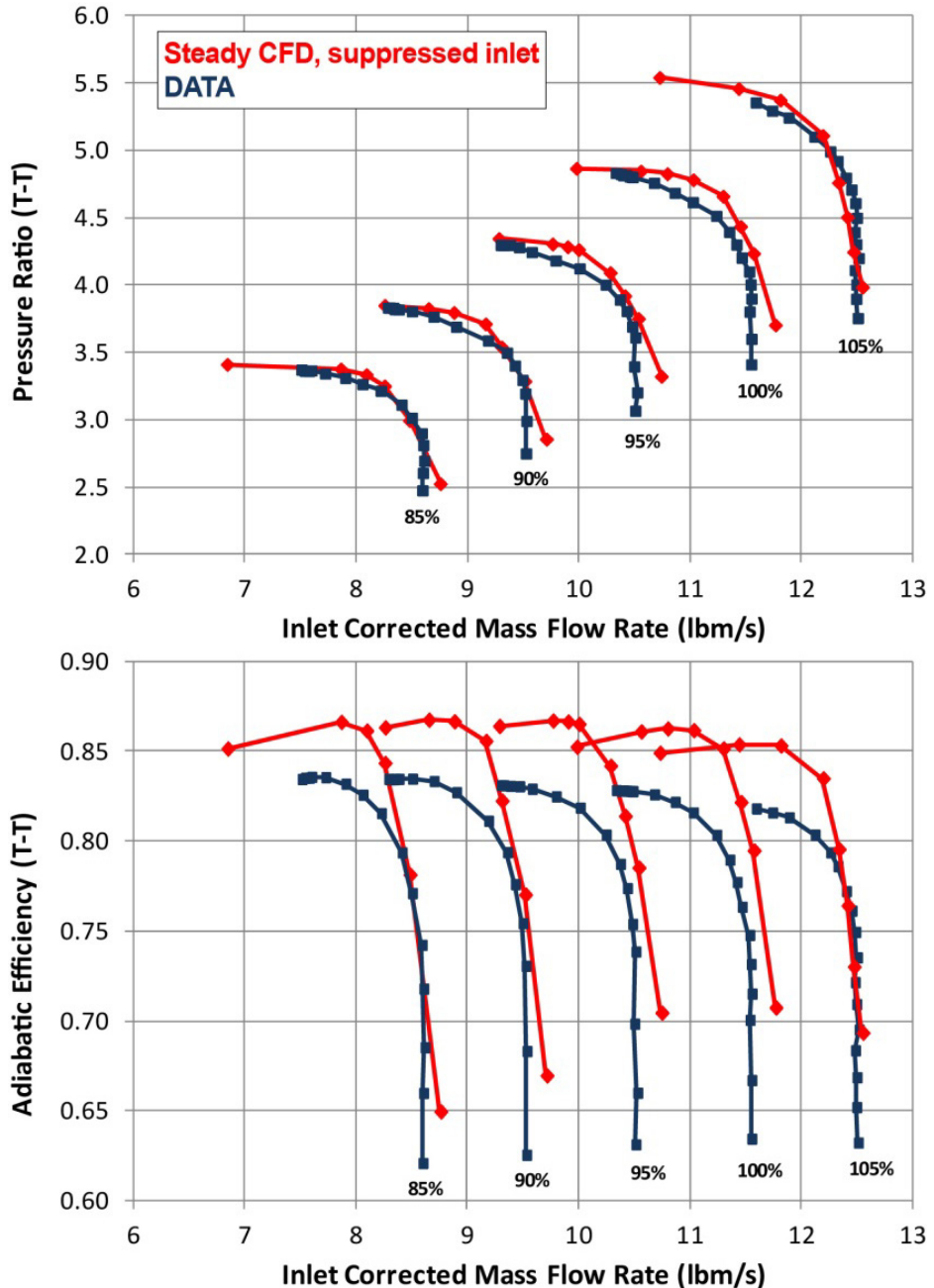


Figure 163.—Full compressor map for speeds 85 to 105 percent obtained during steady post-test CFD analyses using the suppressed inlet conditions, (fixed 12 mil clearance), and the same vorticity-based $k-\omega$ model that was used in pre-test CFD analyses as compared to data at suppressed inlet.

Note that the stall margin is excluded from Table 7. As a part of the post-test CFD computations of these performance maps, no rigorous effort has been put into determining the last stable point at lowest flow. The differences presented in Figure 162 to Figure 164 reflect differences in flow rate computed for same exit static pressures, and as such they are somewhat indicative of changes in range. As already mentioned, and discussed at length in Section 11.0, using steady CFD computations (as well as unsteady CFD computations, with periodic sectors) for the assessment of range is at the least questionable, and could easily lead to misleading conclusions, so this information should be used with caution.

TABLE 7.—COMPARISON OF PERFORMANCE COMPUTED IN POST-TEST CFD ANALYSES USING DIFFERENT APPROACHES PRESENTED IN FIGURE 162 TO FIGURE 164 TO MEASURED DATA ($N_c = 100$ PERCENT, AND 12 mils CONSTANT CLEARANCE)

	Post-test CFD steady UTCFD vorticity-based ambient inlet	Post-test CFD steady UTCFD vorticity-based suppressed inlet	Post-test CFD steady UTCFD strain-rate based suppressed inlet	Data
PR _{TT}	4.83	4.78	4.68	4.68
$\eta_{poly,TT}$, %	89.3	88.8	86.3	85.5
$m_{c,in}$, lbm/s	10.99	11.03	10.99	10.85
M_{exit}	0.155	0.156	0.165	0.18
α_{exit}	9.6°	9.7°	12.3°	34.3°

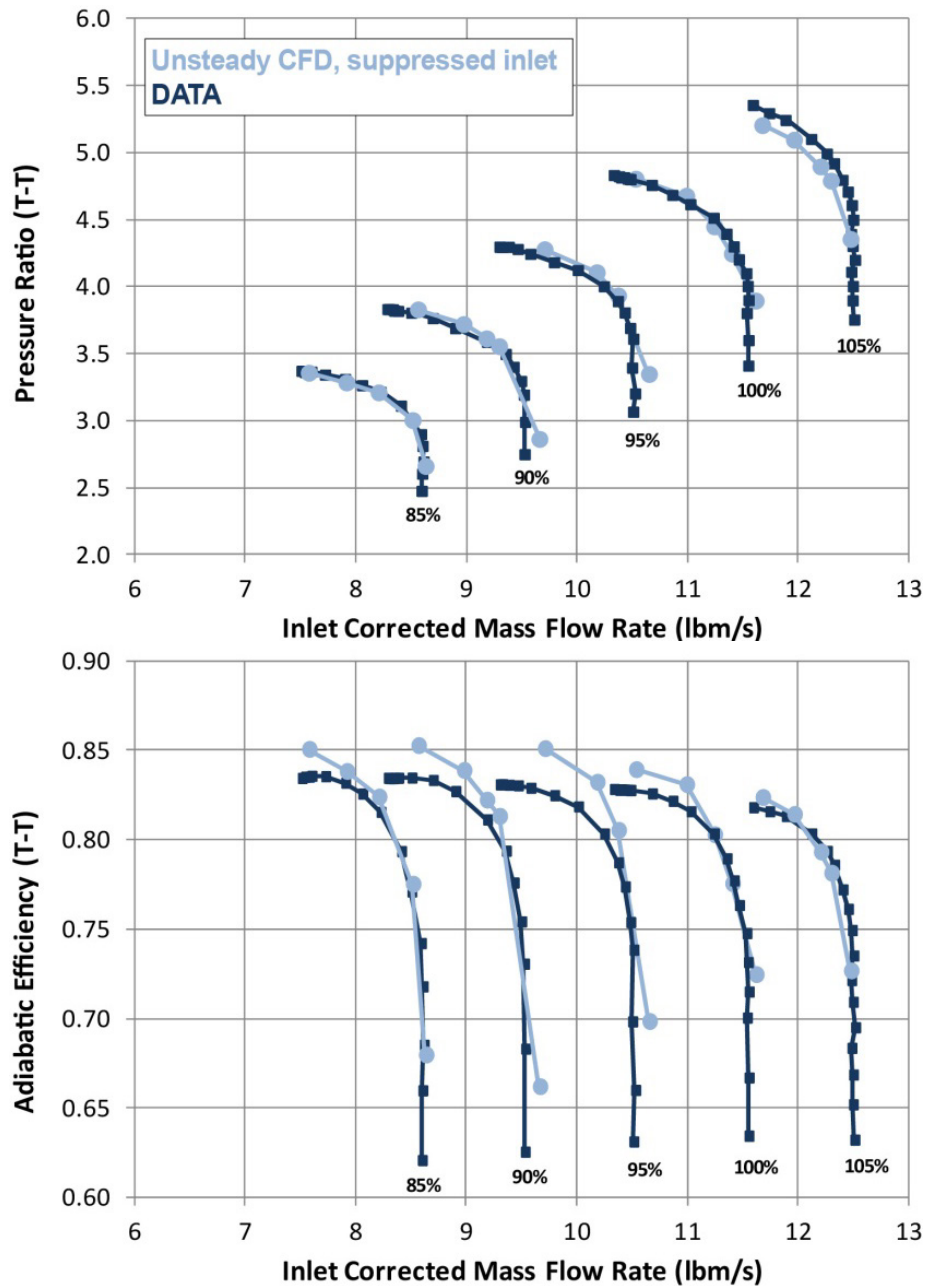


Figure 164.—Full compressor map for speeds 85 to 105 percent obtained during unsteady post-test CFD analyses using suppressed inlet conditions, (fixed 12 mil clearance), and the strain-rate based $k-\omega$ model as compared to data at suppressed inlet.

10.0 Comparison of Post-Test CFD to High-Response Data

As shown in Section 9.7, unsteady CFD simulations are in better agreement with data when it comes to the overall compressor performance. High-response data was also acquired at 100 percent N_c as a part of the test, allowing for a more detailed look into how well does CFD predict the impact of unsteady pressure fields created by impeller and its interactions with the diffuser vanes, and vice versa. This section compares some of these unsteady pressure measurements to the CFD solution. A comparison is made to unsteady CFD simulations using $k-\omega$ model with strain-rate based production at 100 percent speed for the flow rate of approximately 11 lbm/s (design flow rate) and 10.4 lbm/s (near-stall flow rate).

For the installation of the unsteady pressure transducers in the impeller shroud, at the impeller tips (K7, K8 and K9), an orifice/cavity exists between the flowfield and the sensing face of the transducer. This installation and the development of a data correction are fully described in Appendix A. The following experimental comparisons to the CFD show only the corrected data for these locations (see Appendix A for an overlay of both uncorrected and corrected data with CFD). Also, Appendix A contains the corresponding Fourier analyses for both data and CFD.

10.1 Comparison of CFD to Data (100 percent N_c)

Design flow rate: As described in Appendix A, K18 was used to align the CFD with the experimental data (a time shift of 0.05T was found to work well, where T is the period of blade passage). Figure 165 shows the comparison at 11 lbm/s of K18 to CFD to be reasonable in waveform and amplitude. For pressures transducers that are located at different diffuser vanes passages, the experimental data was shifted an additional amount to achieve the correct rotor blade phasing.

The comparisons for the series of pressures in diffuser passage A are shown in Figure 167, Figure 169, Figure 171 and Figure 173 for the design flow rate. For first two locations in this passage (K12, K13, Figure 167 and Figure 169, respectively), again the waveform and amplitude comparison with CFD is reasonable, however there is a phase offset of about 0.06T between the CFD and the data. For the next location in the passage (K19, Figure 171), the phase offset appears to have increased. At the most downstream location (K20, Figure 173) the CFD frequency content is very low, nearly a sine wave. The grid resolution in this region is likely too low to capture the acoustic wave propagation.

Near-Stall Flow Rate: Figure 166, Figure 168, Figure 170, Figure 172, Figure 174, Figure 176, Figure 178 and Figure 180 give the corresponding comparison of the CFD to the unsteady pressure transducers for the near-stall flow rate. All the statements made above regarding the design-flow rate comparison can be restated for the near-stall flow rate. Overall the magnitude of the fluctuations and the waveforms are reasonably predicted by the CFD with the exception of the downstream locations were the higher frequency content is under-predicted likely due to insufficient grid resolution.

The unsteady pressures in the impeller tip region are shown for design flow rate in Figure 175, Figure 177 and Figure 179. Both the CFD and the experimental data show strongly impulsive signatures consistent with the pressure-to-suction surface passage of the rotor blade. The amplitude of the predicted pressure is reasonable for K8, but somewhat low for K7 and high for K9. It should be noted that the transducer correction is only approximate since it is not validated with benchmark data. In addition, the impeller tip region may have other effects (e.g., nonlinear) not accounted for in the model. Finally, note also that the overall magnitude of the oscillations in both CFD and data is significantly higher for these three locations than for the ones further downstream in the diffuser (not surprisingly since these location are in the direct pressure field of the blade loading).

Overall, given the uncertainty of the experimental correction, the comparison of CFD with experimental data appears reasonable (and, in particular, the Fourier decomposition shown in the Appendix A), with the exception of the locations downstream of the diffuser where the grid resolution appears to be insufficient to capture acoustic wave propagation. The importance of capturing the acoustic wave field on performance prediction remains to be determined.

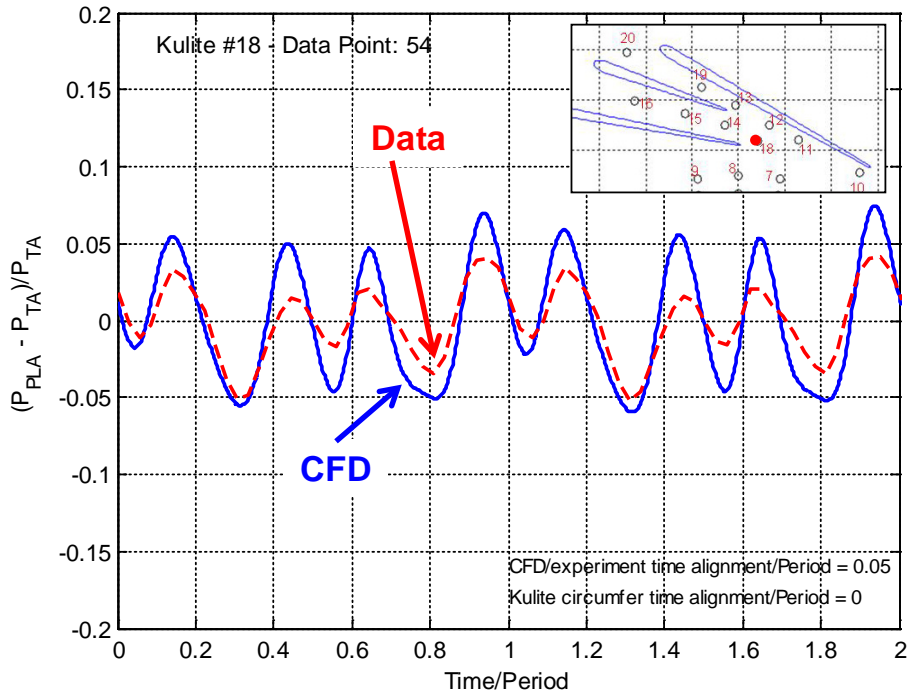


Figure 165.—K18 signal versus CFD at 11 lbm/s (design flow) and 100 percent N_c .

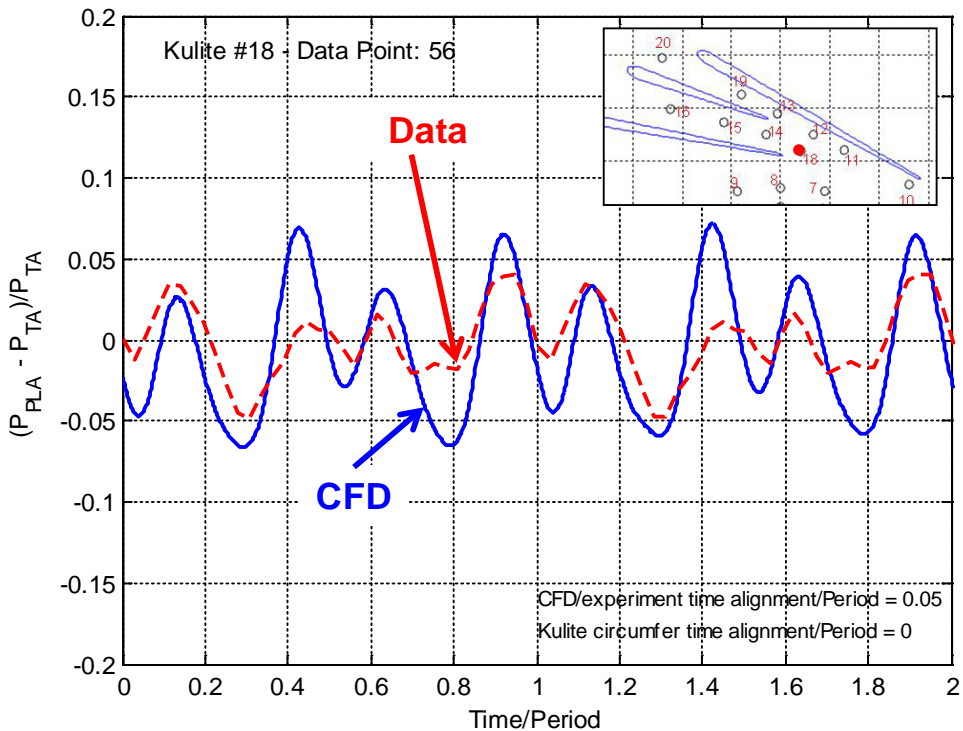


Figure 166.—K18 signal versus CFD at 10.4 lbm/s (near-stall flow) and 100 percent N_c .

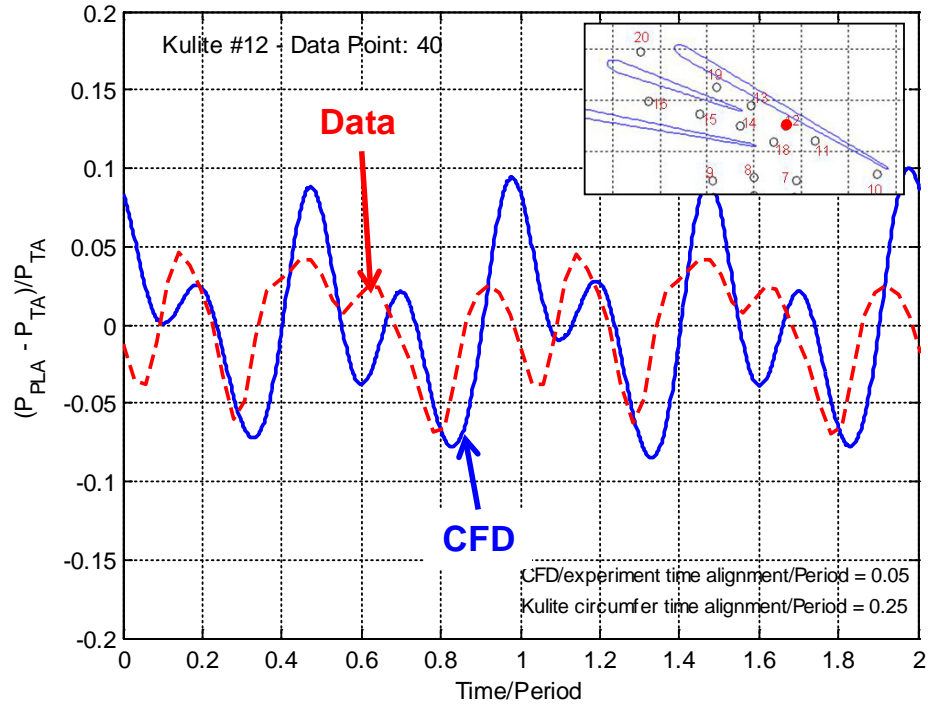


Figure 167.—K12 signal versus CFD at 11 lbm/s (design flow) and 100 percent N_c .

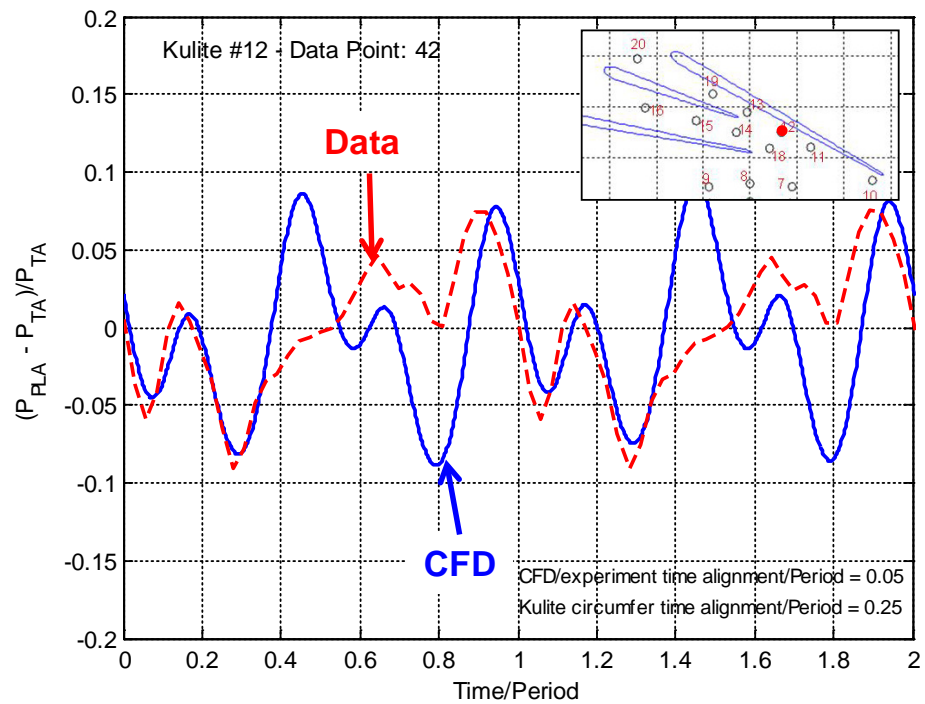


Figure 168.—K12 signal versus CFD at 10.4 lbm/s (near-stall flow) and 100 percent N_c .

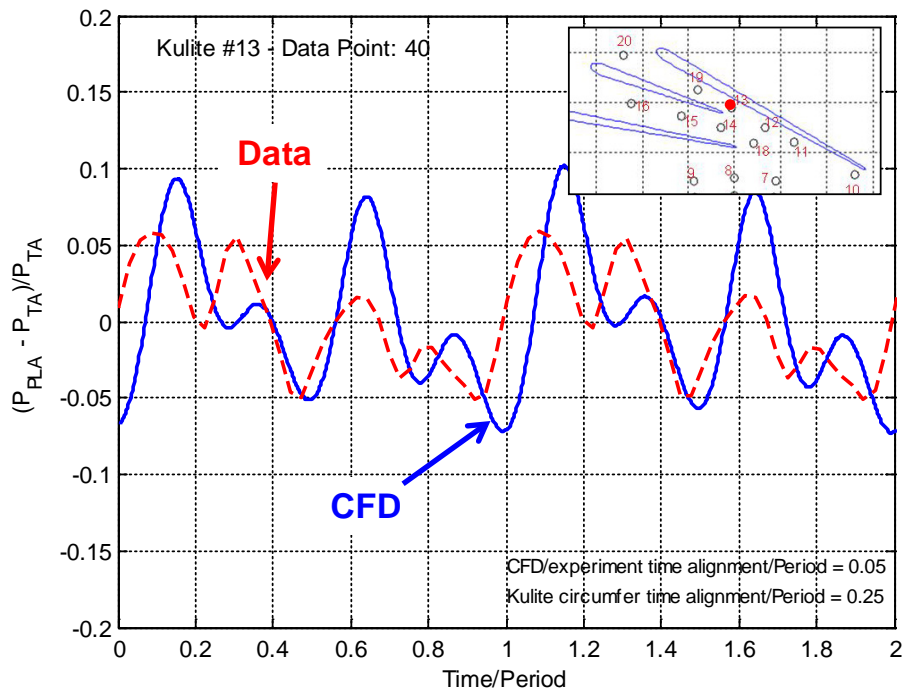


Figure 169.—K13 signal versus CFD at 11 lbm/s (design flow) and 100 percent N_c .

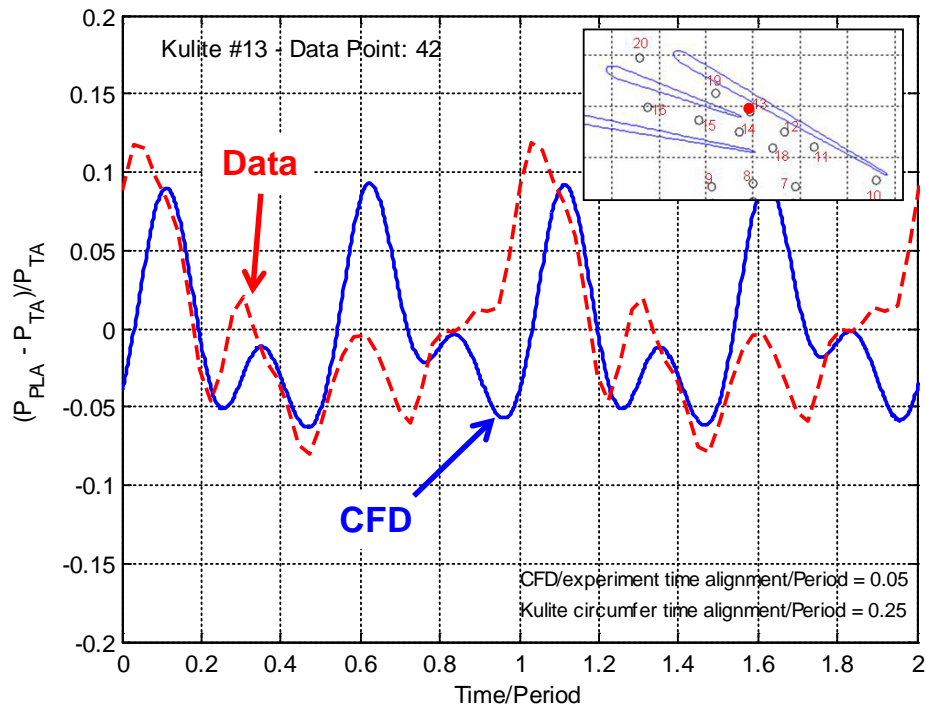


Figure 170.—K13 signal versus CFD at 10.4 lbm/s (near-stall flow) and 100 percent N_c .

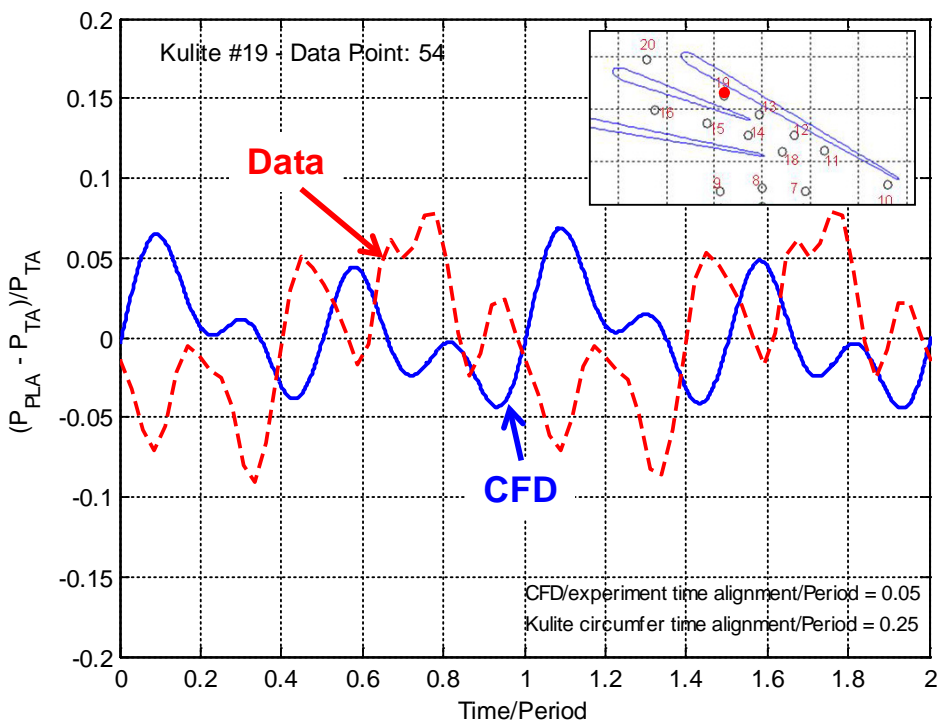


Figure 171.—K19 signal versus CFD at 11 lbm/s (design flow) and 100 percent N_c .

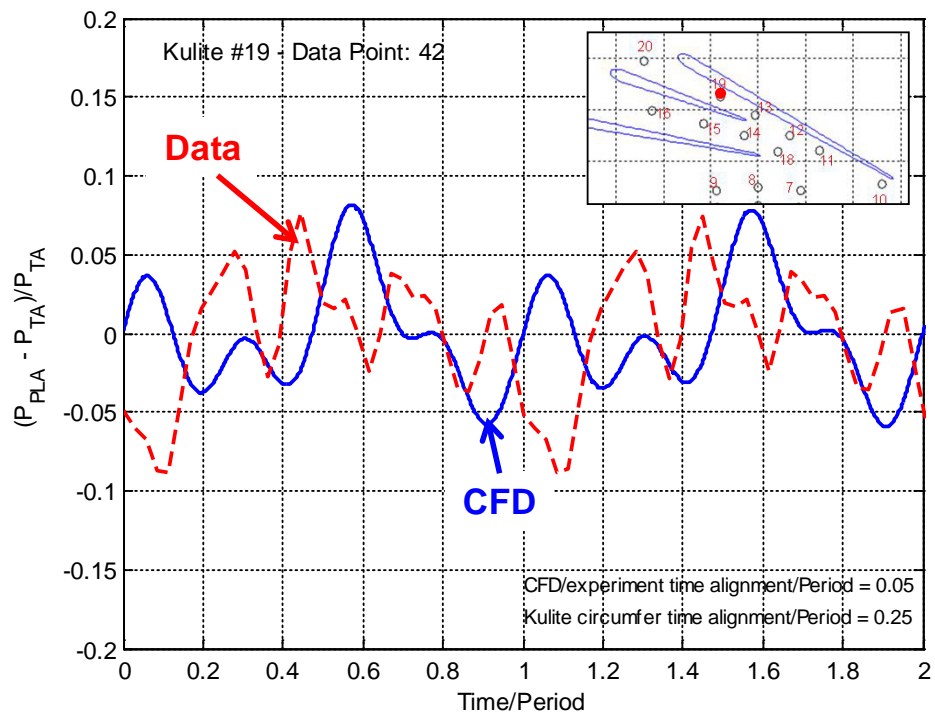


Figure 172.—K19 signal versus CFD at 10.4 lbm/s (near-stall flow) and 100 percent N_c .

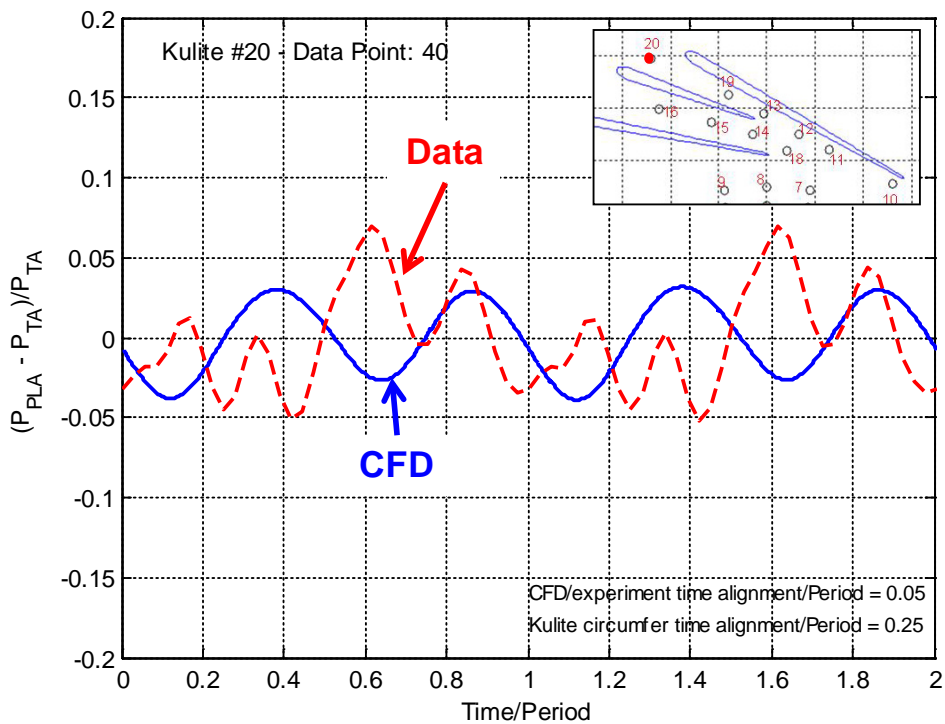


Figure 173.—K20 signal versus CFD at 11 lbm/s (design flow) and 100 percent N_c .

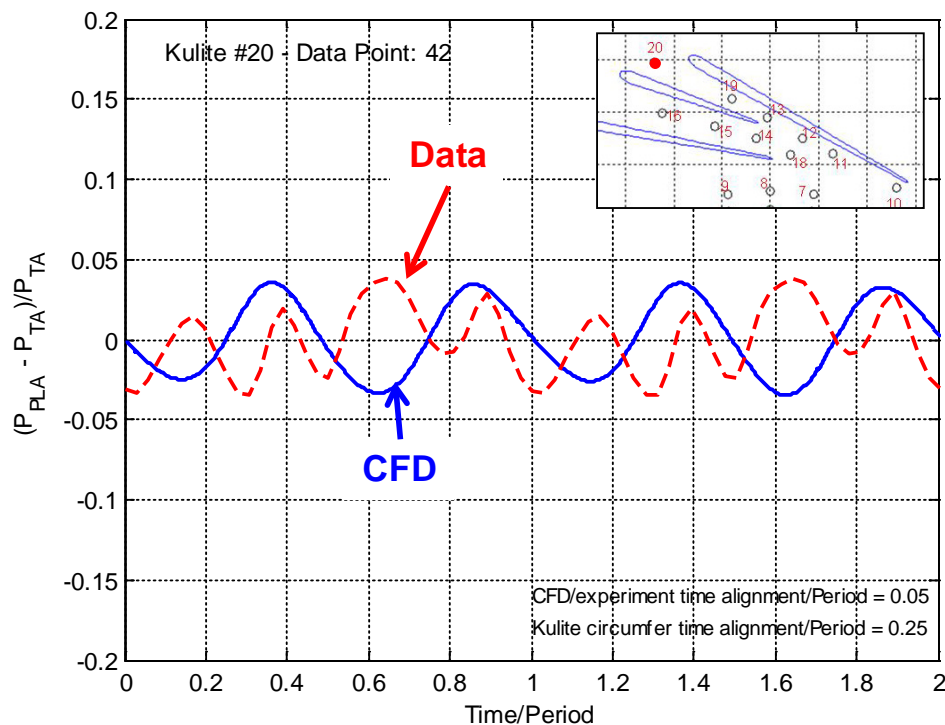


Figure 174.—K20 signal versus CFD at 10.4 lbm/s (near-stall flow) and 100 percent N_c .

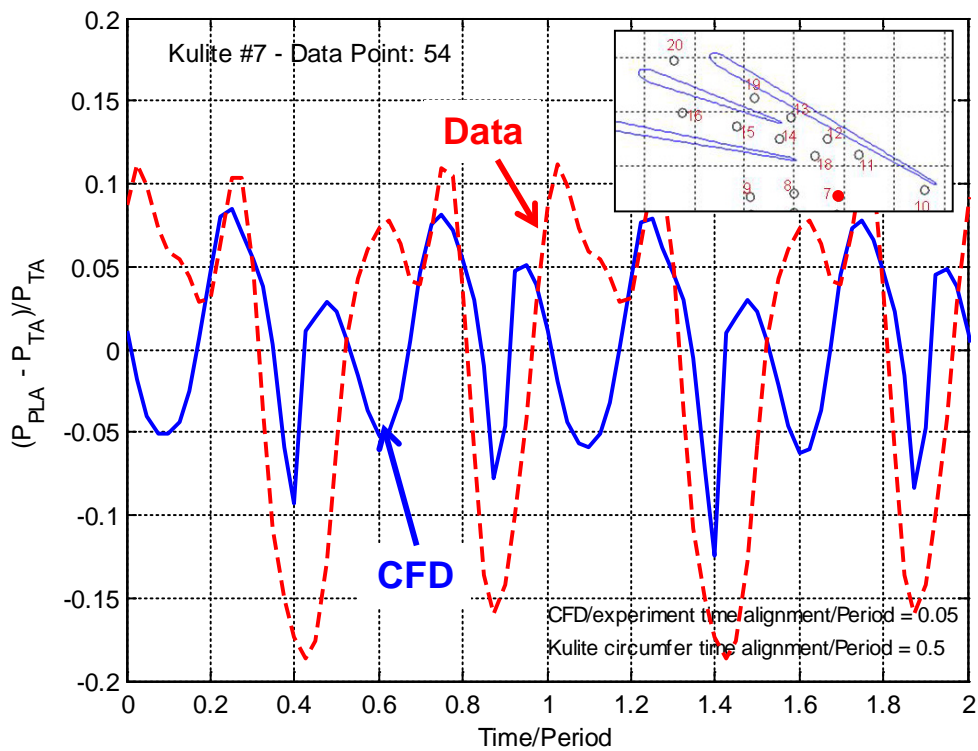


Figure 175.—Corrected K7 signal versus CFD at 11 lbm/s (design flow) and 100 percent N_c .

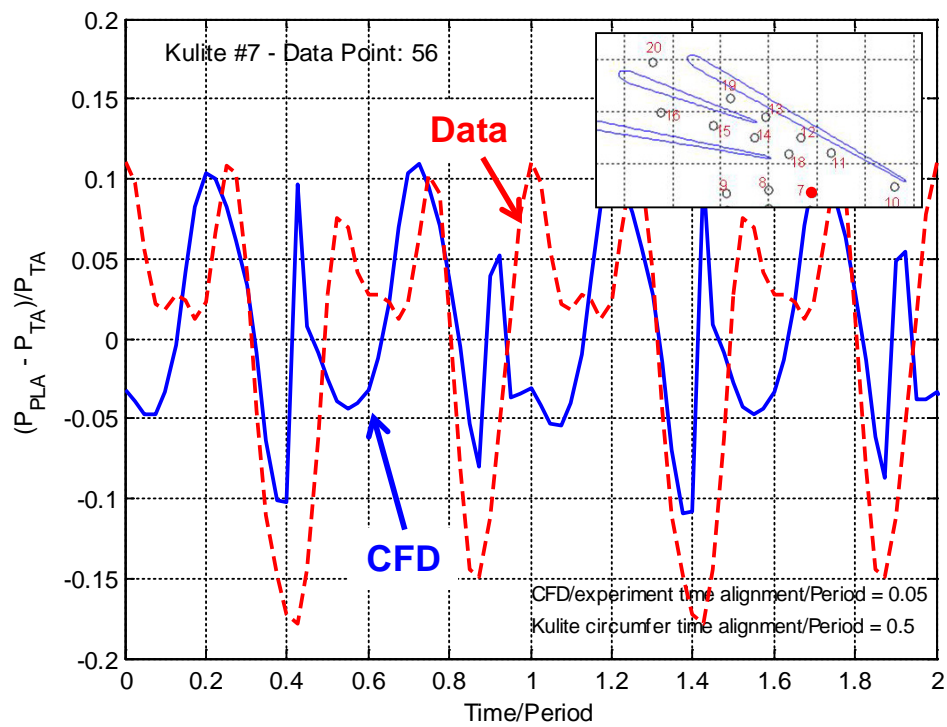


Figure 176.—Corrected K7 signal versus CFD at 10.4 lbm/s (near-stall flow) and 100 percent N_c .

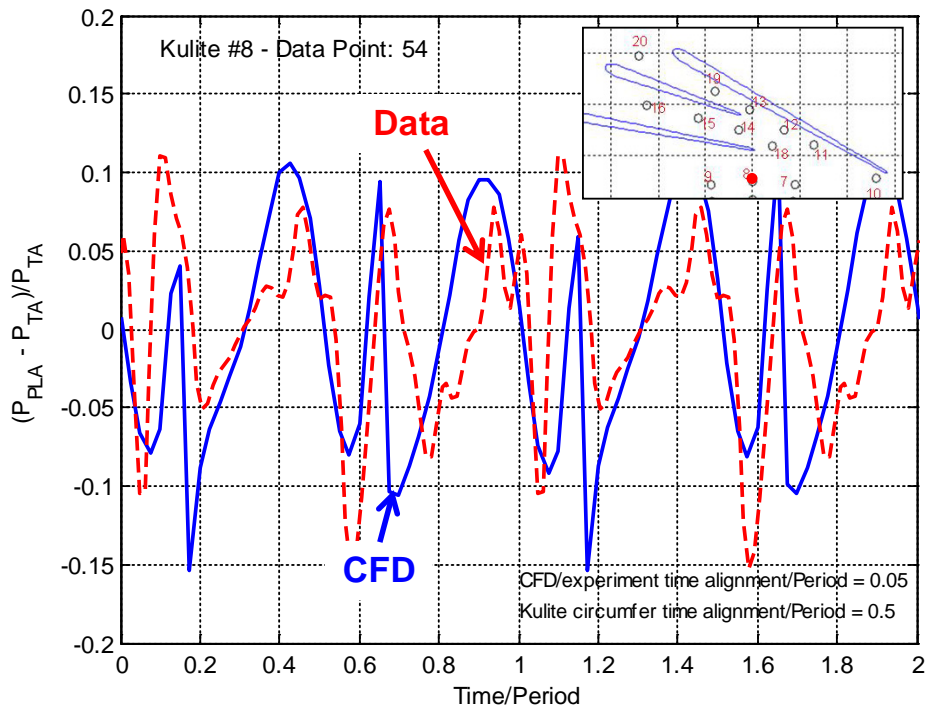


Figure 177.—Corrected K8 signal versus CFD at 11 lbm/s (design flow) and 100 percent N_c .

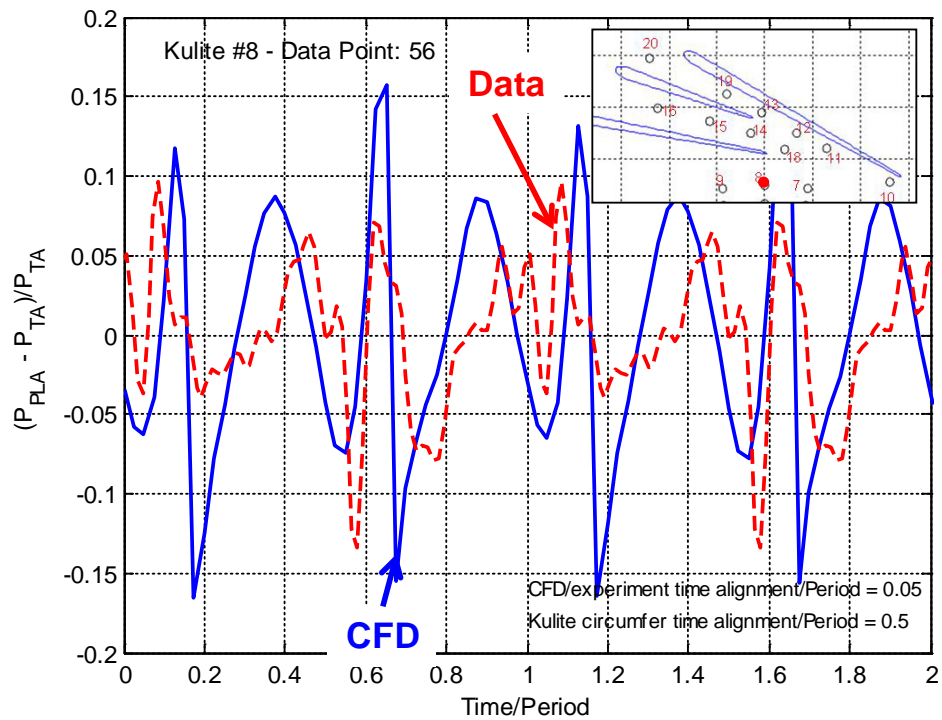


Figure 178.—Corrected K8 signal versus CFD at 10.4 lbm/s (near-stall flow) and 100 percent N_c .

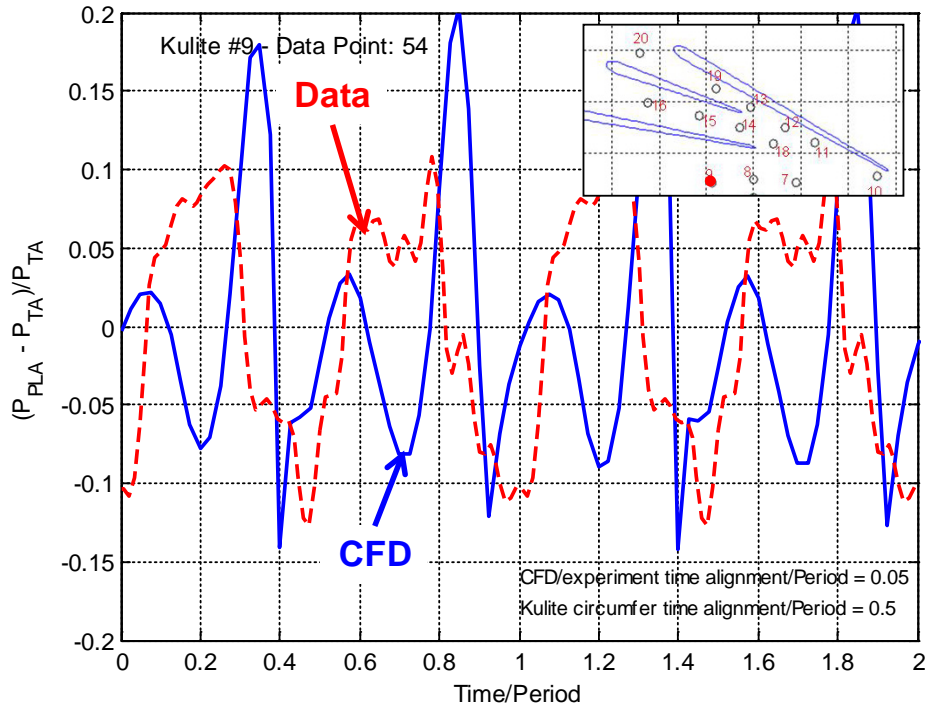


Figure 179.—Corrected K9 signal versus CFD at 11 lbm/s (design flow) and 100 percent N_c .

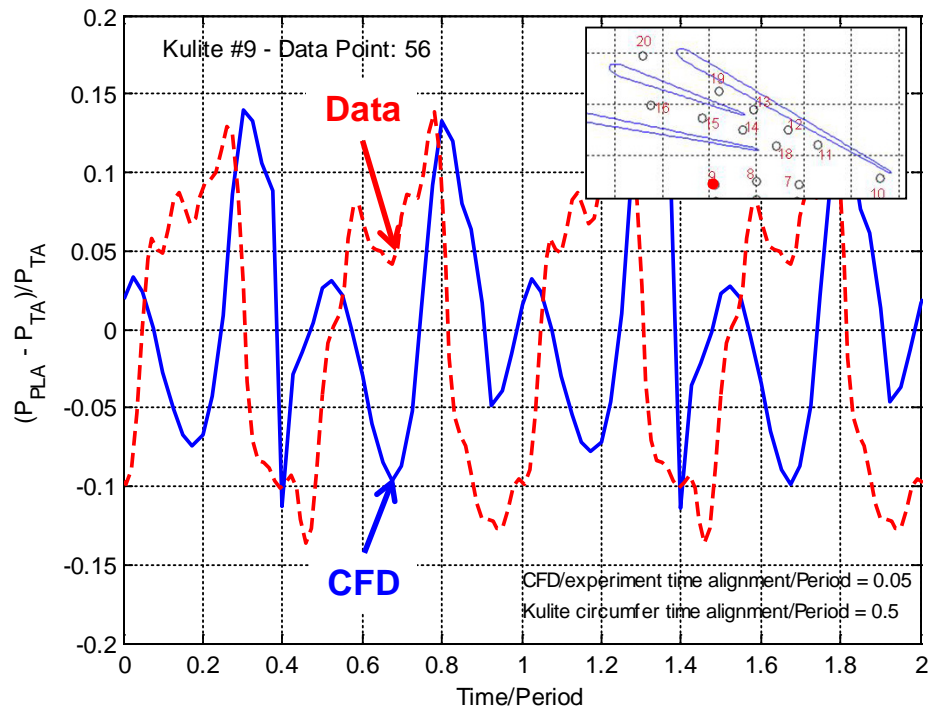


Figure 180.—Corrected K9 signal versus CFD at 10.4 lbm/s (near-stall flow) and 100 percent N_c .

10.2 Assessment of Unsteady Impeller-Diffuser Interactions in Post-Test CFD

Unsteady CFD simulations using strain-based $k-\omega$ model were then further analyzed for impeller-diffuser interactions using Tyler-Sofrin analysis. Design flow rate at approximately 11 lbm/s at 100 percent speed and the near-stall flow rate at 10.4 lbm/s at 100 percent speed are considered.

As first described in (Ref. 16) for axial turbomachinery, adjacent rotors and stators interact to produce spinning modes that may or may not propagate noise to the farfield. Likewise, the impeller and diffuser vanes can generate similar interaction. Noise to the farfield is not as much of an interest herein; rather, is there a performance impact of the “rotor-stator” interaction?

For the centrifugal compressor, the mechanisms responsible for the rotor-stator interactions are impingement of rotor main and splitter blade wakes on the downstream diffuser vanes and reflections of the rotor pressure field from the diffuser vanes. Both mechanisms produce the same spinning m-lobed modes described by the following equation (Ref. 16):

$$m = nB + kV$$

where,

B=number of blades

V=number of vanes

n=harmonic of blade passing frequency

k=....-1, 0, 1....

with a rotating speed of $nB\Omega/m$ where Ω =impeller rotation speed in rad/sec. If the rotation speed of the mode is greater than Mach 1, then the mode will propagate. If below M=1, the mode will decay rapidly. For the compressor in the present study, the following table gives the lowest order modes (B=15, V=20):

To examine the CFD solution for presence and magnitude of rotor-stator interaction modes, the flowfield was spatially filtered for different orders of $m\theta$ to see if there is any energy content at the expected modes in Table 8. As a preliminary investigation, this filtering was done along two circumferential lines shown in Figure 181 (in the vaneless space and downstream of the diffuser)—at mid-span. The spatial filtering is given by the following equations:

$$P_m(r, t) = \frac{1}{2\pi} \int_0^{2\pi} P(r, \theta, t) e^{-im\theta} d\theta$$

$$P_m(r, \theta, t) = P_m(r, t) e^{im\theta}$$

The first equation computes the spatial spectrum for a given instant in time (t). The second equation can be used to recreate the filtered spatial distribution.

The raw CFD pressure distribution along the vaneless space and the diffuser outlet are given in Figure 182 (design operating point) for two different times: t=0 and t=3 percent of one rotation. In the vaneless space, the dominating signature is due to the proximity to the vanes (higher pressure near vane leading edge). The diffuser outlet clearly shows a spinning 5-lobed pattern as predicted by the Tyler-Sofrin equation.

TABLE 8.—LOWEST ORDER SPINNING MODES PREDICTED IN COMPRESSOR

m	n	k
-5	1	-1
10	2	-1
-10	2	-2
5	3	-2

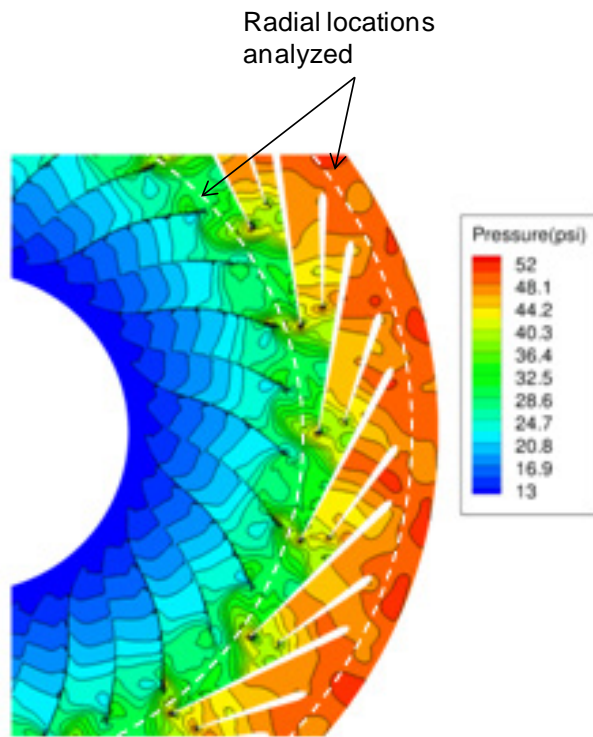


Figure 181.—Circumferential lines studied for rotor-stator interaction—at mid-span (dashed).

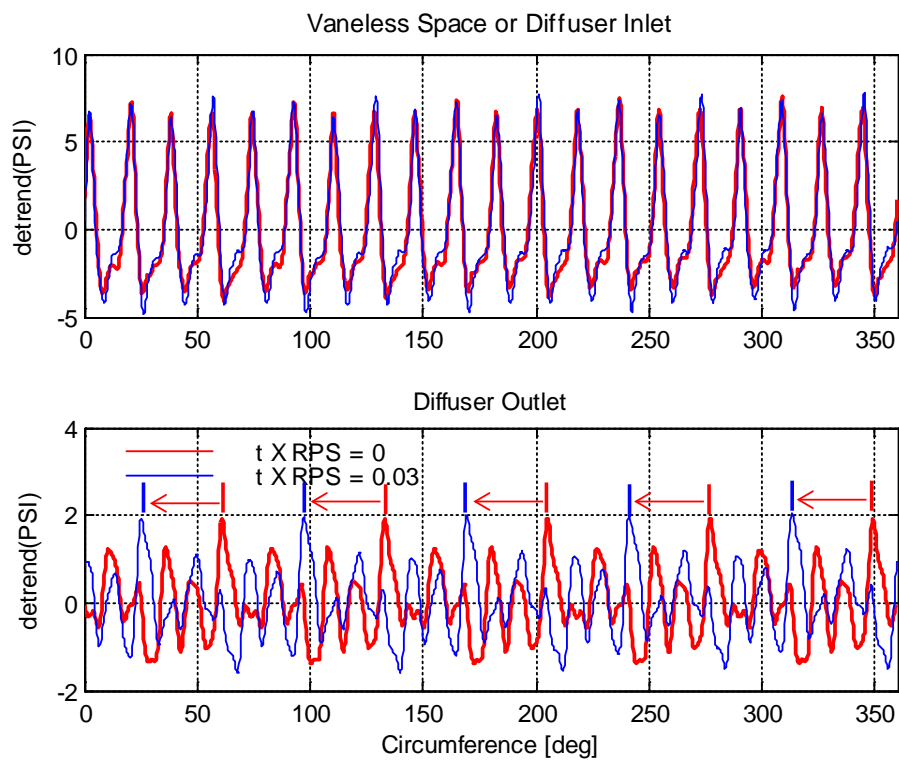


Figure 182.—Raw CFD data for rotor-stator interaction analysis.

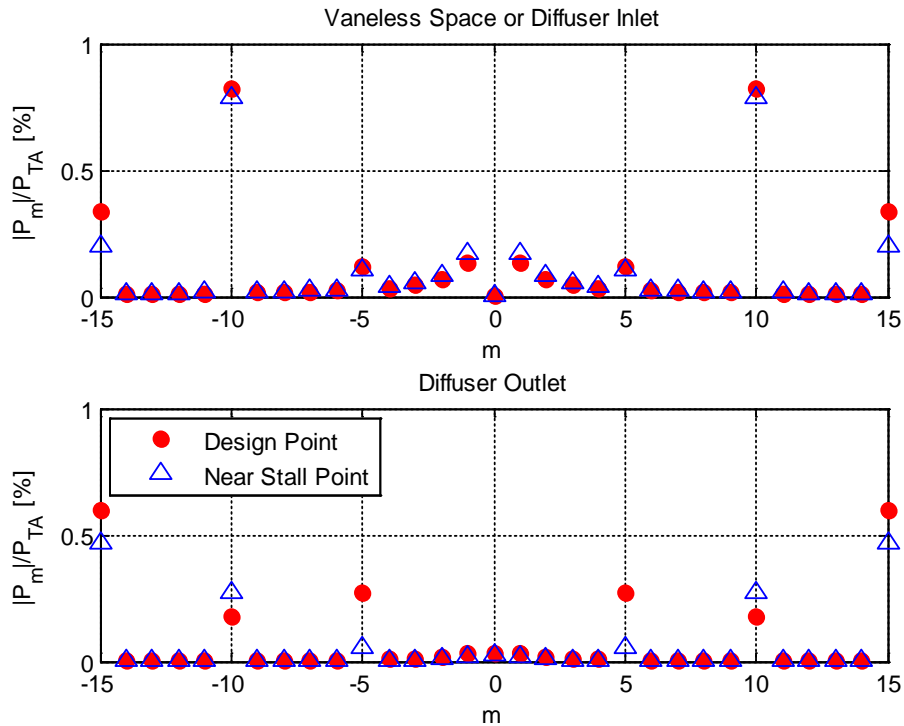


Figure 183.—Spatial Fourier decomposition for rotor-stator interaction analysis—lower order modes.

The more quantitative analysis is shown in Figure 183 which gives the Fourier components of the spatial filter (P_m) averaged of one blade passage, normalized by the mean pressure for the design and near-stall operating points. Several observations can be made.

1. The diffuser outlet flowfield has well defined spinning modes predicted by the Tyler-Sofrin equation.
2. The vaneless space has spinning modes predicted by the Tyler-Sofrin equation, but there is additional energy in unexpected patterns of one and twice per revolution (perhaps due to un converged features in the flowfield).
3. The pressure level of the spinning modes is very low (< 1 percent) and probably not important to compressor performance.
4. The spinning mode content is relatively the same between the design and near-stall operating points.

Figure 184 gives the Fourier components of the spatial filter out to $m=30$. For the vaneless space, the figure clearly shows a dominant spatial pressure variation of 6 percent at $m=20$ which is equal to the vane count. This result shows the presence of the vanes introduces a strong back pressure on the impeller flowfield. For the diffuser outlet, $m=15$ and $m=30$ show moderate levels of pressure (0.6-0.8 percent) which correspond to the blade and blade plus splitter counts.

For completeness of the Tyler-Sofrin analysis, the $m=-5$ mode was reconstructed using the above equation over one rotation of the impeller. This reconstruction is shown in Figure 185 for five instants in time. Since the amplitude of the mode was low, plotting the total pressure (mean plus fluctuating components) would show a circle with a slight wobble. So to better illustrate the mode, a small offset of 0.5 psi was added to the fluctuating component. As seen in the figure, this mode has a 5-lobed pattern as expected, spins in the opposite direction of the rotor, and rotates three times for every rotor revolution.

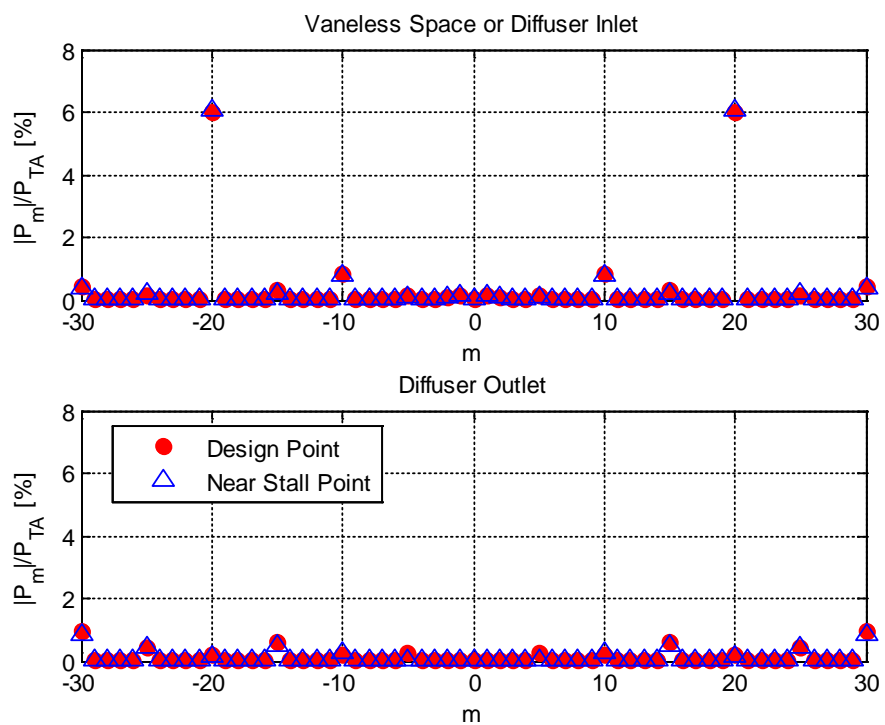


Figure 184.—Spatial Fourier decomposition for rotor-stator interaction analysis—higher order modes.

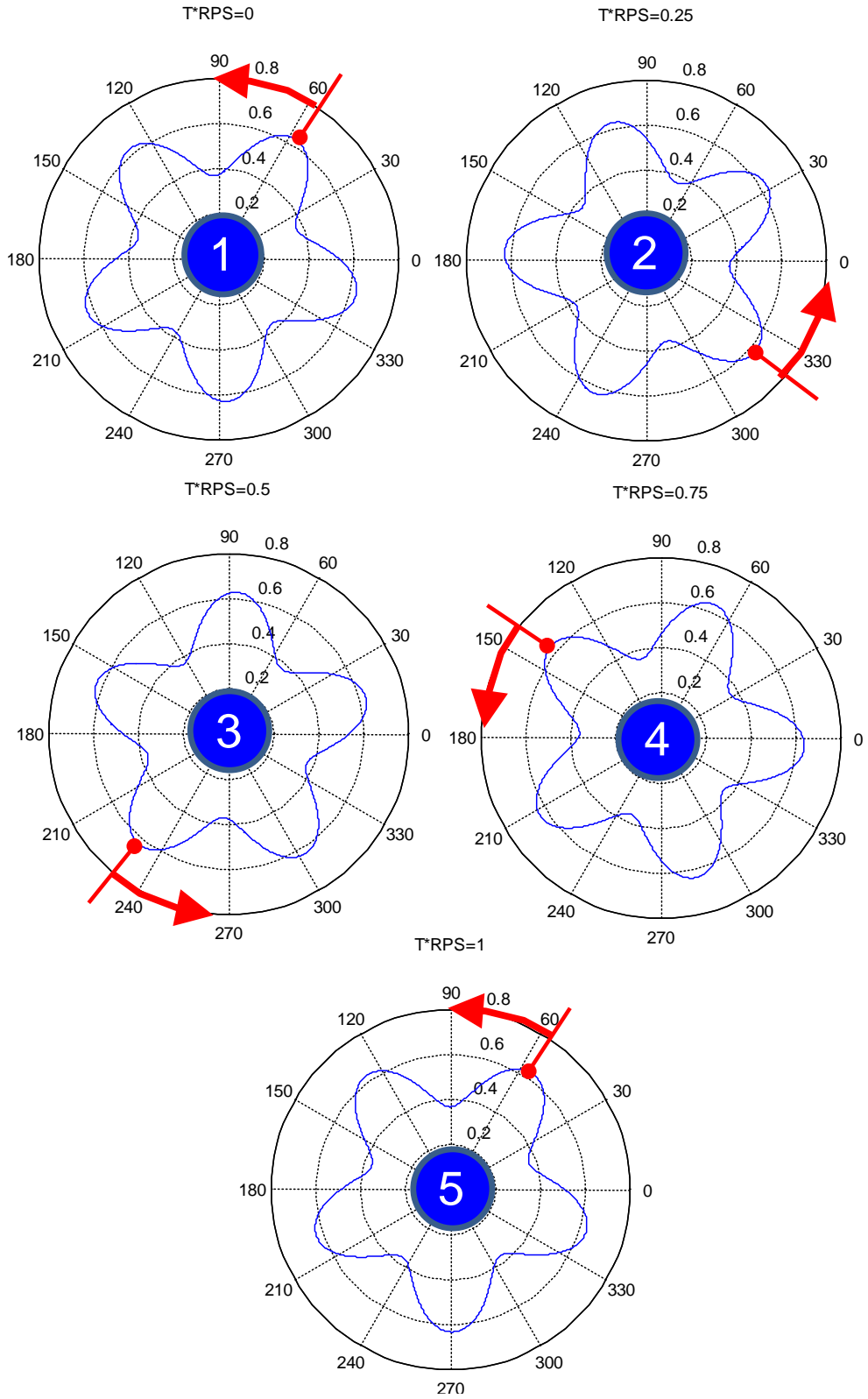


Figure 185.—Reconstructed $m=-5$ mode over one rotor revolution.

11.0 Discussion

In this research effort, a new high-efficiency centrifugal compressor was designed and tested. Overall, measured pressure ratio of 4.68, work factor of 0.81, and exit corrected flow rate of 3 lbm/s met the target. Polytropic efficiency is 2.5 pt below target, having achieved a design condition total-to-total polytropic efficiency of 85.5 percent in test. Stability margin is also lower than the target by 5.5 pt.

As discussed in Section 8.2.2, the measured performance for the impeller is below pre-test CFD predictions. At 100 percent speed, the measured impeller total-to-total adiabatic efficiency for design flow rate is about 87.5 percent, against the predicted value of about 91 percent. The measured pressure recovery in the diffuser yields a peak C_p of 0.67, while pre-test CFD predicted values of about 0.66. Finally, the range and the stability margin are also overestimated in the pre-test CFD simulations. The measured choke flow is approximately 11.5 lbm/s, whereas the predictions yielded 11.9 lbm/s—it is low by about 3.4 percent, which is similar to what was observed when CFD-based design process was assessed for NASA CC3 compressor. Stability margin of 7.5 percent was observed in test, whereas 12 percent stability margin was predicted in pre-test CFD.

Root-cause-analysis was conducted after the test, with a large number of post-test CFD simulations conducted at various conditions. These revealed that suppressed inlet plays a detrimental role on the performance—about 0.6 pt reduction in peak adiabatic efficiency was observed, as well as 1 percent reduction in choke flow. Sensitivities to geometry imperfections (such as a step in the flowpath on the shroud between impeller and diffuser) were also analyzed and a potentially large impact was demonstrated (up to 1 point in efficiency reduction). Similarly, restaggering of the splitter vane was also analyzed with changes in the angle of up to 3°. The restagger produced a significant impact on the static pressure around the vanes and represented the only set of simulations where the peculiar (negative) loading observed in the measurement was also computed with CFD. Furthermore, with such a loading on the diffuser vanes, a significant detrimental impact on the impeller performance was also observed. While such large geometrical differences were not found in the actual compressor hardware, the studies highlight the sensitivity of compressor performance to changes in aerodynamic blockage downstream of the impeller, in particular near the shroud.

Inaccuracies related to turbulence modeling were also identified, showing a large variation in peak efficiency depending on the choice of turbulence model (more than 2 pt variation). Unsteady simulations also showed improved predictions when compared to data, confirming large unsteady interactions. For strain-rate based $k-\omega$ model, unsteady simulations show 2 pt lower efficiency than the corresponding steady simulations, with significant unsteadiness, mainly affecting the impeller performance.

In addition, as a part of this root-cause analysis, a number of shortfalls in both the process and the design itself were identified. Process shortfalls center around the application of the CFD code outside of its domain of validation, the limitations of turbulence modeling and an underestimation of unsteady impeller-diffuser interactions.

Design shortfalls center around the stability of the impeller and the impact on the range of the compressor, the intensity of impeller-diffuser interactions, the diffuser design (in particular the negative incidence in the diffuser and the robustness of the splitter vane design), as well as some other opportunities for improvement (the design of the radial-to-axial bend and the design of EGV airfoils). These are discussed in more detail below.

11.1 Process Shortfalls

11.1.1 Application of Steady CFD Code Outside of its Domain of Validation

The initial successful validation of the steady simulations with the CFD code for the CC3 compressor (with delta between CFD and data of only 0.4 pt in peak efficiency) lead to a faulty assumption that the code could automatically be fully relied on for the design of a higher pressure ratio configuration. With higher work factor at same solidity of impeller blades comes higher diffusion and the CFD tool has not been carefully evaluated for such flows. An additional assessment of the CFD tool for centrifugal

compressors with even higher pressure ratios would have provided a more realistic assessment of the ability of CFD to capture these flows.

Quick turnaround time of steady CFD simulations, that allows rapid evaluation of speedlines for a large number of configurations, makes it attractive as a centerpiece of a design system. However, simply assessing these designs based only on performance numbers obtained from steady CFD, and without careful analysis of detailed results (spanwise profiles, flow angles, leading edge loadings, etc.) can lead to misleading conclusions. Furthermore, a more robust design system should also rely more on the meanline tools and simpler boundary layer codes to confirm the fundamental results observed in CFD. In addition, when an inconsistency occurs between steady CFD and meanline results (or prior experience, e.g., diffuser maps), special attention is needed. An example of that is the diffuser considered in the current design where CFD significantly over-predicted the pressure recovery compared to standard diffuser maps.

Another particular aspect of steady CFD simulations is the assessment of range. Speedlines are usually plotted for all the points for which one is able to compute a stable solution. Sometimes, incipient separation is developing slowly and CFD computations diverge very slowly. In addition, on the near-stall side of the speedline, even a small additional increase in the exit pressure may lead to flow separating, and establishing the last stable operating point can be a very tedious process. This may result in misperception about the range. This turned out to be the case for the final impeller design, which is illustrated in Figure 186.

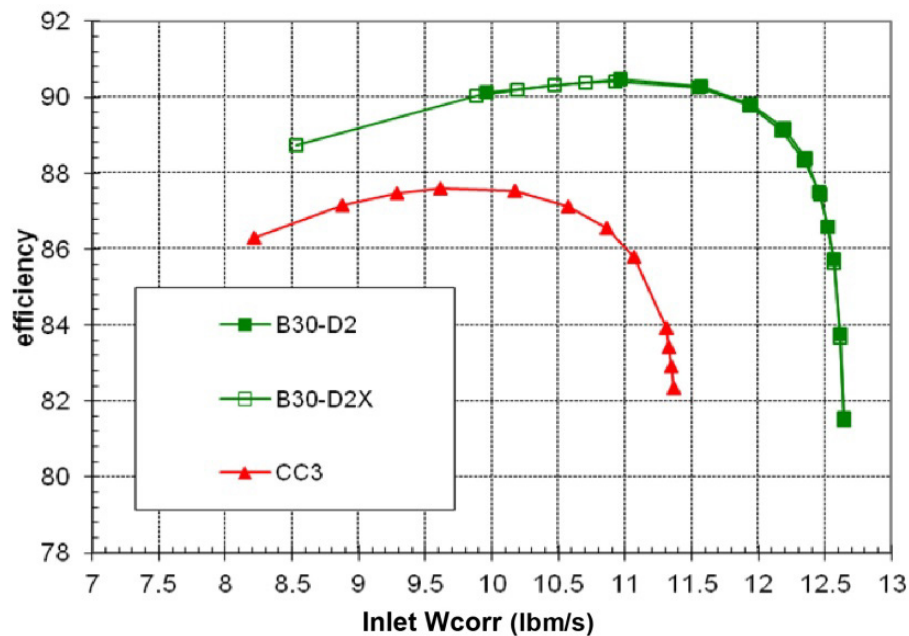


Figure 186.—Two speedlines at 100 percent N_c for the final 30° backsweep design computed with different location of the inlet (open symbols, B30-D2X, has inlet boundary further upstream compared to B30-D2, solid symbols). The leftmost point for B30-D2X is not well converged, and it eventually diverges. CC3 is also shown for reference.

11.1.2 Limitations of Turbulence Models

It is worthwhile repeating that RANS turbulence models are of limited fidelity when it comes to predicting turbulent flow dominated by strong curvature of the flowpath and strong rotational effects, as well as to predicting turbulent separation in adverse pressure gradient, or, in other words—predicting the flow in diffusers. In other words, there is a large uncertainty over their ability to correctly predict these features, and that uncertainty could have been estimated and incorporated in the decrementation of CFD results to define the expected outcome from the experiments in a more conservative way.

As a result of validation of the CFD-based design process for the NASA CC3 compressor, the decision was made to stick with a single code and a single turbulence model—vorticity based $k-\omega$ model—throughout the analyses for HECC. There are clear issues with that model, as discussed in Section 9.4. A better approach would have been to conduct a wider range of sensitivities to turbulence models at critical stages in the design process. None of the models used in the post-test CFD analyses is perfect—they don't take into account the effects of curvature and rotation, but even this initial sensitivity revealed that the results were varying dramatically. As shown in Table 9, there is a variation of more than 2 pt in total-to-total adiabatic efficiency at design flow rate.

Another element of turbulence modeling worthwhile mentioning has to do with laminar-to-turbulent transition in the blade leading edge region. There will always be a certain portion of the blade near the leading edge where the flow is laminar; all CFD computations in this work assumed fully turbulent boundary layers (except to some degree the simulations with Spalart-Allmaras which were intentionally run with lower inlet turbulence). In this way, the CFD simulations might be more forgiving when it comes to large incidence angles and the flow separation might be delayed to some degree. As it will be further discussed in Section 11.2, in the current design, for both impeller and diffuser there are large incidence angles.

11.1.3 Underestimation of Unsteady Impeller-Diffuser Interactions

The CC3 compressor was used to gauge the importance of unsteadiness in the early assessment of the design process. Impeller exit Mach number in this new higher pressure ratio compressor was higher than in CC3, the spacing between the impeller blades trailing edges and the diffuser vanes leading edges is slightly smaller than in CC3, and the impeller and diffuser were mismatched in terms of flow capacities (incidence). These each lead to higher impeller-diffuser interactions and required a more rigorous investigation. The pre-test assessment of the impact of unsteady interactions on the overall performance was somewhat skewed by an insufficient use of unsteady simulations through the design process. Even though a larger role was envisioned for the unsteady CFD at the project proposal stage, mainly due to computational constraints, only limited unsteady simulations were performed. For example, pre-test CFD analyses did include a run for an impeller-diffuser configuration—prior to thickening of diffuser vanes, and the addition of EGVs. These analyses showed about 0.5 pt lower peak efficiency than the corresponding steady runs. Post-test CFD for the final configuration, with the same turbulence model, but finer grid, showed the delta in peak efficiency to be closer to 1.2 pt. With a different turbulence model, this delta was about 2 pt in peak efficiency. Given the higher impeller pressure ratio and exit Mach number, many more unsteady analyses should have been used to optimize the impeller-diffuser gap for optimal performance and minimal detriment to impeller performance, as well as the to assess the impact of diffuser vane leading edge geometry and alignment.

TABLE 9.—COMPARISON OF POST-TEST CFD RESULTS WITH DIFFERENT TURBULENCE MODELS—ADIABATIC EFFICIENCY AT DESIGN FLOW RATE

	Vorticity $k-\omega$	Strain-rate $k-\omega$	Strain-rate $k-\omega$ + SST limiter	Spalart-Allmaras
$\eta_{ad,TT}$, %	86.1	84.8	84.3	83.8

Post-test CFD analyses did include a large number of unsteady simulations. The codes have gotten faster, the setup process simpler, and conducting unsteady simulations in 2013 is much more of a routine than it was in 2009. This allowed for improved spatial and temporal resolution in these unsteady runs, as well as for longer integration times to ensure that the initial transients are not obscuring the conclusions from simulations. Running 10 full revolutions per run produces much more reliable time-averages, than running 2 to 4 revolutions, especially for compressors with such a long flowpath.

As the unsteady CFD simulations conducted as a part of the post-test CFD analyses show, the value of unsteady simulations extends beyond the assessment of the overall performance. They create a wealth of information in addition to time-averaged mixed-out values of 1D profiles. Quantifying the amplitudes of unsteadiness is of particular interest when it comes to impeller-diffuser interactions, both in terms of performance and aeromechanics. The analysis presented in Sections 11.0 based on post-test unsteady CFD simulations is a good illustration of potential value that can be further extracted.

Finally, using the unsteady simulations to create animations of the flowfield and gain insight into the flow physics is potentially of enormous value. It allows the designer to recognize flaws in the design, that might otherwise go unnoticed, and correct them, whether it is flow separation or component interaction. Obviously, these animations come from simulations where the fidelity of the models is still somewhat questionable, as discussed in the previous subsection, but even in that context, they would allow the designer to see what are the models predicting and whether there is something erroneous in the results. No multi-component design should be built without conducting unsteady simulations and creating a large set of representative flowfield animations with the design team examining them very carefully.

11.2 Design Shortfalls

11.2.1 Impeller-Diffuser Interactions

It is well known that a vaned diffuser has an upstream impact on the flowfield leaving an impeller. As already discussed, the measured efficiency of the impeller is lower than that predicted by a steady pre-test CFD analysis. The same configuration was analyzed with unsteady CFD (using strain-rate based $k-\omega$), and the results were more representative of the measured data, as shown in Figure 187; this figure also includes the steady simulations using the same strain-rate based $k-\omega$ model. This is representative of strong interactions between the diffuser and impeller as shown in the plot of unsteady loading on the impeller in Figure 188—stronger than in CC3 due to higher pressure ratio and higher impeller exit Mach number. (This is also indicated by the analysis of impeller-diffuser interactions in Section 11.0 of this report).

The delta in impeller performance between steady and unsteady CFD simulations is about 1.5 to 2 pt, as seen in Figure 187. With a better diffuser design that minimizes the interactions, part of that performance loss could be recovered. This could include shifting the leading edge of the diffuser vanes further down-stream. A more careful assessment of the impact of diffuser vanes on the impeller loading, as a function of the impeller-diffuser spacing, as well as a function of vane leading edge thickness will need to be performed using unsteady CFD simulations—that is the only way to characterize those effects more accurately.

Another indication of the strong impact the diffuser has on the impeller performance comes from the simulations with the rotated splitter vane—these were the only CFD simulations that were able to capture the peculiar measured static pressure distribution around the diffuser vanes. In those steady simulations, the impeller adiabatic efficiency was almost 2 pt lower than in the baseline steady simulations—for design flow rate of 11 lbm/s (Figure 189). Unsteady simulations for that geometry will likely yield the results for impeller efficiency very close to data (if the delta between steady and unsteady simulations of about 1.5 to 2 pt is maintained).

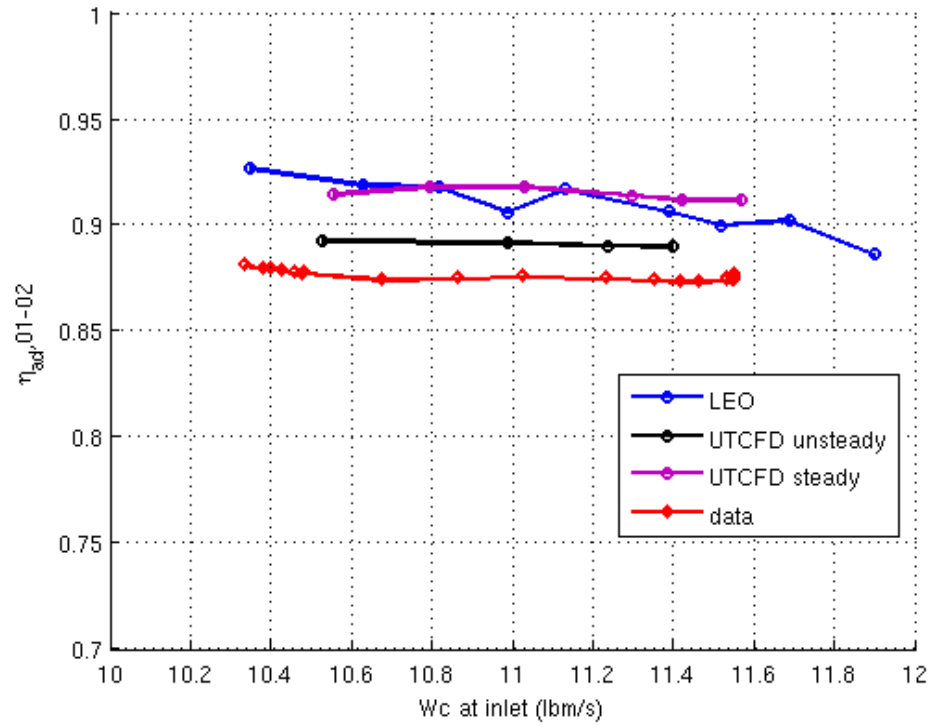


Figure 187.—Impeller efficiency for 100 percent N_c - unsteady CFD results are more representative of the measured data.

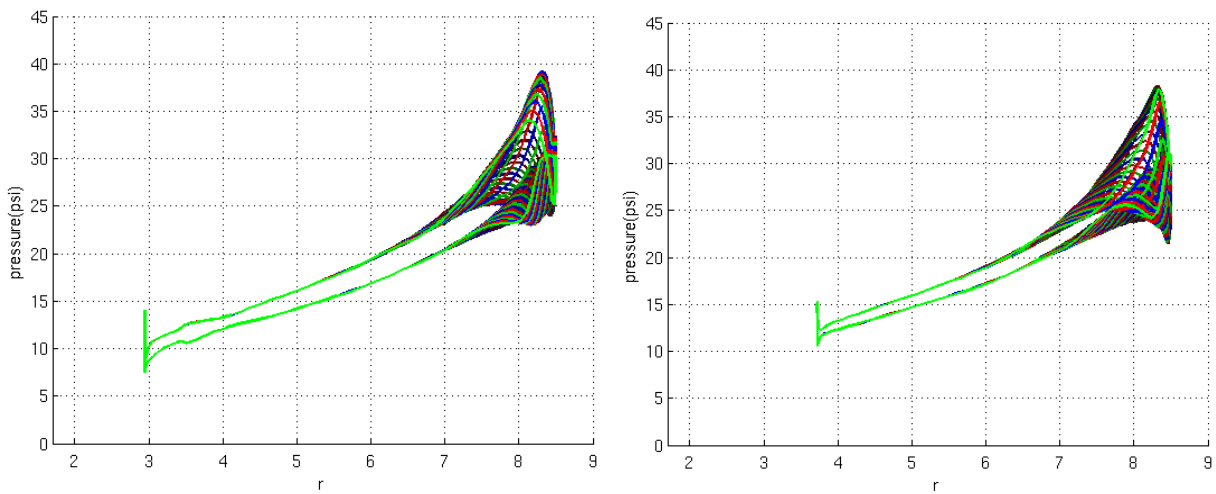


Figure 188.—Unsteady loading on the impeller main-blade (top) and splitter (bottom) at mid-span for design flow rate at 100 percent N_c , as predicted with unsteady CFD using strain-rate based production in $k-\omega$ model.

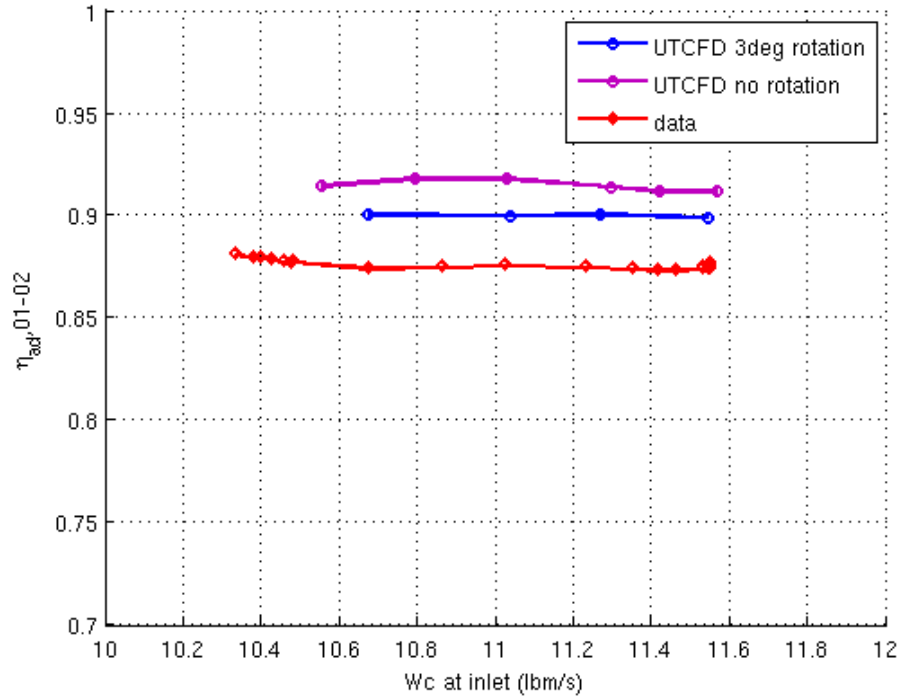


Figure 189.—Adiabatic efficiency for impeller for 100 percent N_c —restaggering the splitter vane by 3° towards the main vane has a large impact on the performance of the impeller.

11.2.2 Diffuser Design

11.2.2.1 Negative Incidence

An instantaneous snapshot of flow features in the diffuser (Figure 190), using a contour plot of turbulent kinetic energy at mid-span, shows an unsteady separation at the leading edge of the pressure side of the main vane—a result of a negative incidence in the diffuser. An interaction of this separation with the flow approaching the splitter vane could be detrimental to the performance of the splitter vane. In the experiment, this effect could have been further amplified due to the fact that the flow at leading edge of the diffuser vane is most likely laminar and the separation in the experiment is possibly even larger.

Figure 191 shows a variation of diffuser incidence as a function of speed, as computed from the averaged values in the measurements. The vanes were staggered at 10° to the tangential direction, and the data shows that the incidence varies from 12° at lowest flow to up to 14.5° at highest flow rate (for 100 percent speed). Unsteady CFD computations show that even for the design point at 100 percent speed, the instantaneous angle varies from 10° to 20° . A better alignment of diffuser vanes should minimize loss generation in the diffuser.

A better alignment of diffuser vanes should minimize loss generation in the diffuser. In addition, restaggering the diffuser vanes to 12° or 13° —instead of current configuration that uses 10° —would also allow for a better matching of impeller and diffuser. In such a configuration, the impeller itself would also operate at a higher flow rate and better incidence angles.

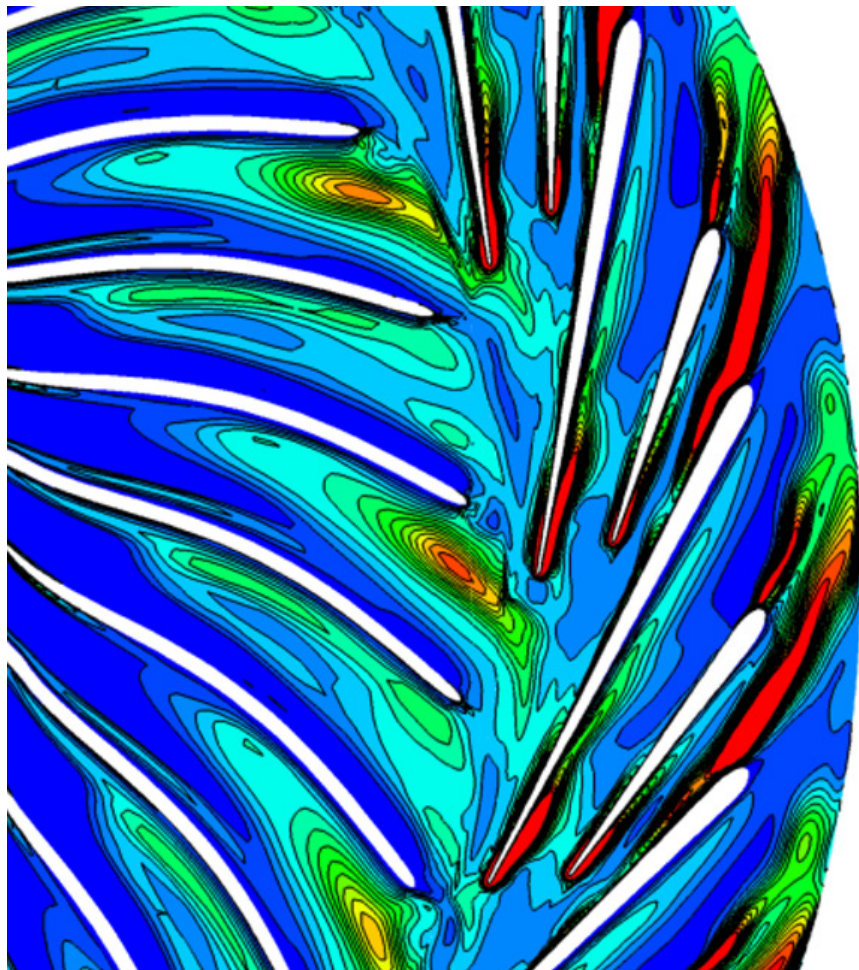


Figure 190.—Instantaneous contour plot of turbulent kinetic energy in the diffuser at mid-span (from a post-test UTCFD unsteady simulation at 11 lbm/s for 100 percent N_c using strain-rate based production $k-\omega$).

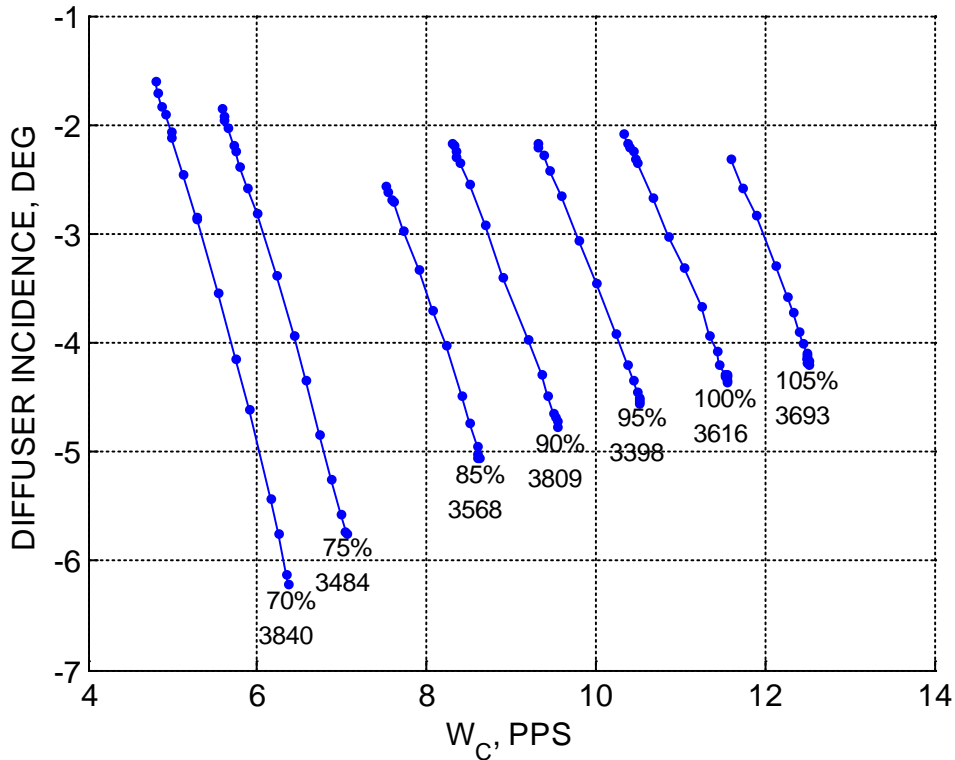


Figure 191.—Average diffuser incidence calculated from measurements of flow rate, exit total temperature, and static and total pressure at modular vane (across all speeds).

11.2.2.2 Robustness of Splitter Vane Design

Figure 192 and Figure 193 show measured static pressure in the diffuser. As discussed previously, an unusual feature that was not observed in the pre-test CFD simulations consisting of negative loading on the splitter vane and a bump on the suction side of the main vane systematically shows in these plots. It would seem that a particular pressure distribution occurs in the diffuser passage between the pressure side of the splitter vane and the suction side of the main vane. This could potentially be due to misalignment of the splitter vane itself (faulty geometry), or a significant misalignment in flow incidence on the splitter.

As a part of the post-test CFD simulations several attempts were made to reconstruct that feature. It only occurred in a handful of simulations: in the geometry sensitivity case study where the splitter vane was rotated for 3° towards the main vane (discussed in Section 9.3.2), and in the simple 2D simulations of the diffuser geometry where inlet angles were varied together with the assumption of laminar leading edges on the main vane—this behavior was only observed in a presence of large separation on the main vane pressure side interacting with the splitter vane, but in that particular case a significantly lower level of recovery was also observed.

These indicate that the positioning of the splitter could be further optimized, both in terms of circumferential alignment and the location of the leading edge with respect to the main-to-main throat.

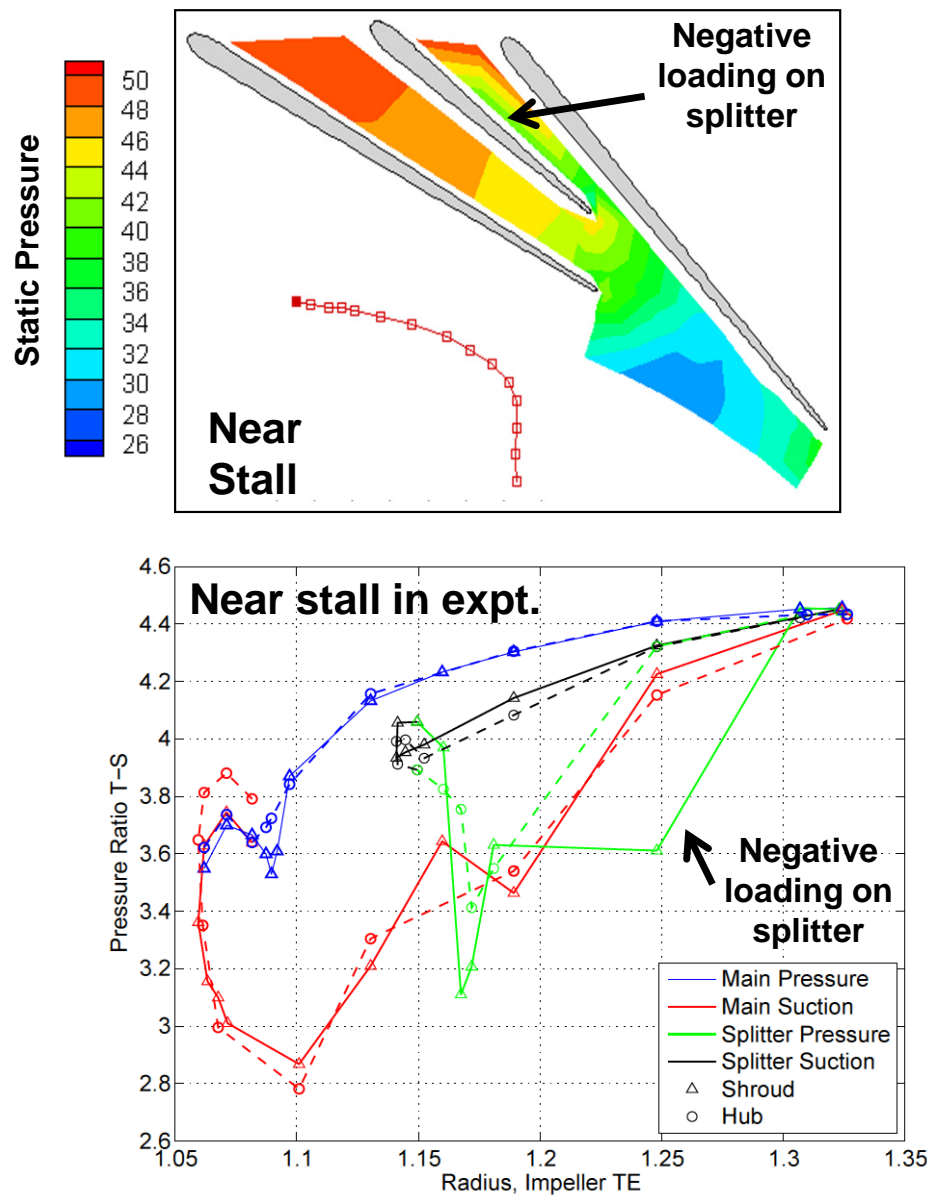


Figure 192.—Measured static pressure near stall for 100 percent N_c shows negative loading on the splitter.

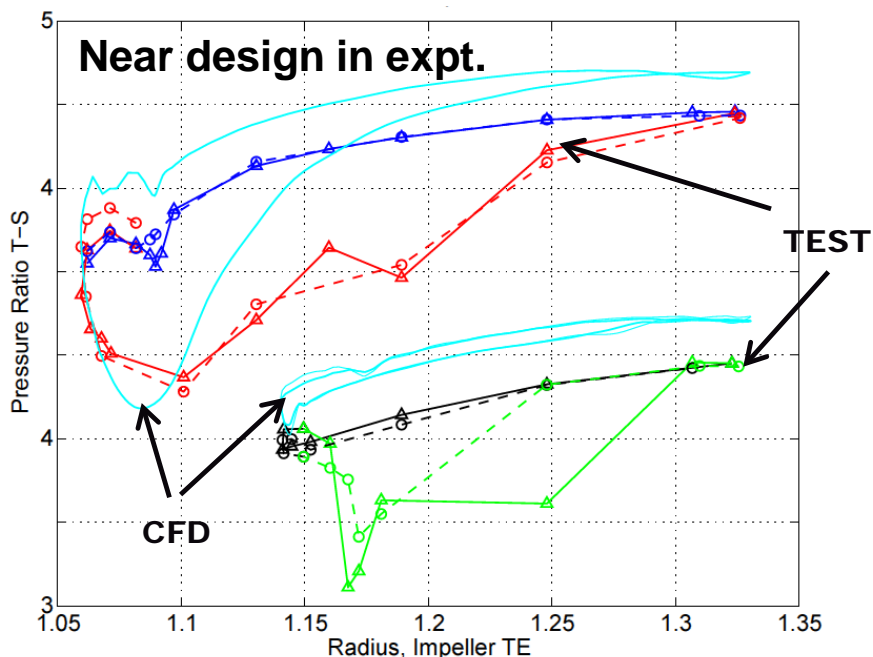
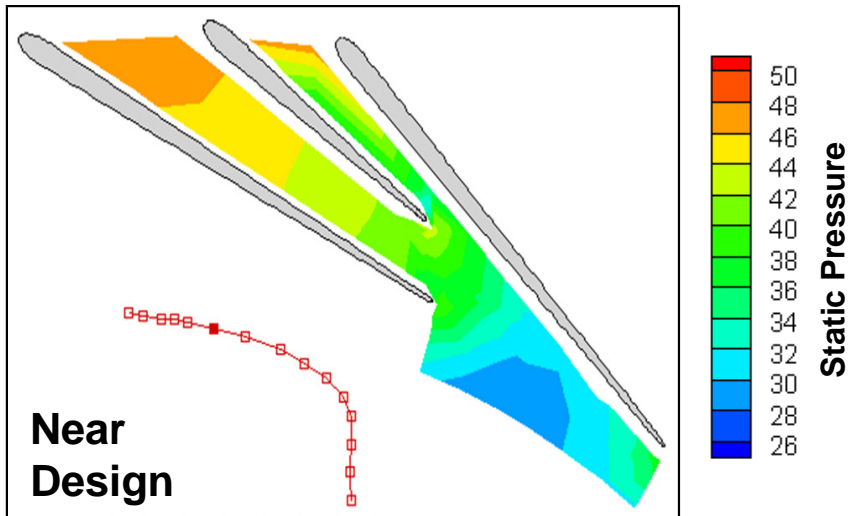


Figure 193.—Measured static pressure near design for 100 percent N_c shows negative loading on the splitter, not predicted by the steady CFD model.

11.2.3 Radial-to-Axial Bend and EGV

11.2.3.1 Separation in the Bend

Pressure recovery as computed from diffuser leading edge to diffuser trailing edge is compared to pressure recovery computed from diffuser leading edge to EGV leading edge in Figure 194. For 100 percent it can be seen that peak CP reduces from about 0.67 to about 0.57. This is an indication of significant losses between the diffuser TE and EGV LE—flow in the bend is separating.

This is further elucidated by considering the pressure taps throughout the bend and into the EGV, as shown in Figure 195. As expected the pressure on the outer wall is increased, but the pressure at the inner wall is not decreasing—it stays almost the same. That could be an indication of flow separating at

the inner wall. CFD result is also included in the same plot (using time-averages from unsteady strain-rate based $k-\omega$ simulations) and shows very similar behavior. Finally, CFD results do indicate the presence of the separation in the bend—this separation originates on the main vane, near the hub and close to the trailing edge and is further convected into the bend—as shown in Figure 196 and Figure 197. A better diffuser design, as well as more consideration for the details of the flow in the bend in the design process, could minimize the extent and the size of the separation in the bend.

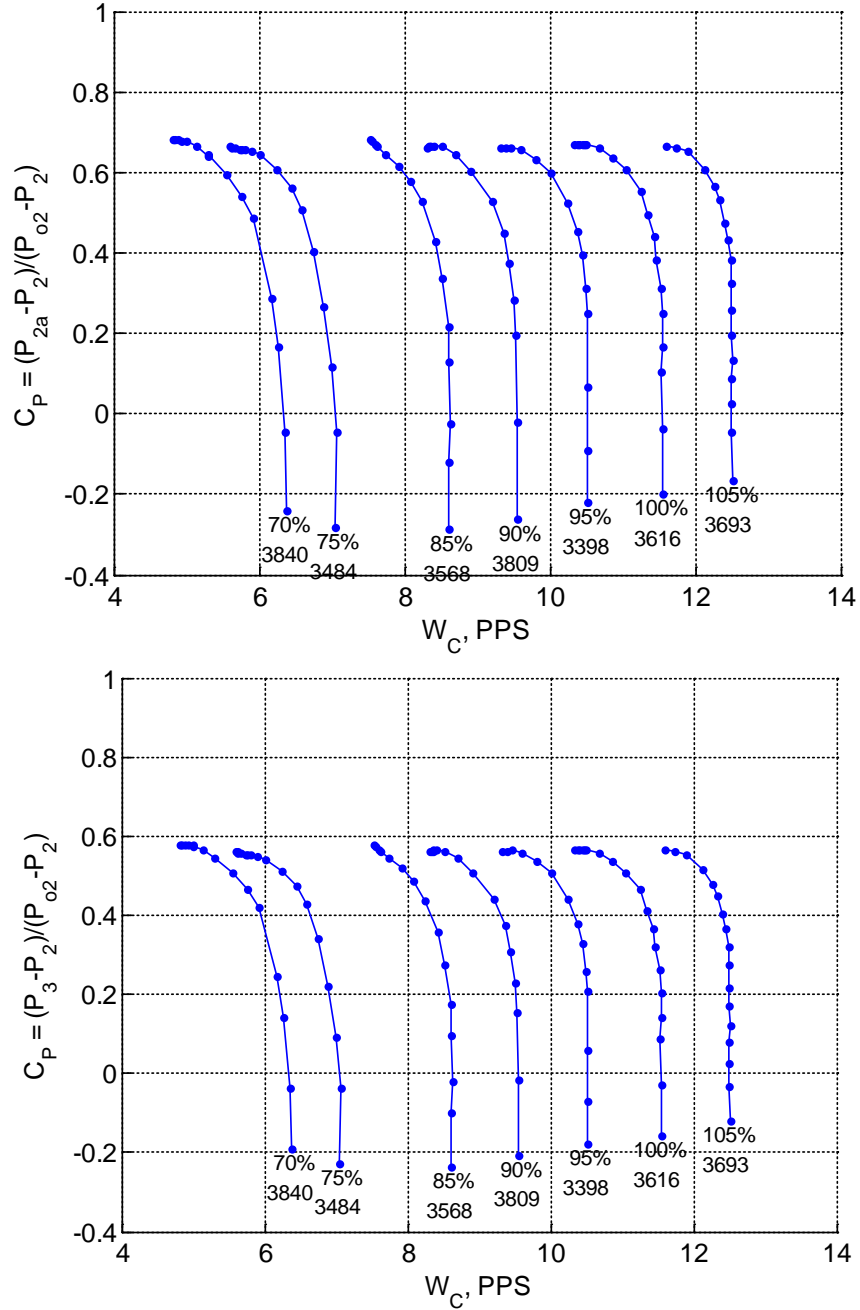


Figure 194.—Pressure recovery: from diffuser LE to diffuser TE (top) and from diffuser LE to EGV LE (bottom).

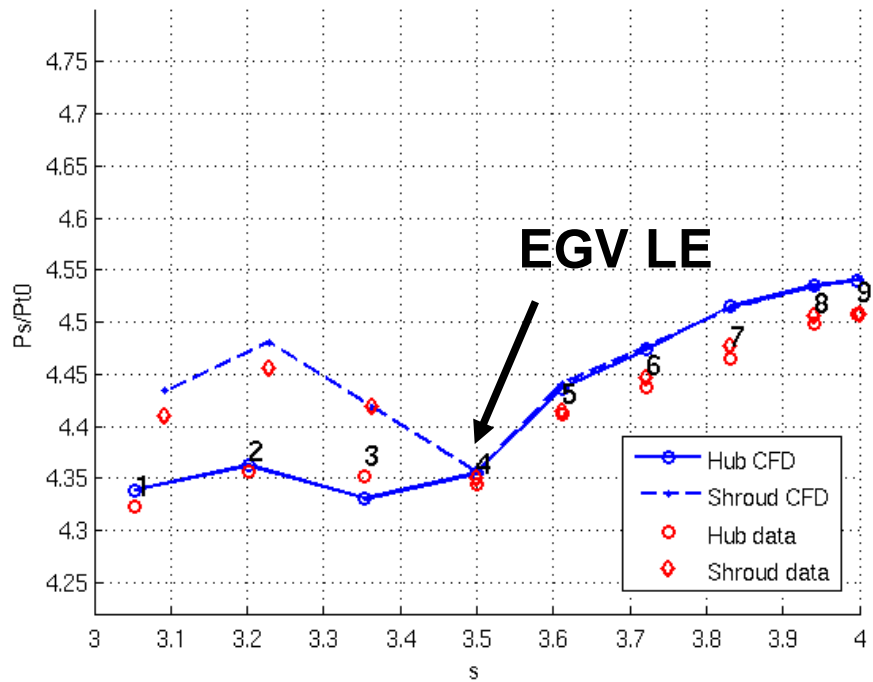


Figure 195.—Pressure throughout the bend—comparison of measurements to post-test CFD (unsteady, strain-rate based $k-\omega$ model) at inlet corrected flow rate of 11 lbm/s for 100 percent N_c .

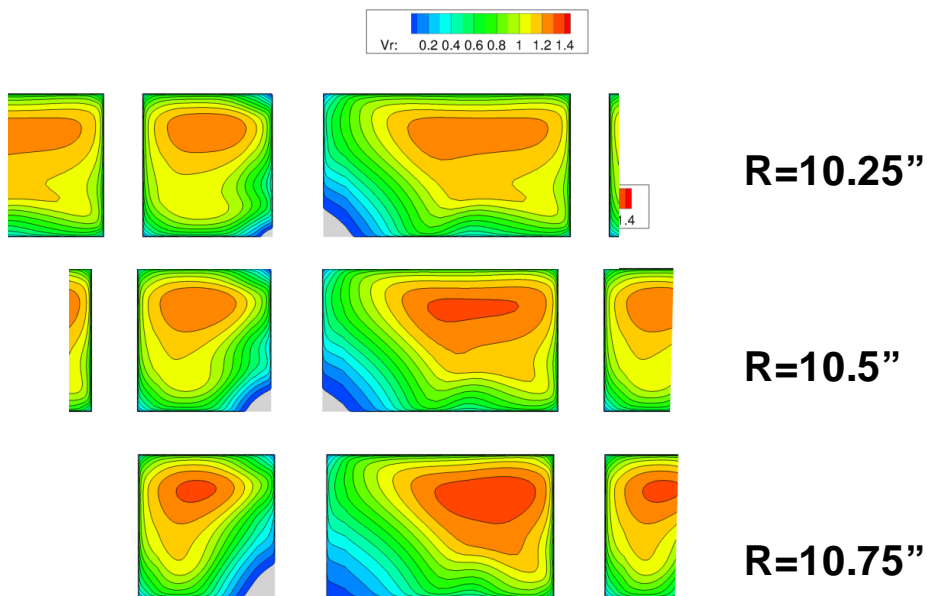


Figure 196.—Contour plots of radial velocity at three radial cross-sections near the trailing edge of diffuser vanes at inlet corrected flow rate of 11 lbm/s for 100 percent N_c . Flow separation near trailing edge; gray indicates reversed flow - time-averaged flowfield from unsteady post-test CFD (unsteady, strain-rate based $k-\omega$ model).

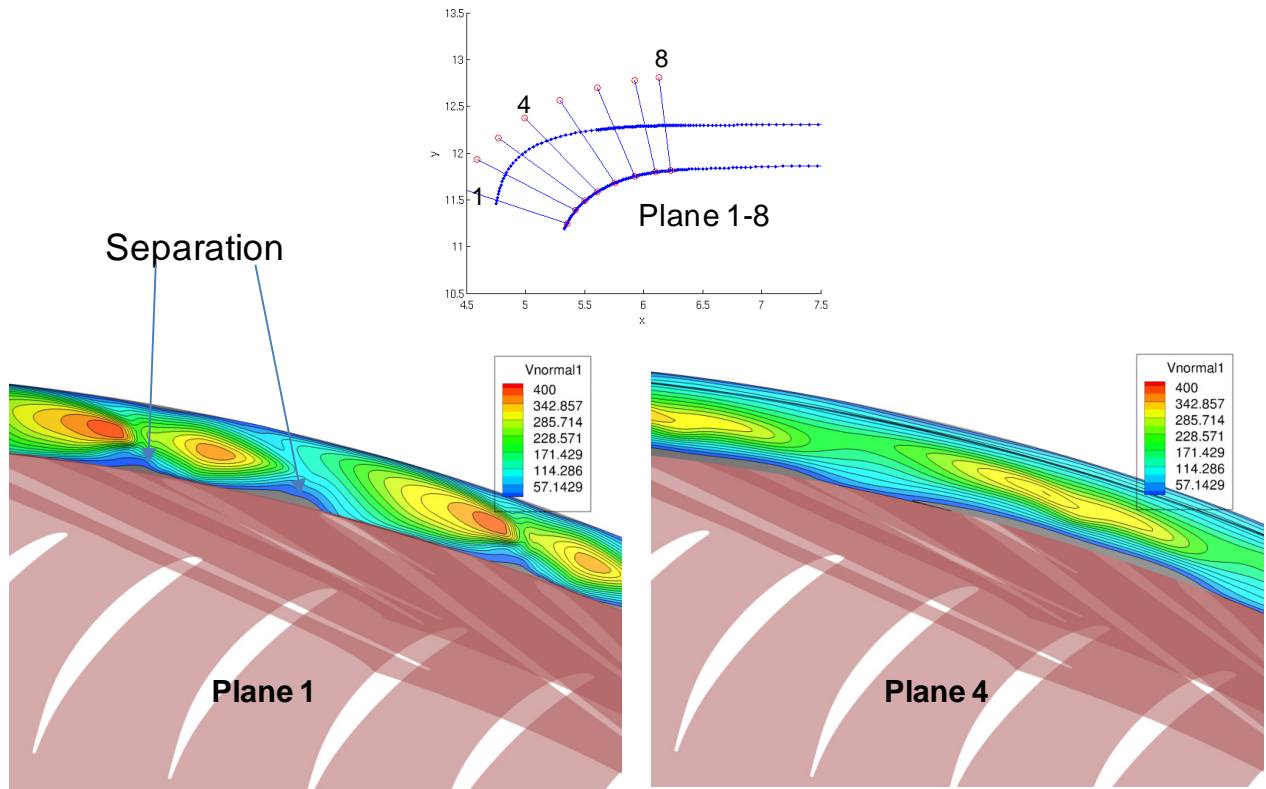


Figure 197.—Contour plots of streamwise velocity at two cross-sections in the bend at inlet corrected flow rate of 11 lbm/s for 100 percent N_c . Flow separation in the bend; gray indicates reversed flow - time-averaged flowfield from unsteady post-test CFD (unsteady, strain-rate based $k-\omega$ model).

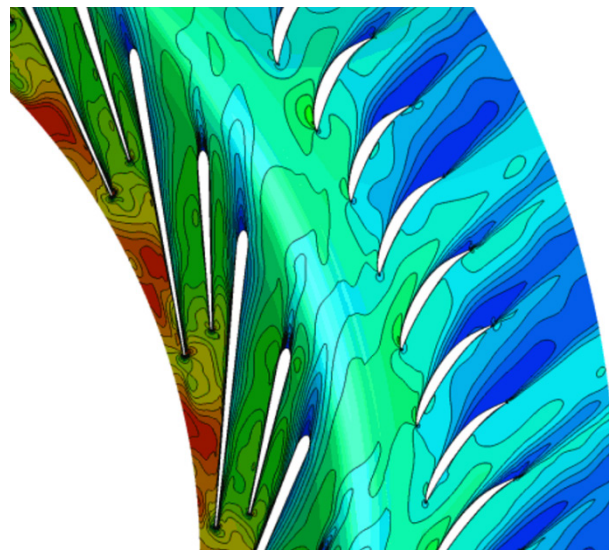


Figure 198.—Contours of instantaneous Ma number in the EGV at midspan indicate flow separation at inlet corrected flow rate of 11 lbm/s for 100 percent N_c (from unsteady post-test CFD, with strain-rate based $k-\omega$ model).

11.2.3.2 EGV Airfoil Design

Examination of the EGV total pressure loss in Figure 117 indicates that the EGV design is probably adequate (with minimum values of about 0.04 for most of the speeds). However, instantaneous snapshots of the flow in the EGVs, such as the plot of Mach number at mid-span in Figure 198 show a fair amount of flow separation at most of the vanes. Furthermore, the measured exit Mach number of 0.18 and calculated exit swirl angle of 34.8° indicate that the EGVs are not as efficient as designed. A better airfoil design could potentially further reduce the losses in the EGVs (as well as exit Mach number and swirl angle).

11.2.4 Stability and Range

As discussed previously and illustrated in Figure 118, for example, the measurements show that the compressor stalls at inlet corrected flow of about 10.3 lbm/s which is fairly close to pre-test CFD results. The range is lower than predicted because the choke flow was overestimated in pre-test CFD by about 4 percent. This is very similar to CC3 results, but was not accounted for when discussing the expected range for the new HECC compressor.

Post-test analyses revealed that it is possible that the stall occurs in the impeller. As Figure 199 illustrates, the lowest stable point predicted in CFD for the impeller with a vaneless diffuser is at inlet corrected flow of about 10 lbm/s, whereas for the stage it is about 10.3 lbm/s. For CC3, on the other hand, the predicted range for the impeller with a vaneless diffuser extends far beyond what is predicted for the stage. In CC3 experiments, the impeller with a vaneless diffuser was stable even for lower flows relative to what was observed for the stage.

Impeller flow incidence angle shown in Figure 200 indicates that for this impeller there is a large positive incidence near the hub even at the design condition (of approximately 11 lbm/s). This large positive incidence only starts to decrease when one approaches the choke flow condition (of approximately 11.6 lbm/s). On the opposite side, as the flow rate is reduced towards 10 lbm/s, the incidence in the lower portion of the span increases over 10°. While even the original CC3 impeller had a relatively large incidence angle near the hub, especially when running at lower flows, this impeller has a different overall loading distribution and it is possible that the impact of this might be different than for CC3 and could lead to impeller stalling at the hub.

Besides the incidence angle, there are other indications that this impeller design might be root sensitive. Backsweep is lowest at the root (as shown in Figure 18), resulting in higher pressure rise being achieved at the root. Also, when the tests were conducted at NASA for various clearances (shown in Table 10), as the clearances were tightened the lowest stable flow rate that was achieved in the test increased and the stall margin reduced—if the impeller was tip sensitive, tighter clearances should have led to an extended range—and the lowest stable flow rate should have decreased.

Finally, hardware inspection shows numerous tool marks, especially at the hub (see Figure 201). If this impeller is indeed root sensitive, a question immediately arises about the impact of those irregularities on the performance and stability. Also, note that the fillets in the actual hardware are somewhat larger than what has been modeled in the pre-test CFD simulations, as shown in Figure 202—in particular on the pressure side of the blade.

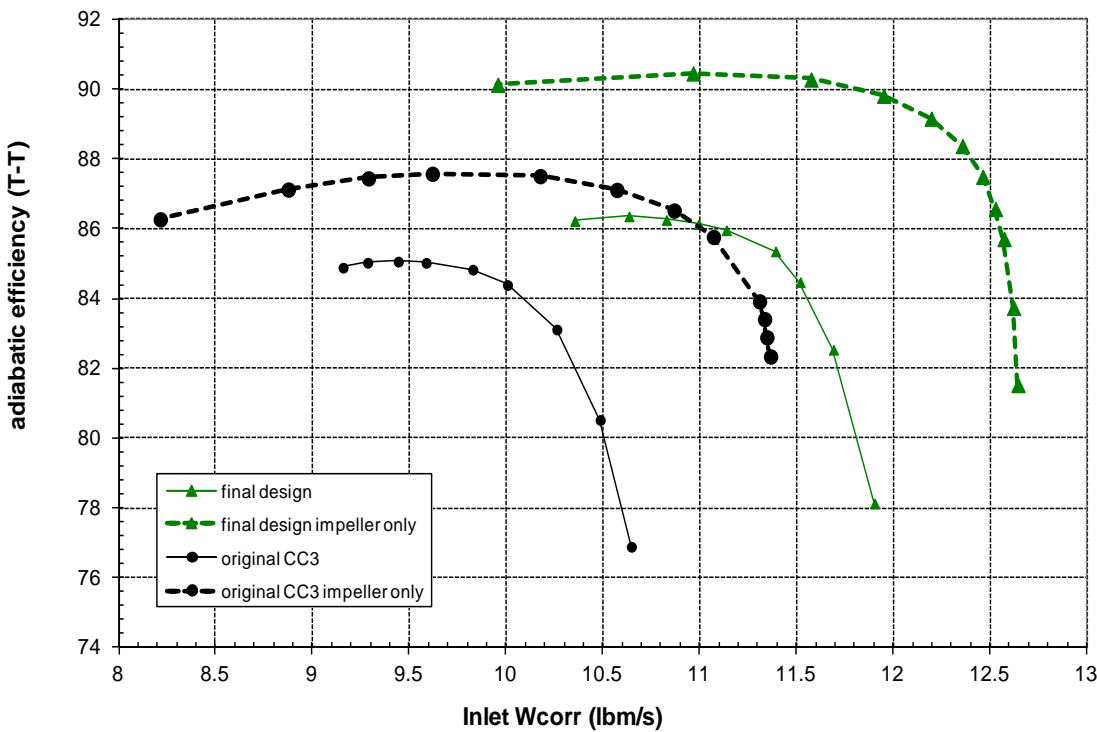


Figure 199.—Range as predicted for HECC and CC3 with both vaned (solid lines) and vaneless diffusers (dashed lines) for 100 percent N_c .

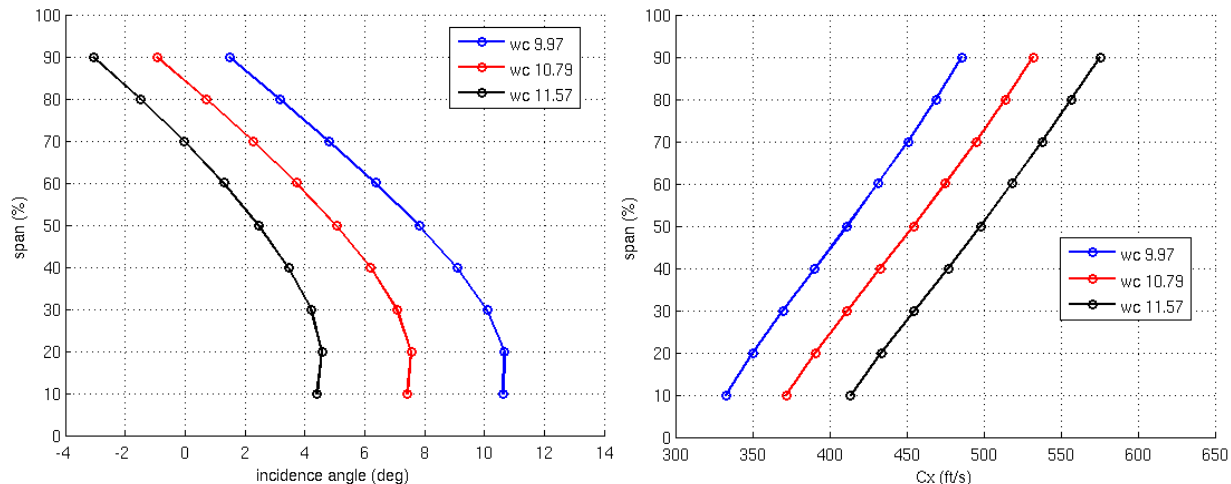


Figure 200.—Flow incidence angle to HECC impeller (left) and axial velocity profile 0.5 in. upstream of the impeller leading edge (right) for near-stall condition (~10 lbm/s), design condition (~11 lbm/s), and choke condition (~11.6 lbm/s)—at 100 percent N_c .

TABLE 10.—LOWEST STABLE FLOW RATE AND STALL MARGIN FOR TESTS WITH DIFFERENT TIP CLEARANCES (AT 100 PERCENT N_c)

	R3635	R3673	R3341
TE tip clearance (maximum), in.	0.012	0.015	0.018
Lowest inlet corrected flow, lbm/s	10.333	10.251	10.196
SM, %	7.5	7.8	7.9

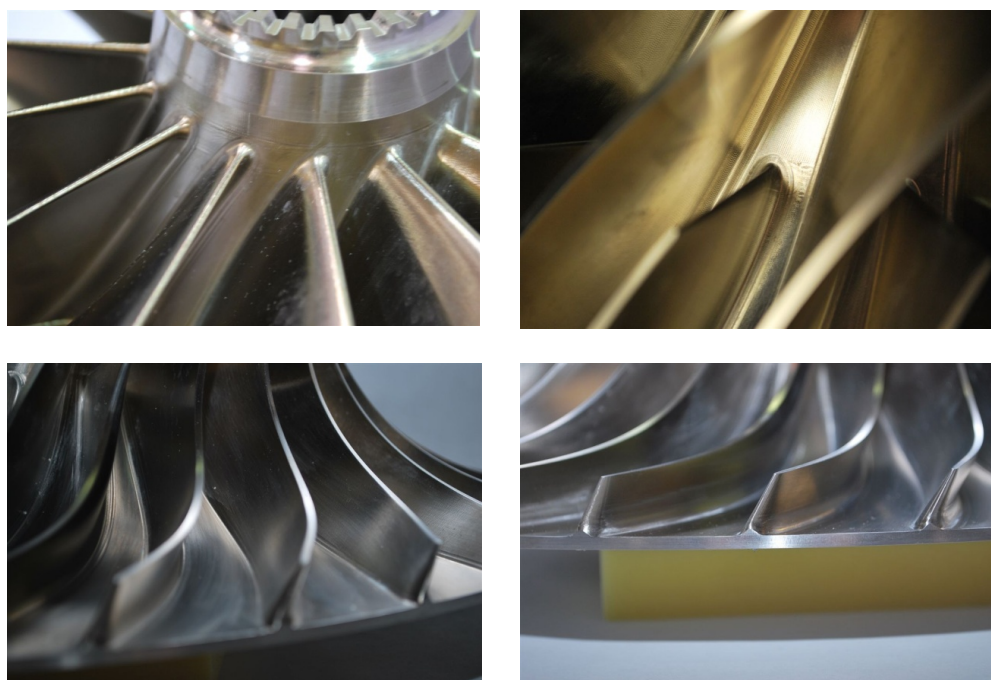


Figure 201.—Toolmarks at the hub of the impeller.

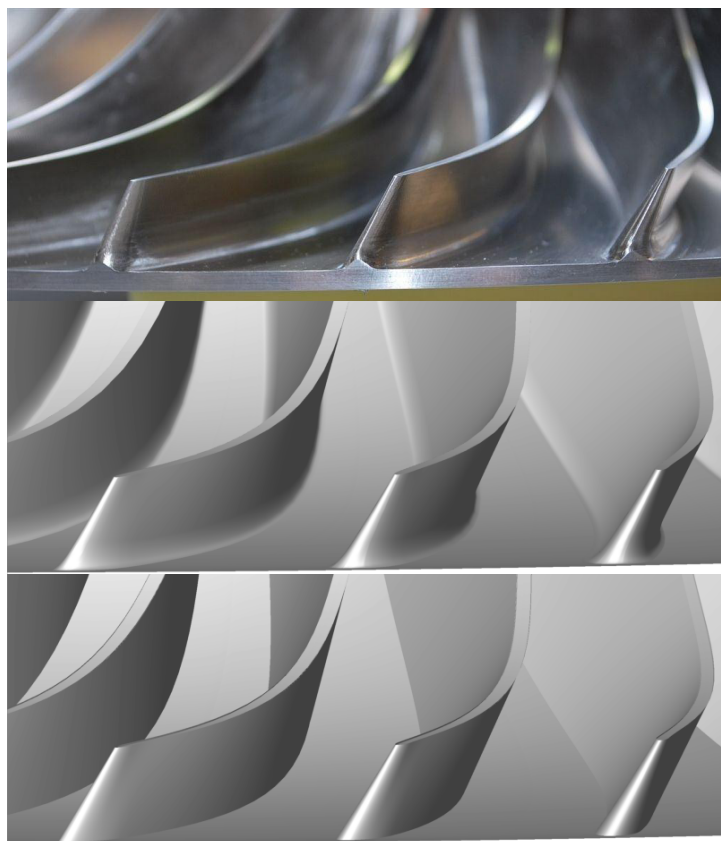


Figure 202.—Impeller fillets at trailing edge, actual geometry (top), CFD geometry with fillets as computed in pre-test simulations (middle), CFD geometry with no fillets (bottom).

11.3 Revisiting Impeller With Vaneless Diffuser

Additional post-test CFD simulations were conducted for the impeller with a vaneless diffuser using UTCFD and the latest computational grids, as well as several turbulence models, with suppressed inlet. The intent was to further verify the pre-test predictions, and perform additional sensitivity analysis of this vaneless configuration. The performance of the impeller is presented using downstream stations at both the exit of the flow domain (at $R \sim 10$ in.), for comparison with the CC3 impeller in a vaneless diffuser configuration (presented in Figure 203), and at the location of the modular vane LE total pressure rakes for comparison with the impeller performance in the vaned configuration (presented in Figure 204).

The results presented in Figure 203, show small differences between pre-test predictions which were run using standard-day inlet condition, most notably a reduction in choke flow by about 2 percent. Note also that all turbulence models predict the last stable CFD computation at the lowest flow of about 9.5 lbm/s—in the CFD simulations for the stage, the variation in range between different turbulence models was more significant (see Figure 151).

The peak efficiency in pre-test predictions (computed at this location) was about 90.45 percent, whereas post-test CFD shows a variation from 90.7 to 89.7 percent—depending on the turbulence model that was used in the simulations. CC3 impeller is also shown for reference, with pre-test CFD predicting peak efficiency of 87.6 percent. Even the post-test CFD indicates that the HECC impeller has at least 2 pt better total-to-total adiabatic efficiency than the CC3 impeller.

The results shown in Figure 204 compare the post-test predictions for the performance of the HECC impeller with a vaneless diffuser to the performance of the impeller with a vaned diffuser, computed using the modular vane LE as downstream station. Only the results with the strain-rate based turbulence model are presented; results from unsteady simulations for the vaned diffuser, as well as the experimental data for the vaned diffuser are also included in the figure for reference. The results indicate that CFD predicts the performance of the impeller with a vaneless diffuser that is about 1 pt better than what steady CFD predicted for the vaned diffuser. Note that the additional drop from steady to unsteady simulation results in the vaned configuration (and ultimately, to data) is a result of impeller-diffuser interactions, absent in the vaneless configurations. A test with a vaneless configuration would allow these CFD predictions to be validated.

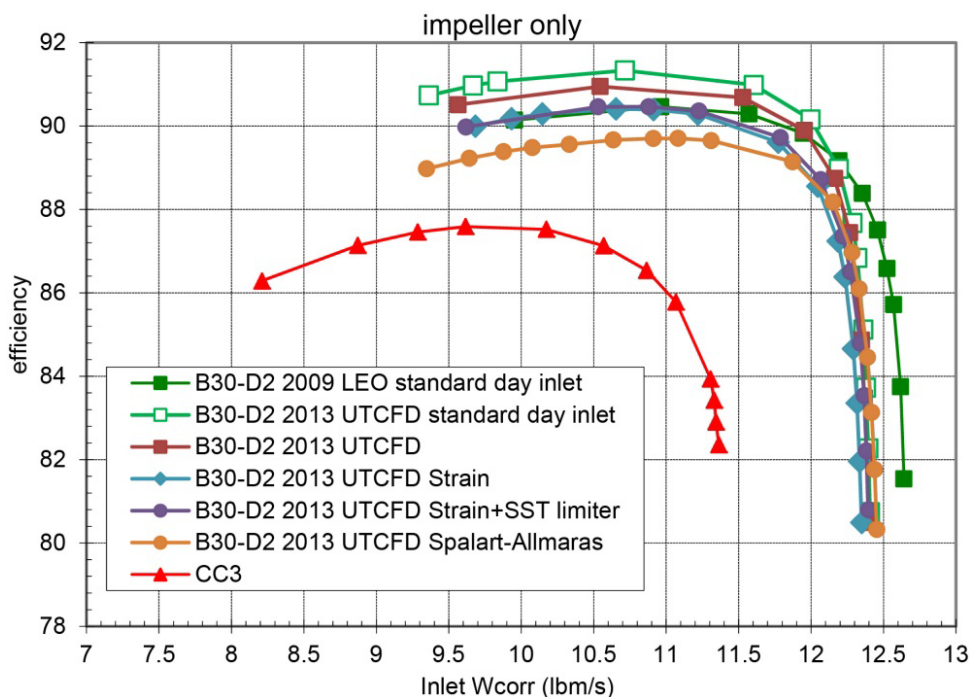


Figure 203.—Total-to-total adiabatic efficiency for the impeller with a vaneless diffuser computed using the exit of the computational domain at $R \sim 10$ in. as downstream station—at 100 percent N_c .

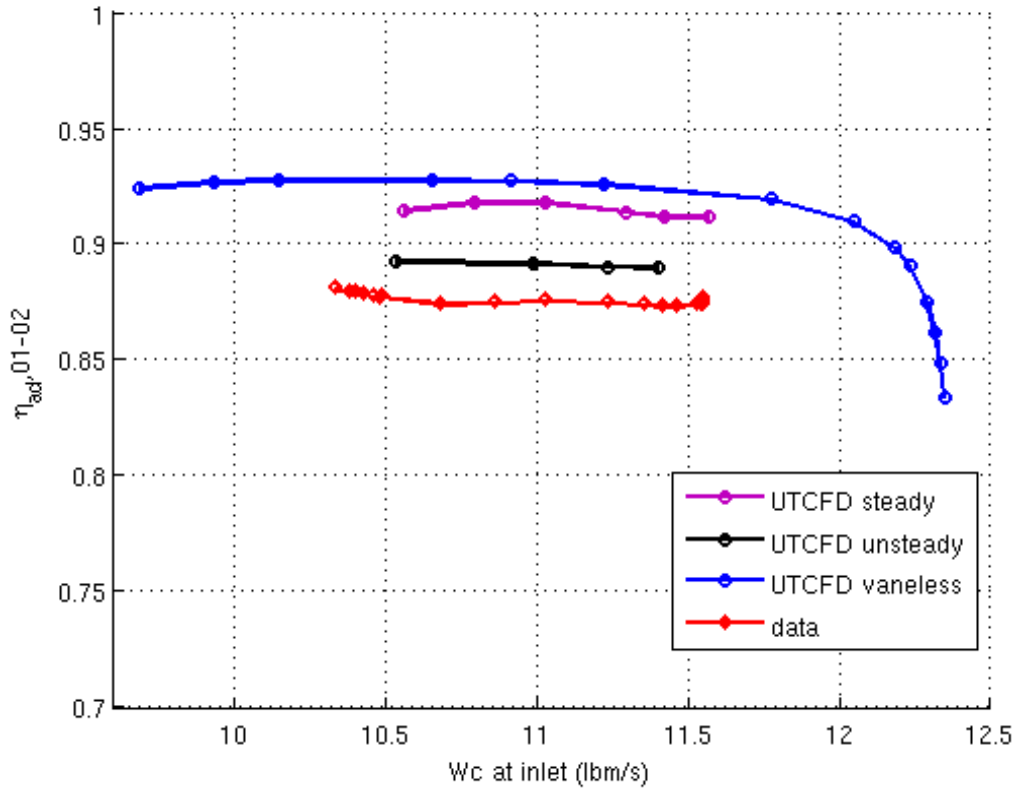


Figure 204.—Total-to-total adiabatic efficiency for the impeller with a vaneless diffuser at 100 percent N_c computed using the radius of modular vane LE ($R \sim 9.1$ in.) as downstream station—a comparison with computations for the vaned configuration (steady and unsteady), using strain rate based $k-\omega$ model. Data for the vaned configuration is also included for reference.

12.0 Conclusions and Recommendations

A new high-efficiency centrifugal compressor was designed with a very challenging reduction in radius ratio. The testing was successful, with no mechanical problems and the running clearances were achieved without impeller rubs. Overall, measured design-point total-to-total pressure ratio of 4.68, work factor of 0.81, and exit corrected flow rate of 3 lbm/s met the design target. Polytropic efficiency of 85.5 percent and stall margin of 7.5 percent were measured at design flow rate and speed.

The measured efficiency and stall margin were lower than pre-test CFD predictions by 2.4 and 4.5 pt, respectively. Initial impression from the experimental data indicated that the reason for the loss in the efficiency and stall margin can be attributed to the design shortfall in the impeller. However, detailed investigation of experimental data and post-test CFD simulations of higher fidelity than pre-test CFD, and in particular the unsteady CFD simulations and the assessment with a wider range of turbulence models, have indicated that the loss in efficiency is most likely due to the impact of unfavorable unsteady impeller/diffuser interactions induced by diffuser vanes, an impeller/diffuser corrected flow-rate mismatch (and associated incidence levels), and, potentially, flow separation in the radial-to-axial bend.

12.1 Test Impeller With a Vaneless Diffuser

A test with a vaneless diffuser should be conducted to determine the impeller performance, including peak efficiency and the stability margin. This test will also allow further evaluation of the accuracy of CFD predictions of the flow in the impeller, as well as to investigate whether the impeller design is root or tip sensitive (with respect to stall). A detailed hardware inspection of the impeller geometry, as well as the diffuser geometry (and the splitter vanes in particular) is also recommended to ensure that the CFD simulations are being conducted for the actual hardware used in the experiments. Polishing the impeller to mitigate the effect of toolmarks and geometry imperfections near hub could also be conducted in order to assess their impact on performance.

12.2 Redesign Diffuser to Minimize Interactions With Impeller

A redesign of the diffuser and the radial-to-axial bend is also recommended. The diffuser needs to be redesigned to eliminate the mismatching of the impeller and the diffuser, targeting a slightly higher flow capacity. Furthermore, diffuser vanes need to be adjusted to align the incidence angles, to optimize the splitter vane location (both radially and circumferentially), and to minimize the unsteady interactions with the impeller. The radial-to-axial bend needs to be redesigned to eliminate, or at least minimize, the flow separation at the inner wall, and its impact on the flow in the diffuser upstream.

12.3 Lessons Learned

Lessons were also learned in terms of CFD methodology and the importance of unsteady CFD simulations for centrifugal compressors was highlighted. Inconsistencies in the implementation of a widely used two-equation turbulence model were identified and corrections were recommended. It was also observed that unsteady simulations for centrifugal compressors require significantly longer integration times than what is current practice in industry.

Appendix A.—Tabulated Data for Key Figures

This appendix contains tabulated data for all key figures in the main body of the report.

TABLE A.1.—DATA FOR FIGURE 48
(a) NASA CC3

Inlet corrected flow rate, lbm/s	Total pressure ratio	Adiabatic efficiency, T-T
10.644	3.612	76.902
10.483	3.838	80.535
10.259	4.031	83.128
10.004	4.160	84.403
9.825	4.224	84.842
9.584	4.287	85.038
9.440	4.317	85.075
9.282	4.346	85.042
9.155	4.361	84.900
8.907	4.374	84.331

(b) Final Design

Inlet corrected flow rate, lbm/s	Total pressure ratio	Adiabatic efficiency, T-T
11.900	4.201	78.142
11.688	4.527	82.548
11.516	4.690	84.484
11.389	4.772	85.367
11.134	4.851	85.973
10.991	4.883	86.146
10.825	4.913	86.266
10.632	4.943	86.370
10.352	4.973	86.237

TABLE A.2.—DATA FOR FIGURE 49

(a) NASA CC3

Exit corrected flow rate, lbm/s	Adiabatic efficiency, T-S	Polytropic efficiency, T-S
3.691	74.792	78.732
3.427	78.773	82.249
3.197	81.649	84.762
3.032	83.099	86.024
2.934	83.631	86.493
2.822	83.948	86.780
2.752	84.072	86.908
2.690	84.122	86.961
2.647	84.022	86.889
2.565	83.518	86.481

(b) Final Design

Exit corrected flow rate, lbm/s	Adiabatic efficiency, T-S	Polytropic efficiency, T-S
3.627	76.599	80.653
3.315	81.250	84.668
3.159	83.304	86.413
3.071	84.248	87.214
2.961	84.940	87.801
2.904	85.154	87.988
2.841	85.323	88.135
2.769	85.486	88.284
2.672	85.415	88.234

TABLE A.3.—DATA FOR FIGURE 50 AND FIGURE 162

(a) Final design, ambient inlet PT 85% corrected speed

Inlet corrected flow rate, lbm/s	Total pressure ratio	Adiabatic efficiency, T-T
8.779212	2.524722	0.651273
8.518392	2.995345	0.784268
8.297230	3.250762	0.847025
8.165322	3.335761	0.865516
7.988421	3.377586	0.871377
7.831730	3.398297	0.872898
7.557555	3.418340	0.870975
7.391085	3.423677	0.868207

(b) Final design, ambient inlet PT 90% corrected speed

Inlet corrected flow rate, lbm/s	Total pressure ratio	Adiabatic efficiency, T-T
9.736385	2.857022	0.671541
9.557709	3.287869	0.773004
9.354516	3.540182	0.825128
9.220375	3.712960	0.859203
8.999178	3.797148	0.871403
8.830737	3.826520	0.873384
8.587759	3.851262	0.872540
8.245239	3.867098	0.868594

(c) Final design, ambient inlet PT 95% corrected speed

Inlet corrected flow rate, lbm/s	Total pressure ratio	Adiabatic efficiency, T-T
10.77434	3.32367	0.70647
10.58331	3.75262	0.78750
10.46443	3.92141	0.81649
10.32798	4.09291	0.84431
10.10822	4.26379	0.86917
10.03506	4.28506	0.87126
9.93704	4.30628	0.87270
9.61165	4.34822	0.87250
8.67725	4.38296	0.85923

(d) Final design, ambient inlet PT 100% corrected speed

Inlet corrected flow rate, lbm/s	Total pressure ratio	Adiabatic efficiency, T-T
11.79910	3.70414	0.70934
11.61221	4.253795	0.798939
11.52197	4.427337	0.823169
11.38212	4.687114	0.85811
11.27571	4.739542	0.861841
10.98969	4.826876	0.86775
10.69117	4.870505	0.86792
10.32661	4.883524	0.863023
9.443664	4.910956	0.852515

(e) Final design, ambient inlet PT 105% corrected speed

Inlet corrected flow rate, lbm/s	Total pressure ratio	Adiabatic efficiency, T-T
12.60795	3.98514	0.69524
12.52466	4.24517	0.73208
12.47524	4.50415	0.76644
12.39734	4.76087	0.79792
12.28437	5.10980	0.83763
11.99842	5.37300	0.85775
11.70288	5.46049	0.85932
11.17302	5.53529	0.85642

TABLE A.4.—DATA FOR FIGURE 118, FIGURE 119 AND FIGURE 120
 (a) Data

Inlet corrected flow rate, lbm/s	Total pressure ratio	Adiabatic efficiency, T-T	Polytropic efficiency, T-T
11.549	3.4105	63.4308	68.9871
11.550	3.6010	66.6904	71.9631
11.534	3.8022	70.0430	74.9746
11.551	3.8999	71.4983	76.2736
11.545	4.0034	73.1452	77.7260
11.531	4.0999	74.7648	79.1392
11.463	4.2035	76.3335	80.5039
11.417	4.2997	77.7126	81.6978
11.353	4.3945	78.9517	82.7674
11.235	4.5133	80.3405	83.9633
11.025	4.6152	81.5834	85.0235
10.862	4.6847	82.1689	85.5290
10.676	4.7581	82.5837	85.8947
10.483	4.8012	82.7716	86.0634
10.479	4.8017	82.7550	86.0501
10.459	4.8051	82.7766	86.0688
10.426	4.8151	82.7943	86.0869
10.400	4.8148	82.8013	86.0925
10.380	4.8236	82.7856	86.0829
10.333	4.8323	82.8254	86.1184

(b) Pre-test CFD LEO

Inlet corrected flow rate, lbm/s	Total pressure ratio	Adiabatic efficiency, T-T	Polytropic efficiency, T-T
11.900	4.201	78.142	81.989
11.688	4.527	82.548	85.768
11.516	4.690	84.484	87.406
11.389	4.772	85.367	88.150
11.134	4.851	85.973	88.662
10.991	4.883	86.146	88.813
10.825	4.913	86.266	88.919
10.632	4.943	86.370	89.017
10.352	4.973	86.237	88.916

TABLE A.5.—DATA FOR FIGURES FIGURE 121, FIGURE 122, FIGURE 123, FIGURE 124, FIGURE 125, AND FIGURE 126

(a) Pre-test CFD prediction

Inlet corrected flow rate, lbm/s	Adiabatic efficiency (T-T) for impeller, %	Total pressure ratio for impeller	Total temperature ratio	Pressure recovery in the diffuser	Pressure recovery in the diffuser and EGV	Total pressure loss from the diffuser to exit
11.900	88.626	4.904	1.642	0.364	0.517	14.096
11.688	90.194	5.064	1.646	0.521	0.640	10.409
11.516	89.961	5.082	1.650	0.606	0.723	7.490
11.389	90.615	5.154	1.652	0.634	0.742	7.213
11.134	91.668	5.274	1.656	0.635	0.734	7.828
10.991	90.574	5.212	1.658	0.675	0.775	6.136
10.825	91.782	5.329	1.660	0.653	0.741	7.661
10.632	91.868	5.360	1.663	0.661	0.741	7.627
10.352	92.654	5.467	1.667	0.646	0.718	8.931

(b) Data

Inlet corrected flow rate, lbm/s	Adiabatic efficiency (T-T) for impeller, %	Total pressure ratio for impeller	Total temperature ratio	Pressure recovery in the diffuser	Pressure recovery in the diffuser and EGV	Total pressure loss from the diffuser to exit
11.550	87.680	4.963	1.658	-0.200	0.044	29.807
11.550	87.590	4.962	1.659	-0.035	0.158	26.271
11.530	87.500	4.962	1.659	0.103	0.278	22.791
11.550	87.400	4.969	1.661	0.166	0.334	20.723
11.540	87.380	4.967	1.661	0.252	0.392	18.585
11.530	87.380	4.959	1.660	0.314	0.448	16.667
11.460	87.340	4.960	1.661	0.383	0.508	14.574
11.420	87.360	4.969	1.661	0.442	0.559	12.822
11.350	87.390	4.988	1.663	0.494	0.605	11.264
11.240	87.480	5.023	1.666	0.554	0.657	9.539
11.030	87.570	5.046	1.668	0.608	0.704	8.075
10.860	87.470	5.072	1.671	0.638	0.732	7.168
10.680	87.440	5.117	1.676	0.662	0.752	6.508
10.480	87.720	5.175	1.679	0.670	0.755	6.561
10.480	87.700	5.174	1.679	0.670	0.755	6.535
10.460	87.750	5.178	1.679	0.670	0.754	6.564
10.430	87.860	5.199	1.680	0.670	0.753	6.655
10.400	87.930	5.203	1.680	0.670	0.752	6.717
10.380	87.950	5.213	1.681	0.670	0.751	6.730
10.330	88.100	5.230	1.682	0.669	0.749	6.844

TABLE A.6.—DATA FOR FIGURE 127
 (a) Pre-test CFD prediction—Main vane on the hub

Radius (in.) at pressure side	Static pressure ratio, P/P0	Data, P/P0	Radius (in.) at suction side	Static pressure ratio, P/P0	Data, P/P0
9.030	3.965	3.649	9.000	3.737	3.719
9.102	3.821	3.722	9.016	3.464	3.434
9.182	3.908	3.545	9.068	3.131	3.048
9.233	3.580	3.559	9.361	2.804	2.796
9.277	3.625	3.544	9.615	3.566	3.236
9.317	4.001	3.670	10.076	4.161	3.317
9.621	4.255	4.033	10.642	4.472	4.013
10.115	4.452	4.179	11.277	4.563	4.300
10.625	4.567	4.298			
11.133	4.551	4.321			
11.277	4.563	4.327			

(b) Pre-test CFD prediction—Splitter vane on the hub

Radius (in.) at pressure side	Static pressure ratio, P/P0	Data, P/P0	Radius (in.) at suction side	Static pressure ratio, P/P0	Data, P/P0
9.706	4.110	3.769	9.701	4.087	3.859
9.772	4.152	3.758	9.719	3.986	3.850
9.850	4.153	3.676	9.792	4.085	3.784
9.906	4.160	3.603	10.110	4.296	3.954
9.948	4.117	3.137	10.613	4.445	4.197
10.070	4.249	3.315	11.271	4.588	4.323
10.070	4.249	3.315			
10.564	4.537	4.196			
11.140	4.584	4.313			

TABLE A.7.—DATA FOR FIGURE 128
 (a) Pre-test CFD prediction—Main vane on the shroud

Radius (in.) at pressure side	Static pressure ratio, P/P0	Data, P/P0	Radius (in.) at suction side	Static pressure ratio, P/P0	Data, P/P0
9.000	3.680	3.425	9.045	3.352	3.220
9.030	3.945	3.566	9.069	3.175	3.151
9.102	3.843	3.666	9.104	3.035	3.039
9.182	3.954	3.576	9.361	2.825	2.891
9.233	3.670	3.424	9.615	3.556	3.138
9.277	3.674	3.273	9.856	3.956	3.498
9.302	3.855	3.372	10.076	4.164	3.199
9.317	3.949	3.705	10.642	4.475	4.085
9.621	4.246	4.001	11.255	4.572	4.330
9.872	4.381	4.115			
10.116	4.444	4.187			
10.626	4.572	4.306			
11.134	4.581	4.335			
11.255	4.572	4.346			

(b) Pre-test CFD prediction—Splitter vane on the shroud

Radius (in.) at pressure side	Static pressure ratio, P/P0	Data, P/P0	Radius (in.) at suction side	Static pressure ratio, P/P0	Data, P/P0
9.706	4.167	3.918	9.701	4.111	3.777
9.772	4.222	3.930	9.719	3.909	3.769
9.850	4.203	3.836	9.792	4.087	3.830
9.906	4.188	2.879	10.110	4.294	4.019
9.948	4.090	2.916	10.613	4.454	4.204
10.071	4.243	3.430	11.247	4.609	4.344
10.071	4.243	3.430			
10.564	4.542	3.982			
11.123	4.605	4.334			

TABLE A.8.—DATA FOR FIGURE 129
Pre-test CFD prediction—Modular vane profile

Span	Total pressure ratio, Pt/P0	Data 1, Pt/P0	Data 2 Pt/P0
0.000	3.955	4.021	3.843
0.125	5.234	5.117	4.948
0.250	5.214	5.087	5.041
0.375	5.271	5.145	5.101
0.500	5.359	5.226	5.191
0.625	5.407	5.310	5.269
0.750	5.405	5.318	5.266
0.875	5.319	5.040	5.003
1.000	3.991	3.825	3.887

TABLE A.9.—DATA FOR FIGURE 130
Pre-test CFD prediction—EGV leading edge profile

Span	EGV 1 total pressure ratio, Pt/P0	EGV 2 total pressure ratio, Pt/P0	EGV 3 total pressure ratio, Pt/P0	Data 1, Pt/P0	Data 2 Pt/P0	Data 3 Pt/P0
0.000	4.697	4.723	4.714	4.422	4.429	4.411
0.249	4.942	4.851	4.909	4.538	4.504	4.608
0.503	5.013	4.920	4.943	4.639	4.569	4.662
0.749	5.037	4.989	5.017	4.714	4.715	4.814
1.000	4.748	4.754	4.760	4.494	N/A	4.443

TABLE A.10.—DATA FOR FIGURE 140, FIGURE 141, AND FIGURE 144
 (a) Final design, ambient inlet PT

Inlet corrected flow rate, lbm/s	Adiabatic efficiency, T-T
11.61221	0.79894
11.52197	0.82317
11.38212	0.85811
11.27571	0.86184
10.98969	0.86775
10.69117	0.86792
10.32661	0.86302

(b) Final design, suppressed inlet PT

Inlet corrected flow rate, lbm/s	Adiabatic efficiency, T-T
11.56969	0.79468
11.45293	0.82157
11.29539	0.85137
11.02834	0.86163
10.79493	0.86255
10.55666	0.86094
9.97914	0.85244

(c) Final design, suppressed inlet PT 0.005 in. step on shroud

Inlet corrected flow rate, lbm/s	Adiabatic efficiency, T-T
11.40966	0.78491
11.22944	0.81368
11.05681	0.83998
10.91876	0.84557
10.59208	0.84661
10.04194	0.84735

(d) Final design, suppressed inlet PT—3° rotated splitter vane

Inlet corrected flow rate, lbm/s	Adiabatic efficiency, T-T
11.547919	0.787881
11.268880	0.827123
11.040149	0.850625
10.674633	0.857872
10.363791	0.858863

TABLE A.11.—DATA FOR FIGURE 145
(a) 3° restagger CFD—Main vane on the shroud

Radius (in.) at pressure side	Static pressure ratio, P/P0	Data P/P0	Radius (in.) at suction side	Static pressure ratio, P/P0	Data P/P0
9.000	3.426	3.425	9.040	3.256	3.220
9.024	3.584	3.566	9.076	3.088	3.151
9.102	3.703	3.666	9.108	2.935	3.039
9.194	3.746	3.576	9.354	2.926	2.891
9.245	3.640	3.424	9.607	3.482	3.138
9.258	3.611	3.273	9.860	3.811	3.498
9.278	3.756	3.372	10.109	3.454	3.199
9.322	3.936	3.705	10.609	4.217	4.085
9.601	4.184	4.001	11.262	4.317	4.330
9.861	4.233	4.115			
10.097	4.274	4.187			
10.610	4.362	4.306			
11.095	4.341	4.335			
11.262	4.317	4.346			

(b) 3° restagger CFD—Splitter vane on the shroud

Radius (in.) at pressure side	Static pressure ratio, P/P0	Data P/P0	Radius (in.) at suction side	Static pressure ratio, P/P0	Data P/P0
9.855	4.280	3.918	9.838	4.286	3.777
9.923	4.053	3.930	9.861	4.240	3.769
10.018	3.831	3.836	9.939	4.192	3.830
10.064	3.506	2.879	10.207	4.206	4.019
10.101	3.453	2.916	10.638	4.264	4.204
10.170	3.862	3.430	11.238	4.406	4.344
10.170	3.862	3.430			
10.678	4.300	3.982			
11.132	4.379	4.334			

TABLE A.12.—DATA FOR FIGURE 146
3° restagger CFD—Modular vane profile

Span	Total pressure ratio, Pt/P0	Data 1, Pt/P0	Data 2, Pt/P0
0.000	4.119	4.021	3.843
0.125	5.155	5.117	4.948
0.250	5.092	5.087	5.041
0.375	5.153	5.145	5.101
0.500	5.255	5.226	5.191
0.625	5.374	5.310	5.269
0.750	5.461	5.318	5.266
0.875	4.501	5.040	5.003
1.000	3.891	3.825	3.887

TABLE A.13.—DATA FOR FIGURE 147, FIGURE 148, FIGURE 149, AND FIGURE 150

(a) 3° restagger CFD

Inlet corrected flow rate, lbm/s	Adiabatic efficiency (T-T) for impeller, %	Total pressure ratio for impeller	Total temperature ratio	Pressure recovery in the diffuser and EGV
11.548	89.872	4.945	1.637	0.475
11.269	90.009	5.014	1.643	0.636
11.040	89.961	5.061	1.648	0.738
10.675	90.016	5.123	1.653	0.765

(b) Data

Inlet corrected flow rate, lbm/s	Adiabatic efficiency (T-T) for impeller, %	Total pressure ratio for impeller	Total temperature ratio	Pressure recovery in the diffuser	Pressure recovery in the diffuser and EGV	Total pressure loss from the diffuser to exit
11.550	87.680	4.963	1.658	-0.200	0.044	29.807
11.550	87.590	4.962	1.659	-0.035	0.158	26.271
11.530	87.500	4.962	1.659	0.103	0.278	22.791
11.550	87.400	4.969	1.661	0.166	0.334	20.723
11.540	87.380	4.967	1.661	0.252	0.392	18.585
11.530	87.380	4.959	1.660	0.314	0.448	16.667
11.460	87.340	4.960	1.661	0.383	0.508	14.574
11.420	87.360	4.969	1.661	0.442	0.559	12.822
11.350	87.390	4.988	1.663	0.494	0.605	11.264
11.240	87.480	5.023	1.666	0.554	0.657	9.539
11.030	87.570	5.046	1.668	0.608	0.704	8.075
10.860	87.470	5.072	1.671	0.638	0.732	7.168
10.680	87.440	5.117	1.676	0.662	0.752	6.508
10.480	87.720	5.175	1.679	0.670	0.755	6.561
10.480	87.700	5.174	1.679	0.670	0.755	6.535
10.460	87.750	5.178	1.679	0.670	0.754	6.564
10.430	87.860	5.199	1.680	0.670	0.753	6.655
10.400	87.930	5.203	1.680	0.670	0.752	6.717
10.380	87.950	5.213	1.681	0.670	0.751	6.730
10.330	88.100	5.230	1.682	0.669	0.749	6.844

TABLE A.14.—DATA FOR FIGURE 151

(a) Data

Inlet corrected flow rate, lbm/s	Adiabatic efficiency, T-T
11.463	0.763335
11.417	0.777126
11.353	0.789517
11.235	0.803405
11.025	0.815834
10.862	0.821689
10.676	0.825837
10.483	0.827716
10.479	0.827550
10.459	0.827766
10.426	0.827943
10.400	0.828013
10.380	0.827856
10.333	0.828254

(c) $k-\omega$ strain based production

Inlet corrected flow rate, lbm/s	Adiabatic efficiency, T-T
11.59117	0.771703
11.27045	0.840295
11.13124	0.848123
10.70478	0.849938
10.27134	0.847475

(d) $k-\omega$ strain based production + SST limiter

Inlet corrected flow rate, lbm/s	Adiabatic efficiency, T-T
11.58326	0.773132
11.28129	0.828448
11.16954	0.837636
11.08792	0.842632
10.80895	0.840867
9.85114	0.825042

(b) $k-\omega$ vorticity based production

Inlet corrected flow rate, lbm/s	Adiabatic efficiency, T-T
11.56969	0.794677
11.45293	0.821567
11.29539	0.851369
11.02834	0.861634
10.79493	0.862548
10.55666	0.860944
9.979137	0.852442

(e) Spalart-Allmaras

Inlet corrected flow rate, lbm/s	Adiabatic efficiency, T-T
11.01461	0.83844
11.29218	0.82611
11.56999	0.76935

TABLE A.15.—DATA FOR FIGURE 154, FIGURE 155, FIGURE 156, AND FIGURE 157

(a) Data

Inlet corrected flow rate, lbm/s	Adiabatic efficiency, T-T	Total temperature ratio	Total pressure ratio
11.463	0.763335	1.661	4.203
11.417	0.777126	1.661	4.300
11.353	0.789517	1.663	4.395
11.235	0.803405	1.666	4.513
11.025	0.815834	1.668	4.615
10.862	0.821689	1.671	4.685
10.676	0.825837	1.676	4.758
10.483	0.827716	1.679	4.801
10.479	0.827550	1.679	4.802
10.459	0.827766	1.679	4.805
10.426	0.827943	1.680	4.815
10.400	0.828013	1.680	4.815
10.380	0.827856	1.681	4.824
10.333	0.828254	1.682	4.832

(b) $k-\omega$ vorticity based production steady

Inlet corrected flow rate, lbm/s	Adiabatic efficiency, T-T
11.56969	0.794677
11.45293	0.821567
11.29539	0.851369
11.02834	0.861634
10.79493	0.862548
10.55666	0.860944
9.979137	0.852442

(c) $k-\omega$ vorticity based production unsteady (Figure 154)

Inlet corrected flow rate, lbm/s	Adiabatic efficiency, T-T
10.5337	0.853318
10.70862	0.852867
10.99281	0.850678
11.22635	0.836379
11.59507	0.780446

(d) $k-\omega$ strain based production steady (Figure 155, Figure 156, and Figure 157)

Inlet corrected flow rate, lbm/s	Adiabatic efficiency, T-T	Total temperature ratio	Total pressure ratio
11.59117	0.771703	1.637394	4.107385
11.27045	0.840295	1.643757	4.604671
11.13124	0.848123	1.646314	4.681182
10.70478	0.849938	1.654173	4.765585
10.27134	0.847475	1.660918	4.810131

(e) $k-\omega$ strain based production unsteady (Figure 155, Figure 156, and Figure 157)

Inlet corrected flow rate, lbm/s	Adiabatic efficiency, T-T	Total temperature ratio	Total pressure ratio
10.53224	0.83936	1.66676	4.805131
10.98705	0.830996	1.659259	4.677855
11.23967	0.802945	1.655152	4.449394
11.39765	0.775579	1.652434	4.246479

TABLE A.16.—DATA FOR FIGURE 163
(a) Final design, suppressed inlet PT—85% corrected speed

Inlet corrected flow rate, lbm/s	Total pressure ratio	Adiabatic efficiency, T-T
8.75695	2.52517	0.64951
8.48008	2.99372	0.78122
8.25613	3.24982	0.84337
8.09212	3.33485	0.86141
7.86327	3.37657	0.86619
6.84376	3.41113	0.85141

(b) Final design, suppressed inlet PT—90% corrected speed

Inlet corrected flow rate, lbm/s	Total pressure ratio	Adiabatic efficiency, T-T
9.70968	2.85632	0.66949
9.51709	3.28569	0.77008
9.30714	3.53918	0.82238
9.16235	3.71156	0.85568
8.87899	3.79611	0.86653
8.65008	3.82513	0.86746
8.25806	3.84853	0.86315

(c) Final design, suppressed inlet PT—95% corrected speed

Inlet corrected flow rate, lbm/s	Total pressure ratio	Adiabatic efficiency, T-T
10.74181	3.32202	0.70444
10.53600	3.75109	0.78513
10.41352	3.91975	0.81385
10.28226	4.09183	0.84181
9.99908	4.26274	0.86504
9.90023	4.28393	0.86645
9.76470	4.30496	0.86700
9.28331	4.34539	0.86396

(d) Final design, suppressed inlet PT—100% corrected speed

Inlet corrected flow rate, lbm/s	Total pressure ratio	Adiabatic efficiency, T-T
11.76634	3.702712	0.707372
11.56969	4.234643	0.794677
11.45293	4.434639	0.821567
11.29539	4.659307	0.851369
11.02834	4.781854	0.861634
10.79493	4.825334	0.862548
10.55666	4.846216	0.860944
9.979137	4.866234	0.852442

(e) Final design, suppressed inlet PT—105% corrected speed

Inlet corrected flow rate, lbm/s	Total pressure ratio	Adiabatic efficiency, T-T
12.548117	3.984351	0.693251
12.468876	4.245480	0.730021
12.412487	4.503318	0.764088
12.333751	4.760130	0.795408
12.191405	5.109489	0.834787
11.810231	5.372682	0.853115
11.436181	5.459034	0.853703
10.726190	5.540816	0.849078

TABLE A.17.—DATA FOR FIGURE 164

(a) Final design, suppressed inlet PT—85% corrected speed unsteady

Inlet corrected flow rate, lbm/s	Total pressure ratio	Adiabatic efficiency, T-T
8.63081	2.6613	0.67974
8.51312	3.004227	0.77527
8.206323	3.210927	0.82406
7.915344	3.284766	0.83836
7.574836	3.357493	0.85072

(b) Final design, suppressed inlet PT—90% corrected speed unsteady

Inlet corrected flow rate, lbm/s	Total pressure ratio	Adiabatic efficiency, T-T
9.66011	2.863736	0.66201
9.29598	3.555927	0.81325
9.18111	3.614036	0.82231
8.97425	3.720712	0.83892
8.562743	3.829934	0.85279

(c) Final design, suppressed inlet PT—95% corrected speed unsteady

Inlet corrected flow rate, lbm/s	Total pressure ratio	Adiabatic efficiency, T-T
10.65084	3.348327	0.69851
10.37123	3.934118	0.80540
10.17821	4.107355	0.83232
9.70624	4.278764	0.85110

(d) Final design, suppressed inlet PT—100% corrected speed unsteady

Inlet corrected flow rate, lbm/s	Total pressure ratio	Adiabatic efficiency, T-T
10.53224	4.805131	0.83936
10.98705	4.677855	0.830996
11.23967	4.449394	0.802945
11.39765	4.246479	0.775579

(e) Final design, suppressed inlet PT—105% corrected speed unsteady

Inlet corrected flow rate, lbm/s	Total pressure ratio	Adiabatic efficiency, T-T
12.47317	4.355273	0.72680
12.2956	4.790427	0.78144
12.20139	4.896855	0.79327
11.96137	5.096011	0.81434
11.67459	5.204656	0.82379

TABLE A.18.—DATA FOR FIGURE 187

(a) Pre-test CFD LEO

(b) Post-test Steady CFD UTCFD

(c) Post-test unsteady CFD UTCFD

Inlet corrected flow rate, lbm/s	Adiabatic efficiency (T-T) for impeller %	Inlet corrected flow rate, lbm/s	Adiabatic efficiency (T-T) for impeller %	Inlet corrected flow rate, lbm/s	Adiabatic efficiency (T-T) for impeller %
11.900	88.626	11.570	91.177	11.398	89.251
11.688	90.194	11.423	91.153	11.237	89.164
11.516	89.961	11.295	91.397	10.9867	89.019
11.389	90.615	11.028	91.790	10.5294	88.955
11.134	91.668	10.795	91.793		
10.991	90.574	10.557	91.438		
10.825	91.782				
10.632	91.868				
10.352	92.654				

(d) Data

Inlet corrected flow rate, lbm/s	Adiabatic efficiency (T-T) for impeller %	Inlet corrected flow rate, lbm/s	Adiabatic efficiency (T-T) for impeller %
11.550	87.680	10.680	87.440
11.550	87.590	10.480	87.720
11.530	87.500	10.480	87.700
11.550	87.400	10.460	87.750
11.540	87.380	10.430	87.860
11.530	87.380	10.400	87.930
11.460	87.340	10.380	87.950
11.420	87.360	10.330	88.100
11.350	87.390		
11.240	87.480		
11.030	87.570		
10.860	87.470		

TABLE A.19.—DATA FOR FIGURE 189

(a) 3° restagger CFD

(b) Post-test Steady CFD UTCFD

Inlet corrected flow rate, lbm/s	Adiabatic efficiency (T-T) for impeller, %	Inlet corrected flow rate, lbm/s	Adiabatic efficiency (T-T) for impeller, %
11.548	89.872	11.570	91.177
11.269	90.009	11.423	91.153
11.040	89.961	11.295	91.397
10.675	90.016	11.028	91.790
		10.795	91.793
		10.557	91.438

(c) Data

Inlet corrected flow rate, lbm/s	Adiabatic efficiency (T-T) for impeller, %	Inlet corrected flow rate, lbm/s	Adiabatic efficiency (T-T) for impeller, %
11.550	87.680	10.680	87.440
11.550	87.590	10.480	87.720
11.530	87.500	10.480	87.700
11.550	87.400	10.460	87.750
11.540	87.380	10.430	87.860
11.530	87.380	10.400	87.930
11.460	87.340	10.380	87.950
11.420	87.360	10.330	88.100
11.350	87.390		
11.240	87.480		
11.030	87.570		
10.860	87.470		

TABLE A.20.—DATA FOR FIGURE 195

Measure station	Hub s-coordinate	Hub CFD, Ps/P0	Hub data, Ps/P0	Shroud s-coordinate	Shroud CFD, Ps/P0	Shroud data, Ps/P0
1	3.052	4.339	4.323	3.092	4.434	4.409
2	3.202	4.363	4.356	3.228	4.481	4.456
3	3.352	4.331	4.352	3.364	4.418	4.419
4	3.500	4.355	4.344	3.500	4.356	4.350
5	3.611	4.437	4.412	3.611	4.441	4.415
6	3.721	4.474	4.438	3.721	4.476	4.447
7	3.831	4.515	4.466	3.831	4.514	4.478
8	3.940	4.534	4.498	3.941	4.534	4.506
9	3.997	4.540	4.508	4.000	4.541	4.508

TABLE A.21.—DATA FOR FIGURE 204

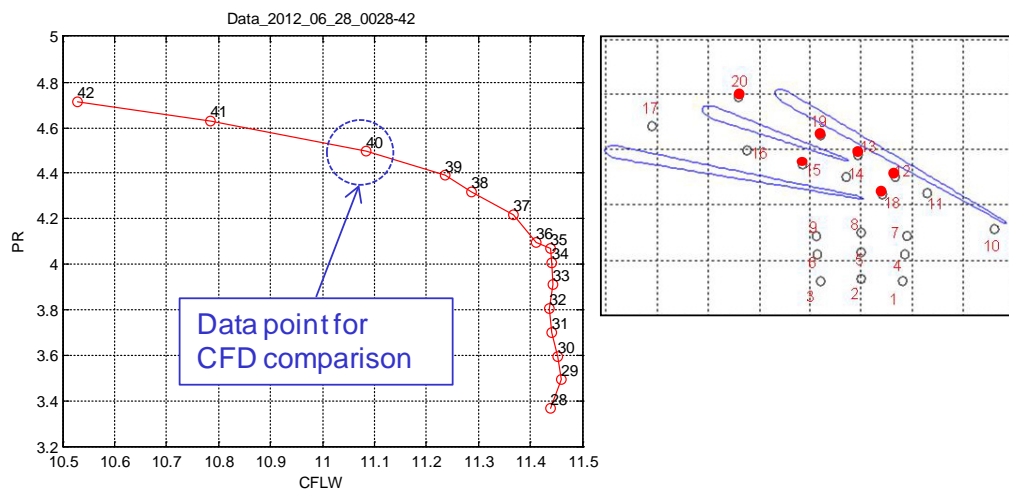
(a) Vaneless Steady CFD UTCFD	(b) Post-test Steady CFD UTCFD	(c) Post-test Unsteady CFD UTCFD
Inlet corrected flow rate, lbm/s	Adiabatic efficiency (T-T) for impeller, %	Inlet corrected flow rate, lbm/s
12.349	83.406	11.570
12.335	84.878	11.423
12.317	86.223	11.295
12.292	87.481	11.028
12.235	89.097	10.795
12.186	89.856	10.557
12.046	91.000	
11.773	91.955	
11.218	92.591	
10.913	92.734	
10.654	92.793	
10.145	92.787	
9.933	92.698	
9.684	92.415	

Appendix B.—High-Response Data and Comparison to CFD

This appendix discusses the processing details of the high-speed pressure signals, comparison to static pressure taps, rotor phase-locked time dependence for range of compressor flows, and comparison to CFD at the design point.

Figure B.1 shows the location of each unsteady pressure transducer (red dots). As shown in the figure, two 100 percent N_c compressor speed lines were obtained for two arrangements of transducers. So-called “Data Set 1” was focused on unsteady pressures in the diffuser passages and “Data Set 2” was focused on the unsteady pressure at the impeller tip. For reference, the compressor design point is approximately where the CFD case was computed as shown in the figure (point 40—Data Set 1 and point 54—Data Set 2).

DATA SET 1



DATA SET 2

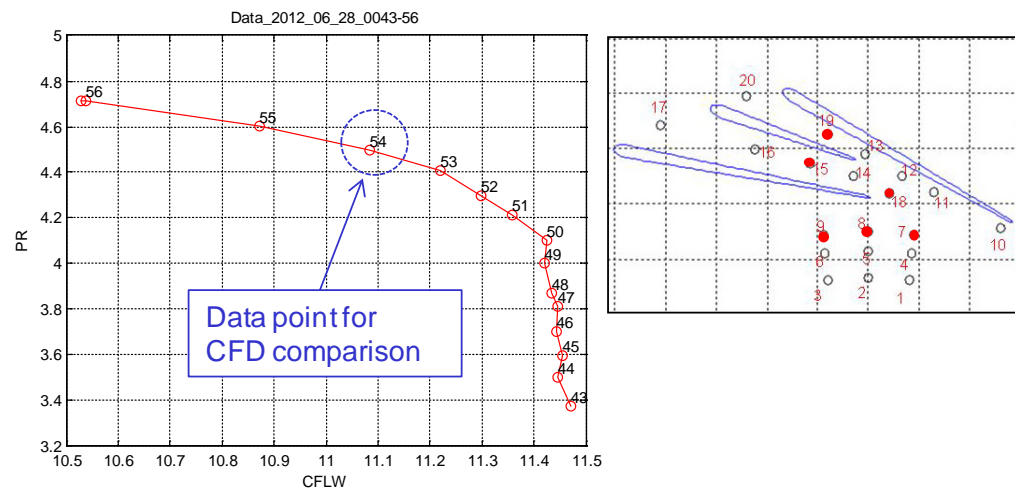


Figure B.1.—Location of unsteady pressure transducers

B.1 Time-Averaged Results

To verify the operating health of the pressure transducers, the time-averaged pressure was computed and compared with nearby static pressure taps. The record lengths of the high-speed pressure data are between 1.8 and 2.1 sec, which corresponds to several hundred rotor revolutions, which provide a repeatable mean value. The circumferential locations of the static taps and the unsteady pressure transducers are shown in Figure B.2. As can be seen, the circumferential locations of static taps and transducers are not coincident (the diffuser high-speed passage transducers are 180° from the diffuser passage static pressure taps and the impeller tip transducers are ~45° away from the closest impeller shroud static taps).

Figure B.3 compares the static tap pressures with the time-averaged, unsteady pressure transducers for the diffuser passages (from data set 1). The red (unsteady pressure) and blue (static tap) symbols in the schematic indicates the relative proximity of their locations. As can be seen in the figure, the static tap and the unsteady pressure compare very well. This agreement was true for all operating points. Since the static taps and unsteady pressures are at different circumferential locations, this agreement suggests the pressure to be uniform in the circumferential direction.

The impeller tip unsteady pressures are compared with the shroud static taps in the bottom of Figure B.4 (from data set 2). There is a significant difference of 4 to 6 psi between the static taps and the unsteady pressure transducers. The diffuser passage static taps and unsteady pressures (top of Figure B.4), like those from data set 1, are in good agreement, ruling out a transducer reference issue (all the unsteady pressure reference tubes were ganged together). Figure B.5 compares the impeller shroud static pressure distribution at two circumferential angles (124° and 304°, see Figure B.2), as well as the diffuser passage static taps, to the unsteady pressures transducers. This figure shows the disagreement between the impeller tip unsteady pressures and the static taps is not likely due to a circumferential variation since the impeller shroud static pressures that are 180° apart are nearly identical in value.

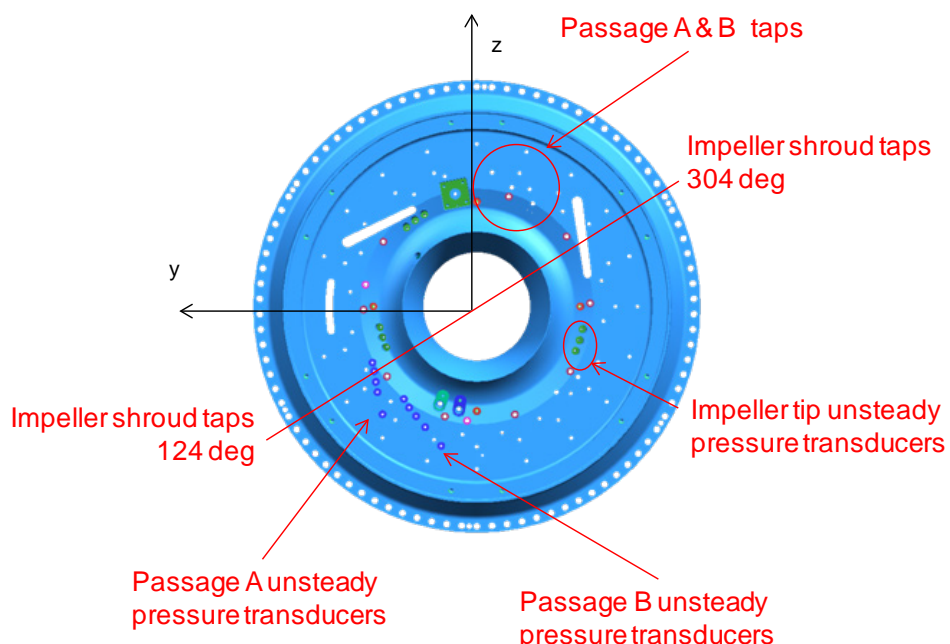


Figure B.2.—Circumferential location of static taps and unsteady pressure transducer (FWD looking AFT).

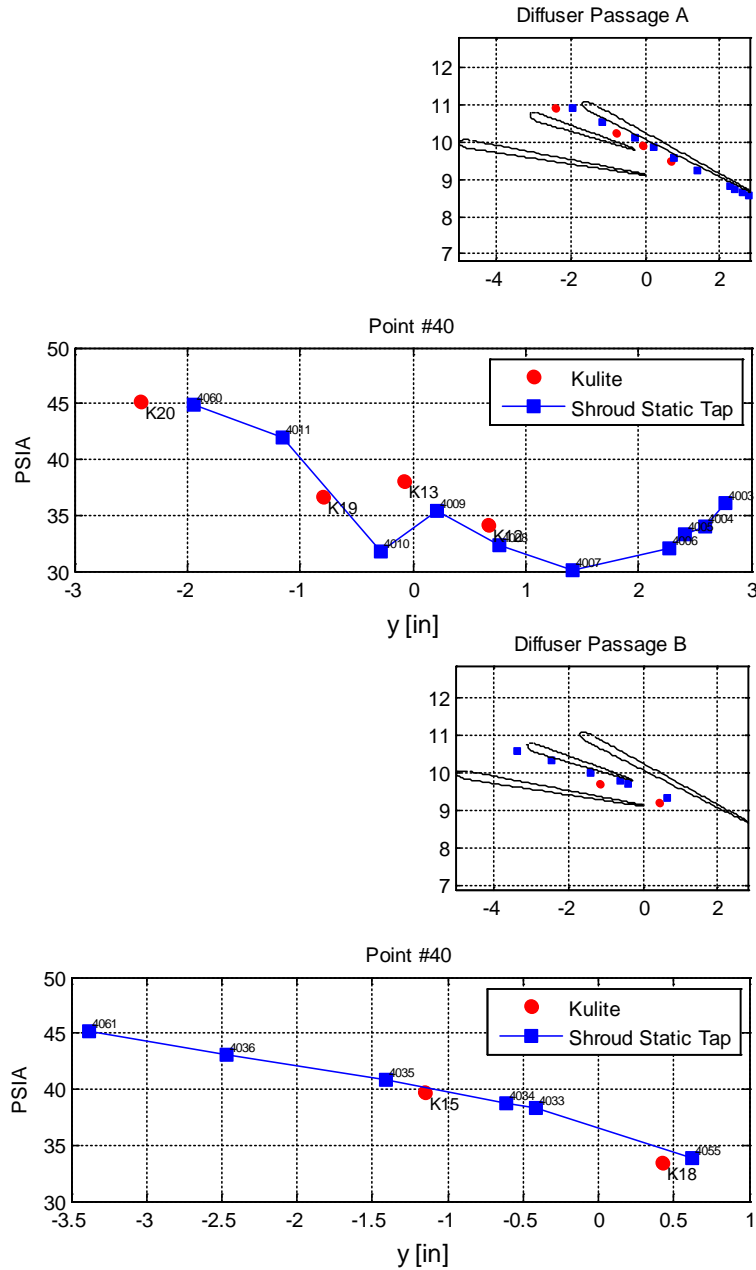


Figure B.3.—Comparison of static taps and unsteady pressure transducers in diffuser passages (at operating point no.40, 100 percent N_c).

A possible explanation for the low time-averaged values of the unsteady pressure transducers in the impeller tip region is as follows. The unsteady pressure transducers in the impeller tip region, as discussed in detailed below, are not flush mounted. The transducers are recessed in cavities connected to the flow via an orifice. This orifice/cavity arrangement creates a Helmholtz resonator with a resonant mode near the blade/splitter passage frequency (see modeled below). It is possible that the blade/splitter passage directly over the orifice entrains the oscillating orifice fluid away creating a net vacuum inside the transducer installation cavity. If this phenomenon is occurring, the effect on the dynamic response of the transducer is expected to be minimal, reducing the inertia of the oscillating fluid thereby changing the resonant mode of the orifice/cavity moderately (square-root dependence).

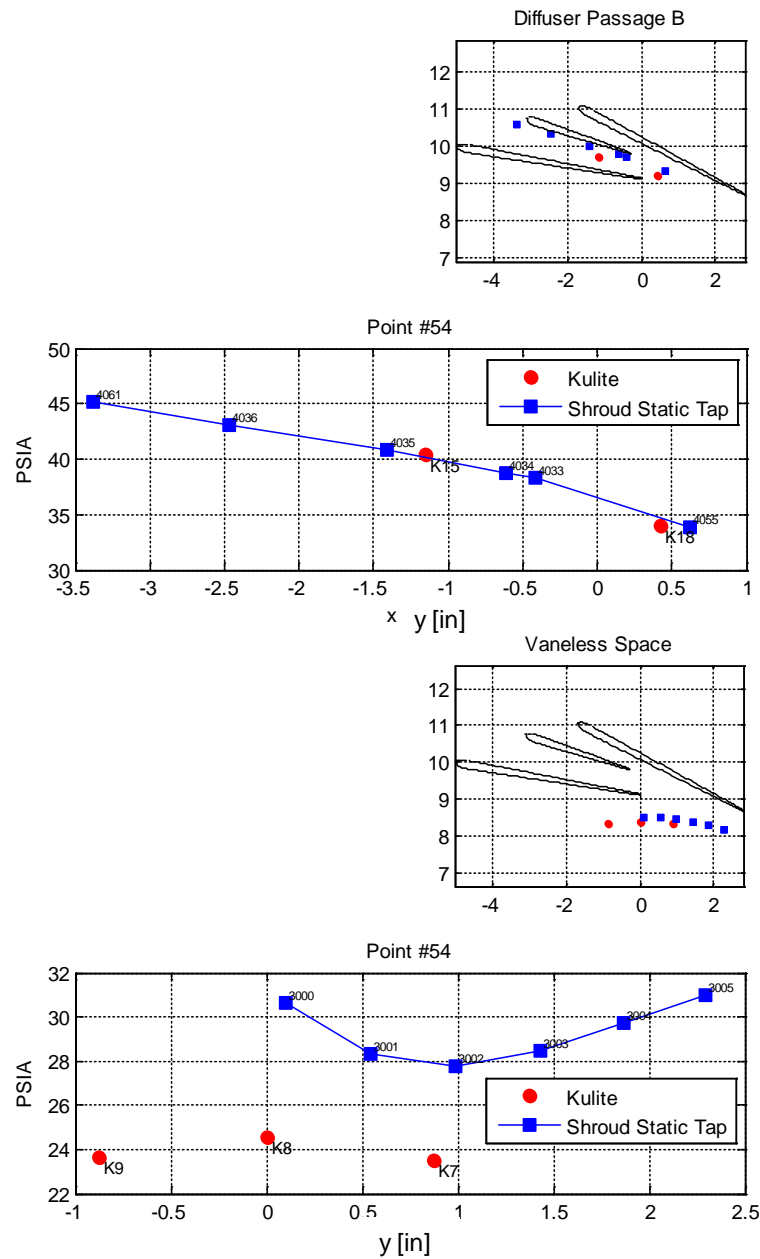


Figure B.4.—Comparison of static taps and unsteady pressure transducers in the impeller tip region (at operating point no.54, 100 percent N_c).

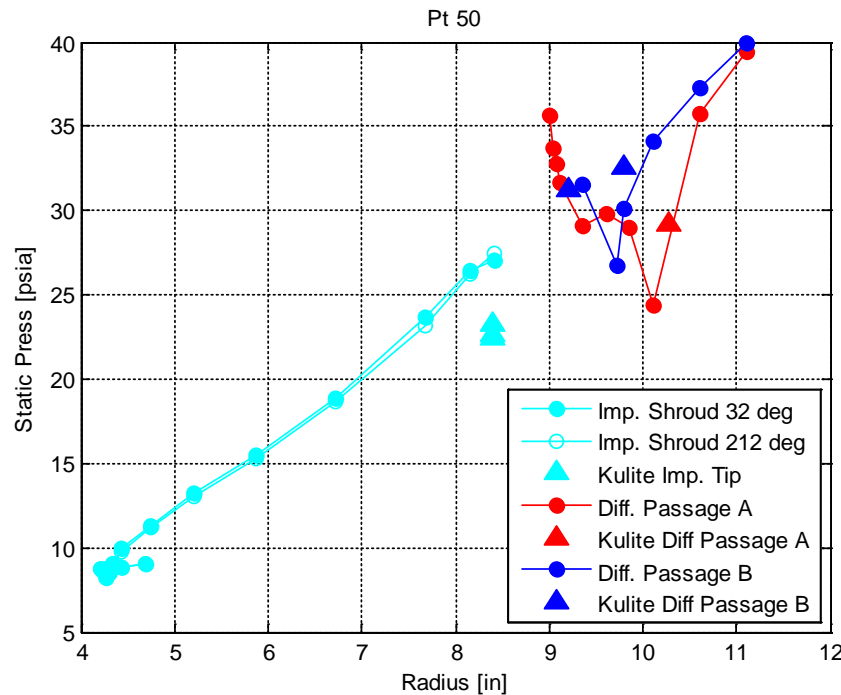


Figure B.5.—Comparison of impeller shroud static taps with unsteady pressure transducers (at operating point no.50, 100 percent N_c).

B.2 Phase-Locked Averaging

In order to understand the deterministic and random components of the high-speed pressure data, the signals were phase-locked averaged using a blade-passage signal that was simultaneously measured with the pressure signals. The result was the deterministic component and the difference between this component and the instantaneous signal was used to compute the random component (quantified by its RMS at each phase of blade position).

The top of Figure B.6 shows the blade-passage signal. The narrow-band (1 Hz frequency increment), ensemble-averaged power spectrum of this signal was computed to determine the blade-passage frequency. Together with the sample rate (2×10^5 Hz), the approximate time steps between blade passages was computed. This information was used to determine the vicinity of the next passage and a peak searching algorithm was used to locate the peak in the blade-passage signal. The blue symbols in the figure confirm that passage times were accurately located. The pressure signals were segmented accordingly and averaged to determine the phase-locked signals. The bottom of the figure shows a comparison of the phase-locked average with a snippet of the instantaneous signal. The parameter “Npassages” allowed phase-locked averaging to be performed over an arbitrary number of passages (Npassages=3 is shown in Figure B.6 with three phase-locked periods plotted). Setting Npassages=15 (number of rotor blades) allowed the full wheel phase-locked average to be computed to understand if there were any local blade imperfections or other once per revolution variations (none were observed).

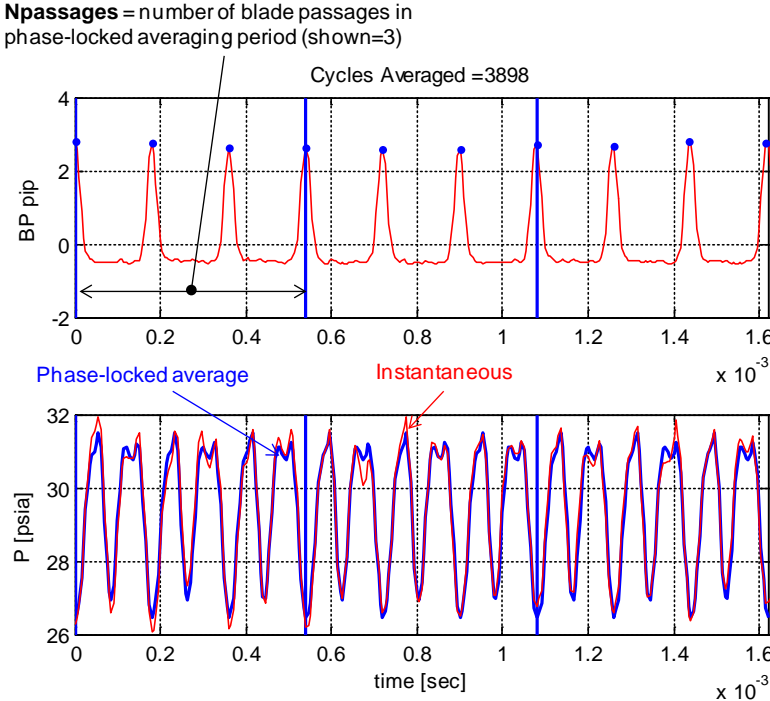


Figure B.6.—Phase-locked averaging approach.

Figure B.7 shows example phase-locked pressure signal from data set 1, point 43 (Npassage=3, one phase-locked period shown). The vertical blue lines correspond to one period of blade passage). In addition to the phase-locked, deterministic component, every segment of the instantaneous signal is shown (blue lines) which gives a clear visualization of the randomness in the signals. As each time step in the segment, the RMS can be computed, resulting in a RMS value as a function of blade passage time or blade phase. The computed RMS signal is shown in the figure (cyan lines) as ± 2 RMS. In addition, the red-dashed lines show the maximum excursion from the phase-locked average signal that occurred in the time record.

For the transducer at the impeller tip (no.7), the signal is very deterministic and the randomness is qualitatively symmetric about average and the ± 2 RMS bounds contain most of the signal (normal or Gaussian-like randomness). In the diffuser passage, the randomness is very asymmetric, showing large excursion compared with the RMS bounds on the high side of the signal.

Figure B.8(a) to (i) give the phase-locked results from the nine transducer locations over a range of compressor flows. Each figure corresponds to one pressure transducer whose location is indicated in the schematic in the upper right of each figure. Results for four operating points across the speed line are given in each figure from deep choke (point A), stall onset (point B), design point (point C) and near stall (point D). The phase-locked averaged pressure (P_{PLA}) ordinate is the fractional variation from the time-averaged pressure (P_{TA}). The time-averaged pressure value is listed in each plot. The abscissa is the time normalized by the blade-passage time. Also shown is the corresponding Fourier components of the phase-locked averaged signal found by:

$$P_n = \frac{1}{T} \int_0^T P_{PLA} e^{-in2\pi f_{BP} t} dt$$

where f_{BP} is the blade-passage frequency.

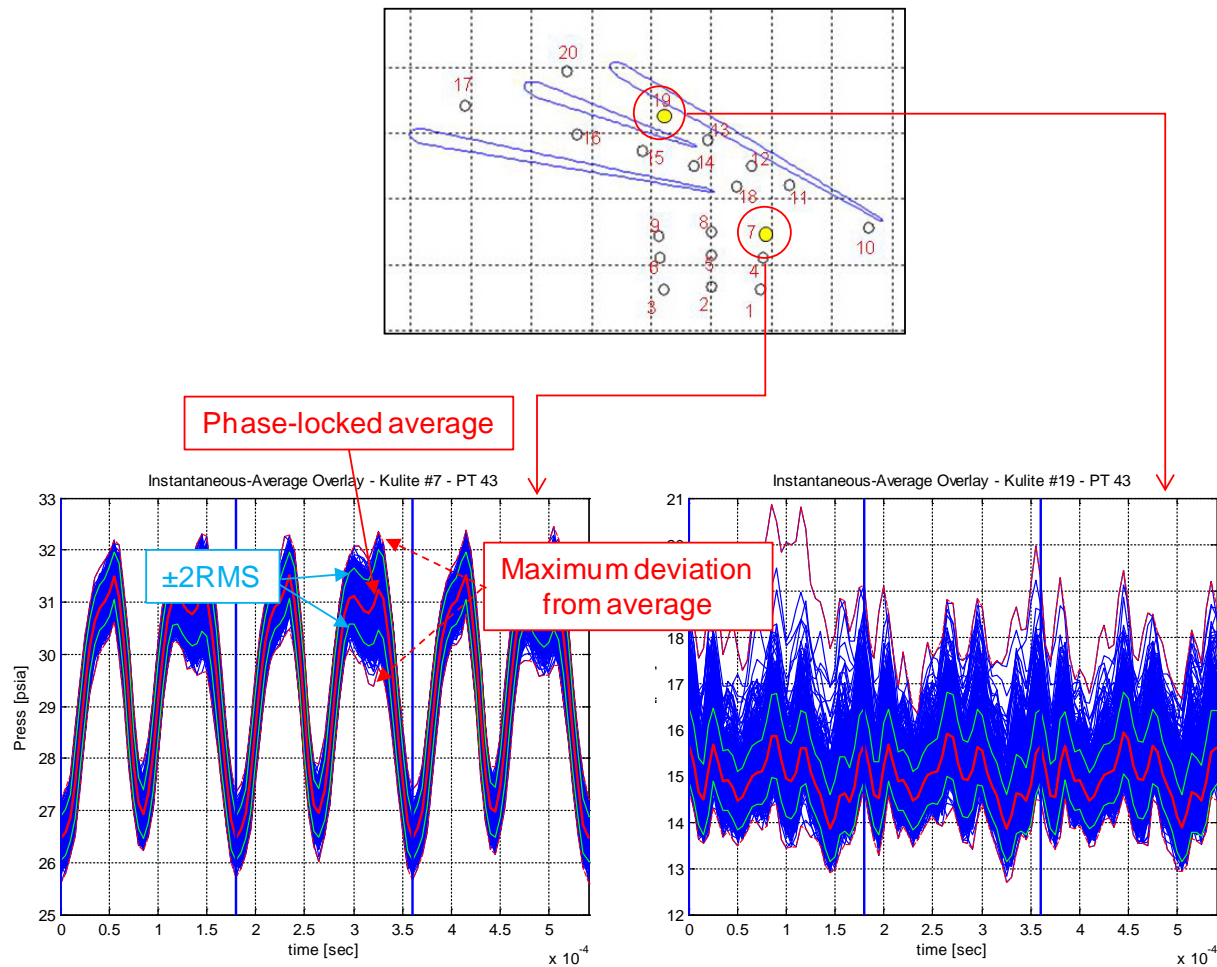


Figure B.7.—Example phase-locked unsteady pressure with random component.

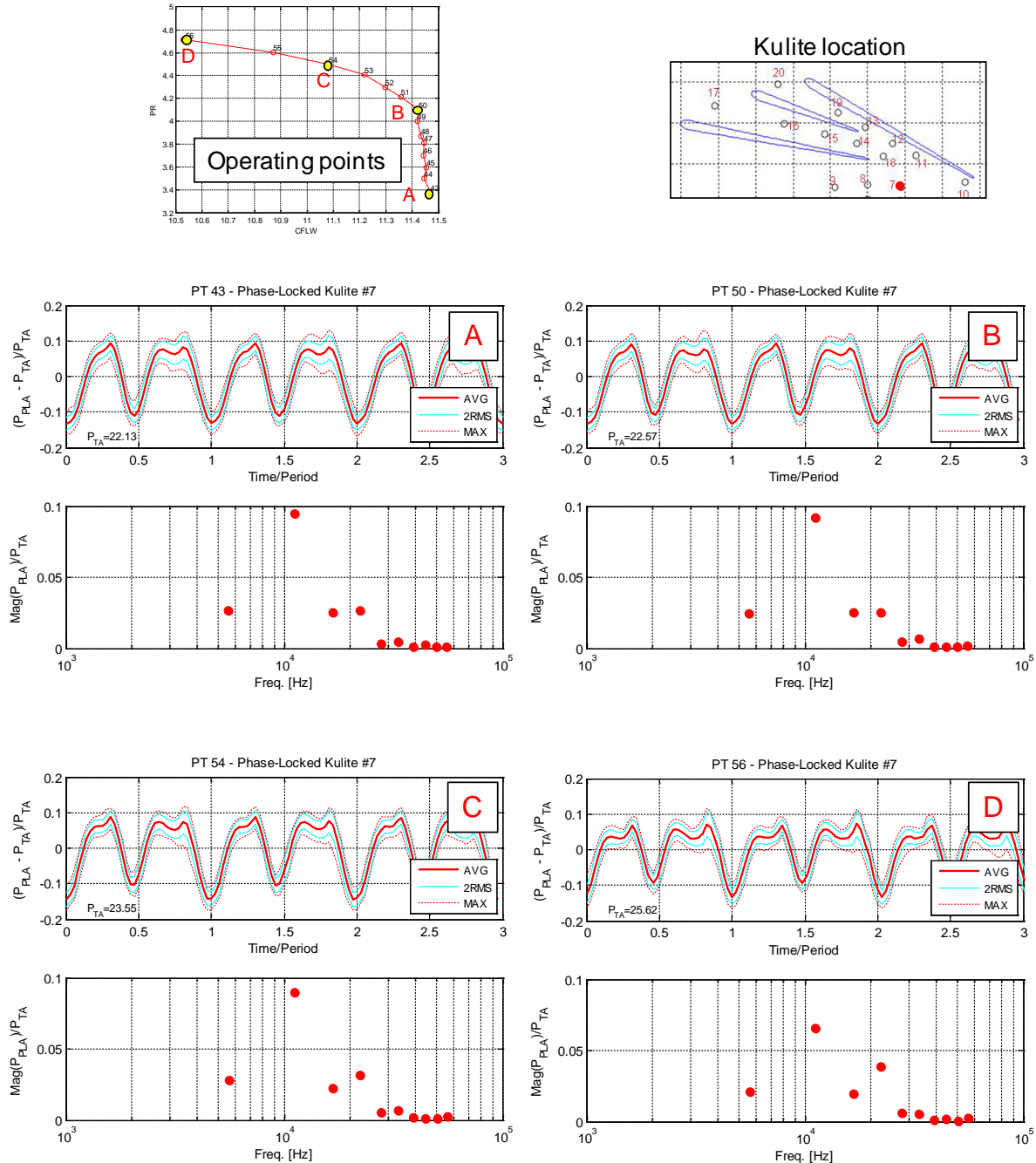


Figure B.8.—(a) Pressure transducer no.7 (operating points 43, 50, 54, and 56; 100 percent N_c).

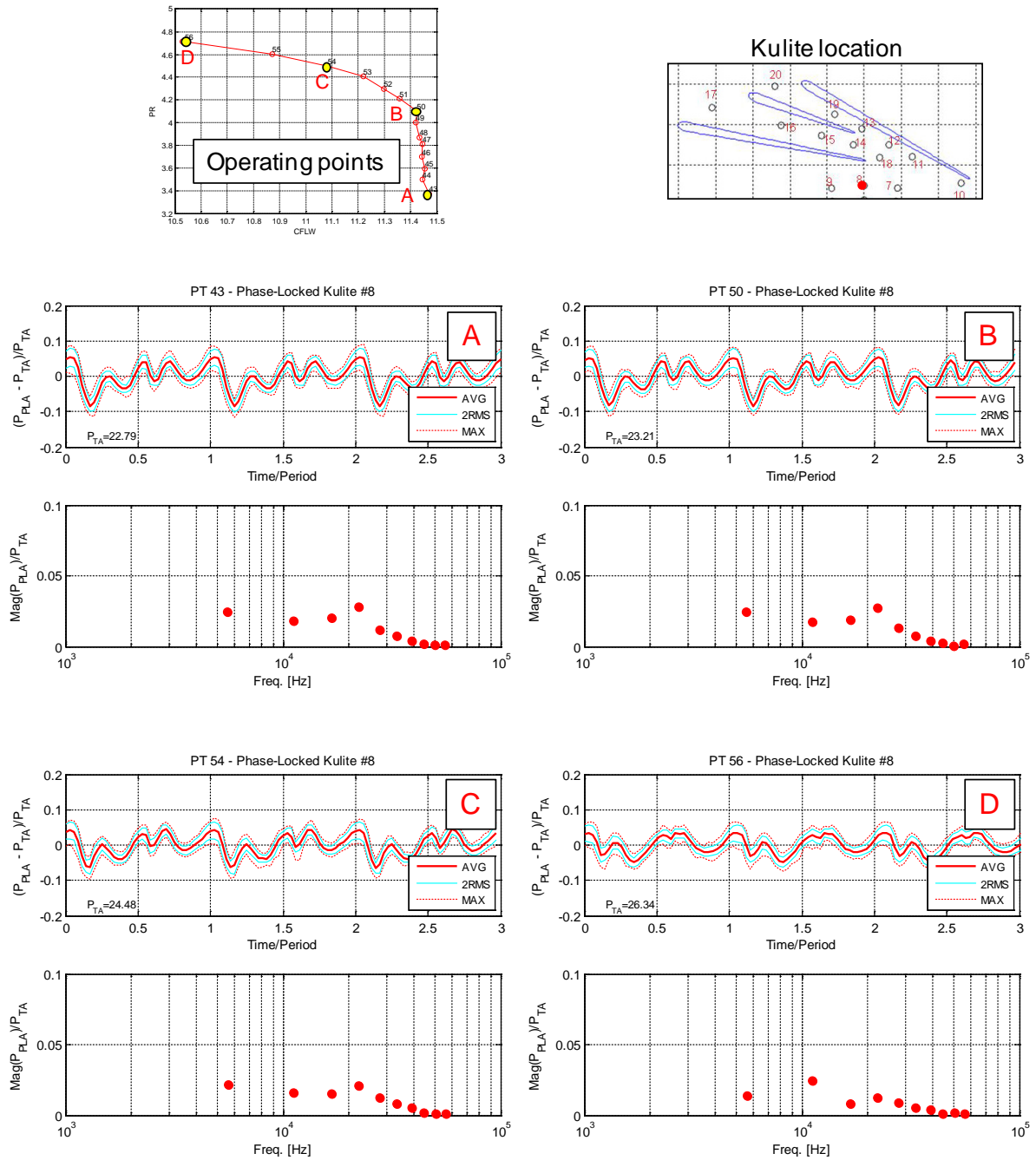


Figure B.8.—(b) Pressure transducer no.8 (operating points nos. 43, 50, 54, and 56; 100 percent Nc).

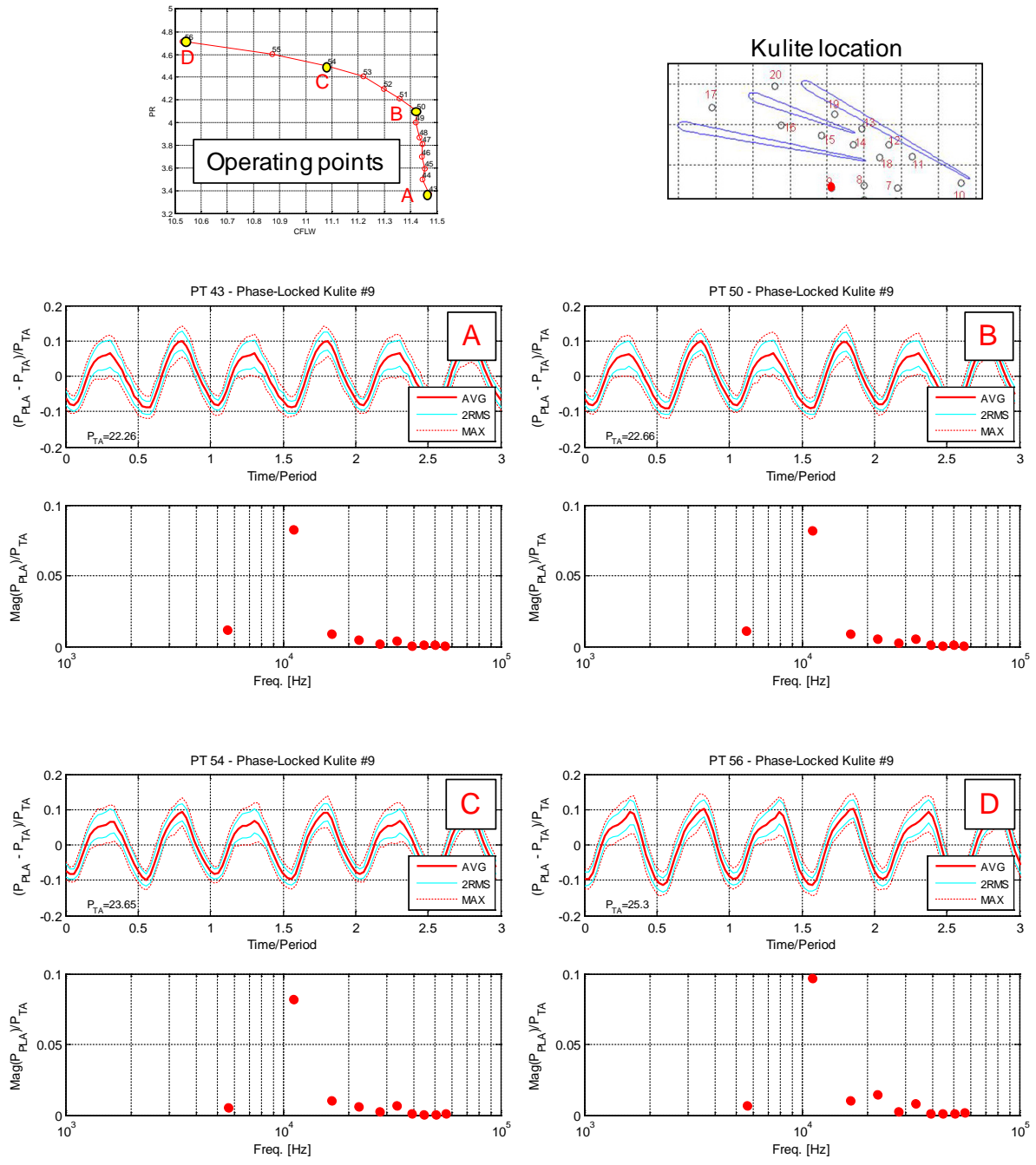


Figure B.8.—(c) Pressure transducer no. 9 (operating points nos. 43, 50, 54, and 56; 100 percent N_c).

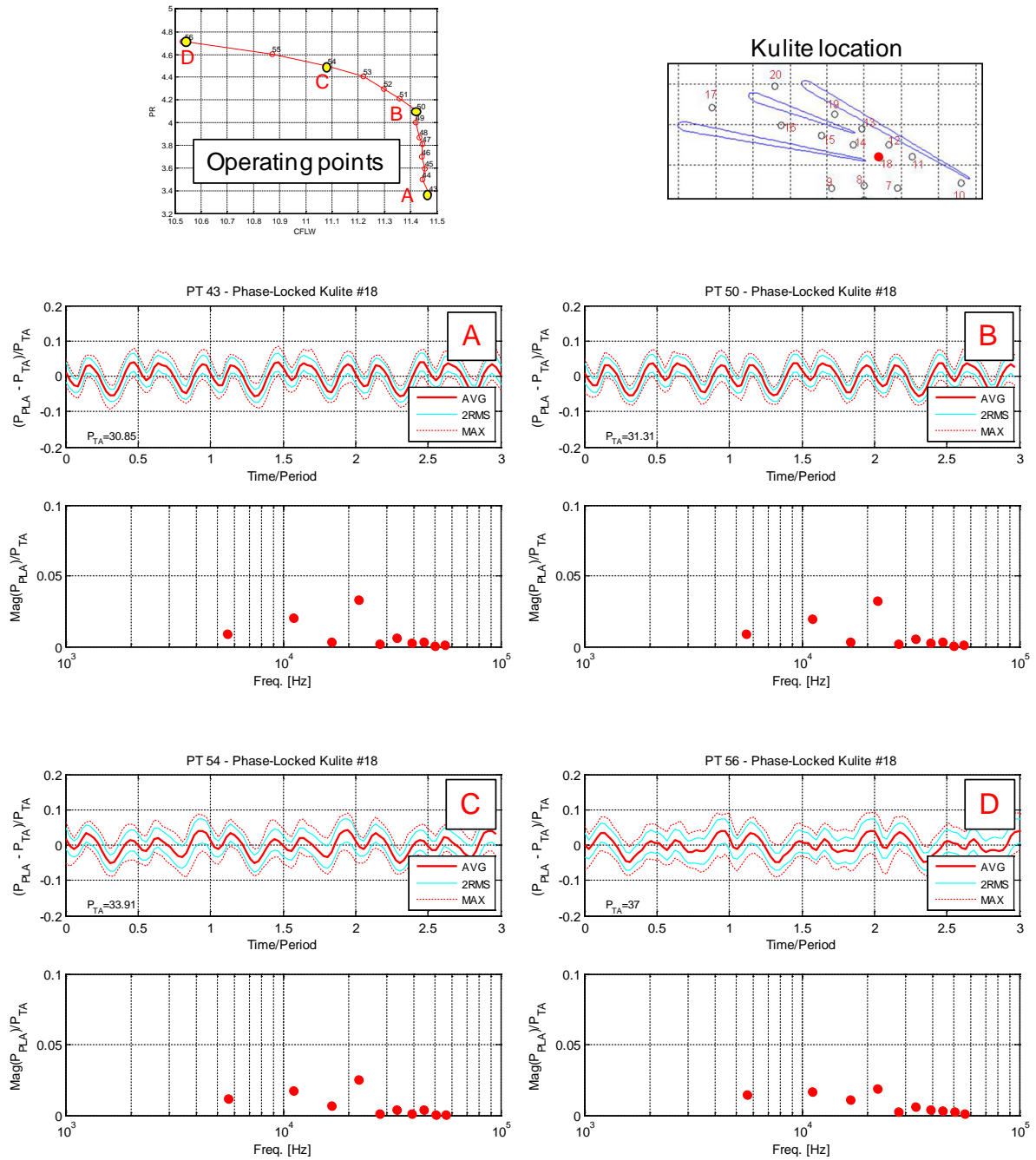


Figure B.8.—(d) Pressure transducer no. 18 (operating points nos. 43, 50, 54, and 56; 100 percent N_c).

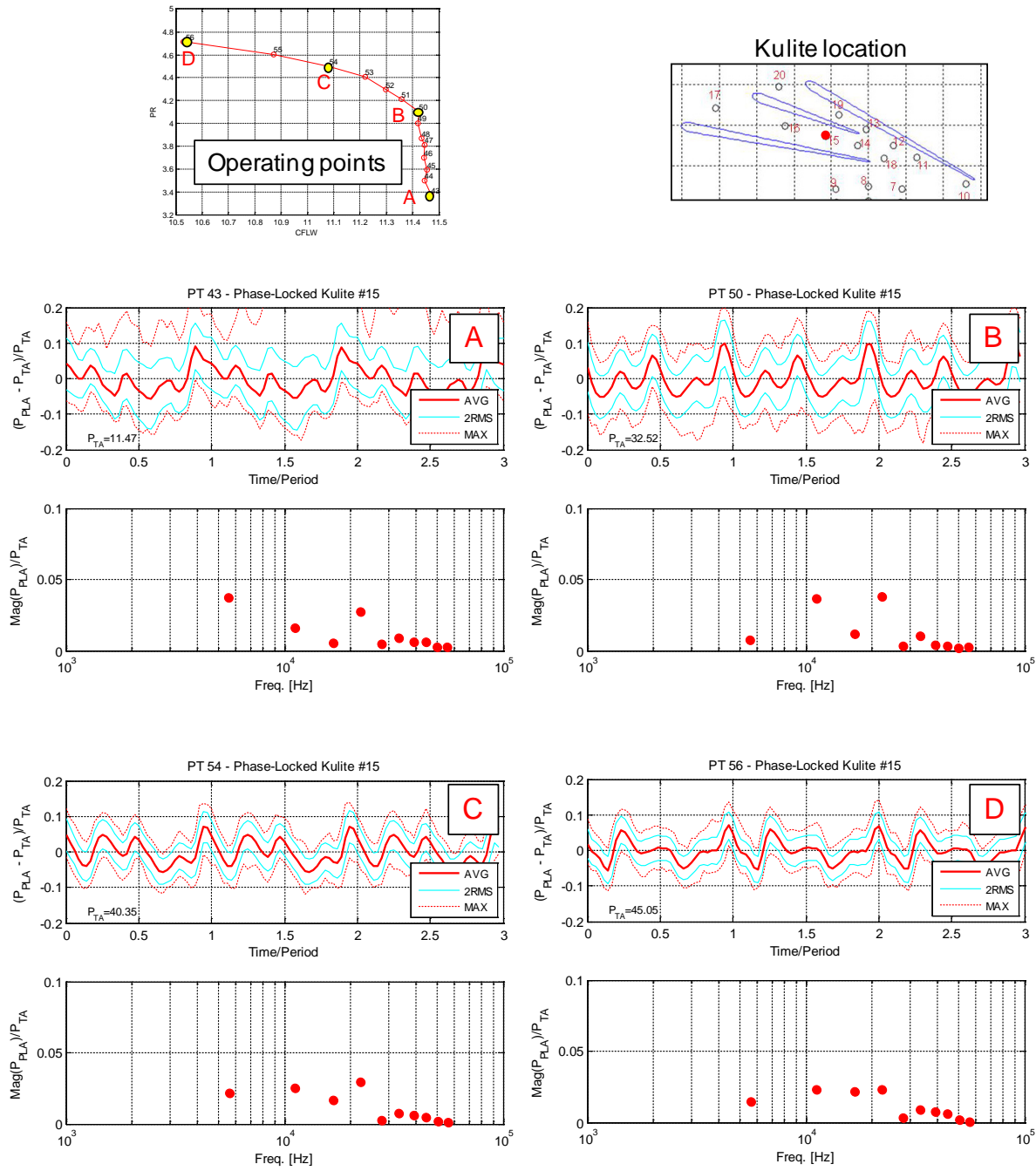


Figure B.8.—(e) Pressure transducer no. 15 (operating points nos. 43, 50, 54, and 56; 100 percent Nc).

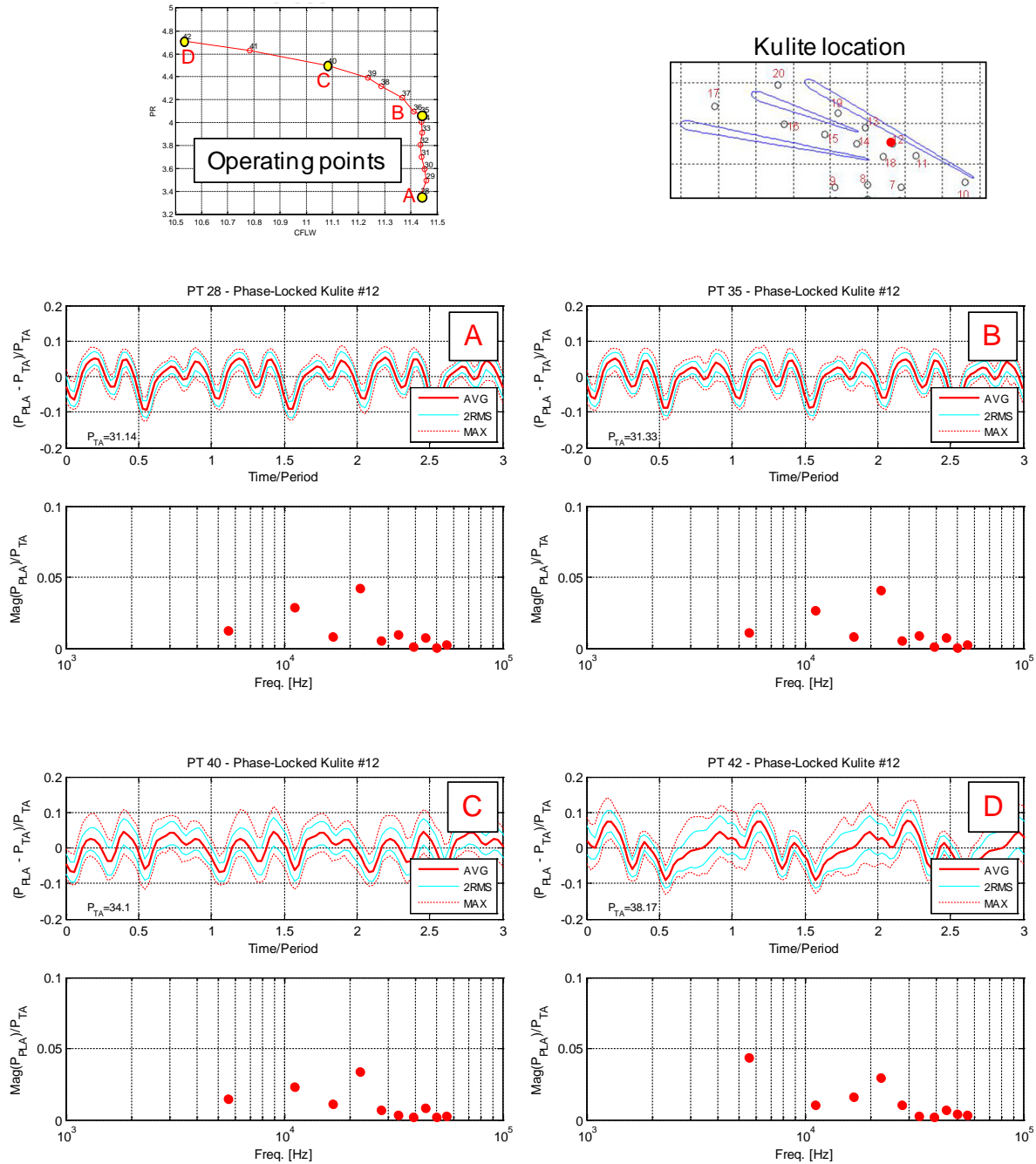


Figure B.8.—(f) Pressure transducer no. 12 (operating points nos. 28, 35, 40, and 42; 100 percent Nc).

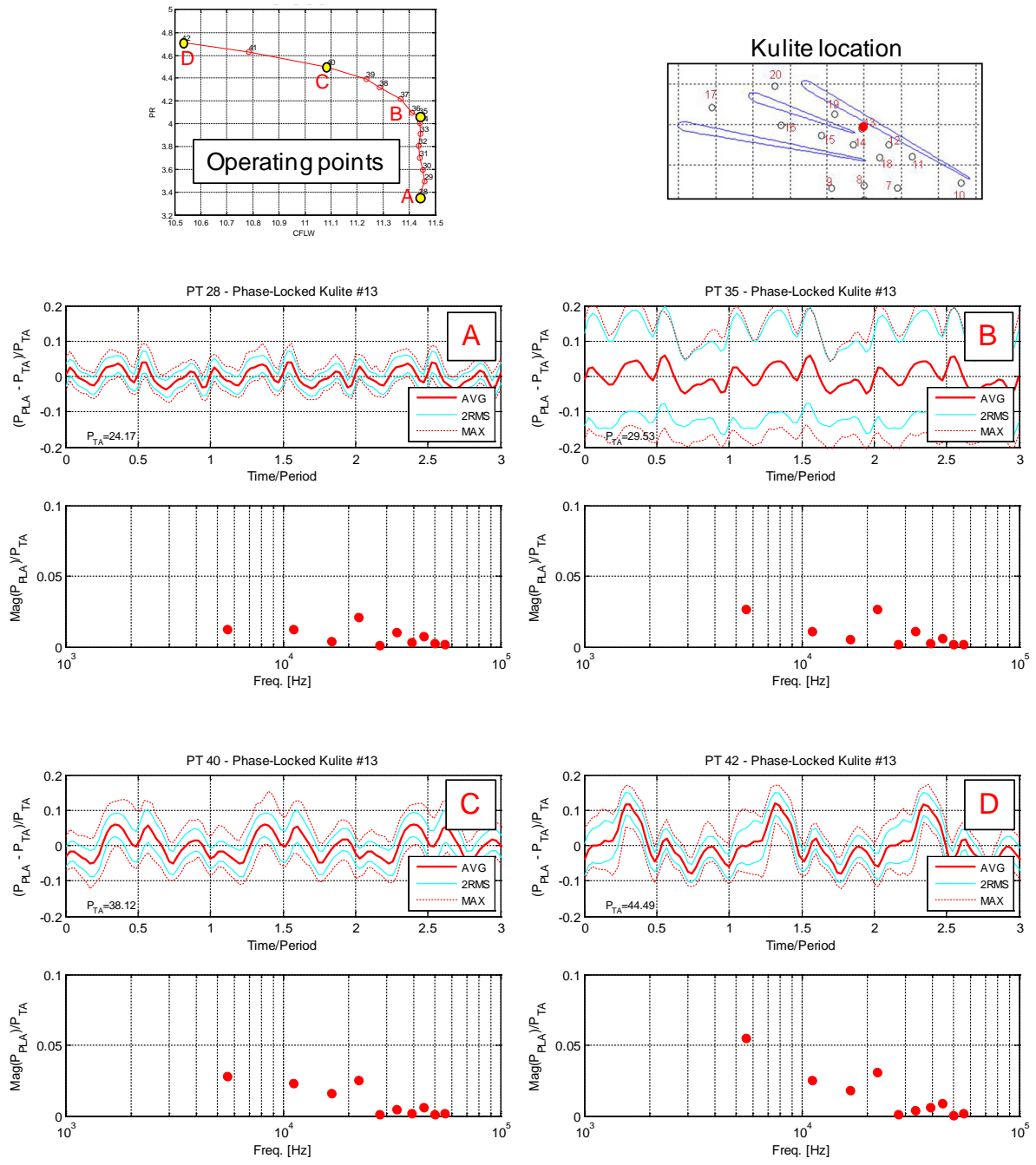


Figure B.8.—(g) Pressure transducer no. 13 (operating points nos. 28, 35, 40, and 42; 100 percent N_c).

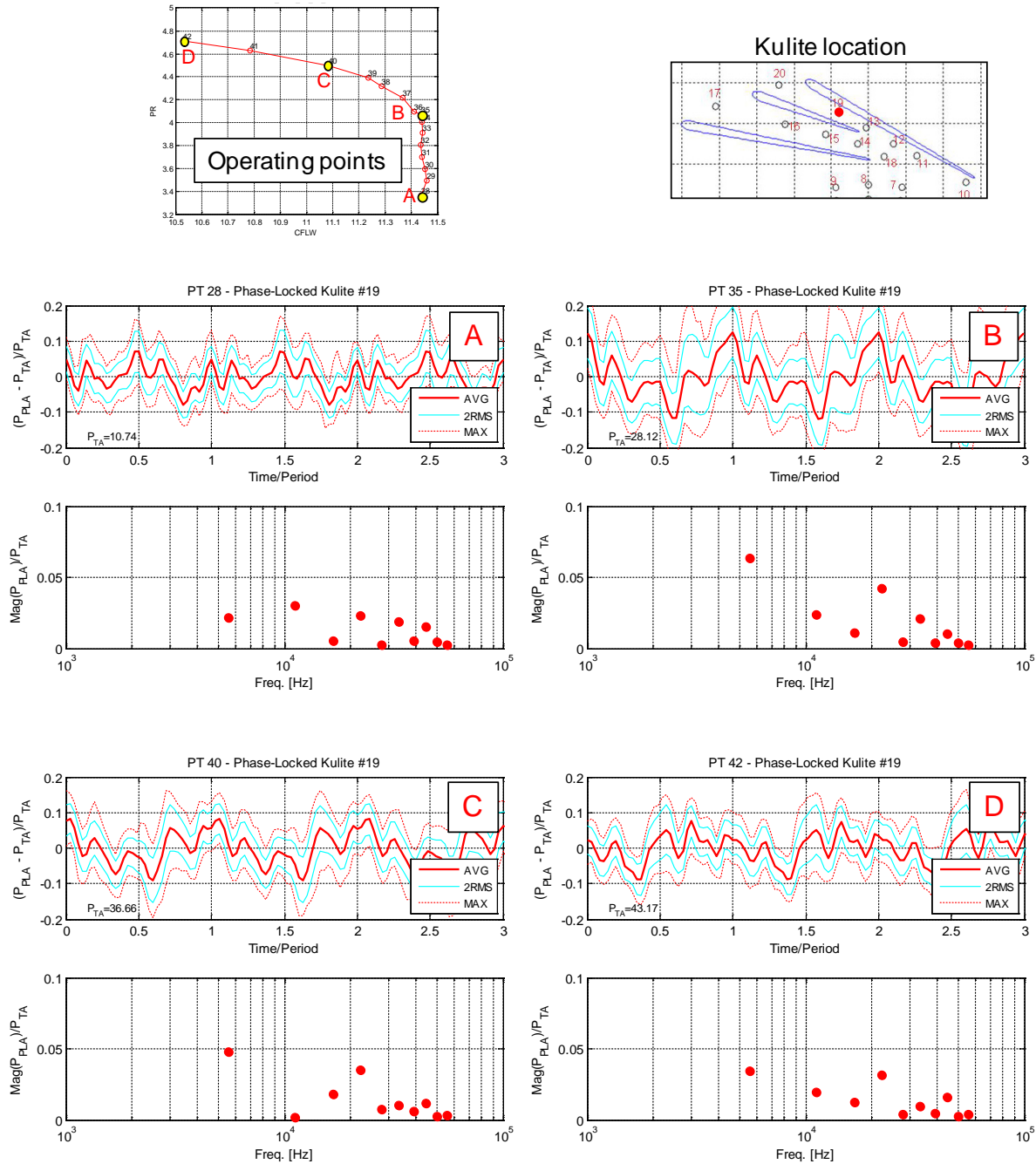


Figure B.8.—(h) Pressure transducer no. 19 (operating points nos. 28, 35, 40, and 42; 100 percent N_c).

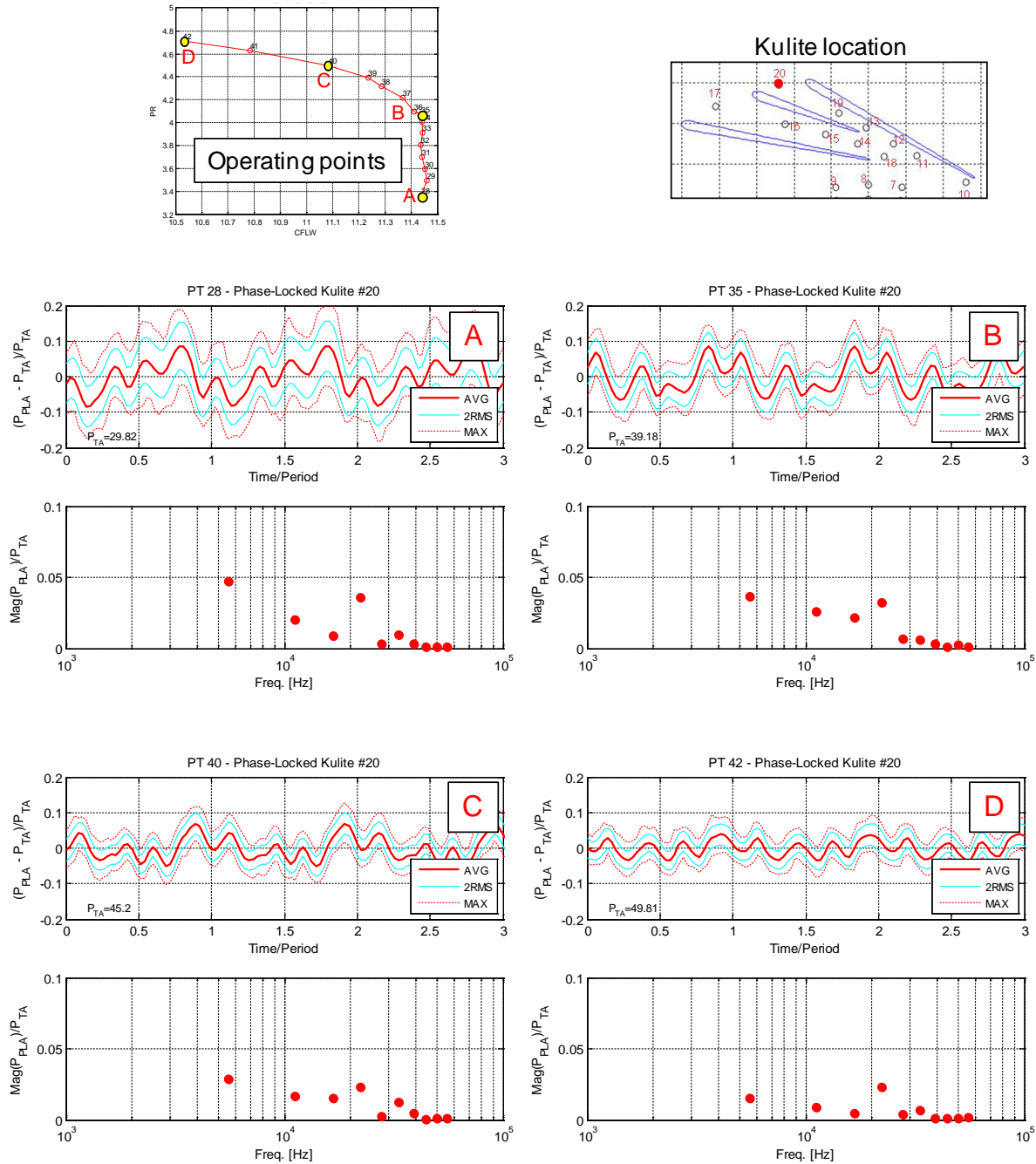


Figure B.8.—(i) Pressure transducer no. 20 (operating points nos. 28, 35, 40, and 42; 100 percent N_c).

B.3 Unsteady Pressure Transducer Correction

The installation of the impeller tip transducers (nos. 7, 8 and 9), an example of which is shown in Figure B.9, consists of an orifice and cavity between the compressor flow field and the face of the Kulite. The fluid in the orifice acts as an inertial acoustic element and the cavity acts as a compliance acoustic element. Together, these acoustic elements have a bulk resonance, otherwise known as a Helmholtz mode.

Two acoustic models, shown in Figure B.10, were constructed to estimate the correction for the unsteady pressure transducer. The lumped-parameter model is a low-frequency approximation which assumes wavelengths are much longer than the geometric dimensions. The model will only capture the bulk mode. For this approximation, the acoustic elements can be represented by an electric circuit. Standard flanged-end corrections were used to approximate the effective length of the orifice (85 percent of the radius on each end). The resistance term of the orifice consists of a radiation term (modeled as a flanged tube resistance), a grazing flow term (Ref. Kraft), and a nonlinear term due to acoustic coupling with turbulences (not modeled).

The second model constructed was based on transmission matrix elements. The conical region was modeled as a series of 50 straight sections and area changes. A grid refinement study showed the results to be well converged above 20 elements. The resistance terms in this analysis are the same as the lumped parameter model. This model has the additional fidelity to capture the longitudinal modes.

The orifice/cavity response in terms of transducer-to-flowfield pressure ratio (P_{CAV}/P_0) is shown in Figure B.11 for a range of grazing flow Mach number. The lumped parameter model and transmission matrix model are in good agreement up to 60 kHz, above which longitudinal modes become important. As can be seen in the figure, the approximate bulk mode is around 18 kHz, very close to the 1st harmonic of blade passing (or the blade-splitter passing frequency). This proximity of the mode with frequencies of interest is unfortunate and can only approximately be accounted for without validation/tuning tests of the actual installation (or mock up).

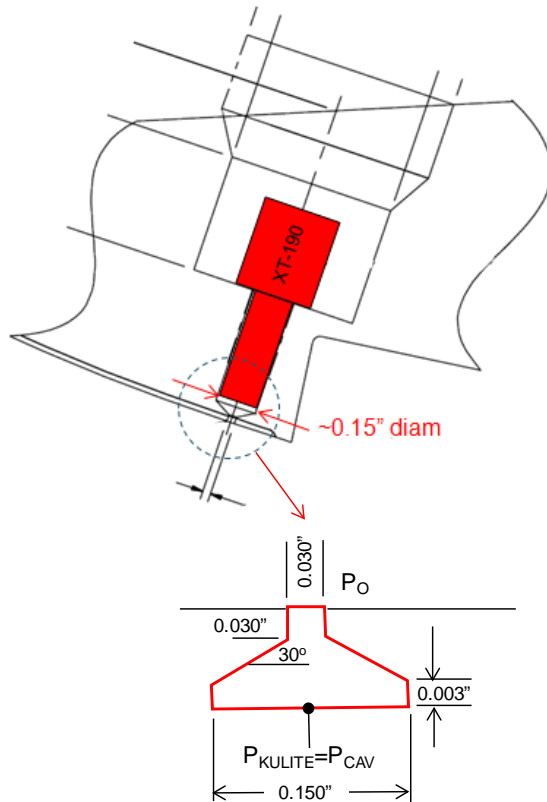
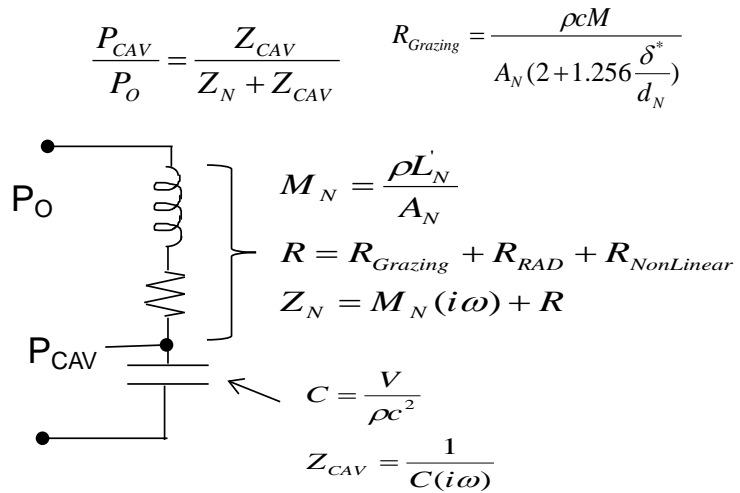


Figure B.9.—Pressure transducer installation details.

Lumped parameter model



Transmission matrix model

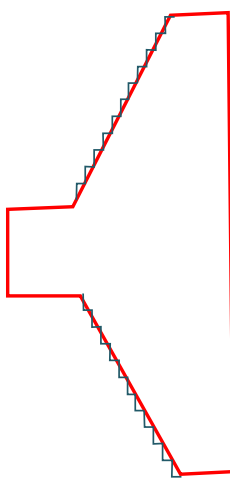


Figure B.10.—Modeling approaches for pressure transducer correction.

The transducer-to-flowfield pressure ratio (transmission matrix) was applied to the experimental data by the following steps

1. Compute Fourier terms of the phase-locked averaged signal (P_n , see above)
2. Compute transducer-to-flowfield pressure ratio (P_{CAV}/P_O)
3. Compute corrected Fourier terms $P_n^{corr} = P_n \frac{P_O}{P_{CAV}}$
4. Reconstruct time domain $P_{PLA}^{corr} = \sum_n P_n^{corr} e^{in(2\pi f_{BP})t}$

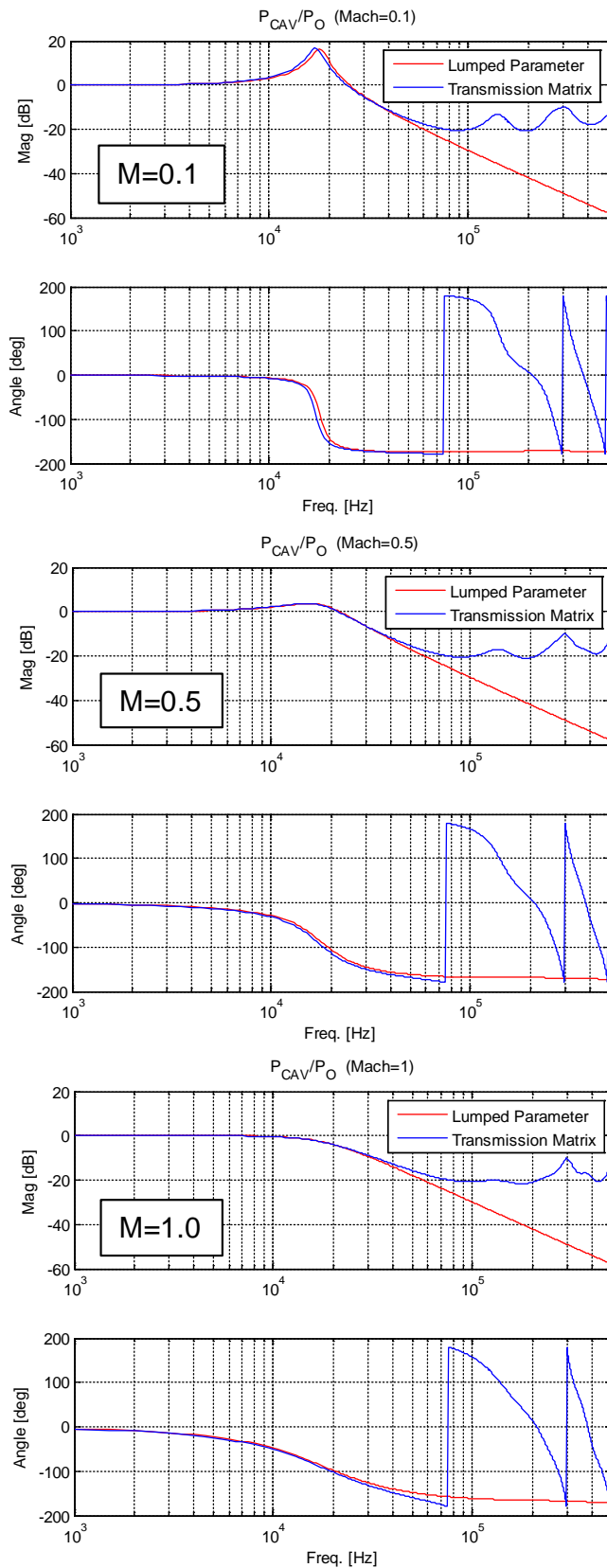


Figure B.11.—Pressure transducer-to-flowfield pressure ratio as a function of grazing Mach number.

To compute the transducer-to-flowfield pressure ratio (P_{CAV}/P_0), the grazing Mach number is needed to compute the grazing flow resistance. The Mach number field from the CFD solution was used to estimate the Mach number. Figure B.12 shows the Mach number distribution for the design point at 50 percent span. Using this distribution with an overlay of the nos. 7, 8, and 9 Kulite locations, show the average grazing flow Mach number to be approximately $M=1.1$. A more accurate time-averaged Mach number computation could have been performed, however the approximate nature of the derived correction and the relatively weak dependence (see Figure B.11) did not warrant such an effort.

Since the experimental rotor orientation was not known, the alignment of the CFD with the experimental for comparison/validation reasons relied on aligning the time domain signals. Transducer no. 18 appeared to show the best agreement, so this signal was used for time alignment. For transducers that are located at different diffuser vanes passages, the CFD was shifted an additional amount to achieve the correct rotor blade phasing.

Figure B.13 gives the comparison of the raw and corrected experimental data to the CFD at the design point for each transducer. The red line and symbols corresponds to the original experimental data, the black ones are the corrected experimental data (only for transducers nos. 7, 8 and 9), and the blue ones are the CFD. A discussion of the agreement and disagreement with the experimental data is given in the main text of the report. In summary, given the uncertainty of the experimental correction, the comparison of CFD with experimental data appears very reasonable with the exception of the downstream locations where the grid resolution appears to be insufficient to capture acoustic wave propagation.

For completeness, the tables at the end of this appendix give the coordinate locations of the unsteady pressure transducers (not all locations were used) for both hot and cold conditions (Table B.1 and Table B.2). Table B.2 gives the actual location relative to the circumference (cold conditions) whereas Table B.1 gives the locations grouped to one vane passage azimuth at top dead center (hot).

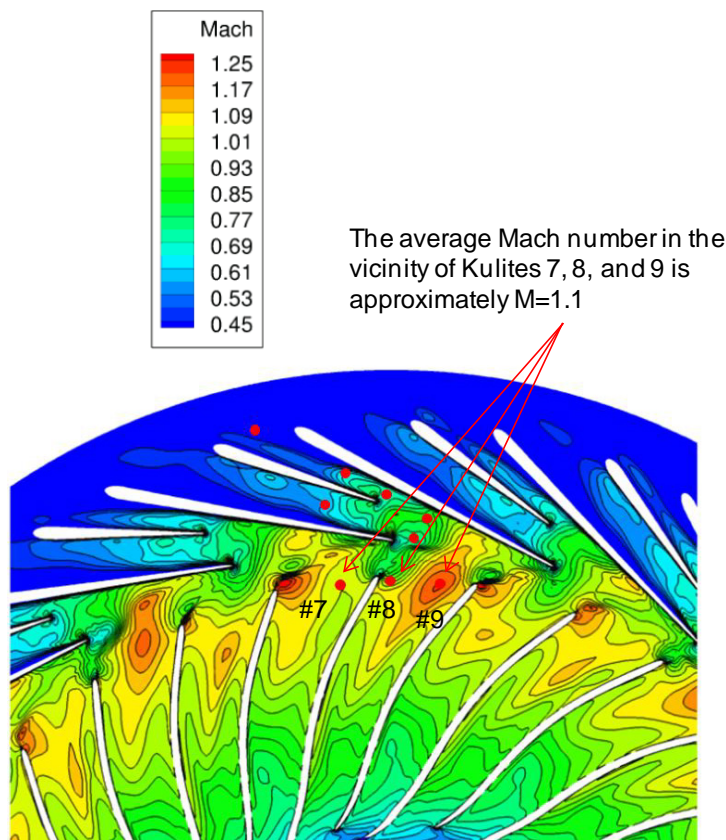


Figure B.12.—Pressure transducer Grazing Mach number (inlet corrected flow of 11 lbm/s, 100 percent N_c).

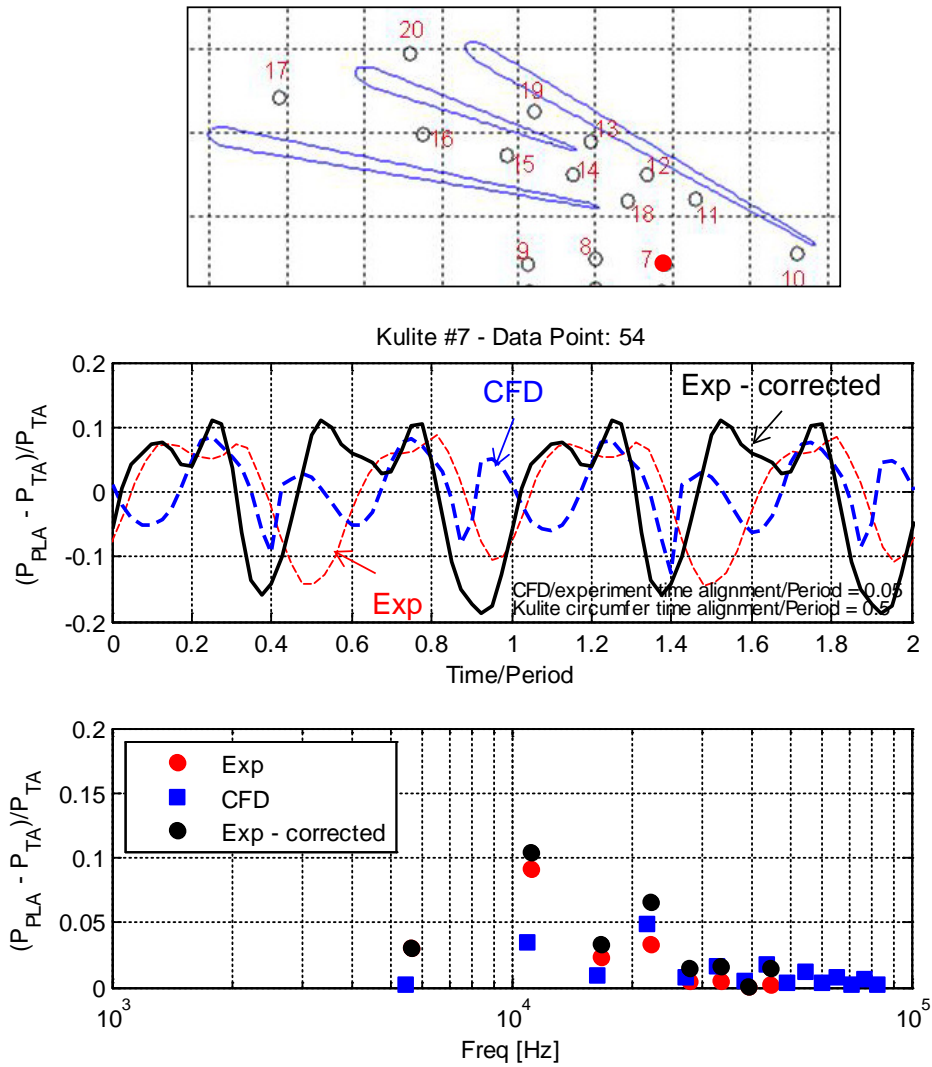


Figure B.13.—(a) Pressure transducer no. 7 comparison with CFD (operating point no. 54 at 100 percent N_c).

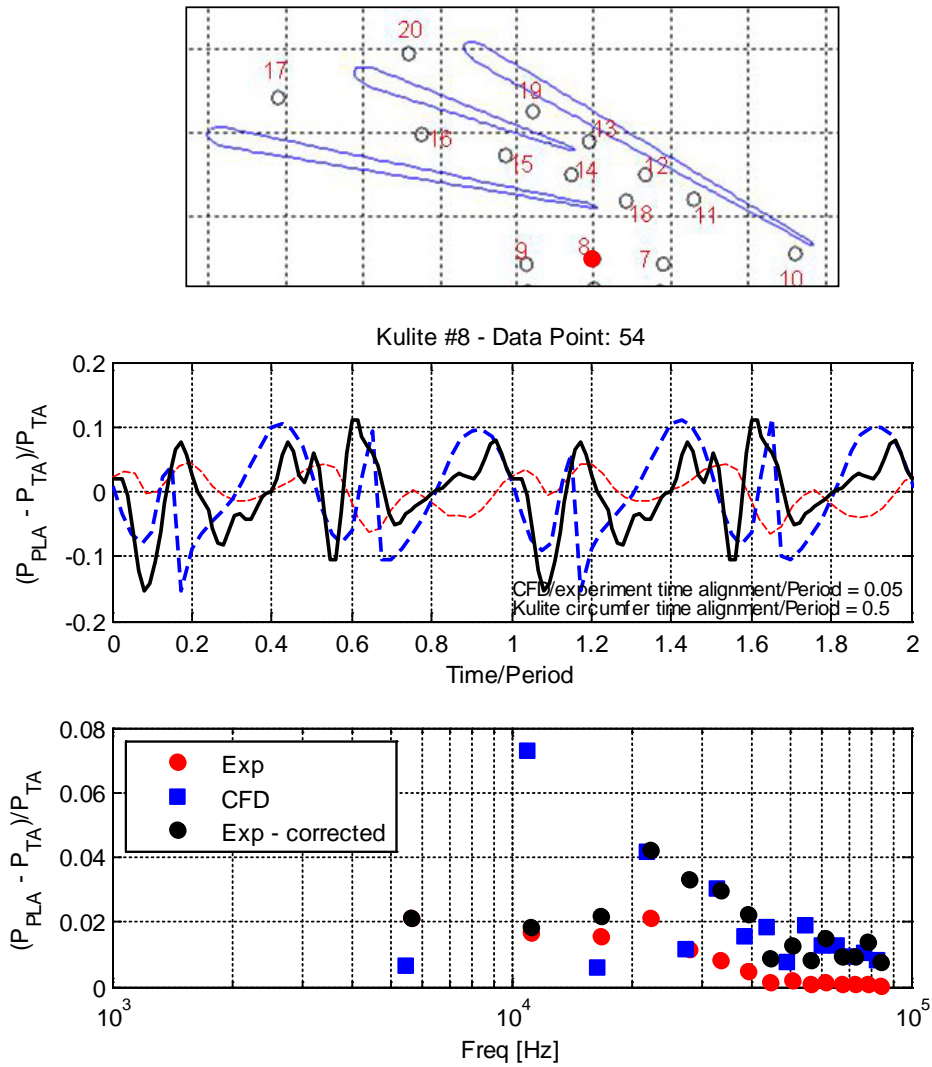


Figure B13.—(b) Pressure transducer no. 8 comparison with CFD (operating point no. 54 at 100 percent N_c).

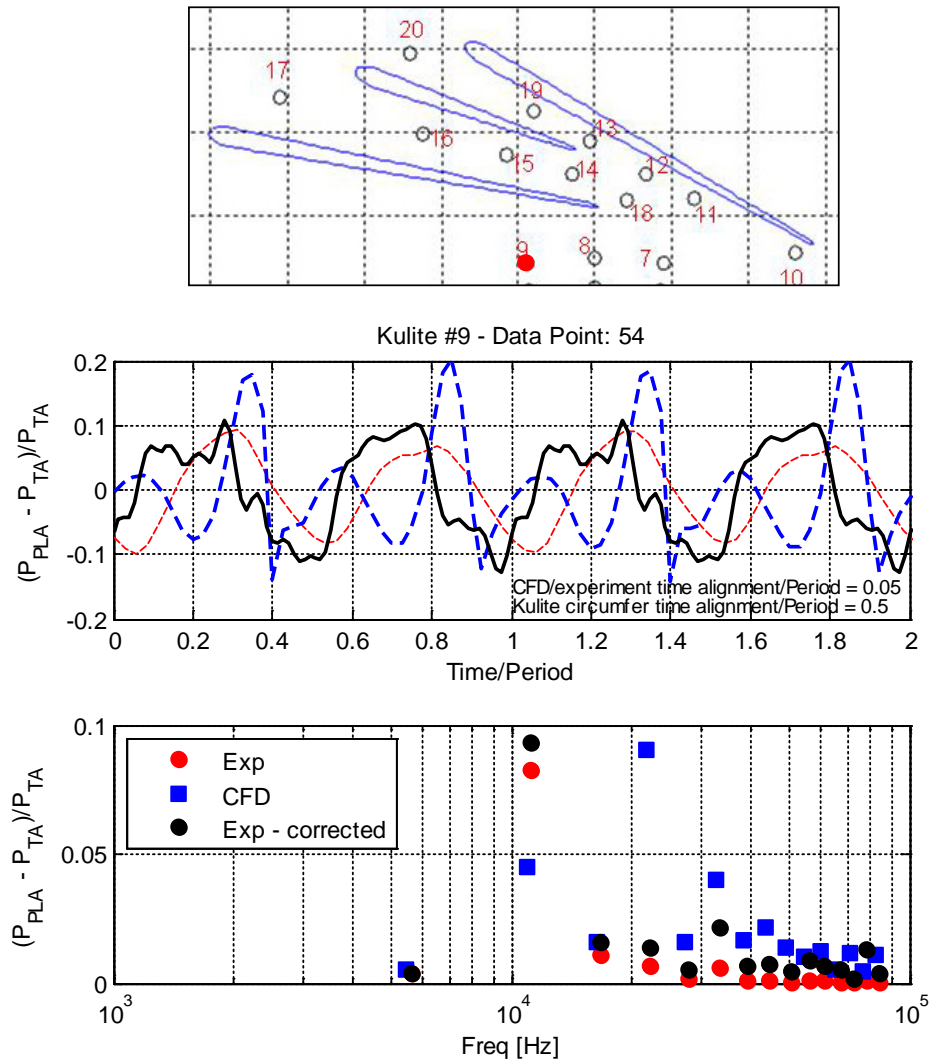


Figure B13.—(c) Pressure transducer no. 9 comparison with CFD (operating point no. 54 at 100 percent N_c).

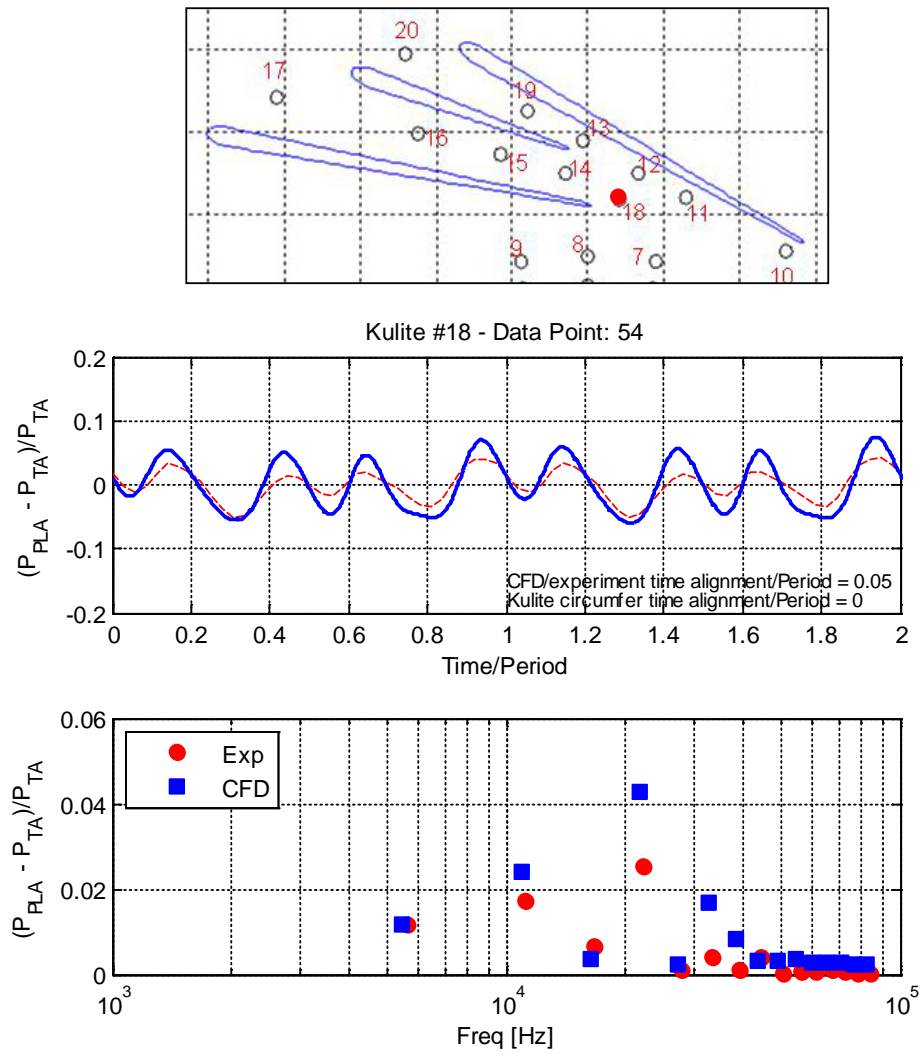


Figure B13.—(d) Pressure transducer no. 18 comparison with CFD (operating point no. 54 at 100 percent N_c).

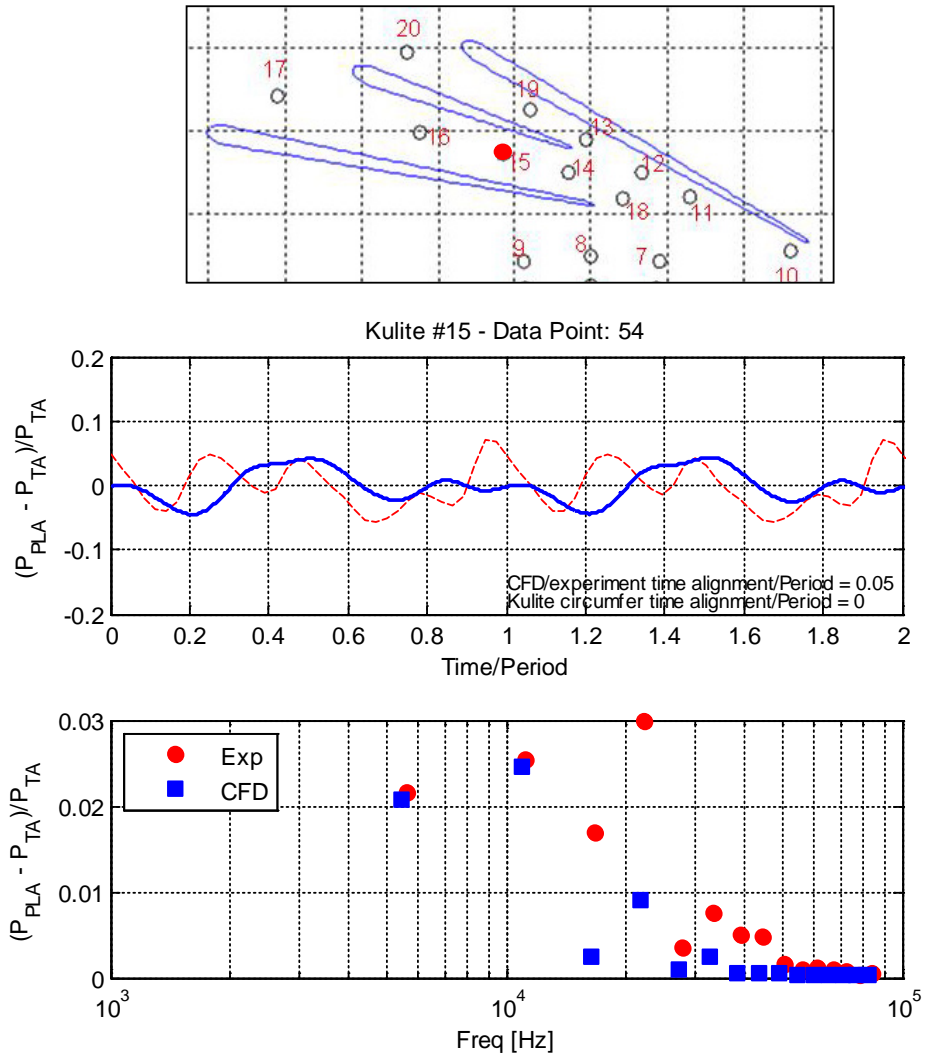


Figure B13.—(e) Pressure transducer no. 15 comparison with CFD (operating point no. 54 at 100 percent N_c).

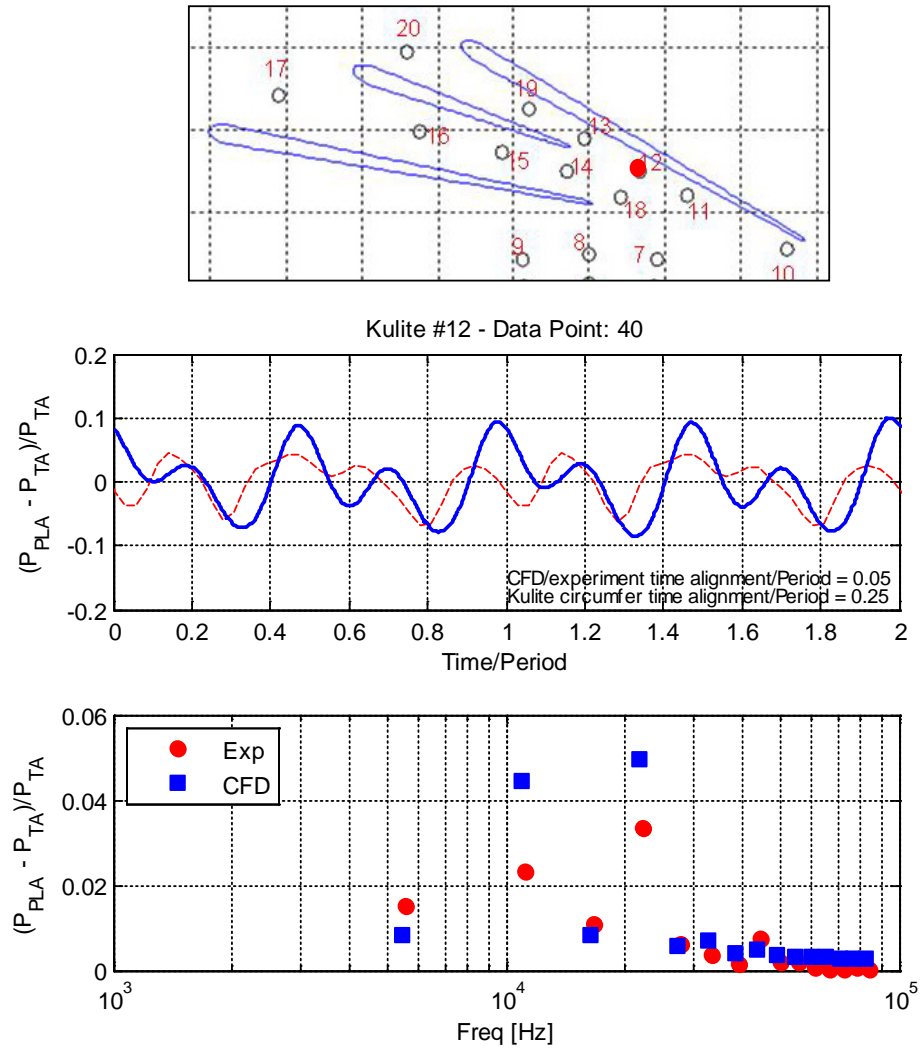


Figure B.13.—(f) Pressure transducer no. 12 comparison with CFD (operating point no. 40 at 100 percent N_c).

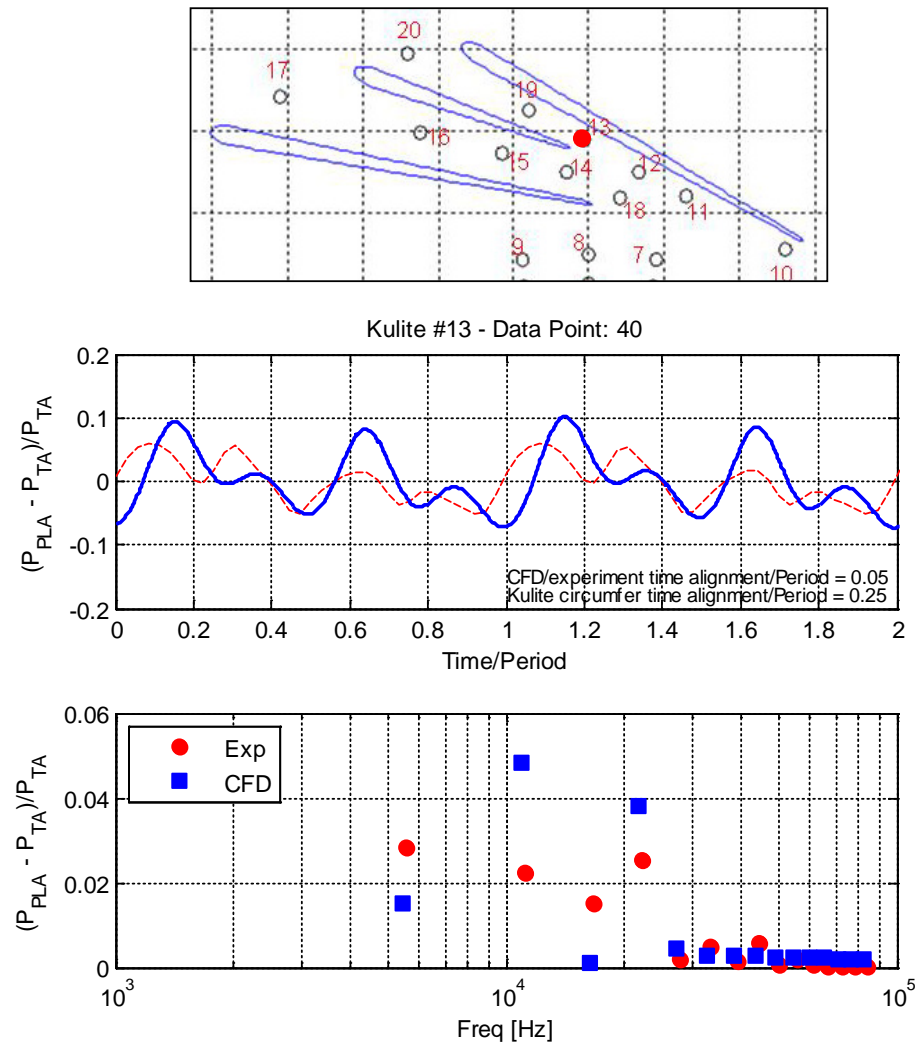


Figure B.13.—(g) Pressure transducer no. 13 comparison with CFD (operating point no. 40 at 100 percent N_c).

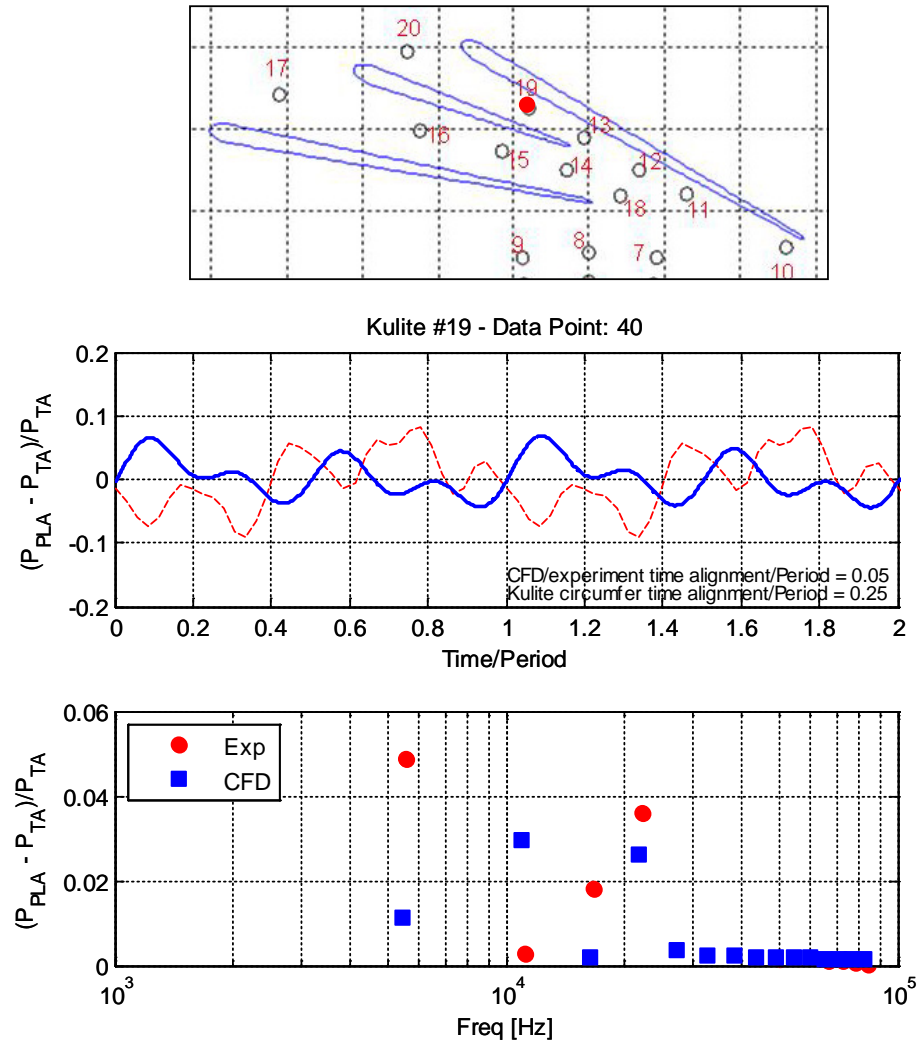


Figure B.13.—(h) Pressure transducer no. 19 comparison with CFD (operating point no. 40 at 100 percent N_c).

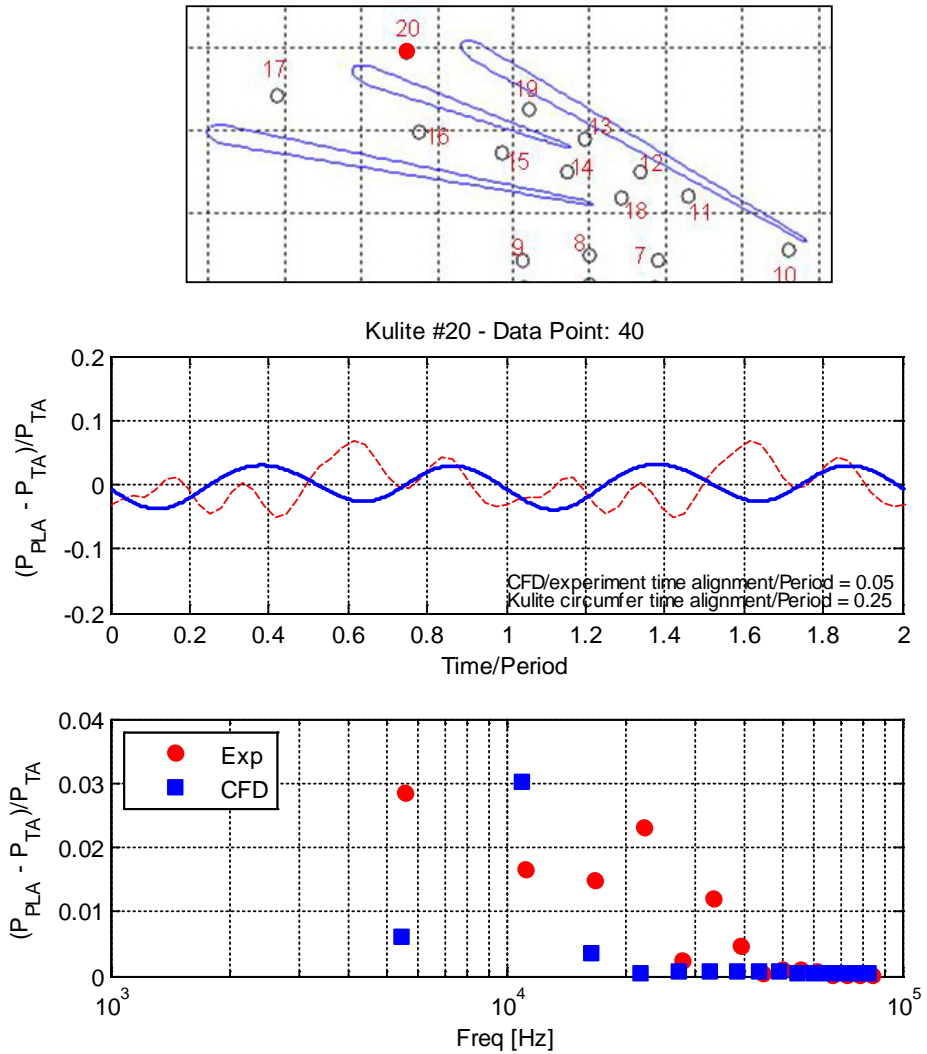


Figure B.13.—(i) Pressure transducer no. 20 comparison with CFD (operating point no. 40 at 100 percent N_c).

TABLE B.1.—ORIGINAL HOT POSITIONING (AS IN CFD SETUP)
FOR PRESSURE TRANSDUCER

Original HOT position (CFD)					
	y	z	θ from TDC in direction of rotation, deg	R, in.	R/Rtip
1	-0.80073	7.61844	-6.00	7.6604	0.902
2	0.00000	7.66041	0.00	7.6604	0.902
3	0.80073	7.61844	6.00	7.6604	0.902
4	-0.85230	8.10911	-6.00	8.1538	0.960
5	0.00000	8.15378	0.00	8.1538	0.960
6	0.85230	8.10911	6.00	8.1538	0.960
7	-0.87674	8.34165	-6.00	8.3876	0.988
8	0.00000	8.38760	0.00	8.3876	0.988
9	0.87674	8.34165	6.00	8.3876	0.988
10	-2.60796	8.56970	-16.93	8.9577	1.055
11	-1.28672	9.22048	-7.94	9.3098	1.097
12	-0.67352	9.50553	-4.05	9.5294	1.122
13	0.07636	9.89282	0.44	9.8931	1.165
14	0.30831	9.50605	1.86	9.5110	1.120
15	1.14861	9.72596	6.74	9.7935	1.154
16	2.23458	9.99213	12.61	10.2389	1.206
17	4.10610	10.41880	21.51	11.1987	1.319
18	-0.41949	9.19770	-2.61	9.2073	1.084
19	0.79434	10.25160	4.43	10.2823	1.211
20	2.41876	10.93830	12.47	11.2025	1.319
21	7.34437	5.12850	55.07	8.9577	1.055
22	8.95617	-0.16787	91.07	8.9577	1.055
10	7.14703	-5.40011	127.07	8.9577	1.055
23	2.60796	-8.56970	163.07	8.9577	1.055
24	-2.92726	-8.46595	-160.93	8.9577	1.055
25	-7.34437	-5.12850	-124.93	8.9577	1.055
26	-8.95617	0.16787	-88.93	8.9577	1.055
27	-7.14703	5.40011	-52.93	8.9577	1.055
28	-2.60796	8.56970	-16.93	8.9577	1.055
29	-1.69790	8.79536	-10.93	8.9577	1.055
30	-0.76923	8.92466	-4.93	8.9577	1.055

TABLE B.2.—FINAL CLOCKED COLD POSITIONING
FOR PRESSURE TRANSDUCER

Final clocked COLD position				
	y	z	θ from TDC in direction of rotation, deg	R, in.
1	5.107	5.672	42.00	7.632
2	5.672	5.107	48.00	7.632
3	6.174	4.486	54.00	7.632
4	7.948	-1.689	102.00	8.126
5	7.728	-2.511	108.00	8.126
6	7.423	-3.305	114.00	8.126
7	-7.638	-3.401	246.00	8.361
8	-7.952	-2.584	252.00	8.361
9	-8.178	-1.738	258.00	8.361
10	7.125	-5.383	127.07	8.930
11	8.190	-4.365	118.06	9.281
12	8.063	-5.027	121.947	9.502
13	7.936	-5.860	126.442	9.865
14	5.323	-7.848	145.852	9.483
15	4.774	-8.519	150.735	9.765
16	4.055	-9.371	156.606	10.211
17	2.795	-10.816	165.510	11.171
18	5.728	-7.173	141.389	9.180
19	7.806	-6.650	130.431	10.255
20	7.409	-8.365	138.47	11.174
21	7.322	5.113	55.07	8.930
22	8.928	-0.167	91.07	8.930
10	7.125	-5.383	127.07	8.930
23	2.600	-8.543	163.07	8.930
24	-2.918	-8.440	-160.93	8.930
25	-7.322	-5.113	-124.93	8.930
26	-8.928	0.167	-88.93	8.930
27	-7.125	5.383	-52.93	8.930
28	-2.600	8.543	-16.93	8.930
29	8.739	1.687	79.07	8.930
30	0.763	-8.867	175.08	8.930

Appendix C.—Hot Coordinates

This appendix contains all hot coordinates which define the flowpath, impeller blades, diffuser vanes and EGVs. These coordinates are used to create CFD grids. The coordinates are given in a cylindrical coordinate system, with x coordinate line being the axis of rotation. The origin of the coordinate system ($x=0$) is set to the leading edge of the main blade of the impeller.

C.1 Flowpath

The flowpath is defined by the curves of the hub and the shroud parts of the flow passage from the inlet to the outlet after EGV. They are expressed in x and r coordinates and begins and ends where the CFD domain begins and ends.

TABLE C.1.—FLOW PATH—HUB

X	R	X	R	X	R
-5.000000	2.480000	-2.720937	1.674509	-0.869580	1.500169
-4.925503	2.444484	-2.666281	1.662600	-0.819300	1.502472
-4.851822	2.409945	-2.611931	1.651132	-0.768956	1.505166
-4.778956	2.376383	-2.557875	1.640102	-0.718538	1.508255
-4.706878	2.343769	-2.504103	1.629502	-0.668035	1.511741
-4.635567	2.312075	-2.450602	1.619330	-0.617437	1.515627
-4.565003	2.281276	-2.397363	1.609579	-0.566734	1.519916
-4.495174	2.251348	-2.344373	1.600247	-0.515916	1.524612
-4.426060	2.222263	-2.291623	1.591329	-0.464972	1.529719
-4.357646	2.193999	-2.239100	1.582820	-0.413893	1.535239
-4.289915	2.166529	-2.186796	1.574718	-0.362667	1.541179
-4.222852	2.139832	-2.134697	1.567018	-0.311284	1.547542
-4.156442	2.113885	-2.082795	1.559719	-0.259734	1.554333
-4.090668	2.088668	-2.031080	1.552817	-0.208005	1.561558
-4.025517	2.064160	-1.979539	1.546310	-0.156088	1.569222
-3.960973	2.040343	-1.928163	1.540194	-0.103970	1.577330
-3.897019	2.017197	-1.876943	1.534468	-0.051641	1.585889
-3.833645	1.994708	-1.825867	1.529130	0.000875	1.594900
-3.770832	1.972856	-1.774926	1.524177	0.053591	1.604369
-3.708568	1.951629	-1.724108	1.519609	0.106551	1.614308
-3.646840	1.931011	-1.673405	1.515424	0.159766	1.624725
-3.585630	1.910988	-1.622806	1.511621	0.213248	1.635629
-3.524929	1.891547	-1.572302	1.508199	0.267008	1.647028
-3.464720	1.872676	-1.521881	1.505156	0.321058	1.658931
-3.404992	1.854363	-1.471535	1.502493	0.375410	1.671348
-3.345728	1.836595	-1.421253	1.500209	0.430076	1.684289
-3.286918	1.819364	-1.371026	1.498303	0.485069	1.697764
-3.228548	1.802658	-1.320844	1.496776	0.540399	1.711785
-3.170605	1.786468	-1.270696	1.495628	0.596081	1.726363
-3.113077	1.770785	-1.220573	1.494859	0.652125	1.741511
-3.055950	1.755600	-1.170465	1.494470	0.708546	1.757242
-2.999212	1.740904	-1.120363	1.494462	0.765355	1.773570
-2.942852	1.726691	-1.070255	1.494835	0.822566	1.790510
-2.886855	1.712951	-1.020133	1.495590	0.880192	1.808077
-2.831212	1.699679	-0.969986	1.496730	0.938246	1.826286
-2.775910	1.686867	-0.919805	1.498256	0.996741	1.845157

TABLE C.1.—FLOW PATH—HUB

X	R	X	R	X	R
1.055691	1.864705	3.578887	3.323974	5.266251	9.997720
1.115110	1.884952	3.660159	3.401878	5.266251	10.306484
1.175009	1.905915	3.741571	3.483453	5.265973	10.351317
1.235405	1.927618	3.822990	3.568923	5.265704	10.396150
1.296310	1.950083	3.904269	3.658526	5.265450	10.440983
1.357739	1.973333	3.985231	3.752506	5.265227	10.485816
1.419705	1.997394	4.065684	3.851120	5.265059	10.530650
1.482222	2.022293	4.145406	3.954628	5.264982	10.575483
1.545304	2.048058	4.224156	4.063294	5.265051	10.620317
1.608965	2.074719	4.301669	4.177379	5.265339	10.665150
1.673219	2.102308	4.377660	4.297145	5.265941	10.709980
1.738080	2.130859	4.451829	4.422840	5.266968	10.754801
1.803557	2.160407	4.523869	4.554702	5.268543	10.799607
1.869665	2.190990	4.593467	4.692949	5.270802	10.844384
1.936420	2.222651	4.660320	4.837779	5.273891	10.889110
2.003833	2.255433	4.724141	4.989365	5.277967	10.933757
2.071916	2.289382	4.784673	5.147861	5.283203	10.978283
2.140680	2.324548	4.841695	5.313399	5.289779	11.022629
2.210137	2.360983	4.895038	5.486094	5.297879	11.066723
2.280295	2.398745	4.944581	5.666044	5.307669	11.110472
2.351162	2.437893	4.990264	5.853344	5.319298	11.153767
2.422748	2.478494	5.032087	6.048088	5.332887	11.196488
2.495055	2.520615	5.070109	6.250375	5.348531	11.238499
2.568089	2.564333	5.104441	6.460317	5.366295	11.279658
2.641851	2.609726	5.135239	6.678039	5.386217	11.319816
2.716338	2.656880	5.162691	6.903679	5.408298	11.358829
2.791547	2.705888	5.187010	7.137410	5.432505	11.396559
2.867470	2.756850	5.208397	7.379423	5.458772	11.432885
2.944096	2.809871	5.227014	7.629930	5.487007	11.467704
3.021407	2.865068	5.242898	7.889168	5.517096	11.500935
3.099380	2.922563	5.255806	8.157410	5.548909	11.532519
3.177987	2.982489	5.264737	8.434949	5.582310	11.562418
3.257190	3.044990	5.266251	8.722079	5.617163	11.590613
3.336943	3.110218	5.266251	9.018761	5.653333	11.617097
3.417190	3.178338	5.266251	9.324941	5.690696	11.641871
3.497864	3.249527	5.266251	9.642654	5.729138	11.664935

TABLE C.1.—FLOW PATH—HUB

X	R	X	R	X	R
5.768557	11.686287	7.361197	11.863051	8.972188	11.868600
5.808859	11.705921	7.406023	11.863913	9.016891	11.868600
5.849954	11.723837	7.450850	11.864697	9.061595	11.868600
5.891752	11.740044	7.495678	11.865405	9.106299	11.868600
5.934166	11.754567	7.540507	11.866039	9.151003	11.868600
5.977107	11.767447	7.585338	11.866599	9.195707	11.868600
6.020492	11.778744	7.630169	11.867090	9.240410	11.868600
6.064241	11.788535	7.675001	11.867514	9.285114	11.868600
6.108282	11.796922	7.719833	11.867871	9.329818	11.868600
6.152548	11.804027	7.764666	11.868162	9.374522	11.868600
6.196982	11.809993	7.809499	11.868387	9.419226	11.868600
6.241537	11.814978	7.854332	11.868545	9.463930	11.868600
6.286176	11.819145	7.899166	11.868635	9.508633	11.868600
6.330873	11.822645	7.944000	11.868654	9.553337	11.868600
6.375608	11.825612	7.988704	11.868600	9.598041	11.868600
6.420369	11.828165	8.033408	11.868600	9.642745	11.868600
6.465146	11.830413	8.078111	11.868600	9.687449	11.868600
6.509933	11.832462	8.122815	11.868600	9.732152	11.868600
6.554725	11.834403	8.167519	11.868600	9.776856	11.868600
6.599518	11.836315	8.212223	11.868600	9.821560	11.868600
6.644310	11.838248	8.256927	11.868600	9.866264	11.868600
6.689100	11.840224	8.301630	11.868600	9.910968	11.868600
6.733889	11.842239	8.346334	11.868600	9.955671	11.868600
6.778677	11.844265	8.391038	11.868600	10.000375	11.868600
6.823466	11.846263	8.435742	11.868600	10.045079	11.868600
6.868258	11.848187	8.480446	11.868600	10.089783	11.868600
6.913055	11.850003	8.525150	11.868600	10.134487	11.868600
6.957857	11.851699	8.569853	11.868600	10.179190	11.868600
7.002663	11.853284	8.614557	11.868600	10.223894	11.868600
7.047472	11.854775	8.659261	11.868600	10.268598	11.868600
7.092283	11.856190	8.703965	11.868600	10.313302	11.868600
7.137097	11.857533	8.748669	11.868600	10.358006	11.868600
7.181913	11.858801	8.793372	11.868600	10.402710	11.868600
7.226731	11.859988	8.838076	11.868600	10.447413	11.868600
7.271551	11.861091	8.882780	11.868600	10.492117	11.868600
7.316373	11.862111	8.927484	11.868600	10.536821	11.868600

TABLE C.1.—FLOW PATH—HUB

X	R	X	R	X	R
10.581525	11.868600				
10.626229	11.868600				
10.670932	11.868600				
10.715636	11.868600				
10.760340	11.868600				
10.805044	11.868600				
10.849748	11.868600				
10.894451	11.868600				
10.939155	11.868600				
10.983859	11.868600				
11.028563	11.868600				
11.073267	11.868600				
11.117970	11.868600				
11.162674	11.868600				
11.207378	11.868600				
11.252082	11.868600				
11.296786	11.868600				
11.341490	11.868600				
11.386193	11.868600				
11.430897	11.868600				
11.475601	11.868600				
11.520305	11.868600				
11.565009	11.868600				
11.609712	11.868600				
11.654416	11.868600				
11.699120	11.868600				

TABLE C.2.—FLOW PATH—SHROUD

X	R	X	R	X	R
-5.000000	5.075000	-2.885694	4.448149	-0.901646	4.210378
-4.938532	5.052105	-2.829484	4.435834	-0.847106	4.210146
-4.877183	5.029724	-2.773371	4.423822	-0.792565	4.210268
-4.815956	5.007859	-2.717351	4.412115	-0.738023	4.210741
-4.754870	4.986437	-2.661419	4.400713	-0.683476	4.211566
-4.693943	4.965392	-2.605574	4.389620	-0.628924	4.212745
-4.633182	4.944698	-2.549812	4.378839	-0.574360	4.214274
-4.572591	4.924329	-2.494131	4.368372	-0.519784	4.216156
-4.512176	4.904264	-2.438526	4.358222	-0.465195	4.218389
-4.451937	4.884483	-2.382996	4.348391	-0.410591	4.220973
-4.391877	4.864980	-2.327537	4.338880	-0.355968	4.223909
-4.331995	4.845738	-2.272147	4.329694	-0.301325	4.227197
-4.272290	4.826753	-2.216821	4.320833	-0.246659	4.230835
-4.212762	4.808024	-2.161558	4.312300	-0.191969	4.234826
-4.153409	4.789541	-2.106354	4.304098	-0.137251	4.239169
-4.094228	4.771304	-2.051208	4.296228	-0.082503	4.243866
-4.035217	4.753315	-1.996115	4.288691	-0.027724	4.248917
-3.976372	4.735577	-1.941073	4.281490	0.031533	4.254777
-3.917694	4.718076	-1.886081	4.274628	0.095278	4.261539
-3.859180	4.700811	-1.831134	4.268106	0.159077	4.268786
-3.800817	4.683824	-1.776231	4.261925	0.222932	4.276519
-3.742594	4.667139	-1.721368	4.256087	0.286847	4.284742
-3.684545	4.650631	-1.666543	4.250594	0.350825	4.293459
-3.626706	4.634160	-1.611755	4.245445	0.414870	4.302675
-3.569019	4.617930	-1.556999	4.240645	0.478984	4.312394
-3.511386	4.602279	-1.502274	4.236191	0.543171	4.322622
-3.453826	4.587127	-1.447577	4.232087	0.607434	4.333368
-3.396427	4.572131	-1.392907	4.228333	0.671776	4.344636
-3.339209	4.557212	-1.338259	4.224929	0.736198	4.356436
-3.282127	4.542536	-1.283633	4.221877	0.800705	4.368775
-3.225153	4.528191	-1.229026	4.219176	0.865297	4.381666
-3.168294	4.514143	-1.174435	4.216828	0.929978	4.395116
-3.111556	4.500364	-1.119858	4.214832	0.994748	4.409139
-3.054931	4.486869	-1.065293	4.213189	1.059610	4.423747
-2.998414	4.473667	-1.010738	4.211899	1.124565	4.438952
-2.942003	4.460761	-0.956190	4.210962	1.189614	4.454771

TABLE C.2.—FLOW PATH—SHROUD

X	R	X	R	X	R
1.254758	4.471217	3.593192	5.730775	4.701683	9.031433
1.319996	4.488309	3.651901	5.794648	4.705420	9.107386
1.385329	4.506064	3.709597	5.860740	4.708714	9.183360
1.450756	4.524501	3.766199	5.929092	4.711563	9.259352
1.516276	4.543641	3.821621	5.999740	4.714074	9.335355
1.581887	4.563504	3.875775	6.072713	4.716335	9.411367
1.647586	4.584116	3.928577	6.148036	4.718279	9.487387
1.713370	4.605499	3.979944	6.225732	4.719931	9.563415
1.779236	4.627680	4.029789	6.305812	4.721295	9.639448
1.845178	4.650686	4.078036	6.388289	4.722376	9.715485
1.911192	4.674546	4.124606	6.473161	4.723213	9.791526
1.977270	4.699293	4.169429	6.560429	4.723834	9.867568
2.043404	4.724957	4.212437	6.650084	4.724262	9.943612
2.109586	4.751572	4.253573	6.742111	4.724496	10.019657
2.175803	4.779174	4.292785	6.836497	4.724580	10.095702
2.242046	4.807802	4.330033	6.933218	4.724561	10.171748
2.308299	4.837496	4.365286	7.032250	4.724478	10.247793
2.374548	4.868295	4.398524	7.133562	4.724346	10.323838
2.440776	4.900245	4.429741	7.237128	4.724151	10.399883
2.506962	4.933389	4.458946	7.342916	4.724015	10.475928
2.573085	4.967774	4.486159	7.450891	4.723989	10.551973
2.639121	5.003449	4.511425	7.561026	4.724142	10.628018
2.705043	5.040467	4.534798	7.673286	4.724625	10.704062
2.770821	5.078877	4.556360	7.787644	4.725461	10.780102
2.836423	5.118735	4.576212	7.904075	4.726450	10.856141
2.901812	5.160096	4.594482	8.022553	4.727319	10.932181
2.966951	5.203017	4.611327	8.143059	4.728013	11.008223
3.031794	5.247553	4.626946	8.265573	4.728911	11.084263
3.096297	5.293766	4.641545	8.390085	4.730604	11.160289
3.160408	5.341711	4.655482	8.516575	4.733644	11.236272
3.224074	5.391451	4.668780	8.645060	4.738477	11.312161
3.287237	5.443042	4.682829	8.775438	4.745367	11.387891
3.349833	5.496545	4.685494	8.803890	4.754385	11.463397
3.411798	5.552015	4.691998	8.879656	4.765884	11.538563
3.473063	5.609509	4.694225	8.908031	4.780701	11.613142
3.533553	5.669078	4.697355	8.955511	4.800087	11.686658

TABLE C.2.—FLOW PATH—SHROUD

X	R	X	R	X	R
4.825348	11.758358	7.370750	12.303631	10.104880	12.304994
4.857393	11.827286	7.446794	12.303931	10.180795	12.304994
4.896505	11.892458	7.522839	12.304185	10.256711	12.304994
4.942518	11.952954	7.598884	12.304406	10.332627	12.304994
4.995067	12.007864	7.674929	12.304592	10.408543	12.304994
5.053551	12.056405	7.750974	12.304738	10.484458	12.304994
5.117057	12.098171	7.827019	12.304857	10.560374	12.304994
5.184457	12.133327	7.903065	12.304933	10.636290	12.304994
5.254595	12.162664	7.979110	12.304983	10.712206	12.304994
5.326590	12.187114	8.055155	12.304994	10.788121	12.304994
5.399878	12.207369	8.131071	12.304994	10.864037	12.304994
5.474076	12.224003	8.206986	12.304994	10.939953	12.304994
5.548833	12.237924	8.282902	12.304994	11.015868	12.304994
5.623903	12.250056	8.358818	12.304994	11.091784	12.304994
5.699186	12.260789	8.434734	12.304994	11.167700	12.304994
5.774672	12.269980	8.510649	12.304994	11.243616	12.304994
5.850350	12.277430	8.586565	12.304994	11.319531	12.304994
5.926173	12.283228	8.662481	12.304994	11.395447	12.304994
6.002093	12.287570	8.738397	12.304994	11.471363	12.304994
6.078074	12.290683	8.814312	12.304994	11.547279	12.304994
6.154084	12.292989	8.890228	12.304994	11.623194	12.304994
6.230110	12.294663	8.966144	12.304994	11.699110	12.304994
6.306149	12.295657	9.042059	12.304994		
6.382192	12.296166	9.117975	12.304994		
6.458235	12.296694	9.193891	12.304994		
6.534277	12.297490	9.269807	12.304994		
6.610317	12.298292	9.345722	12.304994		
6.686359	12.299037	9.421638	12.304994		
6.762401	12.299728	9.497554	12.304994		
6.838444	12.300375	9.573470	12.304994		
6.914486	12.300972	9.649385	12.304994		
6.990530	12.301528	9.725301	12.304994		
7.066573	12.302029	9.801217	12.304994		
7.142617	12.302496	9.877133	12.304994		
7.218661	12.302920	9.953048	12.304994		
7.294705	12.303289	10.028964	12.304994		

C.2 Impeller Main Blade and Splitter

Impeller blades are defined by sections at multiple spanwise locations. Total of 11 sections are given. The sections are uniformly distributed in the span so that they are located from 0 to 100% span with 10% increment. Section 1 refers the hub side and section 11 is for the shroud side. They are expressed in x, $r^*\theta$ and r coordinates.

TABLE C.3.—IMPELLER MAIN BLADE—SECTION 1

X	R*θ	R	X	R*θ	R
5.265840	8.369107	8.491524	5.051690	5.245493	6.148939
5.265822	8.370171	8.490389	5.026255	5.084717	6.019389
5.265763	8.372602	8.486653	4.998027	4.924038	5.887640
5.265629	8.373900	8.479191	4.966726	4.763845	5.753951
5.265376	8.369505	8.465862	4.932078	4.604534	5.618613
5.264959	8.355918	8.445458	4.893832	4.446549	5.481969
5.264369	8.333369	8.419147	4.851705	4.290340	5.344379
5.263578	8.301677	8.387251	4.805416	4.136284	5.206068
5.262564	8.260922	8.350018	4.754643	3.984716	5.067264
5.261296	8.211501	8.307906	4.699144	3.836026	4.928287
5.259747	8.153574	8.261160	4.638699	3.690599	4.789522
5.257883	8.087281	8.210032	4.573173	3.548758	4.651432
5.255694	8.012794	8.154794	4.502501	3.410786	4.514495
5.253166	7.930204	8.095724	4.426658	3.276884	4.379132
5.250285	7.839536	8.033201	4.345679	3.147212	4.245719
5.247030	7.741474	7.967277	4.259661	3.021906	4.114622
5.243333	7.637714	7.897191	4.168773	2.901069	3.986170
5.239152	7.528632	7.822917	4.073239	2.784719	3.860677
5.234442	7.414478	7.744502	3.973357	2.672805	3.738410
5.229160	7.295432	7.662056	3.869446	2.565243	3.619586
5.223263	7.171640	7.575717	3.761849	2.461917	3.504362
5.216700	7.043240	7.485631	3.650929	2.362658	3.392863
5.209407	6.910396	7.391933	3.537085	2.267258	3.285185
5.201313	6.773400	7.294707	3.420713	2.175504	3.181392
5.192338	6.632568	7.194020	3.302190	2.087186	3.081505
5.182378	6.488212	7.089958	3.181895	2.002115	2.985525
5.171341	6.340632	6.982619	3.060195	1.920110	2.893435
5.159098	6.190119	6.872135	2.937446	1.840963	2.805207
5.145524	6.037009	6.758612	2.814019	1.764364	2.720815
5.130467	5.881652	6.642150	2.690286	1.690040	2.640235
5.113753	5.724437	6.522851	2.566574	1.617838	2.563415
5.095197	5.565743	6.400803	2.443183	1.547641	2.490285
5.074584	5.405969	6.276129	2.320418	1.479305	2.420785
5.051690	5.245493	6.148939	2.198578	1.412695	2.354856
5.026255	5.084717	6.019389	2.077950	1.347690	2.292432
4.998027	4.924038	5.887640	1.958807	1.284190	2.233448

TABLE C.3.—IMPELLER MAIN BLADE—SECTION 1

X	R*θ	R	X	R*θ	R
1.841420	1.222102	2.177831	0.082610	0.052117	1.609762
1.726046	1.161354	2.125509	0.108525	0.059902	1.614687
1.612926	1.101898	2.076400	0.138353	0.071341	1.620482
1.502291	1.043713	2.030420	0.171796	0.086737	1.627140
1.394354	0.986790	1.987477	0.208560	0.106361	1.634656
1.289316	0.931132	1.947473	0.249018	0.129240	1.643165
1.187367	0.876744	1.910310	0.293841	0.154060	1.652882
1.088685	0.823630	1.875880	0.342456	0.181716	1.663767
0.993417	0.771851	1.844070	0.395134	0.211647	1.675965
0.901678	0.721507	1.814757	0.452020	0.243475	1.689611
0.813582	0.672674	1.787818	0.512954	0.277356	1.704773
0.729233	0.625399	1.763132	0.577907	0.313205	1.721553
0.648803	0.579580	1.740600	0.646882	0.350856	1.740074
0.572502	0.535031	1.720132	0.719828	0.390230	1.760446
0.500389	0.491869	1.701600	0.796677	0.431267	1.782783
0.432432	0.450367	1.684857	0.877344	0.473915	1.807197
0.368678	0.410601	1.669786	0.961747	0.518109	1.833805
0.309240	0.372528	1.656291	1.049805	0.563750	1.862730
0.254323	0.335954	1.644299	1.141413	0.610766	1.894089
0.204022	0.300882	1.633717	1.236428	0.659150	1.927992
0.158257	0.267588	1.624425	1.334699	0.708889	1.964544
0.116911	0.236357	1.616303	1.436079	0.759940	2.003856
0.080766	0.206276	1.609416	1.540405	0.812274	2.046034
0.050569	0.176787	1.603815	1.647484	0.865899	2.091176
0.026339	0.148380	1.599421	1.757116	0.920843	2.139375
0.008343	0.121396	1.596216	1.869082	0.977146	2.190718
-0.002744	0.096324	1.594266	1.983151	1.034866	2.245289
-0.004987	0.073498	1.593874	2.099079	1.094085	2.303168
0.002103	0.057799	1.595116	2.216610	1.154906	2.364427
0.012239	0.050662	1.596906	2.335476	1.217443	2.429141
0.019231	0.048171	1.598149	2.455402	1.281830	2.497377
0.021636	0.047577	1.598579	2.576101	1.348206	2.569203
0.024060	0.047081	1.599013	2.697272	1.416726	2.644682
0.031407	0.046121	1.600333	2.818615	1.487544	2.723881
0.043744	0.045910	1.602568	2.939809	1.560836	2.806863
0.060908	0.047633	1.605717	3.060496	1.636827	2.893657

TABLE C.3.—IMPELLER MAIN BLADE—SECTION 1

X	R*θ	R	X	R*θ	R
3.180301	1.715776	2.984287	5.208581	6.579598	7.381737
3.298872	1.797897	3.078785	5.216054	6.716549	7.477113
3.415846	1.883356	3.177179	5.222791	6.849420	7.569001
3.530846	1.972333	3.279465	5.228846	6.977937	7.657329
3.643488	2.065026	3.385624	5.234288	7.101800	7.742039
3.753384	2.161631	3.495604	5.239162	7.220691	7.823088
3.860134	2.262317	3.609314	5.243511	7.334323	7.900432
3.963364	2.367236	3.726634	5.247373	7.442436	7.974012
4.062738	2.476491	3.847414	5.250784	7.544855	8.043717
4.157927	2.590160	3.971464	5.253768	7.641367	8.109468
4.248639	2.708270	4.098521	5.256337	7.732812	8.170522
4.334621	2.830810	4.228289	5.258493	7.819610	8.226244
4.415706	2.957690	4.360451	5.260272	7.901248	8.276595
4.491777	3.088765	4.494677	5.261722	7.977185	8.321600
4.562788	3.223883	4.630580	5.262880	8.047019	8.361250
4.628744	3.362891	4.767767	5.263795	8.110371	8.395550
4.689700	3.505520	4.905790	5.264495	8.166768	8.424407
4.745771	3.651424	5.044195	5.265011	8.215819	8.447839
4.797136	3.800262	5.182594	5.265381	8.257406	8.466137
4.844059	3.951703	5.320670	5.265627	8.290732	8.479104
4.886802	4.105439	5.458152	5.265768	8.315276	8.486916
4.925658	4.261205	5.594803	5.265834	8.331919	8.491124
4.960898	4.418654	5.730337	5.265866	8.341609	8.493159
4.992774	4.577321	5.864372	5.265875	8.344790	8.493760
5.021545	4.736779	5.996584			
5.047487	4.896653	6.126735			
5.070851	5.056580	6.254636			
5.091895	5.216196	6.380115			
5.110845	5.375150	6.503039			
5.127912	5.533069	6.623289			
5.143293	5.689599	6.740767			
5.157157	5.844369	6.855359			
5.169660	5.997031	6.966968			
5.180941	6.147236	7.075497			
5.191112	6.294625	7.180853			
5.200296	6.438856	7.282957			

TABLE C.4.—IMPELLER MAIN BLADE—SECTION 2

X	R*θ	R	X	R*θ	R
5.204938	8.335569	8.491771	4.884386	4.777780	5.812257
5.204907	8.336449	8.490571	4.847601	4.621756	5.680077
5.204809	8.338310	8.486651	4.807084	4.467120	5.546778
5.204613	8.338621	8.478919	4.762581	4.314295	5.412728
5.204245	8.333115	8.465455	4.713821	4.163642	5.278187
5.203676	8.318626	8.445209	4.660541	4.015460	5.143385
5.202905	8.295358	8.419269	4.602502	3.870108	5.008682
5.201911	8.263140	8.387960	4.539533	3.727927	4.874459
5.200673	8.222039	8.351557	4.471541	3.589201	4.741175
5.199166	8.172484	8.310468	4.398500	3.454171	4.609296
5.197359	8.114698	8.264864	4.320425	3.323000	4.479227
5.195229	8.048830	8.214980	4.237385	3.195813	4.351337
5.192767	7.975040	8.161076	4.149519	3.072714	4.225971
5.189964	7.893432	8.103406	4.057020	2.953780	4.103447
5.186800	7.804026	8.042314	3.960154	2.839009	3.984043
5.183255	7.707454	7.977850	3.859231	2.728352	3.868018
5.179254	7.605258	7.909332	3.754597	2.621725	3.755563
5.174756	7.497793	7.836741	3.646611	2.519030	3.646822
5.169711	7.385303	7.760120	3.535651	2.420115	3.541893
5.164074	7.267971	7.679570	3.422113	2.324799	3.440861
5.157797	7.145952	7.595216	3.306395	2.232844	3.343760
5.150813	7.019386	7.507194	3.188869	2.143986	3.250590
5.143062	6.888452	7.415623	3.069904	2.058053	3.161332
5.134463	6.753440	7.320578	2.949860	1.974892	3.075958
5.124919	6.614663	7.222123	2.829087	1.894321	2.994417
5.114332	6.472442	7.120332	2.707939	1.816070	2.916666
5.102582	6.327074	7.015301	2.586766	1.739904	2.842661
5.089545	6.178863	6.907148	2.465879	1.665693	2.772326
5.075074	6.028143	6.795983	2.345553	1.593345	2.705580
5.059004	5.875275	6.681907	2.226071	1.522741	2.642347
5.041166	5.720648	6.565023	2.107709	1.453772	2.582549
5.021344	5.564645	6.445443	1.990727	1.386341	2.526109
4.999332	5.407668	6.323293	1.875375	1.320372	2.472945
4.974892	5.250096	6.198709	1.761893	1.255794	2.422975
4.947762	5.092332	6.071866	1.650515	1.192555	2.376118
4.917685	4.934766	5.942956	1.541456	1.130624	2.332285

TABLE C.4.—IMPELLER MAIN BLADE—SECTION 2

X	R*θ	R	X	R*θ	R
1.434925	1.069995	2.291383	0.161931	0.089097	1.922113
1.331113	1.010669	2.253319	0.196770	0.109830	1.929450
1.230200	0.952659	2.217992	0.235141	0.133831	1.937748
1.132360	0.895977	2.185299	0.277644	0.159927	1.947205
1.037750	0.840639	2.155133	0.323770	0.188905	1.957783
0.946505	0.786705	2.127381	0.373762	0.220261	1.969619
0.858733	0.734269	2.101920	0.427751	0.253650	1.982836
0.774553	0.683403	2.078541	0.485601	0.289201	1.997500
0.694347	0.634080	2.054737	0.547292	0.326825	2.013708
0.617885	0.586336	2.032983	0.612835	0.366362	2.031578
0.545351	0.540018	2.013190	0.682186	0.407729	2.051216
0.476805	0.495233	1.995236	0.755284	0.450866	2.072729
0.412230	0.452224	1.978990	0.832317	0.495590	2.094495
0.351681	0.411060	1.964343	0.913110	0.541883	2.117552
0.295270	0.371703	1.951208	0.997484	0.589702	2.142725
0.243183	0.333989	1.939516	1.085346	0.638970	2.170132
0.195497	0.297933	1.929179	1.176566	0.689675	2.199880
0.152132	0.263792	1.920083	1.271000	0.741805	2.232077
0.112976	0.231834	1.912119	1.368509	0.795317	2.266828
0.078714	0.201257	1.905345	1.468964	0.850160	2.304247
0.049996	0.171580	1.899806	1.572210	0.906310	2.344442
0.026830	0.143246	1.895430	1.678029	0.963820	2.387495
0.009447	0.116567	1.892201	1.786153	1.022790	2.433467
-0.001554	0.091981	1.890182	1.896401	1.083236	2.482454
-0.004383	0.069759	1.889666	2.008677	1.145087	2.534602
0.001496	0.054217	1.890740	2.122792	1.208369	2.590017
0.010459	0.046700	1.892388	2.238400	1.273289	2.648736
0.016921	0.043830	1.893584	2.355164	1.340056	2.710798
0.019233	0.043144	1.894013	2.472854	1.408749	2.776294
0.021610	0.042629	1.894456	2.591246	1.479435	2.845331
0.028824	0.041903	1.895804	2.710065	1.552234	2.917998
0.040776	0.042337	1.898054	2.829004	1.627308	2.994362
0.057172	0.045039	1.901178	2.947717	1.704864	3.074472
0.077699	0.050724	1.905147	3.065846	1.785132	3.158374
0.102133	0.059794	1.909955	3.183064	1.868283	3.246121
0.130294	0.072500	1.915612	3.299032	1.954419	3.337766

TABLE C.4.—IMPELLER MAIN BLADE—SECTION 2

X	R*θ	R	X	R*θ	R
3.413378	2.043679	3.433333	5.163590	6.968677	7.672864
3.525703	2.136388	3.532795	5.169406	7.090818	7.755649
3.635605	2.232854	3.636116	5.174635	7.208060	7.834847
3.742706	2.333168	3.743242	5.179320	7.320122	7.910420
3.846651	2.437361	3.854096	5.183507	7.426752	7.982316
3.947078	2.545523	3.968556	5.187233	7.527769	8.050435
4.043635	2.657767	4.086430	5.190524	7.622959	8.114705
4.135990	2.774158	4.207486	5.193393	7.713063	8.174460
4.223877	2.894678	4.331441	5.195848	7.798447	8.229123
4.307088	3.019255	4.458007	5.197918	7.878635	8.278653
4.385473	3.147779	4.586867	5.199639	7.953125	8.323058
4.458942	3.280132	4.717652	5.201049	8.021543	8.362319
4.527467	3.416196	4.849977	5.202191	8.083550	8.396417
4.591047	3.555746	4.983415	5.203089	8.138795	8.425178
4.649770	3.698478	5.117512	5.203775	8.186928	8.448580
4.703782	3.844088	5.251867	5.204284	8.227785	8.466889
4.753287	3.992288	5.386164	5.204640	8.260611	8.479920
4.798536	4.142790	5.520100	5.204838	8.284845	8.487811
4.839788	4.295355	5.653416	5.204942	8.301225	8.491958
4.877283	4.449656	5.785814	5.204988	8.310549	8.493758
4.911273	4.605247	5.916890	5.205000	8.313567	8.494244
4.942005	4.761720	6.046305			
4.969749	4.918708	6.173799			
4.994761	5.075853	6.299155			
5.017295	5.232788	6.422180			
5.037593	5.389158	6.542715			
5.055863	5.544586	6.660629			
5.072325	5.698713	6.775801			
5.087149	5.851164	6.888115			
5.100502	6.001582	6.997468			
5.112534	6.149616	7.103763			
5.123388	6.294904	7.206900			
5.133168	6.437099	7.306817			
5.141992	6.575872	7.403441			
5.149952	6.710919	7.496704			
5.157127	6.841945	7.586533			

TABLE C.5.—IMPELLER MAIN BLADE—SECTION 3

X	R*θ	R	X	R*θ	R
5.143696	8.301844	8.492019	4.800805	4.789888	5.871442
5.143653	8.302536	8.490755	4.761811	4.637114	5.742496
5.143516	8.303828	8.486650	4.718952	4.485804	5.612621
5.143249	8.303139	8.478646	4.672009	4.336358	5.482187
5.142776	8.296522	8.465046	4.620742	4.189112	5.351473
5.142064	8.281134	8.444959	4.564902	4.044343	5.220749
5.141120	8.257142	8.419391	4.504306	3.902366	5.090369
5.139929	8.224398	8.388674	4.438815	3.763487	4.960725
5.138472	8.182951	8.353104	4.368370	3.627953	4.832278
5.136728	8.133255	8.313043	4.292988	3.495958	4.705473
5.134669	8.075604	8.268586	4.212726	3.367631	4.580703
5.132278	8.010153	8.219952	4.127690	3.243061	4.458324
5.129551	7.937056	8.167386	4.038051	3.122321	4.338660
5.126476	7.856412	8.111122	3.944043	3.005461	4.222008
5.123029	7.768251	8.051468	3.845948	2.892467	4.108632
5.119193	7.673150	7.988470	3.744108	2.783280	3.998758
5.114882	7.572484	7.921529	3.638886	2.677826	3.892561
5.110058	7.466600	7.850629	3.530658	2.576016	3.790166
5.104668	7.355734	7.775813	3.419809	2.477704	3.691652
5.098664	7.240068	7.697171	3.306743	2.382541	3.597073
5.091984	7.119762	7.614819	3.191854	2.290297	3.506445
5.084562	6.994966	7.528875	3.075500	2.200810	3.419746
5.076326	6.865869	7.439451	2.958044	2.113925	3.336933
5.067189	6.732763	7.346612	2.839840	2.029516	3.257958
5.057049	6.595962	7.250414	2.721226	1.947433	3.182757
5.045789	6.455783	7.150928	2.602535	1.867446	3.111270
5.033286	6.312534	7.048239	2.484098	1.789357	3.043423
5.019397	6.166525	6.942461	2.366199	1.713065	2.979128
5.003974	6.018101	6.833698	2.249095	1.638501	2.918289
4.986840	5.867624	6.722055	2.133044	1.565571	2.860811
4.967798	5.715488	6.607649	2.018293	1.494192	2.806603
4.946648	5.562083	6.490592	1.905077	1.424296	2.755574
4.923161	5.407813	6.371033	1.793618	1.355827	2.707630
4.897094	5.253064	6.249126	1.684130	1.288738	2.662682
4.868187	5.098236	6.125066	1.576820	1.222997	2.620636
4.836180	4.943719	5.999073	1.471878	1.158591	2.581397

TABLE C.5.—IMPELLER MAIN BLADE—SECTION 3

X	R*θ	R	X	R*θ	R
1.369489	1.095524	2.544870	0.152155	0.091436	2.214407
1.269823	1.033811	2.510958	0.185088	0.113267	2.221523
1.173041	0.973473	2.479559	0.221395	0.138380	2.229565
1.079296	0.914531	2.450570	0.261601	0.165737	2.238713
0.988729	0.857009	2.423887	0.305266	0.196024	2.248938
0.901462	0.800966	2.399401	0.352602	0.228789	2.260363
0.817595	0.746495	2.376995	0.403728	0.263723	2.273103
0.737230	0.693662	2.356559	0.458529	0.300924	2.287221
0.660461	0.642512	2.337978	0.516997	0.340303	2.302812
0.587412	0.592995	2.321151	0.579227	0.381668	2.319317
0.518481	0.544953	2.303214	0.645516	0.424777	2.334468
0.453460	0.498563	2.285894	0.715527	0.469690	2.351213
0.392229	0.454063	2.270201	0.789192	0.516350	2.369656
0.334850	0.411515	2.256037	0.866426	0.564703	2.389907
0.281433	0.370887	2.243320	0.947153	0.614666	2.412072
0.232146	0.332043	2.231986	1.031291	0.666162	2.436266
0.187049	0.295010	2.221952	1.118725	0.719170	2.462592
0.146062	0.260031	2.213110	1.209315	0.773680	2.491151
0.109076	0.227350	2.205358	1.302932	0.829651	2.522045
0.076680	0.196281	2.198743	1.399478	0.887008	2.555391
0.049428	0.166416	2.193307	1.498841	0.945698	2.591302
0.027317	0.138155	2.188982	1.600778	1.005799	2.629852
0.010542	0.111778	2.185751	1.704979	1.067469	2.671079
-0.000374	0.087674	2.183673	1.811307	1.130683	2.715091
-0.003784	0.066050	2.183028	1.919819	1.195217	2.762084
0.000895	0.050665	2.183914	2.030392	1.261025	2.812198
0.008694	0.042771	2.185398	2.142602	1.328399	2.865442
0.014630	0.039524	2.186534	2.256051	1.397628	2.921822
0.016850	0.038748	2.186961	2.370568	1.468728	2.981457
0.019181	0.038214	2.187410	2.486008	1.541677	3.044489
0.026263	0.037721	2.188778	2.602124	1.616562	3.111028
0.037834	0.038793	2.191030	2.718620	1.693529	3.181150
0.053467	0.042469	2.194106	2.835167	1.772761	3.254921
0.072831	0.049342	2.197969	2.951431	1.854463	3.332402
0.095797	0.059687	2.202627	3.067105	1.938762	3.413675
0.122307	0.073648	2.208106	3.181879	2.025688	3.498820

TABLE C.5.—IMPELLER MAIN BLADE—SECTION 3

X	R*θ	R	X	R*θ	R
3.295391	2.115345	3.587881	5.097981	6.959053	7.688483
3.407221	2.208048	3.680838	5.104188	7.079519	7.769329
3.516962	2.304148	3.777658	5.109780	7.195154	7.846666
3.624257	2.403857	3.878335	5.114811	7.305683	7.920458
3.728770	2.507109	3.982835	5.119330	7.410859	7.990661
3.830120	2.613976	4.091058	5.123369	7.510496	8.057186
3.927923	2.724620	4.202825	5.126967	7.604384	8.119969
4.021826	2.839128	4.317917	5.130134	7.693161	8.178418
4.111530	2.957489	4.436086	5.132883	7.777137	8.232017
4.196801	3.079639	4.557063	5.135241	7.855877	8.280722
4.277451	3.205506	4.680547	5.137239	7.928925	8.324524
4.353349	3.335009	4.806190	5.138903	7.995927	8.363394
4.424424	3.468058	4.933620	5.140275	8.056584	8.397287
4.490642	3.604468	5.062420	5.141368	8.110674	8.425953
4.552042	3.743985	5.192148	5.142223	8.157883	8.449326
4.608729	3.886343	5.322401	5.142866	8.198008	8.467646
4.660878	4.031284	5.452841	5.143319	8.230320	8.480742
4.708698	4.178554	5.583151	5.143585	8.254252	8.488710
4.752418	4.327928	5.713053	5.143722	8.270366	8.492795
4.792269	4.479098	5.842219	5.143774	8.279316	8.494360
4.828461	4.631650	5.970252	5.143786	8.282167	8.494729
4.861247	4.785185	6.096788			
4.890882	4.939347	6.221547			
4.917633	5.093774	6.344281			
4.941745	5.248102	6.464781			
4.963468	5.401966	6.582864			
4.983024	5.554987	6.698379			
5.000630	5.706796	6.811194			
5.016474	5.857012	6.921184			
5.030739	6.005273	7.028235			
5.043586	6.151218	7.132252			
5.055150	6.294485	7.233144			
5.065576	6.434722	7.330842			
5.074974	6.571600	7.425284			
5.083447	6.704808	7.516414			
5.091087	6.834049	7.604165			

TABLE C.6.—IMPELLER MAIN BLADE—SECTION 4

X	R*θ	R	X	R*θ	R
5.082113	8.267930	8.492269	4.715899	4.800646	5.931564
5.082058	8.268438	8.490940	4.674618	4.651125	5.805936
5.081883	8.269156	8.486648	4.629357	4.503158	5.679557
5.081543	8.267459	8.478372	4.579918	4.357123	5.552811
5.080964	8.259726	8.464634	4.526090	4.213337	5.426000
5.080112	8.243432	8.444708	4.467673	4.072040	5.299401
5.078999	8.218716	8.419514	4.404503	3.933518	5.173393
5.077611	8.185441	8.389391	4.336482	3.798036	5.048375
5.075937	8.143644	8.354658	4.263607	3.665797	4.924787
5.073957	8.093802	8.315632	4.185921	3.536957	4.803069
5.071656	8.036285	8.272327	4.103519	3.411607	4.683600
5.069011	7.971247	8.224949	4.016559	3.289800	4.566710
5.066027	7.898837	8.173728	3.925234	3.171580	4.452714
5.062677	7.819146	8.118877	3.829810	3.056968	4.341887
5.058950	7.732219	8.060666	3.730604	2.945934	4.234462
5.054816	7.638564	7.999142	3.627972	2.838414	4.130648
5.050191	7.539409	7.933786	3.522301	2.734337	4.030594
5.045030	7.435075	7.864589	3.413982	2.633555	3.934403
5.039284	7.325797	7.791589	3.303405	2.535663	3.842138
5.032894	7.211755	7.714869	3.190978	2.440482	3.753822
5.025787	7.093110	7.634535	3.077087	2.347863	3.669450
5.017906	6.970035	7.550690	2.962085	2.257656	3.588970
5.009161	6.842722	7.463434	2.846316	2.169732	3.512325
4.999452	6.711459	7.372826	2.730128	2.083988	3.439448
4.988668	6.576562	7.278918	2.613845	2.000308	3.370259
4.976695	6.438359	7.181769	2.497782	1.918505	3.304672
4.963386	6.297157	7.081463	2.382240	1.838420	3.242599
4.948597	6.153279	6.978103	2.267481	1.759980	3.183936
4.932159	6.007077	6.871794	2.153739	1.683140	3.128569
4.913891	5.858920	6.762639	2.041244	1.607834	3.076391
4.893584	5.709209	6.650767	1.930216	1.534007	3.027300
4.871028	5.558340	6.536299	1.820863	1.461614	2.981192
4.845987	5.406723	6.419402	1.713378	1.390624	2.937964
4.818216	5.254750	6.300244	1.607947	1.321013	2.897518
4.787447	5.102824	6.179046	1.504752	1.252767	2.859754
4.753428	4.951332	6.056049	1.403958	1.185890	2.824573

TABLE C.6.—IMPELLER MAIN BLADE—SECTION 4

X	R*θ	R	X	R*θ	R
1.305726	1.120401	2.791877	0.142492	0.093748	2.503339
1.210205	1.056322	2.761568	0.173543	0.116664	2.510192
1.117538	0.993683	2.733545	0.207811	0.142874	2.517935
1.027858	0.932516	2.707710	0.245751	0.171478	2.526731
0.941291	0.872850	2.683961	0.286987	0.203056	2.536556
0.857947	0.814744	2.662193	0.331703	0.237212	2.547523
0.777918	0.758286	2.642302	0.380145	0.273610	2.558040
0.701303	0.703538	2.624184	0.432320	0.312274	2.567710
0.628189	0.650543	2.607734	0.488107	0.353157	2.578511
0.558680	0.599273	2.592858	0.547548	0.396096	2.590543
0.492887	0.549653	2.579459	0.610635	0.440993	2.603908
0.430847	0.501788	2.567432	0.677340	0.487770	2.618701
0.372554	0.455872	2.556668	0.747602	0.536370	2.635024
0.318223	0.411964	2.544183	0.821334	0.586745	2.652970
0.267761	0.370081	2.531941	0.898462	0.638817	2.672641
0.221239	0.330119	2.521022	0.978914	0.692510	2.694140
0.178699	0.292122	2.511345	1.062587	0.747796	2.717566
0.140061	0.256312	2.502810	1.149348	0.804668	2.743013
0.105219	0.222916	2.495319	1.239073	0.863085	2.770575
0.074668	0.191360	2.488911	1.331699	0.922952	2.800371
0.048866	0.161308	2.483617	1.427148	0.984185	2.832519
0.027798	0.133118	2.479373	1.525163	1.046890	2.867081
0.011625	0.107040	2.476162	1.625382	1.111280	2.904074
0.000794	0.083412	2.474036	1.727719	1.177291	2.943614
-0.003191	0.062380	2.473259	1.832375	1.244550	2.985944
0.000300	0.047150	2.473939	1.939302	1.312933	3.031230
0.006948	0.038885	2.475242	2.047995	1.382824	3.079452
0.012364	0.035266	2.476308	2.157996	1.454585	3.130593
0.014493	0.034399	2.476729	2.269194	1.528172	3.184791
0.016778	0.033847	2.477181	2.381522	1.603475	3.242223
0.023730	0.033584	2.478561	2.494767	1.680541	3.303013
0.034923	0.035289	2.480800	2.608645	1.759503	3.367245
0.049804	0.039926	2.483807	2.722843	1.840523	3.435006
0.068016	0.047976	2.487536	2.837054	1.923771	3.506372
0.089533	0.059581	2.492011	2.950997	2.009332	3.581445
0.114410	0.074784	2.497276	3.064390	2.097162	3.660336

TABLE C.6.—IMPELLER MAIN BLADE—SECTION 4

X	R*θ	R	X	R*θ	R
3.176884	2.187327	3.743111	5.031972	6.949100	7.704197
3.288040	2.280208	3.829754	5.038595	7.067935	7.783088
3.397447	2.376177	3.920242	5.044569	7.181996	7.858550
3.504771	2.475197	4.014610	5.049958	7.291024	7.930550
3.609699	2.577326	4.112873	5.054810	7.394770	7.999050
3.711837	2.682719	4.214948	5.059167	7.493043	8.063973
3.810761	2.791595	4.320678	5.063076	7.585648	8.125261
3.906102	2.904061	4.429857	5.066538	7.673107	8.182397
3.997532	3.020115	4.542270	5.069575	7.755678	8.234926
4.084787	3.139703	4.657670	5.072219	7.832972	8.282802
4.167645	3.262788	4.775775	5.074495	7.904578	8.325997
4.245935	3.389323	4.896254	5.076417	7.970162	8.364474
4.319544	3.519253	5.018754	5.078025	8.029470	8.398164
4.388399	3.652433	5.142870	5.079324	8.082402	8.426731
4.452497	3.788653	5.268173	5.080347	8.128686	8.450074
4.511896	3.927690	5.394256	5.081123	8.168074	8.468407
4.566739	4.069316	5.520764	5.081674	8.199871	8.481567
4.617198	4.213307	5.647368	5.082004	8.223496	8.489615
4.663465	4.359459	5.773770	5.082169	8.239339	8.493637
4.705740	4.507485	5.899630	5.082223	8.247913	8.494966
4.744230	4.656989	6.024529	5.082234	8.250597	8.495218
4.779163	4.807591	6.148099			
4.810789	4.958944	6.270036			
4.839374	5.110682	6.390069			
4.865154	5.262438	6.507969			
4.888389	5.413844	6.623530			
4.909308	5.564508	6.736582			
4.928134	5.714056	6.846982			
4.945071	5.862096	6.954592			
4.960309	6.008260	7.059297			
4.974020	6.152179	7.160996			
4.986358	6.293484	7.259602			
4.997467	6.431823	7.355050			
5.007474	6.566859	7.447285			
5.016497	6.698280	7.536255			
5.024635	6.825786	7.621907			

TABLE C.7.—IMPELLER MAIN BLADE—SECTION 5

X	R*θ	R	X	R*θ	R
5.020184	8.233826	8.492519	4.629581	4.810399	5.992688
5.020116	8.234148	8.491125	4.585929	4.664165	5.870464
5.019899	8.234285	8.486646	4.538197	4.519591	5.747663
5.019485	8.231576	8.478096	4.486211	4.377029	5.624675
5.018796	8.222716	8.464220	4.429797	4.236773	5.501817
5.017800	8.205512	8.444455	4.368765	4.099040	5.379410
5.016514	8.180063	8.419638	4.303011	3.964075	5.257823
5.014929	8.146250	8.390112	4.232473	3.832099	5.137460
5.013041	8.104100	8.356222	4.157187	3.703280	5.018759
5.010831	8.054108	8.318235	4.077236	3.577730	4.902139
5.008289	7.996723	8.276090	3.992759	3.455499	4.787962
5.005404	7.932100	8.229973	3.903940	3.336608	4.676547
5.002163	7.860369	8.180104	3.811020	3.221063	4.568180
4.998545	7.781626	8.126671	3.714293	3.108860	4.463113
4.994535	7.695920	8.069912	3.614096	2.999954	4.361561
4.990091	7.603691	8.009872	3.510808	2.894270	4.263706
4.985145	7.506027	7.946111	3.404832	2.791600	4.169673
4.979639	7.403222	7.878627	3.296575	2.691519	4.079544
4.973517	7.295499	7.807457	3.186437	2.593903	3.993352
4.966715	7.183040	7.732677	3.074818	2.498622	3.911106
4.959171	7.066027	7.654377	2.962102	2.405538	3.832767
4.950792	6.944624	7.572654	2.848624	2.314526	3.758263
4.941499	6.819042	7.487593	2.734718	2.225474	3.687516
4.931183	6.689574	7.399246	2.620717	2.138311	3.620441
4.919726	6.556536	7.307657	2.506933	2.052953	3.556943
4.906985	6.420251	7.212886	2.393655	1.969259	3.496918
4.892824	6.281043	7.115003	2.281158	1.887110	3.440260
4.877074	6.139243	7.014108	2.169677	1.806461	3.386848
4.859557	5.995209	6.910306	2.059421	1.727293	3.336559
4.840085	5.849323	6.803700	1.950592	1.649569	3.289275
4.818440	5.701993	6.694425	1.843382	1.573260	3.244883
4.794400	5.553622	6.582616	1.737970	1.498347	3.203269
4.767724	5.404629	6.468453	1.634522	1.424821	3.164323
4.738166	5.255414	6.352120	1.533196	1.352682	3.127943
4.705452	5.106381	6.233865	1.434146	1.281934	3.094023
4.669339	4.957920	6.113945	1.337514	1.212597	3.062464

TABLE C.7.—IMPELLER MAIN BLADE—SECTION 5

X	R*θ	R	X	R*θ	R
1.243438	1.144702	3.033167	0.132970	0.096025	2.788028
1.152049	1.078281	3.006033	0.162221	0.119996	2.793283
1.063470	1.013372	2.980968	0.194621	0.147238	2.797926
0.977817	0.950013	2.957873	0.230533	0.176990	2.803253
0.895200	0.888241	2.936654	0.269654	0.209724	2.809276
0.815719	0.828115	2.917216	0.312157	0.245089	2.816078
0.739460	0.769715	2.899459	0.358154	0.282830	2.823743
0.666519	0.713099	2.883291	0.407593	0.322982	2.832334
0.596979	0.658310	2.868620	0.460503	0.365437	2.841931
0.530922	0.605339	2.855355	0.516936	0.410037	2.852630
0.468433	0.554144	2.843406	0.576897	0.456677	2.864519
0.409543	0.504827	2.832680	0.640367	0.505276	2.877690
0.354256	0.457554	2.823081	0.707290	0.555775	2.892231
0.302623	0.412385	2.814529	0.777580	0.608132	2.908226
0.254734	0.369312	2.806952	0.851162	0.662278	2.925766
0.210700	0.328261	2.800287	0.927973	0.718136	2.944947
0.170530	0.289296	2.794458	1.007920	0.775673	2.965863
0.134147	0.252647	2.788289	1.090876	0.834883	2.988593
0.101418	0.218546	2.781110	1.176723	0.895730	3.013231
0.072684	0.186509	2.774953	1.265430	0.958094	3.039889
0.048313	0.156272	2.769838	1.356954	1.021869	3.068693
0.028273	0.128152	2.765706	1.451020	1.087180	3.099688
0.012693	0.102367	2.762539	1.547218	1.154302	3.132874
0.001945	0.079209	2.760378	1.645507	1.223132	3.168372
-0.002606	0.058762	2.759468	1.746237	1.293146	3.206461
-0.000287	0.043685	2.759931	1.849430	1.364147	3.247330
0.005227	0.035053	2.761035	1.954504	1.436607	3.290937
0.010130	0.031067	2.762022	2.060941	1.510962	3.337237
0.012169	0.030112	2.762434	2.168687	1.587108	3.386386
0.014409	0.029541	2.762886	2.277757	1.664846	3.438592
0.021232	0.029506	2.764270	2.387974	1.744185	3.493990
0.032054	0.031834	2.766481	2.499064	1.825241	3.552674
0.046192	0.037419	2.769399	2.610739	1.908151	3.614738
0.063271	0.046629	2.772966	2.722715	1.993056	3.680284
0.083358	0.059477	2.777225	2.834739	2.079992	3.749432
0.106629	0.075903	2.782241	2.946564	2.168841	3.822315

TABLE C.7.—IMPELLER MAIN BLADE—SECTION 5

X	R*θ	R	X	R*θ	R
3.057854	2.259627	3.899025	4.965529	6.938849	7.720015
3.168158	2.352793	3.979546	4.972581	7.056078	7.796935
3.277051	2.448780	4.063876	4.978953	7.168595	7.870507
3.384237	2.547470	4.152082	4.984712	7.276142	7.940703
3.489419	2.648547	4.244231	4.989910	7.378478	8.007488
3.592194	2.752319	4.340263	4.994599	7.475412	8.070797
3.692112	2.859272	4.440027	4.998816	7.566740	8.130584
3.788773	2.969551	4.543350	5.002580	7.652893	8.186399
3.881828	3.083153	4.650043	5.005903	7.734064	8.237852
3.970987	3.200038	4.759882	5.008829	7.809912	8.284894
4.055988	3.320207	4.872606	5.011379	7.880072	8.327480
4.136626	3.443647	4.987907	5.013566	7.944237	8.365561
4.212746	3.570338	5.105445	5.015417	8.002195	8.399044
4.284232	3.700175	5.224835	5.016931	8.053971	8.427514
4.351040	3.832994	5.345656	5.018127	8.099325	8.450829
4.413185	3.968615	5.467505	5.019042	8.137975	8.469172
4.470767	4.106843	5.590011	5.019693	8.169257	8.482397
4.523915	4.247485	5.712837	5.020087	8.192573	8.490525
4.572807	4.390352	5.835650	5.020279	8.208142	8.494483
4.617603	4.535181	5.958106	5.020332	8.216335	8.495575
4.658478	4.681602	6.079786	5.020339	8.218850	8.495709
4.695652	4.829249	6.200302			
4.729369	4.977779	6.319330			
4.759873	5.126831	6.436584			
4.787425	5.276027	6.551798			
4.812262	5.424992	6.664764			
4.834626	5.573327	6.775286			
4.854754	5.720645	6.883207			
4.872857	5.866549	6.988381			
4.889135	6.010657	7.090685			
4.903770	6.152592	7.190023			
4.916936	6.291981	7.286301			
4.928775	6.428463	7.379466			
4.939439	6.561700	7.469460			
4.949046	6.691375	7.556245			
4.957709	6.817183	7.639776			

TABLE C.8.—IMPELLER MAIN BLADE—SECTION 6

X	R*θ	R	X	R*θ	R
4.957893	8.199522	8.492772	4.541736	4.819419	6.054892
4.957811	8.199657	8.491312	4.495659	4.676527	5.936142
4.957550	8.199210	8.486644	4.445399	4.535413	5.816992
4.957052	8.195475	8.477819	4.390814	4.396408	5.697835
4.956246	8.185479	8.463803	4.331766	4.259778	5.579004
4.955101	8.167352	8.444201	4.268105	4.125713	5.460837
4.953637	8.141163	8.419762	4.199759	3.994419	5.343716
4.951853	8.106807	8.390838	4.126720	3.866075	5.228041
4.949751	8.064298	8.357796	4.049046	3.740809	5.114251
4.947324	8.014159	8.320854	3.966879	3.618686	5.002734
4.944553	7.956907	8.279875	3.880392	3.499715	4.893836
4.941429	7.892695	8.235025	3.789800	3.383884	4.787868
4.937935	7.821639	8.186516	3.695385	3.271164	4.685083
4.934050	7.743838	8.134510	3.597465	3.161518	4.585716
4.929746	7.659338	8.079212	3.496401	3.054885	4.489955
4.924989	7.568529	8.020665	3.392600	2.950985	4.397949
4.919702	7.472332	7.958511	3.286469	2.849333	4.309811
4.913834	7.371032	7.892753	3.178434	2.749845	4.225592
4.907320	7.264841	7.823429	3.068900	2.652426	4.145303
4.900094	7.153945	7.750604	2.958263	2.556959	4.068924
4.892069	7.038519	7.674363	2.846896	2.463325	3.996397
4.883172	6.918758	7.594784	2.735117	2.371419	3.927624
4.873299	6.794874	7.511945	2.623245	2.281153	3.862510
4.862330	6.667158	7.425891	2.511599	2.192488	3.800950
4.850143	6.535931	7.336662	2.400473	2.105375	3.742837
4.836593	6.401528	7.244308	2.290130	2.019719	3.688052
4.821518	6.264272	7.148895	2.180818	1.935442	3.636468
4.804747	6.124509	7.050519	2.072741	1.852530	3.587958
4.786085	5.982607	6.949279	1.966083	1.770988	3.542387
4.765335	5.838961	6.845285	1.861019	1.690808	3.499627
4.742275	5.693986	6.738676	1.757709	1.611989	3.459558
4.716670	5.548095	6.629599	1.656304	1.534536	3.422061
4.688276	5.401717	6.518247	1.556941	1.458465	3.387022
4.656839	5.255261	6.404825	1.459752	1.383796	3.354334
4.622106	5.109137	6.289587	1.364867	1.310553	3.323890
4.583815	4.963734	6.172829	1.272400	1.238769	3.295590

TABLE C.8.—IMPELLER MAIN BLADE—SECTION 6

X	R*θ	R	X	R*θ	R
1.182472	1.168488	3.269338	0.124200	0.098123	3.050259
1.095193	1.099749	3.245038	0.151797	0.123063	3.053907
1.010667	1.032599	3.222597	0.182366	0.151292	3.058076
0.928997	0.967083	3.201926	0.216246	0.182165	3.062855
0.850278	0.903242	3.182932	0.253195	0.216056	3.068255
0.774602	0.841134	3.165531	0.293361	0.252664	3.074350
0.702046	0.780834	3.149633	0.336845	0.291764	3.081211
0.632707	0.722394	3.135154	0.383620	0.333363	3.088896
0.566664	0.665853	3.122015	0.433724	0.377351	3.097480
0.503981	0.611226	3.110127	0.487220	0.423570	3.107045
0.444715	0.558500	3.099412	0.544124	0.471913	3.117674
0.388893	0.507772	3.089783	0.604425	0.522294	3.129451
0.336531	0.459184	3.081160	0.668074	0.574652	3.142453
0.287681	0.412789	3.073474	0.734980	0.628955	3.156754
0.242432	0.368586	3.066661	0.805068	0.685141	3.172436
0.200875	0.326528	3.060666	0.878284	0.743131	3.189585
0.163000	0.286691	3.055419	0.954546	0.802890	3.208285
0.128707	0.249276	3.050848	1.033728	0.864414	3.228614
0.097883	0.214482	3.046884	1.115720	0.927669	3.250650
0.070822	0.181954	3.043515	1.200517	0.992518	3.274507
0.047788	0.151506	3.040733	1.288116	1.058824	3.300305
0.028725	0.123420	3.038487	1.378219	1.126741	3.328087
0.013715	0.097893	3.036757	1.470368	1.196601	3.357829
0.003052	0.075171	3.035548	1.564567	1.268263	3.389653
-0.002044	0.055278	3.034975	1.661312	1.341057	3.423871
-0.000852	0.040351	3.035108	1.760699	1.414712	3.460690
0.003573	0.031372	3.035606	1.862065	1.489785	3.500043
0.007986	0.027039	3.036105	1.964832	1.566789	3.541865
0.009941	0.026002	3.036327	2.069006	1.645559	3.586325
0.012139	0.025416	3.036577	2.174685	1.725808	3.633652
0.018845	0.025608	3.037345	2.281725	1.807504	3.683993
0.029321	0.028543	3.038557	2.389869	1.890748	3.737449
0.042769	0.035043	3.040137	2.498850	1.975650	3.794127
0.058797	0.045359	3.042054	2.608414	2.062319	3.854139
0.077576	0.059379	3.044345	2.718336	2.150741	3.917627
0.099397	0.076942	3.047075	2.828405	2.240723	3.984751

TABLE C.8.—IMPELLER MAIN BLADE—SECTION 6

X	R*θ	R	X	R*θ	R
2.938306	2.332241	4.055617	4.898585	6.928309	7.735951
3.047569	2.425805	4.130221	4.906104	7.043963	7.810879
3.155767	2.521919	4.208569	4.912900	7.154960	7.882545
3.262633	2.620396	4.290772	4.919041	7.261046	7.950922
3.367906	2.720800	4.376935	4.924602	7.361989	8.015980
3.471168	2.823153	4.467026	4.929622	7.457592	8.077665
3.571939	2.928057	4.560909	4.934158	7.547657	8.135939
3.669793	3.036017	4.658438	4.938222	7.632506	8.190426
3.764366	3.147034	4.759453	4.941838	7.712284	8.240796
3.855339	3.261081	4.863752	4.945042	7.786684	8.287000
3.942413	3.378200	4.971102	4.947863	7.855394	8.328972
4.025348	3.498413	5.081212	4.950320	7.918141	8.366654
4.103947	3.621735	5.193760	4.952420	7.974744	8.399931
4.178051	3.748105	5.308384	4.954156	8.025362	8.428303
4.247578	3.877404	5.424672	4.955537	8.069788	8.451586
4.312494	4.009497	5.542222	4.956599	8.107699	8.469941
4.372856	4.144226	5.660657	4.957358	8.138468	8.483232
4.428754	4.281426	5.779624	4.957819	8.161474	8.491440
4.480336	4.420928	5.898769	4.958037	8.176768	8.495335
4.527733	4.562487	6.017733	4.958085	8.184578	8.496187
4.571085	4.705765	6.136100	4.958086	8.186921	8.496203
4.610600	4.850411	6.253469			
4.646499	4.996087	6.369501			
4.679028	5.142427	6.483884			
4.708436	5.289053	6.596338			
4.734972	5.435578	6.706627			
4.758876	5.581592	6.814544			
4.780394	5.726697	6.919916			
4.799740	5.870484	7.022592			
4.817130	6.012562	7.122441			
4.832758	6.152542	7.219366			
4.846805	6.290042	7.313273			
4.859434	6.424700	7.404112			
4.870802	6.556172	7.491831			
4.881038	6.684131	7.576400			
4.890262	6.808269	7.657784			

TABLE C.9.—IMPELLER MAIN BLADE—SECTION 7

X	R*θ	R	X	R*θ	R
4.895214	8.165005	8.493027	4.452285	4.827908	6.118233
4.895116	8.164949	8.491500	4.403696	4.688429	6.003052
4.894805	8.163912	8.486643	4.350850	4.550860	5.887630
4.894210	8.159138	8.477539	4.293636	4.415502	5.772360
4.893282	8.147995	8.463384	4.231919	4.282606	5.657620
4.891978	8.128934	8.443944	4.165612	4.152326	5.543747
4.890333	8.101995	8.419887	4.094674	4.024829	5.431134
4.888352	8.067090	8.391567	4.019145	3.900248	5.320180
4.886041	8.024218	8.359381	3.939125	3.778671	5.211313
4.883410	7.973940	8.323490	3.854795	3.660113	5.104902
4.880420	7.916823	8.283682	3.766367	3.544544	5.001274
4.877060	7.853018	8.240109	3.674095	3.431913	4.900715
4.873314	7.782636	8.192967	3.578290	3.322153	4.803462
4.869150	7.705766	8.142398	3.479296	3.215198	4.709725
4.864544	7.622461	8.088572	3.377504	3.110761	4.619661
4.859462	7.533057	8.031529	3.273328	3.008227	4.533401
4.853827	7.438317	7.970992	3.167202	2.907506	4.451019
4.847578	7.338503	7.906976	3.059557	2.808536	4.372552
4.840646	7.233819	7.839516	2.950797	2.711231	4.297985
4.832959	7.124453	7.768669	2.841315	2.615493	4.227275
4.824436	7.010597	7.694508	2.731471	2.521221	4.160337
4.814979	6.892445	7.617102	2.621566	2.428334	4.097054
4.804481	6.770224	7.536517	2.511897	2.336770	4.037306
4.792821	6.644230	7.452791	2.402767	2.246523	3.980985
4.779852	6.514784	7.365963	2.294452	2.157581	3.927964
4.765435	6.382227	7.276071	2.187189	2.069895	3.878109
4.749382	6.246892	7.183183	2.081191	1.983431	3.831282
4.731521	6.109139	7.087381	1.976635	1.898203	3.787347
4.711647	5.969348	6.988766	1.873678	1.814246	3.746158
4.689546	5.827923	6.887450	1.772464	1.731578	3.707588
4.664989	5.685292	6.783578	1.673124	1.650225	3.671506
4.637736	5.541880	6.677310	1.575780	1.570219	3.637791
4.607544	5.398124	6.568846	1.480542	1.491597	3.606327
4.574140	5.254444	6.458419	1.387516	1.414399	3.577005
4.537289	5.111260	6.346292	1.296804	1.338669	3.549721
4.496742	4.968959	6.232779	1.208500	1.264453	3.524374

TABLE C.9.—IMPELLER MAIN BLADE—SECTION 7

X	R*θ	R	X	R*θ	R
1.122703	1.191806	3.500871	0.115720	0.100152	3.303798
1.039507	1.120775	3.479121	0.141671	0.126042	3.307093
0.958999	1.051413	3.459037	0.170459	0.155232	3.310857
0.881267	0.983771	3.440533	0.202361	0.187194	3.315165
0.806394	0.917896	3.423526	0.237194	0.222212	3.320030
0.734462	0.853843	3.407939	0.275081	0.260032	3.325514
0.665548	0.791681	3.393689	0.316116	0.300455	3.331678
0.599743	0.731455	3.380706	0.360290	0.343466	3.338576
0.537126	0.673204	3.368916	0.407653	0.388950	3.346275
0.477744	0.616959	3.358241	0.458277	0.436752	3.354849
0.421627	0.562740	3.348606	0.512187	0.486761	3.364372
0.368802	0.510638	3.339937	0.569382	0.538886	3.374921
0.319291	0.460769	3.332165	0.629815	0.593069	3.386563
0.273154	0.413181	3.325230	0.693394	0.649283	3.399367
0.230475	0.367881	3.319079	0.760040	0.707474	3.413398
0.191327	0.324844	3.313659	0.829710	0.767566	3.428737
0.155685	0.284160	3.308911	0.902327	0.829518	3.445459
0.123447	0.246017	3.304769	0.977770	0.893330	3.463635
0.094501	0.210593	3.301172	1.055932	0.958972	3.483334
0.069057	0.177636	3.298108	1.136837	1.026288	3.504668
0.047295	0.147023	3.295559	1.220516	1.095115	3.527753
0.029148	0.118998	3.293484	1.306649	1.165633	3.552620
0.014667	0.093731	3.291860	1.394731	1.238232	3.579230
0.004078	0.071426	3.290691	1.484808	1.312735	3.607705
-0.001523	0.052053	3.290080	1.577521	1.388328	3.638380
-0.001375	0.037261	3.290096	1.673038	1.464666	3.671475
0.002038	0.027954	3.290469	1.770619	1.542392	3.706902
0.005993	0.023294	3.290901	1.869623	1.622093	3.744578
0.007869	0.022178	3.291108	1.970115	1.703548	3.784678
0.010026	0.021577	3.291347	2.072279	1.786376	3.827451
0.016618	0.021972	3.292078	2.176003	1.870509	3.873055
0.026764	0.025464	3.293215	2.281048	1.956030	3.921591
0.039550	0.032809	3.294667	2.387171	2.043023	3.973179
0.054569	0.044159	3.296403	2.494148	2.131560	4.027939
0.072074	0.059286	3.298466	2.601787	2.221578	4.086035
0.092465	0.077939	3.300925	2.709915	2.312806	4.147644

TABLE C.9.—IMPELLER MAIN BLADE—SECTION 7

X	R*θ	R	X	R*θ	R
2.818240	2.405170	4.212889	4.831089	6.917495	7.752020
2.926272	2.499246	4.281782	4.839100	7.031592	7.824934
3.033588	2.595598	4.354331	4.846338	7.141083	7.894674
3.139952	2.693968	4.430692	4.852889	7.245726	7.961215
3.245143	2.793799	4.511005	4.858822	7.345290	8.024532
3.348731	2.895098	4.595267	4.864197	7.439577	8.084581
3.450205	2.998231	4.683362	4.869061	7.528387	8.141330
3.549118	3.103758	4.775168	4.873436	7.611942	8.194479
3.645093	3.212066	4.870550	4.877344	7.690325	8.243759
3.737781	3.323147	4.969338	4.880831	7.763279	8.289119
3.826850	3.437084	5.071322	4.883925	7.830539	8.330474
3.912022	3.553937	5.176234	4.886649	7.891860	8.367756
3.993057	3.673759	5.283773	4.889002	7.947104	8.400823
4.069765	3.796528	5.393590	4.890966	7.996561	8.429095
4.142011	3.922181	5.505295	4.892543	8.040058	8.452349
4.209720	4.050624	5.618485	4.893763	8.077233	8.470716
4.272901	4.181737	5.732778	4.894639	8.107490	8.484071
4.331600	4.315390	5.847809	4.895171	8.130186	8.492360
4.385935	4.451430	5.963204	4.895416	8.145204	8.496191
4.436009	4.589635	6.078590	4.895455	8.152624	8.496803
4.481934	4.729693	6.193548	4.895449	8.154793	8.496701
4.523877	4.871274	6.307680			
4.562062	5.014043	6.420620			
4.596718	5.157635	6.532043			
4.628082	5.301664	6.641648			
4.656410	5.445730	6.749179			
4.681949	5.589415	6.854412			
4.704944	5.732307	6.957162			
4.725614	5.873985	7.057275			
4.744194	6.014043	7.154608			
4.760886	6.152084	7.249063			
4.775882	6.287716	7.340550			
4.789359	6.420571	7.429020			
4.801483	6.550298	7.514425			
4.812392	6.676564	7.596745			
4.822224	6.799058	7.675950			

TABLE C.10.—IMPELLER MAIN BLADE—SECTION 8

X	R*θ	R	X	R*θ	R
4.832106	8.130251	8.493282	4.361093	4.835994	6.182807
4.831990	8.130003	8.491690	4.309944	4.700010	6.071264
4.831617	8.128364	8.486641	4.254463	4.566078	5.959640
4.830921	8.122540	8.477258	4.194570	4.434475	5.848334
4.829852	8.110229	8.462961	4.130166	4.305426	5.737737
4.828390	8.090229	8.443687	4.061199	4.179056	5.628208
4.826563	8.062533	8.420013	3.987676	4.055488	5.520144
4.824387	8.027075	8.392304	3.909681	3.934809	5.413938
4.821886	7.983851	8.360975	3.827358	3.817061	5.310007
4.819053	7.933426	8.326144	3.740926	3.702213	5.208697
4.815849	7.876444	8.287516	3.650635	3.590188	5.110318
4.812254	7.813045	8.245228	3.556780	3.480895	5.015133
4.808248	7.743325	8.199463	3.459692	3.374233	4.923360
4.803801	7.667380	8.150341	3.359755	3.269924	4.835175
4.798887	7.585268	8.097996	3.257374	3.167231	4.750712
4.793463	7.497254	8.042470	3.152982	3.065986	4.670072
4.787456	7.403953	7.983568	3.047023	2.966125	4.593307
4.780803	7.305608	7.921311	2.939936	2.867593	4.520429
4.773431	7.202414	7.855733	2.832124	2.770320	4.451404
4.765255	7.094558	7.786888	2.723975	2.674223	4.386156
4.756193	6.982244	7.714834	2.615831	2.579224	4.324582
4.746133	6.865672	7.639632	2.507970	2.485272	4.266548
4.734967	6.745090	7.561338	2.400670	2.392326	4.211914
4.722563	6.620791	7.479980	2.294216	2.300418	4.160556
4.708762	6.493099	7.395596	2.188860	2.209576	4.112342
4.693414	6.362364	7.308219	2.084812	2.119796	4.067124
4.676322	6.228928	7.217910	1.982250	2.031089	4.024755
4.657304	6.093168	7.124743	1.881324	1.943499	3.985085
4.636137	5.955471	7.028821	1.782159	1.857089	3.947976
4.612610	5.816261	6.930252	1.684873	1.771904	3.913284
4.586474	5.675973	6.829195	1.589564	1.687998	3.880884
4.557491	5.535047	6.725813	1.496329	1.605427	3.850648
4.525401	5.393930	6.620329	1.405247	1.524250	3.822466
4.489960	5.253059	6.512972	1.316399	1.444528	3.796225
4.450910	5.112855	6.404042	1.229865	1.366320	3.771822
4.408024	4.973713	6.293861	1.145715	1.289689	3.749164

TABLE C.10.—IMPELLER MAIN BLADE—SECTION 8

X	R*θ	R	X	R*θ	R
1.064031	1.214697	3.728158	0.107456	0.102129	3.550898
0.984887	1.141399	3.708720	0.131801	0.128946	3.553879
0.908360	1.069853	3.690767	0.158851	0.159073	3.557284
0.834521	1.000116	3.674222	0.188823	0.192098	3.561170
0.763442	0.932239	3.659008	0.221590	0.228215	3.565557
0.695200	0.866275	3.645052	0.257251	0.267217	3.570494
0.629865	0.802285	3.632289	0.295891	0.308934	3.576038
0.567531	0.740309	3.620650	0.337522	0.353325	3.582232
0.508276	0.680383	3.610073	0.382203	0.400272	3.589139
0.452128	0.622557	3.600486	0.430014	0.449623	3.596826
0.399094	0.566879	3.591820	0.480989	0.501264	3.605361
0.349198	0.513434	3.584012	0.535135	0.555101	3.614809
0.302476	0.462315	3.577001	0.592410	0.611075	3.625232
0.258987	0.413564	3.570740	0.652715	0.669167	3.636686
0.218817	0.367193	3.565181	0.715971	0.729333	3.649233
0.182021	0.323203	3.560278	0.782140	0.791495	3.662942
0.148556	0.281694	3.555976	0.851154	0.855613	3.677883
0.118321	0.242840	3.552218	0.922894	0.921687	3.694114
0.091205	0.206804	3.548952	0.997255	0.989693	3.711698
0.067337	0.173429	3.546157	1.074288	1.059458	3.730742
0.046815	0.142655	3.543819	1.154056	1.130793	3.751363
0.029560	0.114689	3.541893	1.236221	1.203905	3.773577
0.015594	0.089677	3.540364	1.320224	1.279242	3.797328
0.005077	0.067779	3.539230	1.406153	1.356593	3.822740
-0.001015	0.048911	3.538580	1.494795	1.434999	3.850162
-0.001884	0.034252	3.538487	1.586388	1.514044	3.879829
0.000542	0.024625	3.538746	1.680116	1.594457	3.911630
0.004052	0.019647	3.539121	1.775271	1.676899	3.945465
0.005850	0.018454	3.539312	1.871981	1.761092	3.981512
0.007968	0.017836	3.539540	1.970511	1.846566	4.020041
0.014449	0.018429	3.540239	2.070790	1.933211	4.061206
0.024272	0.022463	3.541310	2.172591	2.021095	4.105118
0.036414	0.030633	3.542653	2.275699	2.110271	4.151899
0.050449	0.042989	3.544228	2.379918	2.200779	4.201686
0.066714	0.059195	3.546085	2.485095	2.292502	4.254649
0.085710	0.078910	3.548302	2.591097	2.385089	4.310987

TABLE C.10.—IMPELLER MAIN BLADE—SECTION 8

X	R*θ	R	X	R*θ	R
2.697653	2.478416	4.370843	4.762960	6.906401	7.768239
2.804266	2.573116	4.434228	4.771498	7.018958	7.839114
2.910505	2.669821	4.501171	4.779215	7.126962	7.906907
3.016183	2.768193	4.571853	4.786201	7.230177	7.971592
3.121109	2.867554	4.646463	4.792529	7.328373	8.033152
3.224851	2.967891	4.725020	4.798268	7.421352	8.091550
3.326871	3.069625	4.807424	4.803472	7.508915	8.146763
3.426702	3.172999	4.893580	4.808168	7.591181	8.198563
3.523954	3.278479	4.983386	4.812386	7.668177	8.246744
3.618244	3.386470	5.076702	4.816163	7.739685	8.291253
3.709222	3.497091	5.173333	4.819532	7.805491	8.331986
3.796561	3.610448	5.273045	4.822518	7.865378	8.368865
3.879989	3.726631	5.375554	4.825133	7.919263	8.401721
3.959279	3.845659	5.480526	4.827329	7.967554	8.429894
4.034236	3.967531	5.587603	4.829107	8.010119	8.453117
4.104753	4.092193	5.696375	4.830493	8.046556	8.471495
4.170783	4.219566	5.806459	4.831489	8.076296	8.484917
4.232331	4.349555	5.917479	4.832106	8.098690	8.493287
4.289478	4.482027	6.029043	4.832380	8.113428	8.497053
4.342300	4.616781	6.140764	4.832407	8.120455	8.497424
4.390880	4.753532	6.252220	4.832390	8.122449	8.497202
4.435349	4.891973	6.363020			
4.475916	5.031773	6.472775			
4.512798	5.172565	6.581142			
4.546228	5.313955	6.687803			
4.576455	5.455535	6.792486			
4.603721	5.596871	6.894954			
4.628277	5.737540	6.995010			
4.650367	5.877104	7.092482			
4.670217	6.015146	7.187233			
4.688048	6.151256	7.279159			
4.704065	6.285032	7.368171			
4.718452	6.416096	7.454222			
4.731389	6.544094	7.537272			
4.743025	6.668683	7.617303			
4.753510	6.789549	7.694296			

TABLE C.11.—IMPELLER MAIN BLADE—SECTION 9

X	R*θ	R	X	R*θ	R
4.768517	8.095233	8.493540	4.268064	4.843787	6.248682
4.768379	8.094787	8.491880	4.214294	4.711389	6.140858
4.767943	8.092541	8.486639	4.156134	4.581197	6.033102
4.767140	8.085660	8.476975	4.093526	4.453463	5.925824
4.765923	8.072166	8.462536	4.026411	4.328387	5.819430
4.764298	8.051213	8.443426	3.954779	4.206060	5.714294
4.762294	8.022758	8.420140	3.878683	4.086561	5.610813
4.759935	7.986751	8.393045	3.798252	3.969928	5.509378
4.757245	7.943165	8.362583	3.713677	3.856156	5.410390
4.754222	7.892600	8.328817	3.625212	3.745163	5.314176
4.750802	7.835747	8.291378	3.533145	3.636827	5.221020
4.746967	7.772747	8.250384	3.437810	3.531012	5.131166
4.742694	7.703687	8.206007	3.339563	3.427472	5.044806
4.737952	7.628656	8.158344	3.238819	3.325316	4.962088
4.732716	7.547724	8.107494	3.135999	3.224287	4.883122
4.726930	7.461091	8.053500	3.031548	3.124267	4.807980
4.720531	7.369216	7.996249	2.925922	3.025193	4.736687
4.713446	7.272321	7.935771	2.819565	2.927021	4.669234
4.705599	7.170596	7.872100	2.712882	2.829692	4.605558
4.696901	7.064232	7.805281	2.606244	2.733148	4.545567
4.687256	6.953436	7.735366	2.499975	2.637337	4.489135
4.676552	6.838426	7.662404	2.394330	2.542231	4.436108
4.664669	6.719458	7.586438	2.289563	2.447823	4.386333
4.651465	6.596832	7.507494	2.185938	2.354179	4.339675
4.636771	6.470875	7.425606	2.083683	2.261366	4.295996
4.620427	6.341944	7.340798	1.982980	2.169431	4.255132
4.602231	6.210394	7.253127	1.883970	2.078429	4.216935
4.581975	6.076612	7.162664	1.786773	1.988434	4.181248
4.559442	5.941007	7.069504	1.691487	1.899535	4.147925
4.534402	5.804011	6.973762	1.598198	1.811808	4.116829
4.506608	5.666076	6.875596	1.506976	1.725332	4.087828
4.475802	5.527654	6.775189	1.417887	1.640188	4.060802
4.441738	5.389206	6.672764	1.330987	1.556454	4.035634
4.404159	5.251183	6.568577	1.246330	1.474213	4.012217
4.362828	5.114014	6.462929	1.163972	1.393540	3.990453
4.317530	4.978095	6.356167	1.083965	1.314509	3.970249

TABLE C.11.—IMPELLER MAIN BLADE—SECTION 9

X	R*θ	R	X	R*θ	R
1.006370	1.237192	3.951522	0.099382	0.104060	3.792324
0.931250	1.161651	3.934190	0.122157	0.131784	3.795015
0.858664	1.087949	3.918178	0.147507	0.162826	3.798090
0.788674	1.016146	3.903414	0.175592	0.196890	3.801591
0.721340	0.946299	3.889830	0.206338	0.234083	3.805541
0.656733	0.878455	3.877361	0.239822	0.274242	3.809980
0.594922	0.812670	3.865945	0.276118	0.317225	3.814955
0.535999	0.748977	3.855530	0.315257	0.362967	3.820509
0.480044	0.687408	3.846056	0.357310	0.411347	3.826696
0.427068	0.628033	3.837461	0.402362	0.462217	3.833577
0.377057	0.570926	3.829678	0.450456	0.515458	3.841209
0.330031	0.516168	3.822657	0.501608	0.570975	3.849659
0.286037	0.463826	3.816343	0.555776	0.628710	3.858976
0.245141	0.413938	3.810699	0.612858	0.688650	3.869206
0.207425	0.366521	3.805683	0.672773	0.750759	3.880406
0.172927	0.321599	3.801256	0.735488	0.814963	3.892633
0.141591	0.279285	3.797364	0.800940	0.881219	3.905954
0.113313	0.239737	3.793963	0.869012	0.949530	3.920416
0.087986	0.203103	3.791002	0.939601	1.019879	3.936078
0.065656	0.169320	3.788461	1.012785	1.092073	3.953038
0.046345	0.138389	3.786314	1.088656	1.165903	3.971409
0.029962	0.110481	3.784531	1.166854	1.241600	3.991198
0.016499	0.085716	3.783090	1.246771	1.319670	4.012336
0.006054	0.064216	3.781988	1.328535	1.399871	4.034939
-0.000519	0.045842	3.781303	1.413073	1.481104	4.059376
-0.002382	0.031312	3.781108	1.500695	1.562877	4.085882
-0.000919	0.021374	3.781261	1.590509	1.646006	4.114331
0.002156	0.016083	3.781582	1.681740	1.731229	4.144606
0.003878	0.014816	3.781761	1.774574	1.818210	4.176890
0.005958	0.014182	3.781978	1.869363	1.906390	4.211458
0.012330	0.014969	3.782649	1.966071	1.995618	4.248473
0.021838	0.019532	3.783659	2.064488	2.085946	4.288045
0.033351	0.028507	3.784896	2.164427	2.177398	4.330298
0.046424	0.041847	3.786323	2.265723	2.269977	4.375379
0.061477	0.059107	3.787992	2.368262	2.363513	4.423467
0.079110	0.079859	3.789984	2.471952	2.457570	4.474779

TABLE C.11.—IMPELLER MAIN BLADE—SECTION 9

X	R*θ	R	X	R*θ	R
2.576550	2.551975	4.529472	4.694112	6.895021	7.784629
2.681549	2.647418	4.587562	4.703218	7.006050	7.853437
2.786514	2.744593	4.649094	4.711450	7.112580	7.919256
2.891307	2.843082	4.714276	4.718902	7.214377	7.982064
2.995781	2.942078	4.783334	4.725653	7.311219	8.041847
3.099500	3.041547	4.856312	4.731774	7.402898	8.098579
3.201902	3.141965	4.933130	4.737334	7.489222	8.152240
3.302499	3.243607	5.013722	4.742366	7.570206	8.202680
3.400893	3.346487	5.098011	4.746908	7.645817	8.249753
3.496671	3.451262	5.185895	4.750988	7.715880	8.293404
3.589454	3.558435	5.277200	4.754645	7.780232	8.333510
3.678886	3.668156	5.371713	4.757903	7.838685	8.369982
3.764655	3.780553	5.469174	4.760771	7.891199	8.402627
3.846479	3.895702	5.569284	4.763206	7.938321	8.430699
3.924146	4.013645	5.671681	4.765192	7.979953	8.453891
3.997477	4.134385	5.775979	4.766744	8.015646	8.472281
4.066377	4.257886	5.881791	4.767871	8.044871	8.485768
4.130825	4.384081	5.988719	4.768573	8.066958	8.494221
4.190835	4.512870	6.096375	4.768880	8.081422	8.497922
4.246471	4.644065	6.204344	4.768891	8.088052	8.498049
4.297787	4.777412	6.312208	4.768863	8.089867	8.497706
4.344875	4.912626	6.419576			
4.387925	5.049383	6.526046			
4.427133	5.187314	6.631264			
4.462728	5.326016	6.734887			
4.494945	5.465071	6.836635			
4.524039	5.604028	6.936249			
4.550262	5.742452	7.033523			
4.573863	5.879890	7.128278			
4.595072	6.015908	7.220374			
4.614125	6.150085	7.309704			
4.631239	6.282008	7.396180			
4.646601	6.411288	7.479761			
4.660417	6.537566	7.560404			
4.672840	6.660491	7.638103			
4.684028	6.779741	7.712847			

TABLE C.12.—IMPELLER MAIN BLADE—SECTION 10

X	R*θ	R	X	R*θ	R
4.704408	8.059928	8.493800	4.173073	4.851385	6.315946
4.704249	8.059285	8.492073	4.116630	4.722671	6.211916
4.703746	8.056427	8.486637	4.055750	4.596330	6.108098
4.702818	8.048464	8.476688	3.990399	4.472586	6.004912
4.701453	8.033780	8.462106	3.920557	4.351616	5.902776
4.699667	8.011868	8.443164	3.846261	4.233473	5.802078
4.697490	7.982646	8.420268	3.767611	4.118189	5.703212
4.694951	7.946082	8.393792	3.684779	4.005755	5.606571
4.692082	7.902140	8.364204	3.598012	3.896110	5.512526
4.688860	7.851421	8.331513	3.507589	3.789123	5.421392
4.685219	7.794692	8.295272	3.413843	3.684622	5.333429
4.681134	7.732083	8.255584	3.317138	3.582391	5.248856
4.676585	7.663675	8.212606	3.217863	3.481469	5.167840
4.671542	7.589560	8.166415	3.116456	3.381362	5.090498
4.665960	7.509796	8.117077	3.013350	3.281942	5.016921
4.659794	7.424534	8.064630	2.909010	3.183078	4.947141
4.652974	7.334071	8.009049	2.803891	3.084715	4.881167
4.645424	7.238611	7.950373	2.698445	2.986818	4.818965
4.637065	7.138339	7.888635	2.593072	2.889347	4.760447
4.627804	7.033447	7.823874	2.488124	2.792268	4.705504
4.617533	6.924151	7.756134	2.383907	2.695555	4.653988
4.606134	6.810682	7.685450	2.280648	2.599211	4.605731
4.593476	6.693313	7.611858	2.178574	2.503260	4.560566
4.579412	6.572344	7.535379	2.077927	2.407806	4.518352
4.563759	6.448106	7.456040	1.978913	2.312956	4.478939
4.546349	6.320967	7.373865	1.881678	2.218808	4.442164
4.526971	6.191294	7.288899	1.786329	2.125461	4.407867
4.505408	6.059490	7.201208	1.692956	2.033021	4.375888
4.481435	5.925981	7.110884	1.601626	1.941602	4.346087
4.454796	5.791209	7.018050	1.512397	1.851310	4.318322
4.425252	5.655644	6.922863	1.425309	1.762250	4.292465
4.392546	5.519754	6.825512	1.340401	1.674524	4.268395
4.356417	5.384014	6.726239	1.257702	1.588234	4.245999
4.316625	5.248889	6.625304	1.177243	1.503481	4.225178
4.272931	5.114815	6.523031	1.099059	1.420355	4.205834
4.225137	4.982194	6.419781	1.023180	1.338941	4.187879

TABLE C.12.—IMPELLER MAIN BLADE—SECTION 10

X	R*θ	R	X	R*θ	R
0.949653	1.259320	4.171235	0.091478	0.105951	4.028642
0.878524	1.181560	4.155830	0.112716	0.134562	4.031062
0.809843	1.105727	4.141592	0.136402	0.166500	4.033827
0.743657	1.031887	4.128456	0.162638	0.201582	4.036969
0.680020	0.960097	4.116361	0.191404	0.239828	4.040512
0.618997	0.890403	4.105252	0.222754	0.281120	4.044489
0.560656	0.822853	4.095072	0.256752	0.325344	4.048937
0.505090	0.757474	4.085776	0.293449	0.372411	4.053899
0.452378	0.694293	4.077315	0.332923	0.422197	4.059424
0.402517	0.633398	4.069633	0.375266	0.474557	4.065565
0.355471	0.574890	4.062666	0.420530	0.529371	4.072372
0.311260	0.518845	4.056368	0.468738	0.586538	4.079904
0.269941	0.465306	4.050702	0.519849	0.646004	4.088207
0.231584	0.414304	4.045631	0.573757	0.707763	4.097321
0.196272	0.365863	4.041122	0.630377	0.771788	4.107287
0.164026	0.320030	4.037138	0.689680	0.838006	4.118164
0.134774	0.276927	4.033634	0.751611	0.906373	4.130004
0.108411	0.236699	4.030567	0.816051	0.976897	4.142853
0.084835	0.199481	4.027896	0.882898	1.049567	4.156757
0.064012	0.165298	4.025594	0.952255	1.124172	4.171812
0.045886	0.134213	4.023633	1.024245	1.200481	4.188125
0.030356	0.106362	4.021984	1.098484	1.278753	4.205695
0.017384	0.081841	4.020631	1.174312	1.359552	4.224437
0.007009	0.060729	4.019564	1.251894	1.442605	4.244466
-0.000034	0.042839	4.018846	1.332301	1.526673	4.266156
-0.002869	0.028435	4.018559	1.415913	1.611192	4.289746
-0.002348	0.018191	4.018611	1.501756	1.697063	4.315097
0.000300	0.012596	4.018879	1.588993	1.785103	4.342075
0.001948	0.011255	4.019046	1.677866	1.874918	4.370865
0.003990	0.010607	4.019255	1.768811	1.965861	4.401748
0.010256	0.011583	4.019895	1.861832	2.057740	4.434883
0.019456	0.016664	4.020845	1.956732	2.150590	4.470387
0.030352	0.026426	4.021983	2.053352	2.244406	4.508381
0.042484	0.040729	4.023269	2.151563	2.339154	4.549018
0.056352	0.059020	4.024760	2.251288	2.434609	4.592488
0.072651	0.080788	4.026543	2.352482	2.530249	4.639018

TABLE C.12.—IMPELLER MAIN BLADE—SECTION 10

X	R*θ	R	X	R*θ	R
2.454932	2.625846	4.688776	4.624435	6.883344	7.801217
2.558116	2.722152	4.741791	4.634160	6.992857	7.867922
2.661608	2.819915	4.798108	4.642948	7.097921	7.931739
2.765317	2.918638	4.857969	4.650902	7.198311	7.992646
2.869146	3.017379	4.921633	4.658107	7.293806	8.050630
2.972654	3.116083	4.989171	4.664641	7.384195	8.105675
3.075260	3.215274	5.060519	4.670577	7.469286	8.157769
3.176463	3.315258	5.135636	4.675965	7.548992	8.206835
3.275847	3.416041	5.214486	4.680842	7.623220	8.252790
3.372990	3.517722	5.296980	4.685250	7.691844	8.295573
3.467475	3.621309	5.382984	4.689210	7.754743	8.335048
3.558911	3.727250	5.472309	4.692754	7.811761	8.371109
3.646947	3.835716	5.564721	4.695889	7.862903	8.403540
3.731277	3.946828	5.659931	4.698561	7.908847	8.431511
3.811621	4.060695	5.757618	4.700753	7.949538	8.454672
3.887766	4.177365	5.857390	4.702480	7.984487	8.473072
3.959566	4.296849	5.958859	4.703745	8.013199	8.486627
4.026943	4.419118	6.061626	4.704534	8.034976	8.495162
4.089870	4.544095	6.165291	4.704869	8.049156	8.498797
4.148377	4.671618	6.269428	4.704858	8.055382	8.498678
4.202503	4.801457	6.373607	4.704815	8.057015	8.498215
4.252300	4.933347	6.477446			
4.297927	5.066977	6.580533			
4.339563	5.201975	6.682499			
4.377421	5.337930	6.782990			
4.411742	5.474409	6.881701			
4.442768	5.610950	6.978368			
4.470751	5.747098	7.072775			
4.495948	5.882387	7.164734			
4.518609	6.016367	7.254096			
4.538971	6.148601	7.340757			
4.557254	6.278663	7.424635			
4.573679	6.406160	7.505680			
4.588437	6.530719	7.583865			
4.601713	6.651986	7.659183			
4.613663	6.769627	7.731634			

TABLE C.13.—IMPELLER MAIN BLADE—SECTION 11

X	R*θ	R	X	R*θ	R
4.639735	8.024313	8.494062	4.075991	4.858861	6.384690
4.639551	8.023468	8.492267	4.016831	4.733939	6.284527
4.638974	8.019986	8.486635	3.953198	4.611568	6.184714
4.637922	8.010937	8.476399	3.885082	4.491945	6.085679
4.636404	7.995048	8.461673	3.812501	4.375221	5.987855
4.634458	7.972167	8.442900	3.735549	4.261411	5.891635
4.632111	7.942174	8.420398	3.654374	4.150498	5.797412
4.629389	7.905044	8.394547	3.569185	4.042422	5.705579
4.626332	7.860733	8.365839	3.480290	3.937065	5.616478
4.622908	7.809855	8.334233	3.387999	3.834240	5.530403
4.619035	7.753240	8.299202	3.292676	3.733726	5.447596
4.614690	7.691017	8.260832	3.194722	3.634661	5.368249
4.609855	7.623254	8.219269	3.094557	3.536179	5.292498
4.604490	7.550041	8.174565	2.992636	3.438075	5.220439
4.598546	7.471439	8.126754	2.889413	3.340201	5.152125
4.591968	7.387535	8.075874	2.785352	3.242425	5.087574
4.584691	7.298469	8.021987	2.680923	3.144694	5.026757
4.576639	7.204431	7.965139	2.576572	3.046987	4.969626
4.567727	7.105595	7.905365	2.472691	2.949287	4.916075
4.557850	7.002159	7.842698	2.369616	2.851583	4.865966
4.546907	6.894350	7.777170	2.267628	2.753880	4.819142
4.534755	6.782409	7.708810	2.166924	2.656213	4.775417
4.521266	6.666625	7.637642	2.067700	2.558641	4.734620
4.506268	6.547297	7.563685	1.970178	2.461303	4.696596
4.489597	6.424775	7.486955	1.874536	2.364353	4.661195
4.471048	6.299422	7.407477	1.780889	2.267935	4.628246
4.450414	6.171627	7.325288	1.689306	2.172195	4.597590
4.427468	6.041808	7.240444	1.599844	2.077272	4.569066
4.401959	5.910401	7.153042	1.512543	1.983305	4.542533
4.373650	5.777875	7.063194	1.427431	1.890428	4.517853
4.342273	5.644708	6.971073	1.344520	1.798770	4.494900
4.307570	5.511384	6.876875	1.263822	1.708459	4.473557
4.269301	5.378398	6.780839	1.185341	1.619615	4.453715
4.227206	5.246227	6.683252	1.109086	1.532356	4.435276
4.181075	5.115318	6.584442	1.035068	1.446789	4.418154
4.130713	4.986077	6.484793	0.963302	1.363009	4.402263

TABLE C.13.—IMPELLER MAIN BLADE—SECTION 11

X	R*θ	R	X	R*θ	R
0.893818	1.281104	4.387529	0.083731	0.107804	4.260280
0.826650	1.201147	4.373890	0.103462	0.137285	4.262443
0.761836	1.123208	4.361278	0.125517	0.170102	4.264915
0.699414	1.047356	4.349636	0.149939	0.206182	4.267720
0.639427	0.973652	4.338908	0.176763	0.245461	4.270880
0.581940	0.902136	4.329045	0.206020	0.287865	4.274425
0.527017	0.832850	4.320002	0.237762	0.333306	4.278385
0.474755	0.765812	4.311739	0.272061	0.381673	4.282798
0.425233	0.701048	4.304214	0.309001	0.432840	4.287707
0.378434	0.638660	4.297374	0.348682	0.486664	4.293161
0.334301	0.578778	4.291162	0.391165	0.543023	4.299206
0.292853	0.521470	4.285540	0.436475	0.601814	4.305896
0.254160	0.466757	4.280476	0.484576	0.662983	4.313267
0.218295	0.414663	4.275943	0.535356	0.726534	4.321351
0.185340	0.365218	4.271908	0.588725	0.792447	4.330187
0.155301	0.318491	4.268344	0.644658	0.860654	4.339825
0.128092	0.274615	4.265206	0.703106	0.931107	4.350310
0.103607	0.233722	4.262459	0.763949	1.003821	4.361680
0.081747	0.195931	4.260064	0.827085	1.078789	4.373977
0.062401	0.161356	4.257993	0.892640	1.155787	4.387284
0.045436	0.130121	4.256211	0.960764	1.234560	4.401712
0.030741	0.102326	4.254696	1.031054	1.315396	4.417245
0.018253	0.078043	4.253429	1.102792	1.398918	4.433791
0.007945	0.057312	4.252396	1.176181	1.484822	4.451457
0.000441	0.039896	4.251652	1.252433	1.571731	4.470621
-0.003347	0.025615	4.251279	1.331998	1.659012	4.491524
-0.003750	0.015072	4.251240	1.413822	1.747649	4.514013
-0.001518	0.009178	4.251459	1.497001	1.838539	4.537939
0.000056	0.007765	4.251614	1.581832	1.931231	4.563489
0.002061	0.007102	4.251812	1.668837	2.024990	4.590942
0.008223	0.008263	4.252423	1.758057	2.119585	4.620463
0.017121	0.013852	4.253315	1.849313	2.215031	4.652157
0.027414	0.024387	4.254357	1.942472	2.311296	4.686152
0.038623	0.039633	4.255505	2.037437	2.408310	4.722606
0.051328	0.058935	4.256826	2.134177	2.505788	4.761707
0.066319	0.081698	4.258409	2.232691	2.603124	4.803699

TABLE C.13.—IMPELLER MAIN BLADE—SECTION 11

X	R*θ	R	X	R*θ	R
2.332798	2.700032	4.848757	4.553806	6.871353	7.818031
2.433970	2.797318	4.896910	4.564206	6.979355	7.882596
2.535783	2.895793	4.948219	4.573597	7.082959	7.944378
2.638202	2.994869	5.002946	4.582095	7.181950	8.003352
2.741181	3.093471	5.061384	4.589794	7.276105	8.059512
2.844285	3.191513	5.123625	4.596774	7.365212	8.112848
2.946910	3.289571	5.189627	4.603115	7.449079	8.163357
3.048548	3.387976	5.259369	4.608881	7.527511	8.211032
3.148768	3.486739	5.332853	4.614120	7.600360	8.255856
3.247131	3.585909	5.410022	4.618875	7.667546	8.297764
3.343197	3.685909	5.490762	4.623166	7.728997	8.336599
3.436544	3.787917	5.574912	4.627016	7.784581	8.372246
3.526780	3.892290	5.662265	4.630437	7.834351	8.404460
3.613550	3.999209	5.752566	4.633356	7.879114	8.432329
3.696551	4.108834	5.845498	4.635760	7.918860	8.455459
3.775506	4.221275	5.940692	4.637662	7.953057	8.473870
3.850211	4.336591	6.037761	4.639062	7.981248	8.487493
3.920542	4.454790	6.136302	4.639946	8.002720	8.496111
3.986434	4.575821	6.235894	4.640311	8.016617	8.499681
4.047869	4.699548	6.336113	4.640274	8.022431	8.499314
4.104862	4.825767	6.436524	4.640214	8.023882	8.498728
4.157457	4.954230	6.536733			
4.205752	5.084642	6.636337			
4.249917	5.216628	6.734950			
4.290141	5.349767	6.832204			
4.326668	5.483614	6.927781			
4.359720	5.617689	7.021409			
4.389569	5.751523	7.112851			
4.416464	5.884631	7.201924			
4.440671	6.016548	7.288468			
4.462425	6.146820	7.372386			
4.481974	6.275011	7.453588			
4.499534	6.400716	7.532034			
4.515314	6.523554	7.607698			
4.529506	6.643159	7.680582			
4.542285	6.759193	7.750691			

TABLE C.14.—IMPELLER SPLITTER BLADE—SECTION 1

X	R*θ	R	X	R*θ	R
5.265823	6.559390	8.490460	5.124852	4.422156	6.601000
5.265811	6.560349	8.489702	5.111381	4.317960	6.506653
5.265773	6.562910	8.487269	5.096808	4.213831	6.411033
5.265695	6.566068	8.482649	5.081081	4.110003	6.314284
5.265546	6.567956	8.474846	5.064107	4.006639	6.216583
5.265312	6.565979	8.462500	5.045811	3.903739	6.118000
5.264956	6.558728	8.445310	5.026091	3.801376	6.018591
5.264487	6.546262	8.424077	5.004835	3.700030	5.918387
5.263885	6.528366	8.398974	4.981935	3.600102	5.817438
5.263130	6.504991	8.370125	4.957309	3.501244	5.715952
5.262211	6.476285	8.337801	4.930893	3.403130	5.614189
5.261113	6.442393	8.302233	4.902627	3.306294	5.512337
5.259828	6.403367	8.263554	4.872446	3.211428	5.410575
5.258330	6.359273	8.221922	4.840283	3.118573	5.309089
5.256619	6.310182	8.177506	4.806102	3.027541	5.208036
5.254673	6.256146	8.130463	4.769857	2.938426	5.107576
5.252503	6.197170	8.080982	4.731517	2.851428	5.007867
5.250096	6.133283	8.029262	4.691076	2.766668	4.909057
5.247437	6.065150	7.975274	4.648535	2.684203	4.811299
5.244488	5.993672	7.918616	4.603925	2.604090	4.714780
5.241233	5.919102	7.859316	4.557305	2.526379	4.619683
5.237656	5.841579	7.797428	4.508761	2.451108	4.526180
5.233723	5.761233	7.733013	4.458393	2.378302	4.434443
5.229430	5.678197	7.666120	4.406299	2.307937	4.344583
5.224741	5.592589	7.596810	4.352579	2.239975	4.256686
5.219630	5.504541	7.525139	4.297373	2.174411	4.170865
5.214072	5.414185	7.451170	4.240856	2.111255	4.087247
5.208032	5.321672	7.374978	4.183197	2.050486	4.005930
5.201478	5.227176	7.296628	4.124559	1.992056	3.926972
5.194368	5.130901	7.216195	4.065121	1.935894	3.850414
5.186655	5.033003	7.133757	4.005055	1.881944	3.776304
5.178302	4.933699	7.049370	3.944552	1.830148	3.704670
5.169245	4.833250	6.963122	3.883800	1.780448	3.635536
5.159436	4.731774	6.875079	3.822983	1.732787	3.568920
5.148811	4.629329	6.785318	3.762290	1.687106	3.504820
5.137307	4.526053	6.693926	3.701896	1.643344	3.443240

TABLE C.14.—IMPELLER SPLITTER BLADE—SECTION 1

X	R*θ	R	X	R*θ	R
3.641982	1.601434	3.384163	2.817906	0.993159	2.723409
3.582716	1.561315	3.327572	2.842037	0.998690	2.739608
3.524264	1.522931	3.273448	2.868715	1.006727	2.757700
3.466785	1.486234	3.221769	2.897958	1.016773	2.777752
3.410433	1.451176	3.172502	2.929690	1.028267	2.799780
3.355354	1.417713	3.125622	2.963833	1.041261	2.823798
3.301692	1.385789	3.081096	3.000312	1.055865	2.849834
3.249581	1.355354	3.038891	3.039058	1.072057	2.877922
3.199148	1.326371	2.998977	3.080003	1.089773	2.908100
3.150506	1.298819	2.961310	3.123078	1.108935	2.940417
3.103760	1.272700	2.925851	3.168193	1.129498	2.974913
3.059014	1.248000	2.892563	3.215252	1.151468	3.011625
3.016369	1.224675	2.861419	3.264144	1.174880	3.050585
2.975938	1.202637	2.832395	3.314750	1.199794	3.091828
2.937829	1.181773	2.805475	3.366947	1.226259	3.135390
2.902145	1.161986	2.780642	3.420610	1.254306	3.181302
2.868975	1.143236	2.757878	3.475603	1.283965	3.229601
2.838347	1.125588	2.737122	3.531786	1.315266	3.280323
2.810327	1.109088	2.718352	3.589005	1.348256	3.333493
2.785342	1.093358	2.701792	3.647104	1.382996	3.389134
2.763652	1.077963	2.687545	3.705918	1.419554	3.447275
2.745449	1.062835	2.675682	3.765280	1.457992	3.507928
2.731069	1.048282	2.666369	3.825015	1.498382	3.571105
2.721207	1.034711	2.660011	3.884946	1.540798	3.636812
2.717126	1.023055	2.657388	3.944882	1.585313	3.705053
2.719135	1.014868	2.658678	4.004644	1.631990	3.775808
2.723268	1.010234	2.661338	4.064045	1.680895	3.849055
2.726552	1.007934	2.663453	4.122886	1.732098	3.924770
2.727728	1.007210	2.664211	4.181000	1.785663	4.002910
2.728940	1.006502	2.664994	4.238209	1.841666	4.083427
2.732711	1.004415	2.667429	4.294338	1.900168	4.166261
2.739339	1.000875	2.671719	4.349221	1.961213	4.251336
2.749042	0.996085	2.678016	4.402692	2.024811	4.338535
2.761840	0.991948	2.686361	4.454597	2.090958	4.427727
2.777664	0.989893	2.696735	4.504820	2.159674	4.518810
2.796398	0.990270	2.709100	4.553272	2.231007	4.611701

TABLE C.14.—IMPELLER SPLITTER BLADE—SECTION 1

X	R*θ	R	X	R*θ	R
4.599851	2.304953	4.706250	5.245489	5.686606	7.937488
4.644473	2.381470	4.802268	5.248500	5.760941	7.996511
4.687059	2.460501	4.899567	5.251213	5.832239	8.052893
4.727575	2.541980	4.997949	5.253641	5.900291	8.106572
4.766009	2.625874	5.097292	5.255796	5.965579	8.157293
4.802412	2.712171	5.197523	5.257675	6.028599	8.204516
4.836742	2.800659	5.298323	5.259285	6.089191	8.248124
4.868875	2.890856	5.398992	5.260661	6.147013	8.288139
4.898963	2.982785	5.499603	5.261810	6.201757	8.324544
4.927529	3.077508	5.601700	5.262770	6.253188	8.357312
4.954658	3.175113	5.705433	5.263557	6.301065	8.386443
4.979665	3.273403	5.807793	5.264195	6.345154	8.411899
5.002355	3.371093	5.907098	5.264701	6.385149	8.433600
5.023490	3.469993	6.005934	5.265093	6.420821	8.451621
5.043560	3.571505	6.106280	5.265381	6.452061	8.466150
5.062292	3.674375	6.206490	5.265588	6.478380	8.477036
5.079498	3.777328	6.304927	5.265726	6.499290	8.484281
5.095368	3.880518	6.401889	5.265795	6.514937	8.488653
5.110086	3.984274	6.497928	5.265834	6.525833	8.491153
5.123767	4.088531	6.593140	5.265854	6.532277	8.492421
5.136460	4.193038	6.687406	5.265860	6.534410	8.492807
5.148181	4.297190	6.780157			
5.158960	4.400477	6.870940			
5.168878	4.502708	6.959715			
5.178019	4.603844	7.046609			
5.186479	4.704022	7.131929			
5.194326	4.803176	7.215736			
5.201570	4.900934	7.297712			
5.208250	4.997006	7.377651			
5.214408	5.091264	7.455535			
5.220080	5.183521	7.531305			
5.225298	5.273593	7.604881			
5.230089	5.361330	7.676189			
5.234484	5.446612	7.745168			
5.238497	5.529320	7.811755			
5.242163	5.609359	7.875883			

TABLE C.15.—IMPELLER SPLITTER BLADE—SECTION 2

X	R*θ	R	X	R*θ	R
5.204925	6.526348	8.491270	5.054760	4.420768	6.653220
5.204907	6.527254	8.490522	5.040598	4.318800	6.561452
5.204845	6.529622	8.488100	5.025285	4.216933	6.468451
5.204728	6.532301	8.483413	5.008766	4.115395	6.374361
5.204520	6.533427	8.475508	4.990952	4.014343	6.279354
5.204183	6.530671	8.463213	4.971761	3.913790	6.183512
5.203708	6.522741	8.446283	4.951100	3.813799	6.086896
5.203097	6.509711	8.425468	4.928858	3.714830	5.989549
5.202334	6.491371	8.400942	4.904934	3.617247	5.891537
5.201412	6.467677	8.372839	4.879247	3.520743	5.793073
5.200316	6.438766	8.341434	4.851748	3.425017	5.694400
5.199029	6.404868	8.306916	4.822376	3.330560	5.595716
5.197542	6.366039	8.269383	4.791079	3.238003	5.497195
5.195842	6.322310	8.228981	4.757809	3.147377	5.399017
5.193920	6.273780	8.185867	4.722527	3.058511	5.301349
5.191770	6.220486	8.140185	4.685208	2.971482	5.204343
5.189391	6.162439	8.092110	4.645834	2.886469	5.108157
5.186773	6.099689	8.041827	4.604407	2.803578	5.012936
5.183901	6.032828	7.989319	4.560943	2.722861	4.918831
5.180735	5.962669	7.934223	4.515476	2.644369	4.826029
5.177256	5.889468	7.876568	4.468085	2.568140	4.734689
5.173450	5.813356	7.816406	4.418859	2.494206	4.644983
5.169279	5.734454	7.753795	4.367900	2.422585	4.557076
5.164740	5.652907	7.688780	4.315318	2.353257	4.471070
5.159789	5.568841	7.621421	4.261220	2.286180	4.387044
5.154404	5.482381	7.551769	4.205751	2.221343	4.305107
5.148554	5.393657	7.479882	4.149085	2.158754	4.225374
5.142202	5.302826	7.405831	4.091391	2.098399	4.147932
5.135312	5.210065	7.329678	4.032836	2.040232	4.072833
5.127838	5.115562	7.251493	3.973591	1.984202	4.000113
5.119732	5.019492	7.171347	3.913835	1.930256	3.929805
5.110952	4.922070	7.089299	3.853751	1.878346	3.861937
5.101433	4.823547	7.005429	3.793519	1.828417	3.796528
5.091120	4.724051	6.919805	3.733323	1.780415	3.733584
5.079950	4.623653	6.832503	3.673343	1.734290	3.673100
5.067854	4.522493	6.743608	3.613750	1.689995	3.615067

TABLE C.15.—IMPELLER SPLITTER BLADE—SECTION 2

X	R*θ	R	X	R*θ	R
3.554714	1.647485	3.559467	2.748886	1.030953	2.942511
3.496398	1.606723	3.506279	2.772317	1.037485	2.957497
3.438959	1.567667	3.455475	2.798231	1.046463	2.974242
3.382550	1.530275	3.407027	2.826640	1.057441	2.992806
3.327311	1.494497	3.360899	2.857474	1.069913	3.013209
3.273383	1.460280	3.317059	2.890659	1.083925	3.035464
3.220900	1.427567	3.275470	2.926126	1.099575	3.059600
3.169988	1.396311	3.236097	2.963813	1.116840	3.085652
3.120766	1.366485	3.198902	3.003661	1.135651	3.113665
3.073335	1.338083	3.163842	3.045610	1.155927	3.143688
3.027793	1.311113	3.130869	3.089581	1.177621	3.175767
2.984231	1.285575	3.099946	3.135487	1.200725	3.209938
2.942747	1.261437	3.071038	3.183222	1.225266	3.246242
2.903443	1.238623	3.044123	3.232676	1.251291	3.284711
2.866423	1.217030	3.019180	3.283734	1.278838	3.325383
2.831785	1.196575	2.996194	3.336277	1.307931	3.368301
2.799612	1.177221	2.975140	3.390180	1.338594	3.413500
2.769926	1.159031	2.955962	3.445314	1.370861	3.461021
2.742786	1.142055	2.938634	3.501533	1.404785	3.510892
2.718573	1.125963	2.923337	3.558688	1.440436	3.563151
2.697517	1.110373	2.910158	3.616626	1.477867	3.617821
2.679785	1.095239	2.899147	3.675184	1.517129	3.674924
2.665685	1.080836	2.890447	3.734198	1.558269	3.734481
2.655895	1.067493	2.884436	3.793496	1.601340	3.796503
2.651579	1.056051	2.881793	3.852900	1.646396	3.860994
2.653009	1.047932	2.882667	3.912229	1.693496	3.927952
2.656615	1.043190	2.884877	3.971301	1.742701	3.997361
2.659658	1.040761	2.886743	4.029933	1.794072	4.069196
2.660786	1.039998	2.887435	4.087949	1.847672	4.143429
2.661967	1.039263	2.888160	4.145177	1.903564	4.220019
2.665705	1.037169	2.890460	4.201443	1.961798	4.298913
2.672296	1.033871	2.894519	4.256583	2.022410	4.380040
2.681873	1.029704	2.900439	4.310428	2.085409	4.463300
2.694415	1.026486	2.908225	4.362818	2.150794	4.548572
2.709829	1.025497	2.917849	4.413636	2.218587	4.635760
2.728013	1.026990	2.929283	4.462785	2.288837	4.724779

TABLE C.15.—IMPELLER SPLITTER BLADE—SECTION 2

X	R*θ	R	X	R*θ	R
4.510150	2.361544	4.815500	5.181636	5.674174	7.949616
4.555644	2.436672	4.907736	5.184882	5.747190	8.006970
4.599178	2.514178	5.001317	5.187827	5.817213	8.061773
4.640708	2.594000	5.096047	5.190487	5.884020	8.113967
4.680212	2.676114	5.191807	5.192871	5.948045	8.163309
4.717721	2.760509	5.288521	5.194981	6.009753	8.209313
4.753190	2.846994	5.385886	5.196816	6.068972	8.251872
4.786488	2.935143	5.483264	5.198412	6.125375	8.290999
4.817740	3.024985	5.580710	5.199772	6.178678	8.326665
4.847453	3.117457	5.679566	5.200929	6.228713	8.358867
4.875698	3.212642	5.779953	5.201899	6.275208	8.387569
4.901801	3.308581	5.879185	5.202701	6.318001	8.412722
4.925578	3.404110	5.975722	5.203354	6.356920	8.434232
4.947758	3.500842	6.071851	5.203879	6.391682	8.452136
4.968812	3.600021	6.169322	5.204276	6.422169	8.466608
4.988477	3.700522	6.266646	5.204575	6.447936	8.477513
5.006573	3.801181	6.362344	5.204764	6.468494	8.484853
5.023279	3.902137	6.456670	5.204876	6.483982	8.489332
5.038778	4.003670	6.550103	5.204940	6.494768	8.491856
5.053184	4.105713	6.642714	5.204971	6.501124	8.493100
5.066558	4.208015	6.734373	5.204980	6.503231	8.493473
5.078903	4.310020	6.824569			
5.090262	4.411242	6.912878			
5.100713	4.511495	6.999254			
5.110343	4.610730	7.083805			
5.119258	4.709045	7.166795			
5.127520	4.806368	7.248280			
5.135153	4.902341	7.327962			
5.142187	4.996688	7.405660			
5.148676	5.089262	7.481348			
5.154657	5.179887	7.554974			
5.160167	5.268377	7.626460			
5.165235	5.354578	7.695738			
5.169890	5.438372	7.762753			
5.174159	5.519645	7.827447			
5.178069	5.598290	7.889758			

TABLE C.16.—IMPELLER SPLITTER BLADE—SECTION 3

X	R*θ	R	X	R*θ	R
5.143698	6.493153	8.492085	4.984223	4.418152	6.705771
5.143673	6.494010	8.491347	4.969348	4.318307	6.616613
5.143593	6.496179	8.488935	4.953279	4.218602	6.526257
5.143434	6.498370	8.484181	4.935947	4.119249	6.434857
5.143165	6.498725	8.476172	4.917278	4.020411	6.342570
5.142736	6.495176	8.463930	4.897177	3.922108	6.249498
5.142148	6.486570	8.447261	4.875559	3.824405	6.155701
5.141402	6.472972	8.426864	4.852321	3.727725	6.061235
5.140490	6.454194	8.402918	4.827362	3.632415	5.966186
5.139404	6.430178	8.375567	4.800608	3.538200	5.870764
5.138136	6.401060	8.345082	4.772026	3.444806	5.775195
5.136663	6.367150	8.311621	4.741550	3.352686	5.679692
5.134982	6.328521	8.275236	4.709145	3.262410	5.584419
5.133086	6.285163	8.236070	4.674774	3.173999	5.489555
5.130963	6.237189	8.194264	4.638412	3.087302	5.395265
5.128614	6.184642	8.149946	4.600041	3.002377	5.301703
5.126030	6.127522	8.103281	4.559659	2.919385	5.209022
5.123206	6.065898	8.054442	4.517276	2.838415	5.117370
5.120122	6.000302	8.003418	4.472922	2.759517	5.026889
5.116737	5.931455	7.949890	4.426638	2.682735	4.937766
5.113034	5.859610	7.893887	4.378519	2.608089	4.850142
5.108994	5.784883	7.835459	4.328647	2.535615	4.764195
5.104583	5.707402	7.774658	4.277146	2.465319	4.680062
5.099789	5.627321	7.711531	4.224128	2.397178	4.597845
5.094573	5.544758	7.646132	4.169706	2.331154	4.517623
5.088904	5.459841	7.578510	4.114028	2.267230	4.439497
5.082752	5.372704	7.508719	4.057267	2.205409	4.363569
5.076077	5.283500	7.436823	3.999597	2.145675	4.289917
5.068838	5.192408	7.362882	3.941182	2.087993	4.218583
5.060986	5.099619	7.286961	3.882191	2.032323	4.149600
5.052473	5.005304	7.209127	3.822802	1.978620	4.082994
5.043249	4.909681	7.129437	3.763192	1.926841	4.018786
5.033252	4.813004	7.047966	3.703541	1.876940	3.956983
5.022417	4.715397	6.964785	3.644024	1.828863	3.897586
5.010681	4.616948	6.879966	3.584815	1.782563	3.840587
4.997974	4.517800	6.793595	3.526077	1.738003	3.785970

TABLE C.16.—IMPELLER SPLITTER BLADE—SECTION 3

X	R*θ	R	X	R*θ	R
3.467973	1.695149	3.733714	2.680972	1.072174	3.158104
3.410660	1.653964	3.683785	2.703691	1.079669	3.171967
3.354286	1.614410	3.636154	2.728828	1.089548	3.187462
3.298992	1.576453	3.590792	2.756388	1.101414	3.204646
3.244915	1.540052	3.547651	2.786308	1.114815	3.223536
3.192182	1.505172	3.506697	2.818516	1.129794	3.244149
3.140920	1.471765	3.467891	2.852950	1.146436	3.266511
3.091245	1.439789	3.431196	2.889554	1.164712	3.290662
3.043269	1.409217	3.396569	2.928278	1.184552	3.316647
2.997086	1.380053	3.363958	2.969073	1.205875	3.344519
2.952776	1.352319	3.333322	3.011870	1.228621	3.374322
2.910428	1.326021	3.304613	3.056587	1.252773	3.406101
2.870129	1.301138	3.277797	3.103128	1.278351	3.439897
2.831976	1.277613	3.252850	3.151391	1.305390	3.475742
2.796066	1.255350	3.229749	3.201266	1.333922	3.513676
2.762492	1.234279	3.208479	3.252645	1.363967	3.553745
2.731330	1.214369	3.189014	3.305411	1.395544	3.595992
2.702601	1.195682	3.171299	3.359445	1.428680	3.640457
2.676352	1.178270	3.155304	3.414612	1.463415	3.687176
2.652921	1.161852	3.141176	3.470769	1.499800	3.736190
2.632508	1.146098	3.128982	3.527773	1.537885	3.787525
2.615254	1.130982	3.118757	3.585472	1.577717	3.841209
2.601438	1.116748	3.110625	3.643704	1.619341	3.897274
2.591725	1.103642	3.104935	3.702310	1.662799	3.955734
2.587177	1.092417	3.102280	3.761116	1.708133	4.016597
2.588028	1.084361	3.102777	3.819951	1.755400	4.079868
2.591107	1.079509	3.104573	3.878637	1.804659	4.145540
2.593910	1.076956	3.106214	3.936996	1.855964	4.213595
2.594987	1.076160	3.106844	3.994855	1.909372	4.284013
2.596138	1.075402	3.107518	4.052043	1.964936	4.356762
2.599841	1.073324	3.109687	4.108388	2.022694	4.431793
2.606391	1.070308	3.113535	4.163727	2.082677	4.509048
2.615839	1.066801	3.119102	4.217888	2.144895	4.588436
2.628118	1.064516	3.126375	4.270710	2.209354	4.669851
2.643115	1.064583	3.135305	4.322069	2.276079	4.753201
2.660742	1.067169	3.145876	4.371865	2.345112	4.838400

TABLE C.16.—IMPELLER SPLITTER BLADE—SECTION 3

X	R*θ	R	X	R*θ	R
4.419972	2.416464	4.925332	5.117506	5.661610	7.961797
4.466298	2.490104	5.013820	5.120985	5.733320	8.017475
4.510742	2.565998	5.103709	5.124159	5.802076	8.070695
4.553251	2.644100	5.194812	5.127047	5.867645	8.121395
4.593798	2.724383	5.287002	5.129655	5.930419	8.169353
4.632393	2.806838	5.380203	5.131986	5.990815	8.214133
4.668982	2.891307	5.474136	5.134043	6.048654	8.255638
4.703428	2.977410	5.568224	5.135857	6.103637	8.293873
4.735849	3.065174	5.662486	5.137425	6.155485	8.328797
4.766709	3.155422	5.758081	5.138779	6.204118	8.360428
4.796055	3.248238	5.855118	5.139931	6.249226	8.388701
4.823271	3.341874	5.951187	5.140897	6.290717	8.413549
4.848151	3.435304	6.044927	5.141695	6.328553	8.434867
4.871395	3.529937	6.138319	5.142342	6.362393	8.452653
4.893449	3.626868	6.232883	5.142846	6.392124	8.467069
4.914064	3.725082	6.327290	5.143227	6.417330	8.477994
4.933069	3.823540	6.420217	5.143476	6.437546	8.485427
4.950626	3.922361	6.511880	5.143629	6.452879	8.490015
4.966937	4.021771	6.602669	5.143714	6.463558	8.492562
4.982089	4.121697	6.692648	5.143755	6.469833	8.493783
4.996158	4.221899	6.781675	5.143767	6.471906	8.494143
5.009155	4.321849	6.869283			
5.021114	4.421103	6.955089			
5.032119	4.519473	7.039042			
5.042265	4.616891	7.121222			
5.051657	4.713421	7.201859			
5.060349	4.808993	7.281001			
5.068385	4.903253	7.358372			
5.075790	4.995931	7.433809			
5.082623	5.086883	7.507287			
5.088925	5.175927	7.578755			
5.094736	5.262878	7.648139			
5.100088	5.347587	7.715375			
5.105010	5.429929	7.780416			
5.109538	5.509790	7.843208			
5.113695	5.587063	7.903694			

TABLE C.17.—IMPELLER SPLITTER BLADE—SECTION 4

X	R*θ	R	X	R*θ	R
5.082139	6.459811	8.492903	4.913202	4.414558	6.758683
5.082109	6.460617	8.492176	4.897596	4.316761	6.672162
5.082011	6.462583	8.489773	4.880755	4.219133	6.584480
5.081813	6.464283	8.484952	4.862590	4.121891	6.495800
5.081480	6.463854	8.476841	4.843043	4.025188	6.406267
5.080965	6.459510	8.464651	4.822025	3.929063	6.315986
5.080267	6.450222	8.448244	4.799438	3.833585	6.225034
5.079391	6.436049	8.428268	4.775189	3.739139	6.133479
5.078334	6.416825	8.404904	4.749184	3.646052	6.041418
5.077087	6.392490	8.378307	4.721367	3.554084	5.949049
5.075647	6.363154	8.348749	4.691699	3.462994	5.856604
5.073995	6.329234	8.316349	4.660126	3.373195	5.764288
5.072129	6.290805	8.281118	4.626622	3.285194	5.672271
5.070042	6.247820	8.243192	4.591164	3.199009	5.580721
5.067730	6.200414	8.202697	4.553739	3.114499	5.489804
5.065185	6.148614	8.159750	4.514341	3.031719	5.399672
5.062402	6.092424	8.114500	4.472978	2.950805	5.310479
5.059372	6.031925	8.067110	4.429671	2.871834	5.222369
5.056076	5.967592	8.017576	4.384461	2.794843	5.135487
5.052472	5.900049	7.965622	4.337404	2.719871	5.050002
5.048543	5.829551	7.911279	4.288594	2.646932	4.966057
5.044264	5.756194	7.854592	4.238128	2.576049	4.883812
5.039608	5.680121	7.795611	4.186138	2.507221	4.803394
5.034553	5.601478	7.734383	4.132731	2.440429	4.724911
5.029064	5.520395	7.670954	4.078034	2.375632	4.648429
5.023103	5.436995	7.605375	4.022200	2.312807	4.574040
5.016637	5.351404	7.537693	3.965403	2.251954	4.501836
5.009626	5.263788	7.467968	3.907814	2.193054	4.431885
5.002027	5.174322	7.396254	3.849595	2.136074	4.364225
4.993779	5.083188	7.322618	3.790916	2.080983	4.298883
4.984844	4.990572	7.247113	3.731951	2.027746	4.235874
4.975158	4.896692	7.169804	3.672875	1.976330	4.175214
4.964666	4.801786	7.090755	3.613862	1.926692	4.116902
4.953290	4.705999	7.010042	3.555080	1.878783	4.060935
4.940970	4.609424	6.927733	3.496695	1.832560	4.007302
4.927633	4.512210	6.843913	3.438867	1.787954	3.955971

TABLE C.17.—IMPELLER SPLITTER BLADE—SECTION 4

X	R*θ	R	X	R*θ	R
3.381749	1.744908	3.906921	2.614095	1.117043	3.370403
3.325490	1.703394	3.860117	2.636095	1.125463	3.383219
3.270227	1.663402	3.815525	2.660443	1.136199	3.397551
3.216097	1.624935	3.773102	2.687143	1.148907	3.413449
3.163223	1.587991	3.732807	2.716135	1.163186	3.430929
3.111725	1.552541	3.694597	2.747351	1.179075	3.450007
3.061721	1.518540	3.658432	2.780732	1.196646	3.470711
3.013321	1.485946	3.624266	2.816233	1.215867	3.493081
2.966625	1.454737	3.592063	2.853811	1.236664	3.517163
2.921715	1.424917	3.561766	2.893427	1.258948	3.543010
2.878666	1.396516	3.533324	2.935021	1.282654	3.570673
2.837558	1.369549	3.506694	2.978519	1.307759	3.600196
2.798465	1.344007	3.481839	3.023834	1.334271	3.631620
2.761482	1.319841	3.458732	3.070869	1.362219	3.664980
2.726699	1.296976	3.437355	3.119522	1.391633	3.700318
2.694204	1.275349	3.417684	3.169694	1.422532	3.737678
2.664067	1.254938	3.399699	3.221281	1.454935	3.777110
2.636306	1.235802	3.383343	3.274168	1.488866	3.818657
2.610957	1.217997	3.368585	3.328231	1.524357	3.862364
2.588315	1.201292	3.355543	3.383339	1.561424	3.908266
2.568552	1.185406	3.344264	3.439356	1.600075	3.956398
2.551780	1.170333	3.334769	3.496136	1.640330	4.006797
2.538253	1.156285	3.327164	3.553532	1.682222	4.059490
2.528621	1.143424	3.321774	3.611386	1.725820	4.114506
2.523843	1.132412	3.319108	3.669537	1.771191	4.171854
2.524118	1.124408	3.319261	3.727818	1.818394	4.231547
2.526669	1.119440	3.320684	3.786054	1.867483	4.293590
2.529230	1.116762	3.322115	3.844077	1.918504	4.357967
2.530258	1.115935	3.322689	3.901717	1.971505	4.424664
2.531377	1.115160	3.323313	3.958804	2.026528	4.493657
2.535044	1.113118	3.325365	4.015166	2.083607	4.564911
2.541551	1.110419	3.329011	4.070641	2.142767	4.638373
2.550866	1.107608	3.334253	4.125062	2.204025	4.713959
2.562879	1.106263	3.341045	4.178265	2.267387	4.791573
2.577454	1.107375	3.349332	4.230112	2.332888	4.871141
2.594518	1.111027	3.359102	4.280504	2.400566	4.952571

TABLE C.17.—IMPELLER SPLITTER BLADE—SECTION 4

X	R*θ	R	X	R*θ	R
4.329306	2.470434	5.035757	5.053067	5.648946	7.974037
4.376420	2.542471	5.120534	5.056785	5.719356	8.028030
4.421737	2.616654	5.206760	5.060187	5.786853	8.079659
4.465191	2.692951	5.294258	5.063298	5.851187	8.128859
4.506746	2.771334	5.382900	5.066127	5.912712	8.175426
4.546398	2.851798	5.472604	5.068669	5.971787	8.218977
4.584087	2.934211	5.563107	5.070943	6.028243	8.259424
4.619677	3.018244	5.653892	5.072969	6.081792	8.296762
4.653263	3.103918	5.744955	5.074745	6.132177	8.330940
4.685254	3.191953	5.837289	5.076296	6.179400	8.361998
4.715706	3.282413	5.930950	5.077632	6.223112	8.389838
4.744027	3.373781	6.023843	5.078765	6.263301	8.414380
4.770033	3.465143	6.114750	5.079708	6.300045	8.435505
4.794361	3.557723	6.205370	5.080478	6.332960	8.453173
4.817429	3.652460	6.296998	5.081087	6.361935	8.467532
4.839005	3.748449	6.388460	5.081547	6.386577	8.478477
4.858930	3.844779	6.478590	5.081856	6.406450	8.486005
4.877374	3.941532	6.567546	5.082048	6.421633	8.490702
4.894510	4.038896	6.655664	5.082154	6.432207	8.493274
4.910440	4.136779	6.742970	5.082203	6.438402	8.494470
4.925225	4.234950	6.829335	5.082217	6.440445	8.494815
4.938891	4.332923	6.914329			
4.951473	4.430286	6.997602			
4.963060	4.526839	7.079099			
4.973746	4.622508	7.158881			
4.983626	4.717326	7.237145			
4.992775	4.811196	7.313918			
5.001226	4.903795	7.388960			
5.009023	4.994861	7.462117			
5.016214	5.084228	7.533366			
5.022852	5.171730	7.602659			
5.028974	5.257181	7.669927			
5.034615	5.340421	7.735111			
5.039814	5.421334	7.798164			
5.044607	5.499806	7.859045			
5.049015	5.575721	7.917695			

TABLE C.18.—IMPELLER SPLITTER BLADE—SECTION 5

X	R*θ	R	X	R*θ	R
5.020243	6.426326	8.493726	4.841654	4.410175	6.811987
5.020208	6.427076	8.493010	4.825305	4.314359	6.728129
5.020092	6.428834	8.490617	4.807667	4.218748	6.643154
5.019855	6.430032	8.485728	4.788659	4.123554	6.557219
5.019456	6.428802	8.477513	4.768216	4.028932	6.470473
5.018853	6.423653	8.465376	4.746257	3.934930	6.383018
5.018045	6.413677	8.449233	4.722692	3.841629	6.294938
5.017043	6.398926	8.429679	4.697425	3.749376	6.206315
5.015840	6.379253	8.406901	4.670376	3.658475	6.117256
5.014434	6.354591	8.381064	4.641495	3.568726	6.027957
5.012825	6.325036	8.352436	4.610737	3.479930	5.938655
5.011001	6.291110	8.321101	4.578081	3.392445	5.849532
5.008958	6.252885	8.287030	4.543487	3.306728	5.760774
5.006690	6.210277	8.250349	4.506958	3.222791	5.672536
5.004197	6.163445	8.211170	4.468491	3.140506	5.584984
5.001462	6.112399	8.169599	4.428092	3.059920	5.498269
4.998483	6.057143	8.125771	4.385778	2.981151	5.412543
4.995248	5.997766	8.079836	4.341582	2.904259	5.327951
4.991737	5.934695	8.031799	4.295554	2.829272	5.244633
4.987914	5.868461	7.981427	4.247763	2.756217	5.162748
4.983755	5.799298	7.928750	4.198307	2.685110	5.082439
4.979233	5.727310	7.873814	4.147299	2.615953	5.003841
4.974326	5.652633	7.816663	4.094860	2.548748	4.927091
4.969002	5.575413	7.757344	4.041120	2.483465	4.852272
4.963229	5.495789	7.695900	3.986208	2.420064	4.779454
4.956967	5.413881	7.632376	3.930272	2.358525	4.708730
4.950177	5.329815	7.566818	3.873493	2.298834	4.640171
4.942817	5.243753	7.499281	3.816043	2.240970	4.573834
4.934833	5.155872	7.429817	3.758077	2.184905	4.509759
4.926181	5.066361	7.358481	3.699769	2.130606	4.447957
4.916809	4.975404	7.285328	3.641288	2.078051	4.388439
4.906642	4.883206	7.210424	3.582801	2.027214	4.331222
4.895629	4.790024	7.133825	3.524481	1.978058	4.276291
4.883699	4.695998	7.055603	3.466488	1.930533	4.223639
4.870778	4.601233	6.975829	3.408984	1.884535	4.173243
4.856787	4.505893	6.894591	3.352116	1.839976	4.125078

TABLE C.18.—IMPELLER SPLITTER BLADE—SECTION 5

X	R*θ	R	X	R*θ	R
3.296034	1.796820	4.079107	2.548199	1.165822	3.579588
3.240876	1.755063	4.035296	2.569471	1.175124	3.591432
3.186772	1.714737	3.993606	2.593023	1.186672	3.604678
3.133847	1.675869	3.953992	2.618853	1.200167	3.619373
3.082216	1.638475	3.916409	2.646905	1.215265	3.635534
3.031992	1.602548	3.880808	2.677115	1.231998	3.653176
2.983282	1.568052	3.847146	2.709429	1.250429	3.672326
2.936187	1.534951	3.815380	2.743809	1.270515	3.693023
2.890799	1.503218	3.785467	2.780222	1.292181	3.715316
2.847192	1.472858	3.757350	2.818635	1.315330	3.739260
2.805428	1.443901	3.730977	2.859001	1.339893	3.764905
2.765578	1.416372	3.706304	2.901253	1.365840	3.792295
2.727712	1.390267	3.683290	2.945311	1.393172	3.821475
2.691914	1.365550	3.661911	2.991086	1.421917	3.852481
2.658272	1.342160	3.642144	3.038480	1.452109	3.885355
2.626869	1.320048	3.623969	3.087407	1.483767	3.920140
2.597767	1.299199	3.607365	3.137770	1.516907	3.956893
2.570983	1.279671	3.592278	3.189466	1.551545	3.995656
2.546542	1.261524	3.578672	3.242380	1.587689	4.036476
2.524695	1.244573	3.566639	3.296390	1.625338	4.079395
2.505586	1.228591	3.556210	3.351367	1.664476	4.124454
2.489300	1.213588	3.547396	3.407176	1.705078	4.171689
2.476067	1.199742	3.540282	3.463678	1.747153	4.221133
2.466517	1.187131	3.535174	3.520723	1.790747	4.272822
2.461511	1.176326	3.532503	3.578158	1.835951	4.326771
2.461212	1.168360	3.532344	3.635822	1.882879	4.383000
2.463237	1.163260	3.533423	3.693552	1.931585	4.441511
2.465555	1.160459	3.534661	3.751176	1.982115	4.502311
2.466534	1.159603	3.535183	3.808534	2.034502	4.565381
2.467620	1.158813	3.535763	3.865456	2.088783	4.630713
2.471250	1.156823	3.537702	3.921775	2.144984	4.698271
2.477711	1.154477	3.541163	3.977334	2.203132	4.768007
2.486891	1.152391	3.546097	4.031951	2.263255	4.839868
2.498634	1.151994	3.552441	4.085474	2.325358	4.913750
2.512784	1.154136	3.560127	4.137759	2.389478	4.989590
2.529280	1.158830	3.569154	4.188693	2.455657	5.067304

TABLE C.18.—IMPELLER SPLITTER BLADE—SECTION 5

X	R*θ	R	X	R*θ	R
4.238142	2.523911	5.146789	4.988293	5.636195	7.986340
4.285996	2.594228	5.227898	4.992248	5.705318	8.038641
4.332147	2.666597	5.310487	4.995883	5.771550	8.088668
4.376511	2.740995	5.394404	4.999216	5.834649	8.136362
4.419042	2.817401	5.479517	5.002257	5.894926	8.181532
4.459724	2.895813	5.565733	5.005011	5.952676	8.223847
4.498490	2.976120	5.652813	5.007494	6.007737	8.263231
4.535208	3.058046	5.740293	5.009724	6.059842	8.299666
4.569940	3.141615	5.828159	5.011706	6.108755	8.333096
4.603063	3.227426	5.917213	5.013454	6.154554	8.363577
4.634614	3.315534	6.007483	5.014977	6.196860	8.390983
4.664041	3.404647	6.097179	5.016280	6.235737	8.415217
4.691176	3.493970	6.185235	5.017374	6.271385	8.436147
4.716599	3.584528	6.273055	5.018272	6.303372	8.453695
4.740693	3.677109	6.361717	5.018983	6.331586	8.467998
4.763248	3.770919	6.450199	5.019527	6.355661	8.478963
4.784123	3.865166	6.537488	5.019897	6.375193	8.486586
4.803470	3.959905	6.623706	5.020129	6.390238	8.491391
4.821454	4.055277	6.709118	5.020255	6.400715	8.493988
4.838181	4.151176	6.793721	5.020312	6.406835	8.495160
4.853715	4.247376	6.877383	5.020328	6.408851	8.495492
4.868071	4.343432	6.959729			
4.881301	4.438955	7.040439			
4.893493	4.533753	7.119451			
4.904733	4.627724	7.196812			
4.915127	4.720873	7.272674			
4.924755	4.813097	7.347053			
4.933639	4.904072	7.419744			
4.941838	4.993554	7.490601			
4.949406	5.081376	7.559601			
4.956391	5.167363	7.626703			
4.962836	5.251333	7.691840			
4.968782	5.333127	7.754955			
4.974268	5.412629	7.816008			
4.979330	5.489728	7.874966			
4.983996	5.564294	7.931770			

TABLE C.19.—IMPELLER SPLITTER BLADE—SECTION 6

X	R*θ	R	X	R*θ	R
4.957994	6.392720	8.494554	4.769542	4.405156	6.865712
4.957954	6.393389	8.493848	4.752432	4.311271	6.784547
4.957820	6.394923	8.491466	4.733973	4.217626	6.702315
4.957542	6.395601	8.486509	4.714112	4.124425	6.619150
4.957073	6.393564	8.478190	4.692759	4.031836	6.535219
4.956379	6.387600	8.466106	4.669848	3.939919	6.450619
4.955457	6.376922	8.450228	4.645290	3.848758	6.365437
4.954326	6.361590	8.431099	4.619001	3.758670	6.279768
4.952978	6.341460	8.408911	4.590906	3.669927	6.193730
4.951416	6.316466	8.383835	4.560956	3.582383	6.107525
4.949643	6.286689	8.356144	4.529119	3.495874	6.021373
4.947658	6.252760	8.325880	4.495380	3.410712	5.935455
4.945449	6.214742	8.292973	4.459718	3.327293	5.849951
4.943010	6.172515	8.257543	4.422136	3.245628	5.765023
4.940340	6.126270	8.219687	4.382651	3.165608	5.680825
4.937420	6.075984	8.179497	4.341278	3.087273	5.597511
4.934246	6.021668	8.137096	4.298045	3.010716	5.515232
4.930805	5.963420	8.092624	4.252995	2.935987	5.434130
4.927079	5.901610	8.046092	4.206189	2.863100	5.354342
4.923032	5.836684	7.997310	4.157709	2.792078	5.276015
4.918637	5.768867	7.946310	4.107653	2.722925	5.199294
4.913868	5.698246	7.893135	4.056148	2.655631	5.124295
4.908705	5.624955	7.837824	4.003316	2.590192	5.051148
4.903100	5.549154	7.780429	3.949296	2.526575	4.979929
4.897031	5.470980	7.720983	3.894218	2.464743	4.910714
4.890454	5.390546	7.659531	3.838241	2.404662	4.843570
4.883326	5.307984	7.596114	3.781537	2.346323	4.778575
4.875600	5.223456	7.530785	3.724282	2.289693	4.715767
4.867225	5.137138	7.463587	3.666628	2.234744	4.655182
4.858151	5.049217	7.394574	3.608751	2.181443	4.596818
4.848315	4.959876	7.323801	3.550806	2.129777	4.540700
4.837657	4.869335	7.251322	3.492969	2.079721	4.486811
4.826105	4.777826	7.177200	3.435396	2.031218	4.435152
4.813594	4.685513	7.101500	3.378247	1.984155	4.385698
4.800048	4.592514	7.024293	3.321674	1.938443	4.338425
4.785390	4.498993	6.945664	3.265819	1.894032	4.293300

TABLE C.19.—IMPELLER SPLITTER BLADE—SECTION 6

X	R*θ	R	X	R*θ	R
3.210820	1.850904	4.250287	2.483232	1.218804	3.785823
3.156807	1.809065	4.209347	2.503772	1.228944	3.796756
3.103904	1.768551	4.170434	2.526521	1.241248	3.808988
3.052226	1.729408	4.133500	2.551471	1.255470	3.822558
3.001878	1.691674	4.098496	2.578574	1.271317	3.837483
2.952963	1.655369	4.065375	2.607767	1.288819	3.853776
2.905577	1.620482	4.034092	2.639000	1.308024	3.871466
2.859816	1.586978	4.004601	2.672245	1.328880	3.890590
2.815765	1.554835	3.976853	2.707475	1.351308	3.911201
2.773483	1.524058	3.950796	2.744667	1.375210	3.933349
2.733025	1.494672	3.926375	2.783781	1.400512	3.957093
2.694453	1.466699	3.903543	2.824762	1.427179	3.982470
2.657829	1.440145	3.882261	2.867535	1.455211	4.009527
2.623232	1.414984	3.862503	2.912018	1.484642	4.038300
2.590744	1.391165	3.844245	2.958122	1.515510	4.068830
2.560440	1.368652	3.827476	3.005767	1.547829	4.101167
2.532383	1.347440	3.812163	3.054870	1.581610	4.135361
2.506582	1.327585	3.798260	3.105331	1.616850	4.171470
2.483056	1.309155	3.785730	3.157052	1.653529	4.209530
2.462007	1.292010	3.774640	3.209916	1.691620	4.249591
2.443556	1.275971	3.765007	3.263802	1.731090	4.291699
2.427760	1.261066	3.756826	3.318588	1.771908	4.335891
2.414822	1.247442	3.750172	3.374141	1.814074	4.382207
2.405358	1.235088	3.745329	3.430320	1.857613	4.430686
2.400126	1.224482	3.742661	3.486979	1.902580	4.481350
2.399253	1.216532	3.742217	3.543968	1.949070	4.534219
2.400753	1.211287	3.742980	3.601127	1.997202	4.589309
2.402830	1.208357	3.744038	3.658292	2.047044	4.646628
2.403759	1.207472	3.744512	3.715308	2.098620	4.706165
2.404812	1.206671	3.745050	3.772002	2.151964	4.767925
2.408404	1.204752	3.746885	3.828220	2.207097	4.831865
2.414818	1.202788	3.750170	3.883789	2.264061	4.897971
2.423860	1.201457	3.754817	3.938552	2.322874	4.966166
2.435331	1.202012	3.760740	3.992334	2.383559	5.036387
2.449051	1.205169	3.767867	4.045001	2.446151	5.108558
2.464976	1.210875	3.776196	4.096424	2.510693	5.182610

TABLE C.19.—IMPELLER SPLITTER BLADE—SECTION 6

X	R*θ	R	X	R*θ	R
4.146468	2.577205	5.258442	4.923150	5.623384	7.998714
4.195016	2.645686	5.335921	4.927341	5.691208	8.049313
4.241956	2.716134	5.414911	4.931207	5.756175	8.097731
4.287193	2.788540	5.495270	4.934763	5.818039	8.143908
4.330666	2.862889	5.576872	4.938020	5.877058	8.187673
4.372349	2.939183	5.659616	4.940984	5.933475	8.228746
4.412164	3.017336	5.743283	4.943673	5.987132	8.267060
4.449981	3.097125	5.827470	4.946098	6.037773	8.302589
4.485857	3.178557	5.912124	4.948280	6.085201	8.335264
4.520102	3.262128	5.997884	4.950225	6.129569	8.365166
4.552730	3.347889	6.084763	4.951934	6.170456	8.392134
4.583268	3.434748	6.171238	4.953413	6.208015	8.416059
4.611551	3.522037	6.256404	4.954664	6.242562	8.436792
4.638083	3.610596	6.341395	4.955693	6.273619	8.454222
4.663215	3.701046	6.427062	4.956514	6.301064	8.468466
4.686761	3.792711	6.512533	4.957145	6.324578	8.479451
4.708592	3.884916	6.596957	4.957579	6.343773	8.487170
4.728859	3.977686	6.680404	4.957855	6.358681	8.492086
4.747721	4.071112	6.763068	4.958002	6.369074	8.494707
4.765262	4.165076	6.844935	4.958066	6.375134	8.495854
4.781556	4.259353	6.925867	4.958084	6.377147	8.496173
4.796631	4.353538	7.005528			
4.810534	4.447269	7.083639			
4.823350	4.540352	7.160137			
4.835176	4.632667	7.235042			
4.846116	4.724188	7.308469			
4.856228	4.814788	7.380435			
4.865577	4.904176	7.450743			
4.874198	4.992102	7.519278			
4.882155	5.078398	7.586011			
4.889503	5.162888	7.650901			
4.896288	5.245393	7.713889			
4.902552	5.325756	7.774919			
4.908333	5.403853	7.833958			
4.913671	5.479580	7.890980			
4.918603	5.552804	7.945926			

TABLE C.20.—IMPELLER SPLITTER BLADE—SECTION 7

X	R*θ	R	X	R*θ	R
4.895365	6.358923	8.495386	4.696819	4.399622	6.919891
4.895320	6.359536	8.494692	4.678918	4.307623	6.841461
4.895168	6.360840	8.492319	4.659635	4.215898	6.761993
4.894846	6.360983	8.487295	4.638891	4.124657	6.681641
4.894298	6.358117	8.478870	4.616628	4.034057	6.600544
4.893508	6.351325	8.466839	4.592756	3.944187	6.518823
4.892468	6.339936	8.451228	4.567200	3.855136	6.436565
4.891202	6.324010	8.432529	4.539883	3.767185	6.353871
4.889711	6.303421	8.410933	4.510734	3.680588	6.270882
4.887999	6.278098	8.386624	4.479716	3.595236	6.187785
4.886077	6.248102	8.359875	4.446815	3.511010	6.104785
4.883941	6.214165	8.330687	4.412001	3.428181	6.022084
4.881575	6.176364	8.298950	4.375289	3.347075	5.939831
4.878973	6.134534	8.264776	4.336679	3.267710	5.858203
4.876128	6.088871	8.228251	4.296201	3.189994	5.777348
4.873030	6.039362	8.189449	4.253883	3.113962	5.697418
4.869661	5.986000	8.148484	4.209764	3.039688	5.618561
4.866013	5.928887	8.105482	4.163898	2.967204	5.540919
4.862070	5.868341	8.060463	4.116355	2.896515	5.464624
4.857791	5.804731	8.013282	4.067231	2.827631	5.389814
4.853153	5.738258	7.963969	4.016625	2.760551	5.316630
4.848134	5.669007	7.912565	3.964670	2.695255	5.245180
4.842696	5.597105	7.859111	3.911503	2.631724	5.175570
4.836810	5.522719	7.803650	3.857253	2.569929	5.107892
4.830431	5.445987	7.746219	3.802068	2.509824	5.042202
4.823525	5.367023	7.686857	3.746105	2.451377	4.978564
4.816043	5.285954	7.625600	3.689535	2.394565	4.917048
4.807938	5.202943	7.562497	3.632533	2.339360	4.857682
4.799157	5.118166	7.497588	3.575251	2.285724	4.800492
4.789640	5.031812	7.430923	3.517856	2.233624	4.745480
4.779324	4.944064	7.362553	3.460511	2.183041	4.692644
4.768152	4.855142	7.292528	3.403376	2.133908	4.641987
4.756046	4.765278	7.220908	3.346606	2.086104	4.593486
4.742935	4.674640	7.147760	3.290353	2.039564	4.547119
4.728745	4.583361	7.073150	3.234762	1.994258	4.502854
4.713399	4.491620	6.997162	3.179967	1.950153	4.460653

TABLE C.20.—IMPELLER SPLITTER BLADE—SECTION 7

X	R*θ	R	X	R*θ	R
3.126099	1.907229	4.420477	2.419151	1.276307	3.989249
3.073276	1.865491	4.382285	2.438953	1.287228	3.999327
3.021616	1.824958	4.346026	2.460893	1.300226	4.010610
2.971222	1.785694	4.311649	2.484959	1.315101	4.023122
2.922192	1.747757	4.279104	2.511104	1.331617	4.036887
2.874618	1.711192	4.248344	2.539270	1.349797	4.051914
2.828588	1.676017	4.219317	2.569412	1.369671	4.068233
2.784188	1.642220	4.191982	2.601507	1.391185	4.085880
2.741495	1.609780	4.166288	2.635538	1.414255	4.104904
2.700561	1.578705	4.142179	2.671490	1.438782	4.125361
2.661429	1.549020	4.119597	2.709335	1.464688	4.147304
2.624152	1.520739	4.098501	2.749021	1.491946	4.170777
2.588783	1.493866	4.078850	2.790487	1.520560	4.195819
2.555399	1.468382	4.060617	2.833649	1.550571	4.222477
2.524073	1.444248	4.043782	2.878431	1.582009	4.250783
2.494880	1.421438	4.028324	2.924760	1.614891	4.280789
2.467873	1.399951	4.014223	2.972563	1.649204	4.312552
2.443061	1.379851	4.001432	3.021753	1.684911	4.346120
2.420452	1.361207	3.989908	3.072236	1.721976	4.381543
2.400207	1.343926	3.979699	3.123906	1.760347	4.418871
2.382416	1.327879	3.970809	3.176655	1.799973	4.458147
2.367111	1.313110	3.963224	3.230366	1.840839	4.499414
2.354471	1.299729	3.957000	3.284916	1.882946	4.542718
2.345094	1.287642	3.952407	3.340174	1.926320	4.588098
2.339638	1.277228	3.949746	3.396002	1.970997	4.635584
2.338195	1.269272	3.949041	3.452255	2.017015	4.685206
2.339169	1.263863	3.949517	3.508781	2.064444	4.736980
2.341004	1.260799	3.950412	3.565426	2.113408	4.790917
2.341883	1.259887	3.950841	3.622035	2.163984	4.847021
2.342904	1.259078	3.951339	3.678442	2.216203	4.905293
2.346458	1.257243	3.953073	3.734488	2.270093	4.965712
2.352823	1.255691	3.956192	3.790017	2.325698	5.028250
2.361726	1.255141	3.960568	3.844856	2.383046	5.092866
2.372922	1.256651	3.966096	3.898841	2.442159	5.159489
2.386210	1.260804	3.972700	3.951831	2.503079	5.228054
2.401560	1.267487	3.980377	4.003688	2.565849	5.298499

TABLE C.20.—IMPELLER SPLITTER BLADE—SECTION 7

X	R*θ	R	X	R*θ	R
4.054274	2.630495	5.370728	4.857595	5.610522	8.011166
4.103466	2.697030	5.444622	4.862033	5.677046	8.060049
4.151145	2.765461	5.520053	4.866129	5.740739	8.106849
4.197210	2.835788	5.596888	4.869911	5.801364	8.151501
4.241589	2.908002	5.675001	4.873385	5.859119	8.193852
4.284236	2.982115	5.754292	4.876557	5.914186	8.233676
4.325073	3.058066	5.834556	4.879444	5.966415	8.270914
4.363979	3.135673	5.915440	4.882069	6.015591	8.305531
4.400981	3.214943	5.996879	4.884439	6.061512	8.337447
4.436324	3.296266	6.079350	4.886577	6.104431	8.366764
4.470029	3.379668	6.162814	4.888475	6.143892	8.393292
4.501663	3.464279	6.246059	4.890128	6.180120	8.416905
4.531092	3.549551	6.328320	4.891540	6.213557	8.437443
4.558748	3.636120	6.410448	4.892705	6.243675	8.454751
4.584926	3.724464	6.493090	4.893646	6.270356	8.468937
4.609469	3.814014	6.575522	4.894368	6.293306	8.479943
4.632283	3.904204	6.657038	4.894876	6.312170	8.487759
4.653494	3.995038	6.737675	4.895198	6.326955	8.492784
4.673243	4.086554	6.817564	4.895368	6.337278	8.495430
4.691627	4.178619	6.896652	4.895440	6.343278	8.496553
4.708710	4.271012	6.974812	4.895459	6.345264	8.496858
4.724520	4.363362	7.051757			
4.739118	4.455339	7.127235			
4.752588	4.546742	7.201182			
4.765020	4.637436	7.273600			
4.776515	4.727355	7.344570			
4.787155	4.816361	7.414083			
4.796974	4.904181	7.481989			
4.806040	4.990568	7.548174			
4.814412	5.075352	7.612614			
4.822142	5.158359	7.675272			
4.829278	5.239405	7.736091			
4.835868	5.318339	7.795020			
4.841958	5.395036	7.852027			
4.847590	5.469391	7.907097			
4.852789	5.541270	7.960174			

TABLE C.21.—IMPELLER SPLITTER BLADE—SECTION 8

X	R*θ	R	X	R*θ	R
4.832319	6.325002	8.496224	4.623418	4.393652	6.974577
4.832270	6.325514	8.495541	4.604724	4.303502	6.898902
4.832098	6.326577	8.493178	4.584597	4.213659	6.822233
4.831724	6.326147	8.488086	4.562966	4.124336	6.744718
4.831091	6.322443	8.479556	4.539766	4.035691	6.666495
4.830201	6.314808	8.467578	4.514927	3.947835	6.587679
4.829041	6.302705	8.452236	4.488369	3.860868	6.508368
4.827642	6.286172	8.433968	4.460019	3.775037	6.428675
4.826013	6.265117	8.412968	4.429822	3.690559	6.348744
4.824159	6.239461	8.389432	4.397751	3.607383	6.268761
4.822099	6.209250	8.363629	4.363785	3.525442	6.188932
4.819822	6.175315	8.335524	4.327921	3.444953	6.109441
4.817305	6.137736	8.304965	4.290169	3.366180	6.030447
4.814548	6.096309	8.272055	4.250562	3.289137	5.952102
4.811532	6.051240	8.236865	4.209121	3.213764	5.874575
4.808248	6.002512	8.199462	4.165890	3.140085	5.798008
4.804682	5.950118	8.159941	4.120921	3.068156	5.722549
4.800827	5.894146	8.118419	4.074278	2.997995	5.648334
4.796660	5.834871	8.074923	4.026044	2.929596	5.575494
4.792146	5.772586	8.029352	3.976319	2.862955	5.504161
4.787265	5.707471	7.981737	3.925216	2.798064	5.434459
4.781982	5.639598	7.932118	3.872865	2.734894	5.366498
4.776263	5.569087	7.880534	3.819409	2.673415	5.300373
4.770076	5.496119	7.827026	3.764992	2.613587	5.236158
4.763382	5.420832	7.771624	3.709756	2.555369	5.173920
4.756134	5.343331	7.714370	3.653862	2.498724	5.113716
4.748283	5.263746	7.655295	3.597487	2.443618	5.055592
4.739782	5.182244	7.594441	3.540796	2.390019	4.999578
4.730568	5.098996	7.531848	3.483944	2.337888	4.945689
4.720589	5.014188	7.467558	3.427092	2.287193	4.893928
4.709784	4.928013	7.401614	3.370398	2.237819	4.844284
4.698070	4.840689	7.334076	3.314021	2.189651	4.796749
4.685389	4.752437	7.264990	3.258109	2.142636	4.751298
4.671665	4.663438	7.194421	3.202806	2.096756	4.707904
4.656813	4.573848	7.122438	3.148247	2.052007	4.666532
4.640758	4.483850	7.049125	3.094558	2.008380	4.627144

TABLE C.21.—IMPELLER SPLITTER BLADE—SECTION 8

X	R*θ	R	X	R*θ	R
3.041863	1.965846	4.589691	2.355915	1.338664	4.189990
2.990274	1.924395	4.554128	2.374976	1.350302	4.199267
2.939896	1.884048	4.520403	2.396104	1.363916	4.209653
2.890823	1.844851	4.488469	2.419279	1.379356	4.221177
2.843144	1.806881	4.458269	2.444460	1.396438	4.233850
2.796941	1.770205	4.429752	2.471590	1.415181	4.247688
2.752293	1.734864	4.402874	2.500631	1.435602	4.262714
2.709280	1.700883	4.377580	2.531565	1.457642	4.278968
2.667969	1.668257	4.353829	2.564384	1.481217	4.296498
2.628400	1.637002	4.331561	2.599082	1.506226	4.315357
2.590609	1.607141	4.310720	2.635639	1.532603	4.335599
2.554641	1.578688	4.291263	2.674011	1.560331	4.357269
2.520543	1.551639	4.273145	2.714142	1.589418	4.380410
2.488380	1.525971	4.256350	2.755960	1.619897	4.405057
2.458227	1.501653	4.240850	2.799391	1.651802	4.431249
2.430149	1.478667	4.226629	2.844374	1.685129	4.459037
2.404199	1.457020	4.213664	2.890842	1.719827	4.488481
2.380380	1.436774	4.201913	2.938721	1.755842	4.519629
2.358693	1.418004	4.191334	2.987925	1.793110	4.552532
2.339253	1.400658	4.181951	3.038359	1.831563	4.587242
2.322124	1.384660	4.173756	3.089923	1.871165	4.623801
2.307312	1.370072	4.166730	3.142507	1.911904	4.662264
2.294971	1.356967	4.160912	3.196003	1.953789	4.702668
2.285682	1.345161	4.156557	3.250284	1.996856	4.745065
2.280004	1.334934	4.153906	3.305222	2.041117	4.789487
2.277992	1.326952	4.152968	3.360681	2.086582	4.835964
2.278443	1.321357	4.153178	3.416515	2.133275	4.884522
2.280037	1.318152	4.153922	3.472579	2.181251	4.935179
2.280866	1.317214	4.154308	3.528716	2.230635	4.987944
2.281855	1.316398	4.154769	3.584773	2.281545	5.042819
2.285368	1.314662	4.156410	3.640588	2.334022	5.099798
2.291685	1.313551	4.159369	3.696006	2.388104	5.158863
2.300446	1.313805	4.163488	3.750861	2.443828	5.219970
2.311366	1.316267	4.168646	3.804990	2.501222	5.283063
2.324221	1.321391	4.174757	3.858243	2.560331	5.348086
2.338994	1.329008	4.181827	3.910475	2.621200	5.414983

TABLE C.21.—IMPELLER SPLITTER BLADE—SECTION 8

X	R*θ	R	X	R*θ	R
3.961549	2.683862	5.483661	4.791577	5.597623	8.023705
4.011333	2.748342	5.554014	4.796263	5.662833	8.070863
4.059703	2.814659	5.625925	4.800601	5.725241	8.116031
4.106552	2.882822	5.699267	4.804609	5.784617	8.159147
4.151794	2.952834	5.773920	4.808302	5.841099	8.200074
4.195373	3.024710	5.849773	4.811685	5.894797	8.238639
4.237205	3.098411	5.926642	4.814779	5.945589	8.274795
4.277166	3.173808	6.004240	4.817598	5.993280	8.308493
4.315271	3.250893	6.082468	4.820158	6.037679	8.339645
4.351706	3.329948	6.161633	4.822479	6.079135	8.368375
4.386454	3.410994	6.241689	4.824557	6.117151	8.394459
4.419184	3.493359	6.321682	4.826387	6.152034	8.417759
4.449773	3.576617	6.401003	4.827961	6.184351	8.438097
4.478563	3.661215	6.480242	4.829271	6.213528	8.455284
4.505790	3.747472	6.559833	4.830338	6.239448	8.469412
4.531337	3.834931	6.639197	4.831157	6.261830	8.480438
4.555135	3.923144	6.717780	4.831744	6.280366	8.488351
4.577304	4.012075	6.795572	4.832120	6.295032	8.493486
4.597967	4.101714	6.872643	4.832315	6.305316	8.496159
4.617209	4.191915	6.948919	4.832395	6.311267	8.497255
4.635092	4.282456	7.024276	4.832416	6.313270	8.497547
4.651664	4.373005	7.098463			
4.666980	4.463258	7.171272			
4.681126	4.553010	7.242634			
4.694193	4.642107	7.312528			
4.706278	4.730448	7.381000			
4.717451	4.817881	7.448038			
4.727777	4.904144	7.513505			
4.737309	4.989007	7.577314			
4.746107	5.072289	7.639437			
4.754235	5.153814	7.699839			
4.761744	5.233408	7.758467			
4.768683	5.310911	7.815271			
4.775094	5.386202	7.870230			
4.781023	5.459180	7.923332			
4.786511	5.529707	7.974521			

TABLE C.22.—IMPELLER SPLITTER BLADE—SECTION 9

X	R*θ	R	X	R*θ	R
4.768810	6.290867	8.497068	4.549299	4.387318	7.029796
4.768754	6.291374	8.496396	4.529789	4.298983	6.956915
4.768559	6.292119	8.494043	4.508802	4.210988	6.883081
4.768129	6.291075	8.488882	4.486276	4.123541	6.808430
4.767412	6.286514	8.480247	4.462142	4.036820	6.733101
4.766411	6.278024	8.468323	4.436324	3.950947	6.657220
4.765137	6.265195	8.453251	4.408757	3.866036	6.580880
4.763613	6.248062	8.435417	4.379378	3.782298	6.504204
4.761851	6.226536	8.415018	4.348142	3.699925	6.427346
4.759866	6.200547	8.392260	4.315019	3.618913	6.350495
4.757674	6.170118	8.367410	4.280004	3.539254	6.273842
4.755263	6.136185	8.340394	4.243109	3.461110	6.197557
4.752605	6.098836	8.311019	4.204343	3.384681	6.121814
4.749688	6.057818	8.279382	4.163756	3.309987	6.046753
4.746507	6.013353	8.245537	4.121389	3.236986	5.972529
4.743038	5.965422	8.209540	4.077282	3.165707	5.899302
4.739274	5.914003	8.171474	4.031500	3.096184	5.827211
4.735205	5.859190	8.131441	3.984124	3.028419	5.756391
4.730810	5.801196	8.089479	3.935243	2.962394	5.686966
4.726060	5.740248	8.045530	3.884967	2.898096	5.619061
4.720917	5.676498	7.999629	3.833417	2.835504	5.552790
4.715359	5.610008	7.951811	3.780726	2.774582	5.488257
4.709350	5.540900	7.902113	3.727039	2.715290	5.425550
4.702850	5.469358	7.850574	3.672504	2.657579	5.364739
4.695818	5.395515	7.797226	3.617275	2.601405	5.305879
4.688209	5.319481	7.742102	3.561515	2.546725	5.249021
4.679974	5.241383	7.685230	3.505392	2.493495	5.194205
4.671057	5.161381	7.626652	3.449071	2.441687	5.141457
4.661401	5.079657	7.566396	3.392707	2.391260	5.090777
4.650947	4.996389	7.504507	3.336455	2.342066	5.042166
4.639617	4.911770	7.441027	3.280471	2.293963	4.995611
4.627356	4.826024	7.375999	3.224906	2.246879	4.951095
4.614079	4.739359	7.309478	3.169904	2.200796	4.908591
4.599713	4.651977	7.241528	3.115600	2.155739	4.868061
4.584181	4.564042	7.172206	3.062120	2.111725	4.829476
4.567403	4.475754	7.101598	3.009587	2.068744	4.792781

TABLE C.22.—IMPELLER SPLITTER BLADE—SECTION 9

X	R*θ	R	X	R*θ	R
2.958108	2.026783	4.757939	2.293492	1.406205	4.388150
2.907792	1.985821	4.724893	2.311810	1.418476	4.396675
2.858733	1.945872	4.693594	2.332120	1.432609	4.406224
2.811015	1.906968	4.663989	2.354399	1.448502	4.416816
2.764718	1.869171	4.636021	2.378610	1.466028	4.428463
2.719917	1.832569	4.609637	2.404699	1.485205	4.441182
2.676677	1.797229	4.584795	2.432630	1.506036	4.454992
2.635073	1.763191	4.561441	2.462394	1.528456	4.469932
2.595163	1.730495	4.539530	2.493989	1.552384	4.486050
2.556979	1.699174	4.519005	2.527417	1.577742	4.503401
2.520544	1.669256	4.499809	2.562670	1.604471	4.522037
2.485899	1.640753	4.481896	2.599708	1.632555	4.542002
2.453078	1.613666	4.465231	2.638485	1.661998	4.563337
2.422148	1.587964	4.449786	2.678935	1.692836	4.586076
2.393174	1.563607	4.435543	2.720987	1.725084	4.610261
2.366219	1.540583	4.422484	2.764591	1.758696	4.635945
2.341329	1.518903	4.410587	2.809693	1.793601	4.663179
2.318506	1.498631	4.399815	2.856226	1.829720	4.692016
2.297742	1.479842	4.390123	2.904113	1.866972	4.722510
2.279109	1.462528	4.381513	2.953268	1.905303	4.754715
2.262643	1.446657	4.373972	3.003599	1.944688	4.788675
2.248326	1.432308	4.367469	3.055011	1.985123	4.824442
2.236284	1.419518	4.362035	3.107400	2.026626	4.862061
2.227085	1.408015	4.357907	3.160650	2.069220	4.901586
2.221187	1.397977	4.355270	3.214643	2.112910	4.943049
2.218607	1.389949	4.354120	3.269250	2.157692	4.986486
2.218538	1.384148	4.354089	3.324331	2.203541	5.031934
2.219890	1.380797	4.354693	3.379748	2.250481	5.079413
2.220669	1.379833	4.355040	3.435352	2.298587	5.128936
2.221625	1.379012	4.355466	3.490992	2.348007	5.180512
2.225099	1.377387	4.357017	3.546511	2.398895	5.234138
2.231365	1.376742	4.359825	3.601758	2.451295	5.289803
2.239984	1.377819	4.363702	3.656567	2.505241	5.347478
2.250627	1.381225	4.368511	3.710774	2.560772	5.407115
2.263047	1.387283	4.374156	3.764227	2.617937	5.468668
2.277241	1.395782	4.380655	3.816777	2.676783	5.532075

TABLE C.22.—IMPELLER SPLITTER BLADE—SECTION 9

X	R*θ	R	X	R*θ	R
3.868281	2.737347	5.597256	4.725042	5.584692	8.036343
3.918603	2.799671	5.664115	4.729987	5.648576	8.081759
3.967615	2.863785	5.732546	4.734572	5.709686	8.125282
4.015201	2.929708	5.802429	4.738812	5.767804	8.166851
4.061267	2.997452	5.873646	4.742727	5.822993	8.206343
4.105732	3.067042	5.946090	4.746325	5.875308	8.243640
4.148514	3.138459	6.019590	4.749625	5.924639	8.278704
4.189510	3.211612	6.093902	4.752646	5.970827	8.311476
4.228702	3.286490	6.168914	4.755395	6.013690	8.341860
4.266195	3.363278	6.244785	4.757904	6.053663	8.369997
4.301976	3.441962	6.321418	4.760161	6.090223	8.395635
4.335785	3.522087	6.398147	4.762162	6.123753	8.418619
4.367528	3.603346	6.474515	4.763898	6.154941	8.438757
4.397453	3.685987	6.550840	4.765357	6.183168	8.455821
4.425733	3.770182	6.627353	4.766543	6.208309	8.469890
4.452291	3.855578	6.703617	4.767469	6.230127	8.480937
4.477093	3.941834	6.779225	4.768135	6.248339	8.488947
4.500229	4.028893	6.854143	4.768571	6.262895	8.494195
4.521824	4.116689	6.928356	4.768795	6.273176	8.496892
4.541935	4.205058	7.001787	4.768884	6.279154	8.497964
4.560646	4.293776	7.074297	4.768907	6.281077	8.498241
4.578000	4.382554	7.145687			
4.594057	4.471108	7.215789			
4.608900	4.559236	7.284528			
4.622623	4.646756	7.351864			
4.635318	4.733541	7.417806			
4.647057	4.819408	7.482329			
4.657906	4.904127	7.545329			
4.667920	4.987468	7.606732			
4.677172	5.069246	7.666508			
4.685721	5.149292	7.724626			
4.693620	5.227426	7.781037			
4.700920	5.303495	7.835698			
4.707672	5.377374	7.888585			
4.713917	5.448964	7.939699			
4.719699	5.518122	7.988984			

TABLE C.23.—IMPELLER SPLITTER BLADE—SECTION 10

X	R*θ	R	X	R*θ	R
4.704788	6.256834	8.497919	4.474384	4.380699	7.085609
4.704727	6.257172	8.497258	4.454051	4.294141	7.015550
4.704511	6.257453	8.494916	4.432201	4.207956	6.944576
4.704029	6.255749	8.489685	4.408766	4.122360	6.872822
4.703215	6.250309	8.480943	4.383683	4.037527	6.800423
4.702107	6.240955	8.469073	4.356893	3.953605	6.727494
4.700716	6.227396	8.454275	4.328322	3.870722	6.654144
4.699071	6.209643	8.436878	4.297916	3.789054	6.580504
4.697186	6.187646	8.417085	4.265640	3.708762	6.506739
4.695078	6.161327	8.395109	4.231483	3.629901	6.433024
4.692765	6.130684	8.371219	4.195444	3.552510	6.359540
4.690226	6.096753	8.345301	4.157527	3.476719	6.286476
4.687423	6.059633	8.317119	4.117786	3.402637	6.213960
4.684355	6.019032	8.286762	4.076248	3.330306	6.142168
4.680997	5.975184	8.254274	4.032980	3.259712	6.071239
4.677344	5.928060	8.219694	3.988036	3.190870	6.001324
4.673381	5.877636	8.183092	3.941488	3.123801	5.932568
4.669094	5.823997	8.144561	3.893422	3.058496	5.865104
4.664463	5.767290	8.104146	3.843942	2.994927	5.799050
4.659459	5.707697	8.061834	3.793165	2.933067	5.734526
4.654053	5.645335	8.017660	3.741220	2.872882	5.671635
4.648207	5.580246	7.971660	3.688243	2.814324	5.610471
4.641891	5.512551	7.923866	3.634384	2.757345	5.551113
4.635061	5.442442	7.874320	3.579794	2.701893	5.493628
4.627681	5.370059	7.823043	3.524632	2.647913	5.438070
4.619699	5.295500	7.770073	3.469062	2.595352	5.384480
4.611060	5.218889	7.715430	3.413249	2.544185	5.332890
4.601708	5.140395	7.659155	3.357357	2.494355	5.283316
4.591584	5.060187	7.601270	3.301538	2.445714	5.235755
4.580628	4.978455	7.541814	3.245944	2.398104	5.190199
4.568770	4.895385	7.480821	3.190726	2.351385	5.146630
4.555930	4.811197	7.418344	3.136031	2.305526	5.105027
4.542040	4.726104	7.354422	3.081989	2.260566	5.065364
4.527023	4.640312	7.289117	3.028735	2.216522	5.027594
4.510796	4.554006	7.222490	2.976383	2.173419	4.991684
4.493275	4.467398	7.154625	2.925046	2.131261	4.957580

TABLE C.23.—IMPELLER SPLITTER BLADE—SECTION 10

X	R*θ	R	X	R*θ	R
2.874828	2.090054	4.925233	2.231849	1.479227	4.583835
2.825824	2.049786	4.894595	2.249421	1.492029	4.591653
2.778119	2.010452	4.865611	2.268912	1.506564	4.600411
2.731791	1.972078	4.838224	2.290293	1.522784	4.610126
2.686905	1.934705	4.812384	2.313529	1.540618	4.620809
2.643531	1.898407	4.788030	2.338570	1.560080	4.632470
2.601724	1.863271	4.765122	2.365385	1.581165	4.645132
2.561549	1.829363	4.743607	2.393969	1.603820	4.658835
2.523060	1.796737	4.723440	2.424329	1.627978	4.673622
2.486275	1.765469	4.704563	2.456476	1.653565	4.689549
2.451211	1.735611	4.686923	2.490408	1.680529	4.706667
2.417898	1.707177	4.670471	2.526097	1.708853	4.725016
2.386368	1.680170	4.655170	2.563500	1.738540	4.744639
2.356677	1.654560	4.641000	2.602557	1.769600	4.765574
2.328888	1.630312	4.627943	2.643207	1.802009	4.787851
2.303059	1.607403	4.615978	2.685405	1.835706	4.811531
2.279233	1.585837	4.605087	2.729108	1.870593	4.836663
2.257410	1.565673	4.595230	2.774259	1.906573	4.863300
2.237570	1.546991	4.586370	2.820790	1.943579	4.891496
2.219744	1.529818	4.578489	2.868625	1.981576	4.921305
2.203941	1.514169	4.571564	2.917682	2.020548	4.952774
2.190119	1.500138	4.565554	2.967874	2.060505	4.985955
2.178379	1.487721	4.560482	3.019105	2.101461	5.020900
2.169271	1.476558	4.556570	3.071271	2.143413	5.057660
2.163153	1.466717	4.553954	3.124263	2.186354	5.096272
2.160009	1.458628	4.552611	3.177956	2.230275	5.136783
2.159419	1.452606	4.552360	3.232227	2.275149	5.179218
2.160531	1.449104	4.552835	3.286936	2.320951	5.223619
2.161259	1.448113	4.553145	3.341943	2.367708	5.269996
2.162183	1.447290	4.553539	3.397102	2.415570	5.318363
2.165616	1.445786	4.555006	3.452260	2.464697	5.368725
2.171831	1.445627	4.557669	3.507268	2.515244	5.421079
2.180307	1.447539	4.561314	3.561965	2.567273	5.475404
2.190671	1.451868	4.565793	3.616185	2.620805	5.531660
2.202656	1.458814	4.571003	3.669776	2.675896	5.589807
2.216272	1.468124	4.576961	3.722583	2.732598	5.649786

TABLE C.23.—IMPELLER SPLITTER BLADE—SECTION 10

X	R*θ	R	X	R*θ	R
3.774459	2.790962	5.711525	4.657919	5.571742	8.049091
3.825264	2.851036	5.774941	4.663135	5.634279	8.092751
3.874861	2.912865	5.839937	4.667968	5.694068	8.134615
3.923132	2.976479	5.906403	4.672449	5.750917	8.174621
3.969968	3.041903	5.974222	4.676592	5.804793	8.212666
4.015283	3.109161	6.043275	4.680415	5.855702	8.248682
4.058989	3.178257	6.113414	4.683932	5.903556	8.282645
4.100980	3.249147	6.184457	4.687159	5.948219	8.314485
4.141230	3.321811	6.256262	4.690106	5.989525	8.344092
4.179762	3.396325	6.328833	4.692805	6.028003	8.371633
4.216542	3.472656	6.402048	4.695242	6.063095	8.396820
4.251408	3.550558	6.475510	4.697415	6.095252	8.419485
4.284311	3.629825	6.548896	4.699312	6.125295	8.439422
4.315379	3.710527	6.622279	4.700912	6.152566	8.456363
4.344707	3.792685	6.695690	4.702229	6.176934	8.470372
4.372270	3.876047	6.768831	4.703261	6.198179	8.481440
4.398076	3.960381	6.841438	4.704016	6.216065	8.489549
4.422202	4.045595	6.913437	4.704511	6.230528	8.494908
4.444730	4.131577	6.984765	4.704762	6.240848	8.497631
4.465736	4.218143	7.055306	4.704858	6.246995	8.498678
4.485288	4.305069	7.124929	4.704883	6.249002	8.498941
4.503435	4.392102	7.193489			
4.520253	4.478983	7.260843			
4.535826	4.565502	7.326914			
4.550227	4.651465	7.391654			
4.563553	4.736699	7.455029			
4.575884	4.821017	7.517000			
4.587274	4.904194	7.577498			
4.597800	4.986011	7.636461			
4.607528	5.066286	7.693857			
4.616519	5.144841	7.749661			
4.624827	5.221507	7.803830			
4.632507	5.296126	7.856319			
4.639614	5.368576	7.907112			
4.646196	5.438764	7.956216			
4.652285	5.506541	8.003577			

TABLE C.24.—IMPELLER SPLITTER BLADE—SECTION 11

X	R*θ	R	X	R*θ	R
4.640219	6.221920	8.498777	4.398619	4.373852	7.142056
4.640152	6.222337	8.498128	4.377446	4.289049	7.074857
4.639913	6.222568	8.495796	4.354723	4.204641	7.006774
4.639370	6.220137	8.490496	4.330377	4.120854	6.937946
4.638463	6.213802	8.481645	4.304355	4.037873	6.868490
4.637245	6.203571	8.469830	4.276583	3.955871	6.798545
4.635744	6.189273	8.455307	4.247007	3.874987	6.728208
4.633984	6.170907	8.438352	4.215583	3.795360	6.657619
4.631982	6.148437	8.419169	4.182289	3.717122	6.586949
4.629753	6.121778	8.397983	4.147112	3.640386	6.516377
4.627317	6.090917	8.375060	4.110054	3.565260	6.446079
4.624651	6.056985	8.350248	4.071158	3.491813	6.376210
4.621706	6.020102	8.323269	4.030456	3.420089	6.306930
4.618476	5.979917	8.294204	3.988015	3.350125	6.238375
4.614949	5.936698	8.263083	3.943882	3.281958	6.170719
4.611111	5.890395	8.229931	3.898137	3.215587	6.104093
4.606943	5.840990	8.194806	3.850864	3.151018	6.038640
4.602431	5.788542	8.157789	3.802159	3.088229	5.974489
4.597555	5.733141	8.118937	3.752129	3.027185	5.911764
4.592286	5.674917	8.078279	3.700905	2.967848	5.850567
4.586595	5.613959	8.035852	3.648619	2.910166	5.790999
4.580453	5.550292	7.991687	3.595413	2.854087	5.733143
4.573810	5.484030	7.945821	3.541438	2.799548	5.677070
4.566640	5.415377	7.898287	3.486851	2.746489	5.622842
4.558890	5.344464	7.849109	3.431816	2.694846	5.570508
4.550509	5.271395	7.798320	3.376498	2.644582	5.520102
4.541447	5.196284	7.745937	3.321059	2.595627	5.471647
4.531646	5.119301	7.691992	3.265656	2.547870	5.425158
4.521042	5.040619	7.636506	3.210440	2.501118	5.380620
4.509563	4.960418	7.579517	3.155564	2.455170	5.338018
4.497150	4.878895	7.521050	3.101166	2.409977	5.297339
4.483720	4.796261	7.461154	3.047391	2.365552	5.258551
4.469204	4.712726	7.399862	2.994364	2.321912	5.221622
4.453515	4.628501	7.337243	2.942206	2.279073	5.186507
4.436573	4.543800	7.273348	2.891030	2.237069	5.153162
4.418301	4.458845	7.208256	2.840936	2.195928	5.121538

TABLE C.24.—IMPELLER SPLITTER BLADE—SECTION 11

X	R*θ	R	X	R*θ	R
2.792017	2.155664	5.091585	2.170960	1.557968	4.777124
2.744362	2.116284	5.063249	2.187785	1.571183	4.784279
2.698047	2.077785	5.036472	2.206454	1.585993	4.792294
2.653138	2.040176	5.011205	2.226933	1.602396	4.801182
2.609694	2.003490	4.987384	2.249191	1.620390	4.810956
2.567771	1.967774	4.964963	2.273179	1.639995	4.821624
2.527419	1.933099	4.943889	2.298870	1.661209	4.833206
2.488694	1.899548	4.924118	2.326268	1.683981	4.845738
2.451641	1.867200	4.905604	2.355384	1.708252	4.859270
2.416271	1.836145	4.888286	2.386237	1.733956	4.873850
2.382590	1.806471	4.872116	2.418838	1.761038	4.889532
2.350620	1.778226	4.857044	2.453159	1.789481	4.906355
2.320386	1.751415	4.843035	2.489170	1.819255	4.924358
2.291941	1.726015	4.830067	2.526815	1.850332	4.943578
2.265343	1.701989	4.818122	2.566037	1.882680	4.964048
2.240644	1.679322	4.807189	2.606803	1.916207	4.985822
2.217885	1.658012	4.797243	2.649079	1.950802	5.008951
2.197062	1.638103	4.788251	2.692813	1.986388	5.033494
2.178148	1.619667	4.780173	2.737952	2.022921	5.059498
2.161130	1.602760	4.772974	2.784428	2.060372	5.087019
2.145992	1.587442	4.766626	2.832167	2.098744	5.116104
2.132665	1.573820	4.761081	2.881092	2.138046	5.146809
2.121225	1.561851	4.756353	2.931116	2.178268	5.179188
2.112208	1.551077	4.752647	2.982146	2.219399	5.213290
2.105873	1.541458	4.750055	3.034080	2.261413	5.249162
2.102167	1.533304	4.748541	3.086806	2.304282	5.286844
2.101058	1.527051	4.748090	3.140200	2.347989	5.326378
2.101930	1.523393	4.748445	3.194142	2.392521	5.367797
2.102608	1.522376	4.748721	3.248488	2.437868	5.411125
2.103499	1.521551	4.749084	3.303103	2.484079	5.456376
2.106890	1.520177	4.750472	3.357832	2.531365	5.503566
2.113055	1.520515	4.752994	3.412534	2.579923	5.552696
2.121387	1.523262	4.756421	3.467050	2.629873	5.603751
2.131473	1.528480	4.760587	3.521219	2.681274	5.656701
2.143021	1.536250	4.765386	3.574884	2.734171	5.711512
2.156056	1.546288	4.770841	3.627885	2.788619	5.768127

TABLE C.24.—IMPELLER SPLITTER BLADE—SECTION 11

X	R*θ	R	X	R*θ	R
3.680068	2.844682	5.826488	4.590124	5.558775	8.061969
3.731292	2.902424	5.886516	4.595620	5.619939	8.103850
3.781421	2.961894	5.948124	4.600720	5.678390	8.144037
3.830326	3.023139	6.011208	4.605449	5.733950	8.182466
3.877892	3.086192	6.075656	4.609829	5.786492	8.219048
3.924008	3.151086	6.141348	4.613881	5.835966	8.253773
3.968583	3.217844	6.208159	4.617625	5.882320	8.286624
4.011545	3.286453	6.275939	4.621071	5.925435	8.317520
4.052821	3.356898	6.344546	4.624229	5.965171	8.346345
4.092362	3.429141	6.413820	4.627127	6.002135	8.373283
4.130101	3.503135	6.483629	4.629756	6.035744	8.398016
4.166011	3.578824	6.553807	4.632107	6.066519	8.420360
4.200070	3.656122	6.624192	4.634166	6.095411	8.440092
4.232278	3.734911	6.694611	4.635911	6.121712	8.456909
4.262648	3.815063	6.764898	4.637351	6.145292	8.470859
4.291209	3.896423	6.834892	4.638494	6.165963	8.481947
4.318018	3.978868	6.904471	4.639335	6.183526	8.490155
4.343141	4.062268	6.973516	4.639896	6.197900	8.495628
4.366615	4.146472	7.041921	4.640178	6.208320	8.498377
4.388526	4.231265	7.109534	4.640283	6.214220	8.499398
4.408924	4.316426	7.176239	4.640308	6.216063	8.499647
4.427881	4.401736	7.241924			
4.445479	4.486964	7.306490			
4.461795	4.571895	7.369855			
4.476905	4.656315	7.431953			
4.490887	4.740008	7.492719			
4.503830	4.822772	7.552099			
4.515787	4.904403	7.610058			
4.526846	4.984692	7.666543			
4.537073	5.063448	7.721525			
4.546527	5.140503	7.774983			
4.555269	5.215684	7.826877			
4.563351	5.288832	7.877165			
4.570832	5.359834	7.925837			
4.577767	5.428596	7.972906			
4.584183	5.494966	8.018320			

C.3 Diffuser Main Vane and Splitter Vane

Diffuser vanes are defined in the hub and shroud sides. Section 1 refers to the hub side and section 2 is for the shroud side. The vanes are two dimensional so section 2 is a translation of section 1 in the positive x direction. They are expressed in x, $r^*\theta$ and r coordinates.

TABLE C.25.—DIFFUSER MAIN VANE—SECTION 1

X	$R^*\theta$	R	X	$R^*\theta$	R
5.400000	12.438303	11.204491	5.400000	12.865541	10.294801
5.400000	12.462341	11.202411	5.400000	12.885896	10.257460
5.400000	12.473289	11.200020	5.400000	12.906988	10.220219
5.400000	12.485045	11.196324	5.400000	12.928836	10.183137
5.400000	12.497258	11.191114	5.400000	12.951445	10.146270
5.400000	12.509587	11.184204	5.400000	12.974802	10.109661
5.400000	12.521730	11.175444	5.400000	12.998910	10.073365
5.400000	12.533389	11.164695	5.400000	13.023759	10.037426
5.400000	12.544267	11.151833	5.400000	13.049356	10.001895
5.400000	12.554070	11.136737	5.400000	13.075680	9.966814
5.400000	12.562447	11.119270	5.400000	13.102721	9.932224
5.400000	12.568974	11.099265	5.400000	13.130460	9.898165
5.400000	12.574447	11.077216	5.400000	13.158892	9.864679
5.400000	12.580307	11.053941	5.400000	13.187987	9.831800
5.400000	12.586606	11.029499	5.400000	13.217723	9.799560
5.400000	12.593363	11.003934	5.400000	13.248075	9.767992
5.400000	12.600576	10.977284	5.400000	13.279018	9.737127
5.400000	12.608270	10.949594	5.400000	13.310520	9.706991
5.400000	12.616457	10.920911	5.400000	13.342544	9.677607
5.400000	12.625150	10.891283	5.400000	13.375052	9.648996
5.400000	12.634378	10.860764	5.400000	13.408001	9.621179
5.400000	12.644141	10.829398	5.400000	13.441353	9.594172
5.400000	12.654455	10.797239	5.400000	13.475064	9.567990
5.400000	12.665342	10.764340	5.400000	13.509071	9.542640
5.400000	12.676813	10.730756	5.400000	13.543330	9.518136
5.400000	12.688890	10.696542	5.400000	13.577792	9.494485
5.400000	12.701583	10.661753	5.400000	13.612386	9.471686
5.400000	12.714911	10.626445	5.400000	13.647069	9.449750
5.400000	12.728885	10.590677	5.400000	13.681760	9.428668
5.400000	12.743519	10.554503	5.400000	13.716414	9.408444
5.400000	12.758832	10.517984	5.400000	13.750945	9.389070
5.400000	12.774834	10.481175	5.400000	13.785298	9.370541
5.400000	12.791535	10.444137	5.400000	13.819398	9.352848
5.400000	12.808944	10.406921	5.400000	13.853174	9.335983
5.400000	12.827080	10.369592	5.400000	13.886560	9.319937
5.400000	12.845941	10.332198	5.400000	13.919477	9.304694

TABLE C.25.—DIFFUSER MAIN VANE—SECTION 1

X	R*θ	R	X	R*θ	R
5.400000	13.951847	9.290239	5.400000	14.191944	9.129019
5.400000	13.983611	9.276563	5.400000	14.169162	9.134331
5.400000	14.014686	9.263646	5.400000	14.144849	9.140162
5.400000	14.044987	9.251468	5.400000	14.119063	9.146529
5.400000	14.074464	9.240020	5.400000	14.091873	9.153454
5.400000	14.103028	9.229278	5.400000	14.063347	9.160958
5.400000	14.130619	9.219228	5.400000	14.033552	9.169059
5.400000	14.157157	9.209848	5.400000	14.002564	9.177780
5.400000	14.182584	9.201122	5.400000	13.970454	9.187141
5.400000	14.206824	9.193030	5.400000	13.937316	9.197170
5.400000	14.229832	9.185560	5.400000	13.903213	9.207883
5.400000	14.251533	9.178690	5.400000	13.868221	9.219297
5.400000	14.271873	9.172403	5.400000	13.832428	9.231438
5.400000	14.290793	9.166683	5.400000	13.795919	9.244323
5.400000	14.308247	9.161515	5.400000	13.758764	9.257971
5.400000	14.324194	9.156888	5.400000	13.721055	9.272402
5.400000	14.338577	9.152784	5.400000	13.682866	9.287629
5.400000	14.351370	9.149196	5.400000	13.644275	9.303667
5.400000	14.361513	9.145540	5.400000	13.605361	9.320532
5.400000	14.367230	9.140900	5.400000	13.566200	9.338232
5.400000	14.369020	9.135660	5.400000	13.526867	9.356777
5.400000	14.367285	9.130180	5.400000	13.487442	9.376180
5.400000	14.362803	9.125045	5.400000	13.447995	9.396445
5.400000	14.357780	9.121361	5.400000	13.408585	9.417571
5.400000	14.355692	9.120103	5.400000	13.369284	9.439561
5.400000	14.353402	9.118852	5.400000	13.330162	9.462418
5.400000	14.346222	9.115569	5.400000	13.291276	9.486135
5.400000	14.335153	9.111870	5.400000	13.252684	9.510706
5.400000	14.322085	9.108987	5.400000	13.214441	9.536123
5.400000	14.308168	9.107432	5.400000	13.176600	9.562375
5.400000	14.294189	9.107533	5.400000	13.139216	9.589450
5.400000	14.280896	9.109607	5.400000	13.102321	9.617325
5.400000	14.266597	9.112589	5.400000	13.065971	9.645986
5.400000	14.250505	9.116005	5.400000	13.030203	9.675409
5.400000	14.232666	9.119872	5.400000	12.995050	9.705570
5.400000	14.213128	9.124204	5.400000	12.960551	9.736444

TABLE C.25.—DIFFUSER MAIN VANE—SECTION 1

X	R*θ	R	X	R*θ	R
5.400000	12.926732	9.767995	5.400000	12.226889	10.962811
5.400000	12.893615	9.800195	5.400000	12.227676	10.988912
5.400000	12.861236	9.833009	5.400000	12.231751	11.015071
5.400000	12.829605	9.866398	5.400000	12.238960	11.041086
5.400000	12.798747	9.900323	5.400000	12.249218	11.066771
5.400000	12.768678	9.934744	5.400000	12.262597	11.091969
5.400000	12.739402	9.969612	5.400000	12.279285	11.116481
5.400000	12.710935	10.004885	5.400000	12.299667	11.139991
5.400000	12.683290	10.040517	5.400000	12.323768	11.161630
5.400000	12.656462	10.076455	5.400000	12.350334	11.179408
5.400000	12.630462	10.112650	5.400000	12.375160	11.191711
5.400000	12.605292	10.149051	5.400000	12.395042	11.198473
5.400000	12.580939	10.185597	5.400000	12.409896	11.201891
5.400000	12.557416	10.222241	5.400000	12.420540	11.203476
5.400000	12.534708	10.258925	5.400000	12.427702	11.204147
5.400000	12.512819	10.295592	5.400000	12.431821	11.204369
5.400000	12.491729	10.332181	5.400000	12.433160	11.204410
5.400000	12.471437	10.368637			
5.400000	12.451933	10.404901			
5.400000	12.433204	10.440913			
5.400000	12.415236	10.476614			
5.400000	12.398025	10.511949			
5.400000	12.381560	10.546859			
5.400000	12.365814	10.581280			
5.400000	12.350779	10.615155			
5.400000	12.336446	10.648433			
5.400000	12.322796	10.681054			
5.400000	12.309813	10.712960			
5.400000	12.297481	10.744098			
5.400000	12.285790	10.774415			
5.400000	12.274722	10.803859			
5.400000	12.264262	10.832378			
5.400000	12.254401	10.859925			
5.400000	12.245112	10.886446			
5.400000	12.236404	10.911909			
5.400000	12.229663	10.937032			

TABLE C.26.—DIFFUSER MAIN VANE—SECTION 2

X	R*θ	R	X	R*θ	R
4.600000	12.438303	11.204491	4.600000	12.865541	10.294801
4.600000	12.462341	11.202411	4.600000	12.885896	10.257460
4.600000	12.473289	11.200020	4.600000	12.906988	10.220219
4.600000	12.485045	11.196324	4.600000	12.928836	10.183137
4.600000	12.497258	11.191114	4.600000	12.951445	10.146270
4.600000	12.509587	11.184204	4.600000	12.974802	10.109661
4.600000	12.521730	11.175444	4.600000	12.998910	10.073365
4.600000	12.533389	11.164695	4.600000	13.023759	10.037426
4.600000	12.544267	11.151833	4.600000	13.049356	10.001895
4.600000	12.554070	11.136737	4.600000	13.075680	9.966814
4.600000	12.562447	11.119270	4.600000	13.102721	9.932224
4.600000	12.568974	11.099265	4.600000	13.130460	9.898165
4.600000	12.574447	11.077216	4.600000	13.158892	9.864679
4.600000	12.580307	11.053941	4.600000	13.187987	9.831800
4.600000	12.586606	11.029499	4.600000	13.217723	9.799560
4.600000	12.593363	11.003934	4.600000	13.248075	9.767992
4.600000	12.600576	10.977284	4.600000	13.279018	9.737127
4.600000	12.608270	10.949594	4.600000	13.310520	9.706991
4.600000	12.616457	10.920911	4.600000	13.342544	9.677607
4.600000	12.625150	10.891283	4.600000	13.375052	9.648996
4.600000	12.634378	10.860764	4.600000	13.408001	9.621179
4.600000	12.644141	10.829398	4.600000	13.441353	9.594172
4.600000	12.654455	10.797239	4.600000	13.475064	9.567990
4.600000	12.665342	10.764340	4.600000	13.509071	9.542640
4.600000	12.676813	10.730756	4.600000	13.543330	9.518136
4.600000	12.688890	10.696542	4.600000	13.577792	9.494485
4.600000	12.701583	10.661753	4.600000	13.612386	9.471686
4.600000	12.714911	10.626445	4.600000	13.647069	9.449750
4.600000	12.728885	10.590677	4.600000	13.681760	9.428668
4.600000	12.743519	10.554503	4.600000	13.716414	9.408444
4.600000	12.758832	10.517984	4.600000	13.750945	9.389070
4.600000	12.774834	10.481175	4.600000	13.785298	9.370541
4.600000	12.791535	10.444137	4.600000	13.819398	9.352848
4.600000	12.808944	10.406921	4.600000	13.853174	9.335983
4.600000	12.827080	10.369592	4.600000	13.886560	9.319937
4.600000	12.845941	10.332198	4.600000	13.919477	9.304694

TABLE C.26.—DIFFUSER MAIN VANE—SECTION 2

X	R*θ	R	X	R*θ	R
4.600000	13.951847	9.290239	4.600000	14.191944	9.129019
4.600000	13.983611	9.276563	4.600000	14.169162	9.134331
4.600000	14.014686	9.263646	4.600000	14.144849	9.140162
4.600000	14.044987	9.251468	4.600000	14.119063	9.146529
4.600000	14.074464	9.240020	4.600000	14.091873	9.153454
4.600000	14.103028	9.229278	4.600000	14.063347	9.160958
4.600000	14.130619	9.219228	4.600000	14.033552	9.169059
4.600000	14.157157	9.209848	4.600000	14.002564	9.177780
4.600000	14.182584	9.201122	4.600000	13.970454	9.187141
4.600000	14.206824	9.193030	4.600000	13.937316	9.197170
4.600000	14.229832	9.185560	4.600000	13.903213	9.207883
4.600000	14.251533	9.178690	4.600000	13.868221	9.219297
4.600000	14.271873	9.172403	4.600000	13.832428	9.231438
4.600000	14.290793	9.166683	4.600000	13.795919	9.244323
4.600000	14.308247	9.161515	4.600000	13.758764	9.257971
4.600000	14.324194	9.156888	4.600000	13.721055	9.272402
4.600000	14.338577	9.152784	4.600000	13.682866	9.287629
4.600000	14.351370	9.149196	4.600000	13.644275	9.303667
4.600000	14.361513	9.145540	4.600000	13.605361	9.320532
4.600000	14.367230	9.140900	4.600000	13.566200	9.338232
4.600000	14.369020	9.135660	4.600000	13.526867	9.356777
4.600000	14.367285	9.130180	4.600000	13.487442	9.376180
4.600000	14.362803	9.125045	4.600000	13.447995	9.396445
4.600000	14.357780	9.121361	4.600000	13.408585	9.417571
4.600000	14.355692	9.120103	4.600000	13.369284	9.439561
4.600000	14.353402	9.118852	4.600000	13.330162	9.462418
4.600000	14.346222	9.115569	4.600000	13.291276	9.486135
4.600000	14.335153	9.111870	4.600000	13.252684	9.510706
4.600000	14.322085	9.108987	4.600000	13.214441	9.536123
4.600000	14.308168	9.107432	4.600000	13.176600	9.562375
4.600000	14.294189	9.107533	4.600000	13.139216	9.589450
4.600000	14.280896	9.109607	4.600000	13.102321	9.617325
4.600000	14.266597	9.112589	4.600000	13.065971	9.645986
4.600000	14.250505	9.116005	4.600000	13.030203	9.675409
4.600000	14.232666	9.119872	4.600000	12.995050	9.705570
4.600000	14.213128	9.124204	4.600000	12.960551	9.736444

TABLE C.26.—DIFFUSER MAIN VANE—SECTION 2

X	R*θ	R	X	R*θ	R
4.600000	12.926732	9.767995	4.600000	12.226889	10.962811
4.600000	12.893615	9.800195	4.600000	12.227676	10.988912
4.600000	12.861236	9.833009	4.600000	12.231751	11.015071
4.600000	12.829605	9.866398	4.600000	12.238960	11.041086
4.600000	12.798747	9.900323	4.600000	12.249218	11.066771
4.600000	12.768678	9.934744	4.600000	12.262597	11.091969
4.600000	12.739402	9.969612	4.600000	12.279285	11.116481
4.600000	12.710935	10.004885	4.600000	12.299667	11.139991
4.600000	12.683290	10.040517	4.600000	12.323768	11.161630
4.600000	12.656462	10.076455	4.600000	12.350334	11.179408
4.600000	12.630462	10.112650	4.600000	12.375160	11.191711
4.600000	12.605292	10.149051	4.600000	12.395042	11.198473
4.600000	12.580939	10.185597	4.600000	12.409896	11.201891
4.600000	12.557416	10.222241	4.600000	12.420540	11.203476
4.600000	12.534708	10.258925	4.600000	12.427702	11.204147
4.600000	12.512819	10.295592	4.600000	12.431821	11.204369
4.600000	12.491729	10.332181	4.600000	12.433160	11.204410
4.600000	12.471437	10.368637			
4.600000	12.451933	10.404901			
4.600000	12.433204	10.440913			
4.600000	12.415236	10.476614			
4.600000	12.398025	10.511949			
4.600000	12.381560	10.546859			
4.600000	12.365814	10.581280			
4.600000	12.350779	10.615155			
4.600000	12.336446	10.648433			
4.600000	12.322796	10.681054			
4.600000	12.309813	10.712960			
4.600000	12.297481	10.744098			
4.600000	12.285790	10.774415			
4.600000	12.274722	10.803859			
4.600000	12.264262	10.832378			
4.600000	12.254401	10.859925			
4.600000	12.245112	10.886446			
4.600000	12.236404	10.911909			
4.600000	12.229663	10.937032			

TABLE C.27.—DIFFUSER SPLITTER VANE—SECTION 1

X	R*θ	R	X	R*θ	R
5.400000	14.495933	11.206582	5.400000	14.675404	10.784893
5.400000	14.499725	11.206556	5.400000	14.680651	10.762184
5.400000	14.501868	11.206506	5.400000	14.686136	10.739287
5.400000	14.505373	11.206371	5.400000	14.691874	10.716236
5.400000	14.510116	11.206070	5.400000	14.697854	10.693053
5.400000	14.515947	11.205493	5.400000	14.704085	10.669769
5.400000	14.522687	11.204518	5.400000	14.710562	10.646410
5.400000	14.530161	11.203039	5.400000	14.717298	10.623008
5.400000	14.538186	11.200948	5.400000	14.724272	10.599583
5.400000	14.546595	11.198146	5.400000	14.731504	10.576170
5.400000	14.555221	11.194545	5.400000	14.738985	10.552792
5.400000	14.563902	11.190065	5.400000	14.746709	10.529473
5.400000	14.572484	11.184637	5.400000	14.754667	10.506240
5.400000	14.580836	11.178200	5.400000	14.762877	10.483122
5.400000	14.588814	11.170695	5.400000	14.771312	10.460138
5.400000	14.596265	11.162067	5.400000	14.779965	10.437313
5.400000	14.603071	11.152269	5.400000	14.788850	10.414675
5.400000	14.609070	11.141247	5.400000	14.797942	10.392241
5.400000	14.614104	11.128945	5.400000	14.807244	10.370037
5.400000	14.618002	11.115305	5.400000	14.816739	10.348084
5.400000	14.620602	11.100279	5.400000	14.826407	10.326395
5.400000	14.622575	11.084235	5.400000	14.836254	10.304999
5.400000	14.624826	11.067642	5.400000	14.846265	10.283914
5.400000	14.627203	11.050446	5.400000	14.856414	10.263152
5.400000	14.629724	11.032675	5.400000	14.866708	10.242739
5.400000	14.632433	11.014372	5.400000	14.877108	10.222682
5.400000	14.635327	10.995558	5.400000	14.887626	10.203007
5.400000	14.638395	10.976249	5.400000	14.898223	10.183722
5.400000	14.641662	10.956478	5.400000	14.908891	10.164842
5.400000	14.645127	10.936273	5.400000	14.919616	10.146382
5.400000	14.648800	10.915659	5.400000	14.930359	10.128349
5.400000	14.652676	10.894658	5.400000	14.941130	10.110766
5.400000	14.656765	10.873302	5.400000	14.951892	10.093634
5.400000	14.661087	10.851623	5.400000	14.962628	10.076965
5.400000	14.665630	10.829642	5.400000	14.973321	10.060772
5.400000	14.670401	10.807390	5.400000	14.983943	10.045060

TABLE C.27.—DIFFUSER SPLITTER VANE—SECTION 1

X	R*θ	R	X	R*θ	R
5.400000	14.994474	10.029838	5.400000	15.081760	9.798881
5.400000	15.004893	10.015112	5.400000	15.075419	9.802792
5.400000	15.015184	10.000891	5.400000	15.068603	9.807289
5.400000	15.025319	9.987179	5.400000	15.061146	9.812274
5.400000	15.035276	9.973982	5.400000	15.053040	9.817737
5.400000	15.045034	9.961304	5.400000	15.044321	9.823684
5.400000	15.054566	9.949148	5.400000	15.034990	9.830113
5.400000	15.063862	9.937522	5.400000	15.025090	9.837030
5.400000	15.072892	9.926426	5.400000	15.014623	9.844433
5.400000	15.081636	9.915863	5.400000	15.003615	9.852321
5.400000	15.090074	9.905835	5.400000	14.992106	9.860702
5.400000	15.098182	9.896343	5.400000	14.980110	9.869572
5.400000	15.105943	9.887391	5.400000	14.967646	9.878930
5.400000	15.113343	9.878982	5.400000	14.954751	9.888779
5.400000	15.120359	9.871112	5.400000	14.941441	9.899116
5.400000	15.126969	9.863784	5.400000	14.927749	9.909941
5.400000	15.133157	9.856996	5.400000	14.913715	9.921260
5.400000	15.138914	9.850752	5.400000	14.899349	9.933062
5.400000	15.144231	9.845056	5.400000	14.884691	9.945351
5.400000	15.149069	9.839894	5.400000	14.869762	9.958120
5.400000	15.152988	9.835052	5.400000	14.854599	9.971372
5.400000	15.154671	9.829886	5.400000	14.839213	9.985094
5.400000	15.154398	9.824594	5.400000	14.823657	9.999292
5.400000	15.152400	9.819341	5.400000	14.807945	10.013957
5.400000	15.148902	9.814310	5.400000	14.792106	10.029080
5.400000	15.144280	9.809769	5.400000	14.776164	10.044657
5.400000	15.139419	9.806171	5.400000	14.760150	10.060680
5.400000	15.135792	9.803983	5.400000	14.744090	10.077141
5.400000	15.134482	9.803277	5.400000	14.728011	10.094030
5.400000	15.133087	9.802565	5.400000	14.711934	10.111340
5.400000	15.128840	9.800640	5.400000	14.695895	10.129059
5.400000	15.122143	9.798248	5.400000	14.679901	10.147173
5.400000	15.114092	9.796275	5.400000	14.663983	10.165671
5.400000	15.105601	9.795196	5.400000	14.648164	10.184541
5.400000	15.097149	9.795190	5.400000	14.632460	10.203766
5.400000	15.089083	9.796372	5.400000	14.616897	10.223332

TABLE C.27.—DIFFUSER SPLITTER VANE—SECTION 1

X	R*θ	R	X	R*θ	R
5.400000	14.601487	10.243221	5.400000	14.251467	10.991212
5.400000	14.586258	10.263421	5.400000	14.256261	11.010696
5.400000	14.571220	10.283910	5.400000	14.263062	11.030282
5.400000	14.556389	10.304668	5.400000	14.271830	11.049887
5.400000	14.541782	10.325680	5.400000	14.282581	11.069441
5.400000	14.527412	10.346920	5.400000	14.295391	11.088882
5.400000	14.513294	10.368372	5.400000	14.310421	11.108143
5.400000	14.499439	10.390012	5.400000	14.327841	11.127100
5.400000	14.485848	10.411812	5.400000	14.347915	11.145524
5.400000	14.472549	10.433756	5.400000	14.370616	11.162850
5.400000	14.459541	10.455818	5.400000	14.395068	11.177824
5.400000	14.446831	10.477970	5.400000	14.418665	11.189380
5.400000	14.434429	10.500193	5.400000	14.438899	11.196945
5.400000	14.422339	10.522453	5.400000	14.455284	11.201487
5.400000	14.410562	10.544726	5.400000	14.468274	11.204101
5.400000	14.399116	10.566992	5.400000	14.478421	11.205508
5.400000	14.387991	10.589216	5.400000	14.486198	11.206199
5.400000	14.377193	10.611371			
5.400000	14.366724	10.633431			
5.400000	14.356585	10.655368			
5.400000	14.346776	10.677153			
5.400000	14.337300	10.698757			
5.400000	14.328155	10.720153			
5.400000	14.319343	10.741314			
5.400000	14.310860	10.762209			
5.400000	14.302689	10.782806			
5.400000	14.294849	10.803083			
5.400000	14.287331	10.823011			
5.400000	14.280124	10.842561			
5.400000	14.273219	10.861699			
5.400000	14.266624	10.880406			
5.400000	14.260387	10.898684			
5.400000	14.254339	10.916418			
5.400000	14.250011	10.934380			
5.400000	14.248213	10.952932			
5.400000	14.248750	10.971921			

TABLE C.28.—DIFFUSER SPLITTER VANE—SECTION 2

X	R*θ	R	X	R*θ	R
4.600000	14.495933	11.206582	4.600000	14.675404	10.784893
4.600000	14.499725	11.206556	4.600000	14.680651	10.762184
4.600000	14.501868	11.206506	4.600000	14.686136	10.739287
4.600000	14.505373	11.206371	4.600000	14.691874	10.716236
4.600000	14.510116	11.206070	4.600000	14.697854	10.693053
4.600000	14.515947	11.205493	4.600000	14.704085	10.669769
4.600000	14.522687	11.204518	4.600000	14.710562	10.646410
4.600000	14.530161	11.203039	4.600000	14.717298	10.623008
4.600000	14.538186	11.200948	4.600000	14.724272	10.599583
4.600000	14.546595	11.198146	4.600000	14.731504	10.576170
4.600000	14.555221	11.194545	4.600000	14.738985	10.552792
4.600000	14.563902	11.190065	4.600000	14.746709	10.529473
4.600000	14.572484	11.184637	4.600000	14.754667	10.506240
4.600000	14.580836	11.178200	4.600000	14.762877	10.483122
4.600000	14.588814	11.170695	4.600000	14.771312	10.460138
4.600000	14.596265	11.162067	4.600000	14.779965	10.437313
4.600000	14.603071	11.152269	4.600000	14.788850	10.414675
4.600000	14.609070	11.141247	4.600000	14.797942	10.392241
4.600000	14.614104	11.128945	4.600000	14.807244	10.370037
4.600000	14.618002	11.115305	4.600000	14.816739	10.348084
4.600000	14.620602	11.100279	4.600000	14.826407	10.326395
4.600000	14.622575	11.084235	4.600000	14.836254	10.304999
4.600000	14.624826	11.067642	4.600000	14.846265	10.283914
4.600000	14.627203	11.050446	4.600000	14.856414	10.263152
4.600000	14.629724	11.032675	4.600000	14.866708	10.242739
4.600000	14.632433	11.014372	4.600000	14.877108	10.222682
4.600000	14.635327	10.995558	4.600000	14.887626	10.203007
4.600000	14.638395	10.976249	4.600000	14.898223	10.183722
4.600000	14.641662	10.956478	4.600000	14.908891	10.164842
4.600000	14.645127	10.936273	4.600000	14.919616	10.146382
4.600000	14.648800	10.915659	4.600000	14.930359	10.128349
4.600000	14.652676	10.894658	4.600000	14.941130	10.110766
4.600000	14.656765	10.873302	4.600000	14.951892	10.093634
4.600000	14.661087	10.851623	4.600000	14.962628	10.076965
4.600000	14.665630	10.829642	4.600000	14.973321	10.060772
4.600000	14.670401	10.807390	4.600000	14.983943	10.045060

TABLE C.28.—DIFFUSER SPLITTER VANE—SECTION 2

X	R*θ	R	X	R*θ	R
4.600000	14.994474	10.029838	4.600000	15.081760	9.798881
4.600000	15.004893	10.015112	4.600000	15.075419	9.802792
4.600000	15.015184	10.000891	4.600000	15.068603	9.807289
4.600000	15.025319	9.987179	4.600000	15.061146	9.812274
4.600000	15.035276	9.973982	4.600000	15.053040	9.817737
4.600000	15.045034	9.961304	4.600000	15.044321	9.823684
4.600000	15.054566	9.949148	4.600000	15.034990	9.830113
4.600000	15.063862	9.937522	4.600000	15.025090	9.837030
4.600000	15.072892	9.926426	4.600000	15.014623	9.844433
4.600000	15.081636	9.915863	4.600000	15.003615	9.852321
4.600000	15.090074	9.905835	4.600000	14.992106	9.860702
4.600000	15.098182	9.896343	4.600000	14.980110	9.869572
4.600000	15.105943	9.887391	4.600000	14.967646	9.878930
4.600000	15.113343	9.878982	4.600000	14.954751	9.888779
4.600000	15.120359	9.871112	4.600000	14.941441	9.899116
4.600000	15.126969	9.863784	4.600000	14.927749	9.909941
4.600000	15.133157	9.856996	4.600000	14.913715	9.921260
4.600000	15.138914	9.850752	4.600000	14.899349	9.933062
4.600000	15.144231	9.845056	4.600000	14.884691	9.945351
4.600000	15.149069	9.839894	4.600000	14.869762	9.958120
4.600000	15.152988	9.835052	4.600000	14.854599	9.971372
4.600000	15.154671	9.829886	4.600000	14.839213	9.985094
4.600000	15.154398	9.824594	4.600000	14.823657	9.999292
4.600000	15.152400	9.819341	4.600000	14.807945	10.013957
4.600000	15.148902	9.814310	4.600000	14.792106	10.029080
4.600000	15.144280	9.809769	4.600000	14.776164	10.044657
4.600000	15.139419	9.806171	4.600000	14.760150	10.060680
4.600000	15.135792	9.803983	4.600000	14.744090	10.077141
4.600000	15.134482	9.803277	4.600000	14.728011	10.094030
4.600000	15.133087	9.802565	4.600000	14.711934	10.111340
4.600000	15.128840	9.800640	4.600000	14.695895	10.129059
4.600000	15.122143	9.798248	4.600000	14.679901	10.147173
4.600000	15.114092	9.796275	4.600000	14.663983	10.165671
4.600000	15.105601	9.795196	4.600000	14.648164	10.184541
4.600000	15.097149	9.795190	4.600000	14.632460	10.203766
4.600000	15.089083	9.796372	4.600000	14.616897	10.223332

TABLE C.28.—DIFFUSER SPLITTER VANE—SECTION 2

X	R*θ	R	X	R*θ	R
4.600000	14.601487	10.243221	4.600000	14.251467	10.991212
4.600000	14.586258	10.263421	4.600000	14.256261	11.010696
4.600000	14.571220	10.283910	4.600000	14.263062	11.030282
4.600000	14.556389	10.304668	4.600000	14.271830	11.049887
4.600000	14.541782	10.325680	4.600000	14.282581	11.069441
4.600000	14.527412	10.346920	4.600000	14.295391	11.088882
4.600000	14.513294	10.368372	4.600000	14.310421	11.108143
4.600000	14.499439	10.390012	4.600000	14.327841	11.127100
4.600000	14.485848	10.411812	4.600000	14.347915	11.145524
4.600000	14.472549	10.433756	4.600000	14.370616	11.162850
4.600000	14.459541	10.455818	4.600000	14.395068	11.177824
4.600000	14.446831	10.477970	4.600000	14.418665	11.189380
4.600000	14.434429	10.500193	4.600000	14.438899	11.196945
4.600000	14.422339	10.522453	4.600000	14.455284	11.201487
4.600000	14.410562	10.544726	4.600000	14.468274	11.204101
4.600000	14.399116	10.566992	4.600000	14.478421	11.205508
4.600000	14.387991	10.589216	4.600000	14.486198	11.206199
4.600000	14.377193	10.611371			
4.600000	14.366724	10.633431			
4.600000	14.356585	10.655368			
4.600000	14.346776	10.677153			
4.600000	14.337300	10.698757			
4.600000	14.328155	10.720153			
4.600000	14.319343	10.741314			
4.600000	14.310860	10.762209			
4.600000	14.302689	10.782806			
4.600000	14.294849	10.803083			
4.600000	14.287331	10.823011			
4.600000	14.280124	10.842561			
4.600000	14.273219	10.861699			
4.600000	14.266624	10.880406			
4.600000	14.260387	10.898684			
4.600000	14.254339	10.916418			
4.600000	14.250011	10.934380			
4.600000	14.248213	10.952932			
4.600000	14.248750	10.971921			

C.4 Exit Guide Vane

Exit Guide Vane (EGV) is defined with the hub and the shroud sections. Section 1 refers the hub side and section 2 is for the shroud side. The vanes are two dimensional so section 2 is a translation of section 1 in the positive r direction. They are expressed in x, $r^*\theta$ and r coordinates.

TABLE C.29.—EGV SECTION 1

X	$R^*\theta$	R	X	$R^*\theta$	R
8.921164	-1.109216	11.815770	8.109561	-1.053731	11.815770
8.920464	-1.109229	11.815770	8.069654	-1.046197	11.815770
8.918366	-1.109237	11.815770	8.029328	-1.037934	11.815770
8.914868	-1.109220	11.815770	7.988638	-1.028886	11.815770
8.909980	-1.109233	11.815770	7.947653	-1.019031	11.815770
8.903701	-1.109168	11.815770	7.906423	-1.008370	11.815770
8.896042	-1.109170	11.815770	7.865005	-0.996892	11.815770
8.887007	-1.109080	11.815770	7.823443	-0.984656	11.815770
8.876603	-1.108985	11.815770	7.781775	-0.971711	11.815770
8.864847	-1.108888	11.815770	7.740070	-0.958030	11.815770
8.851747	-1.108714	11.815770	7.698365	-0.943646	11.815770
8.837316	-1.108512	11.815770	7.656720	-0.928571	11.815770
8.821568	-1.108272	11.815770	7.615180	-0.912841	11.815770
8.804521	-1.107934	11.815770	7.573793	-0.896476	11.815770
8.786187	-1.107566	11.815770	7.532594	-0.879510	11.815770
8.766590	-1.107116	11.815770	7.491633	-0.861991	11.815770
8.745749	-1.106580	11.815770	7.450958	-0.843919	11.815770
8.723681	-1.105992	11.815770	7.410611	-0.825341	11.815770
8.700407	-1.105300	11.815770	7.370638	-0.806273	11.815770
8.675960	-1.104497	11.815770	7.331087	-0.786742	11.815770
8.650353	-1.103616	11.815770	7.291995	-0.766780	11.815770
8.623619	-1.102567	11.815770	7.253407	-0.746417	11.815770
8.595783	-1.101407	11.815770	7.215378	-0.725659	11.815770
8.566876	-1.100135	11.815770	7.177931	-0.704564	11.815770
8.536923	-1.098685	11.815770	7.141125	-0.683148	11.815770
8.505959	-1.097022	11.815770	7.104989	-0.661426	11.815770
8.474015	-1.095181	11.815770	7.069571	-0.639453	11.815770
8.441125	-1.093083	11.815770	7.034906	-0.617236	11.815770
8.407330	-1.090701	11.815770	7.001035	-0.594825	11.815770
8.372666	-1.087922	11.815770	6.967989	-0.572265	11.815770
8.337178	-1.084725	11.815770	6.935813	-0.549569	11.815770
8.300910	-1.081031	11.815770	6.904542	-0.526784	11.815770
8.263908	-1.076806	11.815770	6.874211	-0.503926	11.815770
8.226221	-1.072009	11.815770	6.844849	-0.481053	11.815770
8.187902	-1.066590	11.815770	6.816490	-0.458167	11.815770
8.149001	-1.060481	11.815770	6.789167	-0.435309	11.815770

TABLE C.29.—EGV SECTION 1

X	R*θ	R	X	R*θ	R
6.762905	-0.412522	11.815770	6.537887	-0.016053	11.815770
6.737738	-0.389819	11.815770	6.546780	-0.022786	11.815770
6.713670	-0.367269	11.815770	6.556572	-0.030465	11.815770
6.690740	-0.344897	11.815770	6.567287	-0.039029	11.815770
6.668961	-0.322755	11.815770	6.578966	-0.048394	11.815770
6.648347	-0.300899	11.815770	6.591620	-0.058536	11.815770
6.628910	-0.279389	11.815770	6.605249	-0.069434	11.815770
6.610680	-0.258266	11.815770	6.619865	-0.081027	11.815770
6.593662	-0.237577	11.815770	6.635479	-0.093282	11.815770
6.577869	-0.217387	11.815770	6.652086	-0.106172	11.815770
6.563332	-0.197709	11.815770	6.669679	-0.119653	11.815770
6.550037	-0.178607	11.815770	6.688245	-0.133708	11.815770
6.537999	-0.160134	11.815770	6.707776	-0.148301	11.815770
6.527235	-0.142310	11.815770	6.728257	-0.163405	11.815770
6.517782	-0.125192	11.815770	6.749682	-0.178987	11.815770
6.509626	-0.108817	11.815770	6.772041	-0.195012	11.815770
6.502746	-0.093267	11.815770	6.795312	-0.211463	11.815770
6.497181	-0.078582	11.815770	6.819487	-0.228303	11.815770
6.492944	-0.064816	11.815770	6.844543	-0.245515	11.815770
6.489984	-0.052081	11.815770	6.870469	-0.263066	11.815770
6.488196	-0.040483	11.815770	6.897234	-0.280948	11.815770
6.487606	-0.030099	11.815770	6.924828	-0.299119	11.815770
6.488166	-0.021075	11.815770	6.953222	-0.317565	11.815770
6.489679	-0.013551	11.815770	6.982386	-0.336261	11.815770
6.491952	-0.007682	11.815770	7.012308	-0.355170	11.815770
6.494739	-0.003640	11.815770	7.042952	-0.374282	11.815770
6.497450	-0.001412	11.815770	7.074291	-0.393550	11.815770
6.499341	-0.000484	11.815770	7.106290	-0.412961	11.815770
6.500002	-0.000245	11.815770	7.138935	-0.432487	11.815770
6.500641	-0.000056	11.815770	7.172185	-0.452085	11.815770
6.502605	0.000312	11.815770	7.206013	-0.471732	11.815770
6.505928	0.000369	11.815770	7.240393	-0.491420	11.815770
6.510483	-0.000503	11.815770	7.275283	-0.511111	11.815770
6.516083	-0.002542	11.815770	7.310658	-0.530786	11.815770
6.522589	-0.005769	11.815770	7.346483	-0.550397	11.815770
6.529867	-0.010297	11.815770	7.382723	-0.569951	11.815770

TABLE C.29.—EGV SECTION 1

X	R*θ	R	X	R*θ	R
7.419341	-0.589414	11.815770	8.671218	-1.061639	11.815770
7.456298	-0.608768	11.815770	8.695192	-1.065907	11.815770
7.493564	-0.627982	11.815770	8.718110	-1.069821	11.815770
7.531095	-0.647031	11.815770	8.739942	-1.073407	11.815770
7.568858	-0.665917	11.815770	8.760669	-1.076673	11.815770
7.606808	-0.684602	11.815770	8.780258	-1.079671	11.815770
7.644911	-0.703069	11.815770	8.798689	-1.082383	11.815770
7.683136	-0.721278	11.815770	8.815944	-1.084832	11.815770
7.721430	-0.739249	11.815770	8.831999	-1.087045	11.815770
7.759759	-0.756948	11.815770	8.846831	-1.089057	11.815770
7.798092	-0.774343	11.815770	8.860433	-1.090827	11.815770
7.836380	-0.791415	11.815770	8.872784	-1.092402	11.815770
7.874587	-0.808167	11.815770	8.883873	-1.093799	11.815770
7.912684	-0.824554	11.815770	8.893686	-1.094993	11.815770
7.950627	-0.840543	11.815770	8.902209	-1.096021	11.815770
7.988380	-0.856147	11.815770	8.909444	-1.096869	11.815770
8.025909	-0.871299	11.815770	8.915370	-1.097564	11.815770
8.063173	-0.886027	11.815770	8.919989	-1.098086	11.815770
8.100146	-0.900243	11.815770	8.923287	-1.098464	11.815770
8.136785	-0.913968	11.815770	8.925272	-1.098691	11.815770
8.173060	-0.927154	11.815770	8.925932	-1.098754	11.815770
8.208923	-0.939813	11.815770			
8.244336	-0.951915	11.815770			
8.279265	-0.963454	11.815770			
8.313670	-0.974399	11.815770			
8.347513	-0.984765	11.815770			
8.380768	-0.994502	11.815770			
8.413387	-1.003604	11.815770			
8.445323	-1.012097	11.815770			
8.476535	-1.020017	11.815770			
8.506975	-1.027413	11.815770			
8.536606	-1.034261	11.815770			
8.565380	-1.040620	11.815770			
8.593263	-1.046529	11.815770			
8.620221	-1.051982	11.815770			
8.646215	-1.056998	11.815770			

TABLE C.30.—EGV SECTION 2

X	R*θ	R	X	R*θ	R
8.921164	-1.108676	12.296114	8.109559	-1.053185	12.296114
8.920464	-1.108691	12.296114	8.069655	-1.045657	12.296114
8.918366	-1.108695	12.296114	8.029328	-1.037389	12.296114
8.914868	-1.108682	12.296114	7.988638	-1.028346	12.296114
8.909979	-1.108687	12.296114	7.947652	-1.018485	12.296114
8.903703	-1.108626	12.296114	7.906420	-1.007825	12.296114
8.896042	-1.108626	12.296114	7.865004	-0.996348	12.296114
8.887006	-1.108537	12.296114	7.823442	-0.984113	12.296114
8.876603	-1.108443	12.296114	7.781776	-0.971169	12.296114
8.864848	-1.108350	12.296114	7.740070	-0.957480	12.296114
8.851748	-1.108172	12.296114	7.698366	-0.943105	12.296114
8.837315	-1.107972	12.296114	7.656723	-0.928033	12.296114
8.821567	-1.107726	12.296114	7.615181	-0.912299	12.296114
8.804518	-1.107383	12.296114	7.573793	-0.895932	12.296114
8.786187	-1.107026	12.296114	7.532597	-0.878980	12.296114
8.766590	-1.106578	12.296114	7.491635	-0.861451	12.296114
8.745746	-1.106036	12.296114	7.450959	-0.843383	12.296114
8.723680	-1.105449	12.296114	7.410612	-0.824796	12.296114
8.700409	-1.104768	12.296114	7.370638	-0.805732	12.296114
8.675959	-1.103953	12.296114	7.331087	-0.786204	12.296114
8.650354	-1.103085	12.296114	7.291996	-0.766242	12.296114
8.623621	-1.102033	12.296114	7.253408	-0.745873	12.296114
8.595785	-1.100869	12.296114	7.215379	-0.725118	12.296114
8.566875	-1.099593	12.296114	7.177934	-0.704020	12.296114
8.536923	-1.098144	12.296114	7.141125	-0.682603	12.296114
8.505960	-1.096482	12.296114	7.104990	-0.660884	12.296114
8.474014	-1.094640	12.296114	7.069570	-0.638915	12.296114
8.441126	-1.092544	12.296114	7.034906	-0.616710	12.296114
8.407329	-1.090165	12.296114	7.001035	-0.594314	12.296114
8.372666	-1.087384	12.296114	6.967990	-0.571757	12.296114
8.337178	-1.084180	12.296114	6.935814	-0.549060	12.296114
8.300910	-1.080489	12.296114	6.904541	-0.526254	12.296114
8.263911	-1.076270	12.296114	6.874211	-0.503373	12.296114
8.226224	-1.071477	12.296114	6.844850	-0.480470	12.296114
8.187901	-1.066045	12.296114	6.816491	-0.457557	12.296114
8.148998	-1.059937	12.296114	6.789170	-0.434672	12.296114

TABLE C.30.—EGV SECTION 2

X	R*θ	R	X	R*θ	R
6.762906	-0.411862	12.296114	6.537888	-0.015946	12.296114
6.737740	-0.389165	12.296114	6.546783	-0.022696	12.296114
6.713671	-0.366641	12.296114	6.556574	-0.030366	12.296114
6.690742	-0.344325	12.296114	6.567287	-0.038905	12.296114
6.668962	-0.322255	12.296114	6.578967	-0.048251	12.296114
6.648347	-0.300479	12.296114	6.591621	-0.058356	12.296114
6.628910	-0.279052	12.296114	6.605249	-0.069190	12.296114
6.610681	-0.258017	12.296114	6.619865	-0.080733	12.296114
6.593663	-0.237391	12.296114	6.635480	-0.092923	12.296114
6.577869	-0.217242	12.296114	6.652085	-0.105729	12.296114
6.563332	-0.197600	12.296114	6.669678	-0.119145	12.296114
6.550037	-0.178508	12.296114	6.688246	-0.133143	12.296114
6.537999	-0.160026	12.296114	6.707777	-0.147689	12.296114
6.527236	-0.142190	12.296114	6.728260	-0.162763	12.296114
6.517782	-0.125031	12.296114	6.749683	-0.178327	12.296114
6.509627	-0.108619	12.296114	6.772041	-0.194358	12.296114
6.502746	-0.093024	12.296114	6.795311	-0.210822	12.296114
6.497181	-0.078294	12.296114	6.819487	-0.227685	12.296114
6.492944	-0.064502	12.296114	6.844543	-0.244929	12.296114
6.489984	-0.051740	12.296114	6.870466	-0.262505	12.296114
6.488196	-0.040122	12.296114	6.897232	-0.280414	12.296114
6.487606	-0.029733	12.296114	6.924828	-0.298606	12.296114
6.488166	-0.020717	12.296114	6.953221	-0.317054	12.296114
6.489678	-0.013204	12.296114	6.982386	-0.335755	12.296114
6.491952	-0.007350	12.296114	7.012310	-0.354661	12.296114
6.494737	-0.003333	12.296114	7.042952	-0.373755	12.296114
6.497450	-0.001126	12.296114	7.074291	-0.393014	12.296114
6.499340	-0.000211	12.296114	7.106293	-0.412425	12.296114
6.500002	0.000014	12.296114	7.138936	-0.431937	12.296114
6.500641	0.000201	12.296114	7.172182	-0.451535	12.296114
6.502605	0.000554	12.296114	7.206015	-0.471192	12.296114
6.505929	0.000592	12.296114	7.240393	-0.490870	12.296114
6.510483	-0.000310	12.296114	7.275283	-0.510570	12.296114
6.516083	-0.002376	12.296114	7.310656	-0.530238	12.296114
6.522590	-0.005628	12.296114	7.346481	-0.549857	12.296114
6.529865	-0.010175	12.296114	7.382724	-0.569411	12.296114

TABLE C.30.—EGV SECTION 2

X	R*θ	R	X	R*θ	R
7.419341	-0.588878	12.296114	8.671218	-1.061095	12.296114
7.456299	-0.608230	12.296114	8.695193	-1.065366	12.296114
7.493563	-0.627438	12.296114	8.718108	-1.069280	12.296114
7.531097	-0.646495	12.296114	8.739945	-1.072869	12.296114
7.568858	-0.665376	12.296114	8.760669	-1.076138	12.296114
7.606807	-0.684056	12.296114	8.780258	-1.079133	12.296114
7.644912	-0.702531	12.296114	8.798688	-1.081840	12.296114
7.683137	-0.720740	12.296114	8.815944	-1.084292	12.296114
7.721430	-0.738706	12.296114	8.831999	-1.086505	12.296114
7.759761	-0.756411	12.296114	8.846830	-1.088515	12.296114
7.798091	-0.773797	12.296114	8.860434	-1.090291	12.296114
7.836381	-0.790873	12.296114	8.872784	-1.091859	12.296114
7.874589	-0.807630	12.296114	8.883873	-1.093257	12.296114
7.912684	-0.824012	12.296114	8.893686	-1.094451	12.296114
7.950628	-0.840005	12.296114	8.902209	-1.095479	12.296114
7.988380	-0.855607	12.296114	8.909442	-1.096322	12.296114
8.025910	-0.870759	12.296114	8.915368	-1.097018	12.296114
8.063173	-0.885482	12.296114	8.919988	-1.097541	12.296114
8.100144	-0.899699	12.296114	8.923289	-1.097926	12.296114
8.136785	-0.913428	12.296114	8.925269	-1.098142	12.296114
8.173060	-0.926614	12.296114	8.925932	-1.098214	12.296114
8.208922	-0.939265	12.296114			
8.244337	-0.951375	12.296114			
8.279264	-0.962911	12.296114			
8.313670	-0.973861	12.296114			
8.347514	-0.984229	12.296114			
8.380768	-0.993960	12.296114			
8.413387	-1.003062	12.296114			
8.445322	-1.011559	12.296114			
8.476537	-1.019481	12.296114			
8.506974	-1.026866	12.296114			
8.536606	-1.033723	12.296114			
8.565380	-1.040076	12.296114			
8.593261	-1.045987	12.296114			
8.620219	-1.051438	12.296114			
8.646216	-1.056458	12.296114			

Appendix D.—Instrumentation Coordinates

This appendix contains steady state instrumentation location coordinates. The locations of the static taps used listed in the series of tables that follow. The names correspond to the names used in the spreadsheets containing data.

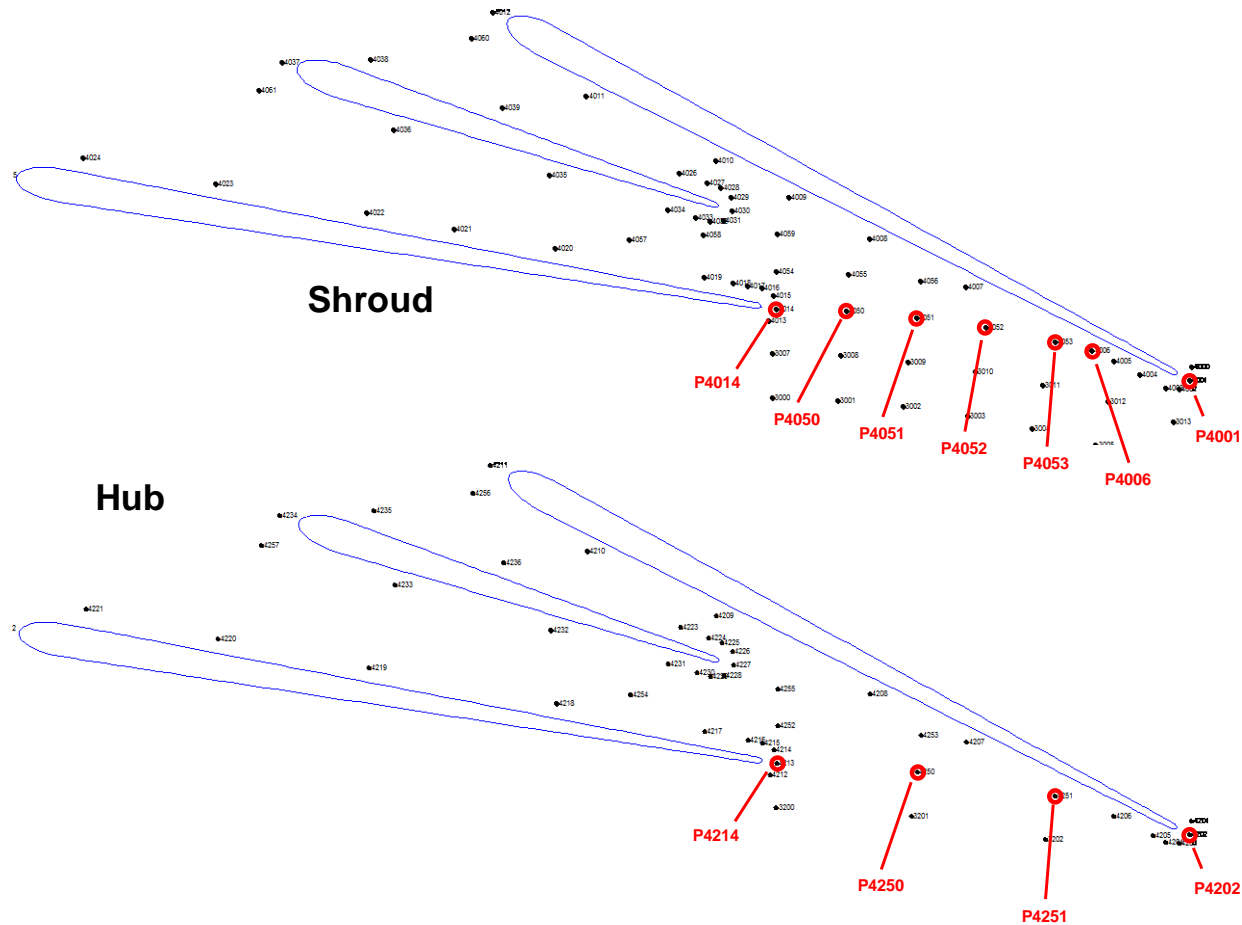


Figure D.1.—Hub and shroud static pressure taps used to compute static pressure at diffuser leading edge

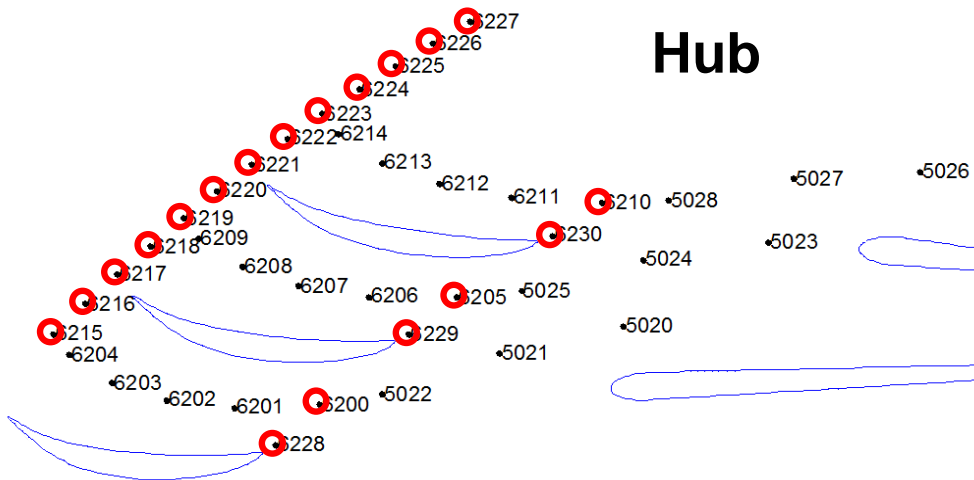
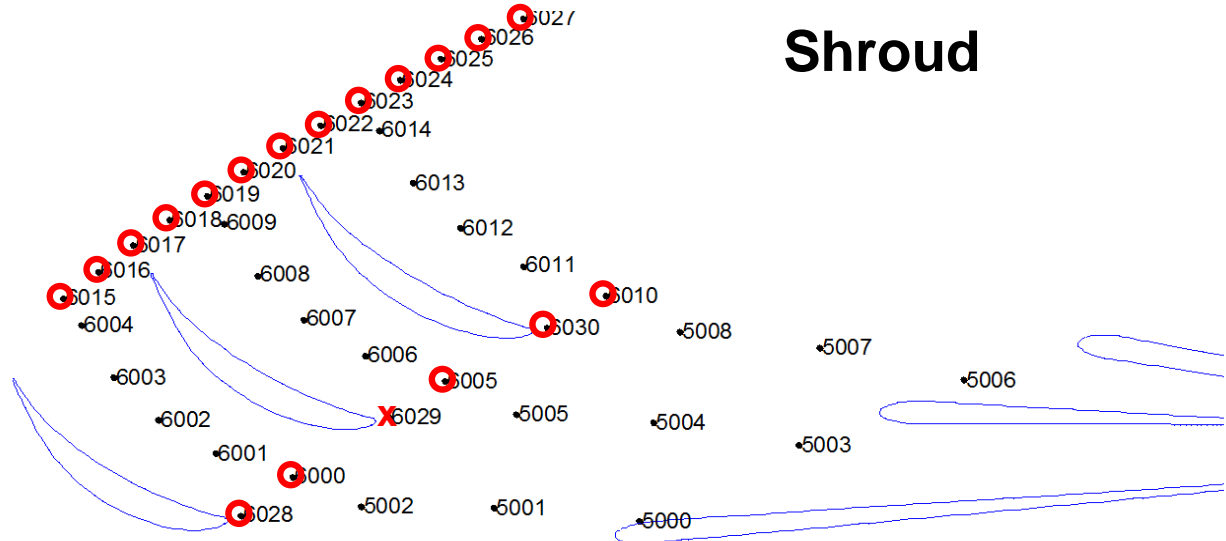


Figure D.2.—Hub and shroud static pressure taps used to compute static pressure at EGV LE and TE

TABLE D.1.—IMPELLER SHROUD
STATIC PRESSURE TAPS

Name	X	Y	Z
P2700	-0.0985	2.2482	3.5978
P2701	-0.3478	2.2386	3.5825
P2702	-0.8475	2.2310	3.5704
P2703	-1.8452	2.2627	3.6211
P2704	-2.8308	2.3509	3.7622
P2705	-3.7996	2.4819	3.9718
P2706	-3.7996	2.4819	3.9718
P2707	-2.8308	2.3509	3.7622
P2708	-1.8452	2.2627	3.6211
P2709	-0.8475	2.2310	3.5704
P2710	-0.3478	2.2386	3.5825
P2711	-0.0985	2.2482	3.5978
P2750	-0.0985	-2.2482	-3.5978
P2751	-0.3478	-2.2386	-3.5825
P2752	-0.8475	-2.2310	-3.5704
P2753	-1.8452	-2.2627	-3.6211
P2754	-2.8308	-2.3509	-3.7622
P2755	-3.7996	-2.4819	-3.9718
P2756	-3.7996	-2.4819	-3.9718
P2757	-2.8308	-2.3509	-3.7622
P2758	-1.8452	-2.2627	-3.6211
P2759	-0.8475	-2.2310	-3.5704
P2760	-0.3478	-2.2386	-3.5825
P2761	-0.0985	-2.2482	-3.5978
P2800	0.1503	2.2616	3.6193
P2801	0.3981	2.2788	3.6468
P2802	0.6449	2.2999	3.6806
P2803	1.1344	2.3536	3.7666
P2804	2.0871	2.5132	4.0219
P2805	2.9707	2.7592	4.4156
P2806	3.7157	3.1101	4.9772
P2807	4.2416	3.5587	5.6951
P2808	4.5337	4.0644	6.5043
P2809	4.6139	4.3258	6.9228
P2810	4.6450	4.4626	7.1417
P2850	0.1503	-2.2616	-3.6193
P2851	0.3981	-2.2788	-3.6468
P2852	0.6449	-2.2999	-3.6806
P2853	1.1344	-2.3536	-3.7666
P2854	2.0871	-2.5132	-4.0219
P2855	2.9707	-2.7592	-4.4156
P2856	3.7157	-3.1101	-4.9772
P2857	4.2416	-3.5587	-5.6951
P2858	4.5337	-4.0644	-6.5043
P2859	4.6139	-4.3258	-6.9228
P2860	4.6450	-4.4626	-7.1417

TABLE D.2.—SHROUD STATIC TAPS
IMMEDIATELY UPSTREAM OF DIFFUSER

Name	X	Y	Z
P3000	4.6535	-0.1006	8.4984
P3001	4.6535	-0.5453	8.4815
P3002	4.6535	-0.9884	8.4413
P3003	4.6535	-1.4289	8.3780
P3004	4.6535	-1.8654	8.2918
P3005	4.6535	-2.2968	8.1828
P3006	4.6536	-2.7219	8.0514
P3007	4.6855	-0.1043	8.8031
P3008	4.6855	-0.5648	8.7855
P3009	4.6855	-1.0239	8.7439
P3010	4.6855	-1.4801	8.6784
P3011	4.6855	-1.9322	8.5890
P3012	4.6855	-2.3791	8.4761
P3013	4.6855	-2.8194	8.3400

TABLE D.3.—HUB STATIC TAPS
IMMEDIATELY UPSTREAM OF DIFFUSER

Name	X	Y	Z
P3200	5.2663	-0.1233	8.8028
P3201	5.2663	-1.0428	8.7417
P3202	5.2663	-1.9508	8.5848
P3203	5.2663	-2.8375	8.3339

TABLE D.4.—DIFFUSER STATIC PRESSURE TAP LOCATIONS

Shroud Instrumentation				Hub Instrumentation			
Name	X	Y	Z	Name	X	Y	Z
P4000	4.7091	-2.9429	8.7101	P4201	5.2663	-2.9429	8.7101
P4001	4.7053	-2.9345	8.6186	P4202	5.2663	-2.9345	8.6186
P4002	4.7014	-2.8639	8.5599	P4203	5.2663	-2.8639	8.5599
P4003	4.7002	-2.7724	8.5683	P4204	5.2663	-2.7724	8.5683
P4004	4.7020	-2.5937	8.6581	P4205	5.2663	-2.6831	8.6132
P4005	4.7038	-2.4150	8.7479	P4206	5.2663	-2.4150	8.7479
P4006	4.7054	-2.2707	8.8204	P4207	5.2663	-1.4149	9.2504
P4007	4.7147	-1.4149	9.2504	P4208	5.2663	-0.7639	9.5776
P4008	4.7207	-0.7639	9.5776	P4209	5.2663	0.2837	10.1040
P4009	4.7238	-0.2103	9.8557	P4210	5.2650	1.1602	10.5444
P4010	4.7246	0.2837	10.1040	P4211	5.3633	1.8196	11.1248
P4011	4.7241	1.1602	10.5444	P4212	5.2663	-0.0786	9.0259

TABLE D.4.—DIFFUSER STATIC PRESSURE TAP LOCATIONS

Shroud Instrumentation				Hub Instrumentation			
Name	X	Y	Z	Name	X	Y	Z
P4012	4.7348	1.7955	11.1102	P4213	5.2663	-0.1276	9.1036
P4013	4.7014	-0.0786	9.0259	P4214	5.2663	-0.1073	9.1932
P4014	4.7053	-0.1276	9.1036	P4215	5.2663	-0.0297	9.2422
P4015	4.7091	-0.1073	9.1932	P4216	5.2663	0.0686	9.2610
P4016	4.7109	-0.0297	9.2422	P4217	5.2663	0.3632	9.3174
P4017	4.7116	0.0686	9.2610	P4218	5.2663	1.3690	9.5099
P4018	4.7123	0.1668	9.2798	P4219	5.2663	2.6484	9.7549
P4019	4.7137	0.3632	9.3174	P4220	5.2650	3.6744	9.9513
P4020	4.7207	1.3690	9.5099	P4221	5.3137	4.5696	10.1517
P4021	4.7238	2.0552	9.6413	P4222	5.3636	5.1682	10.0190
P4022	4.7246	2.6484	9.7549	P4223	5.2663	0.5283	10.0240
P4023	4.7241	3.6744	9.9513	P4224	5.2663	0.3406	9.9551
P4024	4.7294	4.5725	10.1232	P4225	5.2663	0.2467	9.9206
P4025	4.7349	5.1451	10.0105	P4226	5.2663	0.1771	9.8608
P4026	4.7245	0.5283	10.0240	P4227	5.2663	0.1701	9.7692
P4027	4.7243	0.3406	9.9551	P4228	5.2663	0.2300	9.6995
P4028	4.7241	0.2467	9.9206	P4229	5.2663	0.3216	9.6926
P4029	4.7238	0.1771	9.8608	P4230	5.2663	0.4176	9.7205
P4030	4.7230	0.1701	9.7692	P4231	5.2663	0.6097	9.7763
P4031	4.7222	0.2300	9.6995	P4232	5.2663	1.4109	10.0090
P4032	4.7221	0.3216	9.6926	P4233	5.2650	2.4695	10.3165
P4033	4.7225	0.4176	9.7205	P4234	5.3611	3.2571	10.7865
P4034	4.7232	0.6097	9.7763	P4235	5.3138	2.6169	10.8213
P4035	4.7246	1.4109	10.0090	P4236	5.2650	1.7316	10.4657
P4036	4.7241	2.4695	10.3165	P4250	5.2663	-1.0788	9.0439
P4037	4.7342	3.2260	10.7721	P4251	5.2663	-2.0183	8.8816
P4038	4.7294	2.6245	10.7935	P4252	5.2663	-0.1311	9.3571
P4039	4.7241	1.7316	10.4657	P4253	5.2663	-1.1084	9.2921
P4050	4.7054	-0.6040	9.0879	P4254	5.2663	0.8704	9.5685
P4051	4.7054	-1.0788	9.0439	P4255	5.2663	-0.1346	9.6071
P4052	4.7054	-1.5507	8.9750	P4256	5.3071	1.9416	10.9370
P4053	4.7054	-2.0183	8.8816	P4257	5.3071	3.3804	10.5811
P4054	4.7147	-0.1311	9.3571				
P4055	4.7147	-0.6206	9.3374				
P4056	4.7147	-1.1084	9.2921				
P4057	4.7207	0.8704	9.5685				
P4058	4.7207	0.3684	9.6009				
P4059	4.7207	-0.1346	9.6071				
P4060	4.7294	1.9416	10.9370				
P4061	4.7294	3.3804	10.5811				

TABLE D.5.—STATIC PRESSURE TAPS IN BEND BETWEEN DIFFUSER AND EGVS

Shroud Instrumentation				Hub Instrumentation			
Name	X	Y	Z	Name	X	Y	Z
P5000	4.8405	5.0048	10.6813	P5020	5.5091	4.8795	10.4138
P5001	4.8405	3.8609	11.1460	P5021	5.5091	3.7642	10.8668
P5002	4.8405	2.6747	11.4885	P5022	5.5091	2.6077	11.2007
P5003	5.2889	5.9218	10.6368	P5023	5.7982	5.6921	10.2242
P5004	5.2889	4.7775	11.1975	P5024	5.7982	4.5922	10.7632
P5005	5.2889	3.5809	11.6355	P5025	5.7982	3.4420	11.1843
P5006	5.8826	6.7070	10.2862	P5026	6.1343	6.4481	9.8891
P5007	5.8826	5.5951	10.9310	P5027	6.1343	5.3791	10.5089
P5008	5.8826	4.4218	11.4559	P5028	6.1343	4.2511	11.0136

TABLE D.6.—EXIT GUIDE VANE STATIC PRESSURE TAPS

Shroud Instrumentation				Hub Instrumentation			
Name	X	Y	Z	Name	X	Y	Z
P6000	6.4870	7.0278	10.0909	P6200	6.4870	6.7667	9.7027
P6001	7.0965	7.3992	9.8283	P6201	7.0965	7.1467	9.4603
P6002	7.7060	7.6426	9.6434	P6202	7.7060	7.3949	9.2822
P6003	8.3155	7.7903	9.5247	P6203	8.3155	7.5416	9.1619
P6004	8.9250	7.8485	9.4748	P6204	8.9250	7.5947	9.1042
P6005	6.4870	5.9345	10.7702	P6205	6.4870	5.7154	10.3569
P6006	7.0965	6.3313	10.5479	P6206	7.0965	6.1187	10.1555
P6007	7.7060	6.5927	10.3894	P6207	7.7060	6.3841	10.0043
P6008	8.3155	6.7520	10.2869	P6208	8.3155	6.5426	9.9001
P6009	8.9250	6.8151	10.2433	P6209	8.9250	6.6014	9.8482
P6010	6.4870	4.7762	11.3315	P6210	6.4870	4.6015	10.8976
P6011	7.0965	5.1941	11.1519	P6211	7.0965	5.0236	10.7394
P6012	7.7060	5.4706	11.0217	P6212	7.7060	5.3034	10.6169
P6013	8.3155	5.6397	10.9363	P6213	8.3155	5.4719	10.5297
P6014	8.9250	5.7070	10.8995	P6214	8.9250	5.5358	10.4843
P6015	9.2500	7.8816	9.4455	P6215	9.2500	7.5677	9.1156
P6016	9.2500	7.6317	9.6485	P6216	9.2500	7.3268	9.3103
P6017	9.2500	7.3765	9.8449	P6217	9.2500	7.0809	9.4987
P6018	9.2500	7.1164	10.0346	P6218	9.2500	6.8302	9.6805
P6019	9.2500	6.8513	10.2174	P6219	9.2500	6.5748	9.8558
P6020	9.2500	6.5816	10.3932	P6220	9.2500	6.3149	10.0243
P6021	9.2500	6.3073	10.5619	P6221	9.2500	6.0506	10.1859
P6022	9.2500	6.0287	10.7234	P6222	9.2500	5.7823	10.3406
P6023	9.2500	5.7460	10.8775	P6223	9.2500	5.5100	10.4883
P6024	9.2500	5.4594	11.0241	P6224	9.2500	5.2339	10.6287
P6025	9.2500	5.1690	11.1632	P6225	9.2500	4.9543	10.7619
P6026	9.2500	4.8750	11.2947	P6226	9.2500	4.6712	10.8878
P6027	9.2500	4.5778	11.4184	P6227	9.2500	4.3850	11.0062
P6028	6.4610	7.4046	9.8197	P6228	6.4664	7.1127	9.4545
P6029	6.4610	6.3417	10.5374	P6229	6.4664	6.0881	10.1451
P6030	6.4610	5.2095	11.1407	P6230	6.4664	4.9956	10.7252

Appendix E.—Catalog of Electronic Files

This appendix is contained on two supplemental DVDs. The first DVD contains Appendices E.1 to E.7, and the second DVD contains Appendices E.8 to E.10. A detailed list of all the electronic files contained in Appendix E.1.pdf.

E.1 Detailed Catalogue of Electronic Files

E.2 Detailed Compilation of Test Results

E.3 Instrumentation Locations

E.4 Hot Coordinates

E.5 100% N_c LEO Speedline For Final Design (Without Fillets)

E.6 100% N_c LEO Speedline for Final Design (With Impeller Fillets)

E.7 100% N_c LEO Speedline For Final Impeller Design

E.8 Selected Speedlines From Post-Test CFD Simulations

100p_STEADY_BASELINE_SUPPRESSED

100p_STEADY_STRAIN_RATE_PRODUCTION_SUPPRESSED

100p_STEADY_STRAIN_RATE_PRODUCTION_SST_LIMITER_SUPPRESSED

100p_SPALART_ALLMARAS_SUPPRESSED

E.9 Animations From Post-Test CFD Simulations For Design Point

E.10 Meanline Results—Overview

References

1. Peeters, M., and Sleiman, M., "A Numerical Investigation of the Unsteady Flow in Centrifugal Stages," ASME Paper 2000-GT-0426, International Gas Turbine and Aeroengine Congress and Exhibition, Munich, Germany, May 8–11, 2000.
2. Shum, Y. K. P., Tan, C. S., Cumpsty, N. A., "Impeller-Diffuser Interaction in a Centrifugal Compressor," Journal of Turbomachinery, Vol. 122, October 2000.
3. Trebinjac, I., Kulisa, P., Bulot, N., and Rochuon, N., "Effect of Unsteadiness on the Performance of a Transonic Compressor Stage," Journal of Turbomachinery, Vol. 131, October 2009.
4. Welch, G. E., Hathaway, M. D., Skoch, G. J., and Snyder, C. A., "Rotary-Wing Relevant Compressor Aero Research and Technology Development Activities at Glenn Research Center," Proc. AHS Int. 65th Annual Forum, May 2009 (also NASA/TM—2012-217280, Mar. 2012)
5. Cumpsty, N.A., Compressor Aerodynamics, Krieger Publishing Company, 2004.
6. Skoch, G. J., Prahst, P. S., Wernet, M. P., Wood, J. R., Strazisar, A. J. "Laser Anemometer Measurements of the Flow Field in a 4:1 Pressure Ratio Centrifugal Impeller," ASME Paper 97-GT-342, International Gas Turbine and Aeroengine Congress and Exhibition, Orlando, FL, June 2-5, 1997.
7. Larosiliere, L. M., Skoch, G. J., Prahst, P. S., "Aerodynamic Synthesis of a Centrifugal Impeller Using Computational Fluid Dynamics and Measurements," Journal of Propulsion and Power, Vol. 15, (9), Sept-Oct 1999.
8. Ni, R. H., "A Multiple-Grid Scheme for Solving the Euler Equations," AIAA Journal, Vol. 20, (11), 1982.
9. Wilcox, D.C, Turbulence Modeling for CFD, DCW Industries, Inc., 1993.
10. McKain, T.F. and Holbrook, G.J. "Coordinates for a High Performance 4:1 Pressure Ratio Centrifugal Compressor," NASA CR 204134, July 1997.
11. Runstadler, P.W. and Dolan, F.X., "Diffuser Data Book," Creare Inc. TN 186, May 1975.
12. Rodgers, C., and Brown, D., "High Hub/Tip Centrifugal Compressors," GT2009-59012, Proceedings of ASME Turbo Expo 2009, Orlando, FL, June 8-12, 2009.
13. Japikse, D., Centrifugal Compressor Design and Performance, Concepts ETI, Inc., 1996.
14. Lurie, E.A., Van Slooten, P.R., Medic, G., Mulugeta, J.M., Holley, B.M., Feng, J., Sharma, O.P., and Ni, R., "Design of a High Efficiency Compact Centrifugal Compressor for Rotorcraft Applications," Proceedings of American Helicopter Society 67th Annual Forum, Virginia Beach, May 3-5, 2011.
15. Brokopp, R.A. and Gronski, R.S., "Small Engine Component Test Facility Compressor Testing Cell," AIAA 92-3980, July 1992 (also NASA/TM-1992-105686)
16. Tyler, J.M. and Sofrin, T.G., "Axial Flow Compressor Noise Studies," SAE Trans., Vol. 70, pp. 309-332, 1962.

